

The Effect of Turbulence on Stall of Horizontal Axis Wind Turbines

Katrina Elise Swalwell

BSc, BEng(Hon)

Department of Mechanical Engineering

Monash University

Submitted January, 2005

Final Version October, 2005

Table of Contents

Abstract	iii
Declaration of Originality	iv
Acknowledgements	v
1. Introduction.....	1
2. Literature Review.....	5
2.1 Introduction.....	5
2.2 Wind Turbine Characteristics	5
2.3 Aerodynamic Models of Wind Turbine Performance	22
2.3.1 Blade Element Momentum (BEM) Method.....	23
2.3.2 Vortex Wake Methods	23
2.3.3 Computational Fluid Dynamics Models	27
2.3.4 Desirable Characteristics of Future Models	27
2.4 Testing of Wind Turbines	27
2.4.1 Problems in Measurement on Operating Wind Turbines	27
2.4.2 Some Wind Turbine Tests.....	34
2.5 Possible Causes of Delayed Stall.....	43
2.6 Radial Flow of the Boundary Layer	43
2.7 Solidity	51
2.8 Dynamic Stall	54
2.9 Turbulence	64
2.9.1 Field Tests.....	64
2.9.2 Wind Tunnel Tests of Aerofoil Sections in Turbulence.....	67
2.9.3 Acoustic Effects.....	72
2.9.4 Turbulence in the Natural Wind and the Effects of Scale.....	73
2.9.5 Simple Effects of Rotation on Turbulence at the Blade.....	76
2.9.6 Rotational Sampling Effects	78
2.9.7 Induction Effects.....	80
2.9.8 Summary.....	82
2.10 Turbulence Effects on Bluff Bodies	83
2.11 Conclusion.....	88
3. Experimental Method	89
3.1 Introduction.....	89
3.2 Aerofoil Section Models.....	89
3.2.1 Profiles	89
3.2.2 Tapping Locations	90

3.2.3	Model Construction	92
3.3	Wind Tunnel, Model Placement and Grids	94
3.4	Flow Characteristics	98
3.5	Pressure Measurement	109
3.6	Force Calculations	114
3.7	Fluctuating Calculations	117
3.8	Surface Flow Visualisation	117
4.	NACA 0021 Aerofoil.....	121
4.1	Introduction.....	121
4.2	Mean Results.....	121
4.2.1	Low Turbulence Case	121
4.2.2	Comparison with Previously Published Results	127
4.2.3	Effect of Added Turbulence	131
4.3	Fluctuating	153
4.3.1	Lowest Turbulence Case.....	153
4.3.2	Comparison with Computational Results.....	166
4.3.3	Effect of Turbulence on Fluctuations	173
4.3.4	Correlations	183
5.	NACA 4421 Aerofoil.....	197
5.1	Introduction.....	197
5.2	Mean Results.....	197
5.2.1	Comparison	197
5.2.2	Effect of Added Turbulence	198
5.3	Fluctuating	220
5.3.1	Correlations	225
6.	S809 Aerofoil.....	237
6.1	Introduction.....	237
6.2	Mean Results.....	237
6.2.1	Comparison	237
6.2.2	Effect of Added Turbulence	241
6.3	Fluctuating	262
6.3.1	Correlations	266
7.	Conclusions	277
8.	References	289
Appendix A.	Blade Element Moment (BEM) Method.....	297
Appendix B.	Notes on Modelling Dynamic Stall.....	305

Abstract

Wind turbines operate in the natural, turbulent wind. However, prediction of their performance is usually based on simple models which use data from low turbulence wind tunnel tests of aerofoil sections. These models generally underpredict performance where the blade is predicted to stall, this is known as delayed stall. There have been many suggestions as to the cause of delayed stall, including that of turbulence. However there is a surprisingly small amount of data on the effect of turbulence on stall of aerofoil sections. This thesis details tests on three aerofoil sections in various turbulent flows. The detailed measurements of stalled flows have been used as a benchmark for computational simulations of aerofoils at high angle of attack. The tests found turbulence can have a large impact on the aerofoil's performance, especially in the lift force around stall. Given these results it was recommended that turbulence be included in wind tunnel testing of new aerofoil sections for wind turbines and also be considered in the design of new performance prediction methods for wind turbines.

Declaration of Originality

This thesis contains no material which has been accepted for the award of any other degree or diploma in any university or other institution and, to the best of my knowledge, contains no material previously published or written by another person, except where due reference is made in the text.

Katrina Swalwell

Acknowledgements

I would like to thank my supervisors, Professor John Sheridan and Professor Bill Melbourne, for their guidance and support. Also my office mates, Josie Carberry, Jon Dusting, Michael Eaddy, and John Elston, and the other postgraduate students at Monash for making it such an entertaining place to work. I also must thank Michael Eaddy for his help with the wind tunnel equipment, which he had previously used for his PhD experiments, and the Mechanical Engineering workshop staff, especially Mr. Don McMaster and Mr. John Hick, for their advice and the construction of the aerofoil section and supports.

A Monash Graduate Scholarship provided financial support during this research. Thanks must also go to SP Systems, Australia for kindly donating the carbon fibre and epoxy used to construct the aerofoil sections.

There are many others in the wider research community who have kindly taken time to discuss this work. I would especially like to thank David Wood from the University of Newcastle, Australia and Scott Schreck, Sandy Butterfield and Jim Tangler from the National Renewable Energy Laboratory, USA for the long discussions. Also Frank Thiele, Charles Mockett and Ulf Bunge from the Technical University of Berlin for allowing the inclusion of some of their unpublished results in this thesis.

Most of all I would like to express my appreciation to my family, Janene, Terry, Kim and Jeff Swalwell, Lauren Over and Helen and Belle McCoy, and housemates, Kris Ryan, Belinda and Ben Mott, for their encouragement and putting up with me during the writing process. I'd especially like to thank Kris Ryan, Terry Swalwell and Jeff Swalwell for being "wind tunnel safety officers" so I could continue testing over the weekend.

Finally, I would like to dedicate this thesis to Kris Ryan and my parents, Janene and Terry Swalwell.

Chapter 1

Introduction

Horizontal Axis Wind Turbines (HAWTs) are an increasingly common method of generating electricity. However to compete with cheap fossil fuels sources of electricity such as coal, they must become more cost efficient. Fossil fuel technologies have benefited from their gradual refinement since the industrial revolution. However, interest in wind turbines for electricity generation (they are, of course, a much older technology for uses such as water pumping) has fluctuated. Their early use was in remote areas for electricity generation and many small designs are available for this purpose today, where they can be considerably cheaper than extending the electricity grid. There was a surge of interest during the Second World War when electricity generation was difficult, another during the oil crisis of the 1970s and another more recently due to concerns about the finite resource and environmental problems caused by the use of fossil fuels (Gipe, 1995). The recent surge of interest has resulted in turbines that are currently competitive with fossil fuel generation in many parts of the world (in many areas cheaper than all methods except coal, Milborrow, 2005).

One area of wind turbine design that is very important to increasing efficiency is the aerodynamic design and, as a corollary, the prediction of power output. This thesis aims to contribute to continuing improvement in this area. This thesis concentrates on those large scale wind turbines that can justify the cost of thorough aerodynamic blade design. The term “wind turbine” in this thesis will refer to a Horizontal Axis Wind Turbine (HAWT), where the blades turn around an axis parallel to the ground. This has been the most successful commercially design. This thesis will concentrate almost exclusively on them except where useful knowledge for the operation of HAWTs can be gained from studies of the other main type, Vertical Axis Wind Turbines (VAWTs), where the blades turn around an axis perpendicular to the ground. Generally the manufacturers of HAWTs, most notably the Danish companies, have built their turbines based on learning from installed designs and gradually increasing the size and performance over subsequent generations. The other approach where there were dramatic increases in size has resulted in a great deal of useful knowledge but few useful turbines (and some failures of machines, Dodge, 2002).

In 1983 de Vries reviewed the aerodynamic models of wind turbines, which consisted of Blade Element Momentum (BEM) or vortex wake models. He found the existing full-scale data, while useful for accessing the technology, was not detailed enough for validating and improving aerodynamic models. Small rotor experiments in the wind tunnel, conducted by de Vries and den Blanken in 1981, had shown that the theory predicted the overall performance characteristics of the rotor well. However the lift coefficient of the rotor was unexpectedly high beyond stall and the tip loss correction used in the BEM model appeared to be inadequate. This has become known as

“delayed stall”. The experiment was limited by the relatively small Reynolds number of the tests and the large wake blockage corrections that were needed. De Vries concluded his review with the hope “...that in the near future more complete and reliable data on the aerodynamic performance of the HAWT will become available to stimulate and motivate the further development of its aerodynamic theory” (p. 95, de Vries, 1983).

Other reviews of this area have found the problem of “delayed stall” (Hansen, A. C. & Butterfield, 1993). Reviews have also consistently emphasised the need for better understanding of the key processes involved in order to refine current models. Indeed much of the called for full-scale testing, including full scale wind tunnel testing by the American National Renewable Energy Laboratories (NREL) in the Ames wind tunnel, has recently been completed. However, this was conducted in a relatively low turbulence environment with the axial turbulence intensity less than 0.5% (Zell, 1993).

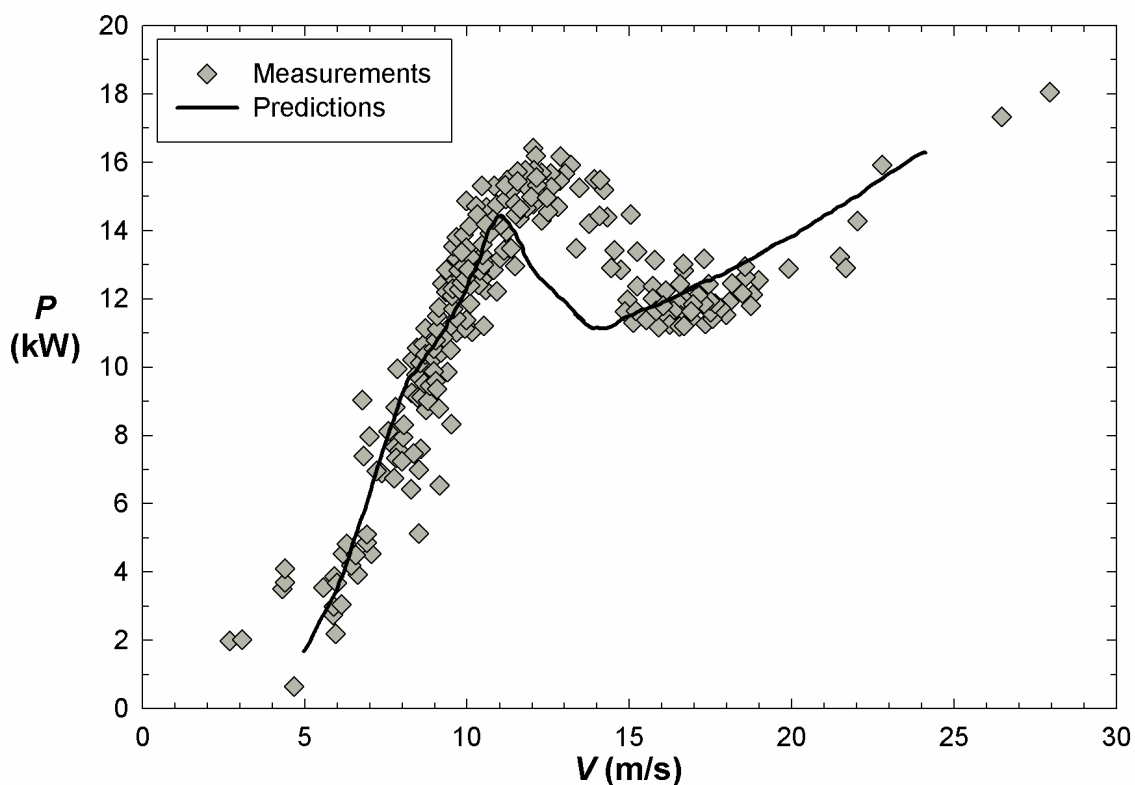


Figure 1-1 - Predictions and field measurements of power (P) versus windspeed (V) on NREL's 10 m test turbine (reproduced from Simms *et al.*, 1999b). The measurements shown were classified as baseline data and excluded the section of the rotation affected by tower shadow. Baseline data were the middle rotation of three rotations when the mean wind speed and direction were relatively constant and the turbine was at minimal yaw.

Delayed stall is important because many turbines are designed so that their maximum power, and therefore load, is limited by allowing the blades to stall. Uncertainty in the loading in this region can lead to overly conservative, and therefore costly, designs. The other main method of aerodynamic load control is pitch control where the blades are equipped with pitching motor to

allow the blades to be pitched during operation (a new trend is for independent pitch control). This offers more control but is more mechanically complex. However this method has become increasingly common on new wind turbine designs. It has been reported that this trend is in part due to the uncertainties caused by delayed stall. However the pitching rate on wind turbines means that even pitch controlled machines will stall in sudden wind gusts, so understanding of the stalling process is important for these machines as well. Delayed stall is likely to have a number of contributing causes. One that has been often suggested, but little investigated, is turbulence.

This thesis looks at an aspect of the aerodynamic design of wind turbines, namely the turbulence at the blade and the effect of turbulence on aerofoil performance near stall. Chapter 2 will show why this area is of importance and what questions remain to be answered.

Chapter 2

Literature Review

2.1 Introduction

The current understanding of the effect of turbulence on wind turbine blades involves many research fields including wind turbine aerodynamics, aerofoils, bluff bodies and, of course, turbulence. This review will begin by briefly examining the characteristics of modern wind turbines. These characteristics will provide limits to the subsequent discussion. Then, as delayed stall is a label given to a region where performance predictions are inaccurate, the various models of wind turbine performance will be briefly outlined. Tests on operating wind turbines are used to validate these models so the next section will detail the possible problems with wind turbine tests and some of the most important tests. The possible explanations of delayed stall will then be considered leading to why the effect of turbulence merits further study. The review will conclude with an examination of the literature on the effects of turbulence on bluff bodies.

2.2 Wind Turbine Characteristics

This brief overview is confined to covering the characteristics of modern wind turbines and the aerofoil requirements for their blades. The literature on aerofoil performance is extensive and undoubtedly many relevant investigations have been overlooked. However, the purpose of this discussion is not to discuss aerofoil theory in detail but to identify the operating conditions of modern wind turbines. These conditions will provide limits for the subsequent discussions, for example by defining the Reynolds number (Re) range of interest. This section will also examine the aerofoil section testing that provides the aerofoil data used in many of the performance prediction methods that will be discussed in the subsequent section.

Modern wind turbines are generally three-bladed, upwind, pitch controlled Horizontal Axis Wind Turbine (HAWT) designs. Tangler (2000) described the reasons for these choices. Vertical Axis Wind Turbines (VAWTs) have complex loading patterns due to the motion into and out of the wind and are generally situated lower in the earth's boundary layer than HAWTs therefore limiting the wind power available. As mentioned in the introduction chapter this thesis will concentrate on HAWTs. Unless specifically stated otherwise, the term "wind turbine" will refer to a HAWT and VAWTs will only be discussed where they give insight into the aerodynamic behaviour of HAWTs. Moreover the discussion will be focussed on the larger HAWTs used for commercial power generation as these designs can economically justify a detailed aerodynamic design process.

One of the main design choices for HAWTs is whether the blades will be upwind or downwind of the rotor. Upwind rotors are favoured over downwind designs because of the lower noise and lower cyclic loading as the blades do not pass through the wake of the tower. Downwind designs have been extensively investigated because this design allows for more flexible blades without the danger of tower strike (where the blade hits the tower). It also allows more coning of the rotor. As the name suggests coning involves tilting of the blades downwind so that the blades outline a cone shape. Coning allows balance of the thrust and centrifugal effects which gives more balance and therefore reduces blade root stresses (p. 56, Eggleston & Stoddard, 1987). Downwind operation has also been favoured for free-yaw designs (designs without motors to yaw the turbine into the wind) as the BEM method predicts almost neutral stability in yaw and if the axial force is taken into account this means the rotor should naturally take a position downwind of the tower (de Vries, 1985). Unfortunately free-yaw wind turbine designs typically spend a lot of time yawed, where the rotation axis of the turbine is not parallel to the wind direction. For example Eggleston & Starcher (1990) investigated three downwind turbines and found all operated at a mean angle to the wind. De Vries (1985) found that using a simple model for small yaw angles that turbines can operate stably when yawed to the wind. Yawed operation means that the blade is passing into and out of the wind thereby adding a cyclic loading to the design and can result in dynamic stall events as will be discussed later Section 2.8.

Three-bladed rotors are more dynamically balanced than the one or two-bladed designs (Tangler, 2000). However the efficiency gained from increasing the number of blades is small. Increasing the number of blades from one to two increases the efficiency by 6% but from two to three blades is only an additional gain of 3% (Tangler, 2000). Also increasing the number of blades for a given radius and aerofoil thickness reduces the blade flap stiffness and therefore increases the chance of the tower strikes (Tangler, 2000).

Power control of wind turbines is achieved by variable speed, variable pitch or stall control. Large turbines have mostly used simple constant speed generators, usually the cheaper induction generators. These can be connected directly to the grid with minimal power electronics and their rotational speed varies only about 1% over their range of operation (Danish Wind Industry Association, 2003). However variable speed designs allow the turbine to optimise the power output for any wind speed and store energy from wind gusts (they have been commonly used in small turbines which are not connected to the grid). Relatively recently some wind turbine companies have found variable speed designs for large wind turbines cost effective (Vestas, 2003), although they require much more power electronics to match the final output to the grid frequency (Danish Wind Industry Association, 2003). For example Vestas now has a variable speed design that allows the rotor speed to vary by 10%. For constant rotational speed the power curve of the turbine can be expressed in terms of the windspeed. However for variable rotational speed it should be expressed in term of the tip speed ratio (λ),

$$\lambda = \frac{\omega R}{U_\infty},$$

Equation 2-1

where ω is the rotational speed, R the tip radius and U_∞ the freestream velocity.

Stall control limits the power and therefore loads in high winds by allowing the blades to stall. However the problem of delayed stall has made it difficult to predict the loading in high winds. It is possible to pitch toward stall or pitch toward feather, the later avoids the problem with stall but can result in high power spikes (Tangler & Somers, 1995). While pitch controlled blades will also stall in wind gusts generally the pitching of the blades will avoid stall. For this reason, despite the extra cost and complexity of the blade pitch motors, pitch controlled turbines have become more common as the following comment indicates.

“One European participant noted that the tendency in the European wind industry has been to move away from stall-controlled designs in favour of pitch-controlled designs because of difficulty in predicting loads for stall-controlled turbines.” (p. 15, Simms *et al.*, 2001)

Wind turbines generally operate in windspeeds of between 5 to 25m/s. They are usually optimised to perform best at the most likely wind at the site, generally around 10 to 15m/s. This is also the performance figure that should be quoted, for instance a 2MW wind turbine will produce 2MW of power at its designed wind speed. Most modern large wind turbines are stopped outside this range of wind speeds to minimise damage, however some smaller designs use tip breaks, where the tip of the blade pitches in high winds. The shape of the tips on all turbines is determined by past design performance. Test experience has shown that a sword tip gives good performance while swept tips limit the noise produced but cause a reduction in performance (Tangler, 2000), see Figure 2-1.

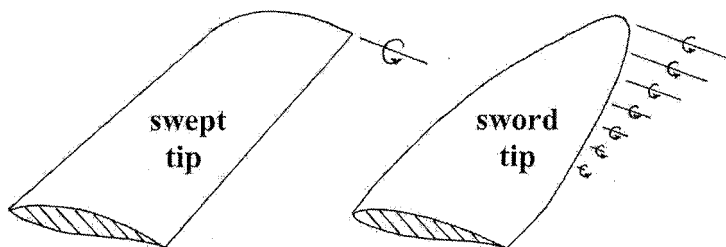


Figure 2-1 - Tip shapes from Tangler (2000).

Wind turbine blades are usually twisted and tapered. Twist alters the angle of attack (α) along the blade to optimise the blades performance. Taper allows thicker sections to be used at the blade root to give greater blade stiffness and strength and thinner higher performance aerofoils towards the blade tips where the greatest power is generated. Cambered aerofoils are used for their higher performance compared to symmetrical aerofoils. The definitions of chordline, midline, chord length (c), maximum camber (h), and thickness (t/c) of an aerofoil section are shown in Figure 2-2. The angle of attack (α) is defined as the angle between the chordline and the freestream flow direction.

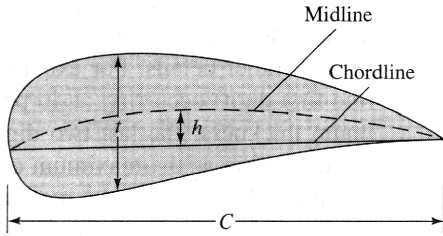


Figure 2-2 - Aerofoil section definitions from White (1999).

The most critical parameter in determining the performance of wind turbine blades is the Reynolds number range in which the blade operates,

$$Re = \frac{Uc}{\nu} \quad \text{Equation 2-2}$$

The operating Re range of wind turbines is shown in Figure 2-3. This figure by Galbraith, Coton, Saliveros & Kokkodis (1987) is very similar to an earlier figure by Lissaman (1983) except the Re range of operation of wind turbines is larger than in Lissaman's figure. This could be due to larger turbines being developed in the four years between publications or different methods of calculating the wind turbine Re number. Neither paper specifies how the Re number range of the wind turbine blades was calculated. The Mach number of large wind turbine operation is well below 0.3 and therefore the flow can be assumed to be incompressible.

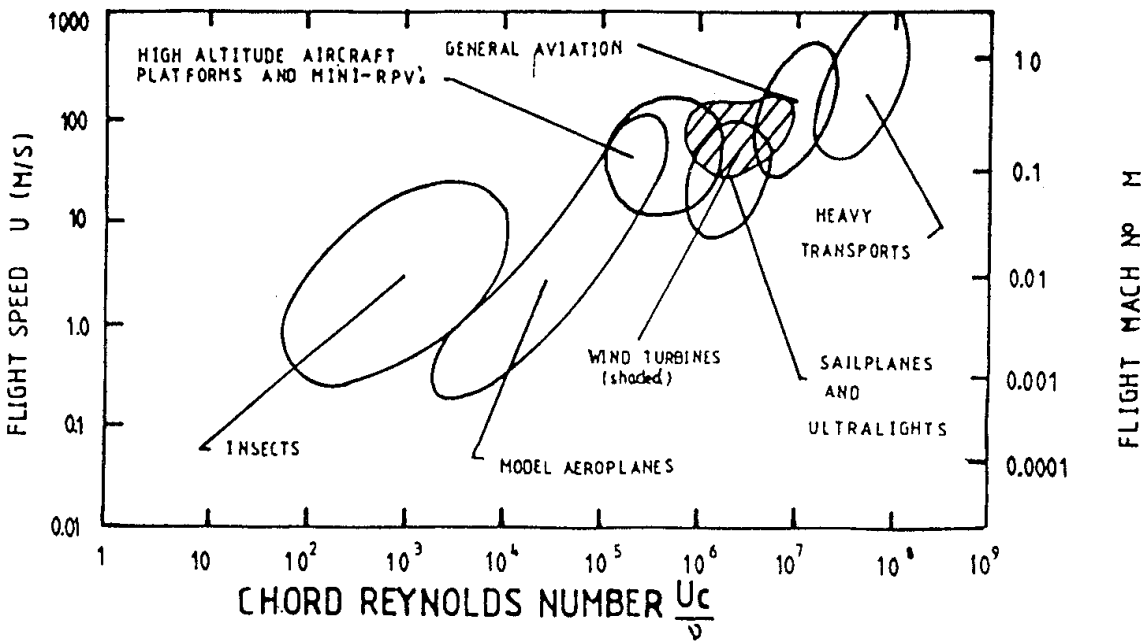


Figure 2-3 – Operating Re of wind turbines by Galbraith *et al.* (1987).

The windspeed (U) at a wind turbine blade is a combination of the blade rotation and the slowed wind approaching the blade, the appropriate windspeeds and therefore the appropriate Reynolds numbers to use to obtain the aerofoil performance data is left to the designers to determine. Blanch (1996) defined a geometric Reynolds number based on a geometric wind speed as

$$V_{geometric} = \sqrt{(V_{wind} \cos \gamma)^2 + (r\Omega)^2}, \quad \text{Equation 2-3}$$

where γ is the yaw angle. This windspeed can be used to give a geometric Reynolds number. A 3m diameter, three-bladed, upwind turbine was attached to a trailer and was towed along the mile long runway at Cranfield Airport generating a low turbulence flow. Rings of pressure taps were placed at 35% and 75% R . This turbine used NACA 4415 aerofoils. Wind tunnel data showing the effect of Reynolds number for this aerofoil has been contradictory with the test by Jacob and Sherman, which showed increasing lift with Re , while Hunt's data for the NACA 4415 aerofoil section showed a decrease in lift in the same Re range and no consistent trend over his larger range of Reynolds numbers (reported by Blanch, 1996). Geometric angle of attack versus lift from the pressure taps on Blanch's turbine did not show clear trends with increased geometric Reynolds numbers; this may have been due to different yaw levels in the tests. However they did show differences in performance which supports the use of a geometric Re .

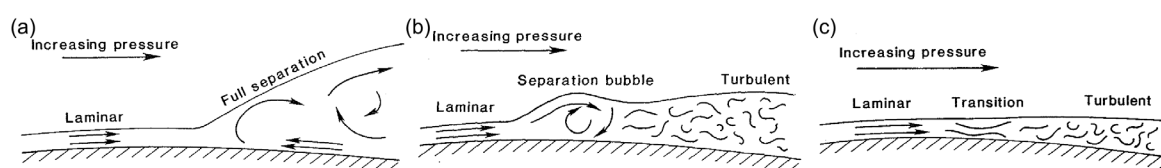


Figure 2-4 - Boundary layer types with Reynolds number, (a) low Re laminar separation, (b) medium Re separation bubbles and (c) high Re turbulent boundary layer. From Miley (1982).

The most important effect of Re on aerofoil performance is on the boundary layer. The boundary layer is the area of the flow where frictional effects are significant; its height is arbitrarily defined as the distance from the surface to the point where the boundary layer velocity is 99% of the freestream velocity (Miley, 1982). There are two types of boundary layers, laminar and turbulent, as the Re increases the laminar boundary layer becomes turbulent. Laminar boundary layers are thinner. Laminar boundary layers produce less skin friction drag than turbulent boundary layers due to the increased mixing in turbulent boundary layers causing larger surface shear. However they separate from the surface easily when the pressure increases in the flow direction, which is called an adverse pressure gradient. Turbulent boundary layers are much less prone to separation. In an adverse pressure gradient the velocity decreases and can eventually reverse causing separation of the flow also known as stall. The suction pressure on the upper surface of an aerofoil helps provide lift and the deceleration of the flow is necessary so that the flows from the upper and lower surface smoothly combine at the trailing edge, referred to as the Kutta condition. Stall occurs when all or part of the flow is separated from the upper surface of the aerofoil. This thesis will use fully stalled to indicate that the flow is entirely separated from the upper surface. Generally thin aerofoils will tend to separate from the leading edge leading to a sharp drop in lift whereas thicker aerofoils will stall more gradually with the separation point moving gradually up from the trailing edge as α increases. Separation bubbles occur when the laminar boundary layer separates from the surface and then reattaches to the aerofoil surface as a turbulent boundary layer (the separated shear layer transitions to turbulence) as sketched in Figure 2-4(b). Miley (1982) believed that a general consensus on the Re range in which separation bubbles occur was

$5 \times 10^5 < Re < 3 \times 10^6$. Above this range the boundary layer is likely to transition to turbulence before separation, as sketched in Figure 2-4(c), and below this range the laminar boundary layer will separate but not reattach, as sketched in Figure 2-4(a).

Carmichael (1981) was more conservative in his estimation of the range of Re over which separation bubbles occur than Miley. Carmichael quoted von Doenhoff's rule of thumb that

$$Re_{reattachment} - Re_{separation} \approx 7 \times 10^4. \quad \text{Equation 2-4}$$

This equation is based on flat plate measurements, smaller values can be found for some thin and/or cambered aerofoils but larger values are common on thick aerofoils. Long separation bubbles can occur for $7 \times 10^4 < Re < 7 \times 10^5$. Long bubbles have more of an effect on performance so efforts in this Re range include trying to encourage short separation bubbles. For $Re > 4 \times 10^6$ Carmichael (1981) identified that laminar separation bubbles are unimportant. Lissaman (1983) asserted that for $Re > 2 \times 10^5$ it is usually possible to design the aerofoil so that transition to a turbulent boundary layer occurs before the adverse pressure gradient. However it is clear that the operation of some wind turbine blades fall into the Re range where separation bubbles and their associated effects would be expected to occur.

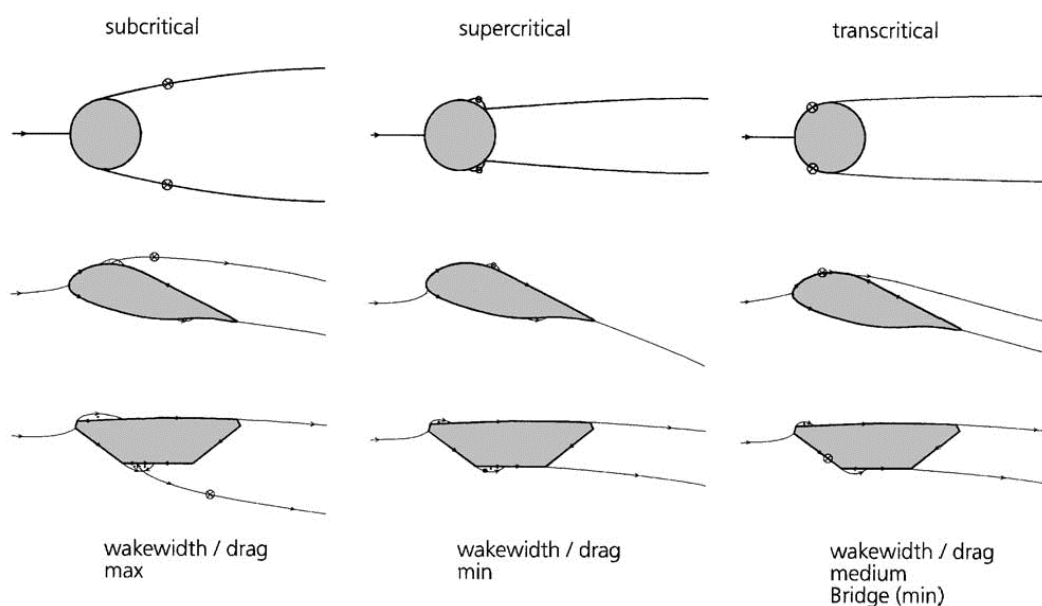


Figure 2-5 - Separation Regimes with increasing Re (p. 1288, Schewe, 2001). The time averaged wake is shown with the symbol \otimes marking the location of the transition from a laminar to a turbulent boundary layer.

Essentially, an aerofoil after separation acts as a bluff body. Schewe (2001) compared the response of three bodies to Re in the range 10^4 to 10^7 where the bodies behaved “more-or-less” as bluff bodies depending on the flow. The bodies spanned the wind tunnel section with a constant cross-section (called a 2D section). They consisted of a circular cylinder, a thick aerofoil at a high α (the aerofoil was part of the Growian wind turbine with a thickness of $27\%c$ and an aspect ratio of 4) and a bridge section (sharp-edged trapezoidal). The types of flow were classified into subcritical (laminar separation), supercritical (separation bubble) and transcritical (turbulent separation). The

separation region was unsteady with the wake forming a Kármán vortex street. The average wake region is shown in Figure 2-5. These three regimes were associated with jumps in the Strouhal number (St) of shedding drag and, where applicable, lift. The Strouhal number (St) is defined as

$$St = \frac{fL}{U_\infty}, \quad \text{Equation 2-5}$$

where f is the frequency of shedding, L is the characteristic length scale of the object and U_∞ is the freestream velocity.

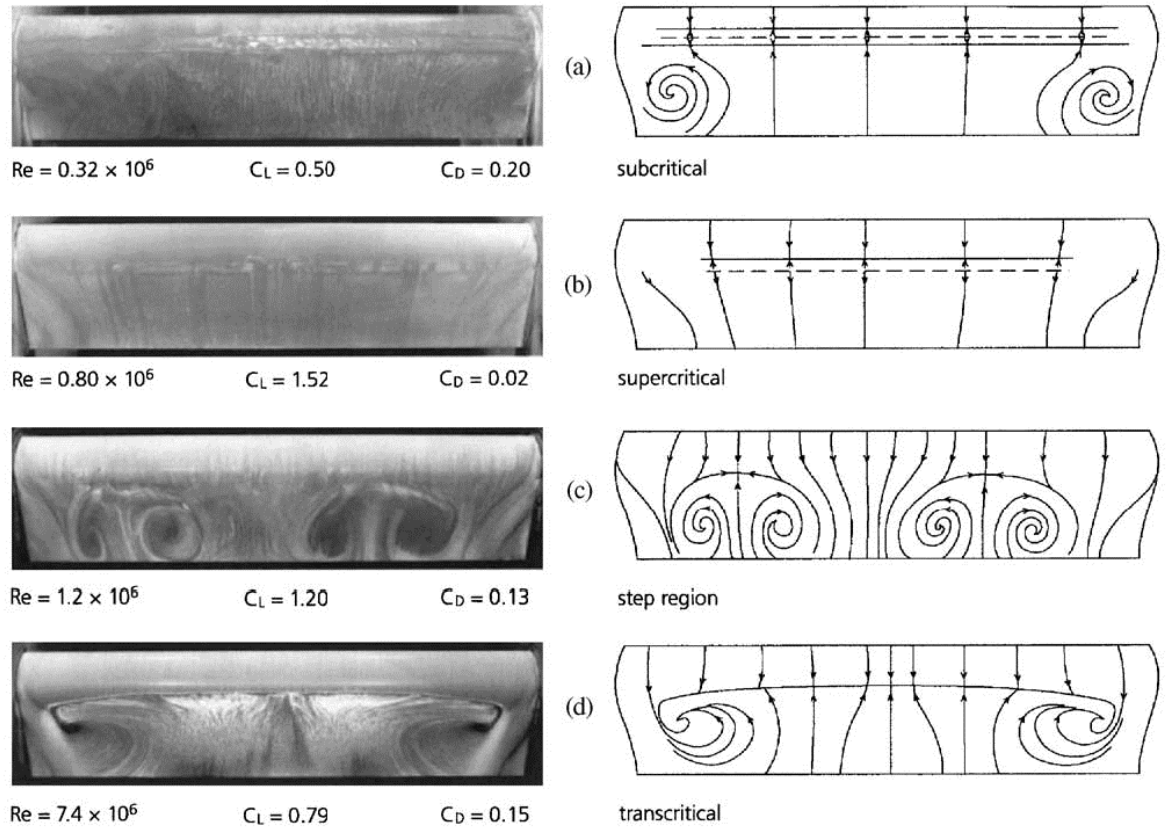


Figure 2-6 – Oil-flow visualisations of surface structures on an aerofoil with increase in Re (p. 1277, Schewe, 2001).

Oil flow visualisation on the surface of the aerofoil is shown in Figure 2-6. The oil added roughness to the surface of the aerofoil that altered the Re at which the different flow regimes occurred so the regimes were matched by lift. The first case, Figure 2-6(a), is a laminar separation (the separated boundary layer changes to turbulent above the aerofoil, the dashed line represents this and is included for topological reasons). The next case, Figure 2-6(b), consists of a separation bubble. The final case, Figure 2-6 (d), is turbulent separation. In the transition between the separation bubble and turbulent separation is a region with a spanwise spatial periodicity, shown in Figure 2-6(c). Schewe describes these features as “mushroom cells” or “owl eyes” and they will be discussed later in this section with regard to aspect ratio effects. Note that these regions are not symmetric. Schewe suggested that

“It is conceivable that both separated regions act, via the owl eyes, like displacement bodies that so strongly accelerate the flow (jet effect) in the space between them that it

overcomes the pressure increase up to the trailing edge without separating. This situation would mean (i) higher lift in the region between the owl eyes and (ii) lower lift in the region of the owl eyes.” (p. 1279, Schewe, 2001)

Schewe noted this may make pressure measurements differ along the span of the aerofoil, so results taken at a single spanwise location may provide an inaccurate view of the total lift.

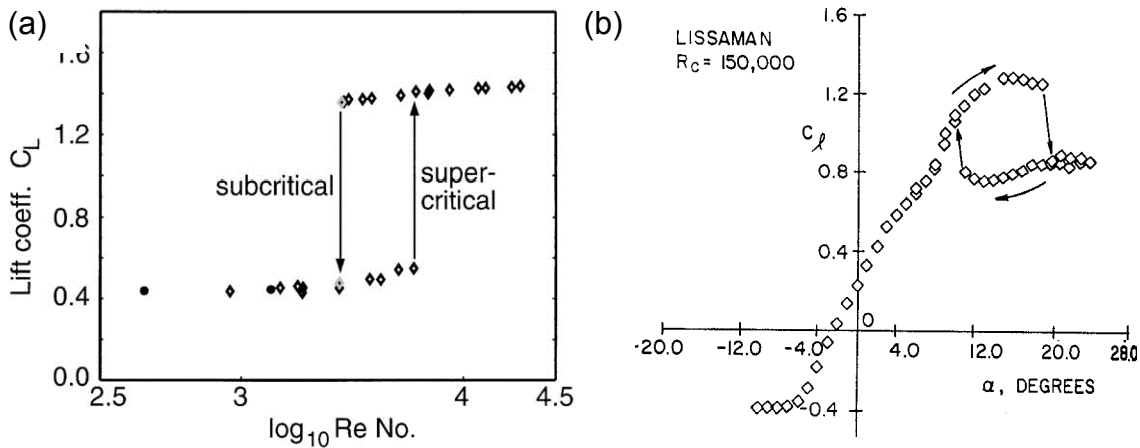


Figure 2-7 - Hysteresis in lift coefficient (a) with Re for the transition from subcritical (laminar separation) to supercritical (separation bubble) from Schewe (2001) and (b) with α for the Lissaman 7769 aerofoil at a Re of 1.5×10^5 (Mueller, 1985).

Interestingly Schewe noted a hysteresis in the lift coefficient with Re number in the transition from the laminar separation (subcritical) to separation bubble (supercritical) states, see Figure 2-7(a). Hysteresis is commonly seen in the forces on an aerofoil with a separation bubble with change of α , for an example see Figure 2-7(b). Smoke visualisation for the Lissaman aerofoil for this Re shows that the attached boundary layer, and therefore separation bubble, does not form until a lower α when α is decreased compared to where it exists when α is increased, see Figure 2-8. Note that this is not a dynamic effect, the angle of the aerofoil was changed while the tunnel was running but the flow is steady and the photos could have been taken any time after the change of angle. A loop in the opposite direction can exist, as Mueller (1985) showed in the same paper on a Miley aerofoil. On this aerofoil the flow was separated from the upper surface at the point of maximum thickness at $\alpha = 0^\circ$. The separation point moved gradually up stream as the α was increased. When the separation point moved far enough upstream, a separation bubble formed which produced a jump in lift. If α was decreased from this point the separation bubble remained for a range of α producing larger lift than for the increasing α case. For both aerofoils the hysteresis is caused by the conditions required to form the separation bubble, once formed the separation bubble will persist to other α .

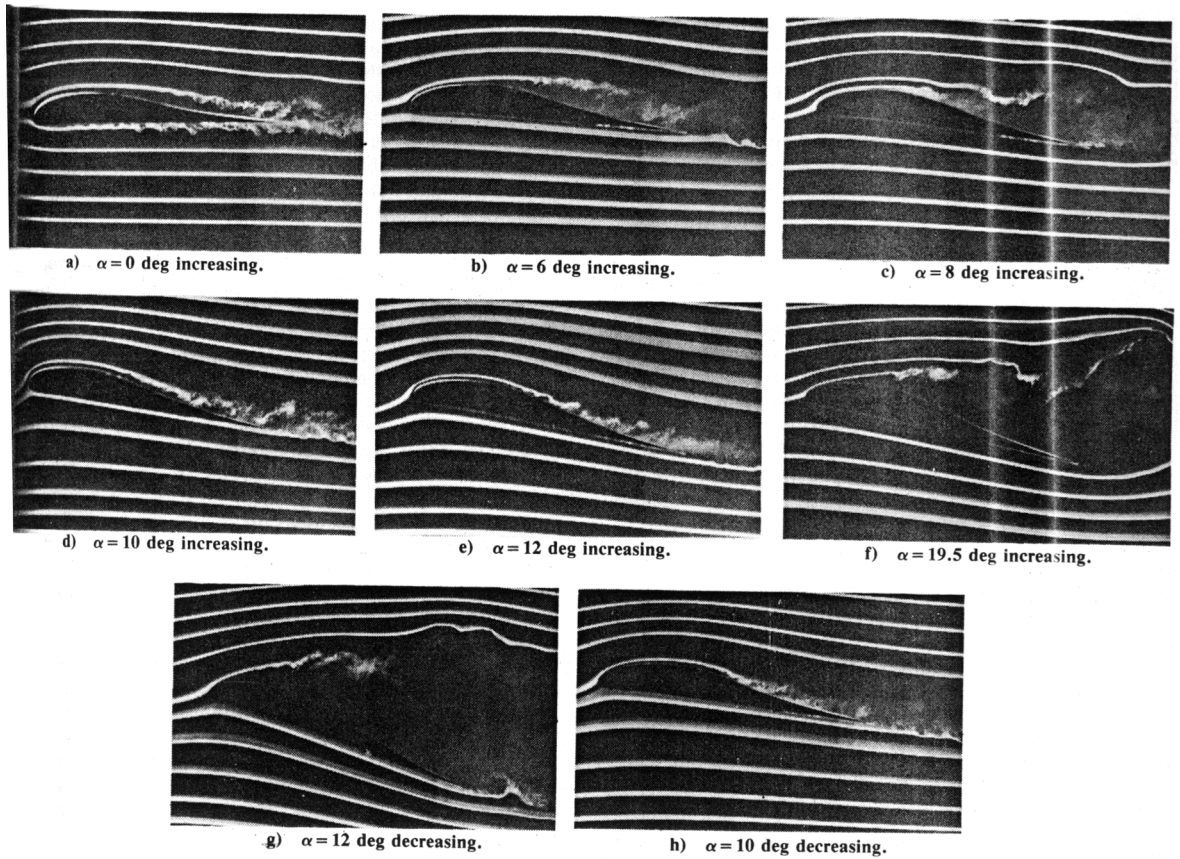


Figure 2-8 – Smoke visualisation of the hysteresis effect for a Lissaman 7769 aerofoil at a Re of 1.5×10^5 (Mueller, 1985)

Mueller (1985) also showed the effect of turbulence on the separation bubble, see Figure 2-9. The turbulence intensity is defined as

$$\begin{aligned}
 I_u &= \frac{\sigma_u}{\bar{U}} \text{ (longitudinal)} \\
 I_v &= \frac{\sigma_v}{\bar{U}} \text{ (lateral)} \\
 I_w &= \frac{\sigma_w}{\bar{U}} \text{ (vertical)}
 \end{aligned}
 \tag{Equation 2-6}$$

where \bar{U} is the mean component of the wind in the longitudinal direction, σ_u , σ_v , σ_w are the standard deviations of the wind in the longitudinal, lateral and vertical directions and I_u , I_v and I_w are the longitudinal, lateral and vertical turbulence intensities respectively. Another important characteristic of turbulence is the dominant size of the turbulence eddies which can be represented by the integral turbulence length scale. L_{uu} , L_{uv} and L_{uw} are the longitudinal, lateral and vertical turbulence integral length scale respectively. By adding turbulence to the freestream the separated boundary layer transitions to a turbulent boundary layer more quickly and therefore reattaches earlier. The length of the separation bubble is reduced causing a smaller hysteresis loop, see Figure 2-9(b). Higher levels of turbulence can cause the boundary layer to transition to turbulence before separation and therefore eliminate the separation bubble altogether, see Figure 2-9(c). Turbulence affects the shear layers and therefore can also affect aerofoils without separation bubbles. However, although turbulence is present in the operating environment of wind turbines, most

aerofoil tests for wind turbine try to eliminate the effect of turbulence as much as possible. Miley discussed the reasoning for this in detail.

“The scale of the turbulence is the deciding factor here. The airfoil boundary layer is sensitive only to turbulent fluctuations on the order of the size of the boundary layer thickness itself. The frequency of these fluctuations is within the audio range. The scale of atmospheric turbulence is too large to have any direct effect on the boundary layer. It may have an indirect effect by causing a fluctuation in the airfoil angle of attack, and consequently, the airfoil pressure distribution. If we consider an aircraft flying through atmospheric turbulence, the turbulence scale is on the order of the size of the airplane, and it responds accordingly by bouncing around. The scale is too large to be seen by the boundary layer as other than a variation in the wing angle of attack.” (Miley, 1982, p.23)

There are points against this argument. However they, and a detailed examination of the effects of turbulence, will be left to later in the thesis since the aim of this section is to discuss common methods of testing aerofoils for wind turbines.

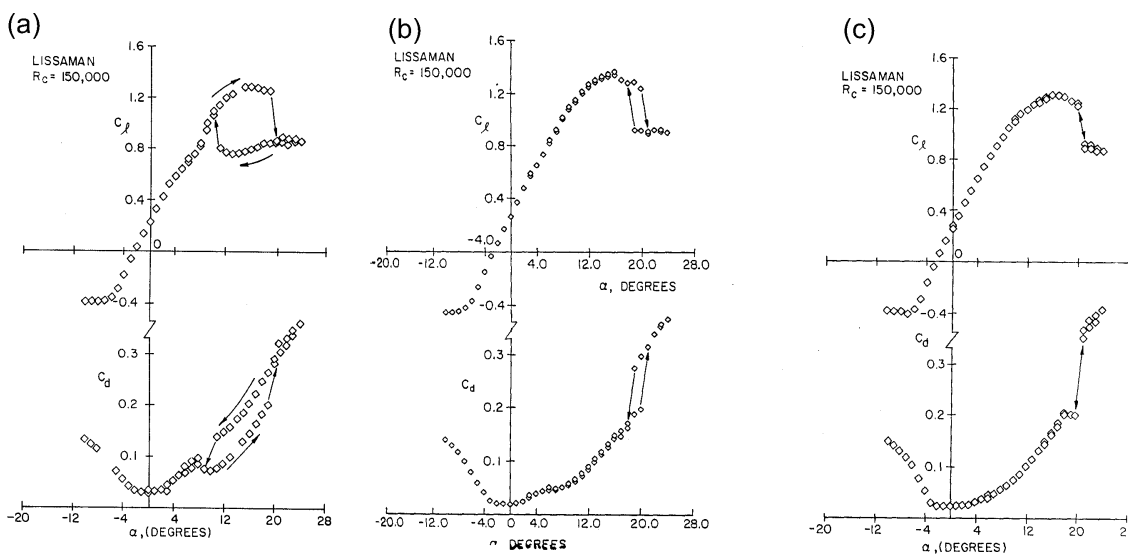


Figure 2-9 – Hysteresis loop for a Lissaman 7769 aerofoil with three turbulence intensity levels in the wind tunnel, (a) 0.07%, (b) 0.16% and (c) 0.3% (Mueller, 1985).

Acoustic disturbances of certain frequencies and surface roughness can also alter boundary layer behaviour, an example of which can be found in Mueller & Batill (1980). In another investigation of the separation bubble on a different aerofoil, a Miley aerofoil, where both a balance model and pressure tapped model were used it was found that

“An understanding of the effect of surface roughness provided a great deal of insight in interpreting the pressure model data. The performance of the pressure model was similar to the performance of the smooth model with a single strip of tape. The surface roughness introduced by the pressure taps altered the airfoil performance significantly at low Reynolds numbers. Any surface roughness or defects in model construction could alter airfoil performance significantly.” (p. 664, Pohlen & Mueller, 1984).

Lissaman (1983) pointed out that roughness may have a favourable effect on performance at lower Re , as shown in Figure 2-10. This fits with observations that insects often have sharp bends in their wings but the wings of birds are smooth.

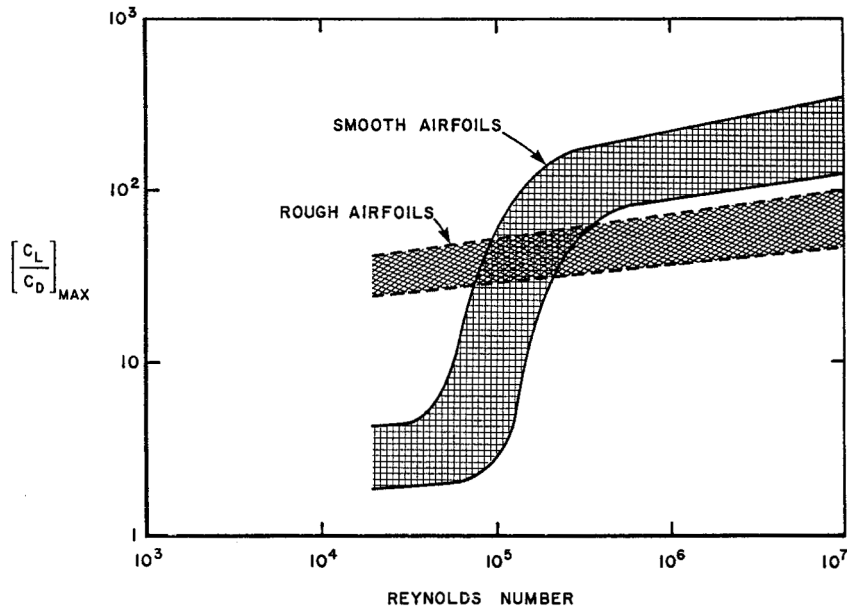


Figure 2-10 - Maximum performance with Re for smooth and rough aerofoils from Lissaman (1983).

Roughness, found on wind turbine blades due to manufacture and/or soiling during operation, is known to increase the thickness of the boundary layer causing earlier stall and higher drag (Tangler, 1999). Roughness partially negates the effect of camber as it causes a thicker boundary layer on the suction surface and therefore causes a lower c_l for a given α , with this effect increasing as the α increases (Tangler, 1999). Most of the NACA four and five digit series, such as the NACA 44XX and NACA 23XXX which were used on early wind turbine designs, achieved their $c_{l,max}$ by leading edge camber which generally results in some laminar flow on the suction surface at $c_{l,max}$. This laminar flow is disrupted by surface roughness and so these aerofoils typically have high losses in $c_{l,max}$. This loss can be expected to increase with increasing $c_{l,max}$ independent of aerofoil thickness. The six digit NACA aerofoils, such as the NACA 63_x-XXX series, were also used in many early wind turbine designs. They used aft camber for achieving high $c_{l,max}$ but

“...leading-edge radius closure can lead to slope discontinuities where it intersects the upper and lower airfoil surface. This discontinuity can result in the formation of leading edge separation bubbles that result in an inconsistent $c_{l,max}$.” p. 4, Tangler (1999).

The reduction in wind turbine performance due to roughness varies with the amount of blade stalled during operation. Losses in annual energy production range from 5% to 10% for variable speed, 5% to 20% for variable pitch (towards feather) and up to 20% to 30% for stall regulated turbines (Tangler, 1999). To try and quantify the effect of aerofoil thickness and $c_{l,max}$ on roughness sensitivity three aerofoils were tested; the S901 and S902 had the same $c_{l,max}$ but different thickness while the S902 had the same thickness as the S903 but a different $c_{l,max}$. These aerofoils were designed with the same principles as the rest of NREL’s wind turbine aerofoil families which will be discussed later in this section. The effect of roughness on $c_{l,max}$ was minimised and the leading edges were designed to alleviate the effect of laminar separation

bubbles, i.e. to have the suction surface transition to turbulence before $c_{l,max}$, therefore requiring aft camber. The aerofoils models had a 45.72cm (18 inch) chord and were tested in the Pennsylvania State University wind tunnel giving an aspect ratio of about 2.22. The clearest trends were seen in the NACA standard roughness tests. Scaled roughness was 0.211mm grit applied from 8% c on the upper surface across the leading edge to 8% c on the lower surface. Comparing the loss in maximum lift with added roughness with other previously published results in Figure 2-11(a) shows that the loss in $c_{l,max}$ is strongly dependent on thickness. Tangler (1999) suggests that this “...trend indicates that it may be difficult to design any roughness insensitivity into airfoils over 24% thick” (p. 4). Figure 2-11(b) shows that, at least for the designs relying on aft camber, the loss of $c_{l,max}$ with roughness is relatively independent of the aerofoil $c_{l,max}$.

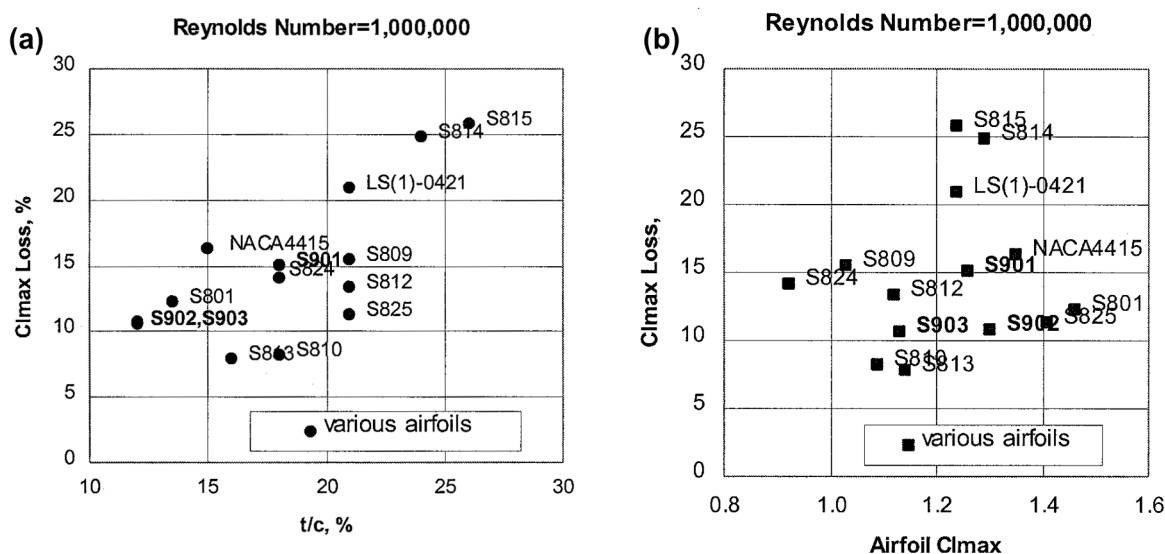


Figure 2-11 - Loss of $c_{l,max}$ with NACA standard roughness, trends with aerofoil thickness (a) and $c_{l,max}$ (b), figures by Tangler (1999).

“Double” or “multiple” stall has been observed on several turbines. Corten & Veldkamp (2001) showed that this can be caused by the accumulation of dead insects on the leading edge of the blades increasing the surface roughness. Corten’s thesis (2001) described this investigation in more detail. Oak Tree Energy had measured very different power levels consistent with “double” stall from their NEG Micron 700kW 44m diameter upwind, stall controlled turbines over different time periods as shown in Figure 2-12(b). Corten developed a number of hypotheses for the cause of double stall, for example that the behaviour was related to hysteresis in stall based on the behaviour at the tip (Corten, 1999), but eventually demonstrated it was caused by the dead insects on the leading edge of the blade shown in Figure 2-12(a). Figure 2-12(c) shows the performance of two NEG Micon turbines located 50 meters apart at the Oak Tree site. The turbine designated P12 had roughness in the form of zigzag tape added to the leading edge of all the blades for the period designated 8-34 okt. This tape was removed for the period designated 34-45 okt. Removing the tape caused an increase in the power generated in high winds to similar levels of the other turbine, P14. Figure 2-12(c) also shows two periods of operation for turbine P14, the first period ends on

12 okt when a small accumulation of bugs was cleaned from the blades. The cleaning increased the turbines performance by about 50kW. Figure 2-12(d) shows the solution adopted for this problem.

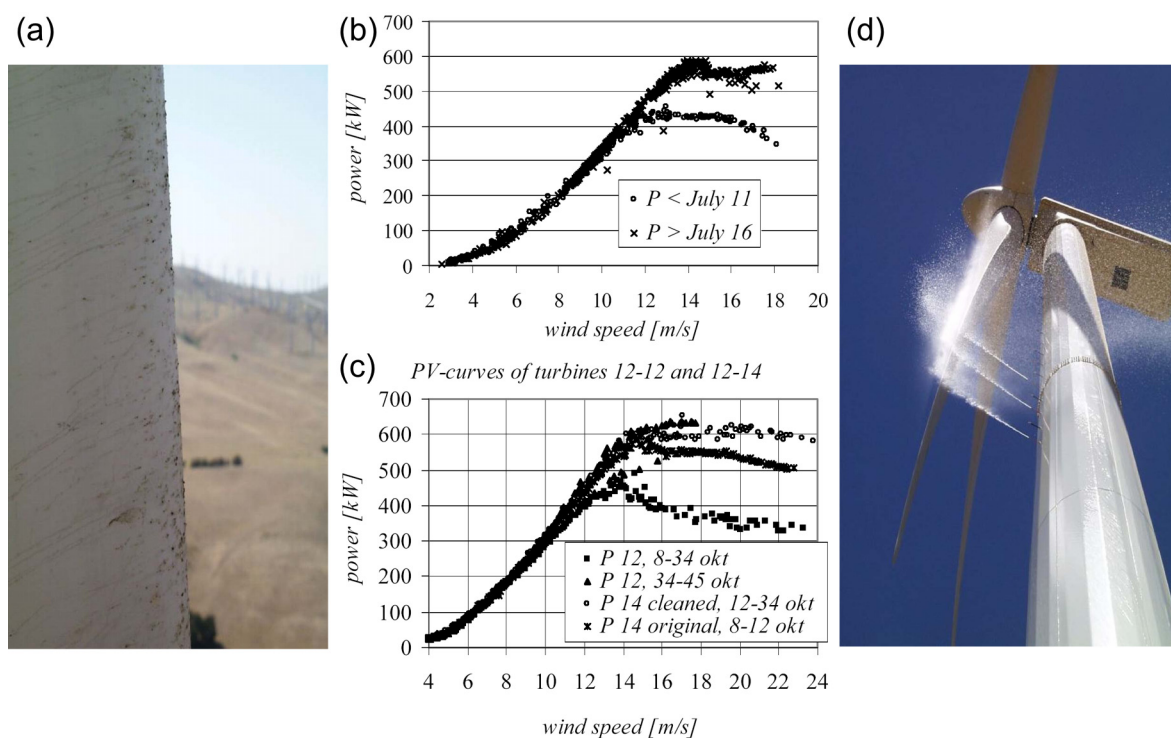


Figure 2-12 - Blade showing the insect caused roughness problem (a). Power performance curves for a 700kW, 44m diameter NEG Micon turbine for different time periods (b). Adjacent turbines of this design with roughness at leading edge (P12, 8-34 okt) and with roughness removed (P12 34-45 okt) (c). The implemented solution of “artificial rain” (d). (a) and (d) from the Oak Tree Energy website (2002) and (b) and (c) from Corten (2001).

Tangler (1999) discussed the conflict in choosing aerofoils for wind turbines. On one hand the designer wants thick aerofoils to reduce blade weight and increase blade stiffness but on the other hand thin aerofoils have lower drag and minimal roughness sensitivity. Similarly, high lift aerofoils are desired for maximum performance but low lift aerofoils limit peak power and allow soft stall. Fugslang (2002) noted that the NACA63-2xx, NACA 63-4xx and the NACA 63-6xx aerofoils have been used on recent wind turbines. NACA aerofoils have been very popular with wind turbine designers because of the availability of wind tunnel measurements, the good geometrical agreement between related aerofoils of different thicknesses and the experience wind turbine designers have with using these aerofoils (Fugslang, 2002). However they can be sensitive to roughness, have unpredictable power in high winds due to the bursting of the separation bubble and can suffer edgewise vibrations due to dynamic stall (Fugslang, 2002).

To obtain the best compromise aerofoil families have been designed specifically for use on wind turbines. One such family is the NREL aerofoils which were designed to have a maximum lift coefficient that was relatively insensitive to roughness effects and soft stall resulting from separation progressing from the trailing edge (Tangler & Somers, 1995). Different aerofoils were designed for different types of power control. For stall regulated rotors thicker (16% to 21%) tip aerofoils were designed with a restrained maximum lift coefficient (the maximum lift coefficient

was limited allow design of aerofoils with gradual stall characteristic) to aid power control near stall. Thinner aerofoils (11% to 15%) with higher maximum lift coefficient were designed for the tip-region aerofoils for pitch controlled and variable speed rotors. The thickness of the root aerofoils varied from 18% to 24% (thicknesses greater than 26% were found to result in unacceptable performance characteristics). The aerofoils were designed by the Eppler Aerofoil Design and Analysis Code (described by Somers, 1992). This program allows aerofoils with prescribed boundary-layer characteristics to be designed and aerofoils with prescribed shapes to be analysed. The velocity distribution can be specified along different segments of the aerofoil at different α . This allows design for the important features of many velocity distributions to be specified from the start of design (other methods specify one condition and then have to iteratively compromise to get desired performance at the off design points). However wind tunnel tests are required as the method is inviscid and incompressible whereas in actual performance viscous effects will be important. This was done for several of the NREL family of aerofoils to verify the code predictions for this type of aerofoil (Tangler & Somers, 1995). A detailed examination of the testing of two aerofoils showed that at high Re the code had trouble predicting the maximum lift coefficient of an aerofoil designed to have a restrained $c_{l,max}$. The aerofoils models had an aspect ratio of two and were tested over an α range of about -10° to 20° . The Delft wind tunnel (Somers & Tangler, 1996) has an octagonal working section (1800 mm wide by 1250mm tall), very low background turbulence (0.02% at 10m/s and 0.04% at 60 m/s) and allowed testing at a wide range of Re (0.7 to 3.0×10^6).

The Eppler Aerofoil Design and Analysis Code (Somers, 1992) is an example of an inverse design method where the shape is determined from the pressure distribution. Inverse methods have been used on most aerofoils designed computationally for wind turbines although “cut-and-try” techniques are still used in the industry (Fugslang, 2002). Risø National Laboratory in Denmark developed a direct design method, where performance is determined from the aerofoil shape, coupled with an optimisation method (Fugslang, 2002). Risø used similar aerodynamic constraints to NREL, including the design of different aerofoil families for different types of power control. However the optimisation method allowed direct inclusion of a wide range of other constraints, including structural requirements, off-design operation, manufacturing limitations, geometrical agreement to allow smooth taper on the wind turbine blade between aerofoil sections and minimum cost of energy as the most aerodynamic design is not necessarily the most cost efficient (Fugslang & Bak, 2003). The aerofoil sections were tested in the VELUX wind tunnel (Fugslang & Bak, 2003), which is a closed return type wind tunnel with an open test section of $7.5\text{m} \times 7.5\text{m}$ open test section containing a $3.4\text{m} \times 3.4\text{m}$ jet. The turbulence intensity in the section was 1% at the maximum velocity of 40m/s which corresponds to a Re of about 1.6×10^6 for the aerofoil section with an aspect ratio of 3.17. Despite some differences from predicted performance with the wind tunnel results, when the Risø-A1 series was tested on operating wind turbines, it cut blade fatigue loading by up to 15% while producing the same annual energy yield (Fugslang & Bak, 2003).

The difference in the magnitude of lift and drag at some angles of attack (they can differ by a factor of 100); the stall region where small changes can have large effects; effects of the walls of the tunnel both in forming a boundary layer and confining the wake from the aerofoil section; effects of turbulence or acoustic disturbances in the tunnel are some of the phenomena that make wind tunnel testing of aerofoils difficult (Lissaman, 1983). These effects can result in very different results being recorded in different measurement facilities. The measurement technique is also important. As noted earlier, experiments by Schewe (2001) demonstrated that even on nominally two-dimensional section (constant cross section across the tunnel), the flow can be three-dimensional. This can result in different results from local measurements, by pressure taps, to those from global measurements, by force balances.

“The steady coefficients can be different, depending on the location of the pressure transducer, if a three-dimensional state exists. A global force measurement has the disadvantage that wall effects, which can differ at different Reynolds numbers, will be integrated over.” (Schewe, 2001, p.1275)

One parameter that is rarely considered on aerofoil section tests is aspect ratio. This is the ratio of the span of the aerofoil section to its chord length. Aspect ratio is known to be an important experimental variable for the measurements of forces on bluff bodies. A stalled aerofoil is, of course, a bluff body. For a cylinder, Szepessy & Bearman (1992) found that small aspect ratios could substantially increase the fluctuating lift force, the effect being dependent on Re ; Szepessy & Bearman tested over a Re range of 1×10^5 to 1.6×10^6 . In the lower end of the range ($Re < 2 \times 10^5$) decreasing aspect ratio could decrease the fluctuating lift force, whereas at the upper end ($Re = 1.3 \times 10^5$) the smaller aspect ratios could suppress vortex shedding. These results have been associated with the number of counter rotating cells on the back surface of the cylinder. Examples of these cells can be seen in the “upper transition” in Figure 2-13. Another explanation is that decreasing the aspect ratio increases the proportion of the cylinder over which effects from the endplates are felt (Blackburn & Melbourne, 1996).

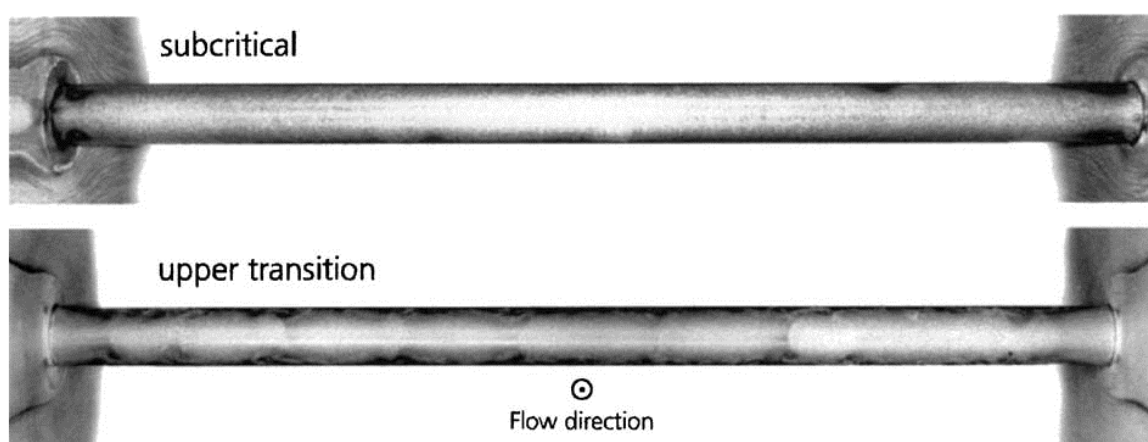


Figure 2-13 - Separation cells can be seen on the downstream side of this cylinder at Re in the “upper transition” range between the range of Re where separation bubbles occur and that where turbulent separation occurs. The subcritical case where separation occurs near the top and bottom of the cylinder is shown to demonstrate that these structures are not an artefact of the visualisation method. From Schewe (2001).

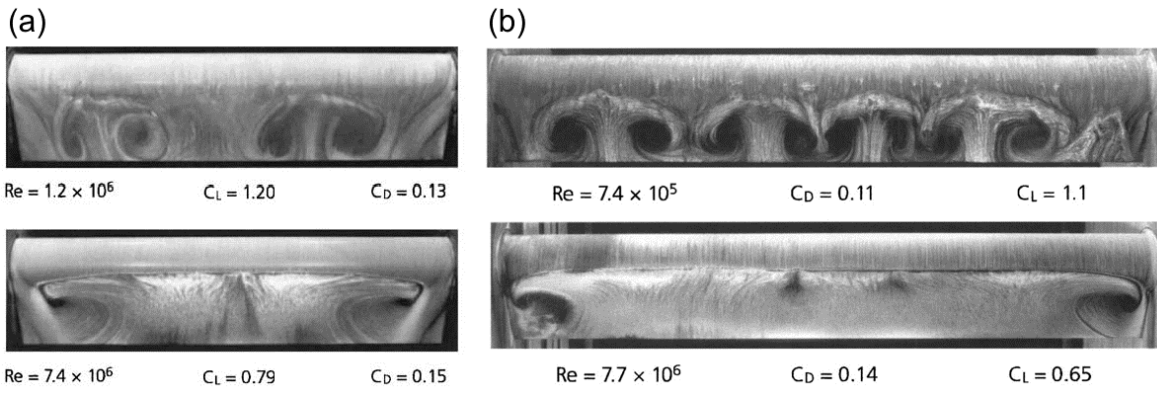


Figure 2-14 – Oil-flow visualisation on an aerofoil section with aspect ratio of 4 (a) and an aspect ratio of 6 (b). The upper photo is during the transition region and the lower photo for turbulent separation in both cases. From Schewe (2001).

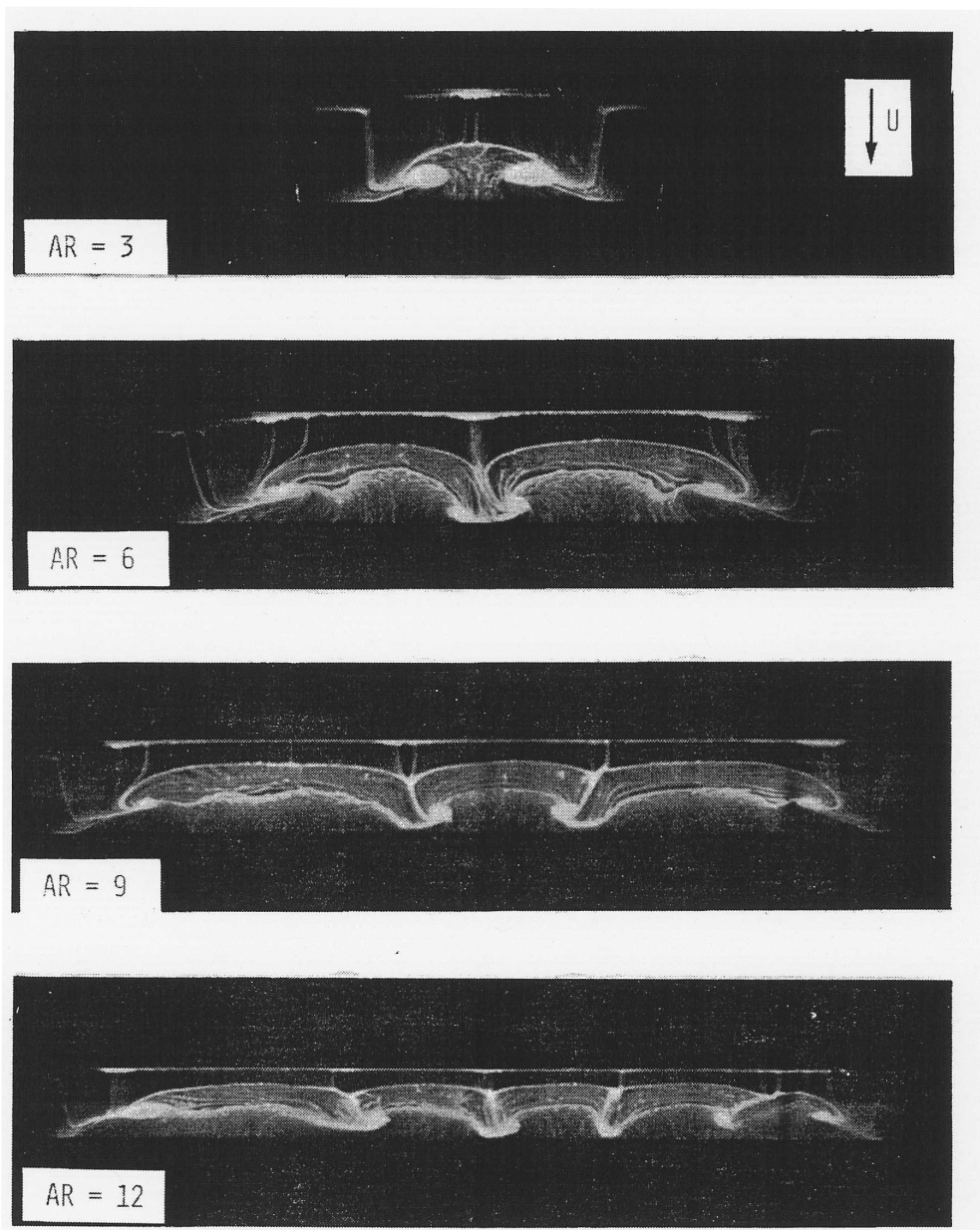


Figure 2-15 - Oil flow patterns on a series of 14% thick Clark Y aerofoil wings of various aspect ratios at $\alpha = 18.4^\circ$ and $Re = 3.85 \times 10^5$. Reproduced from Winkelmann (1982).

Stalling aerofoils have similar cells, called stall cells, mushroom cells, owl eye structures or omega cells, as seen earlier in Figure 2-6. Schewe ran further experiments on a different aerofoil model with an aspect ratio of 6 (his first model had an aspect ratio of 4) to see if the cells were a result of wall effects. The experiments were run at two Re , one during transition and one at a higher Re where the separation is turbulent. Photos of the oil flow visualisations for the two cases at the different aspect ratios are shown in Figure 2-14. Increasing the aspect ratio did not confine the cells to near the wall so Schewe concluded these cells were a feature of this flow regime.

Winkelmann & Barlow (1980) further demonstrated that these structures are not dependent on wall effects by conducting a series of experiments on wing sections (i.e. sharp ends not near the wall of the tunnel). They found more stall cells would develop for higher aspect ratio wings, see Figure 2-15. However as α was increased the cells merged together until only one large cell existed on the wing. At high α only two node points were visible very near the wing tips which looks like the turbulent separation case shown in Figure 2-14. Winkelmann (1982) noted that similar “mushroom” structures have been seen on flat plates, notch back cars, behind bluff objects mounted to a surface, on top of block models, behind a hemi-cylinder model and in shock induced boundary separation. Clearly the number and size of these cells depend on aspect ratio. Therefore reduced aspect ratio would be expected to have a similar effect on the forces measured on a stalled aerofoil as on a cylinder.

Early wind turbine designs used aerofoils with known performance from other applications. The performance prediction codes require knowledge of the aerofoil performance over a wide range of α . Often the data at high α had not been taken as it was not necessary for other applications of the aerofoil and because of worries about the effect of blockage of the wind tunnel on performance. Even recent aerofoil tests of aerofoils designed for use on wind turbines may not include performance data to high α because of concerns about the effect of blockage of the wind tunnel test section on results. In these cases designers will often use flat plate theory to estimate the performance past stall. Assuming the simplified that the plate experiences all the force from the water column immediately upstream, the force exerted on the plate is

$$F = \rho V c \sin(\alpha) \quad \text{Equation 2-7}$$

Resolving the force into lift and drag and normalising by to give the force coefficients results in

$$c_l = 2\sin(\alpha)\cos(\alpha) = \sin(2\alpha), \text{ and} \quad \text{Equation 2-8}$$

$$c_d = 2\sin(\alpha)\sin(\alpha) = 2\sin^2(\alpha) \quad \text{Equation 2-9}$$

A comparison of these equations and the results for the thin, symmetric NACA 0012 aerofoil section are shown in Figure 2-16. The equations give a surprisingly good match for the drag results and for the lift results after the local minimum after stall ($\alpha \geq 20^\circ$). Thicker and/or cambered

aerofoils would not be expected to match as well and in practice, as with all aerofoil section data, the experienced user of the performance prediction method would “massage” the aerofoil section data to best fit the expected performance.

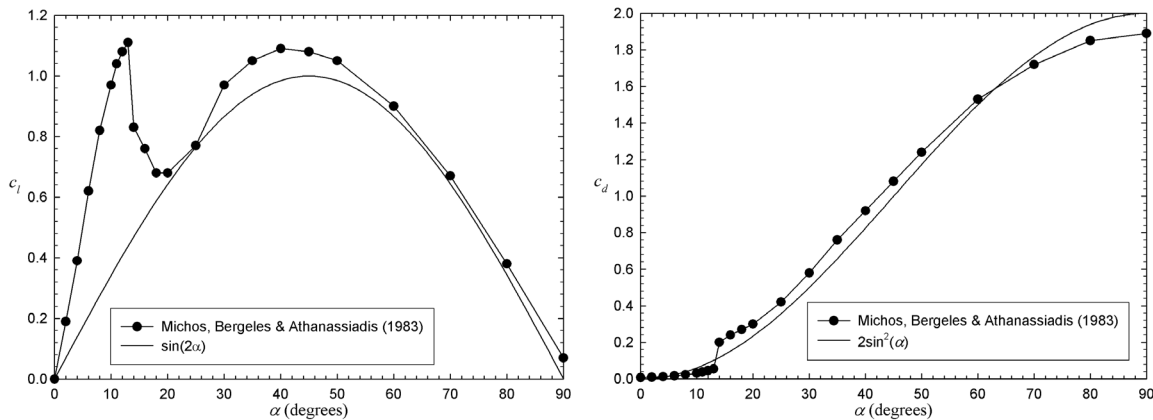


Figure 2-16 - Comparison of the flat plate equations with wind tunnel test results of a NACA0012 aerofoil section by Michos, Bergeles & Athanassiadis (1983).

Michos, Bergeles & Athanassiadis (1983) results for the NACA0012 section shown in Figure 2-16 were taken at a Re of 7.6×10^5 . These measurements were undertaken because there was poor agreement between earlier measurements by other researchers for this aerofoil over the wide range of Re required for VAWT prediction codes. This difference was possibly due to high turbulence levels in the earlier tests. The aspect ratio of the model was 1.7. 16 pressure taps were included on one surface on the tunnel centreline; the complete pressure distribution was formed by taking measurements at both positive and negative α . The data was corrected for blockage by Maskell’s theory. Good agreement was found with balance and integrated pressure measurements of the lift and drag despite the fact that no pressure tap was installed at the trailing edge of the model.

To summarise, in testing an aerofoil section for use in a wind turbine blade the Re is very important. The aspect ratio of the test section can also be important. Performance will obviously differ with aerofoil shape, and thickness can have a significant effect. Before going on to discuss the different wind turbine aerodynamic models it is worth noting that Tangler (2002) found more differences in performance predictions with different aerofoil data sets than between a BEM and a lifting surface, prescribed wake model.

2.3 Aerodynamic Models of Wind Turbine Performance

It is useful to note the characteristics of the various prediction methods to understand what of their features could lead to the failure of prediction known as “delayed stall”. This section will briefly describe the Blade Element Momentum (BEM), vortex wake and Computational Fluid Dynamics (CFD) methods for predicting the aerodynamic performance of wind turbines. It will then discuss the features desirable in new models.

2.3.1 Blade Element Momentum (BEM) Method

The Blade Element Momentum (BEM) method iterates between considering the momentum loss through a streamtube containing the blade element and the aerodynamic performance of the blade element for the given flow conditions (using look-up tables of blade section data) until the results converge. A more detailed description, along with a derivation of the Betz limit and descriptions of the Prandtl tip loss and Glauert corrections, is given in Appendix A for readers who are unfamiliar with this method. Other than when delayed stall is significant, simple BEM models generally give acceptable approximations when the turbine is unyawed and there are no dynamic stall effects (Leishman, 2002). Such models can give good preliminary predictions and considerable insight into basic design parameters (Leishman, 2002).

Engineering models can be added to, or based on, the simple BEM method to attempt to model effects like dynamic stall, which will be discussed in a later section, or induced velocity from the vortex wake. For instance, dynamic inflow modelling considers the lag of the inflow development over the rotor disk to events like changes in rotor thrust or blade pitch. The derivation includes equations from BEM to develop ordinary differential equations to describe the inflow with a time constant (or constants) that represent the dynamic lag. The computational cost of this method is small but it does present the problem of obtaining appropriate time constants. Leishman (2002) gives a more complete description of this method. However, this correction does not embody the physics of the problem and therefore can be inflexible to changes in conditions. Vortex wake methods, which will be considered in the next section, model the effects of the wake directly and so more accurately describe the physical situation, but at the cost of a higher computational overhead.

2.3.2 Vortex Wake Methods

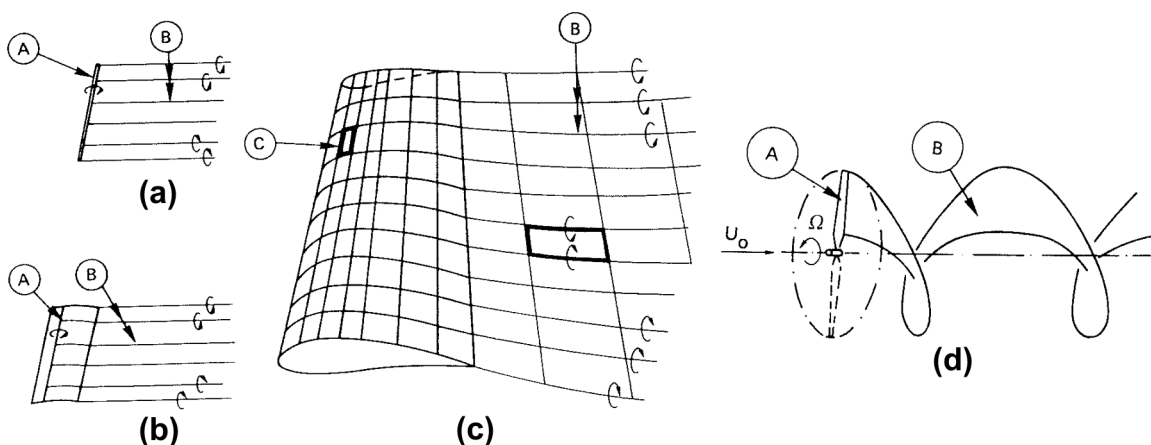


Figure 2-17 - Vortex Theory, (a) lifting-line theory, (b) lifting-surface theory, (c) panel method and (d) rotating blade. A indicates a bound vortex, B the trailing vortex sheet and C a wing contour panel with singularity distribution. From De Vries (1983).

The flow around a finite wing can be modelled in terms of vorticity. The simplest model is lifting-line theory where the wing is modelled as a single bound vortex line and a sheet of vorticity in the wake. The calculation can be simplified by reducing this sheet to a number of discrete vortex lines

as shown in Figure 2-17(a). Other increasingly complex models are lifting surface theory, as shown in Figure 2-17(b), and panel methods, as shown in Figure 2-17(c).

The flow around the wing is assumed to be irrotational except in a thin layer of trailing vorticity. Assuming the boundary conditions that there is no velocity component normal to the wing surface or the vortex sheet, no pressure difference across the vortex sheet and smooth flow at the trailing edge of the wing (de Vries, 1983), the velocity for a fixed wing can be modelled in terms of a perturbation potential, $\phi(x,y,z)$, as

$$V = V_1 + \nabla \phi(x, y, z). \quad \text{Equation 2-10}$$

Vortex wake methods calculate the induced velocity directly from the effect of the vortices trailing the blade (Leishman, 2002). Usually these methods are based on the assumptions of potential flow and that all vorticity is contained in the vortex filaments. The strength of the vortex filaments is determined by the rotor lift distribution. The induced velocity field can be determined by using the Biot-Savart law. For the flow around a HAWT in steady wind with constant rotational speed, Equation 2-10 can be expressed in terms of an unsteady perturbation potential in cylindrical coordinates (x_u, r_u, η_u) which varies with time, t ,

$$V = V_1 + \nabla \phi_u(x_u, r_u, \eta_u, t). \quad \text{Equation 2-11}$$

Relative to the blades, the flow is steady and rotational but the perturbation velocity is still irrotational. The trailing vortex sheet, as shown in Figure 2-17(d), for low perturbation velocities is determined by the velocity of the incoming wind and the rotational speed as shown in the following equation,

$$V_{rel} = V_1 + \Omega \times r + \nabla \phi(x, r, \eta), \quad \text{Equation 2-12}$$

where $\phi = \phi_u$ and $\eta = \eta_u - \Omega t$. However, at large perturbations the vortex sheet will be influenced by the induced velocities and therefore the shape of the wake either has to be assumed or determined by iteration. This will be discussed in more detail later in this section. The effect of the expanding wake also needs to be considered.

The potential flow problem can be solved by modelling the rotor blades and wake by vortices determined by the boundary conditions. Using a lifting-line or lifting-surface model from the vortex system V_{rel} and α at the blade then, using the equation below with C_l from wind tunnel tests, the circulation can be determined,

$$\Gamma = \frac{1}{2} C_l c V_{rel}. \quad \text{Equation 2-13}$$

Panel methods approximate pure potential flow and therefore neglect the effects of viscosity. Semi-empirical methods to approximate the effect of the boundary layer would need to be included for the panel method to work. The other methods get around this problem by using aerofoil section data from wind tunnel tests for their performance data.

The vortex wake can be modelled as either 'prescribed' or 'free' (Leishman, 2002). In a prescribed vortex wake, the position of the vortex elements is specified based on semi-empirical rules derived

from previous experiments and/or free wake code runs (Robison *et al.*, 1995). These methods are only strictly applicable in steady state conditions that closely resemble the conditions under which the experiments used to determine the model were undertaken. These are being surpassed by free wake methods as the power of computers increase. These methods allow the vortex elements to convect downstream with respect to the local velocity field but at the expense of a much more intensive calculation.

The free wake version is also desirable as the wake can and does vary with inflow condition. The experiments of Pederson & Antoniou (1989) found large differences in the wake with windspeed. Pederson & Antoniou (1989) attached smoke grenades to the blades of a 95kW, upwind, stall regulated wind turbine operating in the field to visualise the wake. They found that in low wind speeds (2-4 m/s) the tip vortex was weak (unstable after one revolution, dispersed after three), the flow at 65% span travelled down stream at half the speed of the tip and dispersed quickly and that the expansion of the near wake was uniform. There was very little expansion of the wake in moderate wind speeds (6-8 m/s). The tip vortex was inclined due to the shear layer and was very stable (persisted for five to seven revolutions downstream). In high winds (12-14 m/s), the wake expansion was again very small and the tip vortices travelled very rapidly downstream and dispersed quickly (after three to four revolutions). Higher turbulence and wind shear (seen in one wind direction) caused the tip vortices to dissipate more quickly. The lattice tower caused disruption in the tip vortex and led to its dissipation. However, it did not seem to affect the root vortex which dissipated very quickly (between half and one revolution). This was attributed to the high turbulence from the nacelle and cylindrical blade root. Additionally, free wake methods should be able to model sudden changes such as pitching. Snel & Schepers (1992), using the Tjæreborg 2MW turbine in Denmark, found that suddenly altering the pitch of the blades by 2 degrees caused high torque and blade flapwise bending moments. These loadings were 50% greater than the steady state case predicted by the BEM method.

A typical free vortex system where Lagrangian markers are placed on the vortex filaments leads to the following equation (Leishman, 2002),

$$\frac{\partial \vec{r}(\psi, \zeta)}{\partial \psi} + \frac{\partial \vec{r}(\psi, \zeta)}{\partial \zeta} = \frac{1}{\Omega} \vec{V}(\vec{r}(\psi, \zeta)). \quad \text{Equation 2-14}$$

Here r is the position vector of the filament, ψ is the azimuth and ζ the vortex filament age. Both the left and right hand sides of the equation are discretised leading to a set of finite difference equations that can be solved by numerical integration techniques. The velocity term on the right hand side consists of the freestream velocity, the contributions of other vortex filaments in the wake and from other sources such as turbulence in the wind. Curved vortex segments are usually divided into small straight segments, as shown in Figure 2-18. The induced velocity can then be calculated by repetitive calculation using the Biot-Savart law. This discretisation is second order accurate but there is a relatively high computational cost, although acceleration schemes such as

velocity field interpretation can reduce the computations by an order of magnitude. The formulation of the integration scheme is important and is still a matter of research. Numerical efficiency, accuracy and stability must all be included. It is also necessary to distinguish between physical instabilities in the rotor wakes and numerical disturbances caused by the integration scheme.

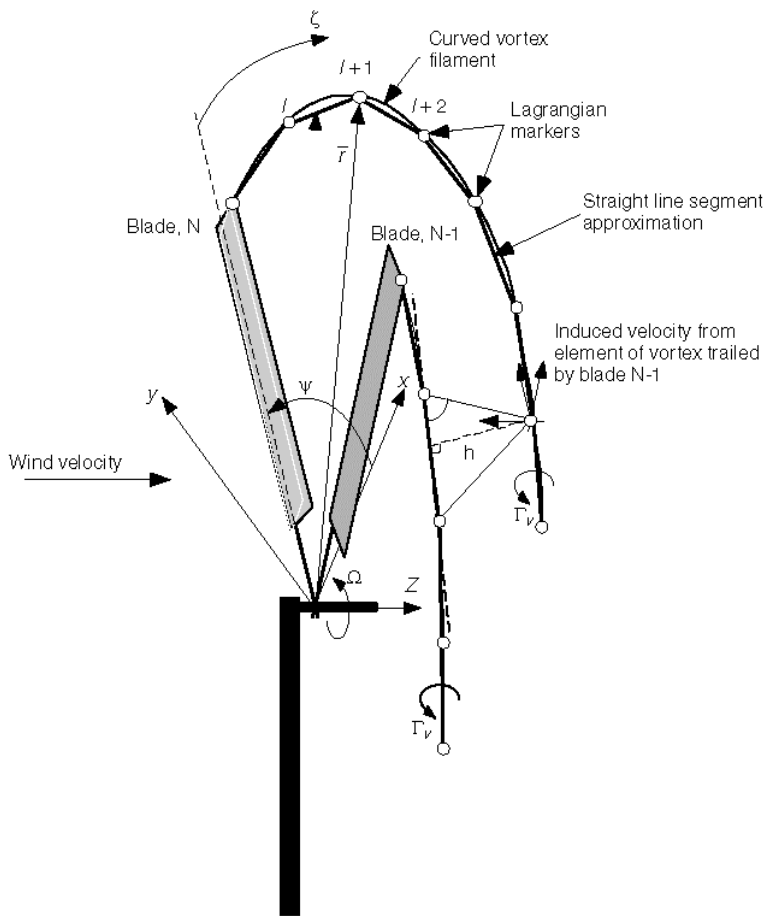


Figure 2-18 - Straight-line Lagrangian discretisation of vortex filaments for a free vortex wake model (Leishman, 2002).

Two main methods of solving the free vortex wake have evolved (Leishman, 2002); time marching methods, which have proved to be more susceptible to instabilities, and relaxation or iterative methods which enforce periodic conditions in the wake. Periodic conditions help to avoid the numerical instabilities but mean the model can only represent steady problems. The modellers also need to include methods of determining the aerodynamic load (this can be done via lookup tables of aerofoil performance as for the BEM model) and the boundary conditions (these can be complicated by blade bending). Other considerations that can be included via semi-empirical rules are stretch of the viscous core, viscous diffusion, tip velocity roll up and the velocity field near the vortex core.

While more complex and computationally expensive, vortex wake methods should be more accurate than BEM methods. They should be able to take into account the effect of the trailing vortices on turbine behaviour.

2.3.3 Computational Fluid Dynamics Models

Computational Fluid Dynamics (CFD) models attempt to solve the discretised Navier-Stokes equations to determine the fluid flow around the turbine and therefore the forces on the blades. CFD approaches are likely to ultimately be the design method of choice (Leishman, 2002). However, CFD modellers encounter problems with computational costs and modelling separated flow, including turbulence modelling and that of the vortices. These methods are yet to be validated sufficiently for the confidence levels necessary for design to be assigned. However, they are currently used to obtain insight into the flow that can be used in more idealised models (for example Chaviaropoulos *et al.*, 2003).

2.3.4 Desirable Characteristics of Future Models

There is a need to improve on the BEM method to improve its physical modelling but retain its relative simplicity and speed that allows for many different wind turbine design options to be easily and quickly compared. There is also considerable work being done on vortex wake methods, which more accurately model the physics of the flow without the extreme computational costs of CFD. It is clearly important to identify the major aerodynamic features of the flows that must be captured for new codes based on either BEM or vortex wake methods to succeed in accurately modelling wind turbine performance. Also, as both of these methods can use aerofoil characteristics obtained from wind tunnel testing, it is important to consider the factors that can affect the aerofoil section results that were discussed in Section 2.2. The next section will detail some important wind turbine tests and some comparisons to performance predictions.

2.4 Testing of Wind Turbines

Wind turbine field data is difficult to analyse as the inflow conditions can only be sparsely measured. Wind tunnel tests of model wind turbines suffer from problems of scaling and duplicating the complex flow encountered in the field. However performance data is necessary for the validation and improvement of aerodynamic performance prediction methods. As discussed in the introduction chapter, experimentally derived performance data has shown delayed stall compared to performance predictions obtained by the commonly used blade element momentum method. This section will examine some general problems with testing. It will then examine some of the most important wind turbine tests to avoid too much repetition in the following section, which will detail many wind turbine tests and what they have shown about the various proposed causes of delayed stall.

2.4.1 Problems in Measurement on Operating Wind Turbines

The method of bins is a way of extracting performance data from variable conditions. Short averages of measurements are allocated to a bin based on the independent parameter of interest. For instance in the common case of determining a power curve, one minute averages say of power

output and wind speed could be determined from field measurements. Each average power measurement would be allocated to a windspeed range bin based on the corresponding average windspeed measurement. The average of the power measurements in the bins would then be determined. Akins (1978) discussed the development of the method of bins for wind turbines with particular emphasis on the determination of power curves. He noted that the density of the air could vary by as much as 15% over a number of hours. As the power available in the wind is a function of density, he suggested that measured torque should be corrected to a standard density. He further noted that that if the measurement point for windspeed was not at hub-height (the standard windspeed measurement position for HAWTs), it should be corrected for vertical wind shear to give a hub-height velocity. Akins compared the measured power output of a VAWT to that calculated from the binned power curve and windspeed frequency based on 0.25s windspeed average from two anemometer locations, one directly above the VAWT and the other on a tower 83m away. Power output was corrected for density variations and windspeed was corrected for vertical wind shear to give windspeed at the centre of the VAWT. There was no detectable difference between measured power and that calculated for the wind speed measured above the VAWT, from the windspeed data measured 83m away the difference was only 0.3%.

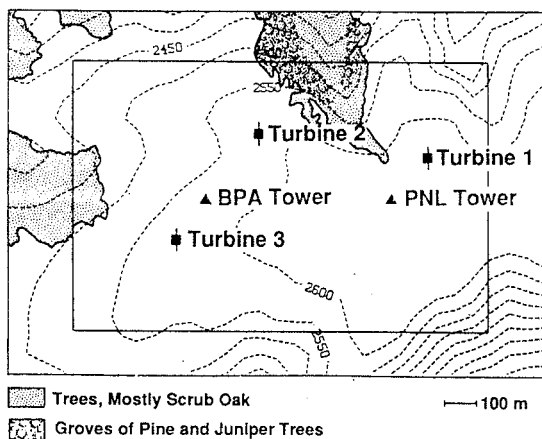


Figure 2-19 - Location of monitoring towers and wind turbines (Elliot & Cadogan, 1990).

The incoming wind speed is necessarily measured away from the wind turbine and, due to the cost of the towers, generally only one meteorological tower is used. The wind measurement can therefore be offset by a varying amount depending on windspeed and direction in space and time from that which the turbine is experiencing. Wind shear can also be a problem if it means that the wind speed at hub height is not indicative of the average wind speed over the turbine. By analysing the performance of three 91m diameter MOD-2 turbines Elliot & Cadogan (1990) were able to assess the effect of turbulence and wind shear on performance. The MOD-2 turbines were an upwind design (Grafton, 1985) so the effect of the tower would not have had an important effect on the results. Data from the turbines and the two meteorological towers, one operated by Bonneville Power Administration (BPA) and the other by Pacific Northwest Laboratories (PNL), were only included if they were not in the wake of another turbine, see Figure 2-19 for relative location of the

towers and wind turbines. They found for all turbines that the power curves were increased by higher turbulence intensity flows, as shown for turbine two in Figure 2-20(a). The data shown in this figure was binned on one minute averages of the wind speed at hub height measured by the BPA tower. Analysis of performance based on the wind direction demonstrated that, while there was an effect due to changes in surface roughness from different approaches, an increase in power with increase in turbulence intensity was apparent even for a single wind direction. Using longer averaging times did not remove the trend.

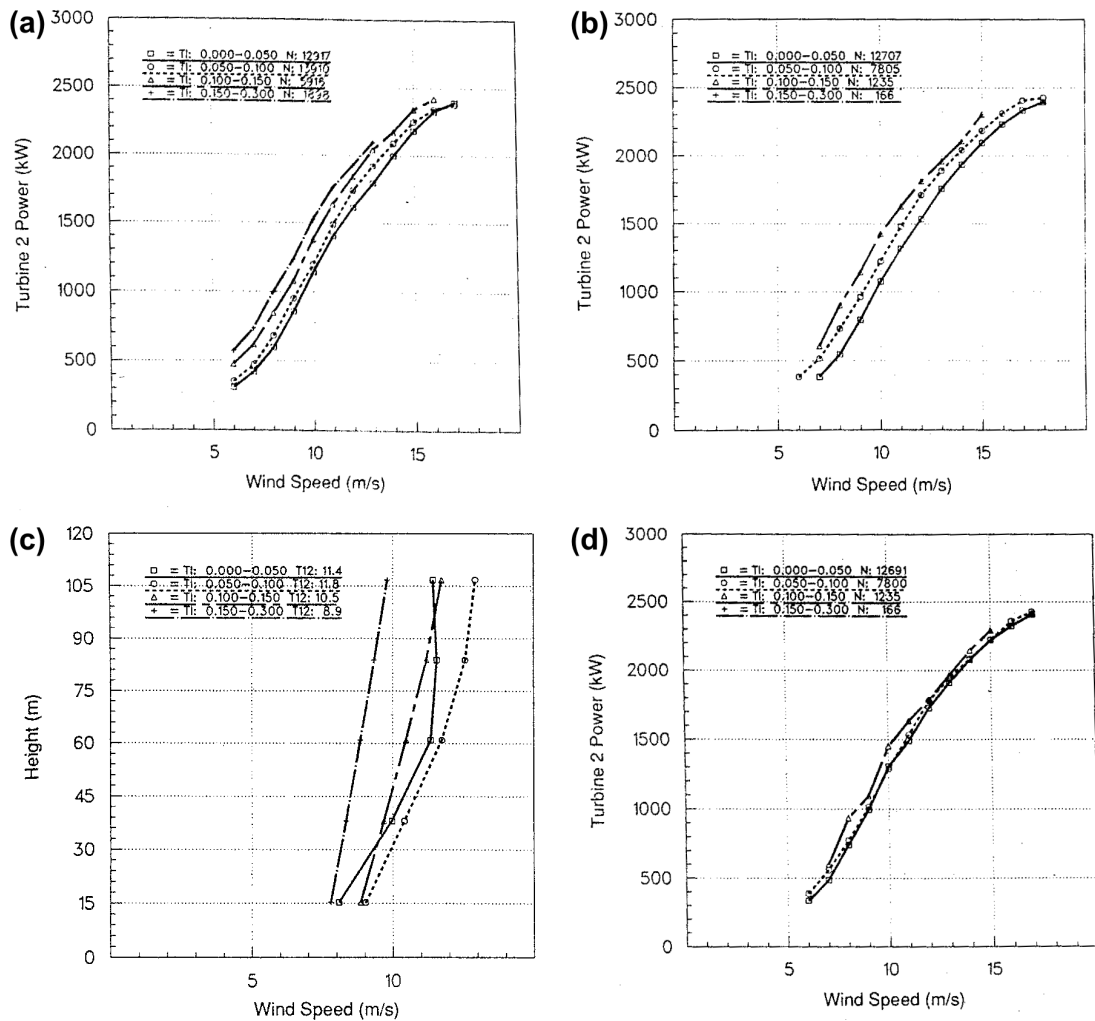


Figure 2-20 - Power curves from one minute averages of a MOD-2 turbine performance based on one minute averages of the velocity at hub height measured by the BPA tower (a) and the PNL tower (b), five minute averages of the wind profile measured by the PNL tower (c) and the power curve based on one minute averages of the rotor area average wind speed from the PNL tower (d). The data is divided into groups based on turbulence intensity (denoted TI in the figures), N is the number of measurements recorded in this range which were binned on wind speed and averaged to give the curves. Figures from Elliot & Cadogan (1990).

To check the effect of the different measurement equipment used by the two towers Elliot & Cadogan (1990) plotted the available performance data based on one minute averages of the hub height wind speed measured by the PNL tower as shown in Figure 2-20(b). This tower was often in the wake of a turbine so there was less data available. The cup and vane system used on the PNL tower measured turbulence intensities that were 10 to 15% lower on average than those measured by the Aerovane on the BPA tower. The authors did not know whether this was an

actual effect or whether it was due to the different measurement equipment. The smaller data set and lower measured turbulence meant there was not enough data in the highest turbulence band to allow it to be plotted for the PNL results; however the increase in power with turbulence intensity was still seen for the other bands. The PNL tower had five sensors spanning the height of the rotor disk. Figure 2-20(c) shows the mean wind profiles based on five minute averages for the different turbulence intensity bands measured by the PNL tower. The turbulence intensity bands are clearly associated with different wind shear profiles. Basing the power curves on one minute averages of the disk-average wind speed, as shown in Figure 2-20(d), removed much of the increase in performance with increasing turbulence intensity, although a smaller effect was still seen. Given these large effects, effects of wind shear must be considered especially at sites with large wind shear or variation in wind shear.

As well as the problems of wind shear Tangler (2002) identified that

“Turbulence-induced errors occur when using the method of bins for measuring power. For each wind speed bin the sum of the wind speeds cubed is greater than the cube of the mean wind speed. This relationship results in the power curve rotating about some mean wind speed value, yielding too high a power value at low wind speeds and too low a value at high wind speeds as stall is encountered.” p. 245.

The effect of smaller cube of the mean windspeed can also be seen in an average by considering the wind to consist of a mean and a fluctuating turbulent component, $u(t)$, which has a zero mean,

$$U = \bar{u} + u(t). \quad \text{Equation 2-15}$$

The cube of this is,

$$U^3 = (\bar{u} + u(t))^3 = \bar{u}^3 + 3\bar{u}^2u(t) + 3\bar{u}u^2(t) + u^3(t), \quad \text{Equation 2-16}$$

and the mean of the wind speed cubed is, cancelling the $u(t)$ terms that average to zero,

$$\overline{U^3} = \overline{\bar{u}^3 + 3\bar{u}u^2(t)} \quad \text{Equation 2-17}$$

This is of course larger than the mean wind speed cubed. Similarly, for short averages assuming measurements are distributed fairly evenly in a wind speed bin, the average of the wind speeds cubed will be larger than the average wind speed cubed. The power available in the wind is proportional to the wind speed cubed. Assuming that the turbine responds immediately to the wind speed fluctuations this would mean that the power in each bin and indeed each measurement would be slightly more than would be predicted from the mean. Although at high wind speeds the blade power is reduced due to stall it is difficult to see how this effect could result in too low a value of power. However the effect is of second order of the windspeed fluctuations and would be small compared to other errors encountered.

The need for data from a variety of different turbines to validate aerodynamic models prompted the International Energy Agency (IEA) to instigate IEA Annex XIV to create a database of performance measurements (Schepers *et al.*, 1997). This project involved two groups from the Netherlands (the Energy Research Foundation (ECN) and the Delft University of Technology

(DUT)), Denmark's Risø National Laboratory, the National Renewable Energy Laboratory (NREL) in the USA and a joint British group (consisting of Imperial College (IC) and the Rutherford Appleton Laboratory (RAL)). All groups ran similar performance tests on their test turbines. This database was extended by IEA Annex XVIII which also included Japan's Mie University and the Greek Centre for Renewable Energy Systems (CRES) but not the joint British group. Test procedures and database setup were reported by Schepers *et al.* (2002). The database of results is freely available on a website hosted by ECN (2002).

Among the problems encountered in setting up the database were differences in the measurements and interpretation of the measurements to determine the equivalent α at the blade (Schepers *et al.*, 2002). The two main measurement devices used to determine α were flow angle flags or multi-hole pressure probes. Flow angle flags consist of a small rigid flag that aligns itself with the local flow and its angular position is measured. They can suffer from oscillations in response to rapid changes in flow conditions, as found by Butterfield (1989a). Pressure probes can have much better dynamic responses provided the sampling rate is high enough and the tubing between the probe and the pressure measurement device is small or the signal is corrected for the tubing response. Both types of probes need to be located close to the blade to record the influence of the wake on the α . However, this close to the blade α will also be influenced by the circulation due to the aerofoil. This is usually corrected by taking measurements of the appropriate aerofoil section in a wind tunnel with the probe attached and therefore getting a relationship between the wind tunnel α and the angle measured by the probe. Assuming this correction is the same in the rotating case allows the determination of the rotating α from probe measurements. Another option used was to estimate from a vortex wake method the influence of the bound vorticity on the probe. This method may compensate for the variation of the bound vorticity along the blade and the resultant shed vorticity that may reduce the influence of the bound circulation seen in the aerofoil section tests. As the probe is upstream of the blade a phase lag may be introduced. An alternative method of determining α used in some experiments was to calculate induced velocity from momentum theory based on the measurements of c_n and c_t and assuming uniform momentum loss over the annular disk. Since the freestream velocity is also measured and the rotational speed known, the effective velocity vector and therefore α can be calculated. The final method used by IEA Annex participants was to determine the stagnation point from the pressure measurements on the rotating blade and match them to that measured in wind tunnel measurements of the aerofoil section. This relies on a unique stagnation point for each α which is not necessarily the case, for example, this was not found for NREL's S809 aerofoil section at high α . A comparison of the various methods showed that in general they agree well in terms of mean values, within a degree for low α and of the order of four degrees for high α . However the differences in standard deviation of α were often in the order of 50%. From this it was concluded that the method based on the measurements of c_n and c_t should not be used in cases where α varies rapidly such as when the turbine is in yaw.

Flow visualisations on an operating HAWT blade using tufts by Butterfield (1989a) found the turbulent wake from the probe holding the flow angle flag caused the separation to move from the mid-chord (where it was either side of the probe) to the trailing edge. However, the flow angle flag was held to the side of this probe before a region that didn't appear to be affected. The effect of probes before the blade was also seen in experiments by Corten (2001). These tests used stall flags, an alternative flow visualisation method to tufts developed by Corten and patented by the ECN (Corten, 2001). Stall flags consist of a small flap covering a reflector. In attached flow the flap is closed but in reversed flow the flap opens, as illustrated in Figure 2-21(a). By illuminating the turbine the reflections from the flags indicate the degree of separation as shown in Figure 2-21(b). This method gives much higher visibility than tufts. Stall flags, like tufts, add roughness to the surface and have the potential to alter the boundary layer flow. They also have the potential to alter the separated flow by providing a barrier to the reversed flow like feathers near the trailing edge of bird wings do as shown in Figure 2-21(c), an effect which has been utilised on gliders to improve performance (Knacke *et al.*, 2004). However wind tunnel surface pressure tests on a 30% thick DU97w300 aerofoil with and without stall flags showed little difference between the two cases over a range of α (Corten, 2001).

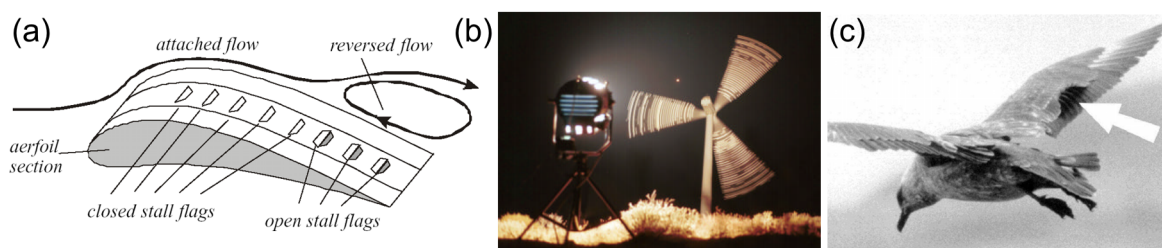


Figure 2-21 - Diagram of the operation of stall flags (a) and stall flags in use on a NEC Micon 700/44 turbine (b), from Corten (2001). Rising of bird feathers to delay separation (c), photo by I. Rechenberg from Knacke *et al.* (2004).

Corten (2001) detailed some field tests of a wind turbine using stall flags. Stall flags were added along 20% and 80% c on one of the blades of an upwind, 300kW, 28m diameter turbine as shown in Figure 2-22(a). The tapered and twisted blades used NACA44xx profiles. In a 12m/s wind, with the turbine operating at 35rpm and no yaw error the position of stall flags was recorded for two revolutions for each of five pitch angles. This resulted in 340 video frames. The number of stall flags open in each video frame was counted. The frames were grouped by this number into three groups. The percentage of time that for any run within the group a stall flag at 20% c at a particular radius was open is given as a probability in Figure 2-22(b), for example the stall flag at a radial position of 12m near the leading edge was open more than 95% of the time in runs where more than 35 stall flags were open on the turbine. Analysis of the effect of pitch was not possible from these figures as the flow conditions were lost in the classification based on number of stall flags showing. The stall flags near the angle of attack probe or connectors for angle of attack probes (the positions of these are shown in Figure 2-22(a) and indicated by dotted lines in Figure 2-22(b)) were more likely to be open than adjacent probes. This was also seen on the trailing edge. The author

attributed this to a severe disturbance of the flow by these connectors and excluded these flags. Figure 2-22(c) and (d) show the probabilities for the leading edge and trailing edge flags respectively excluding these flags. As the plots are for ranges of total number of stall flags open in each frame excluding these flags changes the probabilities at other radial. However, the trends in Figure 2-22(c) and (d) are much smoother trend than Figure 2-22(b) indicating that the flow either side of the probes does not seem to have been significantly effected.

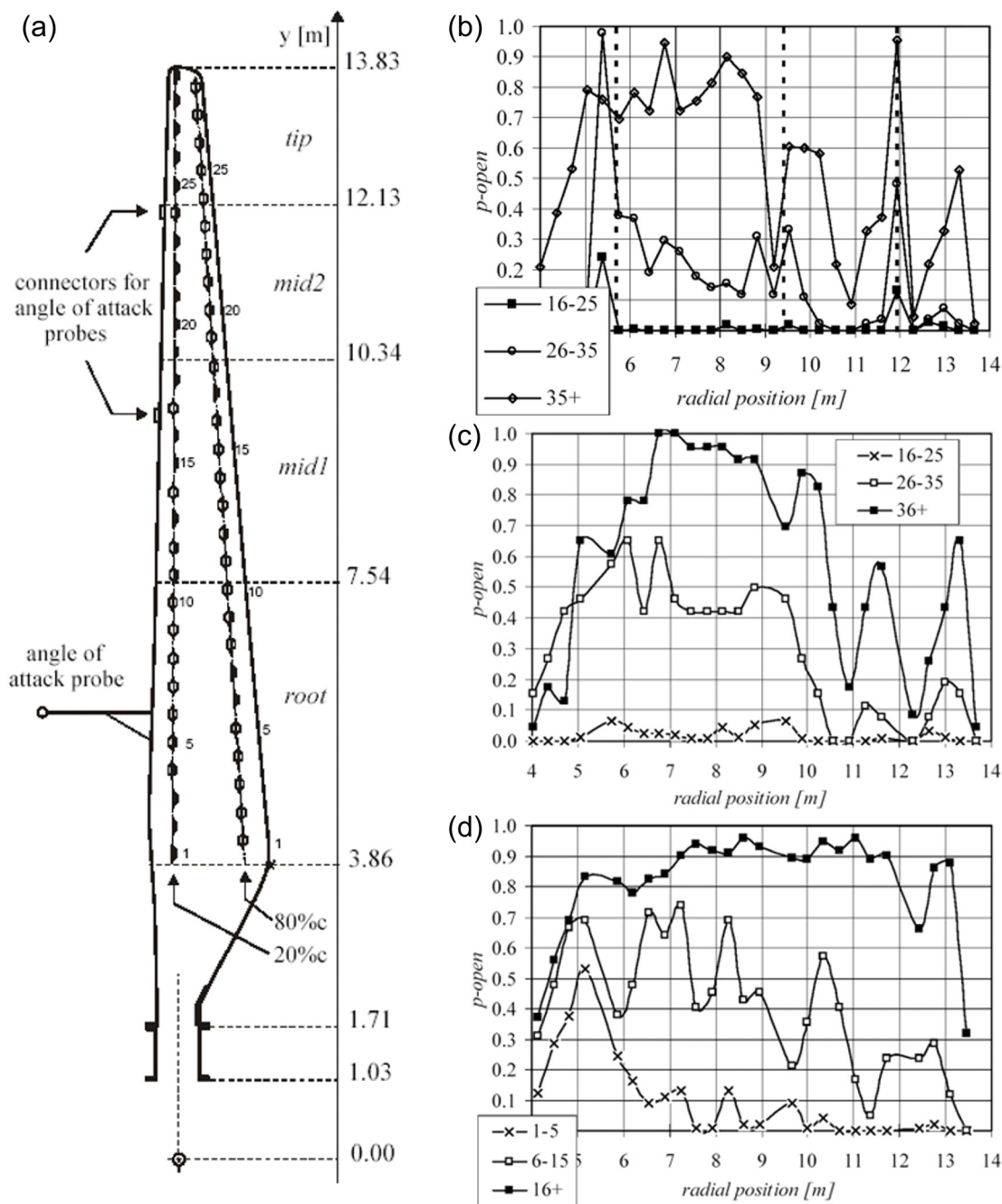


Figure 2-22 – Location of stall flags (a). Probability in runs collected by the number of stalled flags as shown in the legend that a leading edge stall flag is open (b). As for (b) but omitting stall flags influenced by angle of attack probes or connectors (c). As for (c) except for the trailing edge stall flags (d). From Corten (2001).

Both Corten's (2001) and Butterfield's (1989a) visualisation show that the flow can be disturbed by the probe supports (in one case causing separation and in the other attachment). However both

cases also indicated that the flow either side of the disturbance does not seem to be affected. Measurements should therefore be offset from the supports to minimise the effect of any disturbances.

The dynamic pressure ($p_{total} - p_{static}$) is required to determine the coefficient of pressure measured by pressure taps. In wind tunnel tests the pressure coefficient is defined as

$$C_p = \frac{P_{tap} - P_{static}}{P_{total} - P_{static}}. \quad \text{Equation 2-18}$$

However in wind turbine tests an equivalent static pressure does not exist. Instead a reference pressure is used and the total pressure measured from either a Pitot on the blade or estimated from the maximum positive value in the pressure distribution. Comparisons between the Pitot maximum pressure and estimation using a BEM model by NREL found that direct measurement techniques agreed very closely. While the BEM technique showed some differences, the agreement was acceptable and the differences were most likely due to BEM model deficiencies (Schepers *et al.*, 2002).

Flow visualisation on wind turbines has mainly been by surface flow visualisation on the blades or smoke visualisation of the wake. However experiments conducted in 1991 (Smith *et al.*) demonstrated that Particle Imaging Velocimetry (PIV) can be performed on a small wind turbine in a wind tunnel. Images around a blade and in the wake of the turbine were obtained. Unfortunately the 0.9m diameter turbine used had very simple plastic blades and the tip speed was not controlled. The results of this study are therefore of limited applicability but the possibility of the use of this technique in future studies is mentioned for completeness.

When reviewing the evidence from field wind turbine tests consideration should be given to the possible effects of the use of the method of bins, the offset of wind measurements from meteorological towers, wind shear and downwash from probes on measurements. In comparison with aerofoil section tests in wind tunnels possible effects of the method of determining α and the differences in the determination of the pressure coefficient should be considered. However, such measurement difficulties are inherent in obtaining data on a rotating wind turbine blade, especially one operating in fluctuating wind, and care must also be taken not to overestimate these possible problems when considering the data.

2.4.2 Some Wind Turbine Tests

The subsequent sections detail many wind turbine tests and the implication of their results to the proposed causes of delayed stall. However, for conciseness and to serve as an introduction to the next section a few major experiments will be discussed here and referred to subsequently.

Madsen & Christensen (1990) measured the aerodynamic forces on the blade directly using three-component balances instead of the more common method of deriving them from pressure

measurements. This minimised the possible effects caused by the different field and wind tunnel definitions of c_p although they were still present in interpretation of the Pitot measurements. Three 0.5m span segments were floated on balances; segment one was a chord length from the blade root, segment two was at midspan and segment three was at the blade tip. The blade was used on a three-bladed, upwind, stall controlled, 100kW wind turbine which operated at two rotational speeds. The 8.2m long blades were based on NACA 63_n-2nn aerofoil sections. They were both twisted and tapered. A five-hole Pitot tube to measure α was placed just outboard of the midspan segment and about one chord length in front of the leading edge. Madsen (1991) detailed the method used to compute α from the pressures measured by this device. The method was based on wind tunnel tests of the probe mounted on an appropriate aerofoil section and then matching the experimental and predicted power curves to get an appropriate correction for the bound vorticity. Two accelerometers, one placed near the segment closest to the hub and the other close to the midspan segment, were used to measure the flapwise acceleration so the inertia force could be subtracted from the balance measurements.

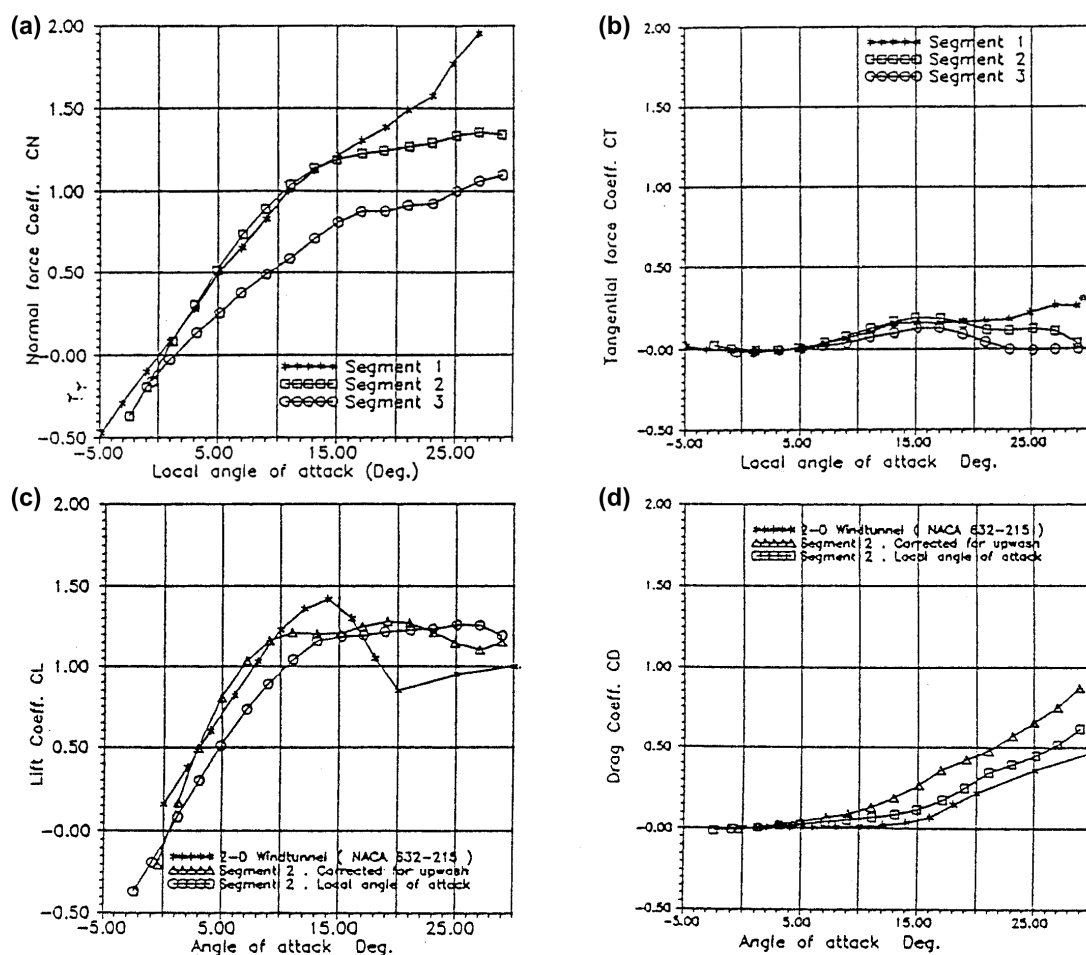


Figure 2-23 - Normal force coefficient (a) and tangential force coefficient (b) versus α measured by five-hole probe. For Segment 2 derived lift (c) and drag (d) coefficients from the normal and tangential coefficients, the same with upwash correction on α and comparison with similar aerofoil. Plots by Madsen & Christensen (1990).

Measurements were taken with non-rotating and rotating blades. In the non-rotating case the rotor was positioned so the tip of instrumented blade was at the highest point. 1Hz data binned on the α

measured by the five-hole probe (which was also corrected for the twist at the blade segments relative to the twist at the probe) is shown in Figure 2-23. In Figure 2-23(a) the C_N at the tip is considerably lower than the other segments, probably due to tip loss effects. The root section did not show stall which the authors suggested might be due to the thickness of the aerofoil (20%) at this span. Similar trends were seen in the C_T data, Figure 2-23(b). An uncertainty of 2° in α was estimated based on experiments of the turbine rotating in still air. It was difficult to zero this test because of the low windspeed compared to normal operating measurements. The C_L and C_D for segment two, the midspan segment, was derived from the C_N and C_T data and as shown in Figure 2-23(c) and (d) respectively. These graphs also show data from tests of a similar aerofoil section in the wind tunnel (the NACA 63₂-215) and curves based on α corrected for upwash by a panel method. The correction for upwash was too strong. While the curves for field and wind tunnel data do not match they are similar at low α but differ at high α , especially in C_L . The segment showed delayed stall compared to 2D wind tunnel data, probably due to turbulent flow and 3D effects, namely finite aspect ratio and spanwise pressure gradients. Also, the drag on the non-rotating blade was increased compared with 2D wind tunnel data. The authors concluded that these effects were of considerable importance to the aerodynamic performance of wind turbine blades.

The wind speed for the non-rotating test averaged 15 m/s, the windspeed range corresponded to a Re range of 0.5 to 0.8×10^6 . When the blades rotated at low rpm $Re = 1.3 \times 10^6$ and at high rpm $Re = 1.7 \times 10^6$. However comparisons of the rotating and non-rotating blades showed the results were similar until the post-stall region. This can be seen in Figure 2-24 where C_N increased by up to 10% for rotating from non-rotating conditions, although the curves showed a similar shape. The authors concluded that rotational effects were of minor importance. However, recent results (Schreck, S. J. & Robinson, 2005) have shown the rotational effects to be moderate at the mid-span location shown in Figure 2-24 and more pronounced inboard.

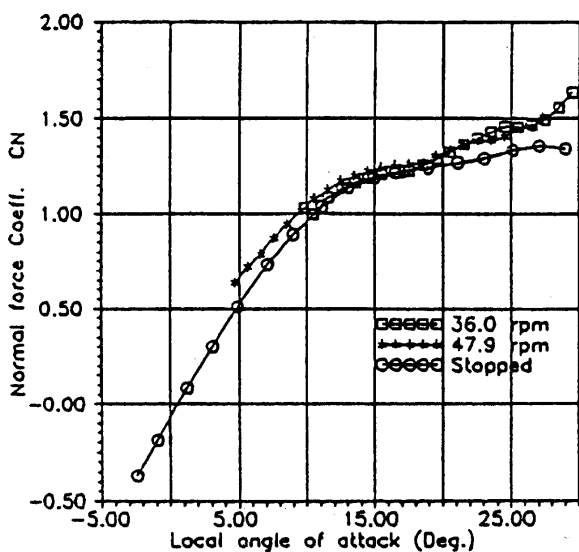


Figure 2-24 - Normal force coefficient for the midspan segment of the blade in rotating and non-rotating conditions (Madsen & Christensen, 1990).

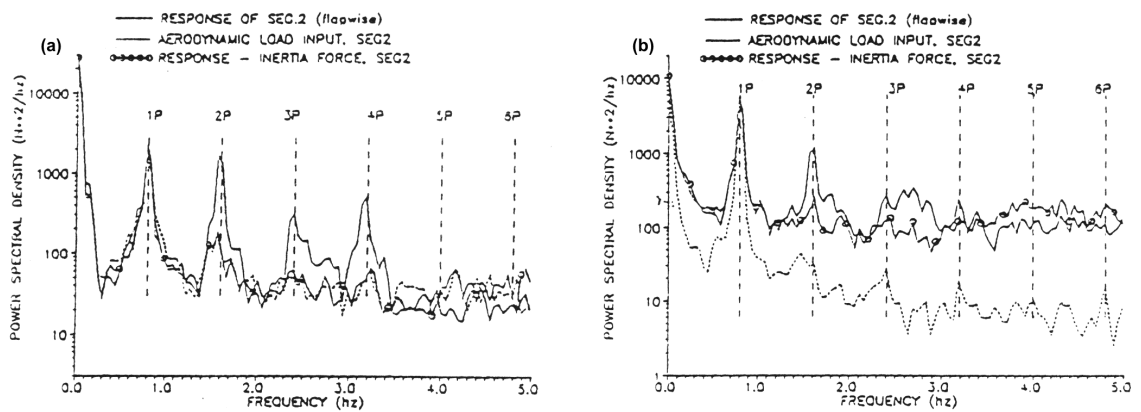


Figure 2-25 – Comparison of power spectra of aerodynamic load input and flapwise response for 8m/s (a) and 18 m/s (b) (Madsen & Christensen, 1990).

For the instantaneous data from the rotating blade in an 8m/s wind, where the blades operate below stall, the power spectra of the total flapwise response and the aerodynamic load with the inertial component subtracted showed excellent agreement as shown in Figure 2-25(a). However in an 18m/s wind, where the blades should have stalled, the standard deviation of aerodynamic load minus the inertial component was about 100% larger than that of the flapwise response, see Figure 2-25(b). The means of the forces were about the same for both wind speeds. After close examination of C_N versus α traces the authors concluded that the increase in the standard deviation was due to stall hysteresis. Madsen & Christensen concluded that the unsteady effects, especially hysteresis loops, were of major importance to aerodynamic performance.

Madsen and Christensen's (1990) wind turbine test showed effects of the tip, turbulence, rotation and stall hysteresis on the blade's performance. More importantly, using mainly the comparison of stationary and rotating blade performance, they were able to assign an importance to the various effects to the performance of the turbine. These effects and their relation to delayed stall will be discussed in the following sections.

A 10m turbine operated by what is now called the NREL National Wind Technology Centre in America has been used for many aerodynamic tests. It was first called the Combined Experiment Rotor because it combined the measurement of loads by strain gauges at every 10% of blade span with pressure measurements using a ring of 32 taps at 80% span, a local flow angle flag and flow visualization using tufts, as described by Butterfield (1989a). Detailed near-field inflow measurements were also made simultaneously by 13 anemometers placed in a vertical plane array one rotor diameter upwind of the turbine. The turbine was a constant rotational speed (74.1 rpm), 10m diameter, rigid hub, downwind, three-bladed design. New blades of constant chord (1.5ft) and thickness ($21\%c$) with zero twist using the well tested S809 aerofoil were used. One of the aims of the instrumentation of this turbine was to investigate the aerodynamic behaviour around stall and to try and assess the relative contributions of turbulence, dynamic stall and spanwise flow to delayed stall (Butterfield, 1989a). Data had to be taken at night to remove the effect of uneven heating on

strain gauges on the black test blade. This made the flow visualization more difficult and tufts in the separated region appeared blurred due to their motion. However at low α the flow was clearly attached and, while the centrifugal force caused slight deflection of the tufts towards the blade tip, there was no significant spanwise flow. For an α of 5° to 10° the boundary layer was separated from around the mid-chord position. The wake from an instrument probe caused attached flow to the trailing edge as mentioned in Section 2.4.1 in the discussion of the effects of probes. The author's sketch of the flow regimes the tufts revealed is shown in Figure 2-26. The author noted that at either side of the thin region where the probe wake caused attached flow the separation boundary location was unchanged which implied that for this flow condition the sections operated independently, arguing against the importance of spanwise flow. No higher α results were available at the time of Butterfield's (1989a) paper. The pressure results revealed the tower wake caused a drop in α , a drop in the leading edge pressure peak and a subsequent drop in lift. Liquid crystal surface visualizations were also undertaken, the results from these will be discussed later in section 2.6.

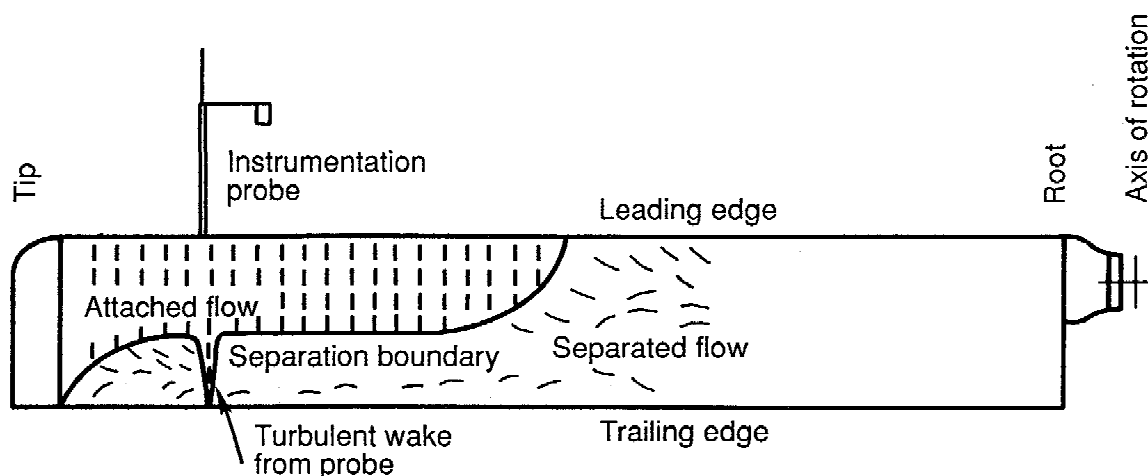


Figure 2-26 - Sketch by Butterfield (1989a) of the flow regimes revealed by tuft visualisation on the combined experiment rotor. Sketch has been altered and simplified to fit the format of this document.

Results at higher α were discussed in a later paper by Butterfield (1989b) that concentrated on the pressure measurements. The pressure measurements could be compared to aerofoil section measurements by the use of a flag type flow angle sensor placed 0.8 chord lengths before the leading edge at 86% span. This sensor also incorporated a total pressure probe at the tip to measure dynamic pressure. The angle of the flag was measured to within 0.1° accuracy. This flow angle sensor was affected by upwash from the blade so wind tunnel tests on the aerofoil section were conducted to give a local flow angle to α conversion. The flow sensor was also subject to damped oscillations, the effect of which was not corrected for in these results. The pressure transducer had a calibration feature that was used while the turbine was running. This was used every five minutes to give results accurate to 2%. The pressure data was not corrected for the frequency effects of the tubing between the pressure taps and the transducers as this effect was found to be insignificant. The wind turbine results were compared to lift curves derived from wind tunnel tests conducted on

the S809 aerofoil section at Delft and Ohio State University (OSU). The differences between these curves (shown in Figure 2-27(a)) were probably due to differences in placement and number of the pressure taps (Butterfield, 1989a). The Delft tests used 108 staggered pressure taps while the OSU tests used 32 taps in a ring on the chord line as was used on the turbine. The later arrangement could cause measurements of a tripped boundary layer due to the roughness introduced by the pressure taps. The wind turbine data for a mean wind speed of 15m/s shown in Figure 2-27(a) was collected at 522 Hz and then block averaged to 10 Hz. The lift coefficient was obtained by integrating the measured pressure coefficients around the aerofoil.

The scatter in the data at high local flow angles in high wind shown in Figure 2-27(a) was attributed to the unsteady inflow and stall hysteresis. The author did not attribute this to dynamic stall because the maximum lift coefficients were generally reduced compared to the wind tunnel data; dynamic stall causes an increase in lift coefficient. The size of the hysteresis loops varied with α and, if the turbine was yawed, they became well defined loops as shown for the azimuth averaged results shown in Figure 2-27(b).

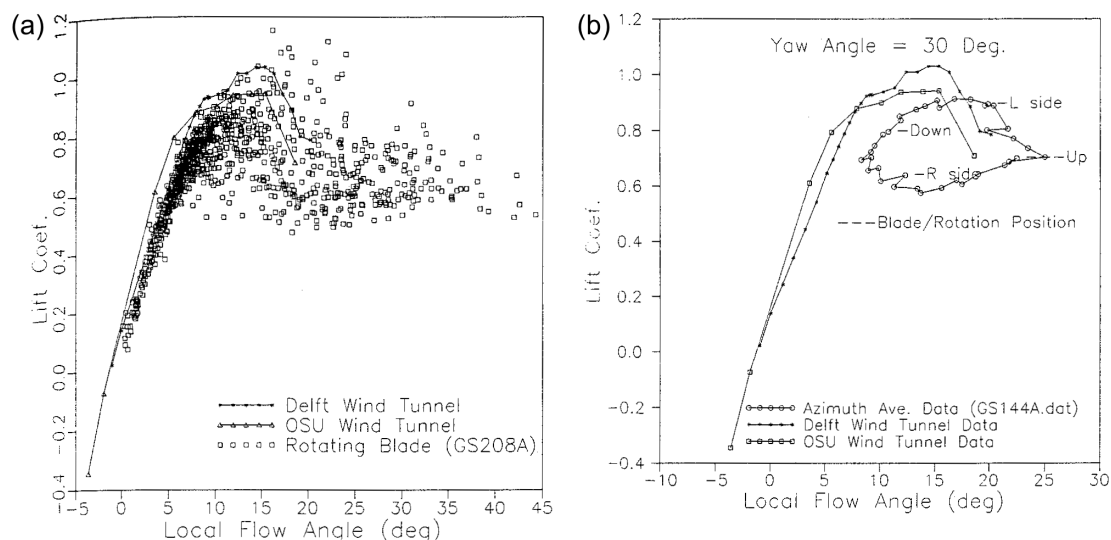


Figure 2-27 - Comparison of free yaw wind turbine operation for a mean wind speed of 15m/s and two aerofoil section performance curves measured from the wind tunnel (a) and azimuth averaged data for fixed yawed operation at 30° (b). Figures from Butterfield (1989b).

Using the Combined Experiment turbine a later experiment by Butterfield, Scott & Musial (1992) again compared the pressure measurements at 80% span and wind tunnel measurements of the S809 aerofoil section. New aerofoil section measurements were used. They were taken in the Colorado State University (CSU) environmental wind tunnel in the 1m x 3.66m (12ft) section. The large cross section allowed testing to high α . The aerofoil section was made from the same mould as the wind turbine blade and had pressure taps in the same chordwise locations. The aerofoil section had a 1m span and 0.46m (1.5ft) chord giving a maximum blockage at $\alpha=90^\circ$ of 12.5%. The turbulence intensity of the tunnel was 1% but most of the energy was at scales much larger than the blade chord. The model also used a Local Flow Angle (LFA) flag as described for the previous experiments; this was again tested to give a transformation between LFA and α . The field

data were binned in 1° increments of α . No tubing correction was applied to the pressure measurements as the CSU data used only mean data and therefore were not effected by the tubing response and the fluctuations in the wind turbine pressure data were less than 20Hz for the tubing used on the wind turbine the response was relatively flat in this region. Comparison of the wind tunnel data, denoted as CSU, and the mean results from the wind turbine bins, denoted HAWT where “sigma” refers to one standard deviation of the data in the bins, are shown in Figure 2-28(a).

The Reynolds number of the wind tunnel tests was 6.5×10^5 , the Reynolds number of the wind turbine blade at 80% span was 8.8×10^5 . Comparison with previous aerofoil section results shown in Figure 2-27 found similar trends but some differences, especially a lower $C_{l,max}$ which may be due to the reduced Re or effects of the presumably coarser mould. However the CSU aerofoil data seemed to match the performance better than that shown in Figure 2-27 and the method of bins made the comparison between the turbine and aerofoil section results easier. In this case it clearly demonstrated that the drop in lift at stall observed in the wind tunnel at α above 16° was not observed when the blade was rotating in the field. The same comparison for the tangential force coefficient is shown in Figure 2-28(b), the even more dramatic influence above stall was significant because it is primarily this force causing the torque and therefore power on a wind turbine. The larger standard deviations above stall are also of interest. However these may be a characteristic of the turbine as Madsen & Christensen (1990) found a slight decrease in standard deviation of the power output in their turbine tests above stall.

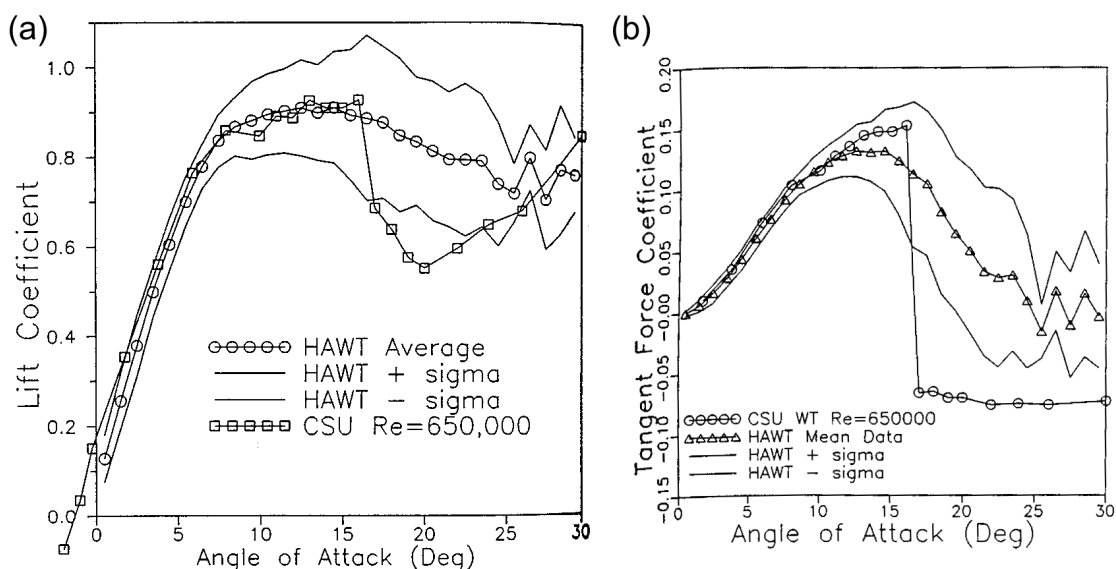


Figure 2-28 - Comparison of blade performance on wind turbine (HAWT) and blade section in wind tunnel (CSU), Lift Coefficient (a) and Tangential Coefficient (b) versus Angle of Attack. Figures from Butterfield, Scott & Musial (1992).

To closely investigate the discrepancy between the wind tunnel and wind turbine C_L and C_T Butterfield, Scott & Musial (1992) compared the C_p measured in the wind tunnel to that measured on the operating wind turbine. They found that at low α the match was very good, for example see Figure 2-29(a). As α was increased to levels below stall the match was poorer, reflected in the increasingly poor match of the C_T and C_L in Figure 2-28, but the general features of the pressure

distributions were still similar. However, for α where the wind tunnel data show the characteristic flat distribution of the stalled aerofoil the wind turbine data still had a distinct leading edge pressure peak, for example see Figure 2-29(b). The suction peak associated with delayed stall persisted up to $\alpha=30^\circ$, as indicated by Figure 2-29(c). There was speculation that the mean profile shown in these figures was the average of two very different profiles. However, the authors argued that the distribution of pressures of the 7.9%*c* pressure tap on the suction side for the α range of 18° to 20° as shown in Figure 2-29(d) appeared to be Gaussian and not bimodal as would be expected for two distinct states, indicating that the mean profile represents a unique flow state.

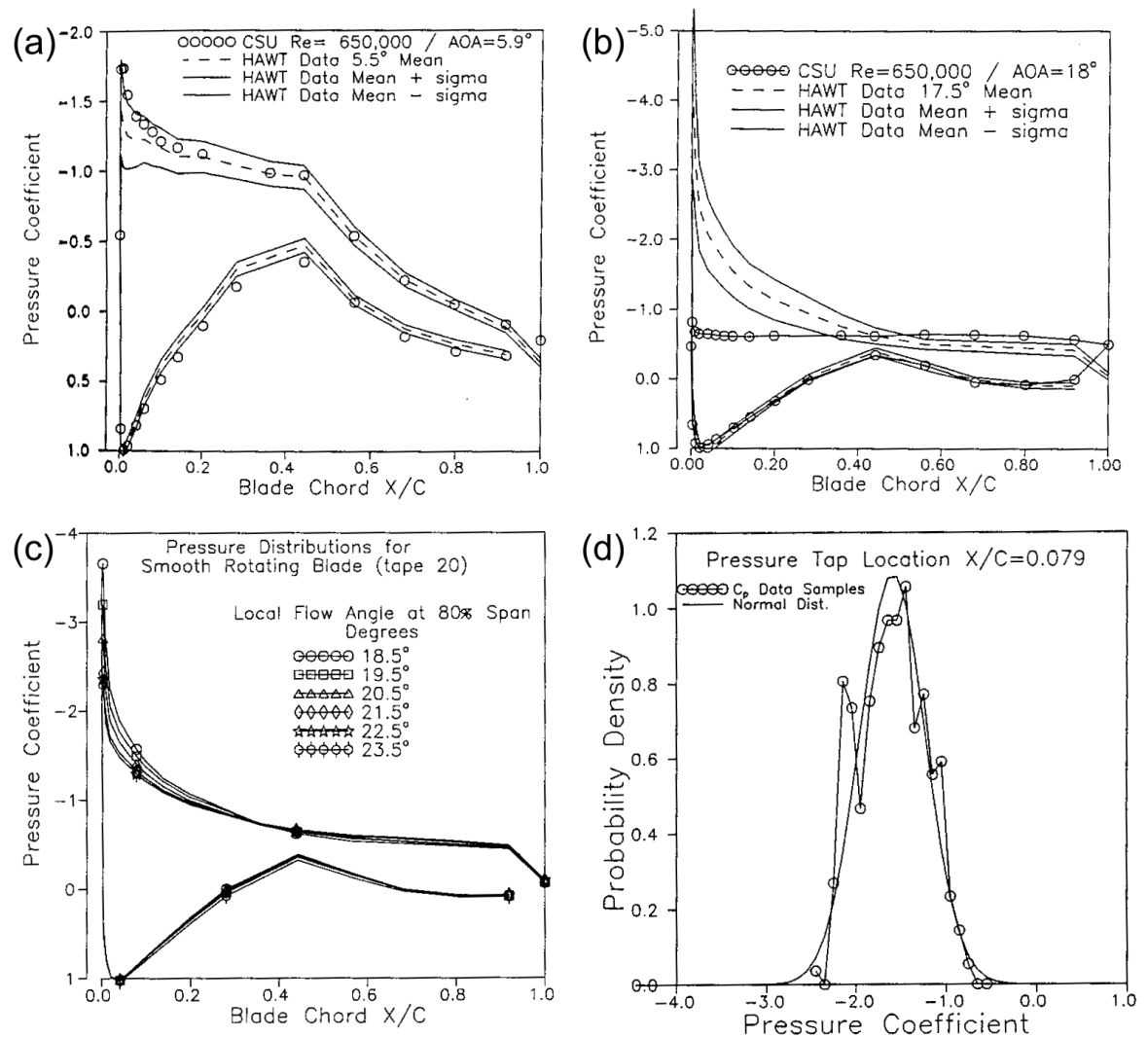


Figure 2-29 - Comparison of pressure coefficients on the HAWT and the aerofoil section in the wind tunnel (CSU) for 5° (a) and 18° (b). Pressure coefficients on the wind turbine for a range of high α (c). Probability distribution at 8%*c* on the suction side of the aerofoil for $\alpha = 18^\circ$ to 20° (d). Figures from Butterfield, Scott & Musial (1992).

Further tests carried out on the combined experiment turbine by Huyer, Simms & Robinson (1996) with added pressure taps giving rings at four locations are described in the later section on dynamic stall. The configuration of the turbine was again changed and the program renamed the Unsteady Aerodynamics Experiment (UAE) as described by Fingersh *et al.* (1995). The turbine blades were replaced with a constant chord, twisted blade set. The new blades included one with five rings of

pressure taps at different span wise locations along with some intermediate taps and five flag α sensors. Five-hole probes could be fitted in place of the flags as an alternative method of determining α . As for the previous measurements the pressure sensors could be calibrated while the turbine was running. The data acquisition system was also upgraded to allow simultaneous monitoring of video, digital and analogue measurements. The duration of these tests allowed the determination of “baseline” cycles for both the untwisted and twisted blade sets (in the later case using α determined by the flags or five-hole probes) as shown in the introduction chapter of this thesis. The data was searched to find three revolutions of the blade where the inflow velocity was fairly constant and the yaw minimal (quantitative definition of this was not provided in the referenced papers). The middle revolution or cycle was averaged to give a baseline measurement. Baseline cycles comprised less than 3% of all data cycles collected (Robinson *et al.*, 1999). In phase V of this project two twisted blades were used, the earlier phases had used three blades.

NREL extended their investigation in 2000 by testing this turbine in the 80 foot \times 120 foot (24.4m \times 36.6m) section of the NASA Ames wind tunnel (the planned experiments were detailed by Simms *et al.*, 1999a, and the completed experiments by Hand *et al.*, 2001). This allowed the performance measurements under controlled conditions in the wind tunnel (which provided a low turbulence flow at known wind speeds, the turbine could be operated at fixed yaw, upwind or downwind). Unfortunately prior to the wind tunnel tests the twisted turbine blade set was destroyed by a failure of the camera support attached to the nacelle. The wind tunnel tests were run with the turbine using a set of two twisted and tapered blades that had only been tested in the field for a limited time at the wrong time of year for high winds to occur at the test site. This meant that there was insufficient data for comparisons between the field and wind tunnel results. Further field tests with the twisted and tapered blades are not currently planned (Schreck, Scott J., 2002b).

One of the most valuable uses of the data from the wind tunnel was as the basis of a blind comparison of wind turbine predictive codes (Simms *et al.*, 2001). The steady inflow of the wind tunnel removed the usual problem of precisely determining the wind conditions in field measurements allowing for a direct comparison between predictions and measurements. Thirty experts using nineteen different types of models tried to predict the performance of the NREL 10 m diameter turbine in a variety of flow conditions. The predictions were run blind to the measurements because many models require expert users to adjust the wind tunnel aerofoil data to make it suitable for the models. The report on this comparison concluded that

“Blind-comparison results were not favorable. Modelers were surprised by the wide variations between their various code predictions. There were also significant deviations from measured wind tunnel results. More disconcerting was the scatter evident under supposedly easy-to-predict typical turbine operating conditions. For the no-yaw, steady-state, no-stall cases, turbine power predictions ranged from 25% to 175% of measured, and blade-bending-force predictions ranged from 85% to 150% of measured. Results at higher wind speeds in stall were especially disappointing - power predictions ranged from 30% to 275% of measured, and blade-bending predictions ranged from 60% to 125% of measured.” (Simms *et al.*, 2001, p. 18).

A 3-D incompressible Navier-Stokes CFD model was consistently the best at predicting aerodynamic forces in cases below and above stall. However the model could only simulate upwind, zero-yaw cases and took days to run a single condition. These are severe restrictions as determination of ultimate lifetime loads requires the calculation of the loading produced by extreme events such as high yaw operation. The modeler also indicated that while the code dealt well with the S809 aerofoil used on this turbine it had been less successful with some other aerofoils.

Later a double issue of the journal *Wind Energy* was devoted to analysis of the database of results from this wind tunnel test (Schreck, Scott J., 2002a). The aims of the investigations were to examine the flow physics around the turbine or to improve the prediction methods. There was a general reluctance to going to full CFD models of turbine behaviour as complexity both in setup and operation of these models limits their usefulness as a design tool. Improvements to existing models were favoured. The limitations in existing prediction methods identified by these studies have also previously been identified as possible causes of delayed stall. For this reason the next section will examine the proposed causes of delayed stall since inclusion of the phenomena that cause delayed stall should improve the prediction methods in other conditions.

2.5 Possible Causes of Delayed Stall

The next sections will discuss the evidence for four possible causes of delayed stall; radial flow in the boundary layer, solidity, dynamic stall and turbulence. It will conclude by explaining why turbulence has been chosen as being in need of further investigation and what questions need to be answered. It is hoped that the results of these investigations can be used in the formulation of improved models of the aerodynamic performance of wind turbines.

2.6 Radial Flow of the Boundary Layer

In his 1945 dissertation Himmelskamp noted stall delay and lift enhancement due to rotation on a fan blade. Himmelskamp attributed this to centrifugal and/or Coriolis forces thinning the boundary layer and inhibiting stall (Schlichting, 1979). Milborrow (1985) proposed that radial flow within the attached boundary layer, as has been seen in some fan flow visualisations, could cause delayed stall on wind turbines.

However a later report by Anderson *et al.* (1987), of which Milborrow was a co-author, found no evidence of radial flow before stall. This study used tufts attached to a 330 kW upwind turbine with a rotor diameter of 26m. The tufts aligned chordwise during attached flow and only indicated radial flow when the flow had separated. By analysing the lift associated with different separation points the lift curve of the turbine could be established. This lift curve showed delayed stall compared with two dimensional wind tunnel data for the GA(W)-1 aerofoil section used.

As discussed in Section 2.4.2 Butterfield's (1989a) experiment on the 10m diameter downwind NREL turbine showed chordwise tuft alignment in the attached boundary layer similar to that seen earlier by Anderson *et al.* (1987) on an upwind machine. Another interesting effect was that the turbulent wake caused by an upstream angle of attack probe caused an attached boundary layer only directly downwind of the probe. Butterfield concluded that

“...at least for this operating condition, adjacent blade sections can be considered to operate independently.” (Butterfield, 1989a)

Similar studies by Brown & Graham (1989), Eggleston & Starcher (1990) and Pederson & Madsen (1998) have consistently shown chord alignment of tufts in the attached boundary layer on different HAWTs. Radial flow within the attached boundary layer has not been seen on operating wind turbines.

Another possible effect of rotation is on the separation bubble. Chaviaropoulos & Hansen (2000) used a quasi-3D Navier-Stokes solver to model a wind turbine. This essentially consisted of the two dimensional form of the incompressible Navier-Stokes equations with some additional weighted radial components. A standard $k-\omega$ turbulence model was used. Predictions at low Reynolds numbers ($Re = 200$) show radial flow in the separation bubble that reduces separation bubble height and therefore increases lift. Similar results (with unsteadiness) were found at high Reynolds numbers ($Re = 2 \times 10^6$). The high Re results were used to “correct” aerofoil section data from wind tunnel tests used in the BEM method predictions. The BEM method using the corrected results overpredicted performance but were more accurate than the earlier BEM method predictions using the unaltered aerofoil section results. A better correction however was achieved with other correction constants.

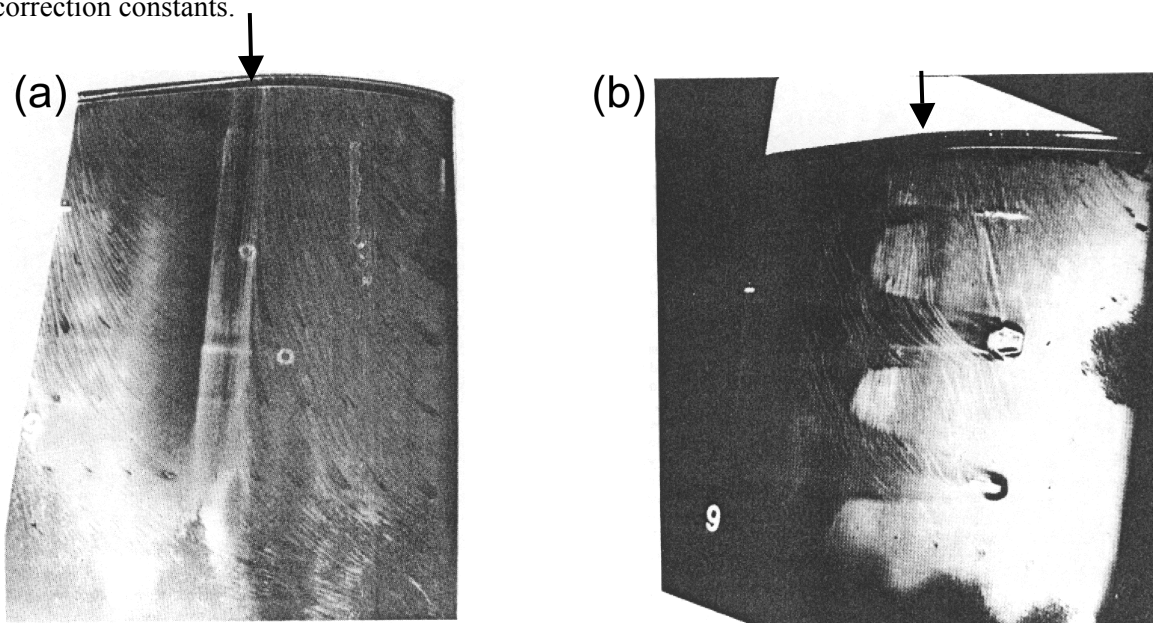


Figure 2-30 - Liquid crystal flow visualisation on the rotating blade (a) and on the rotating blade with protuberances (b). The arrows indicate the location of the separation bubble. The bottom protuberance was a piece of aluminium bent perpendicular to the blade, the middle protuberance, which appears as a hexagon on the picture, was a vortex generator and the top protuberance which appears as a white streak on the photo was a moth impact that occurred shortly after the run began (Butterfield, 1989, p. 254).

Butterfield's 1989 experiment, part of which was mentioned earlier and discussed previously in Section 2.4.2, used liquid crystals to visualise shear stress on the rotating blade surface. A separation bubble had been observed for this aerofoil section in wind tunnel tests. Figure 2-30(a) shows the lines on the surface indicating a separation bubble on the rotating blade surface, the flow in the separation bubble seems to be spanwise. Figure 2-30(b) shows that when small protuberances were added to the blade, the turbulent wakes from these extended chordwise to the trailing edge of the blade. This would suggest spanwise flow exists only in the separation bubble. However, the tests were only carried out for small to moderate angles of attack, which correspond to lower wind speeds and therefore lower Reynolds numbers. They do not demonstrate that spanwise flow in separation bubbles influences stall.

Barnsley & Wellicome (1992) tested a 1.0 m diameter rotor in a wind tunnel. The two-bladed, upwind rotor used NACA 63-02 series aerofoils. The tunnel velocity was kept at 25 m/s and, by varying the load, rotational speeds of 1,000 to 2,000 RPM were achieved. This gave tip speed ratios of between 2.0 and 6.3. The Reynolds number at 70% span was between 150,000 and 450,000. The Reynolds number was limited to this range to avoid supercritical Mach numbers at the tips of the blades (Ma at the tip was between 0.15 and 0.48). Pressure measurements were taken on the upper surface of the wing. These were corrected for the centrifugal pressure component at each tapping. Local hysteresis was found. For 60% span with the blade pitch set at 2° loss of the leading edge suction peak occurred at different rotational speeds over a tip speed ratio of about 0.2 resulting in 20% differences in the normal force for increasing or decreasing rotational speed. The loss of this leading edge suction peak continued gradually towards the root as the rotational speed was increased "...resulting in a range of pressure profiles not normally seen in 2D section behaviour" (p. 14, Barnsley & Wellicome, 1992). The authors attributed this to three dimensional and rotational effects.

Ronsten (1992) used the controlled inflow available in wind tunnel tests to investigate the performance of a 5.35m diameter variable speed turbine in a wind tunnel at CARDC (China Aerodynamic Research and Development Centre). The turbine was tested both rotating and stationary by measuring the pressure at tapping rings at various radial locations. Measurements were corrected for blockage by the wall signature matrix method and also corrected for centrifugal effects. Unfortunately there was no direct measurement of α on the blade. Instead, for the non-rotating case, the equivalent aerofoil section α was found using an iterative process based on lifting line theory. In the rotating case, the equivalent aerofoil section α for each radius was found by estimating the geometric angle α by comparison with the pressures measured at the five pressure taps below the leading edge in the stationary case. Using a linear interpolation the conversion between geometric and equivalent aerofoil section α was found (above 16° , 20° near the hub, the equivalent aerofoil section α was set by lifting line calculations to equal that which would exist if there was no induction on the rotating blade). This conversion was used to find a new dynamic

pressure to scale the pressure coefficients in the rotating case and the process was repeated until α converged. Ronsten found that the coefficient of pressures on the rotating and stationary blades matched well except at high α at 30% span and to a lesser extent at 55% span. Comparison of the rotating blade observations and BEM method calculations found the tip loss correction to be too small and, at small λ , stall did not occur when predicted.

The visualisations mentioned earlier did find the tufts aligned radially in stalled flow. Eggers & Digumarthi (Eggers & Digumarthi) suggested that the radial motion of what they described as “deep stall” flow could increase the power output of wind turbines near stall. They reasoned that centrifugal viscous pumping would lower the pressures in the deep stalled flow. Coriolis forces acting on this spanwise flow would tend to cause positive pressure gradients in the chordwise direction. Using a first order approximation of the spanwise Coriolis and centrifugal forces from the blade-fixed Navier-Stokes equations for incompressible steady flow about thin planar blades, they developed a correction to wind tunnel data. The results of the scaling on surface pressure wind tunnel (CSU) data compared with those taken from the Combined Experiment Rotor (CER) are shown in Figure 2-31. Figure 2-32 shows the effect on power predictions made with the PROPPC code (an early version of the commercial BEM package PROP).

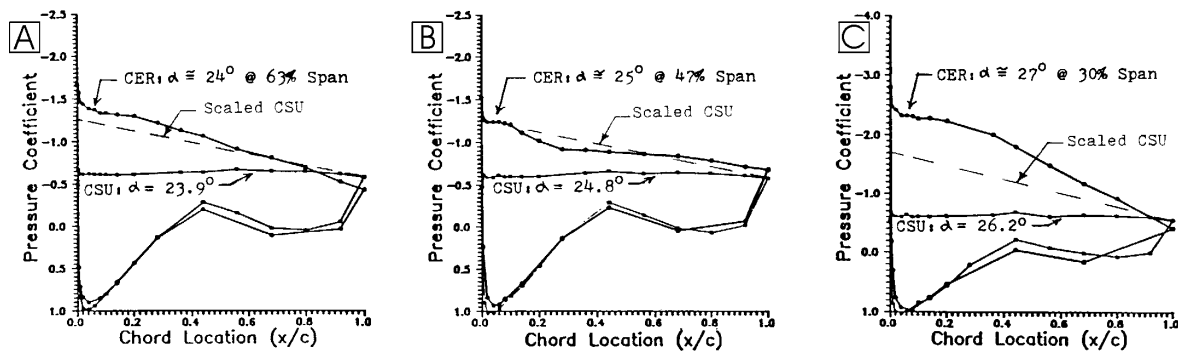


Figure 2-31 - Rotationally scaling of deep stall (Eggers & Digumarthi, 1992, p. 41)

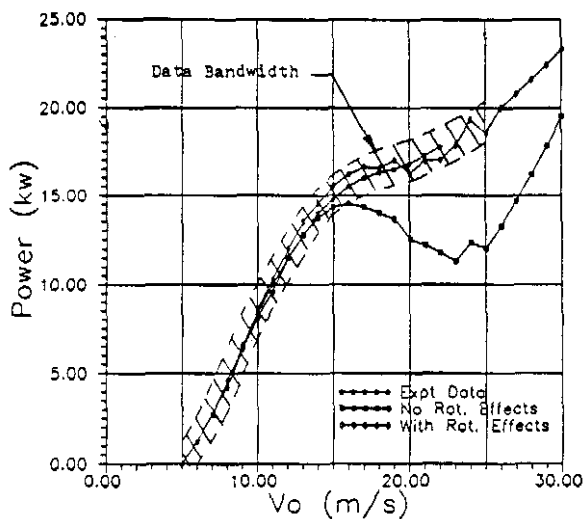


Figure 2-32 – Effect of rotational scaling of performance predictions (Eggers & Digumarthi, 1992, p. 43)

The correction underestimates the effect near the root of the blade (see the 30% span predictions in Figure 2-31). However, this crude correction does improve the predictions markedly as shown in Figure 2-32. It is surprising that these results were not more widely discussed at the time. This may be partly due to later studies which showed yaw and tower shadow have a large effect on this wind turbine (see Section 2.8 on dynamic stall). Other empirical correction methods have been developed by Snel, Houwink & Piers, Tangler & Selig and Corten (according to Schreck, Scott J. & Robinson, 2002).

NREL's UAE 10m diameter wind turbine was operated in the NASA Ames 80ft × 120ft wind tunnel in both rotating and stationary modes to highlight the effect of rotation on performance (Schreck, Scott J. & Robinson, 2002). The data was taken with the stall regulated rotor in a two bladed, upwind, zero cone angle configuration. It was supported on a cylindrical 0.4m diameter tower with the hub at the centre of the tunnel (hub height 12.2m) and a 1.32m rotor overhang. The stationary blade data was taken with the instrumented blade at the 12 o'clock position at windspeeds of 20 and 30m/s. The pitch was increased from -15° to 90° in 5° steps and then decreased in 5° steps back to -15°. At each step the pressure was sampled for 13 seconds. Instantaneous C_p was calculated from tunnel static pressure and the total pressure, which was taken as highest blade surface pressure (on average there was less than 1% error using this method compared to measured tunnel total pressure, the standard deviation was 1.6%). These were integrated to give instantaneous C_n . Instantaneous values were then averaged to give average C_p and C_n . Rotating blade data was taken at a constant rotational speed of 71.6 rpm. The blade pitch was 3° and the windspeed was varied from 5 to 25 m/s in increments of 1 m/s. There was 30s of data taken at each windspeed. Only the data taken while the blade was in the upper half of its rotation (9 to 3 o'clock) was used to avoid any "tower dam" effect.

The blades used a S809 aerofoil and were both twisted and tapered. One blade was instrumented with 22 taps at 5 locations (data from the four inboard locations only were presented). Taps consisted of 0.69mm ID stainless steel tubing connected to pressure transducers less than 0.45m away. They were scanned at 520.8 Hz. Five-hole probes were mounted with their tips 0.8c in front of the blades and 0.04R outboard of each pressure tap row (except for the tapping row closest to the tip, which is not presented, where the probe was mounted 0.04R inboard of the tapping row). The five-hole probes were used to measure the Local Inflow Angle (LFA, the angle of the wind at the probe down from the chord line) and Spanwise Inflow Angle (SFA, the angle across rotor from the chord line, a measurement of the radial flow).

Comparisons of the average normal force coefficients for the parked and rotating cases for different positions along the blade are shown in Figure 2-33. There are clear differences between the parked and rotating cases with rotation causing higher C_n at all LFAs for the two pressure tap rows closest to the hub, while further out the increase appears mainly after stall. The pressure tap row closest to the hub, at 0.30R, showed a reduced slope of the linear part of the C_n curve for parked conditions

where the flow is attached compared with the other tapping rows, see Figure 2-33(a). Schreck & Robinson (2002) suggested that this was due to the vortex trailing from the blade root. The rotating case at 0.3R shows an approximately linear increase in C_n with LFA until 32.6° and has a very different slope to the parked case. Further along the blade at 0.47R the slopes of the linear section of the parked and rotating case curves are similar although the linear section appears to persist to higher LFAs and the C_n values are higher in the rotating than in the parked case, see Figure 2-33(b). Figure 2-33(c) shows that at 0.63R the linear regions of the parked and rotating blade curves are similar until a small drop in C_n in the rotating case. After this point the rotating case exceeds the parked blade C_n for all LFA by as much as 79%. A similar situation was found for 0.80R although the drop in C_n was much larger. There was little difference between results in the parked case for the two windspeeds tested except at 0.80R, Figure 2-33(d), where a hysteresis loop was found.

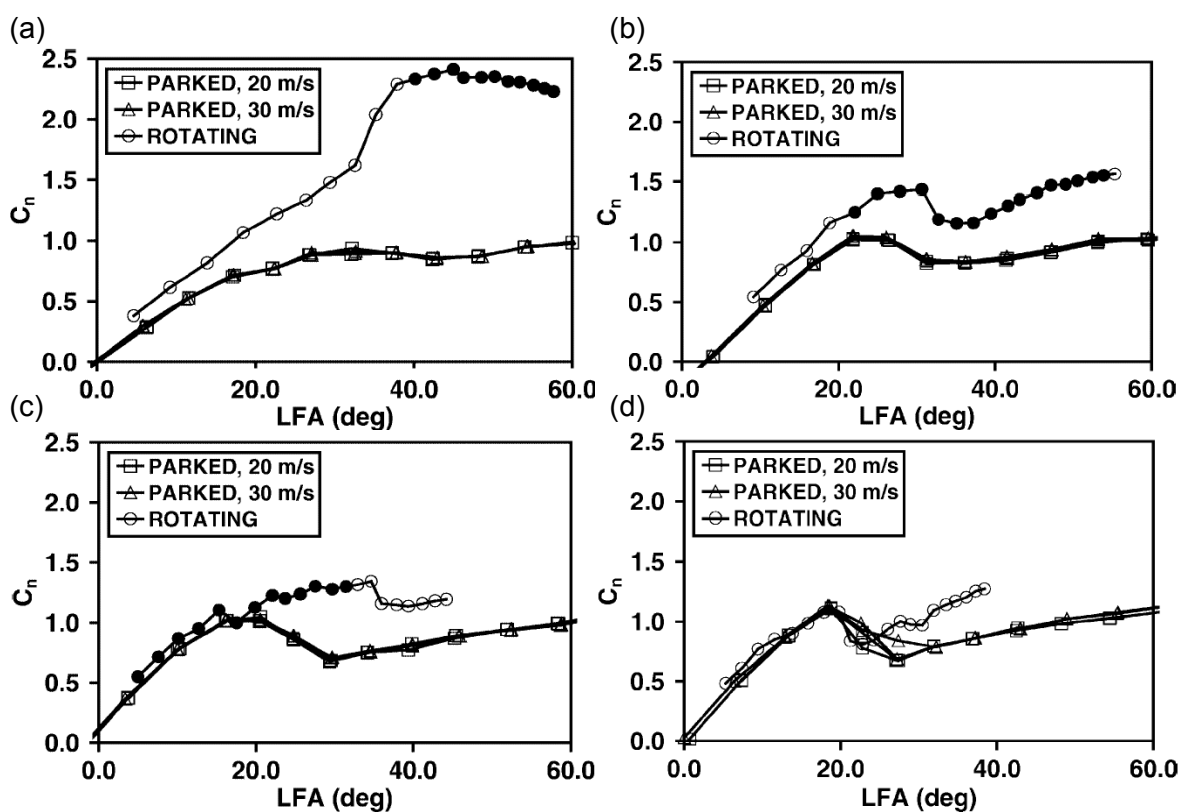


Figure 2-33 - Normal force curves versus local flow angle (LFA) for stationary and rotating blade on the NREL 10m diameter turbine in the NASA Ames wind tunnel at 0.30R (a), 0.47R (b), 0.63R (c) and 0.80R (d). The parked blade data was taken for both increasing and decreasing angles, both cases are plotted. In the rotating case the filled circles indicate data that are in the Reynolds number range of the parked runs. From Schreck & Robinson (2002).

Figure 2-34(a) shows the standard deviations of C_n with LFA. The rise in standard deviations at 0.63R and 0.80R occurred around LFAs where C_n first dropped after the linear increasing region, as shown for the rotating case in Figure 2-33. The standard deviation was 5% to 10% of the mean C_n from which Schreck & Robinson (2002) concluded that the surface pressure enhancement in the rotating case was not associated with prominent unsteady effects. However, a later paper by Schreck & Robinson (2005) showed the standard deviations of the stationary and rotating C_n versus

LFA and showed for $LFA \geq 30^\circ$ the standard deviation was much higher for the rotating case. They identified the separation point reached the leading edge for all rows between $19.9^\circ \leq LFA \leq 26.4^\circ$ and associated this with the steep increase in standard deviation around these LFA. They hypothesised that the increased standard deviation at larger LFA was associated with an unsteady impinging shear layer.

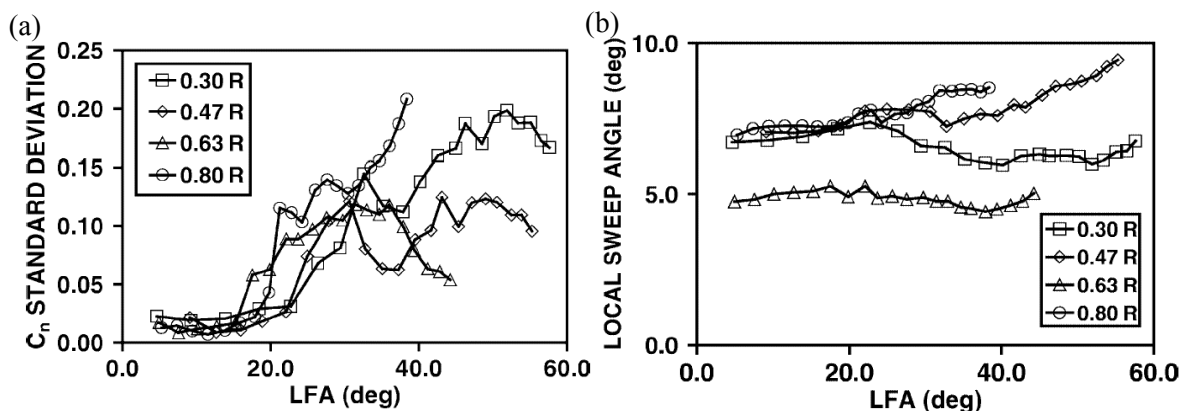


Figure 2-34 – (a) Local flow angle (LFA) versus the standard deviation of the coefficient of normal force (C_n). (b) Local sweep angle (angle of flow along blade) versus the local flow angle (LFA, the angle from chord line). From Schreck & Robinson (2002).

Local sweep angle (LSA) shown in Figure 2-34(b) was less than 9.4° in all cases and varied by less than 2.3° over the entire LFA range. C_n magnitude and the amplification from the rotating case varied significantly in this same range implying that influences other than LSA drove the C_n amplification in the rotating case. Schreck & Robinson (2002) did not provide an explanation why the LFA in the $0.63R$ case was lower than for all the other locations.

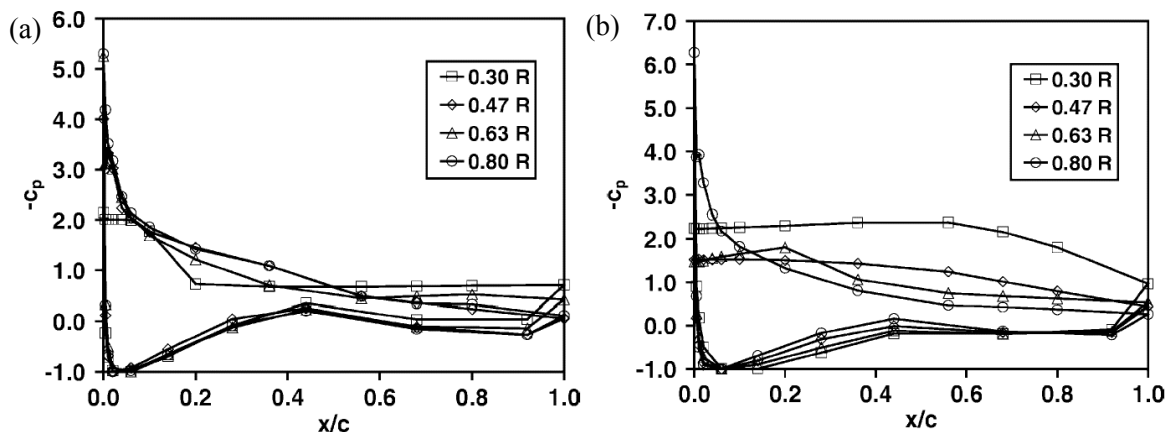


Figure 2-35 - Stall surface pressure distributions for the stationary (a) and rotating blade (b). From Schreck & Robinson (2002).

Figure 2-35(a) shows the average pressure distributions for what Schreck & Robinson (2002) described as “at stall”, which meant at the LFA with the maximum C_n (Schreck, Scott J., 2005). All the curves are similar and the differences were probably mainly due to the coarse changes in pitch (5° steps) causing the comparisons to be between slightly different conditions. All cases show a suction peak near or at the leading edge. The suction peak at $0.30R$ is presumably reduced because of the influence of the vortex from the blade root. The comparison of the average pressure

distributions for the rotating case to the parked case at the same LFA and for each span is shown in Figure 2-35(b). For $0.80R$ the pressure distributions for the parked and rotating case are very similar as would be expected for the similar values of C_n in Figure 2-33(d). The pressure distribution at $0.63R$ features a broad suction peak at $0.2 x/c$ and is somewhere between the pressure distribution at $0.80R$ and that found for the inboard tapping rings. At $0.30R$ and $0.47R$ there was no leading edge suction peak for the rotating case and very small suction surface pressure gradients. This was very different to the stationary profiles and appears to indicate that three-dimensional effects are occurring in the rotating case (Schreck, Scott J. & Robinson, 2002).

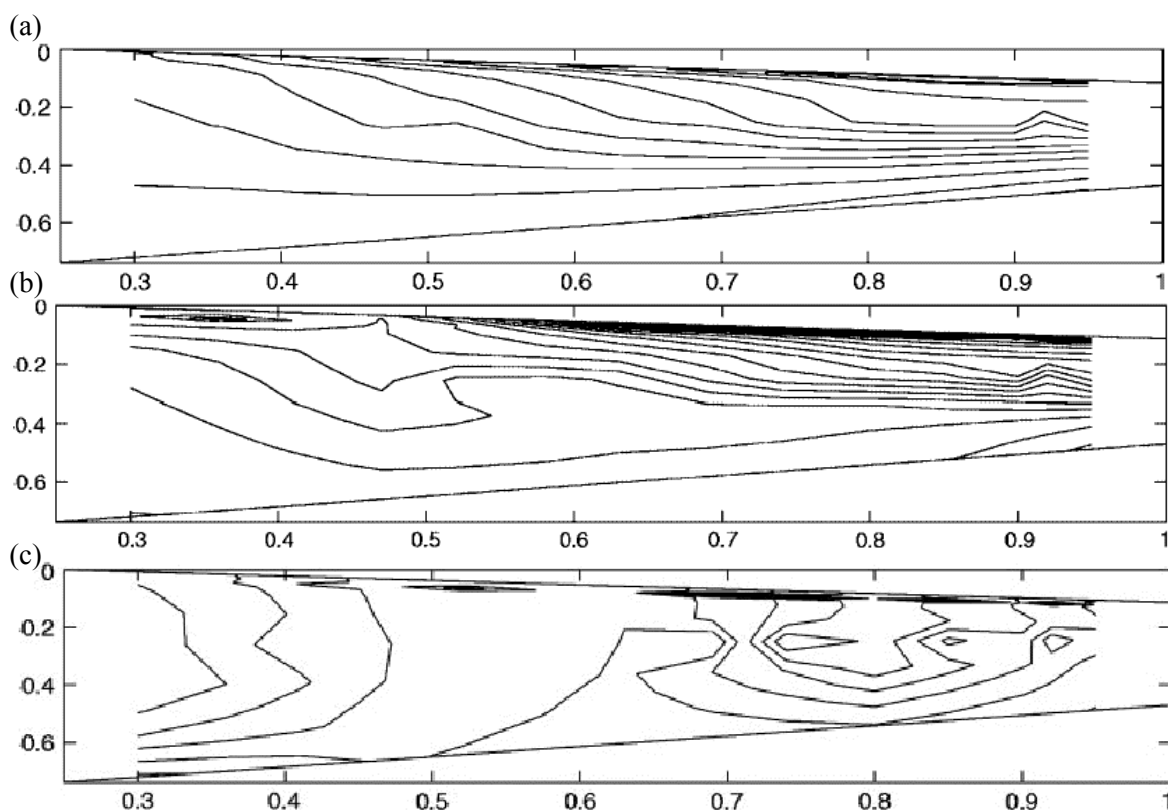


Figure 2-36 – Rotating blade surface pressure topology for $U_\infty = 7$ m/s (a), 10 m/s (b) and 24 m/s (c). These plots were created using linear interpolation between taps. The contour intervals are 100Pa. From Schreck & Robinson (2002).

By linearly interpolating between pressure taps Schreck & Robinson (2002) developed an indication of the pressure contours across the blade. At a low windspeed of 7m/s the flow is fairly uniform radially, as shown in Figure 2-36(a). At this windspeed all the LFAs were below stall for a stationary blade. At a windspeed of 10m/s, Figure 2-36(b), a surface feature at $0.50R$ disrupts the radial contours. Inboard of this feature sharp radial pressure contours have achieved steep gradients near the blades leading edge. Outboard the radial uniformity remains. The LFAs at $0.30R$ and $0.47R$ were ones where the C_n from the rotating blade exceeded stationary blade levels by 40% to 50%. In contrast the LFAs outboard of this feature were at angles where the rotating blade C_n levels for these sections were very close to the corresponding LFAs of the stationary blade. At a windspeed of 24m/s the surface pressures are highly three dimensional, Figure 2-36(c), and the LFA at all sections was one where the rotating C_n exceeded that of the stationary case.

From these results it was concluded that spanwise gradients are associated with higher values of C_n (Schreck, Scott J. & Robinson, 2002).

In summary Schreck & Robinson (2002) were able to conclude from these experiments that rotational influences delay stall and augment blade normal forces especially on the inboard section of the blade. The Re number did not seem to play a part. The augmentation was predominately a steady effect and span wise pressure gradients were associated with this normal force augmentation.

The non-rotating and rotating wind turbine tests of Madsen & Christensen (1990) discussed in Section 2.4.2 came to the conclusion that rotation has a minor effect on performance. This is clearly different to the conclusions reached from the wind tunnel tests of Barnsley & Wellicome (1992), Ronsten (1992) and Schreck & Robinson (2002). One possible explanation for this difference is the effect of yaw, Schreck & Robinson commented that

“Typically, dynamic stall dominates turbine blade flow fields at large to moderate yaw angles. It remains prominent even under low yaw conditions due to inflow turbulence, tower wake and similar effects. However, low yaw angles appreciably attenuate dynamic stall effects, permitting emergence of rotational influences. At zero yaw, rotational effects comprise the principal increment to blade aerodynamic response.” (p. 133, Schreck, Scott J. & Robinson, 2002).

The turbine Madsen & Christensen tested had a yaw drive system (Madsen, 1991) so it would not be expected to operate for long times at yaw. Yaw will be discussed more fully in Section 2.8 on dynamic stall. Another difference between the field and wind tunnel tests is the level of turbulence. Turbulence and 3D effects were given as possible causes for the differences between field and stopped turbine curves Figure 2-23(c). In the wind tunnel the aerofoil began to stall at around 15° and reached a local minimum in lift at 20° . In the field the difference between the normal coefficients in the rotating and non-rotating cases was not apparent until $\alpha \geq 20^\circ$. It seems that rotation for this wind turbine in the field had an effect when the aerofoil was fully stalled. As will be discussed later in Section 2.9 turbulence can prolong the stalling process, acting to delay the progress of the separation point from trailing to leading edge with increasing α . However it is clear from the wind tunnel tests that rotation of the stalled boundary layer can be a cause of increased power from HAWTs.

2.7 Solidity

A small shrouded wind turbine was tested at the outlet of a wind tunnel by Clausen, Piddington & Wood (1987). The shroud consisted of a 260mm diameter pipe that extended 115mm upstream of the turbine. It ensured that the tip losses (the tip clearance was between 1 and 2mm) were minimised, as was the expansion of the streamtube around the turbine. The turbine was held in the pipe by four equally spaced radial supports that were located before the blades; these were shown to have no significant effect on the flow. Performance predictions were made using the BEM

method. The power produced was greater than that calculated when the blade was predicted to be stalled. The authors suggested a number of possible causes of this difference; the Reynolds number of the aerofoil data used by the BEM method was too high, the lower solidity of an actual turbine to what is assumed by the BEM method (BEM is only strictly valid for an infinite number of blades), radial motion within the blade boundary layer or other forms of three dimensionality caused by the vortices at the hub and/or blade tip

The suggestion of solidity as a cause of delayed stall was new and, in another paper in 1987, Wood further investigated the possible affects of solidity on performance. One aspect of finite solidity is that the flow around a blade element will affect the adjacent blade elements below it. Figure 2-37 shows diagrammatically the equivalence between a narrow streamtube around a blade element and an infinite cascade of blade elements. In this situation the flow around any blade element will be affected by the flow around the other blade elements.

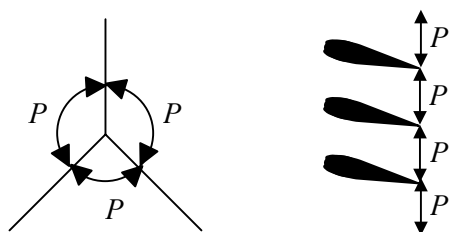


Figure 2-37 - Cascade of blade elements.

The other component of solidity, which Wood (1987) considered more important, was discussed in a paper by Taylor (1963). Taylor attempted to explain the “rotational inflow factor” that designers had found necessary to assume in order to predict the performance of propellers. Using Kelvin’s theorem, that in an inviscid fluid the circulation around any circuit of particles remains constant, he argued that there was little rotation before the blades. For example consider a ring of fluid that was stationary before the propeller acted on it, i.e. there was no circulation. The circulation in this ring will remain zero until affected by viscosity very near the blades. Taylor (1963) quoted the work of Pannel & Jones that showed no rotation two inches in front of the propeller they tested within the limit of the accuracy of their measurements. Taylor suggested that the “rotational inflow factor” was due to the influence of the circulation of the other blades on the blade being considered. Wood (1987) explained this idea in terms of the trailing vorticity. In a later article he explained the point about trailing vorticity further

“Since the conventional mean flow changes direction across the blades, the vorticity trailing from the hubs and tips does not flow in the upstream flow direction. It was argued by Wood that this change in direction, which does not occur for a two-dimensional aerofoil of finite span, could alter the generation of surface vorticity on the blade.” (Clausen & Wood, 1988, p. 307)

Wood tried two computational models to predict these effects; a crude cascade model (1987) and a panel method (1991). Both of these were based on the assumption that the flow did not separate.

Clausen & Wood (1988) analysed the turbine further using phase-locked averaged measurements (based on blade position) of the wake to investigate the tip and hub vortices. Little change in the axial vortices was found between situations where the BEM method produced accurate and inaccurate predictions. However they concluded that the presence of vortices of both rotational directions was not accounted for by the BEM method and these might create a pressure field that delayed separation. The point being made here was that for a 2D blade element the circulation altered the flow before the blade and after the blade. Taylor (1963) showed that for a rotating blade the speed of the flow but not its circulation was altered before the blades. Betz (Glauert, 1963) showed that the maximum efficiency was obtained when the vorticity followed a constant diameter screw surface. These conditions are obviously very different to those encountered by the 2D blade element.

In a series of three papers Ebert & Wood (1997, 1999, 2001) examined the results from X-probe measurements taken in the wake of a small wind turbine. The performance of this turbine had previously been investigated by Clausen, Piddington & Wood (1987), as described earlier in this section. Instead of the shroud used in the earlier experiment the 250mm diameter turbine was supported in a 400mm diameter pipe with the tip of the nacelle level with the outlet of a 250mm “diameter” hexagonal wind tunnel. Due to the high solidity of the turbine, wake measurements were restricted to within two chord lengths of the blades. The authors expected no qualitative change in the wake due to the blockage. This setup also meant the wake was expanding into an essentially quiescent fluid. The measurements were taken by an X-probe driven to a radial position by a traverse that also allowed the probe to be rotated for measurements in other planes. The probe was triggered when the blades were at a certain point and sampling continued for most of a revolution. There was a brief gap to allow processing of the data before sampling was again triggered at the same (arbitrary) point; this meant that there was a gap in the presented measurements. Averages of the measurements taken when the probe was in the same position relative to the blades were presented. Three tip speed ratios (λ) were investigated. The turbulent kinetic energy, k , defined by the following equation,

$$k = \frac{1}{2} \left(\overline{u^2(\theta_*, t)} + \overline{v^2(\theta_*, t)} + \overline{w^2(\theta_*, t)} \right), \quad \text{Equation 2-19}$$

where $u(\theta_*, t)$, $v(\theta_*, t)$ and $w(\theta_*, t)$ are the time dependent components of the velocities in the wake averaged at position θ_* . Figure 2-38 shows k for the turbine operating at $\lambda=2$, normalised by the wind speed squared. The large turbulent energy from the blade can clearly be seen. The highest contour plotted for the $\lambda=2$ case was 0.10. The turbulent kinetic energy for the two other tip speed ratios investigated, four and six, were also plotted in the 1999 paper. However the turbulent kinetic energy in the wake was much less for these tip speed ratios, the maximum contour level was set to 0.03 for these cases. This suggested that the flow had separated from at least some part of the blade. The highest coefficient of power was near a tip speed ratio of four, the wake in this case was

simple with the velocity deficit in the wake almost constant with radius. At a high tip speed ratio of six the coefficient of power was lower. As tip speed ratio increased the tip vortices showed increasing amounts of angular momentum. This trend implied that at runaway, a condition where blade rotate rapidly but the turbine doesn't generate electrical power, the power extracted from the wind is instead being used to counteract the tip vortices.

The turbulence levels in the wake indicate boundary layer separation in the “delayed stall” region. As the cascade and panel methods assume attached flow predictions in this region they will be inaccurate. These results indicate that the increased “delayed stall” lift is due to effects while the blade is at least partially stalled rather than a delay of all separation as Wood models previously assumed.

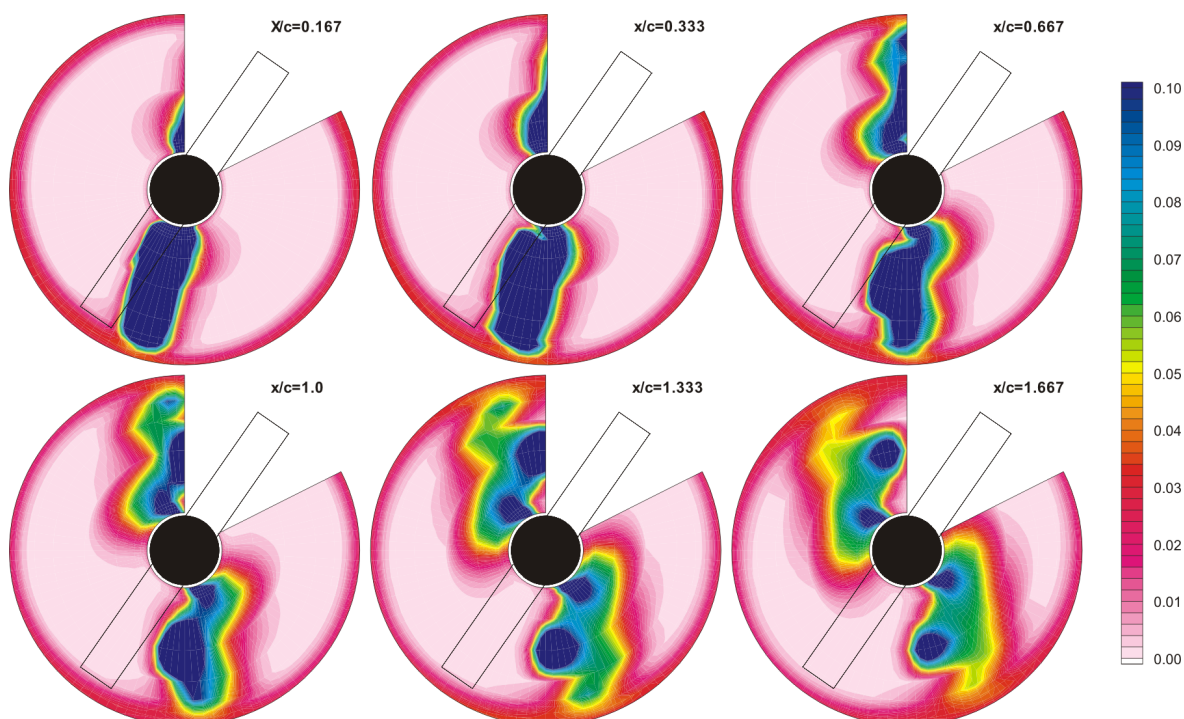


Figure 2-38 – Downstream development of the turbulent kinetic energy normalised by the square of the windspeed at a tip speed ratio of two. From Ebert & Wood (1999), colour version kindly supplied by the authors.

2.8 Dynamic Stall

Dynamic stall was first identified on helicopter rotor blades but has also been observed in rapidly manoeuvring aircraft, jet engine compressor blades, insect wings and wind turbines. In many cases it is the primary limiting factor on performance (Carr, 1988). Dynamic stall is an effect caused by the unsteady motion of the aerofoil relative to the fluid around it (Carr, 1988, McCroskey, 1982). It can delay the α at which stall occurs resulting in increased normal force and pitching moment. These quantities are shown in Figure 2-39(a) for an aerofoil undergoing dynamic stall along with the features of the boundary layer. This shows stall is delayed before the appearance of a vortex whose travel over the surface of the aerofoil causes the peaks in normal force and pitching moment. The effect is hysteretic; as α is reduced the forces are much lower than when it is increased.

Hydrogen bubble visualisations on a pitching aerofoil in water give a picture of the vortex movement, see Figure 2-39(b). The sequence of events shown in Figure 2-39(a) is typical of virtually all aerofoils in fully developed dynamic stall (Carr, 1988). A high effective pitching rate is needed for dynamic stall to be observed (McCroskey, 1982). If the effective angle of attack is not far beyond the point of static stall, a small hysteresis loop will develop. At higher α , the flow will be dominated by a viscous zone which is of the order of the aerofoil thickness, and, at higher α again, the vortex dominated flow shown in Figure 2-39 is seen (McCroskey, 1982).

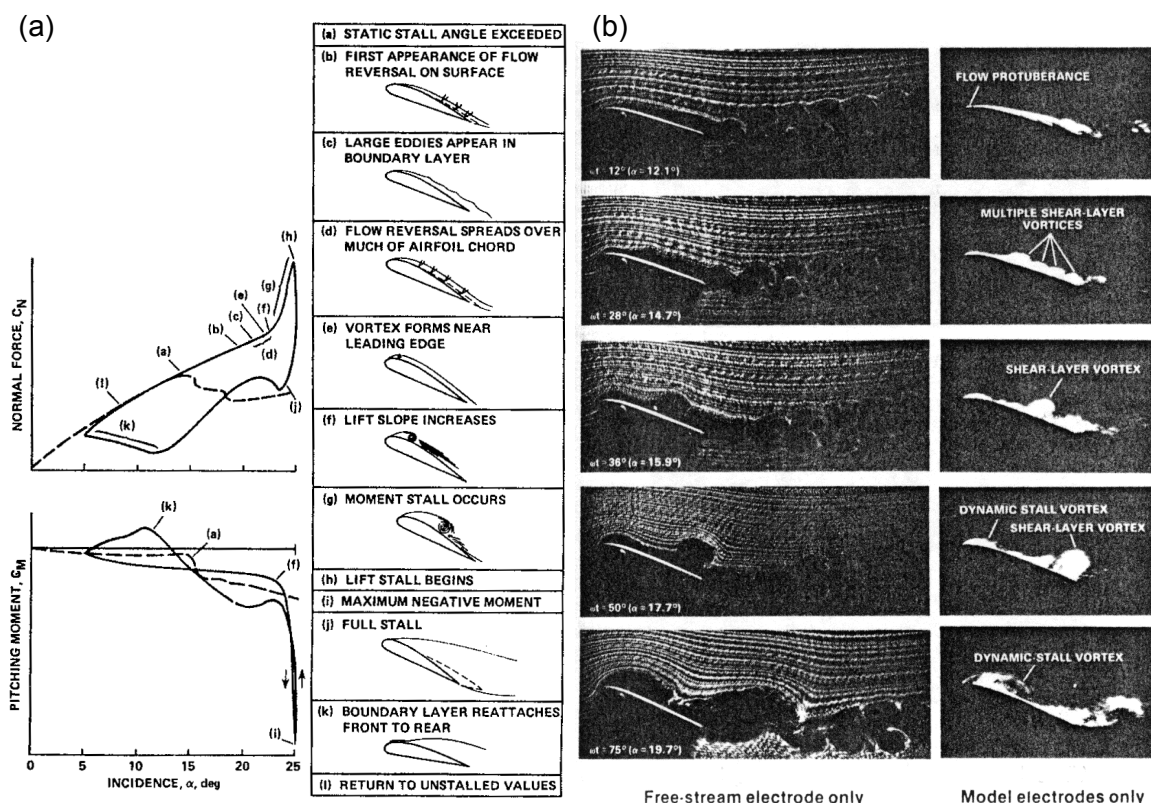


Figure 2-39 - Dynamic stall events on a NACA 0012 aerofoil oscillated in pitch (a) (Carr, 1988). Hydrogen bubble visualisations of a modified NACA 0012 aerofoil oscillating in pitch (b) (McAlister & Carr, 1979).

Dynamic stall occurs when the aerofoil's motion takes the effective α above the static stall α (Leishman, 2002). Note that significant unsteady effects can be produced on aerofoils undergoing unsteady motion even when operating with fully attached flow (Leishman, 2002). Predicting these effects (despite the apparent simplicity compared with stalled flow) is a non-trivial problem. The unsteadiness can be quantified in terms of the reduced frequency, k .

$$k = \frac{\Omega c}{2 V_{rel}}, \quad \text{Equation 2-20}$$

where Ω is a characteristic physical frequency of the flow. k values tend to be higher on the inboard part of the blade (lower values of V_{rel}).

Dynamic stall can be caused by pitching, plunging or in-plane oscillations (Carr, 1988). Pitching obviously changes α rapidly. Inviscid modelling can relate plunging to an equivalent pitching motion. However, viscous effects mean that the quantitative flow of the plunging motion can be

quite different from the inviscid equivalent α pitching motion (Carr, 1988). The general features of dynamic stall seen for pitching remain similar for plunging, as shown in the visualisation of plunging dynamic stall in Figure 2-40. In-plane oscillation is equivalent to changes in free stream velocity. Saxena, Fejer & Morkovin (1978) used this equivalence in their investigation by fluctuating the free-stream velocity in a wind tunnel over a NACA 0012 aerofoil section. They found that the flow was quasi-steady for α below where the aerofoil stalls in steady flow or for low frequencies of oscillation. However, for high frequencies of oscillation at α above where stall occurs in steady flow, the average normal force was 60% greater than the mean and there were large periodic excursions from the mean. Pitching, plunging or in-plane oscillations could occur on an operating wind turbine. For instance a wind gust could be equivalent to an in-plane motion or it could be considered to alter α and cause pitching motion. This is true for all turbines,

"Even for pitch controlled turbines, because of changing wind and flow directions, unsteady aerodynamic and stall effects can still be important contributors to the blade airloads and wind turbine performance." p. 86 (Leishman, 2002)

The dynamic stall motions and possible equivalent wind turbine motions are given in Table 2-1. The effects of dynamic stall could also be similar to blade vortex interactions from other sources, for example in the wake of other turbines (Horner *et al.*, 1995).

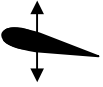
Dynamic Stall Motion	Pitching	In-plane oscillation	Plunging
Diagram			
Possible Equivalent Wind Turbine Motions	Yaw Wind Shear In-plane gusts	Wind Gusts Tower Shadow	Blade teetering or elastic bending

Table 2-1 – Dynamic stall motions and possible equivalent wind turbine events. Some motions from Leishman (2002).

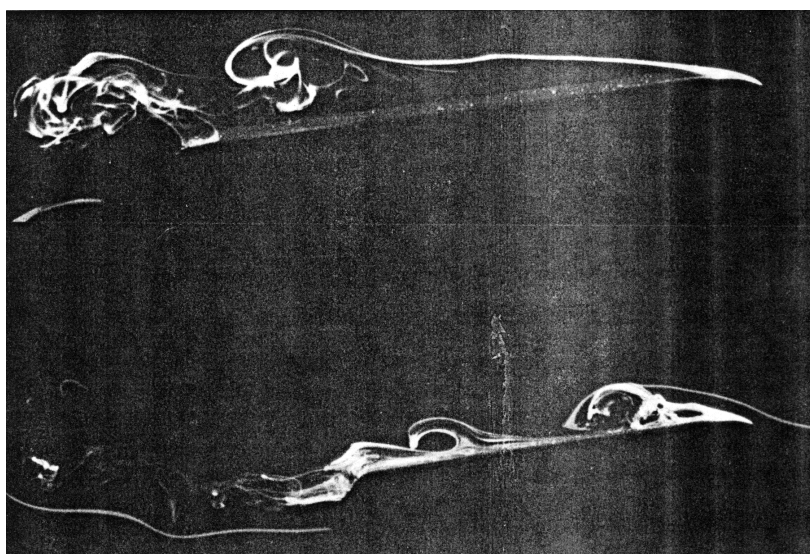


Figure 2-40 – Dye visualisation of steady (top) and unsteady separation (lower) caused by plunging on a flat plat at $\alpha = 6^\circ$ (Foussekis, Fraunié & Béguier, 1992).

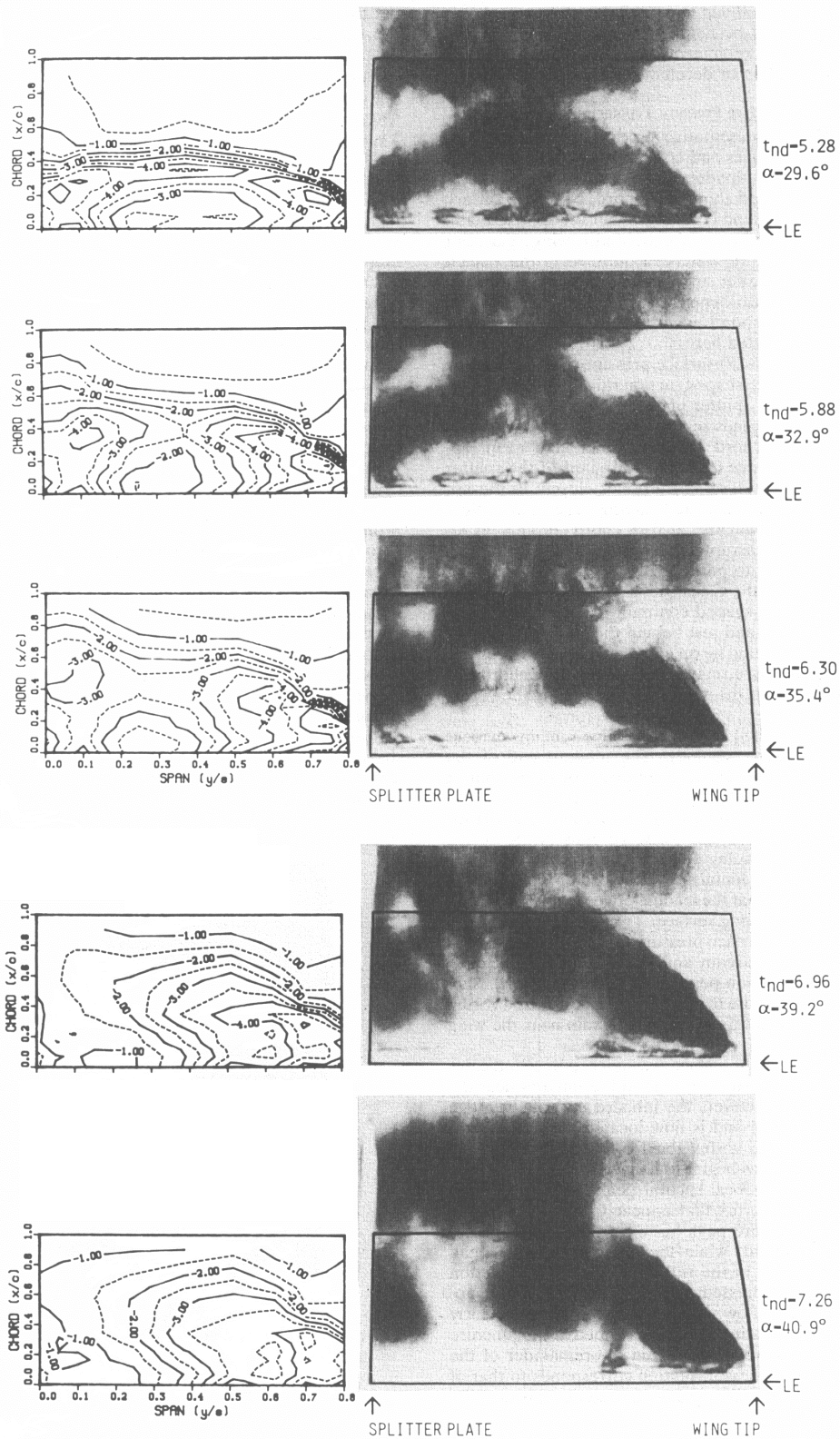


Figure 2-41 - Contour lines of surface pressure taken from pressure tap measurements in a wind tunnel and dye visualisations from a different model, where the dye was injected via a slot in the leading edge of the model, taken in a water tunnel. Both models had a constant chord of 15.24cm, a NACA 0015 aerofoil cross-section and were 29.10cm long with a square tip. The pitch rate was 0.1 around a pitch axis at 0.33c. The non-dimensional time is indicated by t_{nd} and the leading edge of the model by LE. From Schreck & Helin (1994).

Dynamic stall is a complex phenomenon. Parameters which can have a significant effect and which are likely to affect wind turbines include the type of motion, aerofoil shape, pitch axis,

amplitude of oscillation, mean α , frequency of oscillation, Mach number (for Mach numbers greater than 0.2), Reynolds number and three dimensional effects (McCroskey, 1982, Carr, 1988). Three-dimensional effects on a wind turbine could be caused by coning or by effects from the wing tip or hub on the adjacent sections of blade. For the assumption of incompressible effects to be valid, not only must the local Mach number based on velocity be low (which it generally is for wind turbines), but the frequency of the unsteady effects must be small with respect to the sonic velocity, a (Leishman, 2002). This leads to the requirement

$$\omega c / a \ll 1. \quad \text{Equation 2-21}$$

Using the definition of Mach number (M) and k this can be expressed as

$$Mk \ll 1. \quad \text{Equation 2-22}$$

This condition may be exceeded in situations with high k , for example the case of tower shadow. The modelling of compressible effects is substantially more complex and computationally intensive. However capturing the incompressible effects is, in many cases, more important (Leishman, 2002).

Both McCroskey's and Carr's reviews noted that the effect of wind tunnel walls on measurements needed further investigation. Surface pressure measurements have shown that unsteady spanwise distributions are augmented near the wingtip and that unsteady flows near the wing-wall junction can be just as complex (Schreck, Scott J. & Helin, 1994). Schreck and Helin's (1994) investigation of the pitching of a short wing, see Figure 2-41, showed the vortex is deformed via slower convection near the wall and tip. The vortex shape resembles the stall cells seen on the surface of static aerofoils during stall. The shape of the wing tip is also known to influence the vortex formation (Wagner, 1987).

Eggleston & Starcher (1990) performed tuft and oil-flow visualisation on three downwind turbines (rotor downwind of the tower), the 7.3 m diameter Enertech 21-5, the 9.9 m diameter Carter 25 and the 13.5 m diameter Enertech 44-50. They found that the flows were different on all turbines, but the smallest turbine showed reattachment due to the tower shadow. The work showed that the tower wake can affect the aerodynamic performance significantly in some turbines.

To investigate whether dynamic stall occurs on an operating wind turbine, the NREL 10 m diameter turbine was run as a three bladed, downwind rotor, at a constant RPM (72 RPM) and with rectangular untwisted NREL S809 section blades of 0.457 m chord (Shipley, Miller & Robinson, 1995). Rows of pressure tappings were placed at 30%, 47%, 63% and 80% span and the angle of attack at each section was measured by flag probes. Dynamic stall events were identified to have occurred when the minimum measured pressure coefficient at one of these rows of pressure taps was less than -10 (a conservative definition). Dynamic stall occurred mostly at 30% span but this may have been due to this section of the blade being far more likely to have angles of attack above stall. Interestingly, when data away from the tower shadow was considered, the number of occurrences was far closer at each span location and 30% span no longer had the maximum number

of occurrences. The range of wind speeds and yaw angles for which the angle of attack for part of the cycle would exceed the stall angle were calculated. Using a contour plot of dynamic stall occurrences on a yaw angle versus wind speed axis they found that, for 47%, 63% and 80% span, stall mostly occurs in the areas expected (see Figure 2-42A). Removing data from near the tower shadow showed dynamic stall primarily occurred for yaw angles greater than 15° or less than -15° (see Figure 2-42B). For 30% span, dynamic stall seems to occur at higher inflow velocities than predicted. The authors attributed this to either “delayed stall” or to a larger effect of tower shadow perhaps due to higher turbulence generated by the nacelle and tower.

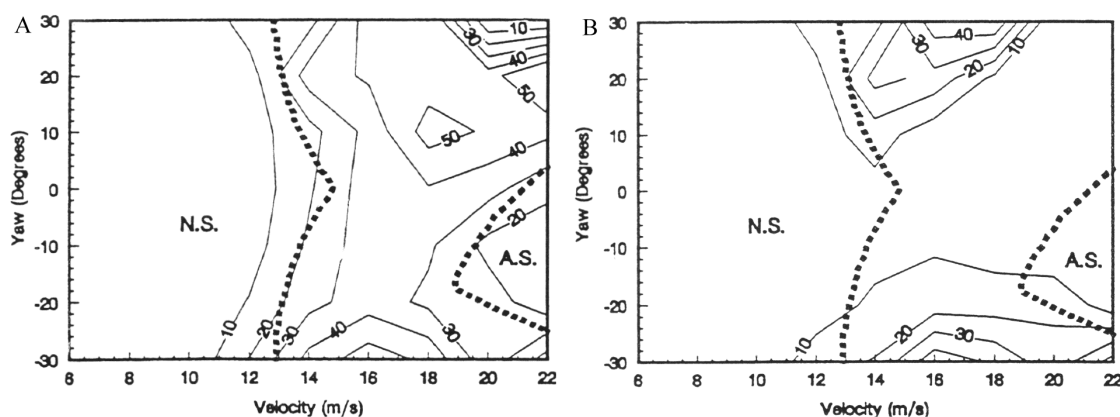


Figure 2-42 - NREL Data at 63% Span. A is a contour map which shows the number of occurrences of minimum $C_p < -10$, which was taken as an indication of dynamic stall, during the tests. B excludes data when the blade is in, or close to, the tower shadow. N.S. indicates the region where no stall is expected on the blades and A.S. the region where the blade is predicted to be completely stalled.

Robinson, Hand, Simms and Schreck (1999) analysed pressure coefficients from pressure taps on NREL’s 10 m turbine with untwisted and twisted non-tapered blades. They found that the tower shadow could cause the stalled boundary layer to attach, the attached boundary layer to separate, or cause no change. They identified several unsteady parameters that can affect this bifurcation response, namely the free stream wind speed, the yaw angle, the wake and three-dimensional stall of the blades. Further investigation would have been required to identify which of these are most important. They also found that the blades behaved two dimensionally below the static stall angle.

From Shipley, Miller & Robinson (1995) and Robinson *et al.* (1999), it seems clear that dynamic stall is likely to occur due to high yaw angles and tower shadow. Further investigation of both these parameters is discussed below. However, it should be emphasised that there is no evidence so far for dynamic stall occurring due to any other blade motions.

Huyer, Simms & Robinson (1996) analysed results from the 10m diameter combined experiment rotor, described earlier for the work by Butterfield and others (Butterfield, 1989a, 1989b, Butterfield, Scott & Musial, 1992), which had added tapping rings of 36 1mm diameter taps at 30%, 47% and 60% span in addition to the one at 80% span. Wind tunnel tests of the S809 aerofoil section used on this turbine showed that trailing edge separation began from an α of about 8° but the aerofoil did not fully stall until an α of 16° . Pressure data was taken at 520.8Hz and then

aliased filtered at 100Hz (analysis of the frequency content of the signals showed that it remained below 50Hz). Calibration of the pressure transducers using the in blade system was undertaken every 10 minutes. If the drift was too large between calibrations on any tap, the entire data set was discarded. Calibration was also regularly performed on other components. Surface pressure data was normalised by the freestream dynamic pressure, q_o , unless otherwise mentioned.

$$q_o = \frac{1}{2} \rho (V \omega^2 + Vr^2). \quad \text{Equation 2-23}$$

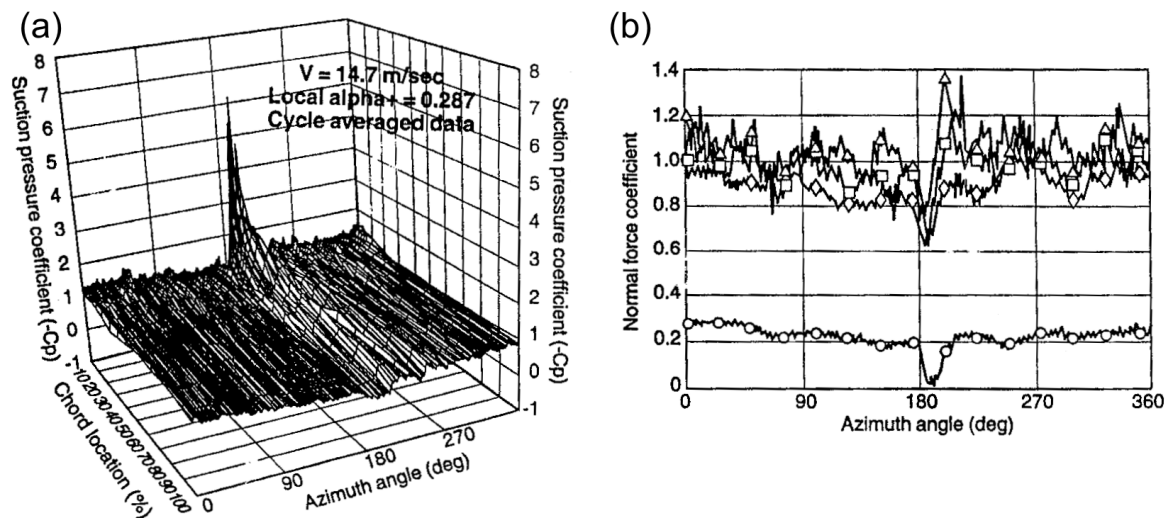


Figure 2-43 - (a) Upper surface pressure coefficient of five data cycles ensemble averaged on azimuth angle for the 47% span location at zero yaw at a wind speed of 14.7m/s. (b) Normal force coefficients averaged on azimuth angle at 80% span for zero yaw; mean wind 7.7m/s circles, 14.7m/s diamonds, 18.7m/s squares and 23m/s triangles. From Huyer, Simms & Robinson (1996).

Figure 2-43(a) shows the upper surface pressure coefficients at 47% span ensemble averaged across the azimuth angle for five cycles. The peak is at an azimuth angle of 190° , which is just after the blade passes through the tower wake (corresponding to an azimuth angle of 180°). The tower caused reattachment of the boundary layer. The same effect can be seen in the normal force coefficient at 80% span in Figure 2-43(b). A clear dip in normal force coefficient (c_n) is seen around 190° azimuth angle in low winds (7.7m/s, indicated by circles on the graph). The average c_n were about 10% lower than the section data recorded in wind tunnel tests. For the higher wind speeds, the average c_n was higher than static wind tunnel tests and transitory peaks were seen as the blade passed out of the tower wake.

The effect of tower wake and yaw combined creates more complicated changes in the suction surface pressure as seen in Figure 2-44. For 30° yaw in a wind of 15m/s at 30% span, as shown in Figure 2-44(a), there is a peak associated with blade passage through the tower wake at an azimuth angle of 140° (wake passage occurs at a lower azimuth angle due to the high yaw) and a larger peak at 180° azimuth angle associated with a pressure ridge that moves down the chord as the azimuth angle increases. Looking at this second peak in more detail by examining the suction surface pressure coefficients during one cycle in Figure 2-44(b) shows this feature is associated with the movement of a suction pressure peak along the chord as would be expected for a dynamic stall event. Figure 2-44(c) shows the cycle averaged suction surface pressure coefficients for 63% span.

The shape is considerably different to the 30% span case with passage through the tower wake, at an azimuth angle of 165°, causing the loss of a leading edge pressure peak. The leading edge pressure peak is regained after this event and continues to grow until an azimuth angle of 280°, after which the blade stalls abruptly. During one cycle at 63% span, shown for some azimuth angles in Figure 2-44(d), the suction pressure peak remained near the leading edge.

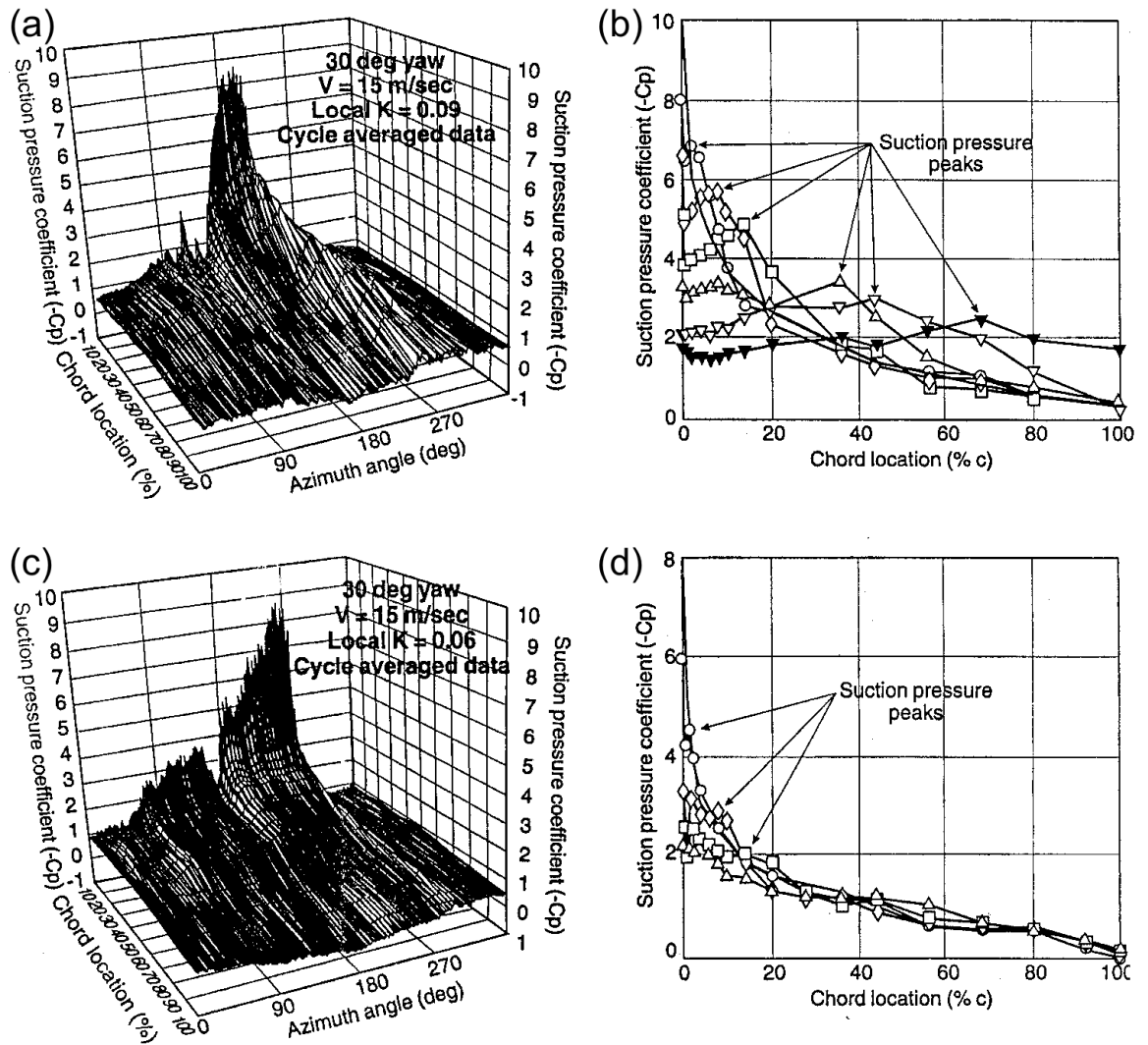


Figure 2-44 - (a) Upper surface pressure coefficient averaged for five cycles across the azimuth angle for the 30% span location at a yaw angle of 30° at a wind speed of 15m/s. (b) Suction surface pressure coefficients during a single cycle under the conditions of (a), azimuth angle 186° line only, 192° circles, 196° diamonds, 205° squares, 218° triangles points up, 227° triangles points down and 245° filled triangles. (c) 63% span location under the same inflow conditions as (a). (d) Suction surface pressure coefficients during a single cycle of (c), azimuth angle 276° line only, 278° circles, 281° diamonds, 284° squares and 288° triangles. From Huyer, Simms & Robinson (1996).

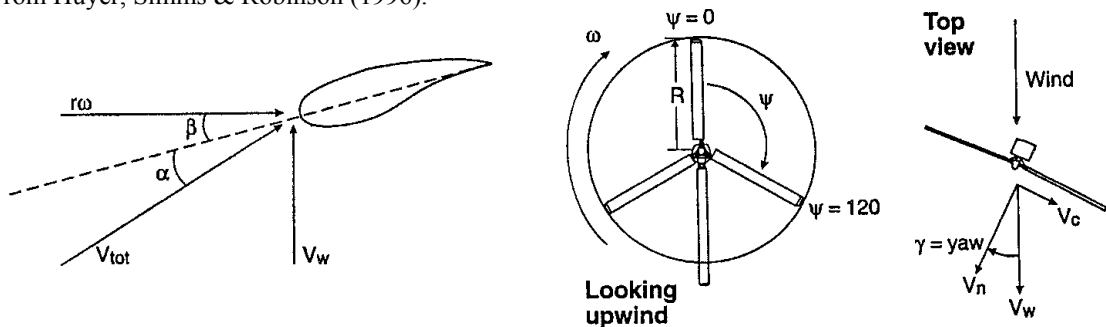


Figure 2-45 - Variable definitions for the simple model of yaw developed by Huyer, Simms & Robinson (1996).

Yaw will affect the α the blade encounters. Huyer, Simms & Robinson (1996) developed a simple model for this, the variables used are defined in Figure 2-45, by considering the wind (V_w) after passing through the rotor to have a component normal to the rotor (V_n) modelled by

$$V_n = V_w(1 - a) \cos(\gamma), \quad \text{Equation 2-24}$$

where a accounts for the slowing of the wind by the rotor and γ is the yaw of the rotor. The mean component parallel to the rotor plane (V_c) is then

$$V_c = -V_w \sin(\gamma). \quad \text{Equation 2-25}$$

The blade travels into and out of the wind according to the azimuth angle ψ so the tangential velocity (V_t) the blade sees consists of the local rotational velocity $r\omega$ and the V_c modified by the azimuth angle (ψ) as shown below,

$$V_t = r\omega + V_c \cos(\psi). \quad \text{Equation 2-26}$$

There will also be a spanwise component (V_s)

$$V_s = V_c \sin(\psi), \quad \text{Equation 2-27}$$

giving a total velocity of

$$V_{total} = \sqrt{V_n^2 + V_t^2 + V_s^2}. \quad \text{Equation 2-28}$$

This leads to the instantaneous local dynamic pressure, q , being modelled as

$$q = \frac{1}{2} \rho V_{total}^2, \quad \text{Equation 2-29}$$

and the α , as these blades have no twist and considering a pitch angle β , as

$$\alpha = a \tan\left(\frac{V_n}{V_t}\right) - \beta. \quad \text{Equation 2-30}$$

A simple model of the velocity deficit in the tower wake was added to this. The wake was modelled as half a cosine function with a maximum deficit of 30% of the total wind velocity and a width of two tower diameters. It should be noted that this model did not include factors such as wind shear, skewed wake effects or induced velocity (due to the slowing of the flow near the rotor) as the authors believed these effects would be of smaller magnitude. Plots of q and α using this model for the different span locations are shown in Figure 2-46(a) and (b) respectively for a yaw angle of 30° . This model was used to compare the wind tunnel aerofoil section results with yawed turbine data. The wind tunnel data was normalised by the constant dynamic pressure, q_o , defined as

$$q_o = \frac{1}{2} \rho (V_\omega^2 + V_r^2), \quad \text{Equation 2-31}$$

and the wind turbine data by q as defined earlier. Note Equation 2-31 has been modified from that given by Huyer, Simms & Robinson (1996) to have ω and r as subscripts, this was presumably a typographical error as the version in the paper was not dimensionally consistent. The comparison is shown in Figure 2-46(c) for 30% and 63% span. A hysteresis loop is seen at low α for 30% span and a smaller loop at all α for 60% span. At both locations the maximum c_n values were observed

at maximum α and the authors found they were qualitatively consistent with wind tunnel data for oscillating wings.

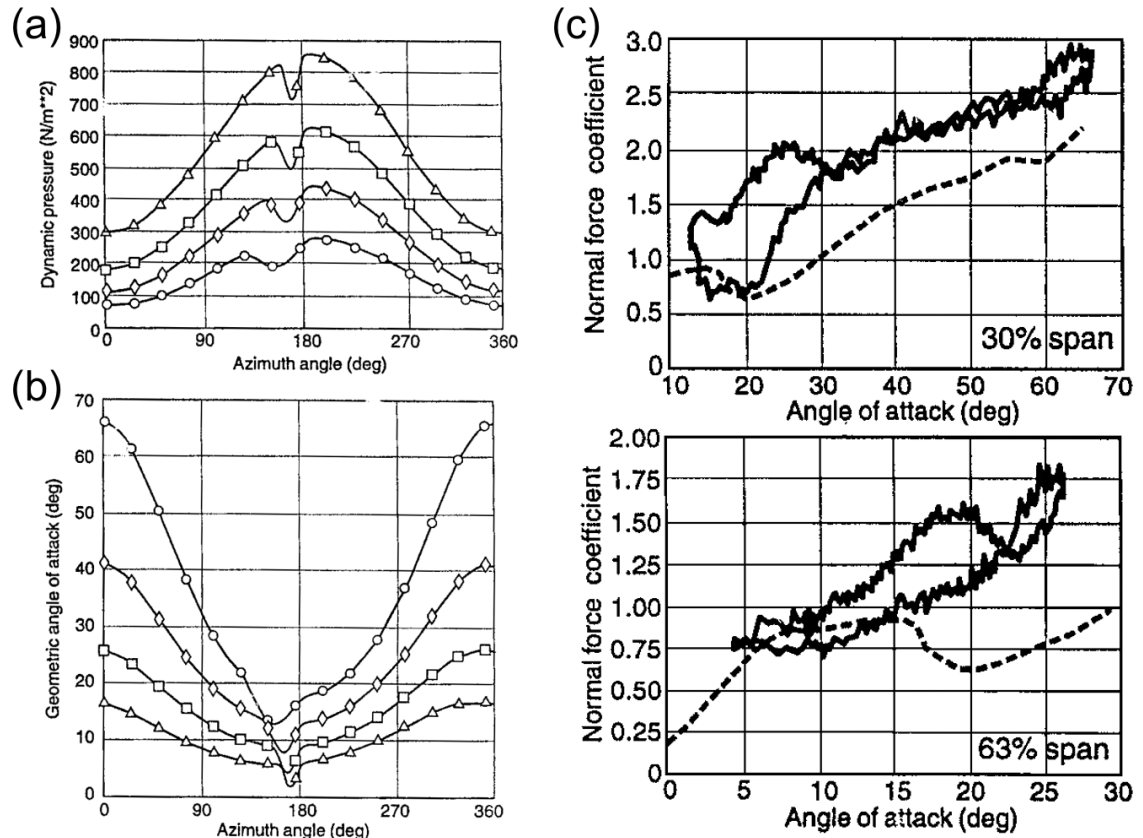


Figure 2-46 - (a) Instantaneous dynamic pressure, q , and (b) theoretical angle of attack versus azimuth angle for a yaw angle of 30° and a wind speed of 15m/s , 30% span circles, 47% span diamonds, 63% span squares and 80% span triangles. (c) Field data normalised by q compared with wind tunnel data (dashed line) normalised by the constant dynamic pressure, q_0 . From Huyer, Simms & Robinson (1996).

Schreck *et al.* (2000) investigated dynamic stall due to yaw by comparing the pressure coefficients of different tapped sections. They found that a dynamic stall vortex convected along the wing. The vortex formed earliest towards the hub and latest towards the tip but was convected chordwise along the blade faster at the middle of the blade span and slowest at the hub and near the tip. These three-dimensional results are qualitatively the same as for a pitching wing where the vortex rises furthest from the blade surface in the centre of the blade and is convected faster because of the influence of the free stream (Schreck, Scott J. & Helin, 1994, shown earlier). Schreck, Robinson, Hand & Simms (2001) tested the same turbine with different blades in the low turbulence of the Ames wind tunnel. This allowed them to control the wind speeds and yaw angles. They found at small yaw angles and low wind speeds that the dynamic stall vortex was fairly two-dimensional. However at moderate wind speeds and yaw angles the vortex was highly three-dimensional. In both cases the passage of the vortex increased the normal force.

Dynamic stall occurs on wind turbines due to yaw and tower wake. Appendix B includes a brief description of some methods and issues with including dynamic stall models in prediction methods. However, delayed stall also occurs in other flows, for example the plot shown in Chapter 1 of delayed stall was taken in cases of minimal yaw and ignored data in the tower wake. While

dynamic stall should rightfully be included in wind turbine models, other factors need to be considered to fully account for delayed stall.

2.9 Turbulence

Turbulence in the natural wind has often been proposed as the cause for anomalous wind turbine field results. As was discussed briefly in Chapter 1, the wind tunnel experiments of wind turbine performance by de Vries and den Blanken (1981) which were among the first to identify the problem of delayed stall also looked at using grids to add different levels of turbulence to the wind tunnel flow. The results were limited by the high blockage correction needed and the relatively low Re . However, other tests have been more successful as this section will discuss.

2.9.1 Field Tests

Anderson, Milborrow & Ross (1982) tested a 3 meter diameter wind turbine in the wind tunnel and field. The coefficient of power versus tip speed ratio results for these conditions and BEM momentum predictions are shown in Figure 2-47. There was a good match between the predictions and the wind tunnel data at the two wind speeds. There was not enough data at low tip speed ratios for any differences to be observed between the measured and the predicted performance when the blades were expected to be stalled. However the field data power output is over predicted in the 5m/s curve. The authors suggested this reduction in performance was caused by turbulence; predominately by large scales of turbulence causing yawed operation.

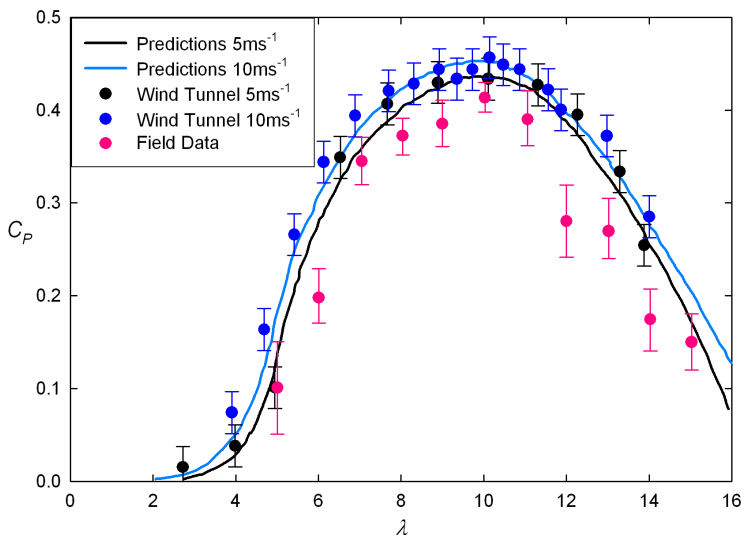


Figure 2-47 - Comparison of predictions, wind tunnel and field data of the coefficient of power (C_p) versus the tip speed ratio (λ) for a 3m diameter HAWT. Error bars on wind tunnel tests indicate the typical error. Field data should be compared with the 5m/s prediction and wind tunnel measurements. Data from Anderson, Milborrow & Ross (1982).

Elliot & Cadogan (1990), discussed in detail in Section 2.4.1, reported the opposite trend to that seen by Anderson, Milborrow & Ross (1982), as turbulence increased on their 91-m MOD2 turbines the performance improved slightly, see Figure 2-20. This may be due to the different scale

of the turbines, both in terms of the Reynolds number and the far smaller chance of encountering a turbulence eddy that would encompass the larger rotor. Like the Anderson, Milborrow & Ross (1982) study, there was not enough high wind conditions observed by Elliot & Cadogan (1990) to comment on the effect of turbulence near stall.

It is difficult to isolate the effects of different wind characteristics on performance. For instance, Elliot & Cadogan (1990) found an increase in performance with turbulence at all wind speeds. However, when they examined the wind data more closely they found that the low turbulence conditions generally occurred at night when there was usually a very high wind shear at their site. The wind shear had a larger effect and made the determination of the effect of turbulence alone difficult.

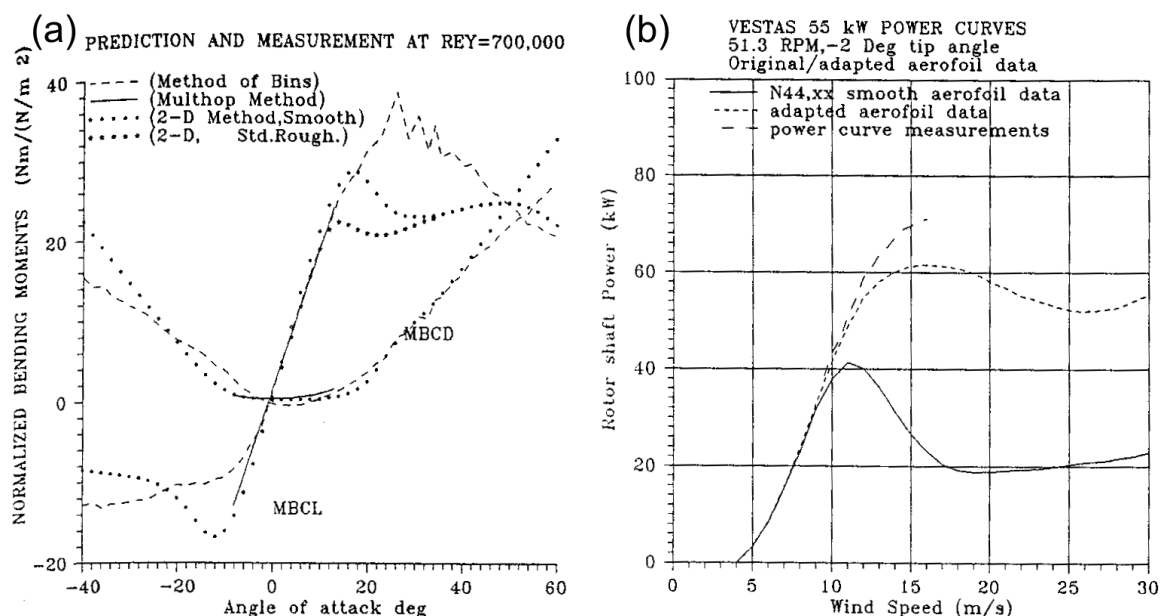


Figure 2-48 – (a) Normalised bending moments in the lift and drag directions from test measurement (method of bins), three-dimensional predictions below stall (Multhop method) and two-dimensional predictions from smooth (2-D Method, Smooth) and rough aerofoil section data (2-D, Standard Roughness). (b) Power predictions from smooth aerofoil section data and field data from this test compared with measurements on a Vestas 55kW wind turbine. Plots from Paulsen (1989).

Paulsen (1989) tested a 6.4m, tapered, twisted wind turbine blade based on NACA 44xx aerofoil profiles mounted vertically above a 12m tower on a moment balance. The accuracy of the bending moments was within 1.5%. The oncoming wind was measured 2m before the blade at a height of 15.8m. The chord based Re varied from 5×10^5 to 1×10^6 . The normalised bending moment in the direction of lift in rough weather exceeded that in dry weather by about 7%. Comparing curves based on the method of bins for increasing and decreasing α , hysteresis was evident at all α in the normalised bending moment in the direction of lift. Paulsen suggested this may be due to rapid blade flapping. Two-dimensional predictions of the stationary blade characteristics were made based on both smooth and rough aerofoil section data under the assumptions of constant wind speed along profile, no Re effect at different chord sections, an infinitely stiff blade and neglecting downwash. Three-dimensional predictions were also made but these were valid below stall only.

Comparison with binned measurements at a Re of 7×10^5 showed that the maximum normalised bending moment in the direction of lift was much larger in the field data as shown in Figure 2-48(a). From the field data, adapted aerofoil section data was derived by what Paulsen described as an interactive process. The wind tunnel section data and this adapted section data was used to predict the performance of a 55kW Vestas turbine as shown in Figure 2-48(b). The adapted data provided a better match than the original data but still under-predicted the maximum power output.

Liu (1986) studied a wing in natural turbulence using the Wortmann FX 63-137 aerofoil with a wing span of 3.66 m and a chord of 0.61 m, corresponding to an aspect ratio of 6:1. The wing was placed in natural wind on a mount that allowed the pitch to be changed. A balance measured the forces on the aerofoil. The wind speed ranged from 6.3 to 11.5 m/s (corresponding to Reynolds numbers of 2.5×10^5 to 4.5×10^5) and the turbulence intensity was between 8% and 20%. These tests were compared to wind tunnel measurements using a wing of the same aspect ratio with a chord length of 5 inches in a 6ft x 6ft wind tunnel at $Re = 300,000$ (Marchman III, Sumantran & Schaefer, 1987). The reported turbulence level for the wind tunnel (Marchman III, Sumantran & Schaefer, 1987) was 1.8% at 10m/s and 4.5% at 30m/s, these tests corresponded to a velocity of about 38m/s. Compared to wind tunnel results, the lift at high angles of attack was noticeably higher and stall was delayed in the natural wind. The maximum C_L for the wind tunnel data was 1.5 at an angle of attack of 13° . The maximum C_L measured in the field was 1.8 at an angle of attack of 19° . The drag coefficient was lower at low angles of attack and showed very large standard deviations at high angles of attack. The moment coefficient was noticeably lower at all angles of attack and showed no hysteresis loop at higher angles of attack, instead showing a sharp drop as angle of attack increased. Plots of C_L and C_D versus angle of attack are shown in Figure 2-49 A and B respectively.

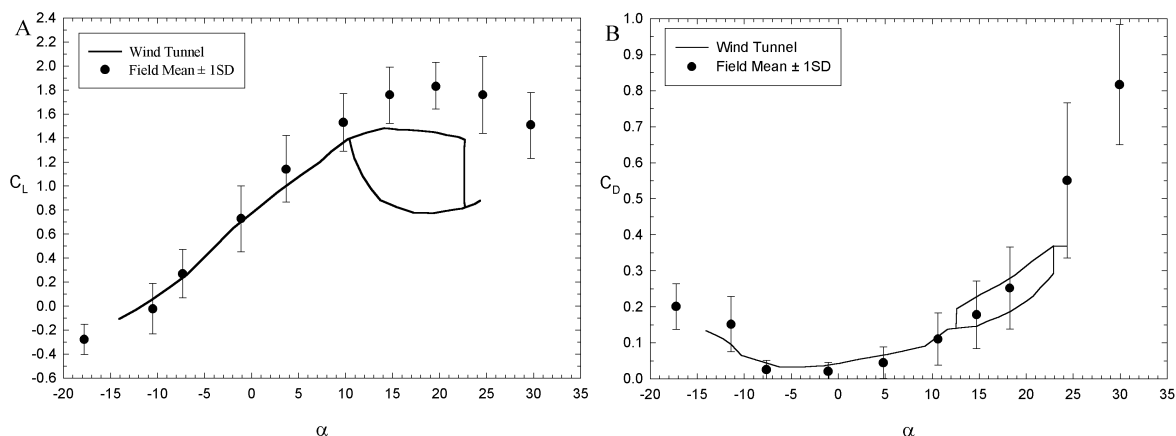


Figure 2-49 - Performance of the Wortmann FX 63-167 aerofoil in the natural wind (Aspect Ratio = 6:1, $Re_c = 2.5 \times 10^5$ to 4.5×10^5) and wind tunnel ($Re_c = 3 \times 10^5$) from Liu (1986).

Interestingly Liu (1986) drew parallels between this performance and that of aerofoils undergoing dynamic stall, specifically plunging motion. The similarity between the “delayed stall” seen in Figure 2-49A for this aerofoil in the field and that seen on wind turbines in the field is obvious, for

example see the results of Butterfield, Scott & Musial (1992) in Section 2.4.2. Unfortunately, due to the measurement technique used, there was no information on what was occurring in the boundary layer.

2.9.2 Wind Tunnel Tests of Aerofoil Sections in Turbulence

Surprisingly little work has been done in wind tunnels on the effect of turbulence on the performance of aerofoils. Wind tunnels studies are generally performed with grid generated turbulence. Grids generate turbulence that is approximately isotropic. However, the mean velocity just behind the grid bars is not uniform because of overshoots in line with the grid openings. This non-uniformity decays rapidly if a square grid is used although the uniformity should always be checked (Bearman & Morel, 1983).

The first major study of the effect of turbulence on aerofoil performance was conducted by Stack (1931). Stack (1931) tested the performance of five aerofoil sections of 5 inch chord and 30 inch span between Reynolds numbers of 1×10^5 to 3×10^6 with and without a turbulence inducing grid in a wind tunnel. Unfortunately, due to the limitations in available technology and knowledge at the time of the tests, the scale and turbulence intensity produced by the grid were not measured. The existence of turbulence was detected by comparing the drag on a 20 cm sphere with and without the grid. This early method of detecting turbulence is based on the sensitivity of the drag of a sphere to the boundary layer. The laminar boundary layer separates shortly after the flow first reaches the rear of the body. However the turbulent boundary layer enables the flow to remain attached further around the sphere, thus reducing the drag. As the level of turbulence in the flow increases, the transition to turbulence occurs earlier. However according to Hoerner (1965) this can only be a qualitative indication of the turbulence intensity as the stiffness of the suspension of a sphere in the wind tunnel, mechanical vibrations, surface roughness and even sound waves have an effect. Therefore the drag data only shows that grids increased the turbulence, they cannot allow direct comparison with other data.

The aerofoils Stack tested (1931) were thin (NACA 0006) and thick (NACA 0021) symmetrical sections, a medium thickness aerofoil with camber (Clark Y) and two thick aerofoils with camber (USA 35-A and USN PS6). It should be noted that the aerofoil sections tested had an aspect ratio of 6:1. Stack's results for the NACA 0021 aerofoil are shown in Figure 2-50.

Figure 2-50 shows that, for a Re of 83 000 without a grid, the aerofoil stalls abruptly at an α of about 16° . The lift is still increasing at α beyond 16° for a similar Re with turbulence. No data points were taken between α of 4° and 16° for this case, so where the results deviate from the low turbulence case is unclear. A similar delay in stall is observed between measurements for a Re of 735 000 without a grid and a Re of 730 000 with a grid. Stall in the low turbulence flow at a Re of 735 000 is less abrupt than at a Re of 83 000. It was found for aerofoils where C_{Lmax} increased with increasing Reynolds number (NACA 0021 and Clark Y), that the addition of turbulence decreased

C_{Lmax} at low Re but increased C_{Lmax} for high Re (the cross over point was between 1 to 2×10^5 for both aerofoils). The effect of turbulence on profile drag was found to be small at the higher Reynolds numbers tested. Thick cambered aerofoils are usually used at the root of wind turbine blades, the part of the blade that stalls first. However, for the two thick cambered aerofoils he tested, Stack found that adding turbulence decreased the maximum C_L . For the USA 35A aerofoil the decrease was observed over a Re range of 1.7×10^5 to 2×10^6 . Stack also found a similar reduction in the maximum C_L on the NACA 0006 section. This occurred when turbulence was added to the flow for a Re range of 1.8×10^5 to 1.8×10^6 .

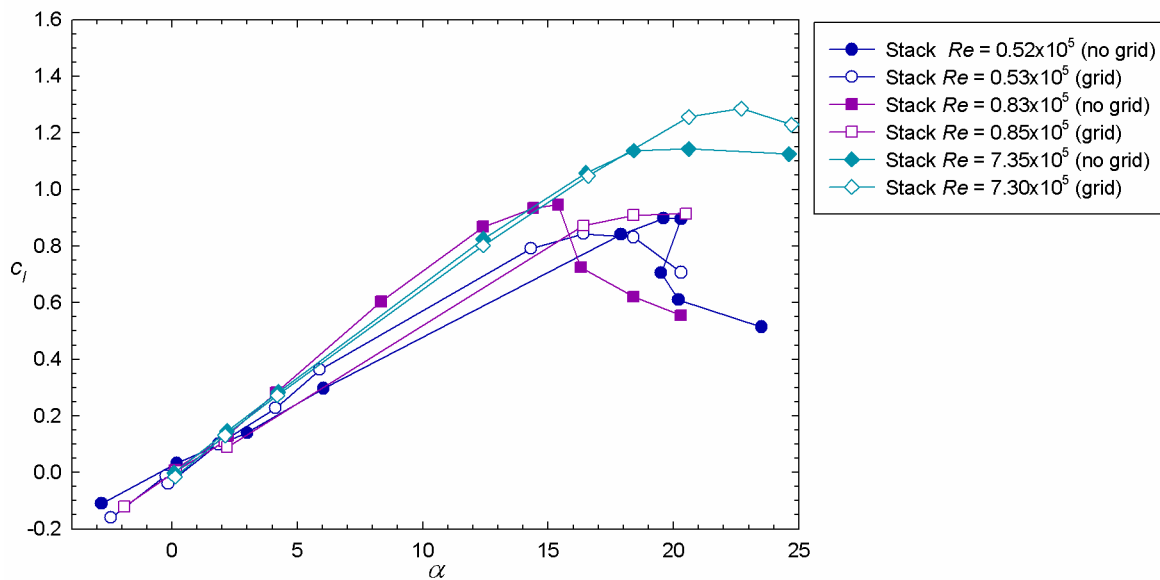


Figure 2-50 - NACA 0021 results from Stack (1931).

As part of his doctoral thesis on the effect of turbulence on bridge like structures, Jancauskas (1983) tested the NACA 0006 aerofoil section at similar Reynolds number to Stack's 1931 tests. His findings contradict those of Stack. Jancauskas found that the addition of turbulence delayed stall on the NACA 0006 aerofoil at a Re of 2×10^5 , see Figure 2-51. He also found that, as the turbulence intensity was increased from 0.6 % to 16 % stall was further delayed. The aspect ratio of the section in these tests was 8 to 3 (2.67).

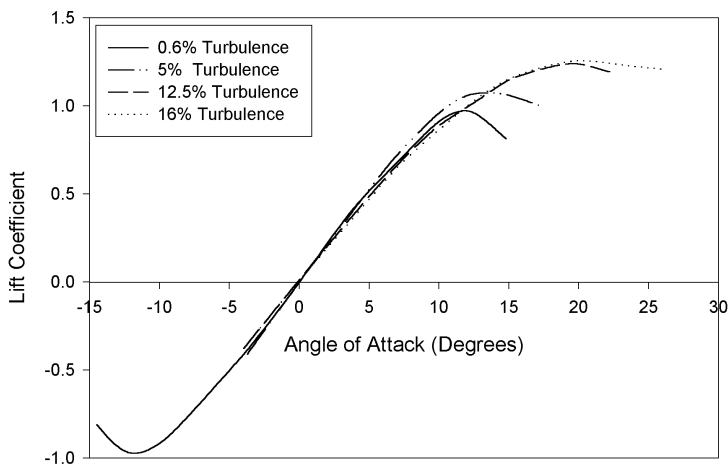


Figure 2-51 - NACA 0006 aerofoil section in turbulence ($Re \approx 2 \times 10^5$) from Jancauskas (1983).

Wind turbines typically use tapered, twisted blades consisting of cambered aerofoils. The “delayed stall” occurs on the root section of the blade first, i.e. the thickest section of the blade. So, if the effect of turbulence on the aerofoil section’s performance is important to the stall behaviour of HAWTs turbulence, it would be expected to “delay stall” on thick cambered aerofoils. Stack’s results (1931) indicate that this does not happen. However the results obtained with the NACA 0006 aerofoil by Stack (1931) and Jancauskas (1983) are different. The reasons for this difference require further investigation. Possible reasons for the difference include turbulence scale and intensity, Re , aspect ratio and surface roughness effects.

Because of the lack of aerofoil section data in turbulence for wind turbine applications, Devinant, Laverne & Hureau (2002) tested a NACA 65₄-421 aerofoil section in various intensities of turbulence up to an angle of attack of 90°. The model was installed between two panels 3.5m long, 2m high and 1.1m apart in the main 2m×2m test section. The aerofoil section had a chord length of 0.3m giving an aspect ratio of 3.67 between the panels and a maximum blockage at $\alpha = 90^\circ$ of 27%. Three grids were used; all were placed 1.9m upstream of the centre of the test section. They produced turbulence intensities that diminished slightly over the aerofoil chord from an average I_u of 4.3% to 3.9% for grid 1 ($I_v = I_w = 3.8\%$), from 10% to 9.2% for grid 2 ($I_v = I_w = 9\%$) and from 17.1% to 15.4% for grid 3 ($I_v = I_w = 14.5\%$). The integral length scale of the turbulence was not determined but, based on the increasing size of the grids, the scale should increase from grid 1 to grid 3.

Balance measurements were used for low α measurements and pressure tap measurements for high α results. The results for the different turbulence intensities on the lift, drag and moment at a Re of 4×10^5 are shown in Figure 2-52. The lowest turbulence flow shows a flat region in the c_l curve with a dip after the linear attached portion of the plot. As measurement points are not shown on the plot for the balance measurements, it is difficult to tell if this is just due to a minimal number of measurement points in this region. On increasing the turbulence intensity, the c_l plots revert to a more anticipated profile and have a higher maximum c_l associated with stall for $I_u = 4\%$ and 9% . However, the c_l maximum associated with stall decreases for $I_u = 16\%$. Also, in all cases, increasing turbulence intensity decreases the slope of the linear attached region of the curves. In all cases, except $I_u = 16\%$, a second maxima in c_l is seen around $\alpha = 40^\circ$ to 50° and for all cases c_l reduces as α increases further to 90° (in this region the aerofoil is stalled and the forces are associated with windward-leeward pressure differentials). The drag and moment show similar results in all cases, the most notable feature being a jump in drag and drop in moment for the lowest turbulence intensity case at the same α at which the aerofoil shows a drop in c_l . These results show delayed stall on a thick, cambered aerofoil. However, the aspect ratio of the test was low and the turbulence was only classified in terms of intensity when integral turbulence length scale was being changed along with intensity. So, while the results support the idea of turbulence

effecting stall on wind turbines, they don't answer all of the questions raised by the Stack and Jancauskas comparison.

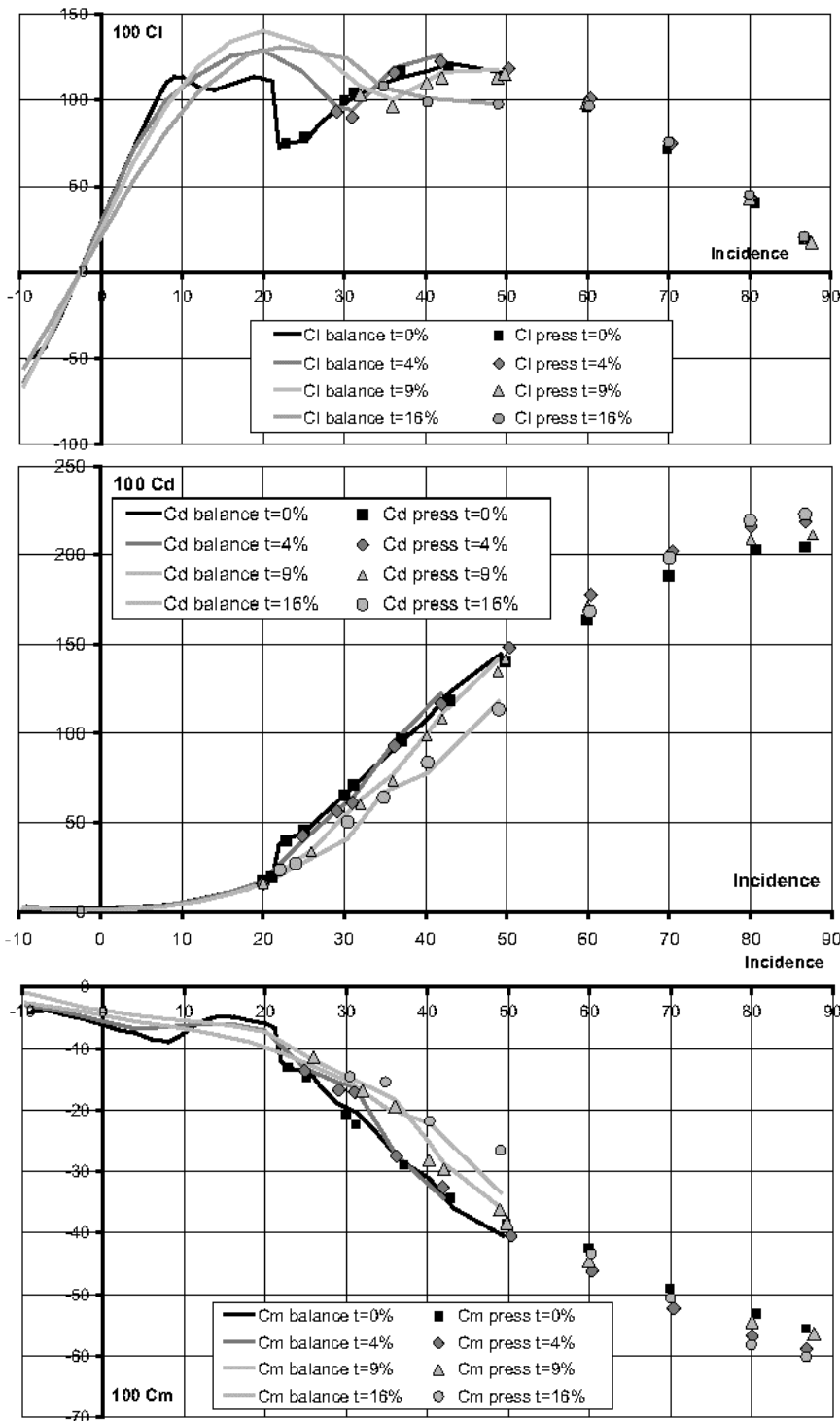


Figure 2-52 – Lift, drag and moment curves at different turbulence intensities for the NACA 65₄-421 aerofoil section at $Re = 4 \times 10^5$ (Devinant, Laverne & Hureau, 2002). Note I_u is designated in the plot legends and the data taken without grid induced turbulence is indicated by black lines and points and corresponds to a turbulence intensity of 0.5%.

Huang & Lee (1999) tested a NACA 0012 wing in various levels of turbulence using balance measurements and surface oil flow visualisations. The wing was attached to the balance at one end where there was also an end plate; the tip of the wing was at half the tunnel width. The aspect ratio

of the model was 5. The surface visualisations at a Re_c of 5.9375×10^4 and a turbulence intensity of 0.2% show that, at small angles of attack ($\alpha = 1^\circ$), there is a small trailing edge separation. By $\alpha = 5^\circ$ a laminar separation bubble formed at about half the chord and the flow at the trailing edge had reattached. At $\alpha = 8^\circ$ the laminar separation bubble had moved to the leading edge. By $\alpha = 10^\circ$, flow had again begun to separate at the leading edge. Finally, while there is still a laminar separation bubble at the leading edge, the aerofoil at $\alpha = 12^\circ$ can be considered to be stalled. These surface flow patterns, along with the separation and vortices that occur near the tip and hub, are shown in Figure 2-53.

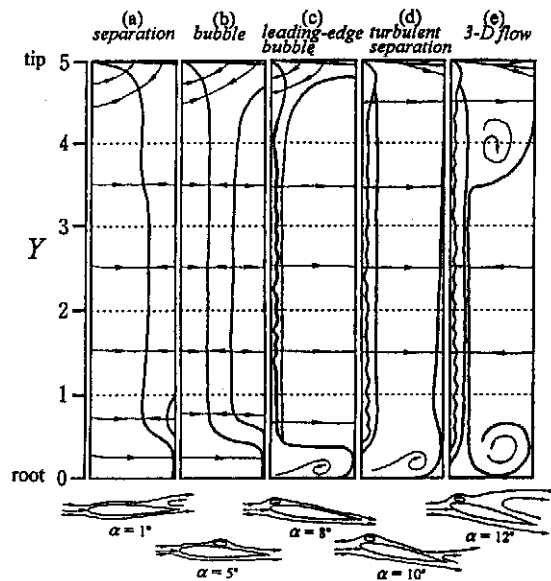


Figure 2-53 - Sketch of typical surface-flow patterns (Huang & Lee, 1999).

Turbulence was induced by the use of screens with different sized meshes. This would also induce different integral length scales of turbulence; however the integral length scales were not examined in this investigation. Adding turbulence to the stream did not alter the flow regimes but did delay the angle of attacks at which they occurred. There was little difference between the effect of 0.45% turbulence intensity and 0.5% or 0.65% but this may be due to integral length scale effects. Correspondingly, the stall angle and the maximum lift increased with turbulence intensity to a plateau from approximately 0.45% turbulence intensity onwards. This occurred at all the Re_c tested ($\sim 3 \times 10^4$ to 1.2×10^5). Increasing Re_c , i.e. increasing the tunnel velocity, for the same turbulence intensity, decreased the angle at which a bubble occurred and the angle at which the leading edge bubble formed. It also increased the angle at which turbulent separation occurred.

A study by Kentfield (1996), based on the differences in performance of aerofoils equipped with Gurney flaps (small, rigid flaps attached to the trailing edge on the pressure side of the aerofoil), suggests that the boundary layer thickness increases as the turbulence intensity increases. Also, similar to a flat plate, the boundary layer thickness increases as the chord based Reynolds number (Re_c) decreases.

2.9.3 Acoustic Effects

In 1975 Amiet discovered that a lifting surface passing through turbulence produces pressure fluctuations that can radiate broadband noise. Although a considerable amount of theoretical work has been done to model the acoustic effect, there have been surprisingly few experimental studies. Mish & Devenport (2001) only identified one paper prior to their own that experimentally investigated the effect of angle of attack and turbulence on noise and performance. This paper by McKeough & Graham (1980) displayed the balance measurements from the NACA 0015 section in comparison with the predictions of unsteady thin, aerofoil theory. Mish & Devenport's reproduction of these results to compare with their own experimental results in terms of lift and angle of attack is more convenient for this discussion (see Figure 2-54).

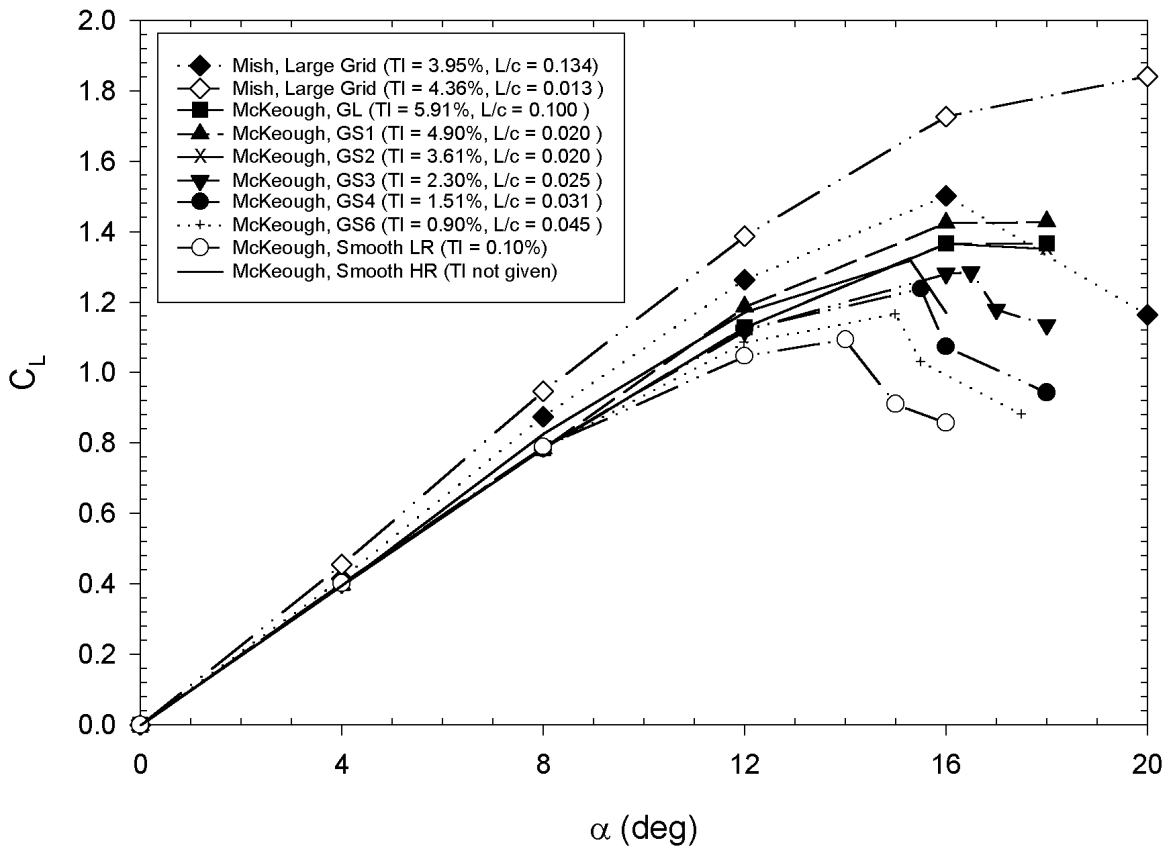


Figure 2-54 - Lift Coefficient versus Angle of Attack in Various Levels of Turbulence Mish & Devenport's results at $Re = 1.17 \times 10^6$, McKeough Smooth HR $Re = 0.76 \times 10^6$ all other McKeough Data at $Re = 0.26 \times 10^6$ (Mish & Devenport, 2001)

Mish & Devenport's study (2001) used a NACA 0015 section with an aspect ratio of three. The model had pressure tappings and microphones embedded in it. The chord based Reynolds number used was 1.16×10^6 . Two turbulence grids were used which produced similar turbulence intensities but very different integral length scales. The large grid gave a turbulence intensity of 3.93% and a longitudinal integral length scale of $0.134c$ and the small grid produced a turbulence intensity of 4.35% and a longitudinal integral length scale of $0.0127c$. Both grids delayed stall compared to the aerofoil response in smooth flow. The large scale turbulence delayed stall until an angle of attack of around 16° , the small scale turbulence caused the aerofoil not to stall in the range

of angles of attack tested (up to 20^0). Mish & Devenport's analysis of the microphone response showed that after stall the response in large scale turbulence was very similar to that with no grid. The small grid turbulence was still evident in the measurements at similar angles of attack. This seems to indicate that the small scale turbulence is more effective in interacting with the boundary layer. They also looked at the correlation of the signals in the chordwise and spanwise directions. Some of these results contradicted those of McKeough & Graham (1980). This contradiction, and Mish & Devenport's use of a very small aspect ratio aerofoil section (which is known to affect correlation on bluff bodies), makes the validity of the correlation results doubtful so they will not be presented here.

Using a force balance and pressure taps, Marchman, Sumantran & Schaefer (1987) tested the response of a Wortmann FX-63-137 aerofoil with an aspect ratio of 8 and $Re = 100,000$ to low turbulence (0.02% and 0.2% intensity) and acoustic disturbance (4830, 5200 and 5500 Hz). This study was performed because of different values of the hysteresis loop (large, small and non-existent) reported for this wing in different tests. The tenfold increase in turbulence level reduced the size of the hysteresis loop by restoring attached flow over the rear half of the blade, but not the leading edge. They also reported that the effect was reduced as Re was increased. The acoustic tests showed,

“A 4830-Hz signal was capable of fully restoring an attached upper-surface flow whereas 5200- and 5500-Hz disturbances, all at the same 110-dB sound level, resulted in only partial restoration of the flow. It is interesting that, for these cases, flow attachment was forced within the prebubble, laminar portion of the boundary layer and not the postbubble, turbulent portion as seen with added turbulence.

Acoustic disturbance tests showed that a disturbance of the proper frequency and pressure level can often completely restore a fully separated flow to a fully attached flow, which remain stable and after the disturbance signal is removed. It was shown that the sound levels as low as 95 dB at frequencies around 500 Hz can be used to force flow reattachment.” (Marchman III, Sumantran & Schaefer, 1987, p. 50)

2.9.4 Turbulence in the Natural Wind and the Effects of Scale

Turbulence has long been known to increase the structural loading on wind turbines. Mouzakis, Morfiadakis & Dellaportas (1999) used a multivariate regression analysis to determine the effect of various wind parameters on the fatigue loads of a wind turbine. The four parameters were wind characteristics (mean wind speed, wind shear and mean wind inclination), wind turbulence (standard deviation and integral length scale components), wind speed distribution (skewness and kurtosis) and wind speed coherence (delay factors from three different elevations). They found that the turbulence structure was the primary factor inducing fatigue. Using the same technique (with various levels of the lateral and vertical turbulence ratios and corresponding integral length scales to simulate different terrain) they predicted that, in complex terrain, fatigue loading could reach over 30% of that found in flat terrain.

Another study by Sacre, Flori & Duchene-Marullaz (1987) analysed the wind at different heights at two very different sites. The first, at Corsica, was located at the top of a steep hill, 600 m above sea level and 2 km from the sea. The prevailing winds coming from the sea showed acceleration of the mean wind flow for the lowest (10 m height) measurements and very low turbulence intensity at all tested heights. The second site at Lastours was located on a plateau surrounded by hills and 300 m above sea level. The plateau was bare but the slopes around it were covered with low, dense vegetation. The turbulence intensity varied very slightly with height. It was 0.17 at 20 m, 0.16 at 30m and 0.15 at 40 m. The lateral turbulence was of the same order as the longitudinal. A spectral analysis of the longitudinal component showed that, when compared to flat, open terrain, the low frequencies were reduced and high frequencies increased.

Wind turbines operate in turbulent wind. The current practice of installing many turbines together in wind farms can increase the turbulence encountered as some turbines operate in the wake of other turbines. The wake of a turbine has been found to increase turbulence intensity and to increase the turbulence length scales (Taylor, G. L., 1987). Structural modelling of the turbine predicted that this will increase extreme loads and therefore the likelihood of fatigue damage of a turbine operating in the wake of another (Taylor, G. L., 1987).

The NREL Ames wind tunnel tests did not measure the effect of turbulence on performance. Unfortunately the instrumented, untapered, twisted, turbine blade, which had been extensively field tested, was destroyed when an instrumentation boom broke off the wind turbine. Therefore, a new set of tapered, twisted blades were used. These blades only had shakedown tests in the field prior to the wind tunnel tests. As part of the current study these shakedown tests were investigated but there was insufficient high wind speed data to compare to the lower turbulence wind tunnel tests. There are currently no plans to test the tapered, twisted blades in the field (Schreck, Scott J., 2002b). The axial turbulence in the Ames tunnel was less than 0.5% (Zell, 1993). Adding turbulence would have been difficult to achieve practically in such a large tunnel. However field tests would have provided comparison data in the natural, turbulent wind. The argument against the need of testing the effect of turbulence was that the

“...issue is instead related to the characteristic scale, rather than the amount or quantity, of the turbulence. Characteristic scales of turbulence generated in small wind tunnels can be on the order of the size of the airfoil dimensions and can certainly affect airfoil performance. Scales found in naturally occurring planetary boundary layer turbulence are typically much larger - on the order of the size of the rotor or larger - with little energy at the characteristic scale of the blade chord.” (p.15, Simms *et al.*, 1999b).

This argument was even more strongly made in *A Catalog of Low Reynolds Number Airfoil Data for Wind Turbine Applications* (Miley, 1982) which was quoted in Section 2.2.

The integral length scale is the area under the curves of the u component with the components of velocity in the longitudinal (L_{uu}), lateral (L_{uv}) and vertical (L_{uw}) directions. The integral length

scale may be viewed as being representative of the average size of the most energetic turbulence eddies (Bearman & Morel, 1983). Turbulence decays by the effect of viscosity at smaller scales, having a large main integral length scale of turbulence necessitates the existence of smaller scales although there will be less turbulence intensity at these scales.

To investigate how much less the intensity is at smaller scales, the commonly used von Kármán-Harris equation for the longitudinal turbulence spectra (Holmes, 2001) was employed. This can be written in non-dimensional terms as

$$\frac{n.S_u(n)}{\sigma_u^2} = \frac{4\left(\frac{nL_{uu}}{\bar{U}}\right)}{\left[1 + 70.8\left(\frac{nL_{uu}}{\bar{U}}\right)^2\right]^{5/6}} \quad \text{Equation 2-32}$$

where n is the frequency, L_{uu} is the longitudinal turbulence integral length scale (L_{uv} and L_{uw} are the lateral and vertical integral length scales) and $S_u(n)$ is the spectral density function for the wind velocity $u(t)$. $S_u(n)$ is the contribution to the variance (σ_u^2) by a frequency, integrating over all frequencies,

$$\sigma_u^2 = \int_0^{\infty} S_u(n) dn. \quad \text{Equation 2-33}$$

This non-dimensional curve is shown for some typical values of L_{uu} , \bar{U} and I_u for a wind turbine site. L_{uu} from Sacre, Flori & Duchene-Marullaz (1987) and typical value of I_u for open farm land at a height of 50m (Holmes, 2001) is shown in Figure 2-55.

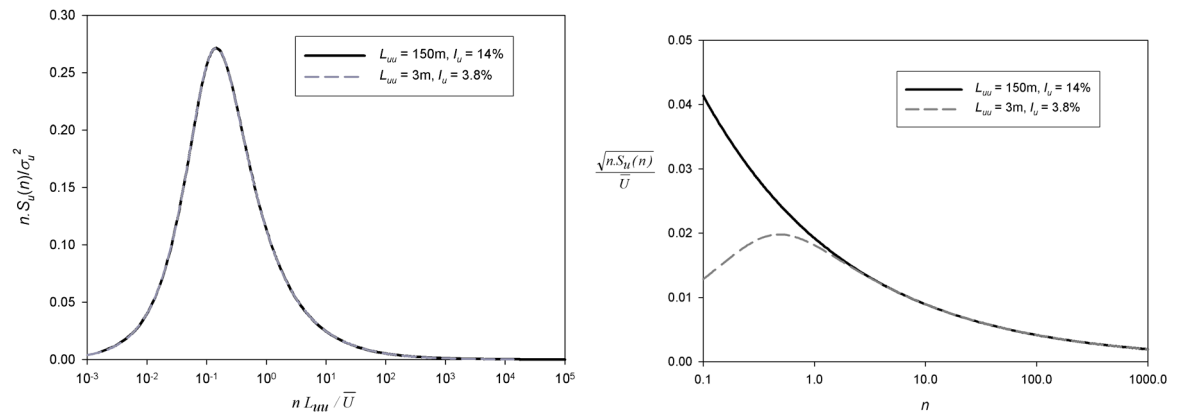


Figure 2-55 - Non-dimensional (left hand side) and dimensional (right hand side) von Kármán - Harris spectra for some typical values at a wind turbine site and a matched curve at a length scale of the chord length near the hub at a large turbine. Both curves are for a mean wind speed of 10m/s.

Also shown in Figure 2-55 is a matched curve for a lower length scale equal to the size of the chord length near the hub of a large HAWT. A better comparison is obtained by rewriting Equation 2-32 in terms of the dimensions of turbulence intensity,

$$\frac{\sqrt{n.S_u(n)}}{\bar{U}} = \frac{1}{\bar{U}} \sqrt{\sigma_u^2 \frac{4\left(\frac{nL_{int}}{\bar{U}}\right)}{\left[1 + 70.8\left(\frac{nL_{int}}{\bar{U}}\right)^2\right]^{5/6}}}$$

Equation 2-34

The square root of the integral of $S_u(n)$ divided by the mean wind speed gives the turbulence intensity. Equation 2-34 does not give the turbulence intensity at a specific frequency n but rather an indicative measure of this. A plot of Equation 2-34 for the data shown is given in Figure 2-55. As expected, this shows that the curves do not match at low frequencies (large scales) but match very well for the smaller scales, higher frequencies that are of interest (difference less than 6% for frequencies greater than 1, for frequencies greater than 10 the difference is less than 0.07%). Therefore, even for very large integral length scales there will be non-negligible turbulence intensity at smaller length scales.

2.9.5 Simple Effects of Rotation on Turbulence at the Blade

Another factor that will limit the turbulence intensity encountered by a blade element is the steady rotational component of the apparent wind due to the rotation of the blade. Watkins, Saunders & Hoffman (1995) outlined a method for resolving the turbulence intensity in the wind into the relative turbulence intensity experienced by a moving vehicle. They found that predictions for a vehicle travelling at 100 km/h matched well for terrain with low roughness but that in cases with obstructions, for example trees, the method under-predicted the longitudinal and, particularly the lateral turbulence intensity. The method assumes that the intensity of turbulence fluctuations are not affected by wind speed. Adapting this to the case of a wind turbine for the geometrically simpler case of wind turbine at zero yaw, the intensities is shown in Figure 2-56.

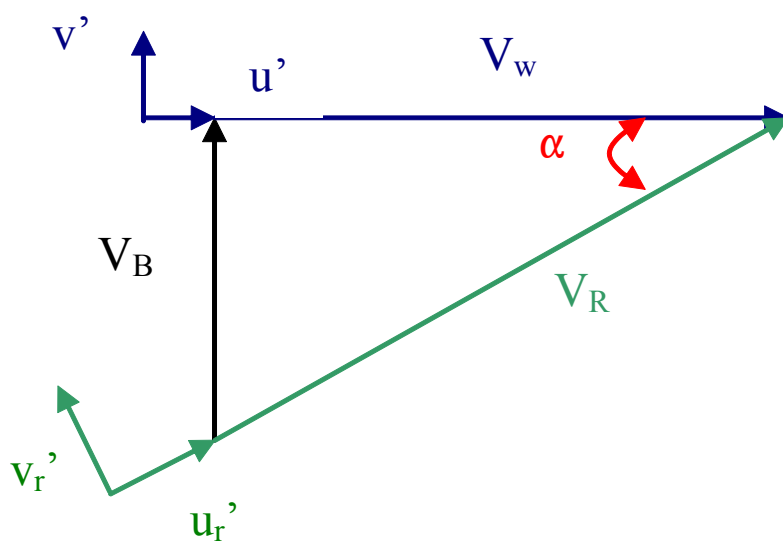


Figure 2-56 – The wind and turbulence components near a wind turbine blade.

Where V_w is the wind speed at the blade, V_B is the wind speed caused by the rotation of the blade, V_R is the relative wind speed at an angle of attack, symbol α , u' , v' and w' (w' is not shown as it is out of the page) are the instantaneous velocity components of turbulence in the wind speed at the blade and v_r' , u_r' and w_r' (w_r' is also not shown as it is out of the page) are the resultant instantaneous velocity components in the relative wind. From these the turbulence intensities in the wind speed at the blade (I_u , I_v and I_w), see Equation 2-35, and in the relative wind (J_u , J_v and J_w), Equation 2-36, can be defined

$$I_u = \frac{\sqrt{u'^2}}{V_w}, \quad I_v = \frac{\sqrt{v'^2}}{V_w}, \quad I_w = \frac{\sqrt{w'^2}}{V_w}; \quad \text{Equation 2-35}$$

$$J_u = \frac{\sqrt{u_r'^2}}{V_R}, \quad J_v = \frac{\sqrt{v_r'^2}}{V_R}, \quad J_w = \frac{\sqrt{w_r'^2}}{V_R} = I_w. \quad \text{Equation 2-36}$$

Also u_r' can be defined in terms of u' and v'

$$u_r' = u' \cos(\alpha) + v' \sin(\alpha). \quad \text{Equation 2-37}$$

Therefore,

$$u_r'^2 = u'^2 \cos^2(\alpha) + v'^2 \sin^2(\alpha) + 2u'v' \cos(\alpha) \sin(\alpha), \quad \text{Equation 2-38}$$

and taking the mean gives

$$\overline{u_r'^2} = \overline{u'^2} \cos^2(\alpha) + \overline{v'^2} \sin^2(\alpha) + 2\overline{u'v'} \cos(\alpha) \sin(\alpha). \quad \text{Equation 2-39}$$

In natural wind $\overline{u'v'} \ll \overline{v'^2} < \overline{u'^2}$ because u' and v' are usually not well correlated. Assuming they are uncorrelated (i.e. $\overline{u'v'} = 0$)

$$\overline{u_r'^2} = \overline{u'^2} \cos^2(\alpha) + \overline{v'^2} \sin^2(\alpha), \quad \text{Equation 2-40}$$

$$\frac{\overline{u_r'^2}}{V_w^2} = \frac{\overline{u'^2}}{V_w^2} \cos^2(\alpha) + \frac{\overline{v'^2}}{V_w^2} \sin^2(\alpha), \quad \text{Equation 2-41}$$

$$I_\alpha^2 = I_u^2 \cos^2(\alpha) + I_v^2 \sin^2(\alpha). \quad \text{Equation 2-42}$$

Therefore,

$$J_u = \frac{I_\alpha V_w}{V_R}. \quad \text{Equation 2-43}$$

Similarly it can be shown that

$$J_v = \frac{I_{\alpha+90} V_w}{V_R}$$

Equation 2-44

However for a wind turbine the wind speed seen at the blade is reduced compared to that in the natural wind due to the expansion of the wake behind the turbine. Similarly, due to the swirling of the wake, the wind component due to the rotation of the blade is increased. These are accounted for by the Blade Element Momentum (BEM) method via axial (a) and tangential (t) induction factors. Assuming that the wake is formed by the mean wind speed and is not altered by the instantaneous turbulence fluctuations, there are two alternate ways of viewing the effect of these factors on the turbulence intensity. One, the turbulence intensity is not at all altered by the wake (so the explanation outlined above with axial and tangential induction factors applied to give V_B and V_w holds). Some preliminary calculations based on this assumption for a turbulence intensity of 14% for the Tjæreborg wind turbine using a simple BEM method gave a turbulence intensity range for a wind range of 4m/s to 24 m/s of about 1.25% to 3.4% near the hub to 0.3% to 1.25% near the blade tip. Two, the wake also affects the turbulent vectors and so the axial and tangential induction factors should be applied to the instantaneous velocity components as well. There are legitimate arguments for both of these positions (and for arguing that the wake would be affected by the turbulence fluctuations) and further experimental investigation would be needed to confirm which is accurate. However it should be remembered that the effect of the rotation of the blade will be smallest on the thick blade sections used near the hub of the turbine, the section of the blade which stalls first.

2.9.6 Rotational Sampling Effects

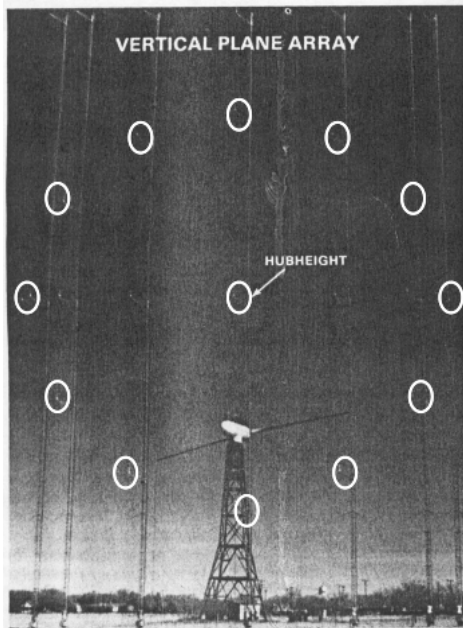


Figure 2-57 - The vertical plane array of anemometers Connell & George (1987) used for their tests (the circular ring of anemometers used for the tests have been circled) in front of the MOD-OA1 turbine. The anemometers were two rotor diameters (76.2m) upstream of the turbine and wind records were only taken when the turbine was within $\pm 20^\circ$ of being directly upstream of the turbine.

The turbulence intensity experienced by a wind turbine blade is further complicated by the rotational sampling induced by the blade's motion. Connell & George (1987) used a circular array of anemometers upstream of a turbine, see Figure 2-57, to calculate the turbulence that a blade would encounter. While their analysis of the effect on the turbine will not be reported here, as it did not account for the effect of the tower wake producing a cyclic loading on the downwind blades, they did gain some valuable insights on the effect of blade motion on the turbulence encountered. They generated a simulated time history of the blade as it rotated once every 1.5s. However the anemometers sampled only every 0.25s. The simulated blade passed the position of an anemometer every 0.125s so the wind speed measurements were interpolated in time and space to determine the simulated wind time history. This interpolation has the potential to exaggerate the periodicity that was found in the results but, since these results agree with other researchers' results, which will be presented later in this section, they probably did not influence the results greatly.

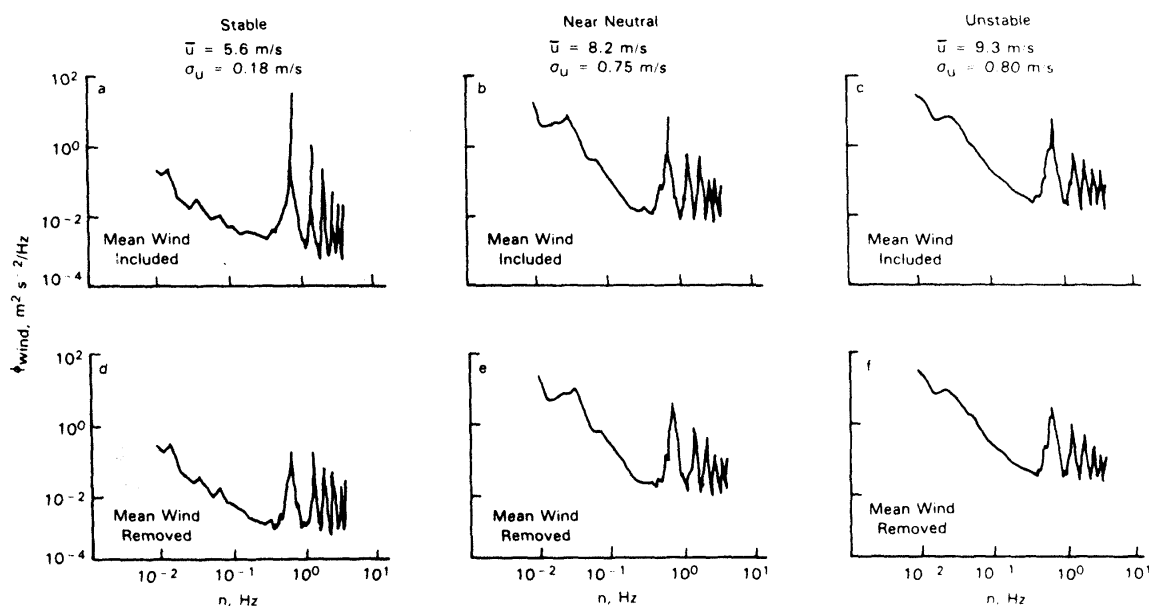


Figure 2-58 – Examples of power spectral density function of the simulated wind for stable, neutral and unstable layering of the atmosphere (Connell & George, 1987). The top row of plots (a, b and c) includes the mean wind speed where the bottom row (d, e and f) has had the mean wind removed.

The power spectral density of the wind speeds for various types of the earth's boundary layer are shown in Figure 2-58. Connell & George (1987) pointed out that cyclic motion of the blade causes rapid travel through two-dimensional gradients of velocity and that the blade repeatedly passes through persistent gradients. These persistent gradients are organised into peaks at multiples of the frequency of rotation. However these gradients are not only due to the wind shear. The lower row of plots in Figure 2-58 has had the mean wind removed from each anemometer before simulation of the rotational wind and therefore doesn't have the effect of wind shear. It seems the effect of the mean wind shear effects the peaks at the frequency of rotation and twice the frequency of rotation of the blade but turbulent effects are more important at higher multiples of the blade rotational frequency. As higher frequencies equate to smaller turbulence scales, the sampling of the wind due

to the blade's rotation could increase the turbulence intensities at the smaller scales that the blade experiences. Smaller scales are more likely to affect the performance of the aerofoils.

Verholek used eight Gill *uvw* anemometers equally spaced on the circumference of a circle of diameter 24.4m which was 24.4m off the ground and scanned them cyclically to simulate a moving blade (reported by Kristensen & Frandsen, 1982). The results of this experiment in comparison with a simple kinematic model developed by Kristensen & Frandsen (1982) are shown in Figure 2-59 and agree well with the observations of Connell & George (1987). Kristensen & Frandsen (1982) noted that Verholek's results showed the variance shifted from lower to higher frequencies as can be seen by comparing the power spectrum of the blade and the hub in Figure 2-59. The model assumed that the turbulence was stationary, homogeneous, isotropic, incompressible, Taylor's hypothesis was valid and that the turbulence energy spectrum had the form suggested by von Kármán. These assumptions should be invalid given the wind shear effects due to the earth's boundary layer, but the results matched well. The authors argued that the vertical wind profile over the time of a blade revolution is so erratic that the difference in wind speed seen at the top and bottom of the rotation are of the order of, and often less, than the root mean square of the wind speed (which is related to the standard deviation).

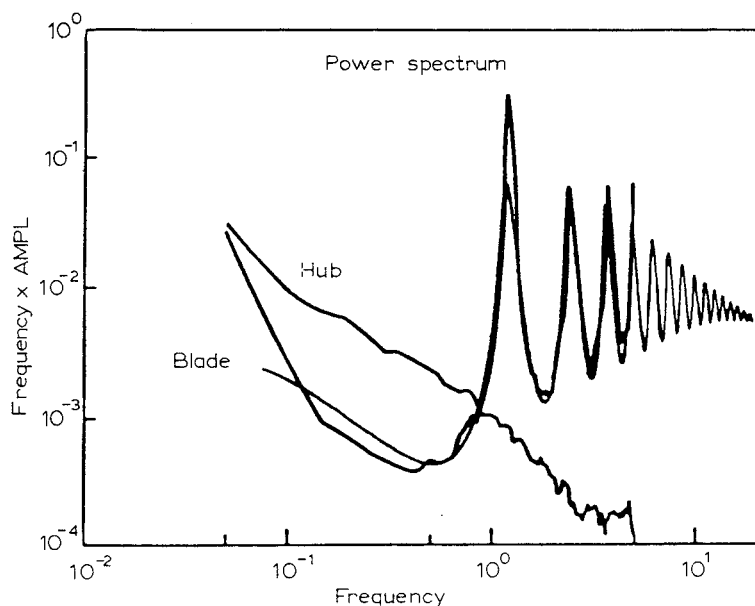


Figure 2-59 –The experimental spectrum obtained by Verholek with the theoretical results from the model by Kristensen & Frandsen (1982). The experimental results stop around 5Hz but the model results extend to about 20Hz. Verholek's hub spectrum matched a power law spectrum with an exponent of about -1.2 instead of the expected -2.3. Therefore the theoretical spectrum was shifted along the axis and normalised to match the experimental spectrum for frequencies lower than the first maximum.

2.9.7 Induction Effects

Neff & Meroney (1985) studied the effects of induction on the mean wind and turbulence using a 0.53m diameter model rotor in the 1.83m x 1.83m section of the Meteorological Wind Tunnel at Colorado State University. The mean axial velocity change and turbulence intensity relative to the rotor location is shown in Figure 2-60 for a wind speed of 7.6m/s and two different turbulence intensities, 0.1% and 1.5% (the higher turbulence intensity was generated by a grid). The

measurements were made with three-dimensional hot-film probes that had three orthogonally mounted, cylindrical hot films.

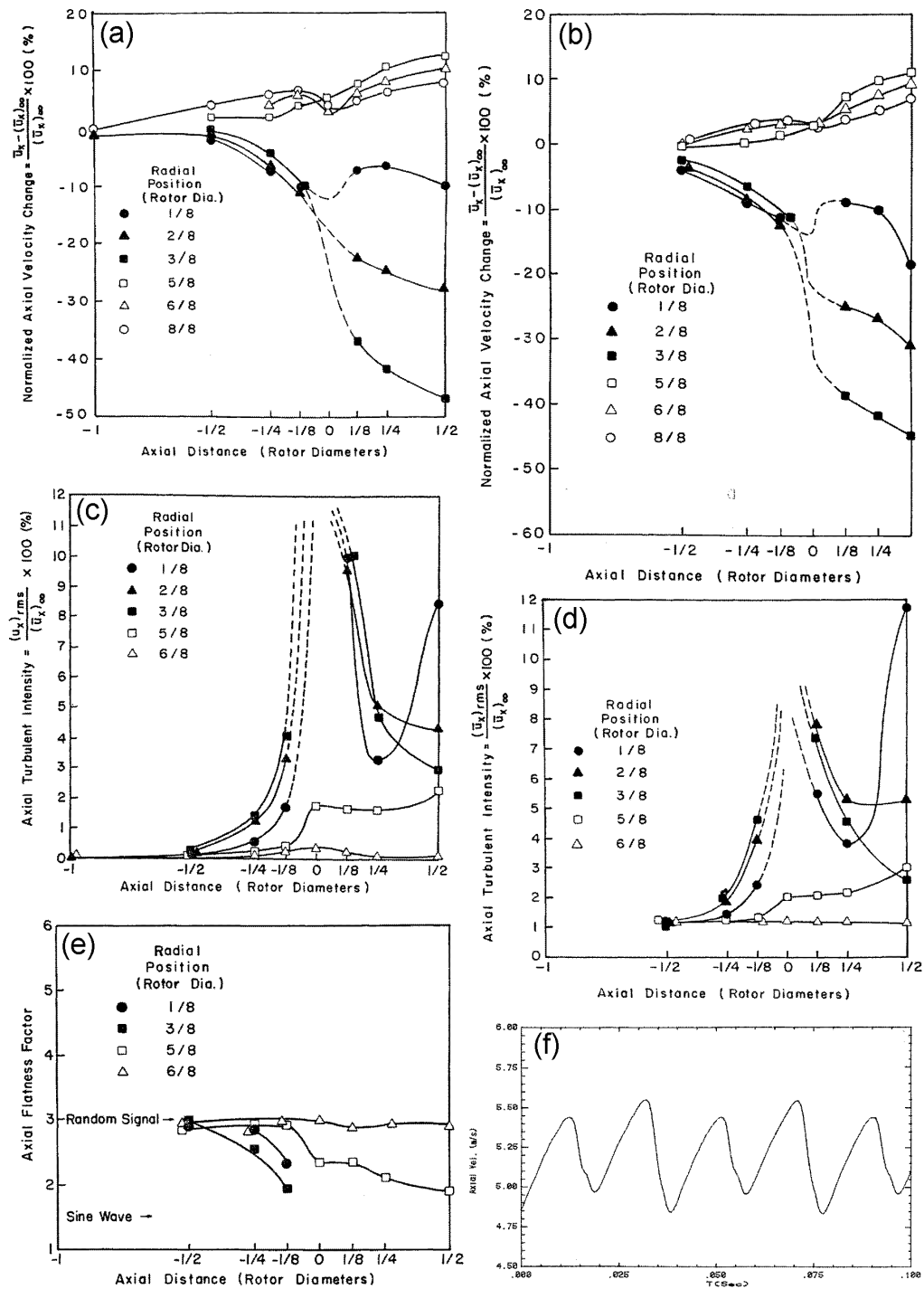


Figure 2-60 –The normalised mean axial velocity change versus axial distance for a wind speed of 7.6 m/s and a turbulence intensity of 0.1% (a) and 1.5%(b). The axial turbulence intensity versus axial distance for a mean wind speed of 7.6 m/s and a turbulence intensity of 0.1% (c) and 1.5%(d). The axial flatness factor versus axial distance for a wind speed of 7.6 m/s and a turbulence intensity of 1.5% (e) and a representative time series of the axial velocity just before the rotor (f).

The axial velocity results in Figure 2-60 did not show much difference for the different turbulence intensities. As expected within the radius of the blade, the flow was decelerated by the rotor. The flow was accelerated outside this radius. The turbulence intensity increases towards the rotor for points within the radius of the blade and then decreases in the wake (Neff & Meroney attribute the

increase for point $R = 1/8$ at $x = 1/2$ to the growing wake of the turbines hub and support mechanism). The point at $5/8D$ shows an increase in turbulence past the turbine rotor, presumably due to spreading of the wake. Neff & Meroney state

“...the axial flatness factor versus axial distance shows that most of this turbulence intensity in the non-wake region is due to an organized periodic structure, approaching that of a sine wave.” (p. 24, Neff & Meroney, 1985)

The plot of axial flatness factor is also shown in Figure 2-60 along with a representative plot of the axial velocity just before the rotor. It would be interesting to know if this almost sinusoidal velocity variation exists in a full scale case along with a corresponding increase in turbulence intensity.

2.9.8 Summary

It would also be useful to have instantaneous wind speed measurements near the blade to determine the turbulence encountered in a natural wind with all the factors of rotation included. (As part of the current study this was attempted using the five-hole probe on the instrumented blade of the NREL wind turbine in some tests, which was kindly lent to the author, but found that the frequency response of the tubing would have effectively damped out the high frequency variations in the results).

This section has shown that turbulence has the ability to alter the performance of wind turbines and can delay stall on aerofoils. Further work is necessary to test this for thick cambered aerofoil sections with an aspect ratio greater than 7. Thick cambered aerofoils sections are used near the hub of wind turbine blades, the part of the blade that stalls first and typically shows the greatest deviation from the behaviour of non-rotating aerofoil sections. While the natural wind is usually of large integral turbulence length scales, this requires there to be energy, although of a lower intensity, at the scales equivalent to the chord length. These scales are likely to effect aerofoil performance. The effect of induction, at least on a model rotor, can increase the turbulence intensity towards the turbine. Also operating in the wakes of other turbines increases the turbulence levels encountered. Furthermore, from the perspective of the blade, while the steady rotation of the blade would be expected to reduce the turbulence intensity experienced, the rotational sampling of the natural wind increases the turbulence intensity at multiples of the blade's rotational frequency. Therefore the assumption that the blade experiences minimal turbulence at the scale of the blade chord is not valid, and turbulence should be considered as a possible cause of delayed stall.

The aerofoil is acting as a bluff body past stall so it is useful to consider the effect of turbulence on bluff bodies, which has been studied in much more depth than the subset of aerofoils at high α . Therefore the next section will briefly detail the main findings of interest to the current study of the effect of turbulence on bluff body flows.

2.10 Turbulence Effects on Bluff Bodies

After over a century of effort by researchers and engineers, the problem of bluff body flow remains almost entirely in the empirical, descriptive realm of knowledge. ... The features that characterize a "bluff body" in aerodynamics are a large region of separated flow, a high value of the coefficient of drag (almost all pressure drag) and, traditionally, the phenomenon of vortex shedding, particularly in "two dimensional" flow. (pp. 79-80, Roshko, 1993)

The quotes Roshko placed around two-dimensional emphasise that although bodies of a constant cross section that span the tunnel are generally termed two dimensional, they produce three-dimensional flow. For example, for the most studied of bluff bodies, the circular cylinder, a close approximation to two-dimensional flow can be achieved for $Re < 180$ provided careful attention is paid to the end conditions. However for greater Re the flow is intrinsically three-dimensional (Roshko, 1993).

The drag on a bluff body is dependent on Re . Factors that may effect this dependence include free stream turbulence intensity and scale, aspect ratio, roughness, end conditions and blockage ratio (Roshko, 1993). Roshko (1993) noted that a change of Re does not necessarily imply direct effects of viscosity on the wake flow and that large separation and high drag can occur without vortex shedding. Turbulence is found in natural wind and wakes. It produces buffeting loads on bluff-bodies and changes in the mean flow field (Bearman & Morel, 1983).

Roshko (1993) stated that the variable separation point from circular cylinders means that this is actually a complex case of a bluff-body and uses data from flat plates normal to the flow to provide a case with fixed separation points. The case of an aerofoil is somewhere between these two cases with a fixed separation point from the sharp trailing edge and a variable separation point from the rounded leading edge. However, as more bluff body data exists for circular cylinders than any other shape, it is useful to know the features in the flow for the area with separation bubbles or turbulent separation with which this thesis is concerned. This corresponds, for flow around a cylinder, to the critical regime where separation bubbles form, and to the post or trans critical regime of turbulent separation, with a wider wake and higher drag. In the critical regime, there are exceptionally high values of shear stress in the boundary layer. At separation, the boundary layer is so thin ($\theta/d \sim 10^{-3}$) that it can develop Kelvin-Helmholtz instability and high Re stress while still close to the cylinder (Roshko, 1993)

The resulting enhanced entrainment requires the layer to reattach to the wall. The Reynolds stress in the boundary layer after reattachment is still at free-shear-layer values, i.e. considerably higher than in a boundary layer that has not experienced a separation bubble. This allows the boundary layer to survive a greater adverse pressure gradient than in the post critical regime where transition finally occurs *before* separation. (Roshko, 1993)

This results in an exceptionally narrow wake and low drag in the critical regime and a wider wake with associated higher drag in the post critical regime.

Much work has been performed on the effect of turbulence intensity and scale on bluff bodies. Turbulence is known to interact with boundary layers, promoting their transition from laminar flow to turbulent flow. In free shear layers, separating from the leading edge, added turbulence causes a higher radius of curvature of the shear layer and therefore earlier reattachment (Melbourne, 1993). In cylinders it is known that for all three transition states if the turbulence length scale is less than the diameter and intensity is greater than a certain value the turbulence becomes a governing factor (Zdravkovich, 1997).

There are three basic mechanisms by which freestream turbulence interacts with bluff-bodies; accelerating the transition to turbulence in shear layers, enhanced mixing and entrainment and distortion of the freestream turbulence itself (Bearman & Morel, 1983). The overall effect is often the result of more than one of these mechanisms. The excitation of the shear layer by turbulence entrained into it and by the pressure fluctuations, causes the transition to turbulence to occur earlier, i.e. a laminar boundary layer will become turbulent earlier with increased turbulence in the freestream. For attached boundary layers, the enhanced mixing and entrainment caused by increasing turbulence in the freestream increases skin friction. For free shear layers, the spreading rate is increased by the turbulence. One example of the distortion of turbulence occurs at a body's surface. As there can be no velocity component normal to the surface, this component's energy will be transferred to the component parallel to the surface. This blocking effect begins to take effect about one integral length scale from the wall. Also, the turbulence components at the wall will be attenuated by viscosity. This results in the freestream turbulence chiefly influencing the outer part of the boundary layer. These effects also mean that the structure of turbulence near the body may be quite different to that in the freestream. Turbulence can be distorted by the mean flow field (the mean strain field acts to rotate and stretch some vortex lines more than others).

For a situation where the separation layer closes up in the near wake, for instance in the wake of a short, thin plate, increasing turbulence levels in the freestream increases the curvature of the shear layer leading to a smaller separation region. Large scales dominate in this process. In contrast, for a flat plate spanning the tunnel, turbulence was shown to have little effect. It was reasoned that the vortex shedding was dominant and not significantly effected by turbulence (Bearman & Morel, 1983). Small scale turbulence is more likely to effect the thin shear layer at separation. To have an impact, the turbulence scale must be between one order of magnitude smaller than the shear layer thickness and one order larger than the typical body dimension (Bearman & Morel, 1983). However, as is discussed above, in some cases the turbulence intensity is the only important factor and the integral length scale does not have an effect. Bearman & Morel (1983) concluded that

“... free-stream turbulence can have a significant influence on the flow, and it is not always clear beforehand what and how significant an effect one should expect. Consequently, it is advisable (depending on the nature of the flow under study) to complement smooth-flow tests with tests in streams of elevated turbulence levels.” (p. 121).

Post stall aerofoils are bluff bodies. Shedding of vortices from bluff bodies causes fluctuating forces on the bodies. Designers must ensure that the shedding frequency does not coincide with the natural frequency of the body or a harmonic of this frequency. Some large wind turbines have suffered from stall-induced vibrations. This has prompted increased interest in the structural response of wind turbines to stall induced vibrations, for example the recent paper by Hansen (2003). The shedding from an aerofoil could also be of interest to designers of other structures who are required to use such aerofoils at high α .

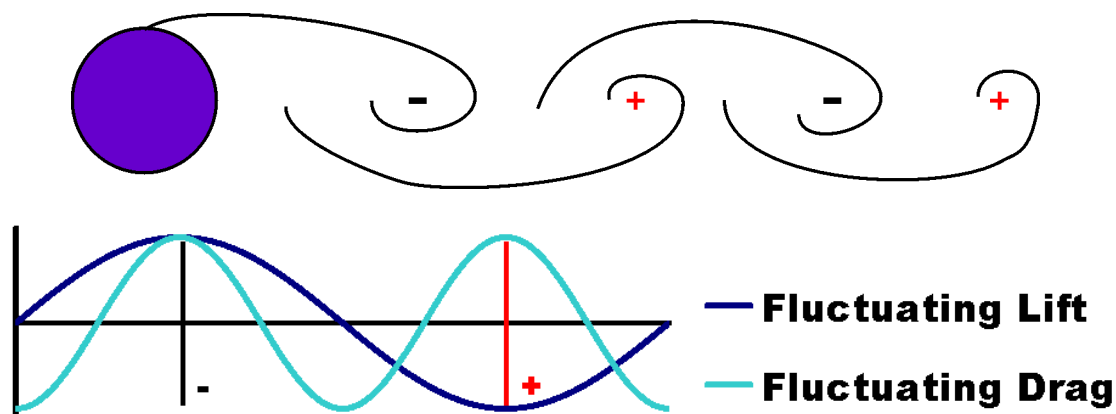


Figure 2-61 - Sketch of the Kármán vortex street behind a cylinder and the resulting fluctuating lift and drag forces.

For a stationary circular cylinder, vortices are alternately shed from the top and bottom surfaces of the cylinder and braid together to form a Kármán street. The vortices shed from the top surface are of negative sign and pull the cylinder up and in the direction of the flow; the vortices shed from the bottom of the cylinder are of positive sign and pull the cylinder down but still in the direction of the flow. The vortex shed from the top of the cylinder results in a peak in the lift and drag force. The vortex shed from the bottom of the cylinder results in a trough in the lift force but another peak in the drag. This results in the drag force oscillating at twice the frequency of the lift. A sketch of this is shown in Figure 2-61.

The fluctuations in c_d at higher Re are still at twice the frequency of c_l but appear in bursts, see Figure 2-62. The bursting intervals are an order of magnitude greater than the St time and they are not periodic. This has been associated with the spanwise modulation of the vortex shedding by Szepessy & Bearman (1992). The time scale of bursting has been shown to be dependent on end effects (for example, by Szepessy & Bearman (1992)) however it was not evident that it is related solely to end effects. Roshko (1993) suggested that it could be caused by spanwise structure (i.e. cellular structure on cylinder).

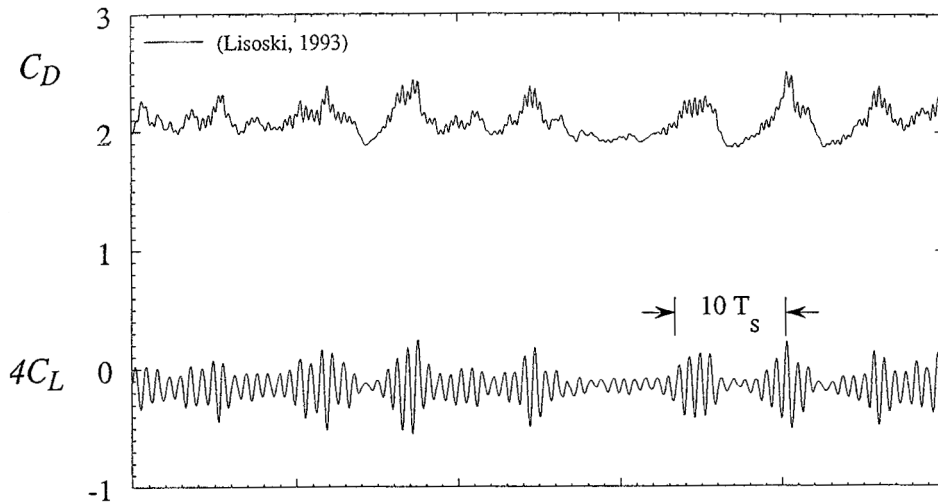


Figure 2-62 - Experimental Lift and Drag histories for a flat plate (thickness 10%). Data by Lisoski reproduced by Roshko (1993).

Stalled aerofoils have long been known to produce vortex wakes, as discussed for instance in the work of Fage & Johansen (1928). This compared measurements in the wake of several bluff bodies including two asymmetric bodies, an inclined flat plate and an aerofoil section at various α . They measured the boundaries of the vortex sheets at several positions in the near wake. The vortex sheets were found to shed from the leading and trailing edges of the aerofoil but did not join in the near wake, although the vortex sheets did expand and therefore became closer to each other, see Figure 2-63. The distance between the sheets increased with α and therefore the vertical distance between the leading and trailing edges increased. Fage & Johansen's most important conclusion was that the frequency and spacing of vorticity in the wake was dependent on the lateral spacing between the vortex sheets.

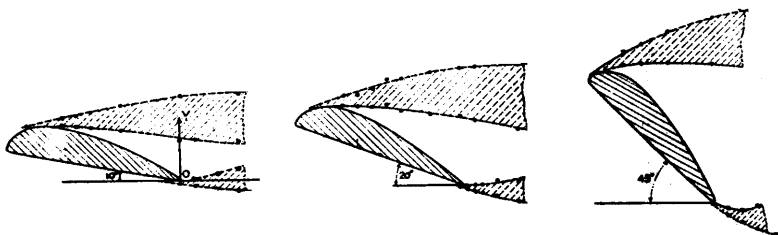


Figure 2-63 - Vortex sheets behind an aerofoil from Fage & Johansen (1928).

Their second conclusion was in part the impetus for Roshko's definition (1955) of a universal Strouhal number (St^*) based on a length scale equal to the width of the wake (d') and the characteristic velocity of the wake (U_s),

$$St^* = \frac{f d'}{U_s} \quad \text{Equation 2-45}$$

This can be related to the traditional definition of Strouhal number by the base pressure parameter (k)

$$k = \frac{U_S}{U_\infty} = \sqrt{1 - C_{ps}}, \quad \text{Equation 2-46}$$

$$k \left(\frac{d}{d'} \right) = \frac{St}{St^*} \approx \frac{St}{0.16}, \quad \text{Equation 2-47}$$

where C_{ps} is the base pressure coefficient. The 0.16 estimate for Roshko's universal Strouhal number given in Equation 2-47 was derived from observations on various different shapes. Using Equation 2-47 and the measured St , a relationship between k and d/d' can be derived. Roshko's paper also provided generic curves for several bluff-bodies. Using these and the relationship between k and d/d' , an estimate of the coefficient of drag for the body can be made.

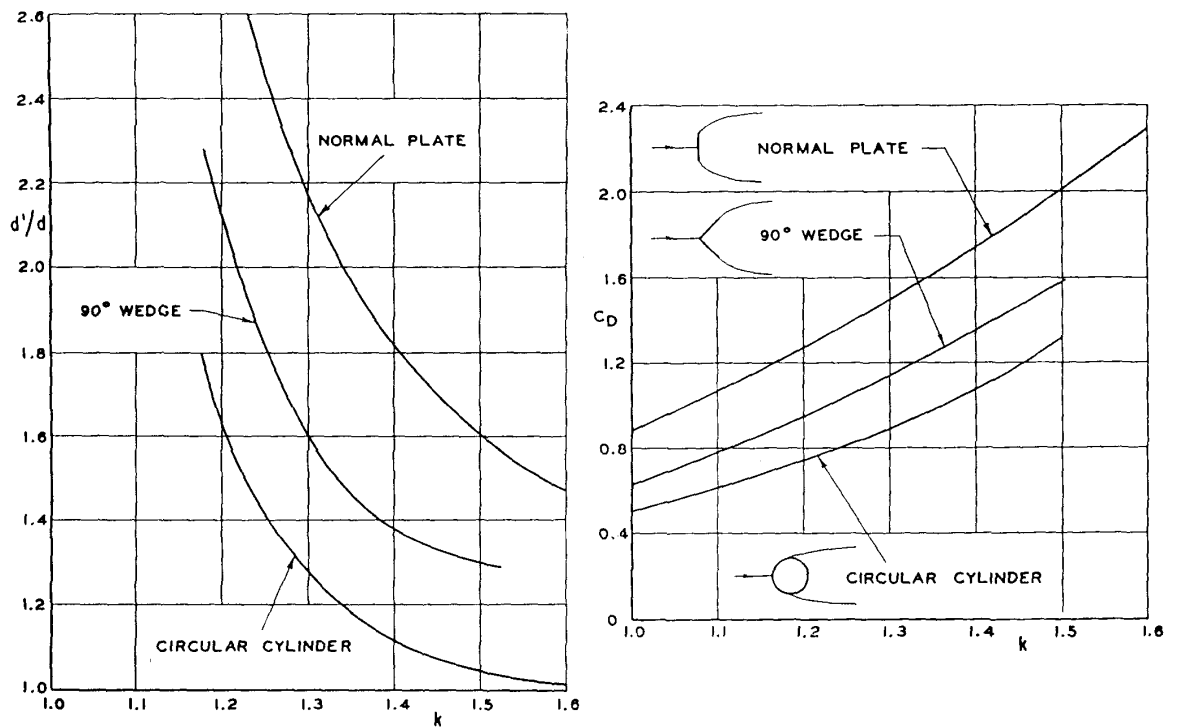


Figure 2-64 – Relationships between the base pressure parameter k and the ratio of wake width D' to object dimension D and the coefficient of drag c_d for a variety of cross-sections. Reproduced from Roshko (1955).

Roshko's universal Strouhal number is the most widely used of several variations that have since been proposed (Nakamura, 1996). Griffin (1979) demonstrated that using this formation with the natural frequency of the incident flow, the measured wake width at the end of the vortex formation region and the velocity at the edge of the separated boundary layer St^* collapses the d' and k data from 2D bluff cylinders, vibrating cylinders, cylinders in confined flow and cylinders at yawed incidence to a uniform flow to single curves. However, obtaining such measurements in the wake is difficult in many situations. Nakamura (1996) showed that while Roshko's universal Strouhal number is applicable to bluff bodies without after bodies, it may not be applicable to bluff bodies with afterbodies as the afterbody can significantly alter the vortex formation region.

Chen & Fang (1996) studied flat plates with bevelled sharp edges and found that the St based on the width of the plate normal to the freestream between separation points remained approximately

constant over a range of $0 < \alpha < 90$ degrees, a small variation being most evident for $\alpha < 45$ degrees, see Figure 2-65. They found jumps in St associated with the changing of shedding position from the back to the front edge of the bevel.

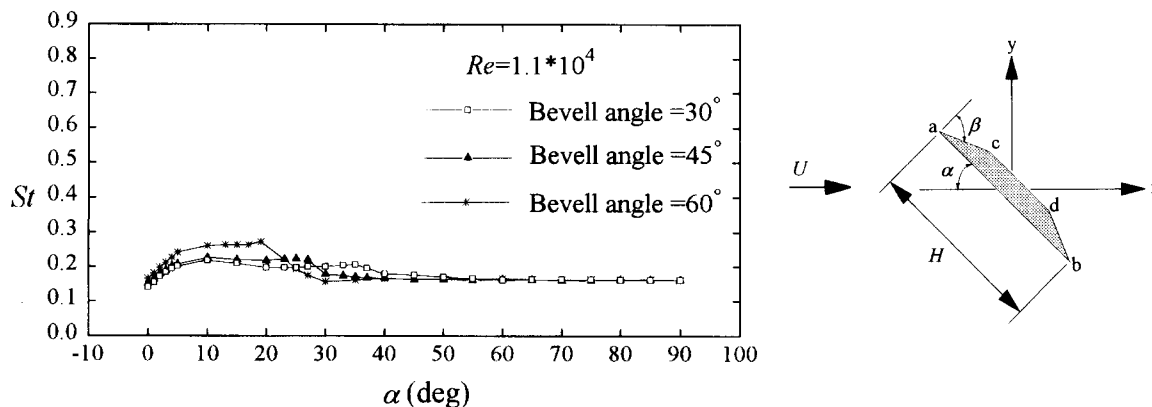


Figure 2-65 - Strouhal number based on the distance normal to the freestream between separation points (flow could separate from the upstream, a or b, or downstream, c or d, points of the bevel). Reproduced from Chen & Fang (1996).

In conclusion the bluff body studies have shown that large turbulence scales can influence the curvature of the shear layers and small turbulence scales the transition of the boundary layers to turbulence. Also, for the aerofoil sections at high α vortex shedding would be anticipated. The frequency of this shedding should give an indication of the wake width. Using the length of the aerofoil section normal to the freestream as an indication of the wake width it may be possible to calculate a fairly constant Strouhal number.

2.11 Conclusion

This chapter has shown that radial flow of the stalled boundary layer has the potential to cause the effect of “delayed stall”, along with dynamic stall and freestream turbulence. Dynamic stall, while very important in the cases of yawed flow or that affected by the wake of the tower, has not been demonstrated for other flow situations. Turbulence has the potential to slow the progress of the separation point from the trailing edge with increasing α . However, although turbulence is known to do this on some aerofoils, there are questions about the effects of aspect ratio, turbulence scale and intensity that have not been answered. Also, turbulence has been neglected from aerodynamic models and from the NREL Ames wind turbine tests designed to provide data to verify these models. For these reasons it was decided to investigate the effect of turbulence on thick aerofoil sections to discover if turbulence should be considered in future aerodynamic models of wind turbines.

Chapter 3

Experimental Method

3.1 Introduction

All experiments were conducted in the Monash University 450 kW Wind Tunnel. This section begins with descriptions of the models tested, the wind tunnel and the measurement equipment. It then details the results of experiments to determine the flow characteristics of the tunnel. The methods used to interpret the results are then examined, specifically the tubing response correction, the calculation of forces and the methods used in the analysis of fluctuations. The chapter concludes with a description of the method used to obtain surface flow visualisations.

3.2 Aerofoil Section Models

3.2.1 Profiles

Three 21% thick aerofoil sections were investigated. The first two were 4-digit NACA profiles. For the NACA XXXX series aerofoils the first digit is the percentage camber (m) with respect to chord (c), the second gives the position of maximum camber (p) as a tenth of chord and the last two digits give the maximum thickness (t) as a percentage of the chord length. The thickness (y_t) is given by

$$y_t = \frac{t}{0.20} \left(0.29690\sqrt{x} - 0.12600x - 0.35160x^2 + 0.28460x^3 - 0.10150x^4 \right), \quad \text{Equation 3-1}$$

where x is the position along the chord. The position of the mean line for $x \leq p$ is given by

$$y_m = \frac{m}{p^2} \left(2px - x^2 \right), \quad \text{Equation 3-2}$$

and for $x > p$ by

$$y_m = \frac{m}{(1-p)^2} \left(1 - 2p + 2px - x^2 \right). \quad \text{Equation 3-3}$$

The angle of the mean line is

$$\theta = \tan^{-1} \left(\frac{dy_m}{dx} \right), \quad \text{Equation 3-4}$$

and the upper (x_u, y_u) and lower (x_l, y_l) surface coordinates taken from the leading edge are given by

$$\begin{aligned} x_u &= x - y_t \sin \theta \\ y_u &= y_m + y_t \cos \theta \\ x_l &= x + y_t \sin \theta \\ y_l &= y_m - y_t \cos \theta \end{aligned} \quad \text{Equation 3-5}$$

These formulae are from Abbot & Doenhoff (1959).

The 0021 and 4421 were chosen from the NACA aerofoils to give a contrast between a symmetrical and a cambered aerofoil section. The NACA 0021 was previously investigated by Stack (1931) who found a difference between the effects of turbulence on thick symmetrical and cambered models, see Section 2.9.2. The NACA 4421 has been used on wind turbines (Hansen, A. C. & Butterfield, 1993), for example, the 2MW Tjæreborg test turbine in Denmark. On this turbine it was used on a section of the blade between root and mid-span; this inboard section of the blade stalls first. NREL's S809 aerofoil is also 21% thick. It was specifically designed for use on wind turbines (Somers, 1989) and was used on the turbine tested in the NASA Ames wind tunnel. This aerofoil was designed to be insensitive to roughness, have a restrained maximum lift and a gradual stall (Somers, 1989). Somers (1989) lists the surface coordinates for the S809. A comparison of the aerofoil profiles is shown in Figure 3-1. The S809, when compared to the two NACA profiles, has much narrower leading and trailing edges. The thickest part of the aerofoil is slightly more towards the trailing edge and, from the thickest part, the lower surface is more cambered.

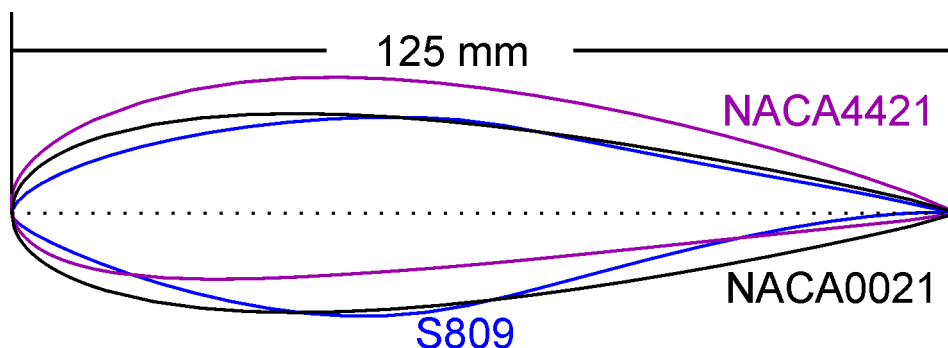


Figure 3-1 - Aerofoil cross-sections of the NACA0021, NACA4421 and NREL's S809 (to scale).

The 125mm chord length (c) gave an aspect ratio (span/chord) of over seven, in line with the limits found for the testing of other bluff bodies (see the work on a circular cylinder by Szepessy & Bearman (1992) discussed earlier in Section 2.2). The aspect ratio of the models was $7.28c$. This chord length meant that the blockage of the tunnel was minimal, less than 1.32% for $\alpha=0^\circ$ increasing to a maximum of 6.25% at $\alpha=90^\circ$. Because of the small blockages encountered no blockage corrections were applied to the results. However, the small chord length also limited the maximum Re to about 4×10^5 with no grids in the tunnel. With the large grid the maximum Re was about 2.7×10^5 .

3.2.2 Tapping Locations

The NACA 0021 and NACA 4421 had taps at the same locations along the chord as shown in Figure 3-2. There were two tapping rows (B1 and B2) each placed one chord length either side of the tunnel centreline. On the NACA aerofoil sections these rows contained 28 taps. However, due to the narrower leading and trailing edge of the S809 aerofoil section and therefore the smaller internal volume, the B rows were limited to 22 taps on this model. There were 4 tap rows designated A that surrounded the rows B at one chord length either side. The positions of the taps along the chord are shown in Figure 3-3. The 4 tap rows had taps on the leading edge, trailing edge

and near the point of maximum thickness. The rows designated B aimed to catch the surface distribution of pressure and so had a complete ring of taps which were concentrated towards the leading edge in order to obtain better coverage of the higher gradients expected there. They also contained the same chordwise taps as the four tap (A) rows. The taps were labelled according to row and then numbered from the trailing edge across the top surface, around the leading edge and then back towards the trailing edge.

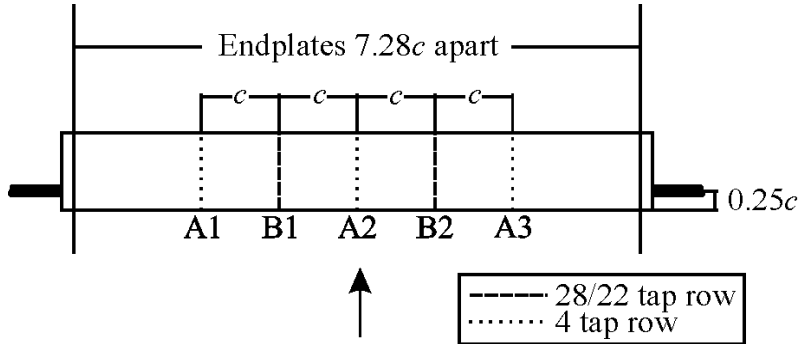


Figure 3-2 - Tapping row locations, each row designate A had 4 taps, on the NACA aerofoils the rows designated B had 28 taps but on the S809 they had only 22 taps. The aspect ratio between the endplates was $7.28c$ and the aerofoil sections were supported by steel bars located at $0.25c$.

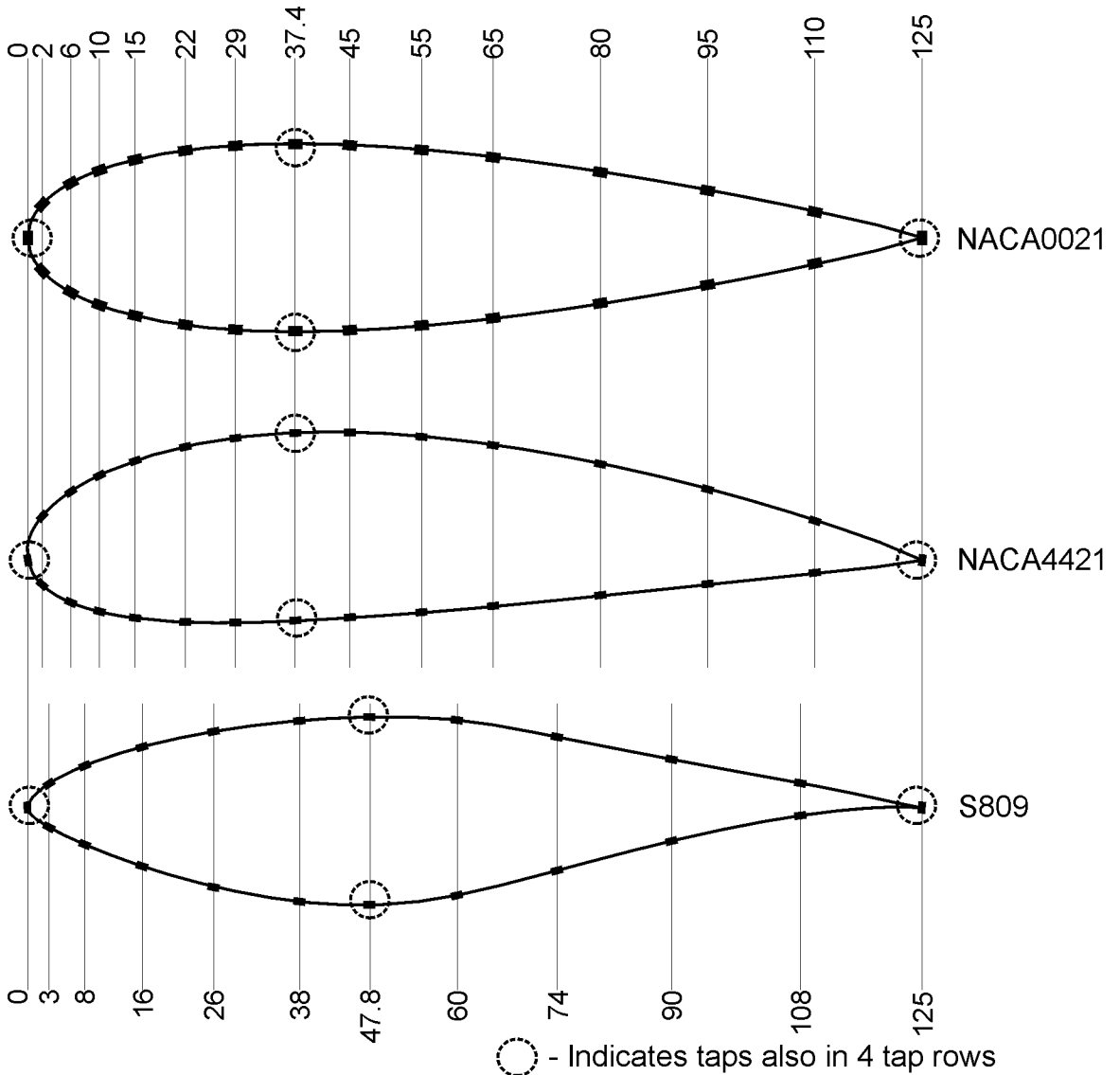


Figure 3-3 - Tapping locations along the chord in mm for all three aerofoil sections.

3.2.3 Model Construction

The chief design constraint was a desire for minimal deflection of the aerofoil section during testing. A maximum deflection (y_{max}) of 0.5mm at the centre of the aerofoil was chosen (equivalent to a deflection of less than 0.055% of the span of the aerofoil section between the endplates). Modelling the aerofoil as a simply supported beam (all equations from Roark's Formulas for Stress and Strain, Young, 1989), the maximum deflection at the centre of the beam ($x/2$) is

$$y_{max} = \frac{-5\omega_a l^4}{384EI} \tag{Equation 3-6}$$

Initial calculations were performed by modelling the aerofoil as a rectangle,

$$I = \frac{1}{12}bd^3, \tag{Equation 3-7}$$

where the width is b and the height is d . At $\alpha = 0^\circ$

$$I = \frac{1}{12}c(0.21c)^3 \approx 7.7 \times 10^{-4}c^4, \tag{Equation 3-8}$$

whereas at $\alpha = 90^\circ$ the second moment of inertia is a factor of 100 larger

$$I = \frac{1}{12}(0.21c)c^3 \approx 1.75 \times 10^{-2}c^4. \tag{Equation 3-9}$$

Therefore the greatest deflection of the aerofoil is expected to occur for low α and, as a consequence, will be induced largely by the lift force. The sectional lift coefficient (c_l) is defined as

$$c_l = \frac{L}{\frac{1}{2}\rho V^2 c}, \tag{Equation 3-10}$$

where L is the lift force per metre span. Therefore the force per unit length (ω_a) is 182 N/m (assuming a maximum c_l of 1.2 (around what was observed by Stack, 1931) a wind speed of 45 m/s, which is the maximum expected in the wind tunnel section used, and a chord length of 125mm). Using a span (l) of 0.95m (the actual length of the aerofoil section including segments concealed behind the endplates and a force per unit length (ω_a) of 220 N/m), this gave the condition

$$EI = \frac{-5\omega_a l^4}{384y_{max}} = \frac{-5(182)(.95)^4}{384(-0.0005)} \geq 3860 \text{ Nm}^2. \tag{Equation 3-11}$$

To simplify the calculation, and provide a quasi safety factor, this force was assumed to apply to the aerofoil at $\alpha = 0^\circ$. Modelling the aerofoil as a collection of rectangles as shown in Figure 3-4, the results in Table 3-1 were obtained.

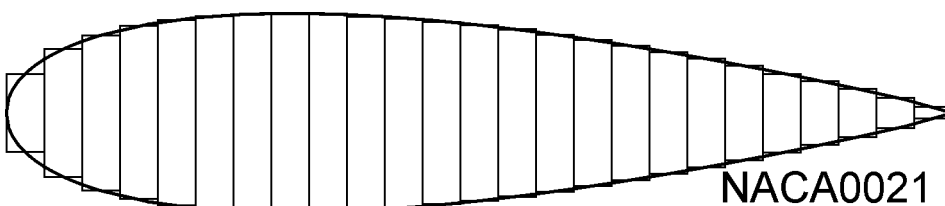


Figure 3-4 – Simple model to allow the calculation of the second moment of inertia of the aerofoil.

Number of Rectangles	Whole Aerofoil		2mm Thick Shell		3mm Thick Shell	
	Area ($\times 10^{-3} \text{ m}^2$)	I ($\times 10^{-8} \text{ m}^4$)	Area ($\times 10^{-3} \text{ m}^2$)	I ($\times 10^{-8} \text{ m}^4$)	Area ($\times 10^{-3} \text{ m}^2$)	I ($\times 10^{-8} \text{ m}^4$)
125	2.2266	8.7407	0.5022	3.8893	0.7352	5.2706
250	2.2276	8.7433	0.5026	3.8906	0.7357	5.2723
2500	2.2282	8.7441	0.5029	3.8910	0.7361	5.2728
12500	2.2282	8.7441	0.5029	3.8910	0.7361	5.2728
125000	2.2282	8.7441	0.5029	3.8910	0.7361	5.2728

Table 3-1 – Second moment of inertia of the NACA 0021 aerofoil modelled as a collection of rectangles.

Therefore, even in the unrealistic case of a solid aerofoil (where there would be no room for tubing), $E \geq 44 \text{ GPa}$. Due to the requirements for stiffness, carbon fibre and steel were chosen as materials. To find the second moment of area for different wall thickness the coordinates of the surface to a smaller size were determined (by computing the points at a specified distance from the surface using the known angles of the surface segments and computing a specified distance inwards normal to the surface). Using the rectangle method the second moment of area for this shape was determined. Subtracting this from the value for the whole aerofoil it was found that for 2mm thick walls $I=3.8910 \times 10^{-8} \text{ m}^4$ and for 3mm walls $I=5.2728 \times 10^{-8} \text{ m}^4$. Choosing the 3mm thick walls and using an E of 125 GPa for the carbon fibre gave an EI of 6590 Nm^2 which exceeds the criteria given by Equation 3-11.

The value of E obtained was for prepreg carbon laminate, the actual value achieved with hand lay-up would be less. Therefore two steel bars were added along the length to provide additional stiffness. The bars were located along the chordline, one at $1/4c$ and the other at about $0.55c$. The main bar at $1/4c$ that was also used to support the aerofoil between the bearings had a diameter of 16mm. The diameter of the second bar was 12mm. As the modulus of steel is $E= 200 \text{ GPa}$, the second moment of area is

$$I = \frac{\pi}{4} R^4 = \frac{\pi}{4} \left((0.008)^4 + (0.006)^4 \right) = 4.2 \times 10^{-9} \text{ m}^4, \quad \text{Equation 3-12}$$

so the EI of just the bars was 840 Nm^2 . The weight of the bars, given per unit length by Equation 3-13, did not provide a significant force on the structure (in general the weight would oppose the lift force anyway),

$$F_{weight} = \left((\rho A)_{bars} + (\rho A)_{shell} \right) g = \left(7860 \frac{\pi}{2} (0.008^2 + 0.006^2) + 1500 (7.361 \times 10^{-4}) \right) (9.8) = 23 \text{ N/m} \quad \text{Equation 3-13}$$

The outer shell of carbon fibre was firmly connected to the two metal bars around bracings. The outer carbon fibre shell was constructed by making a wooden shape of the aerofoil. From this model female fibreglass moulds were constructed, and then the carbon fibre was laid up in these moulds. The carbon fibre aerofoil segments were then tapped. The inner supports were made to fill the internal section of the model at the far end that contained no tubing. In the rest of the model, the supports did not reach the leading or trailing edges and there was a gap between the two

bars as can be seen in Figure 3-5. The model was then glued together with filler, being careful not to deform the tubing. Yoshida, Kurita and Tamura (2000) showed that provided that bending did not greatly reduce the sectional area of the tubing the positions and number of bend points in the tubing produced negligible effect on the fluctuating pressures compared to the same pressures measured with a straight tube. Unfortunately during this process in the construction of the S809 aerofoil section, the top surface slipped sideways, resulting in the upper and lower taps being out of alignment by 1mm. The leading edge tap remained in line with the top surface taps and the trailing edge tap in line with the lower surface taps. The tubing for the NACA 4421 came out the wrong side so the model was tested upside down. After the aerofoil was bonded together the surface of the model was filled and sanded back to give a very smooth surface. The next section will describe the wind tunnel and how the model was installed.

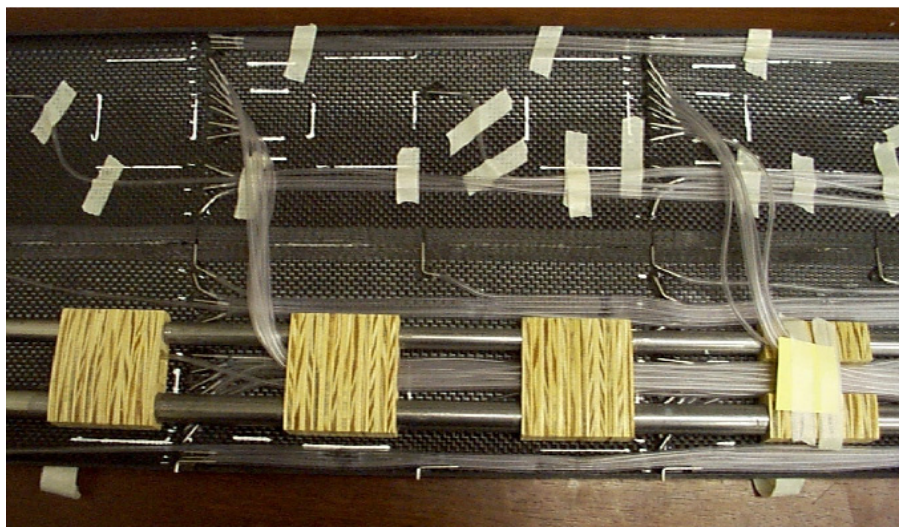


Figure 3-5 - Internals of the NACA 0021 aerofoil section showing tubing, bracing and support bars.

3.3 Wind Tunnel, Model Placement and Grids

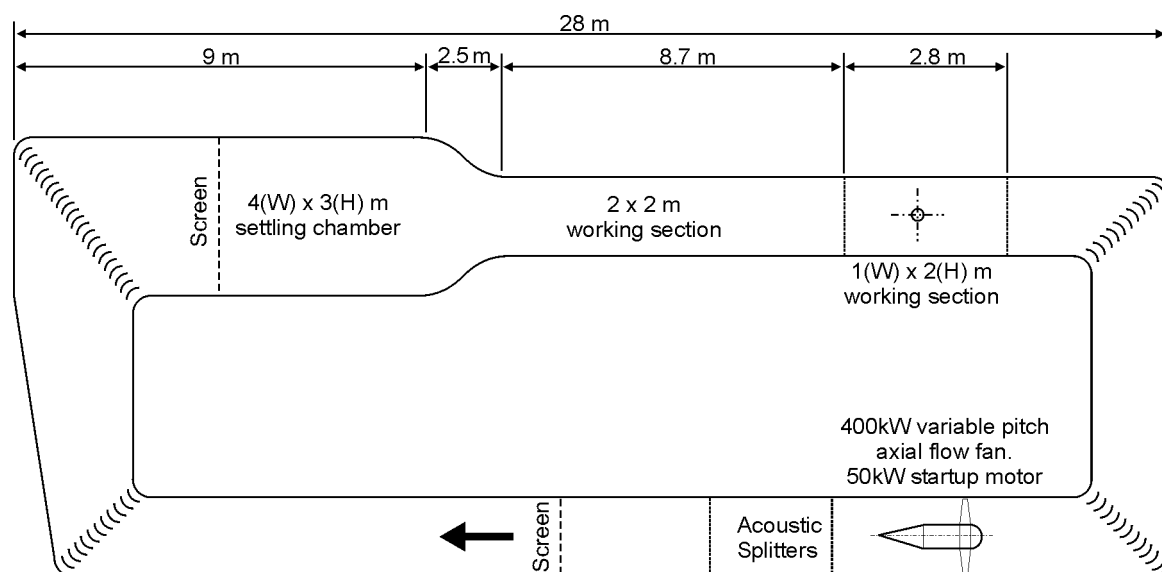


Figure 3-6 - Diagram of the 450kW Wind Tunnel, Department of Mechanical Engineering at Monash University (reproduced from Eddy, 2005).

A diagram of the 450kW wind tunnel at the Department of Mechanical Engineering, Monash University is shown in Figure 3-6. The tunnel is of closed circuit design and is powered by a 400kW electric constant-rotational speed, variable-pitch axial-flow fan and a 50kW start-up motor which are situated in the return circuit. The experiments were conducted in the 1m wide by 2m high working section.

End plates were installed in the working section to minimise the effects of the wall boundary layers and create a more two-dimensional flow. The endplates were designed to the criteria of Stansby (1974) for circular cylinder testing modified slightly for aerofoil testing. Stansby's recommendations were endplates that extended 2.5 diameters upstream, 6 diameters downstream and 6 diameters above and below the centre of the cylinder. An aerofoil's dimension perpendicular to the flow changes with α . The conservative criteria of $2.5c$ was used upstream of the model, the rest of the dimensions were taken as the maximum possible with the existing supports. The endplates were made of 6mm Medium Density Fibreboard (MDF), were situated 45 mm off the wall (using aluminium tube spacers) and had a shaped leading edge to prevent separation. The positions of the endplates, model, reference Pitot and electronic scanivalve in the working section are shown in Figure 3-7.

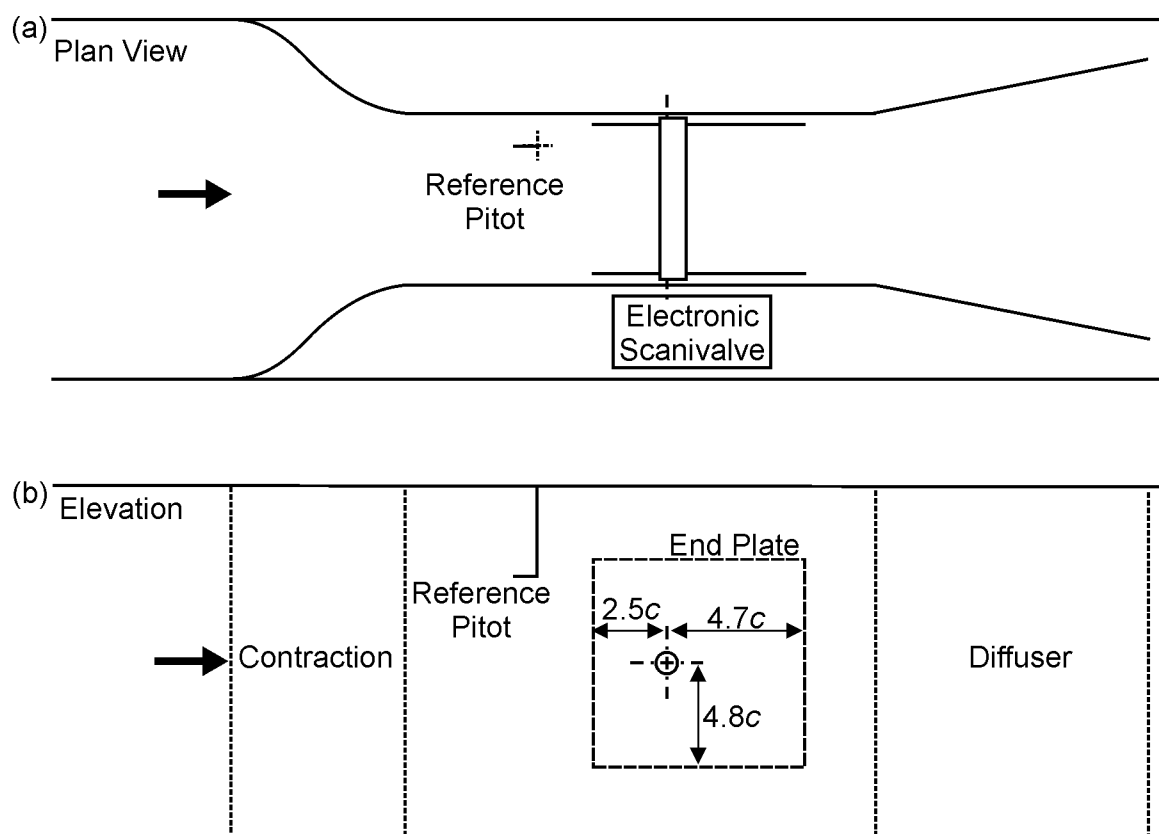


Figure 3-7 – Diagram of the 450kW wind tunnel 2m × 1m working section and the endplates, adapted from Eaddy (2005).

The models were slid in through the side of the tunnel where the electronic scanivalve was later placed. The two circular endplates were placed on the model before the steel bar at $1/4c$ was slid

into a nylon bearing on the far tunnel wall. The main endplates had a circular hole with a flange that fitted a similar flange on the circular endplates that rotated with the model, see Figure 3-8. The circular endplates were held in place by this flange and large washers that were attached to the bolts around the holes, see Figure 3-9(a). (The original design used screws but these occasionally came loose. A hot glue gun was used to apply glue over the nuts to ensure this did not happen with the bolt design). A similar nylon bearing was located on the near end of the bar via a positioning arm that was held fast to the shaft. The model was positioned to $\alpha = 0^\circ$ by matching the upper and lower pressures around the leading edge of the symmetric NACA 0021 model and for the other two cambered models by using an inclinometer on the flat upper surface of jigs that had the model shape cut out of their lower surface. The model was held at this angle by securing the second bearing-brace to the tunnel wall.

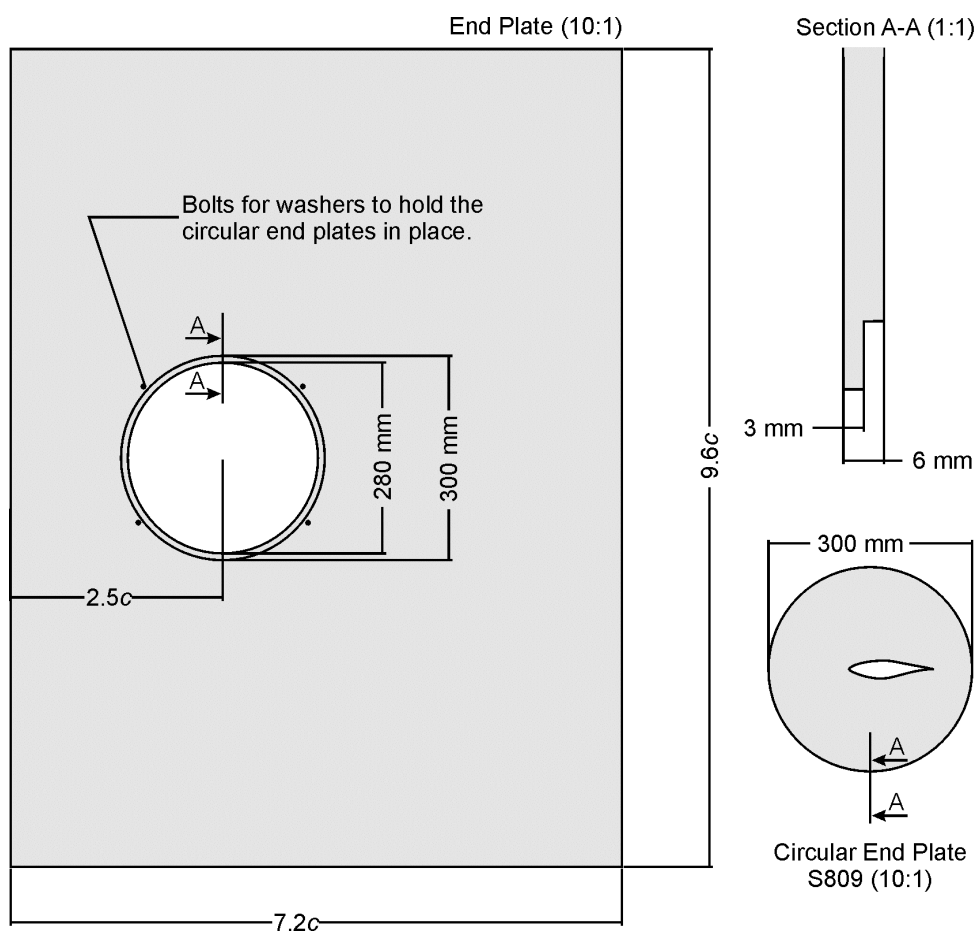


Figure 3-8 - Drawing of end plates for the wind tunnel wall furthest from where the Scanivalve was located.

α was changed while the tunnel was running by removing a small panel on the outer tunnel wall, reaching over the electronic Scanivalve (see Figure 3-7 for a diagram showing the inner and outer tunnel walls and the Scanivalve), unscrewing the bolt which fed through the positioning arm, altering α using a pair of multigrips and screwing the bolt in at the new position, see Figure 3-9(b). The small panel was then replaced. This allowed α to be changed while the tunnel was running with minimal disturbance to the flow. The braces had an outer ring of threaded holes every 5° from -90° to 90° and an inner ring of threaded holes every 5° from -27.5° to 27.5° , see Figure 3-9(b). The

original positioning arm, shown in Figure 3-9(b), was black plastic and was held to the shaft by an interference fit (controlled by bolts which allowed the arm to be removed). In general this worked well, however, it did slip a couple of times so a new positioning arm was constructed of aluminium and held to the shaft by grub screws. The new positioning arm was used for the NACA 4421 and S809 tests.

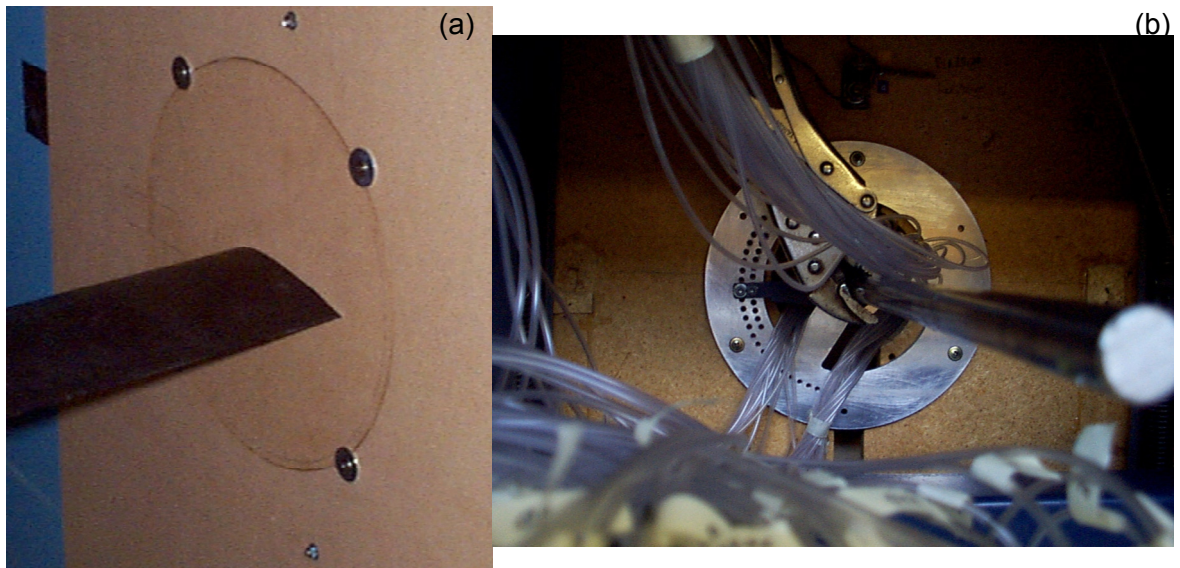


Figure 3-9 – Photos of (a) the model and endplate assembly (original version that used screws to hold the washers that held the circular endplates in place) and (b) the near side of the tunnel showing the bearing and positioning brace, the positioning arm (original plastic version), the multigrips used to change α and the steel rod which was located at quarter chord in the model.

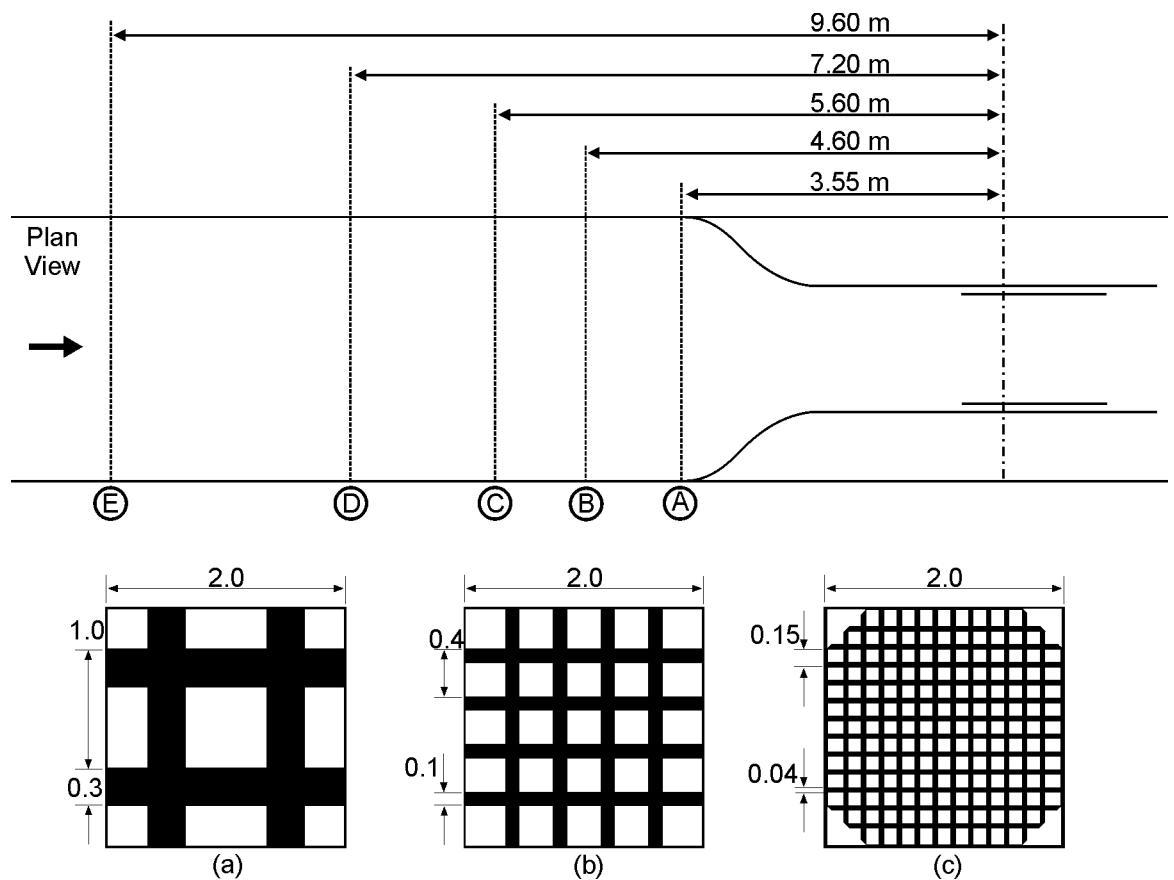


Figure 3-10 - Diagram of grid positions measured from the quarter chord of the model (and labelled A to E) and grids, the grids will be referred to as the large (a), medium (b) and small (c) grids. Diagram adapted with permission from Eaddy (2005). All dimensions in metres.

Three grids were used to give different turbulent scales. These will be referred to as the small, medium and large grids. They were placed at five different positions in the $2\text{m} \times 2\text{m}$ section of the tunnel, upstream of the contraction to the $1\text{m} \times 2\text{m}$ to section used for the tests. This configuration was mostly due to flow speed considerations but the contraction would also have made the grid-generated turbulence more isotropic. The grids and their positions, labelled A closest to the model and E furthest from the model, are shown in Figure 3-10. The small grid had corners cut out (triangles of approximately 0.3m base and 0.3m height) to allow it to fit over light fittings in the $2\text{m} \times 2\text{m}$ section. The large grid was not used in the closest position to the model because the turbulent flow did not have enough time to develop so that the turbulence intensities in the longitudinal, lateral and vertical directions were similar (Eaddy, 2005). This meant that, including the no-grid case, each model was tested in 15 different turbulent flows. The next section will examine the characteristics of these flows.

3.4 Flow Characteristics



Figure 3-11 – One of the cobra probe's used (a) and a close-up of the head (b).

The flow characteristics of the bare tunnel and those with the grids were measured by cobra probe traverses. The cobra probe measures the pressure on different facets of an angled probe head, see Figure 3-11, and then combines these measurements to deduce the three components of velocity. The spatial resolution of the cobra probe was limited by the 2.5mm size of the faceted head. Measurements were taken for 60 seconds at 2500Hz with a digital filter applied at 1250Hz . This resolution was adequate to produce the well-defined turbulence spectra shown later in this section. The cobra probe results matched earlier hotwire results for the same flow conditions taken by Mr. Michael Eaddy (2005) but gave smaller uncertainties in the measurements. Two Turbulent Flow Instrumentation (TFI) cobra probes were used along with the accompanying software to obtain the measurements of velocity and turbulence intensity across the tunnel. One probe remained at the centre of the tunnel while the other was moved to various positions relative to this probe as shown in Figure 3-12. Probe 0 was placed in the centre of the tunnel where the $1/4c$ of the model was located when the model was in the tunnel. The other probe (Probe 1) was moved to the other positions on the grid. Every probe location was tested for the flows most likely to be inhomogeneous, the clear tunnel (no grid) case and flows where the turbulence producing grids

were placed in the positions closest to the test section. For the other grid positions, only the Probe 1 positions in the middle row (same row as Probe 0) were measured. Some experiments were repeated at higher wind tunnel fan blade angles to ensure tunnel speed did not influence the results.



Figure 3-12 – Photograph of the cobra probes in the tunnel with the small grid and diagram of the cobra probe positions for measurements. Note the Pitot at the top of the image.

The ratio of the U velocities is shown in Figure 3-13 for the no grid and the three grids in the positions closest to the model at which they were tested. These were the extreme cases with the largest differences in velocity. The maximum difference between the two velocities measured was only 5%, which was considered a very good result given the nature of the flow. Also there is little structure in these results, indicating that the grids were not affecting the mean velocities. The vertical bands in the medium grid results seem to be due to the interpolation (there were no Probe 1 measurements taken at $x = 0$), this is confirmed by the following analysis of the turbulence intensities.

The turbulence intensity in the u , v and w directions for all of the measurements are plotted in Figure 3-14. The results at $x = 0$ were taken as the average of all the measurements taken with Probe 0; all other results were from the averaged measurements of Probe 1. Probe 0 tended to measure a slightly higher intensity than Probe 1. In the absence of a turbulence producing grid the turbulence intensity was slightly higher at $x = -300\text{mm}$ than at the other positions, the addition of the grids removed this bias. The tests for the different speeds showed good agreement except for I_w for the case of No Grid Lower (30) at $x = 100\text{mm}$. This measurement is much higher than the others and was assumed to be an anomaly given the tests at the other flow speeds (which matched well in all other cases) did not detect it. In conclusion, the turbulence intensities across the tunnel were considered to be reasonably uniform.

The Pitot used in the experiments to measure the dynamic pressure was connected during the cobra probe tests. The comparison between the velocities measured with the Pitot and Cobra Probe 0 are given in Table 3-2. It can be seen that the Pitot always reads a lower velocity than the cobra probe. This is not surprising given the Pitot's location 0.3m from the top of the tunnel (as can be seen in the photograph in Figure 3-12). It is also 0.5m upstream of the cobra probes and so there is a possibility of some acceleration of the flow contributing to this effect. The standard deviation of the ratio was small, indicating that these results were not due to fluctuations in the flow. Excluding the large grid in the two positions closest to the section, the no grid case showed the smallest ratio of Pitot velocity to Cobra Probe velocity. This can be seen more clearly by noting the ratio of the averages for each condition to that found for the no grid condition. These results were taken for the moving probe (Probe 1) measurements in the middle row at a fan blade angle of 20°. Apart from the large grid in the two positions closest to the model, lower Pitot measurements for the no grid case would cause the Re to be underestimated for the no grid case more than the others. As turbulence would be expected to replicate some of the effects of higher Re increasing turbulence should minimise differences between the flows rather than increase them. However the effect on Re was small, less than variations during the runs which will be discussed next, and so no correction to the results for this was attempted.

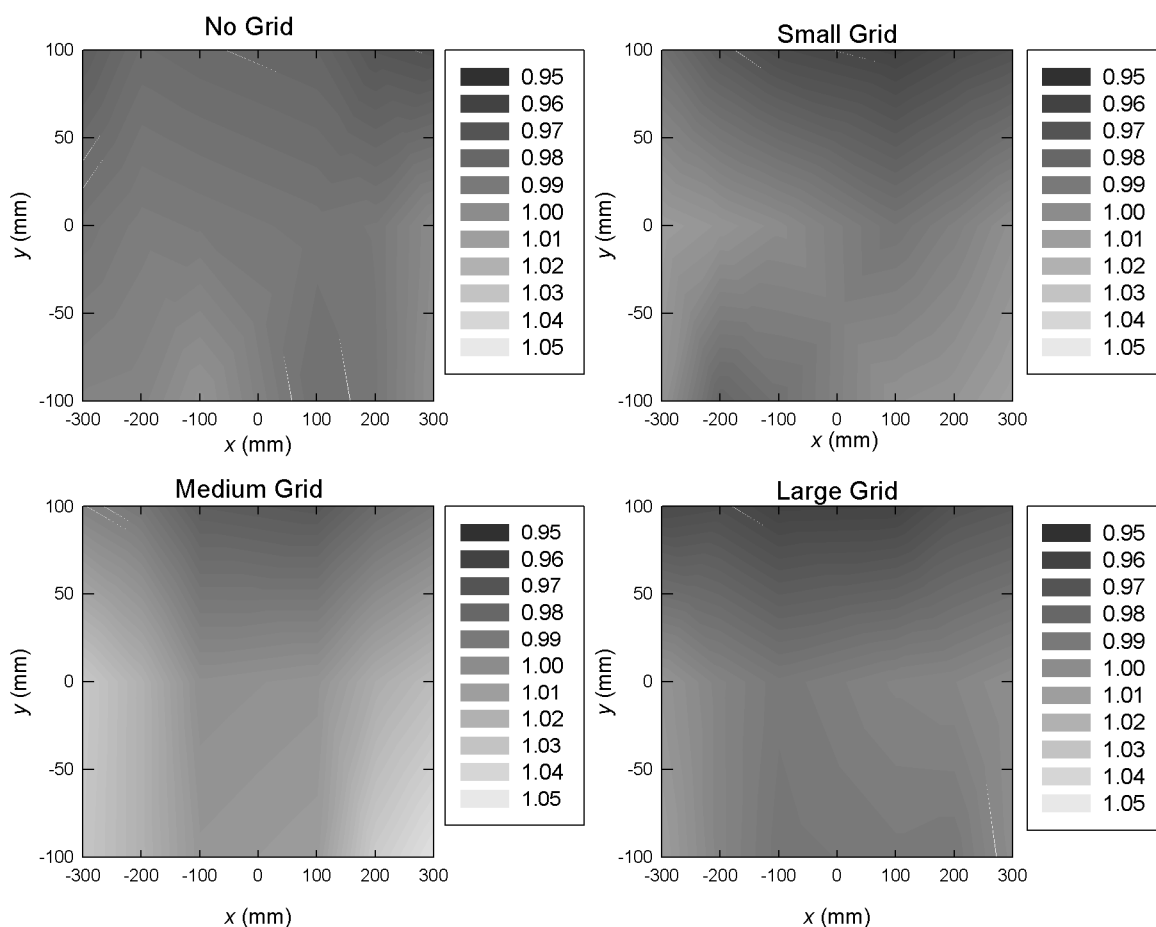


Figure 3-13 – Contour plots showing the ratio of velocities measured by the two probes at the positions shown in Figure 3-12 ($U_{\text{Probe 1}}/U_{\text{Probe 0}}$). The grids are in the positions closest to the model (3.55 m from measurement position for the small and medium grids and 4.60 m for the large grid).

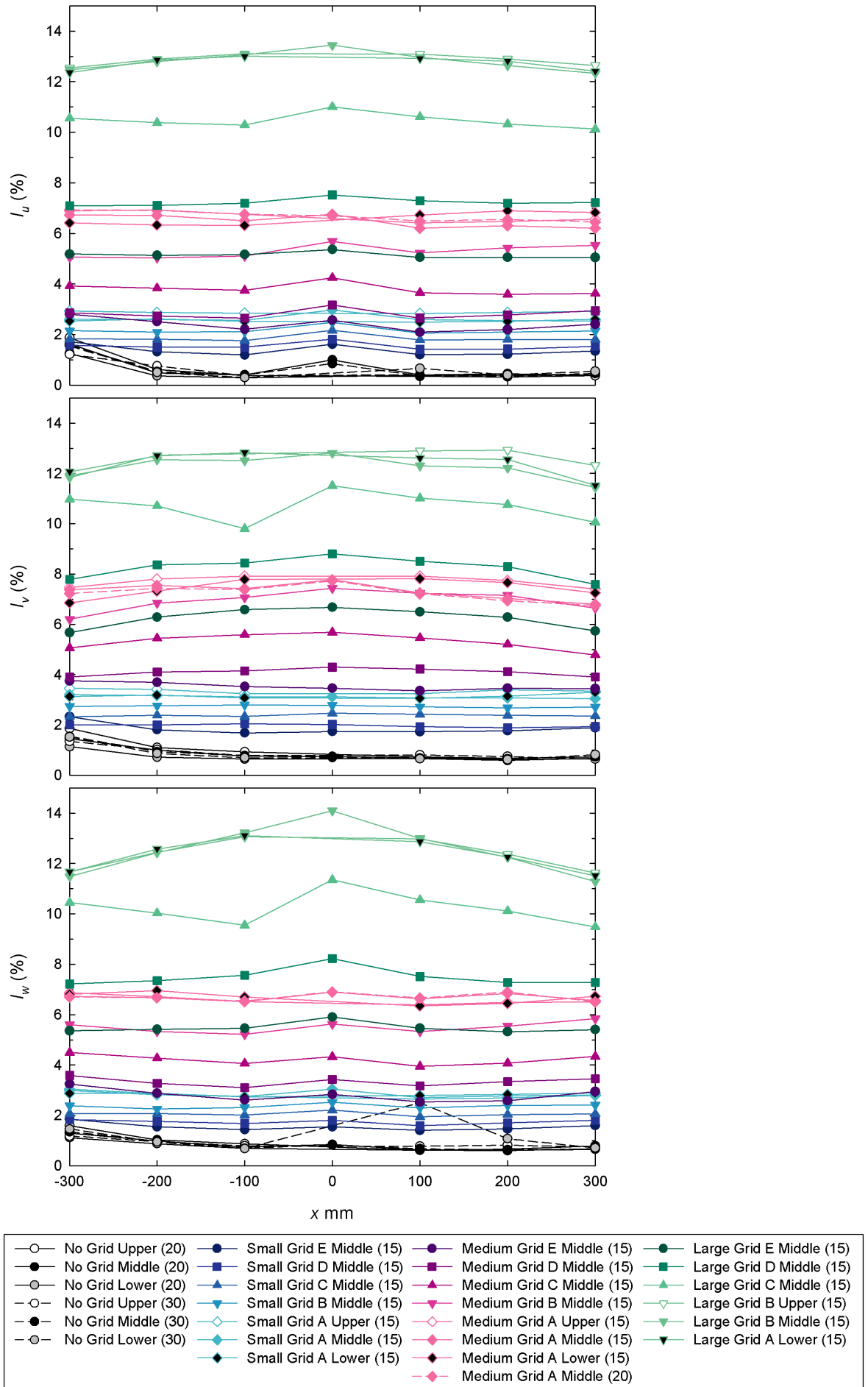


Figure 3-14 – Turbulence intensities across the tunnel (number in bracket is fan blade angle in degrees).

Grid	Position (m)	Blade Angle (°)	Moving Probe Row	Pitot Velocity / Cobra Probe 0 (Average)	Standard Deviation	Average ratio (ratio to no grid, middle, 20° data)
No Grid	-	20	Upper	0.954	0.006	1.02
			Middle	0.939	0.005	1.00
			Lower	0.939	0.008	1.00
	-	30	Upper	0.933	0.007	0.99
			Middle	0.921	0.004	0.98
			Lower	0.923	0.008	0.98
Small	A (3.55)	15	Upper	0.968	0.001	1.03
			Middle	0.967	0.002	1.03
			Lower	0.966	0.003	1.03
Small	B (4.60)	15	Middle	0.958	0.003	1.02
Small	C (5.60)	15	Middle	0.954	0.003	1.02
Small	D (7.20)	15	Middle	0.958	0.004	1.02
Small	E (9.60)	15	Middle	0.957	0.004	1.02
Medium	A (3.55)	15	Upper	0.967	0.001	1.03
			Middle	0.967	0.001	1.03
			Lower	0.966	0.002	1.03
	A (3.55)	20	Middle	0.966	0.001	1.03
Medium	B (4.60)	15	Middle	0.988	0.001	1.05
Medium	C (5.60)	15	Middle	0.965	0.002	1.03
Medium	D (7.20)	15	Middle	0.962	0.002	1.02
Medium	E (9.60)	15	Middle	0.943	0.002	1.00
Large	B (4.60)	15	Upper	0.917	0.002	0.98
			Middle	0.919	0.002	0.98
			Lower	0.916	0.002	0.97
Large	C (5.60)	15	Middle	0.930	0.002	0.99
Large	D (7.20)	15	Middle	0.954	0.002	1.02
Large	E (9.60)	15	Middle	0.935	0.001	1.00

Table 3-2- Pitot measurements compared to Cobra Probe 0 measurements.

The mean dynamic pressure (reference pressure, $R_{dynamic}$) was recorded from the Pitot along with the temperature for each run. The density of the air was calculated according to the perfect gas law, assuming an atmospheric pressure of one atmosphere (atmospheric pressure was not measured during the experiments but the small variations expected were considered unlikely to affect the results).

$$\rho = \frac{p}{RT}, \text{ where } p = 1 \text{ atm} = 101,350 \text{ Pa and } R_{air} \approx 287 \text{ J kg}^{-1} \text{ K}^{-1}. \quad \text{Equation 3-14}$$

The velocity was calculated by

$$V = \sqrt{\frac{2R_{dynamic}}{\rho}}. \quad \text{Equation 3-15}$$

The viscosity for the recorded temperature was calculated by the power law

$$\frac{\mu}{\mu_0} \approx \left(\frac{T}{T_0}\right)^{0.7}, \text{ where } \mu_0 = 1.71 \times 10^{-5} \text{ kg m}^{-1} \text{ s}^{-1} \text{ and } T_0 = 273 \text{ K}. \quad \text{Equation 3-16}$$

With the values calculated from the above equations, the Reynolds number (Re) based on chord length (c) was determined from the Pitot measurements,

$$Re = \frac{\rho V c}{\mu} \quad \text{Equation 3-17}$$

The Pitot was connected to the Scanivalve by very long tubing (several meters long), as the mean pressure was the only measurement of interest. Therefore these measurements were excluded from the tubing correction and the low pass filter. The standard deviation of the Pitot measurements varied according to the grids in the tunnel. For example with the NACA 0021 model in the no grid case, the standard deviation was at most 1.5% of the measurement. However, for the small grid it varied between a maximum of 2% for the grid furthest from the model and a maximum of 5% for the grid closest to the model. The standard deviation of the Pitot measurements for the medium grid varied correspondingly between maximums of 3 and 11% and for the large grid between 9 and 17%. To give an idea of this variation, the Re for the dynamic pressure plus or minus one standard deviation was determined according to the equation below and plotted as error bars,

$$Re \pm \sigma = \frac{\rho c}{\mu} \sqrt{\frac{2R_{dynamic} \left(1 \pm \frac{\sigma_{R_{dynamic}}}{R_{dynamic}}\right)}{\rho}} = Re_{R_{dynamic}} \sqrt{1 \pm \frac{\sigma_{R_{dynamic}}}{R_{dynamic}}} \quad \text{Equation 3-18}$$

The Re versus α plot for the S809 aerofoil is shown in Figure 3-15 as typical of what was seen for all the aerofoil sections. There is definitely variation in Re with α and some of this will be due to blockage effects. However, unaccounted for effects of temperature seem to account for the largest variation. This may partly be effects on the atmospheric pressure which would affect the Re through the equation for density (Equation 3-14). As α was only increased on most runs and the tunnel temperature increased during a run, increasing α in most cases equates to increasing tunnel temperature. However, for the checks for hysteresis and when a second zero was taken at the end of the run the temperature increased with decreasing α . The second zero measurements (easily located on the plot due to the straight line running from the right hand side point at 90° to the left hand side point at 0°) show some increase in Re with decrease in α , presumably the component due to blockage. However, they all show much lower Re than the first measurement and this variation is presumably due to temperature. The decreasing α runs were not usually conducted immediately after the increasing α runs so the initial temperature of the runs were different and direct comparisons between the lines should not be made. However, the decreasing α cases show decreased Re with decreased α which, in these cases, is related to increasing temperature.

Correcting for these trends in Re was considered. However the aerofoils tested were, depending on flow condition and α , operating with a laminar separation bubble, laminar to turbulent boundary layer transition, partially separated flow (which was highly three-dimensional) or as a bluff-body exhibiting vortex shedding. A post-processing blockage correction to successfully account for all these flow states does not exist and considerable difficulty would have been found in trying to decide where and how to transition between different blockage corrections. Attempting to remove

the variation due to temperature without applying a blockage correction ran the risk of attributing changes due to blockage to variations in temperature and therefore adding more uncertainty to the results. While the variation in Re is the largest failing in the experimental technique, it was therefore decided that attempting a correction would have increased the uncertainty. However, the variation should be remembered when comparing results.

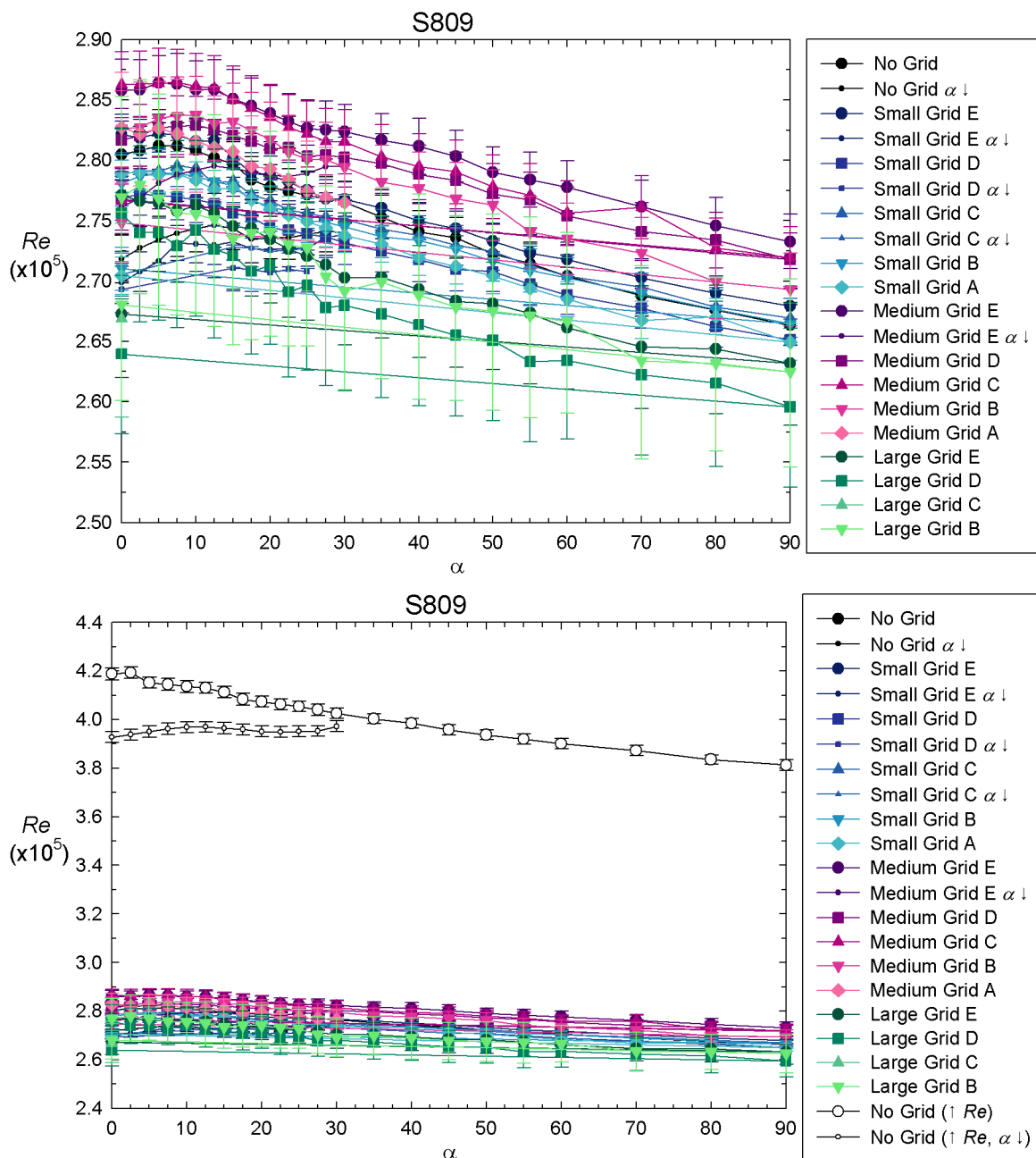


Figure 3-15 - Variation of Re during runs of the S809 aerofoil section.

The last flow condition that needed to be calculated was the integral length scale of turbulence. The integral length scale was determined by using a curve fitting technique described by Iyengar & Farell (2001). The technique involved fitting an inverted parabola to the peak region of the spectrum by eye and then shifting the von Kàrmàn spectrum to match the fitted peak with the von Kàrmàn peak. This considerably improved the determination of integral length scale from a

relatively small number of data points (compared to just fitting the von Kàrmàn peak to the experimental spectrum, finding the zero measurement or using the area under the autocorrelation curve). The von Kàrmàn spectrum is defined as

$$\frac{f S(f)}{\sigma^2} = \frac{4 \left(\frac{f L}{U} \right)}{\left(1 + 70.7 \left(\frac{f L}{U} \right)^2 \right)^{5/6}} \quad \text{Equation 3-19}$$

where L is the integral length scale, f is the frequency, σ is the standard deviation of the velocity component, $S(f)$ the turbulence spectrum, and U is the mean longitudinal velocity. A Matlab program was used to find the turbulence spectrums from the time histories of the velocity components. A comparison of the spectrums determined from experiment (the experimental spectrums were the average of 36 individual spectrums with a block size of 4096 data points) which have been normalised compared to the fitted von Kàrmàn spectrums are shown for the three grids closest to the model in Figure 3-16, Figure 3-17 and Figure 3-18. The integral turbulence length scales for the lowest turbulence flow (no grid) could not be determined. To conclude this section a summary of all the flow conditions is given in Table 3-3.

Grid	Panel width (m)	Position (in m)	I_u (%)	I_v (%)	I_w (%)	L_{uu}/c	L_{uv}/c	L_{uw}/c	NACA 0021 Re	NACA 4421 Re	S809 Re
None	-	-	0.6	0.9	0.8	-	-	-	2.66×10^5	2.72×10^5	2.75×10^5 4.00×10^5
Small	0.04	E (9.60)	1	2	2	0.4	0.7	0.5	2.69×10^5	2.73×10^5	2.75×10^5
Small	0.04	D (7.20)	2	2	2	0.3	0.6	0.4	2.72×10^5	2.69×10^5	2.72×10^5
Small	0.04	C (5.60)	2	2	2	0.3	0.6	0.3	2.72×10^5	2.70×10^5	2.74×10^5
Small	0.04	B (4.60)	2	3	2	0.3	0.4	0.2	2.72×10^5	2.68×10^5	2.74×10^5
Small	0.04	A (3.55)	3	3	3	0.3	0.3	0.3	2.66×10^5	2.71×10^5	2.74×10^5
Medium	0.10	E (9.60)	2	4	3	0.6	0.6	1.0	2.71×10^5	2.69×10^5	2.81×10^5
Medium	0.10	D (7.20)	3	4	3	0.5	1.1	0.5	2.69×10^5	2.72×10^5	2.79×10^5
Medium	0.10	C (5.60)	4	5	4	0.5	1.0	0.5	2.68×10^5	2.74×10^5	2.81×10^5
Medium	0.10	B (4.60)	5	7	5	0.6	0.9	0.4	2.71×10^5	2.77×10^5	2.79×10^5
Medium	0.10	A (3.55)	6	7	7	0.5	0.6	0.4	2.70×10^5	2.71×10^5	2.77×10^5
Large	0.30	E (9.60)	5	6	5	0.8	1.3	0.8	2.65×10^5	2.69×10^5	2.71×10^5
Large	0.30	D (7.20)	7	8	7	1.0	1.1	0.8	2.67×10^5	2.65×10^5	2.68×10^5
Large	0.30	C (5.60)	10	11	10	1.1	1.0	0.9	2.68×10^5	2.67×10^5	2.63×10^5
Large	0.30	B (4.60)	13	12	12	1.1	0.8	0.8	2.70×10^5	2.69×10^5	2.71×10^5

Table 3-3 - Summary of test conditions. Grid sizes, positions, resultant three components of turbulence intensity (I_u , I_v & I_w) and scale (L_{uu} , L_{uv} & L_{uw} normalised by chord length, c), and the average Reynolds numbers (Re) of the experiments.

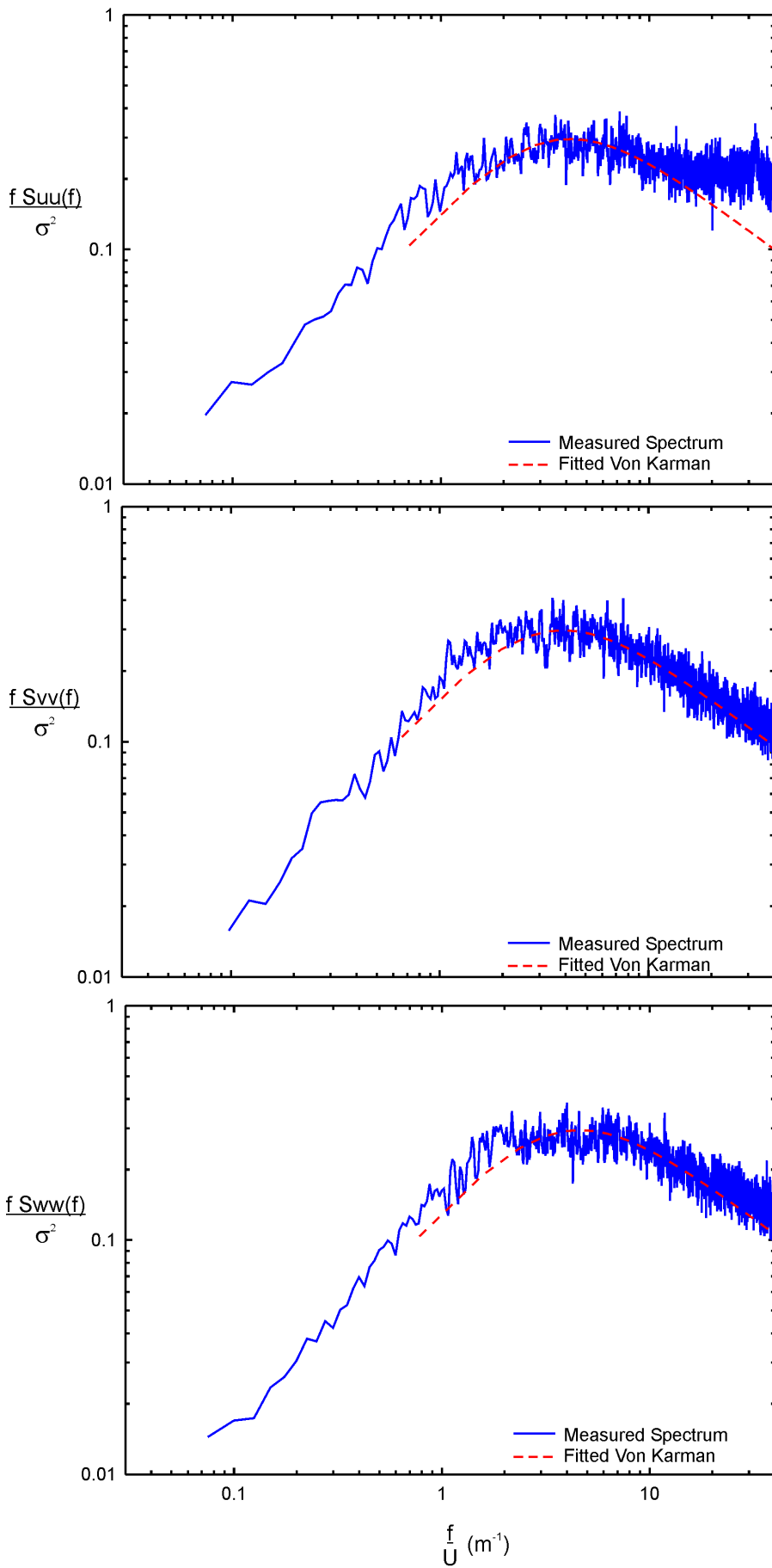


Figure 3-16 - Normalised turbulence spectra for the u, v and w components produced by the small grid in position A.

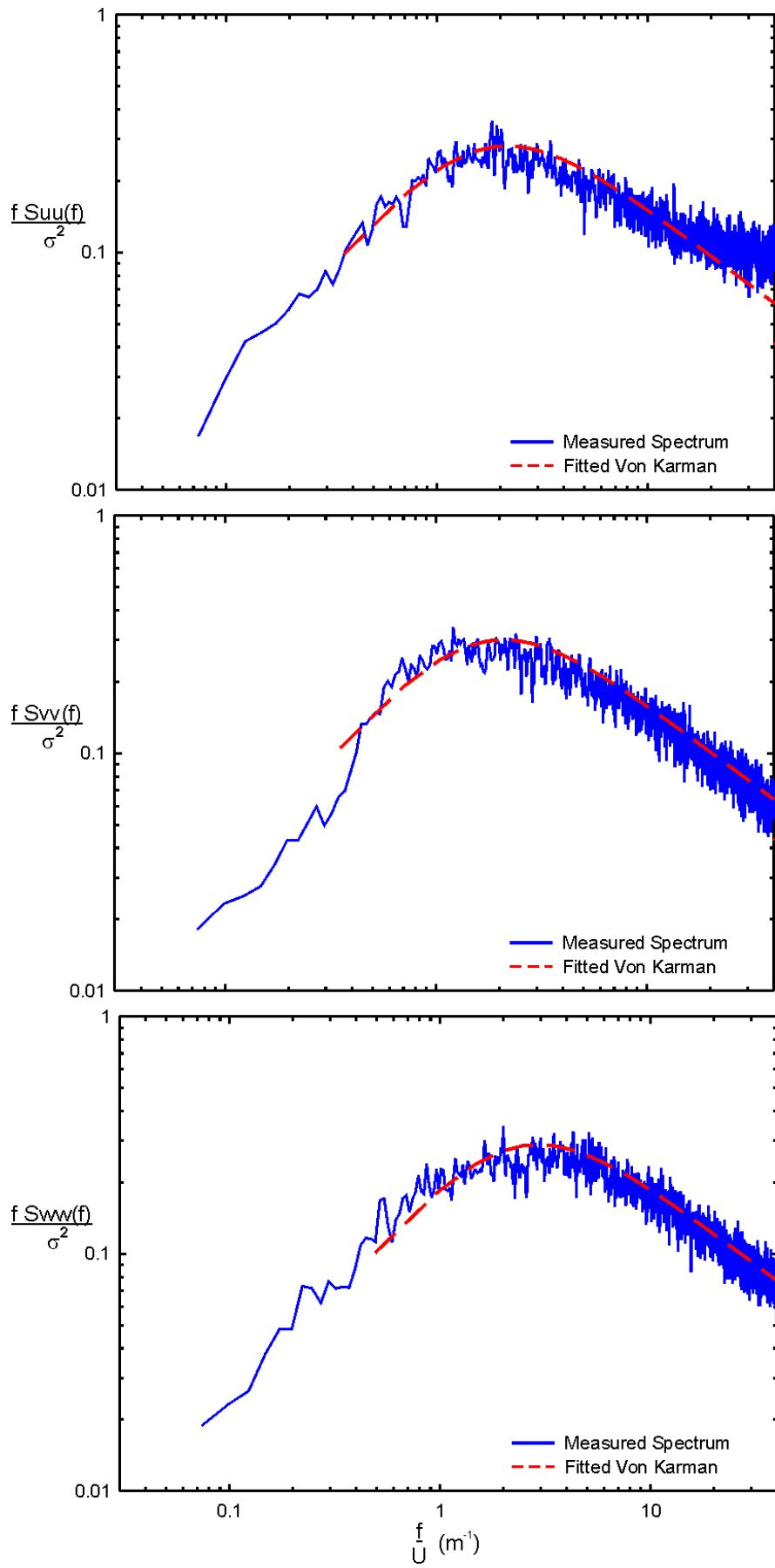


Figure 3-17 - Normalised turbulence spectra for the u, v and w components produced by the medium grid in position A.

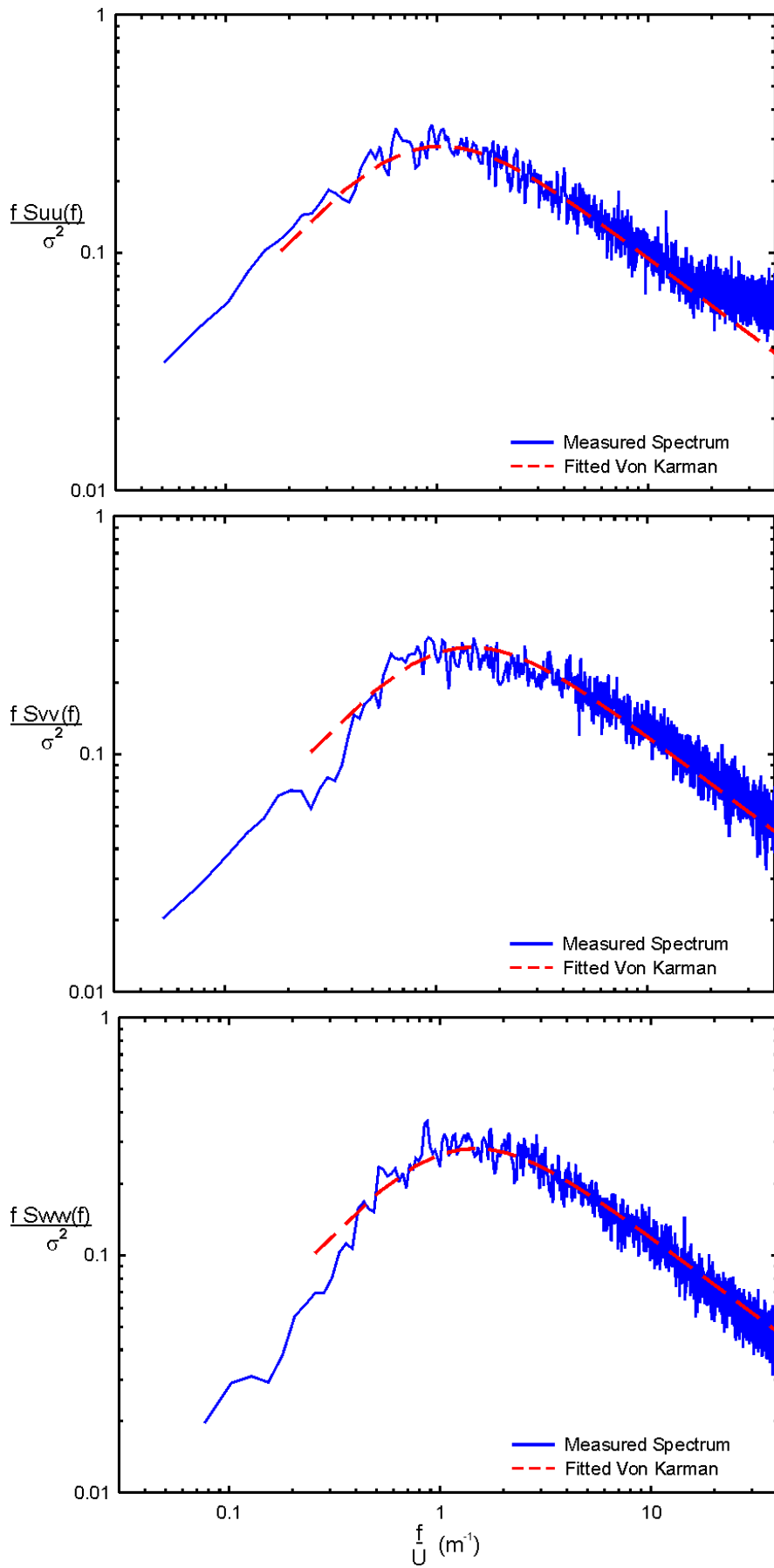


Figure 3-18 - Normalised turbulence spectra for the u, v and w components produced by the large grid in position B.

3.5 Pressure Measurement

A Scanivalve box containing 128 1psi temperature compensated pressure transducers divided into 8 modules containing 16 transducers was used to measure the pressure (the part number for the modules was ZOC16TCIP/16Px-1psid). To minimise temperature fluctuations the transducers were installed in large aluminium blocks. A multiplexer in each of the modules allowed the 16 signals from a module to be sent via a single analogue channel. This system meant that not all transducers were sampled simultaneously. The three digital signals sent to the Scanivalve specified the number of the transducer in the module that was to be read. The delay between sampling transducers within a module was determined by the time needed for the amplifiers to respond to the changed input voltage. This delay was 56 μ s, which equates to a maximum delay of 840 μ s between sampling of any two transducers in a module.

The Scanivalve box was connected via an interface box to a computer containing an Analogue to Digital Board that ran the in-house software that allowed the pressure transducers to be sampled at up to 1000Hz, see Figure 3-19. Differential signals were sent from the Scanivalve box, the interface box converted them to referenced single ended signal by voltage subtraction just prior to the signals being sent to the Analogue to Digital board. This minimised the effect of electrical noise picked up during transmission from the Scanivalve box as the noise was likely to be similar on the differential lines and therefore was removed by the subtraction process. The analogue to digital card was a sample and hold type (an Eagle Technology PC-30DS board with a maximum throughput of 100 000 samples per second). Therefore, all of the analogue signals were sampled and the voltages held while the signals were converted to digital signals. This method meant that the analogue to digital conversion did not introduce a time lag between signals.

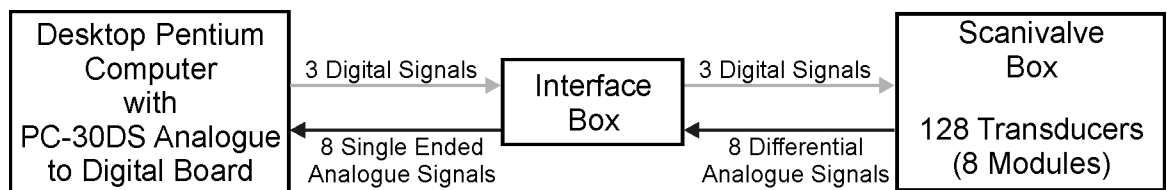


Figure 3-19 - Diagram of the connections between the scanivalve system and the computer, adapted from Eaddy (2005).

The static pressure measured by the Pitot upstream of the model was used as the reference pressure to the Scanivalve (effectively subtracted from all the measured pressures). The transducers were sampled at 1000 Hz for 35s. The computer used was an Intel based personal computer running MS-DOS 6.22. The signals from the analogue to digital board were converted to Pascals and the time series saved to hard disk. The conversion factors for each channel to allow the conversion to Pascals were found using applied pressures and the calibration tool in the control software. The system was calibrated at the start of each day's testing after the tunnel had been run for a while to allow it to warm-up and minimise temperature fluctuations during the run. It was also recalibrated

periodically during the experiments. The calibration was performed by applying atmospheric pressure or suction to the reference line with the wind tunnel fans off (effectively zero or the same positive pressure on all the taps) which was also measured by a Betz water manometer, sampling from the transducers at the same frequency as the experiments (generally for a shorter sampling time of around 10s) and then entering the applied pressure in mm of water into the control software to set the calibration. This process was repeated until the calibration for all taps gave repeatable zero and applied pressure readings. There were two calibration ranges for the taps supported by the software, 0.25psi and 0.5psi. Most measurements were performed using the smaller range but in some cases, notably with the large grid in the tunnel near the model, the larger range was required. The computer reported out of range errors if the smaller scale was inadequate. After the range had been changed on the taps they had to be recalibrated.

The temperature was recorded manually at the start of each sampling period. As mentioned in the previous section, this was used to determine correct values for the density and viscosity and to compute the Re of the tests. The temperature was measured inside the wind tunnel using a K type thermocouple that produced a signal of $10\text{mV}/^\circ\text{C}$ displayed as a temperature on the Monash University thermocouple unit (MEC829).

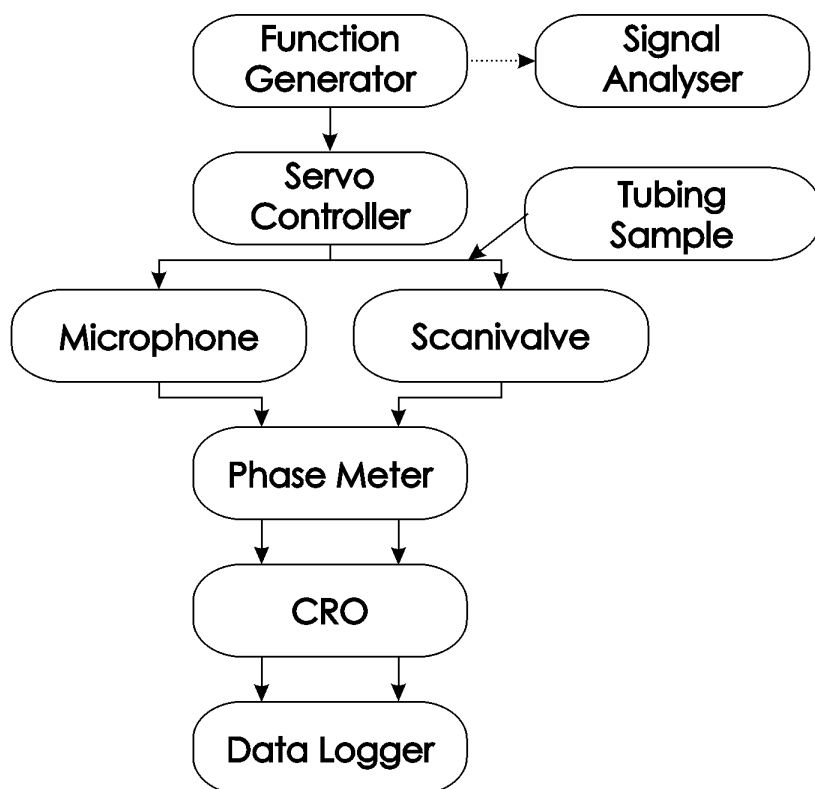


Figure 3-20 - Layout of equipment for the tubing response tests.

The measurements were corrected for the amplitude and phase response of the tubing by the method detailed by Irwin, Cooper & Girard (1979). The tubing consisted of 20mm long, 1.50 mm internal diameter metal taps (external diameter 1.6mm) that were connected from the model's surface to the Scanivalve by 1.7m long 1.50 mm internal diameter plastic tubing (the plastic tubing

had an external diameter of 2.70 mm, was supplied by BIOCORP Australia and was of the type used for intravenous drips). The response of this tubing was determined using the experimental setup shown diagrammatically in Figure 3-20. A signal analyser was used to precisely measure the frequency of the sinusoidal signal generated by the function generator. This known electronic fluctuation was applied to a servo controller that was connected to a speaker to produce a known pressure fluctuation. The pressure fluctuation was passed both through the tubing setup used in the model to the Scanivalve and directly to a microphone. The phase difference between the electronic signals generated by the microphone and the Scanivalve were measured by a phase meter. The data log was able to visualise the signals (for testing purposes) and measure the amplitude of both signals. The ratio of the amplitudes was found and normalised by the lowest frequency fluctuation response so that the lowest frequency fluctuation had an amplitude ratio of one, as there should be no change to a constant pressure by the tubing system. This enabled the amplitude and phase response of the tubing to be determined, as shown in Figure 3-21.

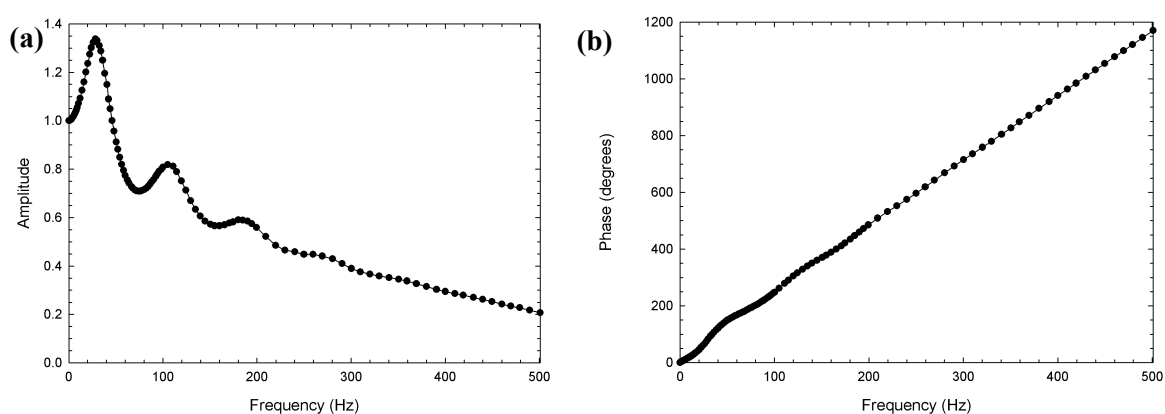


Figure 3-21 - Tubing response amplitude (a) and phase (b) for 1.7m plastic tubing with a 20mm metal tap, all having an internal diameter of 1.5mm.

The measurements taken during testing were corrected for the tubing response using the phase and amplitude response of the tubing. A computer program to correct the tubing response was written by the author using a Visual C++ 6.0 compiler. The program took as inputs the name and locations of the standard files produced by the pressure sampling software, a text file containing the tubing response amplitude and phase and whether or not a low- or band-pass filters were to be applied. If a filter was chosen further inputs were required, namely the numbers of points of the filter and the cut-off and, for the band-pass filter, the cut-in frequency. The data presented in this thesis used a 151-point low-pass filter with a cut-off frequency of 250 Hz. The details of the filter applied will be discussed later in this section.

The program also had the option to nominate a range of taps to ignore. This was used to omit the Pitot measurements from the correction since they were not obtained through the same tubing. The program read in the sampling information from the pressure files. Using the sampling frequency, f , and sampling time, T , the highest power of two, N , that fitted into the number of samples was determined by rounding down the result of Equation 3-20 to get an integer value,

$$N = \frac{\ln(f * T)}{\ln(2)}. \quad \text{Equation 3-20}$$

The program read in 2^N data points from each pressure tap. The average pressure from each tap was determined and subtracted from the tap pressure data to ensure each pressure record had a zero mean and therefore a zero component at $f = 0$ in frequency space (large mean components can potentially lessen the accuracy at which the smaller fluctuating components are determined). A Fast Fourier Transform (FFT) was then applied to the pressure records. The computer used had an Intel Pentium III 733MHz processor (the motherboard used the 815e chipset) and used the real FFT provided in the Intel Signal Processing library that was optimised for this chip. The computer ran either Microsoft Windows 98 or XP operating systems.

The program also read in the amplitude and phase of the tubing response and used them to calculate the real and imaginary components, t_{real} and t_{imag} , of the tubing response. Using the equations below, these components were used to correct the real and imaginary parts of the pressure signals, p_{real} and p_{imag} , to give the corrected pressure, $p_{c, real}$ and $p_{c, imag}$,

$$p_{c, real} = p_{real}t_{real} - p_{imag}t_{imag} \quad \text{Equation 3-21}$$

$$p_{c, imag} = p_{real}t_{imag} + p_{imag}t_{real} \quad \text{Equation 3-22}$$

An inverse FFT was then applied to the processed signals after which the averages were added back into the signals.

The maximum frequency of interest was 200Hz as the amplitude response of the tubing was about half above this frequency. As there was little information content in the signal above this frequency the tubing response correction could have potentially amplified noise above this frequency excessively. Therefore a low-pass filter was applied to the time series data after the tubing response correction. A filter with the form

$$h_D(0) = 2f_c, h_D(n) = \frac{\sin(n2\pi f_c)}{n\pi} \quad \text{Equation 3-23}$$

was used, where f_c was the cut-off frequency, $h_D(0)$ was the midpoint of the filter and n specified the coefficients above, up to $n = (N-1)/2$, and below, down to $n = -(N-1)/2$, this midpoint, where N is an odd-number which specifies the total number of coefficients in the filter (Ifeachor & Jervis, 1993).

This filter is derived from the ideal rectangular cut-off in frequency space, and in the limit of an infinite number of taps does produce this response and a perfect linear phase-response. However, truncating the filter to use a finite number of taps causes ripples in the filter in frequency space known as the Gibbs phenomenon, as shown in Figure 3-22. As can be seen in the figure the increase in the number taps reduces the ripples and the filter tends towards a perfect square filter.

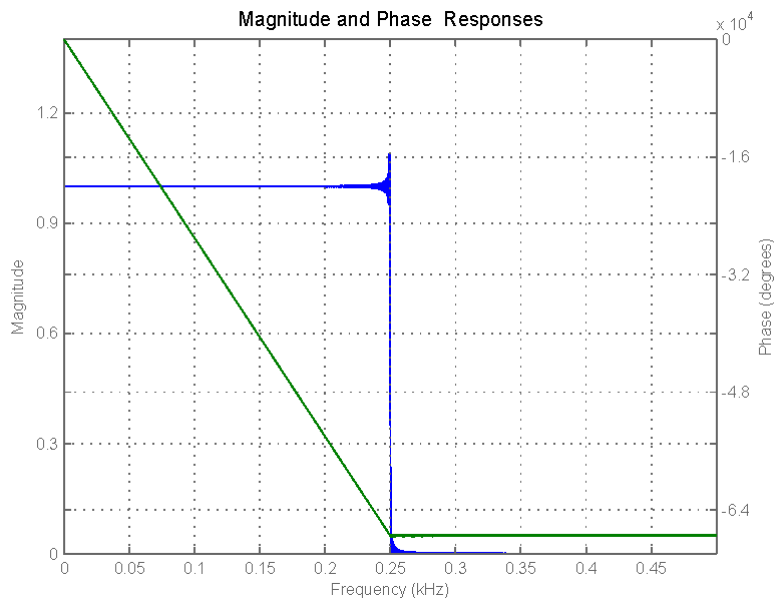
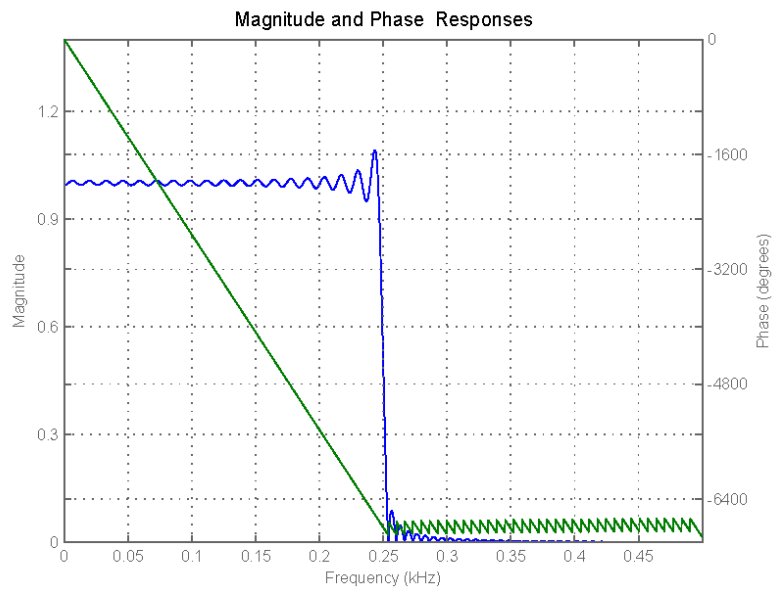
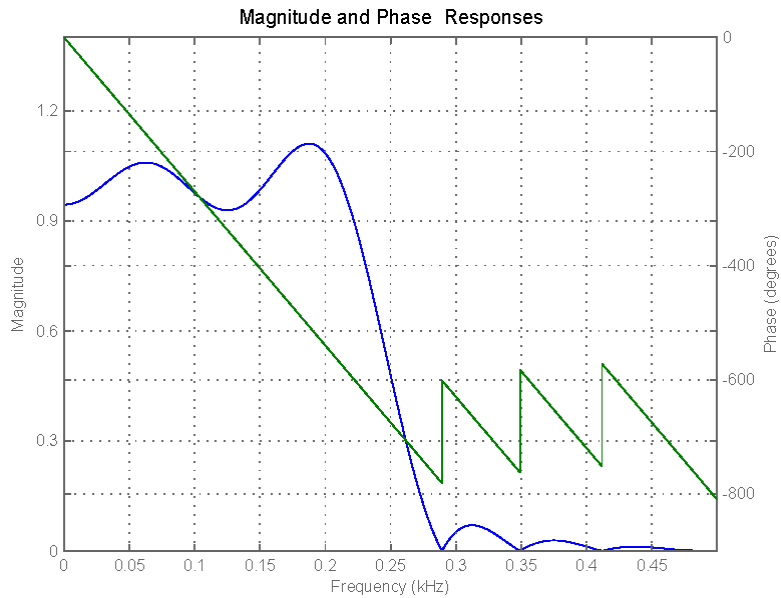


Figure 3-22 - The effect of a finite number of taps on the low-pass filter's response for a cut-off frequency of 250Hz. Top 15 taps, middle 151 taps and lower 1501 taps. The magnitude response is in blue and the phase response in green. Plots generated by Matlab's filter design and analysis tool.

However, as the filter needs to be applied symmetrically to the N-1 points either side of the current point of interest the data must be padded with zeros either side to allow the filter to be applied. The zero padding meant that the beginnings and ends of the pressure records affected by the zero padding ((N-1)/2 points at the beginning and end of the records) had to be omitted from future analysis. To minimise the effect of the zero padding only 151 taps were used in the filter (see the middle plot in Figure 3-22) and the cut-off was chosen to be 250Hz which was above the maximum frequency of interest so that the data of interest would not be affected by the “ringing” near the cut-off frequency or the slight slope of the cut-off.

After these processes were complete a new file including the sampling information from the original file, details of the applied corrections, the mean and standard deviations of each tap and the corrected pressure signals was created.

3.6 Force Calculations

All the calculations of force were done using Matlab after the tubing response correction and lowpass filter had been applied. The mean dynamic pressure measured by the Pitot was used to normalise the pressure measurements to give coefficients of pressure (C_p). The aerofoil surface was divided into small segments for force calculations. The pressures at the centre of these segments (the positions indicated by a dot in Figure 3-23) were found by interpolating, using the Matlab spline function, the pressures measured in the 28 or 22 tap rows. At this point any blocked taps were excluded from the calculation. The taps were numbered from the trailing edge across the upper surface around the leading edge and then back along the lower surface. The blocked taps were tap 25 in Row B2 on the NACA 0021 and tap 19 in Row B2 on the NACA 4421. There were no blocked taps in the S809 section.

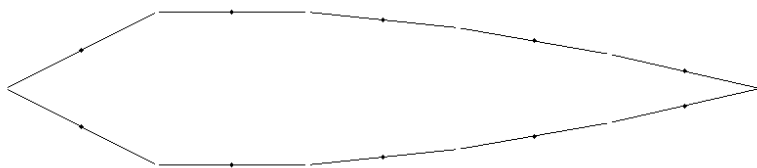


Figure 3-23 - Example of how the NACA 0021 aerofoil was divided into small segments for force calculations showing 10 segments with small gaps between segments for clarity, in the calculations 500 segments were used and there were no gaps between segments.

The sectional coefficients of normal (c_n) and tangential force (c_t) can be calculated from the splined pressures by summing the coefficient of pressure (c_p) on each small segment times the length of that segment in the vertical or horizontal direction normalised by the chord length. As a positive pressure on the upper surface will produce a force downwards, all forces calculated for the upper surface (the first half of the points) for c_n are subtracted. This problem is automatically solved for the c_t calculations as Δy for cases where the forces should be subtracted will be negative,

$$c_n = \sum_{i=segments/2+1}^{i=segments} C_{P_i} \frac{\Delta x_i}{c} - \sum_{i=1}^{i=segments/2} C_{P_i} \frac{\Delta x_i}{c}, \quad \text{Equation 3-24}$$

$$c_t = \sum_{i=1}^{i=segments} C_{P_i} \frac{\Delta y_i}{c}. \quad \text{Equation 3-25}$$

Using the angle of attack (α) c_n and c_t were resolved into the coefficients of lift (c_l) and drag (c_d).

$$c_l = c_n \cos(\alpha) - c_t \sin(\alpha), \quad \text{Equation 3-26}$$

$$c_d = c_n \sin(\alpha) + c_t \cos(\alpha). \quad \text{Equation 3-27}$$

The sectional moment coefficient taken around $1/4c$ position ($c_{m, 1/4c}$) is more complicated. To calculate the moment the size and angle of the moment arm was first calculated for each centre position around the object. The arms for the simple example shown in Figure 3-23 are shown in Figure 3-24.

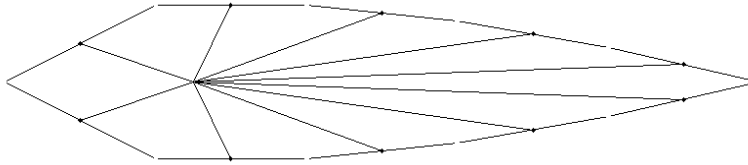


Figure 3-24 - Moment arms for the simple case shown in Figure 3-23.

By calculating the angle of the moment arm and the angle of the surface to the horizontal the angle between the force due to the pressure (F_P) and the component of this force providing the moment (F_M) can be calculated, and therefore F_M can be determined. This calculated is complicated by the pressure changing orientation on the surface (pressure is of course always applied to the outside of the object). Looking at the geometry for $\Delta y > 0$

$$F_M = F_P \cos(\theta + \phi) \quad \text{Equation 3-28}$$

and for $\Delta y < 0$

$$F_M = F_P \cos(\pi - \theta + \phi). \quad \text{Equation 3-29}$$

Where θ is the angle of the moment arm of length l , and ϕ is the angle of the surface segment from the horizontal. As the aerofoil is turned about the $1/4c$ position, changing α does not change $c_{m, 1/4c}$ the formula for $c_{m, 1/4c}$ is for $\Delta y > 0$

$$c_{m, 1/4c} = C_P \frac{\sqrt{\Delta x^2 + \Delta y^2}}{c} \cos(\theta - \phi) \frac{l}{c} \quad \text{Equation 3-30}$$

and for $\Delta y < 0$

$$c_{m, 1/4c} = C_P \frac{\sqrt{\Delta x^2 + \Delta y^2}}{c} \cos(\pi + \theta - \phi) \frac{l}{c}. \quad \text{Equation 3-31}$$

Adding these components together across the total surface of the aerofoil gives the total $c_{m, 1/4c}$. There is no need to consider the α since this changes the angles of all the moment arms by the same amount.

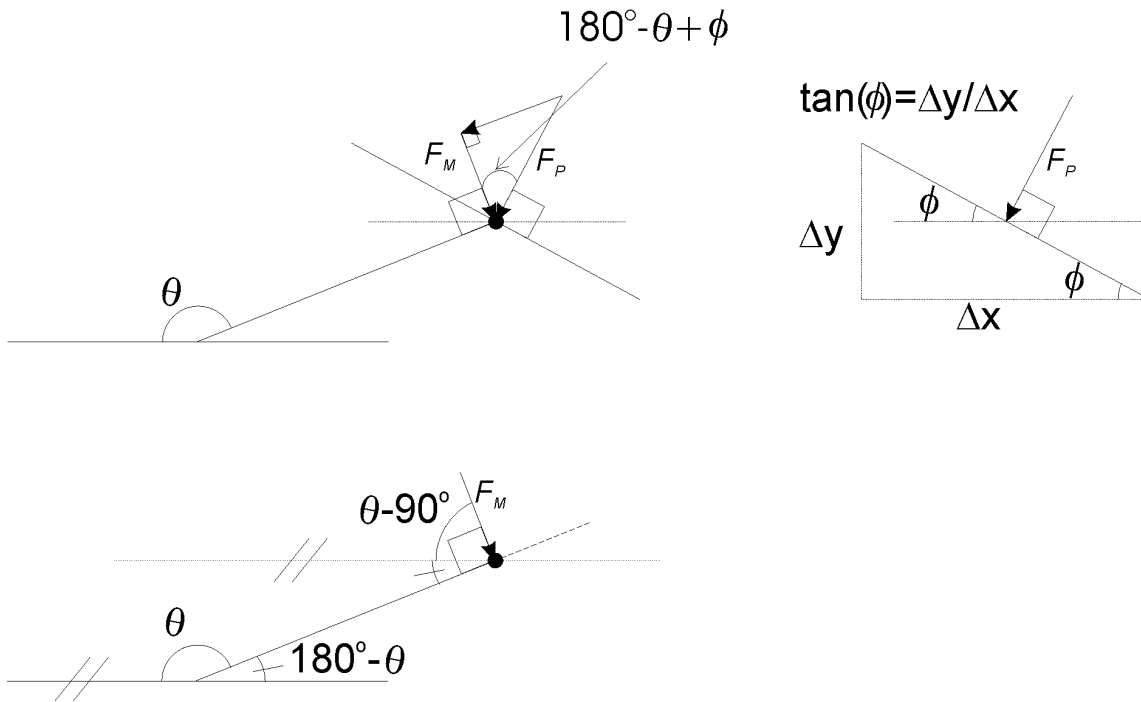


Figure 3-25 - Geometry of the surface segments, the moment arm, the force due to pressure (F_P) and the component of this force normal to the moment arm (F_M). θ is the angle of the moment arm and ϕ is the angle of the surface segment from the horizontal

Number of segments used	$\alpha = 0^\circ$						$\alpha = 10^\circ$					
	c_l		c_d		c_m		c_l		c_d		c_m	
	B1	B2	B1	B2	B1	B2	B1	B2	B1	B2	B1	B2
10	0.03	0.03	-0.14	-0.14	0.00	-0.01	1.06	1.06	-0.01	-0.01	0.01	0.00
100	0.02	0.02	-0.01	-0.01	0.00	-0.01	1.07	1.07	0.02	0.04	0.02	0.01
200	0.02	0.02	0.00	0.00	0.00	-0.01	1.06	1.06	0.02	0.05	0.02	0.01
400	0.02	0.02	0.00	0.01	0.00	-0.01	1.06	1.06	0.03	0.05	0.02	0.01
500	0.02	0.02	0.00	0.01	0.00	-0.01	1.06	1.06	0.03	0.05	0.02	0.01
1000	0.02	0.02	0.01	0.01	0.00	-0.01	1.06	1.06	0.03	0.05	0.02	0.01
Number of segments used	$\alpha = 45^\circ$						$\alpha = 90^\circ$					
	c_l		c_d		c_m		c_l		c_d		c_m	
	B1	B2	B1	B2	B1	B2	B1	B2	B1	B2	B1	B2
10	1.04	1.04	1.22	1.22	-0.26	-0.26	0.09	0.09	2.04	2.06	-0.55	-0.55
100	1.05	1.04	1.12	1.11	-0.25	-0.25	0.16	0.15	1.95	1.97	-0.52	-0.52
200	1.05	1.05	1.11	1.11	-0.25	-0.25	0.16	0.15	1.95	1.97	-0.52	-0.52
400	1.06	1.05	1.11	1.10	-0.25	-0.25	0.15	0.15	1.95	1.97	-0.52	-0.52
500	1.06	1.05	1.11	1.10	-0.25	-0.25	0.15	0.15	1.95	1.97	-0.52	-0.52
1000	1.06	1.05	1.10	1.10	-0.25	-0.25	0.15	0.15	1.95	1.97	-0.52	-0.52

Table 3-4 - Demonstration of convergence for 500 segments used in the determination of c_l , c_m and c_d for the NACA021 aerofoil (with no grid in the tunnel).

To demonstrate that the 500 segments used in the force calculations are sufficient c_l , c_d and c_m , $1/4c$ were calculated using different numbers of segments for several α for the NACA 0021 aerofoil section with no grid in the tunnel. The results are presented above in Table 3-4. It can be seen that the calculated values of force are well converged for 500 segments.

3.7 Fluctuating Calculations

As described earlier the tubing response correction produced 2^{15} (32 768) corrected samples which were then low-pass filtered to 250Hz using a low-pass filter with 151 terms. Before applying the filter the time series was zero padded. The zero padding affected the filter output for the first and last 75 samples which were therefore omitted from the subsequent calculations. Either the raw pressure measurement (not normalised by the dynamic pressure) or the force calculated from the instantaneous values of pressures by the method detailed in the previous section (the average dynamic pressure was used to normalise the pressures for the force calculations) was used. The frequency content of the signals was analysed using Matlab's implementation of the Welch method over small segments. The signals were broken into eight segments with 50% overlap. Each of these segments was windowed with a Hamming window. The Power Spectral Density of these segments was then determined and the final result averaged to give a clearer indication of the frequency content of the signals.

The other tool used to investigate the fluctuating signals was the correlation coefficient (R). Between two signals (x and y), R is given by (p. 21-3, Newland, 1993)

$$R_{xy} = \frac{\sum_{i=1}^{i=N} [(x_i - \bar{x})(y_i - \bar{y})]}{\sigma_x \sigma_y} . \quad \text{Equation 3-32}$$

This was used to find the correlation between the pressure signals at various positions on the aerofoil and the correlations between the instantaneous force coefficients. Matlab was used to carry out these calculations.

3.8 Surface Flow Visualisation

Oil flow visualisation was chosen as the most practical visualisation technique for the relatively high speed turbulent flow that was studied. A detailed examination of this technique has been provided by Maltby (1962). In the current study the oil used was kerosene and it was combined with Kaolin to make a paint. Kaolin or China Clay (in pure form Kaolin is a hydrated silicate of alumina $\text{Al}_2\text{O}_3 - 2\text{SiO}_2 \cdot 2\text{H}_2\text{O}$) is a fine white powder that is transparent when suspended in the kerosene. As the kerosene evaporated the Kaolin dried, forming a white pattern that showed an unevenly weighted average of the movement of the kerosene on the model's surface. A very small amount of Linseed oil (no more than a drop or two) was used as a dispersing agent to limit the size of the clumps of Kaolin particles in the kerosene and therefore result in a finer pattern. The first application was one part Kaolin to two parts kerosene by volume. A weaker solution of kerosene and Kaolin was used after the first run to replace particles lost off the surface.

The paint alters the flow by as the boundary condition between the air and the kerosene is different to that between the air and the aerofoil surface and by adding roughness to the surface. By solving the equations of motion for a thin oil sheet moving on a surface under the influence of a boundary layer Maltby (1962) concluded that

“The oil follows boundary layer surface streamlines except near separation where it tends to form an envelope upstream of the true separation envelope. This early indication of separation is expected to occur for both compressible and incompressible flow; it is less marked for turbulent than laminar layers. The distance by which separation is apparently altered depends on the oil thickness, and the model size, but it is independent of the oil viscosity (provided this viscosity is much greater than the viscosity of the fluid of the boundary layer).

...The effect of the oil flow on the motion of the boundary layer... is very small in most practical cases but increases as the oil viscosity decreases.

...Interpretation of the oil pattern at low Reynolds number... should be treated with caution as transition could be erroneously interpreted as separation.” p. 23

The paint will also tend to run downhill on the curved surface of the aerofoil. These limitations must be considered when interpreting the dried patterns. Another factor to consider is that the dried pattern is an unevenly weighted average of the kerosene flow during the run. Because of this interpretation of the final dried patterns was greatly helped by a video record of their development.

A digital video camera was placed above the tunnel, focussed through a Perspex window directly down onto the model. Two lights were placed above other Perspex windows on the tunnel centreline, one upstream and one downstream of the video camera. Unfortunately the arrangement of the lights caused a slight shine off the liquid kerosene in the centre of the model. However, as this did not impact on the dried images and using frosted windows would have increased the problem of overheating of the Perspex windows by the lights, this problem was ignored. The video camera was connected to a television beside the tunnel to allow the development of the flow to be observed during the run.

Surface flow visualisation was conducted on the NACA 0021 and S809 aerofoil sections. Taps were plugged with 1.2mm diameter cylindrical rod ‘strip styrene’, sanded to size and forced into the holes. This allowed for cleaning the aerofoil and removing the plugs to permit further pressure testing. Fortunately, no repeat pressure runs were necessary. On the NACA 0021 aerofoil section the plugs sat just above the surface, which added to the roughness caused by the taps but made them easier to remove. On the S809 aerofoil section the plugs were recessed into the taps, reducing their possible effect on the flow. However, not all of the taps could be filled using this method (for example none of the trailing edge taps were able to be filled).

Two people were required at the beginning of these runs. The angle of attack was set before the run started. The tunnel was run at a slow speed, the video started (via a remote control) and the upper surface of the model painted. A dustpan brush was used as a paintbrush as it was found to allow the most even coverage. Once the first person closed the rear door of the tunnel the second person immediately started to increase the wind tunnel fan blades angle thus increasing the wind

tunnel speed. The first person watched the development of the flow on the monitor beside the tunnel to ensure the pattern had not dried before the tunnel reached full speed. On the digital video tape full speed was indicated either by later analysis of the sound recorded by the video (NACA 0021 tests) or by flicking the tunnel lights off and on (S809 tests). In the first runs the tunnel was run until enough kerosene had evaporated so that drips would not alter the dried pattern. The rest of the pattern was then dried using hot lights. Unfortunately, the hot lights caused some patches of the aerofoil surface to delaminate causing white patches, which can be seen in the final photographs. The patch near tapping row A3 delaminated to such an extent that the weave of the carbon fibre could be felt causing a rough patch. The S809 runs were run for a long time to allow the kerosene to evaporate, the run time could be up to an hour if most of the kerosene pooled in small areas. The final dried patterns were captured by both digital video and by handheld cameras.

Chapter 4

NACA 0021 Aerofoil

4.1 Introduction

This chapter examines results from the symmetric NACA 0021 aerofoil section. Subsequent chapters detail the results from the two cambered aerofoil sections and then the final chapter compares the results for all the aerofoils. This chapter is split into two parts. The first deals mainly with an analysis of the mean results. The second examines the fluctuating results in detail.

4.2 Mean Results

Pressure coefficients were measured for α between 0° and 35° at 2.5° increments, from 35° to 60° at 5° increments and at 10° increments from 60° to 90° . These measurements were repeated for a total of 15 different flow conditions. In addition for 0° to 20° the measurements were carried out for both increasing and decreasing α to check for hysteresis for the lowest turbulence case for each integral turbulence length scale (no grid case and for each grid case with the grid furthest from the model). For the two rows with 28 taps the average coefficient of pressure measured at each tap was splined across the surface and used to calculate the coefficients of lift (c_l), drag (c_d) and moment about the quarter chord ($c_{m, 1/4c}$). Also, surface flow visualisations were conducted at selected α for some flow conditions. The details of the flow conditions, see Table 3-3, force calculations and surface flow visualisations are described in Chapter 3 on experimental method.

This section begins with an in depth examination of the results from the lowest turbulence case (no grid in the tunnel). A comparison with previously published results is then presented. This order allows a full examination of the features of the present experimental results to be made before adding the complication of comparisons with results taken in different facilities. The effects of turbulence were then examined. By comparing results for the same grid in the different positions of the tunnel the effect of similar length scales but different intensities was examined. The effect of turbulence on hysteresis was observed for each grid in the furthest position from the model. Finally the effect of similar intensities but different length scales was examined by comparison of results with different grids in positions that produced similar turbulence intensities.

4.2.1 Low Turbulence Case

The lowest turbulence flow results (no grid in the tunnel) are shown in Figure 4-1. The c_l curve shows a linear region for α between 0° and 10° . A hysteresis loop is very evident between 10° and 17.5° . In the increasing α case, the c_l stays around the same level until 15° where there is a sharp drop in c_l . The c_l values calculated from the measurements from the pressure taps in rows B1 and

B2 is not the same at all α . These differences are most pronounced for the decreasing α case, where row B1 shows a very abrupt stall at 12.5° , but then continues at a similar value of c_l until the end of the hysteresis loop at 17.5° . In contrast the c_l for row B2 falls only about two thirds as much as the c_l for row B1 at 12.5° . The c_l calculated from row B2 then falls again at 15° to below the value from row B1 at this angle. However, at the end of the hysteresis loop at 17.5° the values from both rows are very similar. As α increases further the c_l increases to a local maximum at 45° . This local maximum is characteristic of c_l curves over a wide range of α and is due to the general deflection of air downwards, such as would be caused by a flat plate at high α . Interestingly, the c_l is not zero at 90° . It seems reasonable that this is due to the non-symmetrical shape presented to the flow at this α . If the separation point from the rounded leading edge of the aerofoil was past the tip, then this combined with the fixed separation from the sharp trailing edge would result in a wake that was bent slightly downwards, therefore creating a small lift force.

Also shown in Figure 4-1 are plots of c_d and $c_{m, 1/4c}$. The c_d values were calculated from the surface pressure measurements (there was no wake rake used in any of these experiments) and so only give the pressure drag. There is a sharp jump in c_d associated with stall that results in a small hysteresis loop. However, at higher α the coefficient of drag increases to around 2, which is the value of c_d that would be expected for a flat plate at 90° in this Reynolds number range (White, 1999, p. 458). That it does not reach 2 may be due to the deflection of the wake, which causes a positive c_l at this α . The $c_{m, 1/4c}$ also shows a hysteresis loop between 10° and 17.5° . However, it shows sharp changes for both the increasing and decreasing α cases. There is a sharp increase in $c_{m, 1/4c}$ at 12.5° for the increasing α case but there is a sharp decrease to negative values of $c_{m, 1/4c}$ for the decreasing α case. Before full separation $c_{m, 1/4c}$ is near zero or positive, after full stall $c_{m, 1/4c}$ is negative in all cases.

The coefficients of pressures (C_p) and standard deviations (σ) from each of the pressure taps can help to interpret the c_l , c_d and $c_{m, 1/4c}$ results. Plots of these for selected α are shown in Figure 4-2. As the model is symmetric the C_p measured at $\alpha = 0^\circ$ should be the same for the upper and lower surfaces, Figure 4-2 shows they match very well. Interestingly there is a small increase in σ for a tap in row B1 just past $x/c = 0.6$ for both the increasing and decreasing α cases. There may be a slight imperfection in the model that causes slightly unsteady flow at this tap at this angle of attack. In general the σ of taps in row B1 is slightly higher than that for row B2 near the leading edge. By $\alpha = 5^\circ$ the suction pressures on the top surface have increased, especially near the leading edge. The leading edge σ has also increased slightly but the values from taps in row B1 are still slightly higher than for row B2 in this region. At 10° , the largest angle in the linear attached flow region of the c_l plot, the trend of increasing suction peak continues. There are some slight differences between C_p recorded from the taps in rows B1 and B2 near the leading edge. The σ continues to increase near the leading edge.

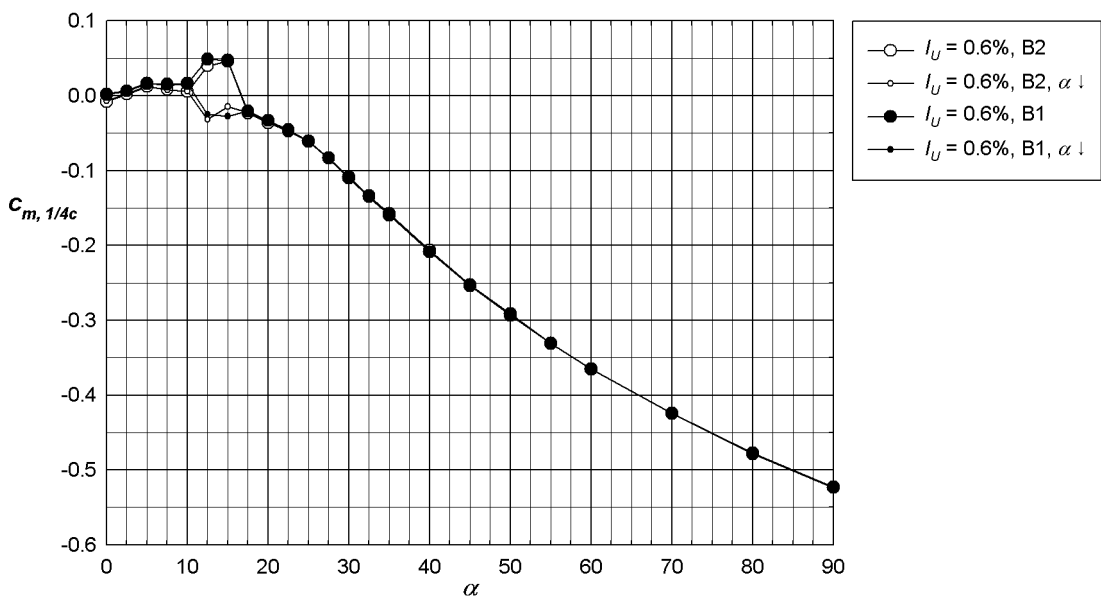
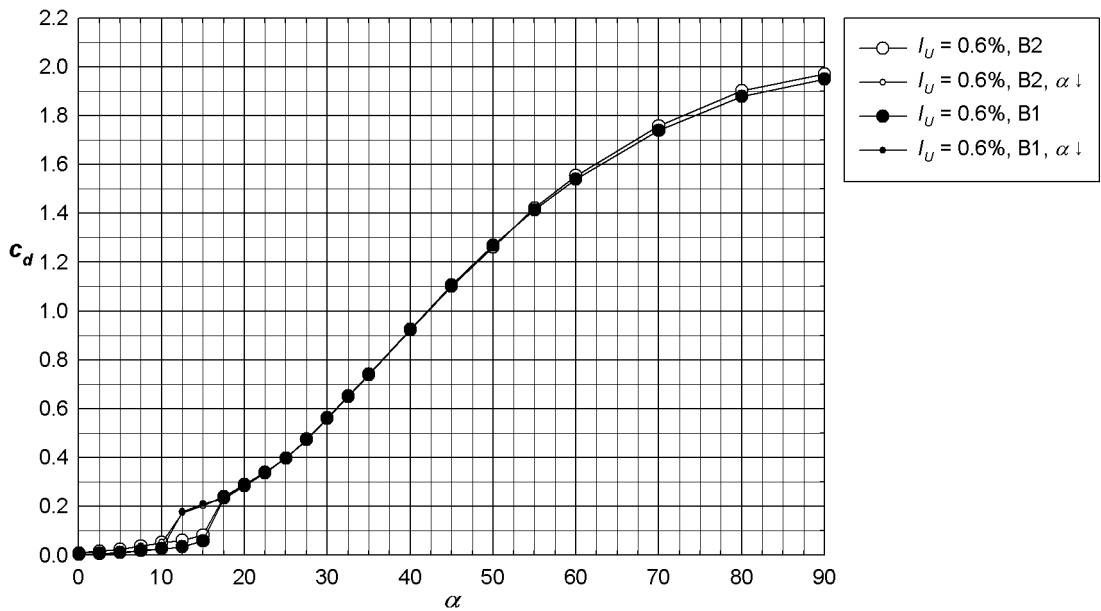
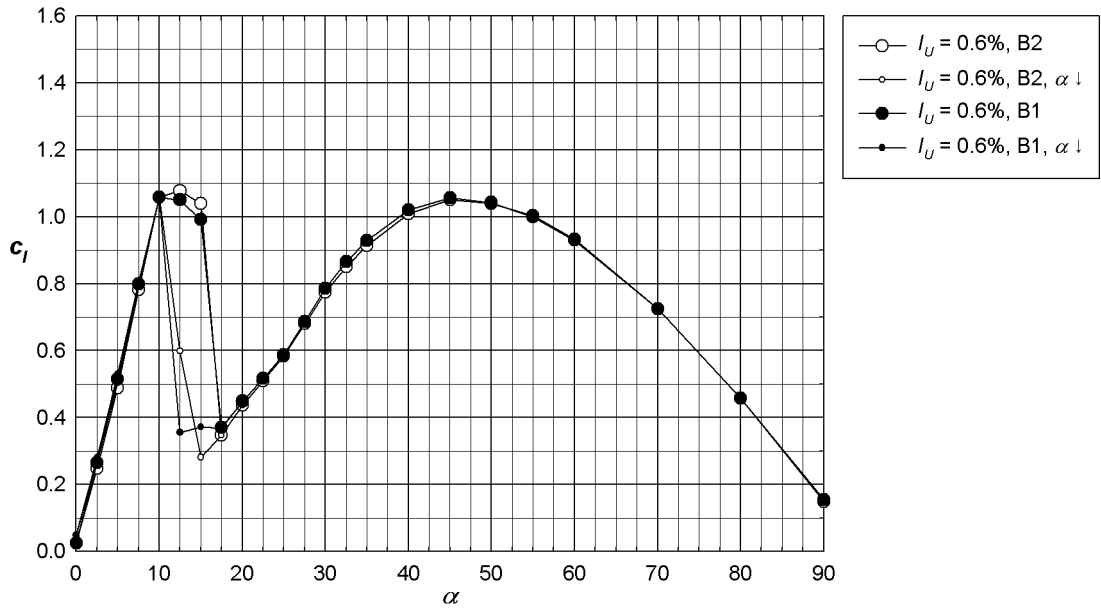


Figure 4-1 – NACA 0021 mean coefficients of lift, drag and of moment about the quarter chord for the lowest turbulence flow (no grid).

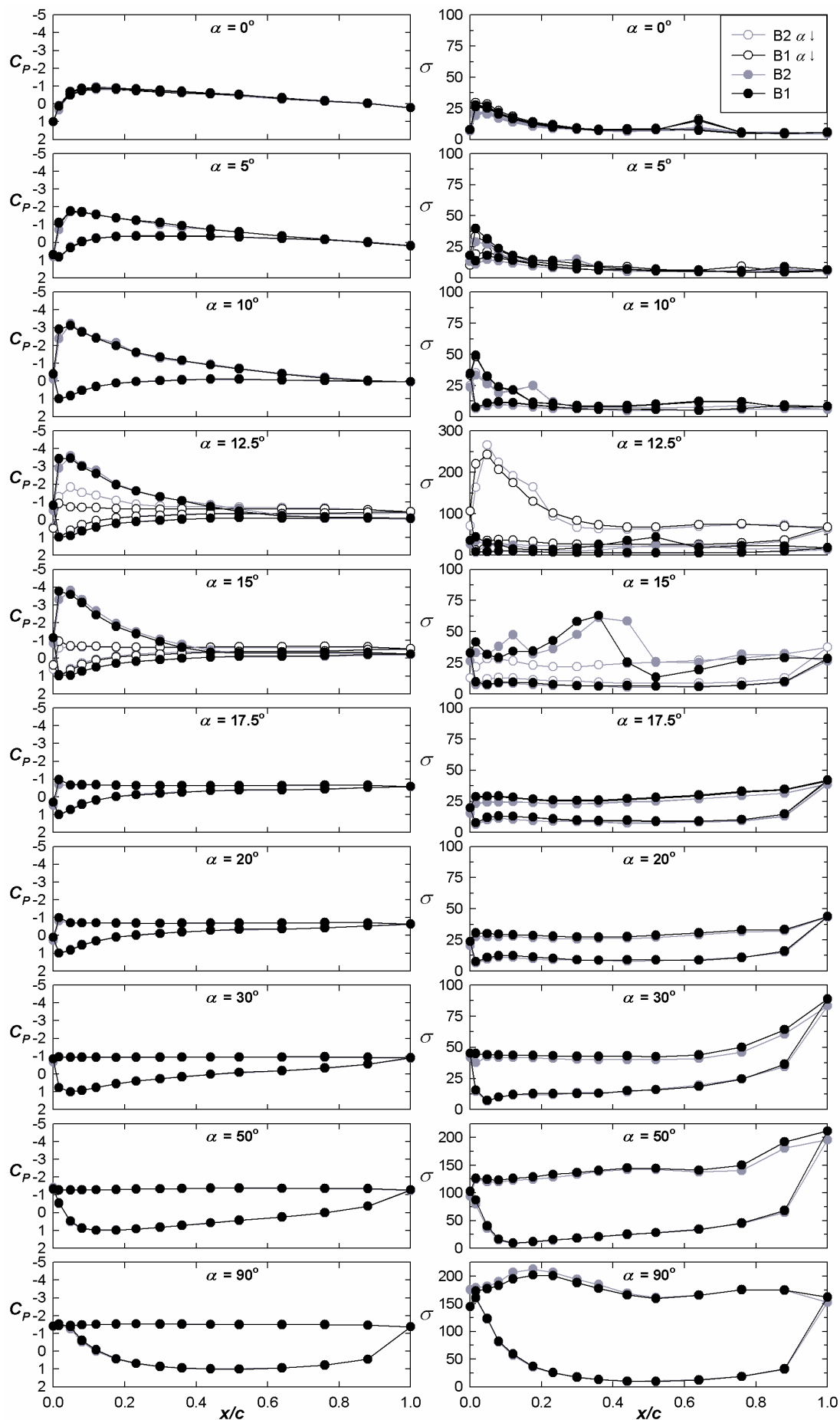


Figure 4-2 – NACA 0021 coefficients and standard deviations of the pressures around the aerofoil around stall for the lowest turbulence flow (no grid in the tunnel). Note the change in scale of the σ plots at 12.5° , 50° and 90° . The closed circles indicated increasing and the open circles decreasing α .

At $\alpha = 12.5^\circ$ there are clear differences between the results for the increasing and decreasing α cases. The C_p plot shows a suction peak at the leading edge for the increasing α case. For the decreasing α case tapping row B1 appears to be fully stalled but row B2 still has a small suction peak at the leading edge. These differences result in the different mean c_l values observed. The scale of the σ plot had to be increased threefold to compensate for the much larger σ observed in the decreasing case. This plot is repeated in Figure 4-3 below along with a plot at the same scale as used for other α results to allow examination of σ for the increasing α case. The decreasing α case is dominated by a large degree of variation near the leading edge. This is consistent with an intermediate state where the flow is attached at times. By contrast, in the increasing α case there is a peak in σ , indicating a peak in shedding, around $0.5c$. This is consistent with the mean C_p plot, as shown in Figure 4-2, where separation appears to be located around mid-chord.

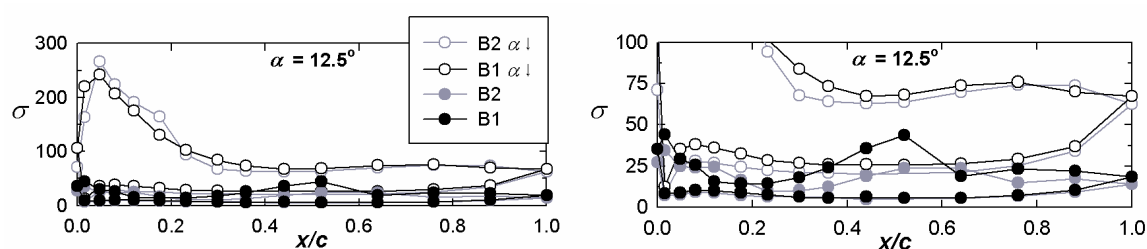


Figure 4-3 – Standard deviation of the pressure recorded at taps at the same and smaller σ scales than in Figure 4-2 so the differences in the attached and separated standard deviations can be seen.

By $\alpha = 15^\circ$ the σ in the decreasing α case have returned to low levels. However the increasing α case has a peak around $0.4c$ again consistent with the C_p plot indication of separation around this region. However, by $\alpha = 17.5^\circ$ there is full separation in all cases and a fairly flat σ on the top surface. As α increases further the magnitude of C_p increases on both the upper and lower surface, although the increase is more gradual on the upper surface. σ also increases with a peak forming at the trailing edge. However by $\alpha = 90^\circ$ the highest σ is near the quarter chord. The C_p measurements at this α reveal a suction pressure on both sides of the rounded leading edge which would result in the slight lift seen in the mean c_l results.

Aerofoils during and post stall are known to produce three dimensional flows. Schewe (2001) gives an example of this which was discussed in Section 2.2. To determine the likely effects of this three dimensional flow on the results surface flow visualisation was conducted as discussed in the experimental method, Chapter 3. In these tests hysteretic effects could not be examined as the tunnel was run up to speed after the kerosene/kaolin paint was applied. The results near stall with no grid in the tunnel are shown in Figure 4-4. The white patches visible in the same place in each run are due to imperfections on the model surface caused by drying under high heat. The pictures were taken with the digital video camera situated on top of the tunnel, directly above the model. It did not have a wide enough field of view to capture the entire model; therefore the section near the wall on the right hand side of the pictures was omitted. Note that the leading edge of the model is

at the top of the pictures, this means tapping row B2 is on the left side of the picture and row B1 on the right hand side.

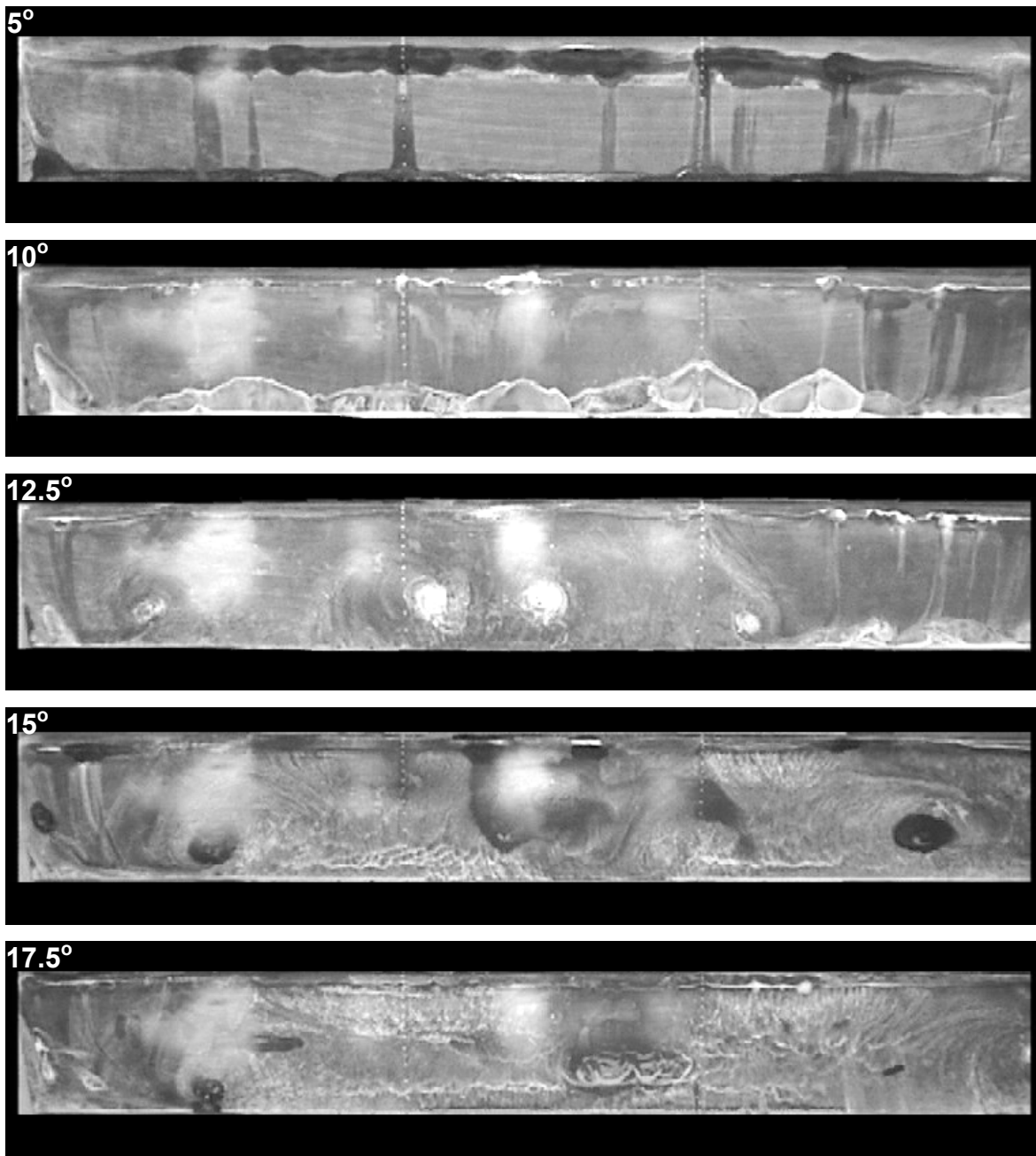


Figure 4-4 - Surface flow visualisation on the NACA 0021 around stall for the lowest turbulence flow (no grid).

The paint for the surface flow pattern shown in Figure 4-4 for $\alpha = 5^\circ$ is only partially dried; the area where the fluid dries slowly is still dark. The band near the leading edge is a separation bubble however, apart from this region, the flow is attached. At $\alpha = 10^\circ$ the fluid has started to separate from the trailing edge. The trailing edge shows paired regions of rotating flow. By $\alpha = 12.5^\circ$ there are some regions of swirling flow (see white sections near trailing edge) but in general the flow across the aerofoil is disorganised. This seems consistent with the decreasing α case. At this α there are two “mushroom” structures visible. Their different locations relative to the tapping rows B1 and B2 may explain the difference in c_l between the two rows at this α .

Similarly for $\alpha = 15^\circ$ and 17.5° there are some regions of swirling flow but the pattern is, in general, disorganised. These results are also consistent with the separated flow found for the decreasing α case. The disorganised regions show patterns similar to that formed by small waves.

4.2.2 Comparison with Previously Published Results

Comparison of aerofoil section results is notoriously difficult. Aerofoil sections can be greatly affected by the flow characteristics of the tunnel they are tested in. This section will compare the current results with previous results from three different studies. The first study, by Stack (1931), was discussed in Section 2.9.2. In this section only Stack's results for the no grid cases for the NACA 0021 aerofoil section nearest in Re to the present experiments will be examined. Stack's aerofoil section had a 5 inch chord and a 30 inch span, giving an aspect ratio of 6. Unfortunately, the turbulence intensity in wind tunnels was not routinely measured at the time Stack took his measurements and so the background intensity for these results is not known. The second experiment was conducted by Raghunathan, Harrison & Hawkins (1988) and tested a NACA 0021 aerofoil section at a Re of 2.6×10^5 . In their study, the tunnel test section was $0.84 \times 1.145\text{m}$ and had a background turbulence intensity of 0.2%. The model was instrumented with 28 pressure taps (one each at the leading and trailing edges and 13 each on the upper and lower surfaces). The model had a chord length of 100 mm and spanned the width of the section giving an aspect ratio of 8.4. The maximum blockage at $\alpha = 90^\circ$ was 8.7%. The authors reported that the measurements were corrected for blockage effects but did not specify the method used.

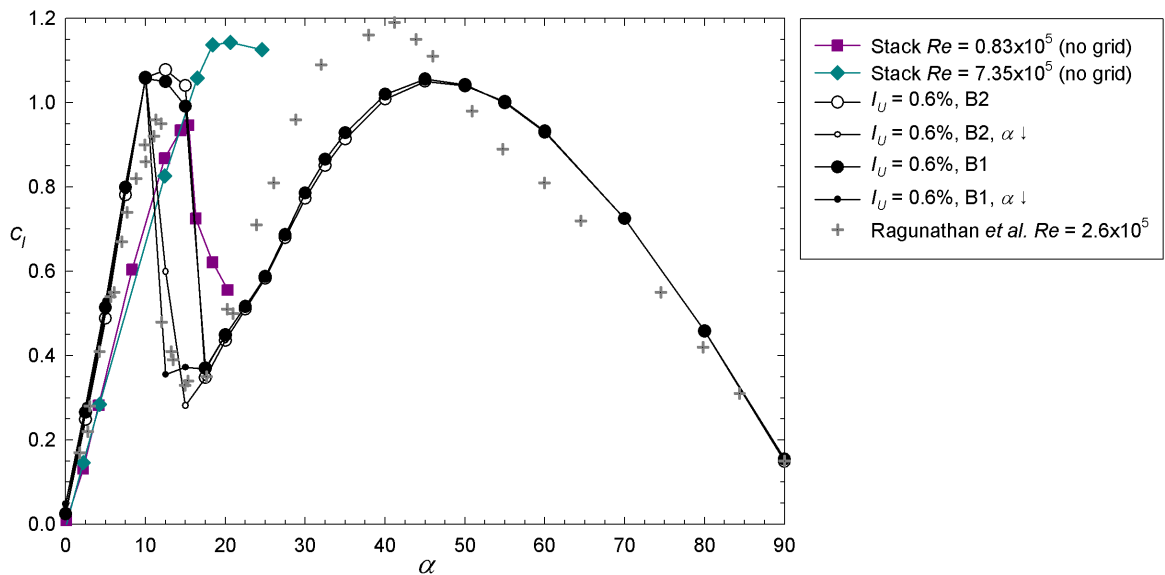


Figure 4-5 – NACA 0021 results from Stack (1931), Raghunathan, Harrison & Hawkins (1988) and this study for the no grid case for both tapping rows.

Comparisons of the c_l results are shown above in Figure 4-5. It can be seen that the slopes of the linear portion of the c_l curves from Stack do not match the other results well. Given the consistency between the slopes of the curves for the two Re cases reproduced from Stack's results, it does not seem to be a Reynolds number effect. It is possible that there is a systematic

measurement error. As will be seen later in this section, the slope for the current results and those of Raghunathan, Harrison & Hawkins resemble that of predictions by Sheldahl & Klimas (1981) using the Eppler method for the NACA 0021 aerofoil. The first local maxima for c_l seen by Raghunathan, Harrison & Hawkins (1988) is lower than that seen in the present results although the first local minima matches well. Raghunathan, Harrison & Hawkins found the second local maxima at about $\alpha = 42^\circ$, whereas the current results found the second local maxima at around $\alpha = 45^\circ$, which is where it would be expected given the symmetry of the aerofoil. However the two tests match well around $\alpha = 90^\circ$.

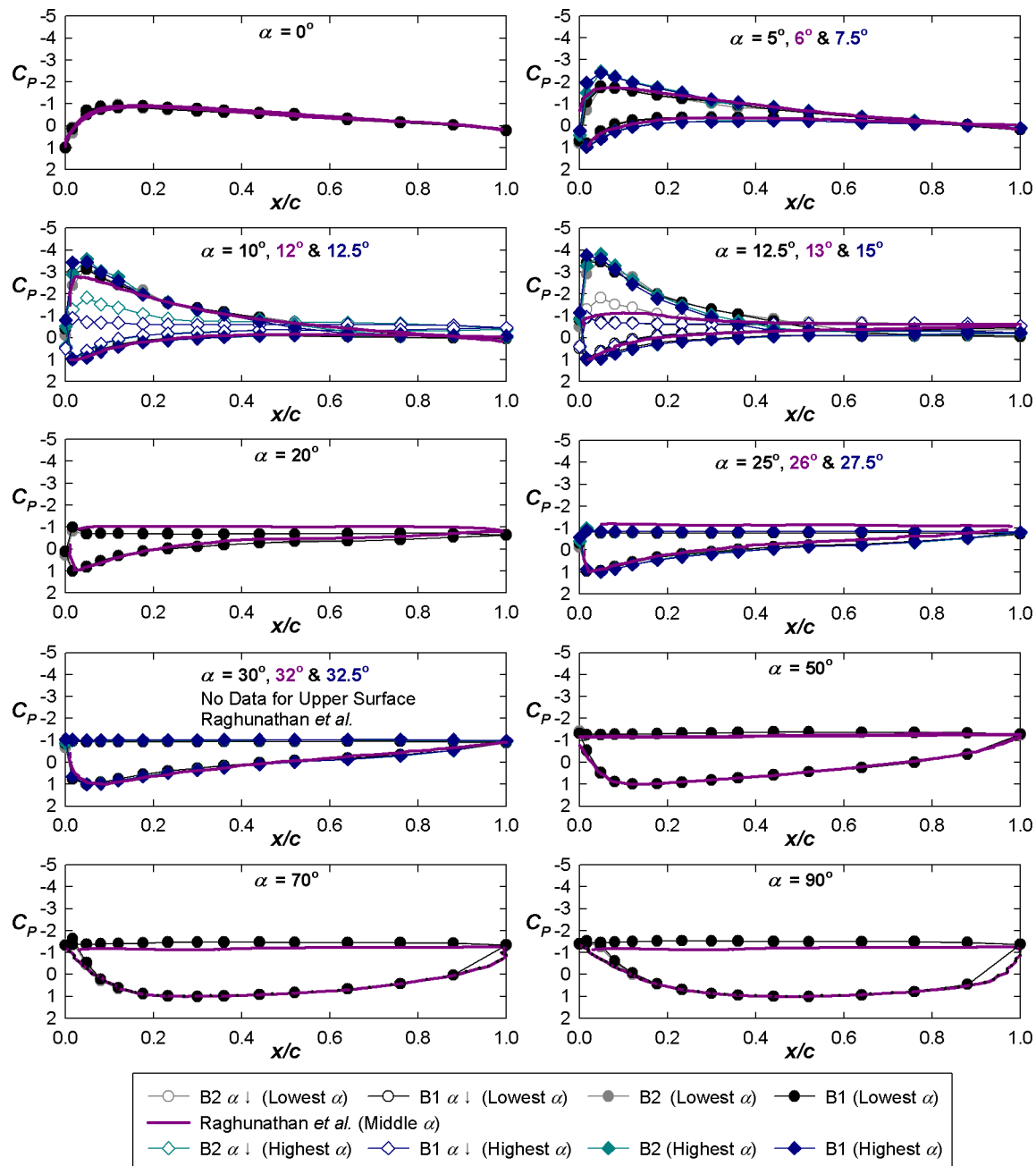


Figure 4-6 - Comparison of the mean C_p from the present results with those measured by Raghunathan, Harrison & Hawkins (1988).

Raghunathan, Harrison & Hawkins (1988) also provided surface pressure plots for their results. They did not indicate on their plots the location of the pressure taps (only lines were plotted) but

the results can still be compared, as shown in Figure 4-6. In cases where there were no results for the current experiment at the same α as the Raghunathan, Harrison & Hawkins results, the current results at the two closest α were plotted. There is excellent agreement for the cases at 0° and 6° , as would be expected considering the good match for c_l at these α . At $\alpha = 12^\circ$ the c_l from Raghunathan, Harrison & Hawkins is between the results for the increasing and decreasing α cases from the present results. From the C_P plot this seems to be due to a lower peak at the leading edge, although the general shape of the C_P plots match the current increasing α results for this case. However at $\alpha = 13^\circ$ the Raghunathan, Harrison & Hawkins results much more closely resemble the decreasing α results found in the current study. The shape of the C_P curves at higher α match well although the values for the upper surface are different. This accounts for the difference in predictions of c_l at these α (although the c_l values match well at $\alpha = 90^\circ$).

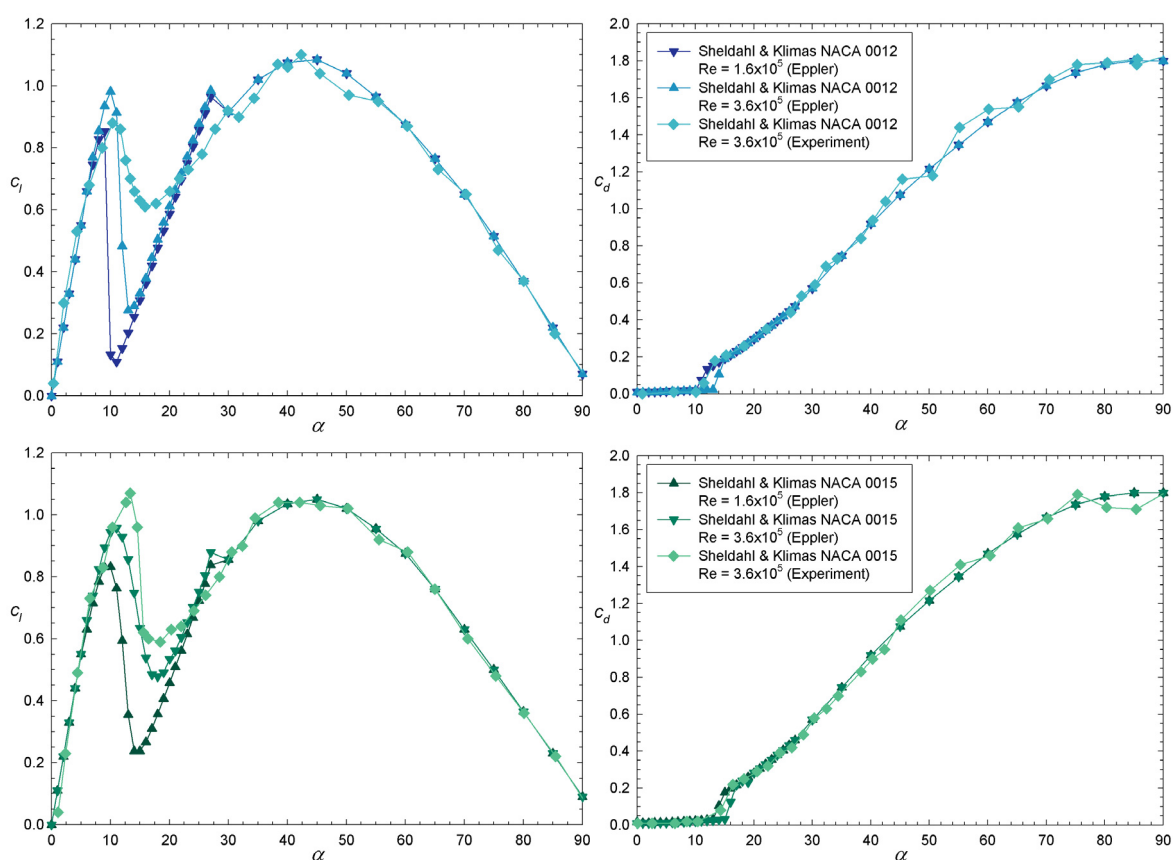


Figure 4-7 - Comparison of Eppler code (low α) and predictions based on experimental results (high α) with experimental data for NACA 0012 and NACA 0015 aerofoil sections.

Following Raghunathan, Harrison & Hawkins (1988) the current results have also been compared to results from NACA 0012 and 0015 aerofoil sections, although the data used for the comparison is from a later report than they used. Sheldahl & Klimas (1981) tested some symmetrical NACA sections over a wide range of α . The sections tested had a 6 inch span, giving an aspect ratio of 6 in the test section used and a maximum blockage at 90° of 7.1%. Forces were measured using a balance. A wake rake was also used to obtain drag results at low α . The turbulence level in the tunnel was not given. They also used an Eppler code to predict performance of several

symmetrical NACA aerofoil sections. The results from this code matched predictions well enough for the authors to feel justified in using the Eppler code for the linear and earlier non-linear portions of the c_l curve. The experimental data for all aerofoils above this region was considered close enough for this to be used for the remaining α . A comparison of these predictions and this study's experimental results is shown in Figure 4-7. The predictions match well for c_d . They also match well for c_l except around stall where the Eppler code seems to underpredict c_l values for the first local maxima and minima. The Eppler predictions for the NACA 0021 section were compared with the experimental results from the NACA 0012 and NACA 0015 as well as with the results from the current set of experiments and those of Raghunathan, Harrison & Hawkins (1988) shown earlier. The Eppler code predictions for the NACA 0021 aerofoil section are expected to provide a reasonable prediction except around stall.

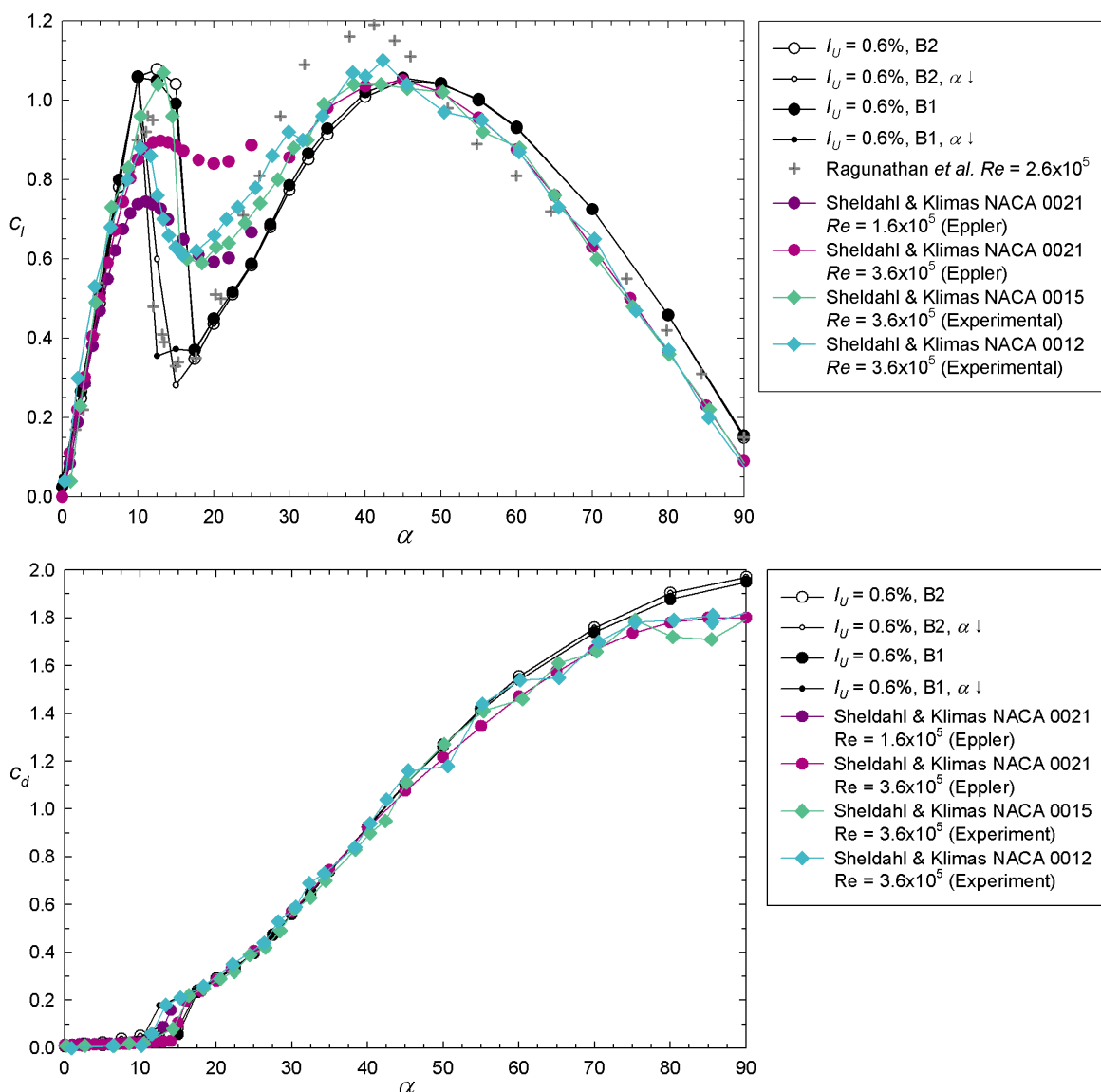


Figure 4-8 – NACA 0021 results from this study, Raghunathan, Harrison & Hawkins (1988) (c_l only) and Eppler predictions from Sheldahl & Klimas (1981). Also experimental results from Sheldahl & Klimas (1981) for the NACA 0015 and NACA 0012 aerofoil sections.

The comparison of c_l results in Figure 4-8 show the current results have features that match those seen in previous experiments but the curve does not match any one previous experiment over the complete range of α . The linear portion of the graph from 0° to 7.5° has a similar slope for all the results shown. The current results are the only ones to show such a high value of c_l at $\alpha = 10^\circ$, this may be due to the tapping rows' positions in the structure or the presumably higher turbulence levels of this experiment. The current results for the increasing α case match results from the NACA 0015 aerofoil section reasonably well for $\alpha = 12.5^\circ$ to $\alpha = 15^\circ$, at these angles the decreasing α case of the current results more closely resembles the results of Raghunathan, Harrison & Hawkins. Around $\alpha = 20^\circ$ the present results match those of Raghunathan, Harrison & Hawkins best, although by $\alpha = 45^\circ$ the current results show a better match to those of Sheldahl & Klimas, (which have their second local maxima at $\alpha = 45^\circ$ as would be expected for a symmetric aerofoil). This discrepancy may have been caused by the blockage correction applied to the Raghunathan, Harrison & Hawkins results. However by $\alpha = 90^\circ$ the results are again closer to those of Raghunathan, Harrison & Hawkins. Raghunathan, Harrison & Hawkins did not supply a c_d plot in their paper so the c_d results can only be compared with those of Sheldahl & Klimas. They seem to match well, as can be seen in the lower plot in Figure 4-8, including the jumps in drag associated with stall, except at high α where the present results tend to a higher level of drag. This may be due to the thickness of the aerofoil causing a wider wake; Sheldahl & Klimas' predictions for the c_d at this α are based on experimental observations for thinner aerofoil sections.

In conclusion these results, while not matching any one set of previously published results exactly, show the general features of previous results. Given the difficulty in matching results for aerofoil sections tests conducted in different wind tunnel facilities, the degree of matching found is reassuring, giving confidence in the methodology and findings of the current study.

4.2.3 Effect of Added Turbulence

This section will report on the effect of grid-generated turbulence on the mean values of c_l , c_d and c_m , $1/4c$. The effect of turbulence intensity was examined for similar integral length scales by comparing the coefficients for the same grid in different positions. The effect of turbulence integral length scales was examined by comparing results from different grids with similar intensities but with different integral length scales. The C_p and σ from taps in tapping rows B1 and B2 were used to aid interpretation of the force and moment coefficients. Surface flow visualisations allowed the effect of turbulence on separation to be observed directly. Comparisons at low α (0° to 20°) allowed the effect of turbulence on hysteresis to be examined.

This section first looks at the effect of turbulence intensity. It should be stressed that due to the decay of turbulence, the integral length scale changes as the grid is moved further away from the model. Therefore, the effect of turbulence intensity could not be examined in isolation. The results from the small grid are presented in Figure 4-9. The legend shows the results for rows B2 and B1

in order of grid position, with the symbols for the grid furthest from the model (position E) being at the top of the legend and the grid closest to the model (position A) at the bottom. The effect of decreasing α was examined only with the grid in the position E. Hysteresis was clearly present for this case and was therefore likely to be present for at least some of the other cases. The hysteresis loop will be examined in more detail later in this section.

The lift results for the small grid, presented in Figure 4-9, show that the increase in turbulence intensity causes more gradual change in c_l around stall, causing a “softer” stall. The slope of the attached region was slightly reduced by higher turbulence intensities. The c_l at $\alpha = 12.5^\circ$ was reduced by the addition of turbulence but at $\alpha = 15^\circ$ it was increased, meaning the maximum c_l remained similar. Although in all cases there was a reasonably sharp drop in c_l for $\alpha > 15^\circ$, the drop became smaller as the turbulence intensity was increased. This could correspond to turbulence in the flow promoting a more turbulent boundary, by causing the boundary layer to transition to turbulence earlier and/or by entering boundary layer and increasing turbulence production. The boundary layer seems to be better able to resist adverse pressure gradients. This enables the separation line to move more slowly towards the leading edge with increasing α . Interestingly, there is a large difference between the two tapping rows in this region with results for tapping row B2 tending to lie on the values from row B1 found for the previous grid position. This will be examined in more detail by looking at the mean and standard deviations of the C_p measurements later in this section. The c_l response does not appear to be greatly affected by increased turbulence intensity for $\alpha > 20^\circ$.

The c_d plots in Figure 4-9 show little difference across the range of turbulence intensities generated by the small grid. There seems to be a slight difference at low α between the results from rows B1 and B2. This will be examined further when the effects of hysteresis are examined. The sharp jump in c_d associated with stall is seen between $\alpha = 15^\circ$ and $\alpha = 17.5^\circ$ in all cases except for the decreasing α case where it is seen 2.5° earlier. There appears to be a slight decrease in the maximum c_d with increasing turbulence intensity.

$c_{m, 1/4c}$ shows a variation in results as a function of turbulence intensity in the range $10^\circ < \alpha < 22.5^\circ$, which is similar to the range of α where the variations in the c_l results were seen as discussed previously. When α is around 15° , a sudden drop in $c_{m, 1/4c}$ is noted which seems to be associated with stall. Before this sudden drop, $c_{m, 1/4c}$ appears to subtly increase with increasing α , however little variation was noted across the range of turbulence intensity investigated. For $17.5^\circ \leq \alpha \leq 22.5^\circ$ the addition of turbulence seems to cause slightly more negative values, this again promotes the idea of the boundary layer being attached for a short distance from the leading edge. This will be examined further by looking at the surface pressures at the pressure taps.

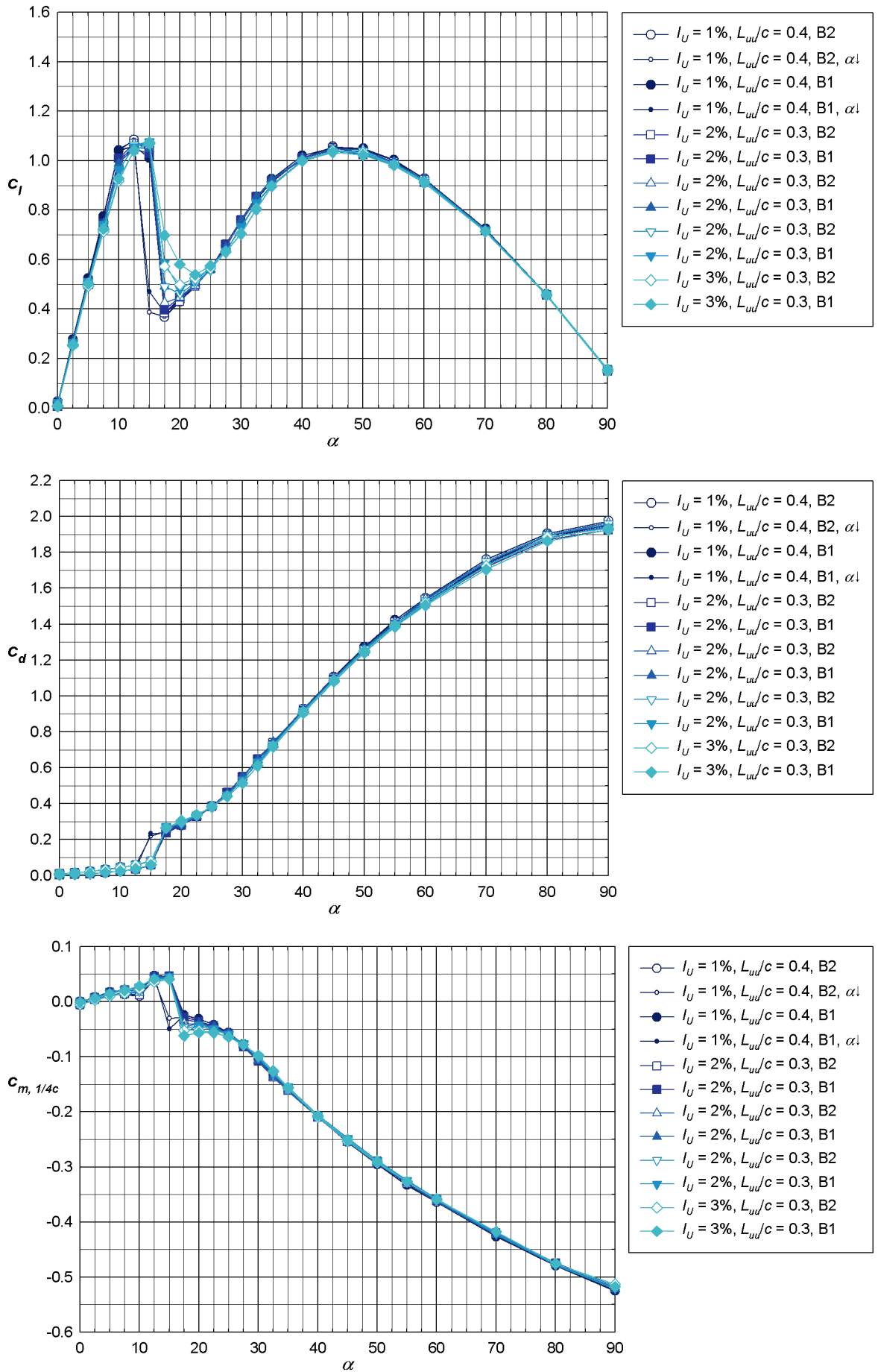


Figure 4-9 – NACA 0021 mean coefficients of lift, drag and of moment about the quarter chord with the small grid.

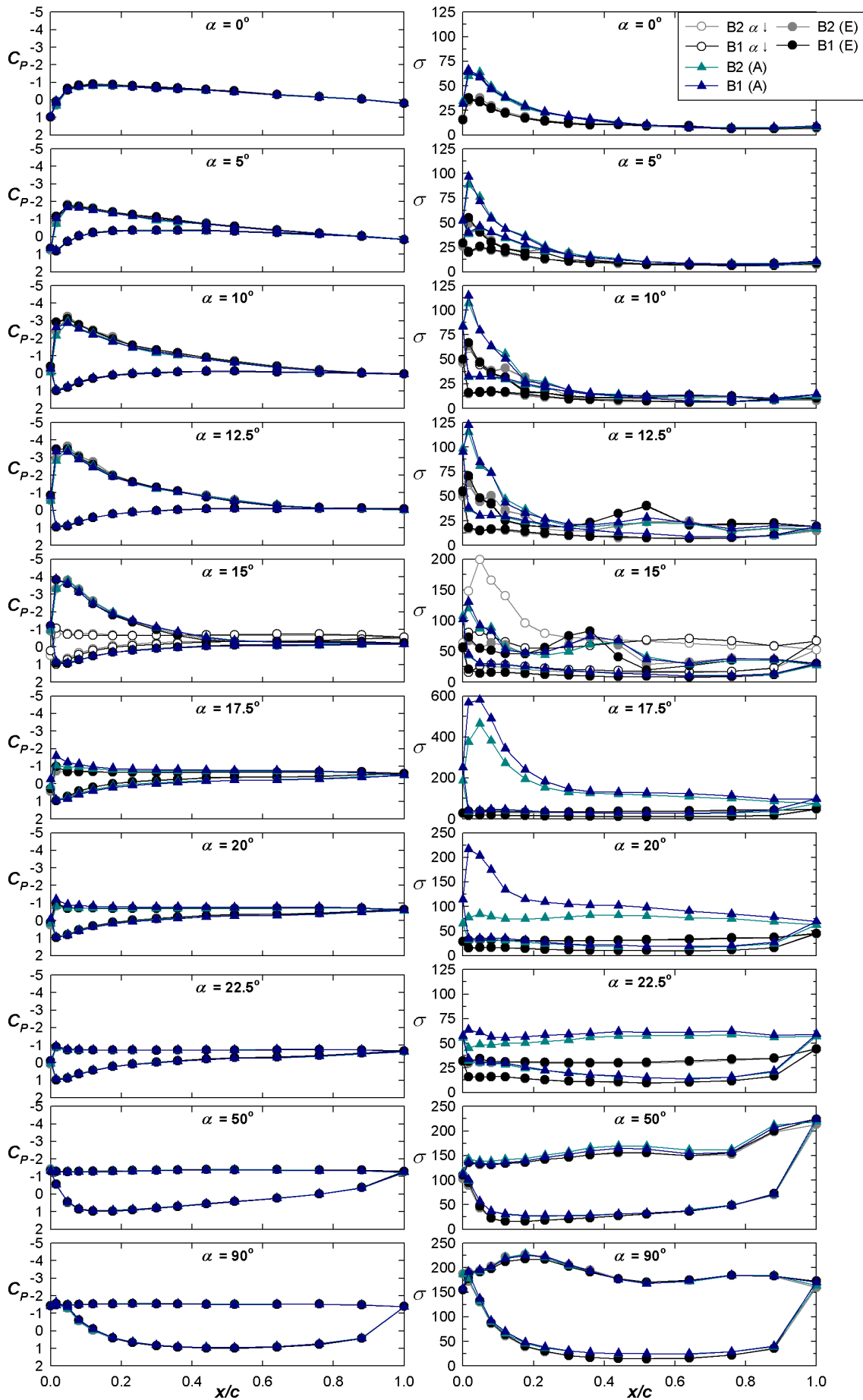


Figure 4-10 – NACA 0021 coefficients and standard deviations of the pressures around the aerofoil around stall with the small grid in the tunnel at the closest (A) and furthest positions (E) from the model. Note the change in scale of the σ plots at 15° , 17.5° , 20° , 50° and 90° .

Figure 4-10 shows the mean C_p and the standard deviation of the pressure measured by the Scanivalve (pressure at the tap minus the static pressure from the Pitot) at a variety of α for the small grid in the position closest, position A, and furthest, position E, from the model. For the cases $\alpha \leq 20^\circ$, the plots for decreasing α with the grid in position E are also shown. While the C_p values are very similar for all taps at $\alpha = 0^\circ$, the σ on the front half of the aerofoil is larger for the grid in position A. The turbulence in the freestream seems to be increasing the variation in the pressure signals on the forward half of the aerofoil. A similar effect can be seen at $\alpha = 5^\circ$. At $\alpha = 10^\circ$ and, to a lesser extent, at $\alpha = 12.5^\circ$, the C_p values for the taps on the suction surface near the leading edge for the grid in position E are higher than those for position A, causing the difference in c_l noted earlier. The σ at $\alpha = 10^\circ$ again has higher values near the leading edge for the grid in position A compared to position E. There are also differences in σ between the two rows (although no differences between the increasing and decreasing α cases for the same row) with the grid furthest from the model; row B2 shows increased standard deviation around $20\%c$. A similar difference is seen between the two rows at $\alpha = 12.5^\circ$ and at this angle there is also an increased σ near mid chord for row B1. At $\alpha = 12.5^\circ$ the grid closer to the model causes a peak in σ on the suction surface near the leading edge. The peak at this α has increased in size compared to at $\alpha = 10^\circ$.

At $\alpha = 15^\circ$, the two flow conditions give similar values of C_p for the increasing α case showing attached flow until about mid-chord. The separation corresponds to increased σ around $0.4c$. However in the decreasing α case, the mean C_p appears to show separated flow. Row B1 has slightly higher values of C_p at the leading edge and at the first tap on the suction side, which corresponds to the higher c_l , slightly higher c_d and lower $c_{m, 1/4c}$ seen in Figure 4-9. Comparing the two flow conditions, the σ on the suction surface are very different. Row B1 shows increased σ compared to those found at $\alpha = 12.5^\circ$ with similar values for all suction surface taps. However, row B2 shows much increased values of σ on the suction surface near the leading edge (note the change of scale of this plot). This is similar to what was seen for both rows at $\alpha = 12.5^\circ$ in the decreasing α case with no grid in the tunnel, the increased turbulence from in the boundary layer from the freestream seems to have delayed the progress of the separation line towards the leading edge. The σ peaks at the leading edge are consistent with a small attached region which varies from being attached and separated, for row B1 the variation appears less than for row B2 leading to a higher suction peak but smaller σ peak at the leading edge.

At $\alpha = 17.5^\circ$, the flow condition with the grid closest to the model seems to have produced a similar flow to that seen at 15° for row B2 in the decreasing α case with similar C_p and a large leading edge peak in σ . However, the peaks on the suction surface at the leading edge in C_p and σ are larger than at 15° for row B2 in the decreasing α case (note the even larger scale of the σ plot), corresponding to the higher c_l and lower $c_{m, 1/4c}$ recorded at this angle. Also row B1 shows the

higher C_p and σ than row B2. The results at 17.5° for the lower turbulence intensity case are reproduced at a different scale in Figure 4-11 to allow the results to be examined. However, no major features are seen and the results resemble those found at $\alpha=20^\circ$ for this flow condition. For the higher turbulence flow condition at $\alpha=20^\circ$, small peaks in σ are observed which are similar, but smaller in magnitude to that found for $\alpha=17.5^\circ$. These small peaks cause a spread in the c_l and $c_{m, 1/4c}$ results that is similar to that found for $\alpha=17.5^\circ$, however the variation is reduced in size.

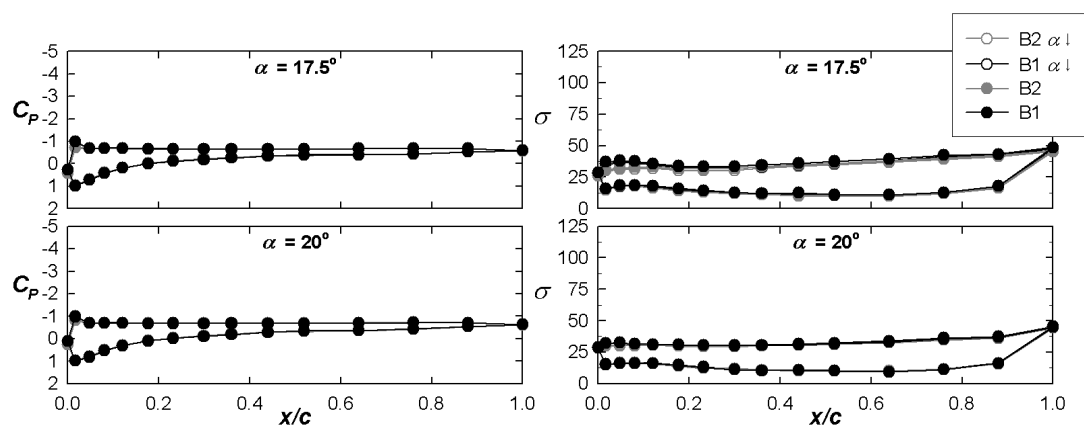


Figure 4-11 – NACA 0021 coefficients and standard deviations of the pressures around the aerofoil around stall with the small grid in the tunnel at the furthest position from the model, position E. Same data as in Figure 4-2 at $\alpha=17.5^\circ$ and 20° for the grid position E but at a different σ scale.

Figure 4-10 shows that, at $\alpha=22.5^\circ$, the C_p values for all cases look similar. However, the σ for the grid closest to the model is larger on all taps, which may be due to turbulence in the flow affecting the tap response, as was found for low α . At $\alpha=50^\circ$ the C_p are again very similar but the σ are only slightly increased for the taps on the suction surface and on the lower surface from the leading edge to about mid-chord. As expected the C_p are similar at $\alpha=90^\circ$, the σ are only slightly different for the two flow conditions showing increased variation for the case where the grid is closest to the model on the central taps on the lower surface (buffeting) and a few taps near 20% chord on the upper surface.

Surface flow visualisations, using china clay, are presented in Figure 4-12. These images show an unevenly weighted time average of the surface flow and, therefore, are unlikely to capture the variations identified in the σ analysis. The image taken for the case $\alpha=5^\circ$ shows a separation bubble similar to that seen for the case where there was no turbulence grid upstream of the model. However, the results for the no grid and small grid in position A are not similar at 15° . With no grid in the tunnel at $\alpha=15^\circ$ the flow appeared to be totally separated, in agreement with results from the decreasing α case in the force measurements. With the small grid closest to the model the flow is not fully separated, there are mushroom shaped pairs of counter-rotating vortices. These structures seem to allow flow to be attached from the leading edge until these structures form and are consistent with the increasing α case (the only pressure measurements taken for this flow condition). As the tunnel had to be run up to speed after the paint had been applied for the surface

flow visualisation and would be equivalent to the decreasing α case this indicates that the decreasing α case would have been similar to the increasing α case in this flow. The two pictures are of sequential experiments. They show that the formation of these structures is very sensitive to initial conditions. However the mushroom structures have disappeared by 17.5° and 20° and there are very few structures visible except near the walls. This is similar to the flows seen at 15° and 17.5° for the no grid flow condition.

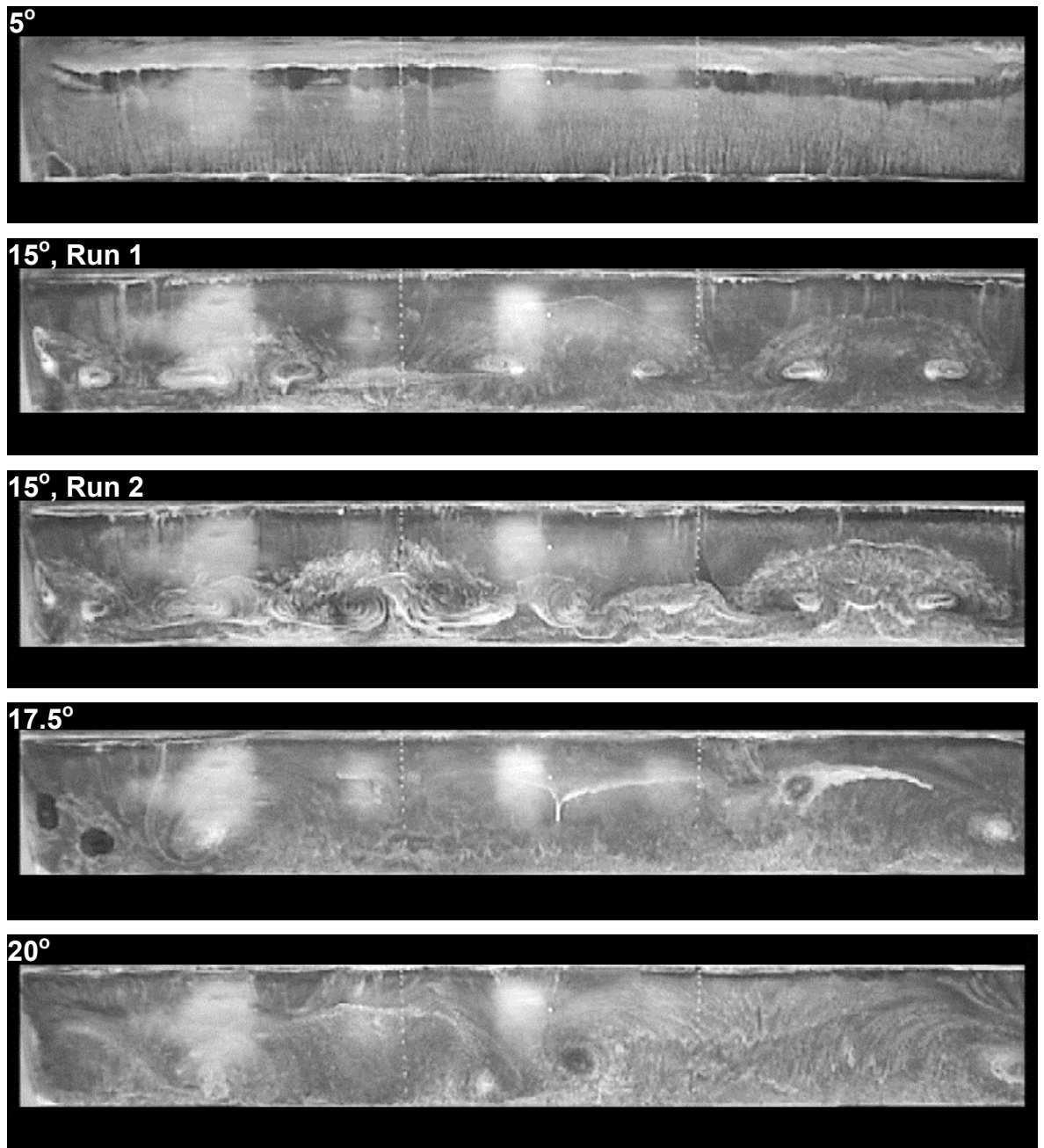


Figure 4-12 - Surface Flow Visualisation on the NACA 0021 around stall with the small grid in the closest position to the model.

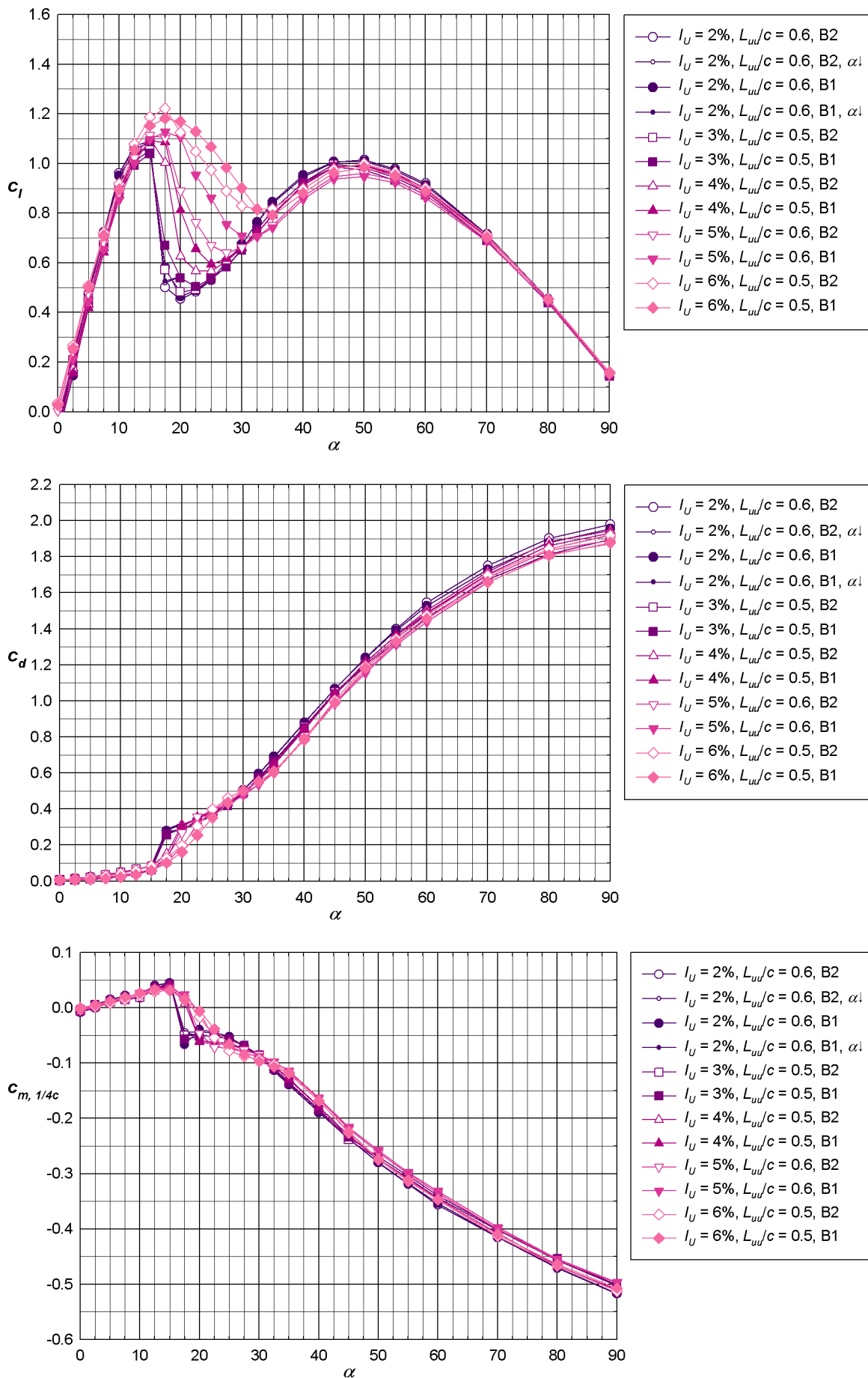


Figure 4-13 – NACA 0021 mean coefficients of lift, drag and of moment about the quarter chord with the medium grid.

Figure 4-13 shows c_l , c_d , and $c_{m, 1/4c}$ for the flow conditions with the medium grid in the tunnel. The integral length scale of the turbulence in the flow direction was between 0.5 to 0.6 c . The turbulence intensity ranged from about 2 to 3% with the medium grid furthest from the model, which was similar to the small grid in some positions close to the model, up to 6% with the medium grid closest to the model. These higher levels of turbulence have a more dramatic influence on the stall. Hysteresis was checked for with the grid in the furthest position from the model, and no effect was found. This is consistent with the earlier conclusion from the surface flow visualisations with the small grid in the tunnel closest to the model (which produced a slightly higher turbulence intensity), that hysteresis effect was likely to have been removed with the addition of turbulence of this intensity.

The c_l plot in Figure 4-13 shows that for the flow conditions with $I_u \geq 4\%$ the maximum lift was increased and, in all but the row B2 results for the $I_u = 4\%$ case, the maximum lift occurred at a higher α . There were pronounced differences again between results for the two tapping rows during stall presumably due to the tapping rows being in different locations in the stall cells, this will be examined later in this section using the surface flow visualisations. As the turbulence intensity was increased, the stall became more gradual with smaller changes in c_l as α was increased. Above the stall region there was a spread in the c_l results that reduced as α increased towards 90°.

In the c_d plots in Figure 4-13, increasing the turbulence intensity affected the jump in drag associated with stall. As the turbulence intensity increases, the jump is smoothed out. There is also a spread in the c_d results, similar to that observed in the c_l results, but in this case the spread increases as α increased towards 90°. The flow with the highest turbulence intensity produces the smallest maximum drag at 90°. This may be due to the increased turbulence causing increased curvature of the streamlines and therefore a smaller wake. The $c_{m, 1/4c}$ plots also show a similar smoothing of the jumps associated with stall. There is a spread in the results for $\alpha \geq 35^\circ$ but, in this case, the spread remains fairly constant. Plots of C_p , to be presented next, will give a better understanding of these features.

Figure 4-14(a) and (b) shows the mean C_p and σ of the pressure measured for each tap in rows B1 and B2 at a variety of α for the medium grid in the closest and furthest positions to the model. More angles have been shown than for the no grid and small grid flow conditions as there was a larger range of α where there were significant differences between the force measurements. At $\alpha = 0^\circ$ there was some slight differences between the upper and lower surfaces for the grid in position E, which may indicate the aerofoil was not as well aligned as in the other flows (the NACA 0021 tests used the first design of the positioning arm that did slip on a few occasions requiring the model to be realigned). The most noticeable feature is the difference in the σ on the taps on the front half of the aerofoil for the grid in positions A and E. The medium grid in position E shows a

similar level of σ to that seen for the small grid at this angle for position A (compare the results for $\alpha = 0^\circ$ in Figure 4-2 with those in Figure 4-14(a)). The plots do not show significant differences between the increasing and decreasing α cases, confirming the absence of a hysteresis effect over more than 2.5° (the angular separation of α between measurements).

The C_p plots at $\alpha = 5^\circ$ and 10° show very little difference between the results for the grid in position E and in position A. The σ at these angles shown in Figure 4-14(a) are of similar shape but of greater magnitude to that seen in the small grid case, shown in Figure 4-10. The trend of increasing peaks on the upper surface near the leading edge in both C_p and σ , is continued to 12.5° . In the small grid σ plot at this angle, there was a small local maximum around $0.5c$ that was not seen in the medium grid case. However by $\alpha = 15^\circ$, a similar small local maximum is seen around $0.4c$ in σ . This is similar to what was seen on the small grid in the increasing α cases at this angle. The C_p plot at $\alpha = 15^\circ$ in Figure 4-14(a) shows all attached flow (and no evidence of the hysteresis seen with the small grid in position E). However by $\alpha = 17.5^\circ$ with the medium grid in position E, the aerofoil appears to have stalled, with the exception of a small region of attached flow near the leading edge. Interestingly, the σ for the increasing α case are high across the suction surface aerofoil but are low in the decreasing α case. The grid in position A appears to still have an attached boundary layer and the σ has increased between the leading edge to about mid-chord. The C_p on the lower surface is also different in this case, being slightly larger than for the grid in position E.

This difference in C_p for the lower surface persists for $20^\circ \leq \alpha \leq 30^\circ$. In this range the leading edge suction peak reduces for the grid in position A. In position E the flow continues to be stalled. There are also differences in the suction peak sizes for rows B1 and B2 in position A that results in the different force coefficients for these rows in this range. This σ for the grid in position A increased (note the change in scale on these plots) and also showed differences between the two rows. The σ increase to a maximum leading edge peak for row B2 at $\alpha = 22.5^\circ$ and for row B1 at $\alpha = 25^\circ$ and then decrease again.

Figure 4-14(b) shows that for $\alpha > 30^\circ$, the C_p values for both cases are very similar with only slight differences in the suction surface values. However the σ show major differences (note the scale on these plots has changed back to what it was for the low α cases), the leading edge peak for the case with the grid in position A reduces and has disappeared by $\alpha = 70^\circ$. However, lower surface differences between the cases where the grid is in position A or E spread back further along the chord with increasing α . The σ at the trailing edge increases from $\alpha \geq 35^\circ$ for the grid in position E, the σ at the trailing edge increases for the grid in position A also for $\alpha \geq 40^\circ$ but does not match that for the grid in position E until $\alpha = 70^\circ$. By $\alpha = 90^\circ$ the differences are along the entire lower surface.

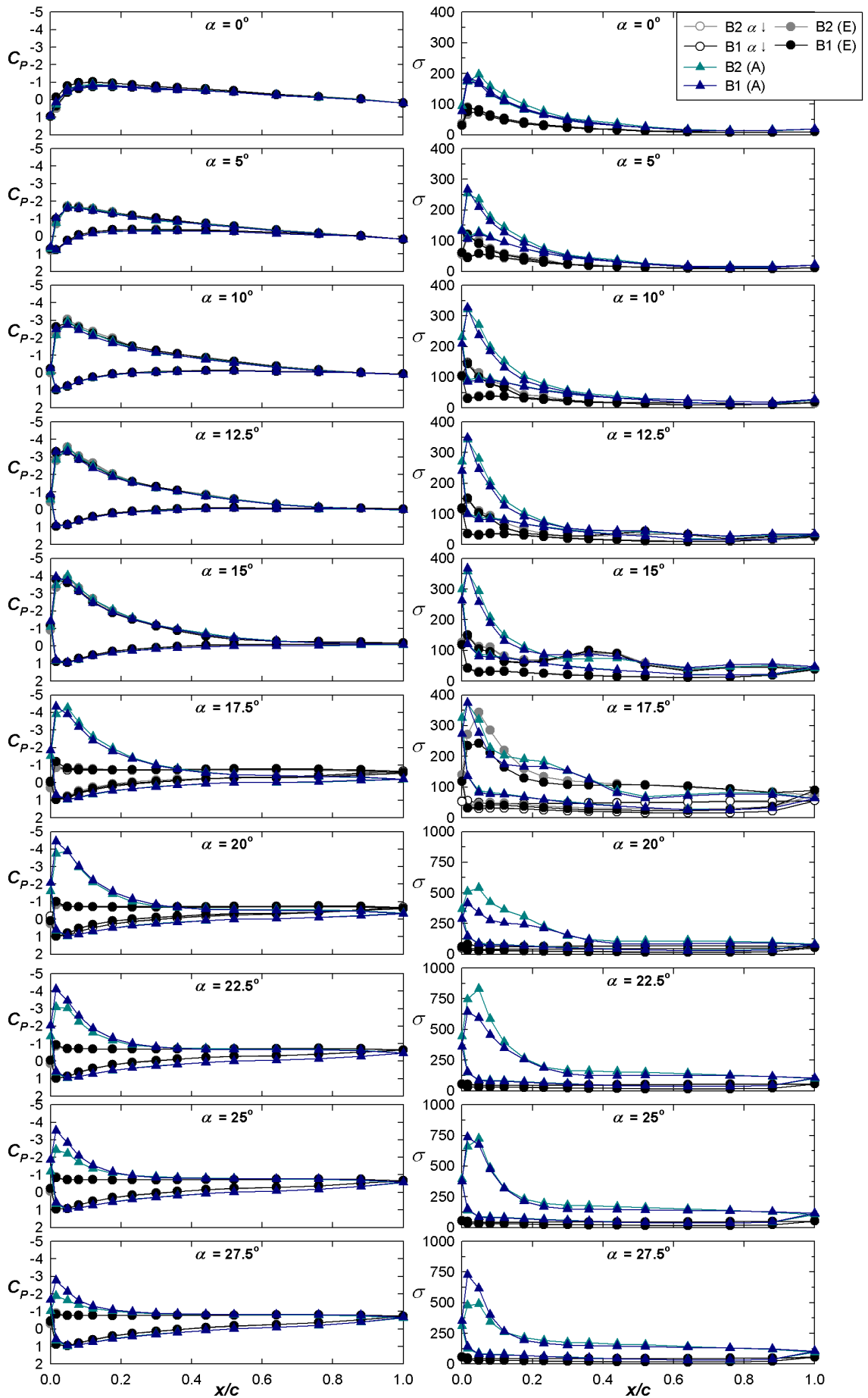


Figure 4-14(a) – NACA 0021 coefficients and standard deviations of the pressures around the aerofoil around stall with the medium grid in the tunnel at the closest (A) and furthest positions (E) from the model. Note the scale of the σ plots changes from a maximum of 400 to a maximum of 1000 for $\alpha \geq 20^\circ$.

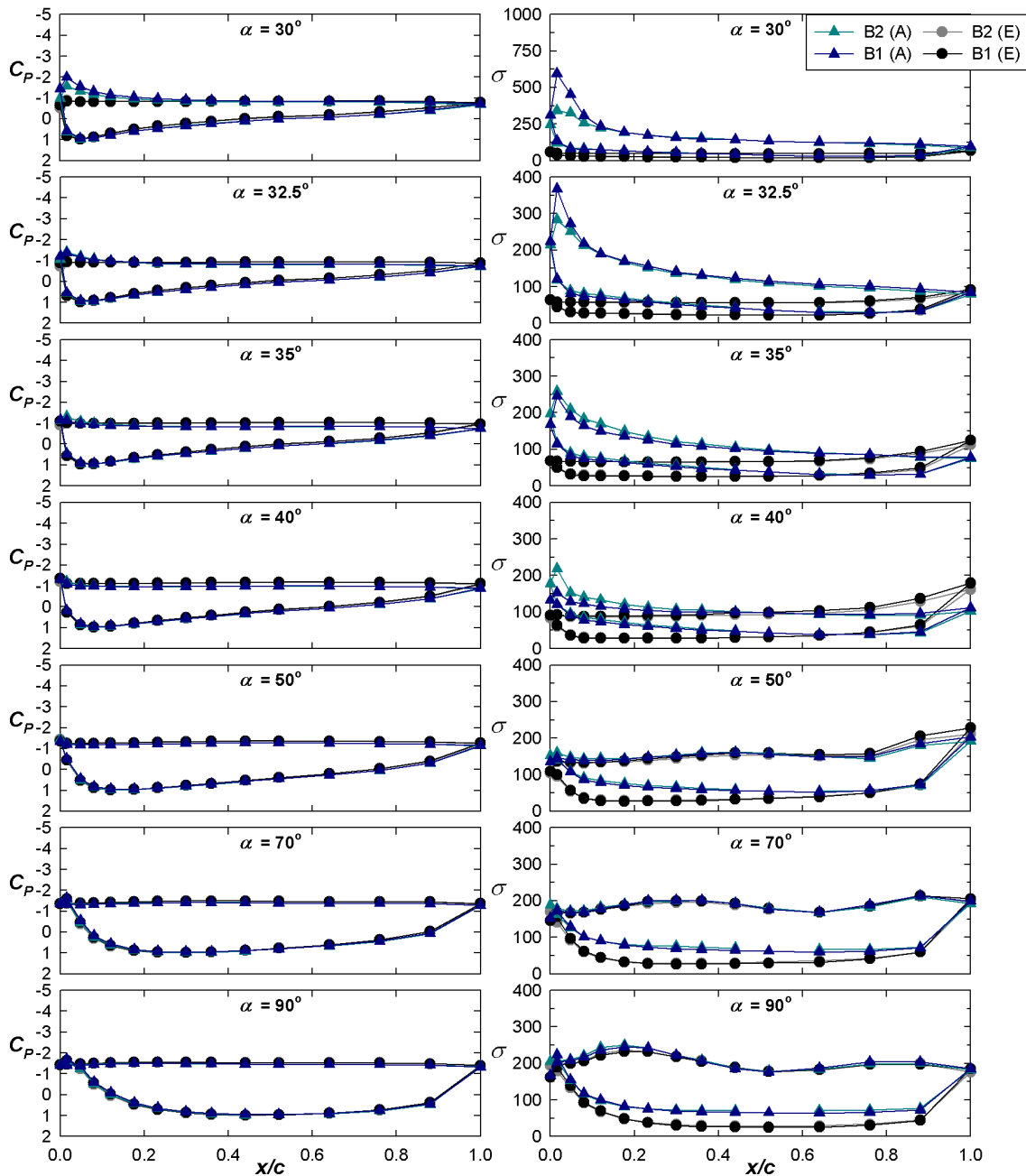


Figure 4-14(b) – NACA 0021 coefficients and standard deviations of the pressures around the aerofoil around stall with the medium grid in the tunnel at the closest (A) and furthest positions (E) from the model. Note the scale of the σ plots changes from a maximum of 1000 $\alpha = 30^\circ$ to 400 for the other plots.

Surface flow visualisations for the medium grid in position A are shown in Figure 4-15. At $\alpha = 5^\circ$ there was perhaps a laminar to turbulent boundary layer transition just before quarter chord but, unlike the no grid and small grid surface flow visualisations at this α , no separation bubble was visible. At 15° separation is visible midway along chord. The dark spots are where fluid collected and not yet dried (the white patterns as noted for the other visualisation pictures were caused by delaminated regions on the model surface which seemed to have no effect on the flow). These regions may be similar to the pairs that occur at 10° with no grid. At 20° and 25° , “mushroom” shaped structures are visible. The higher σ seem to be associated with these structures and the partial separation that goes along with them. By $\alpha = 30^\circ$ the flow patterns were fairly disorganised and the flow appears to have separated.

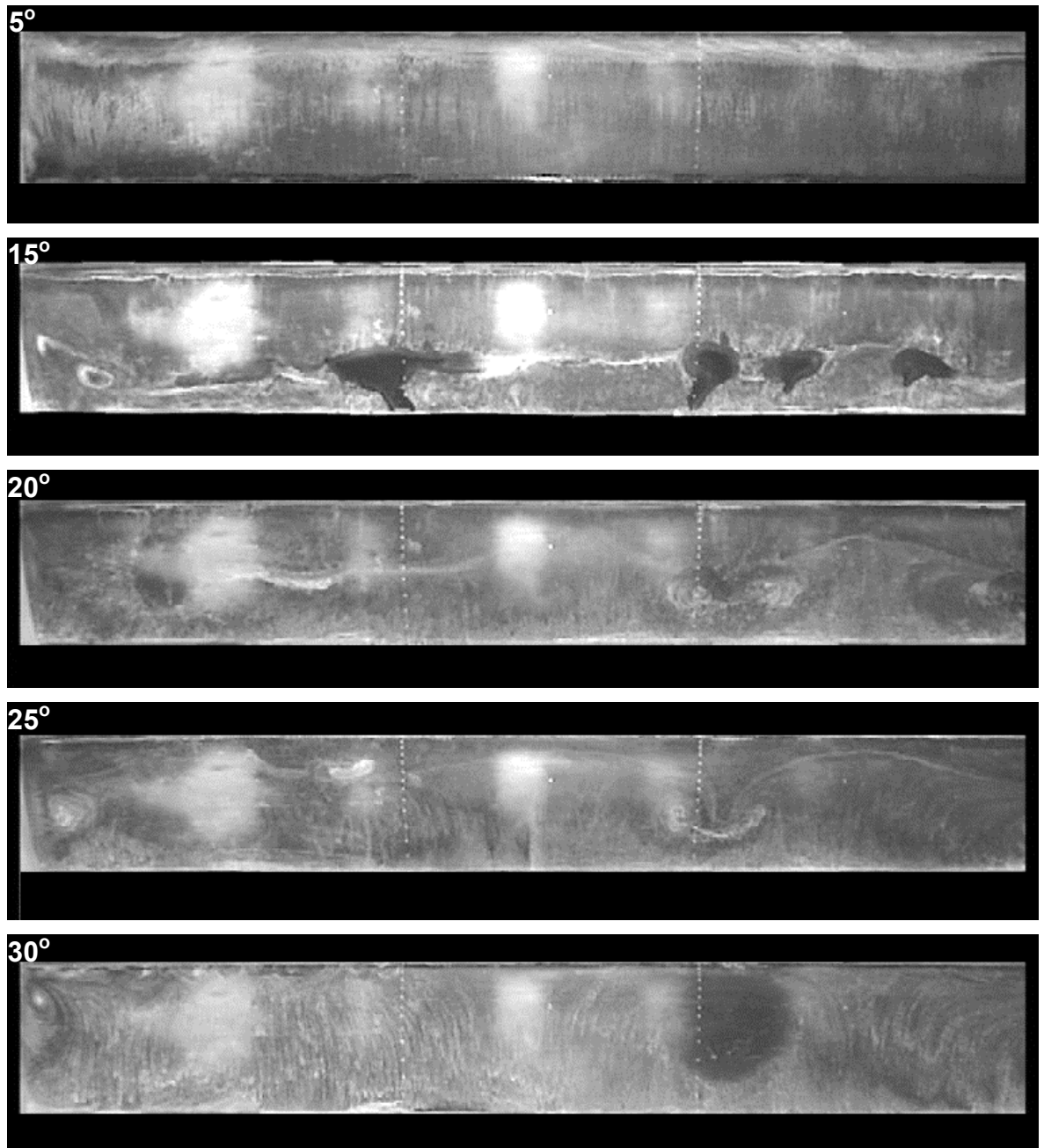


Figure 4-15 - Surface Flow Visualisation on the NACA 0021 around stall with the medium grid in the closest position to the model.

The large grid produced dramatic effects on the sectional coefficient of lift, as shown in Figure 4-16. With the grid in positions E and D, stall was delayed and the first local maximum slightly increased (with the grid in position D the maximum was delayed until 17.5°). With the grid in positions C and B, the lift coefficient around stall increased compared to other cases especially from 10° on. The maximum lift occurred at $\alpha = 20^\circ$. With the grid in position C the curve did not rejoin the deep-stall trend until 40° . The shape of the lift curve with the grid in position B also resembled the deep-stall trend by this angle but with increased values until about 70° when it joined the other curves. As for other cases, there were significant differences between the lift values from row B1 and B2 during stall.

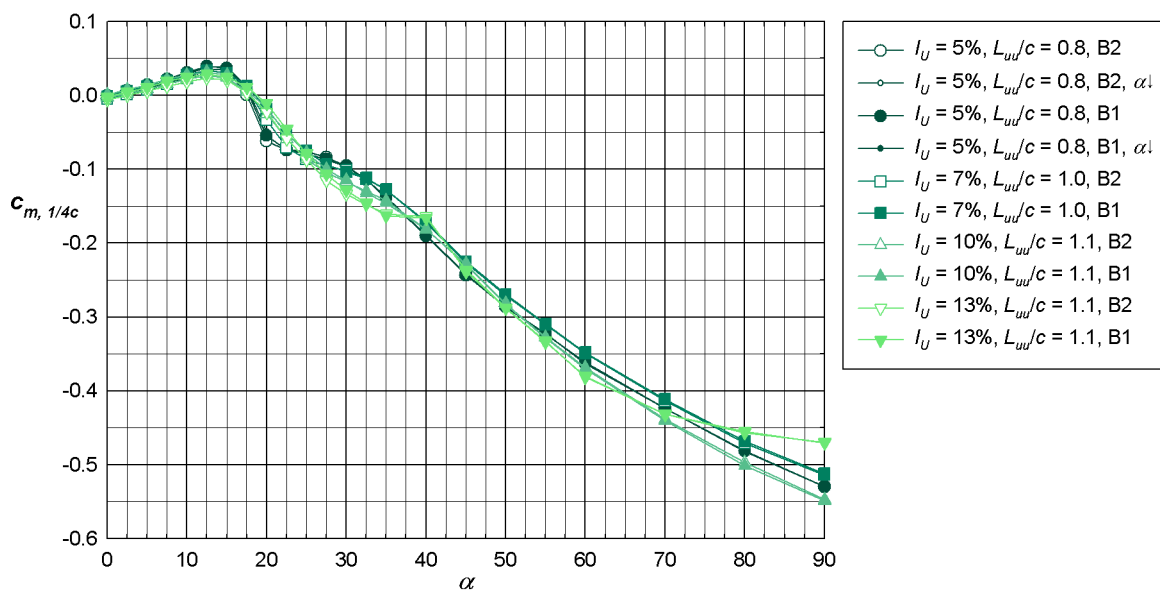
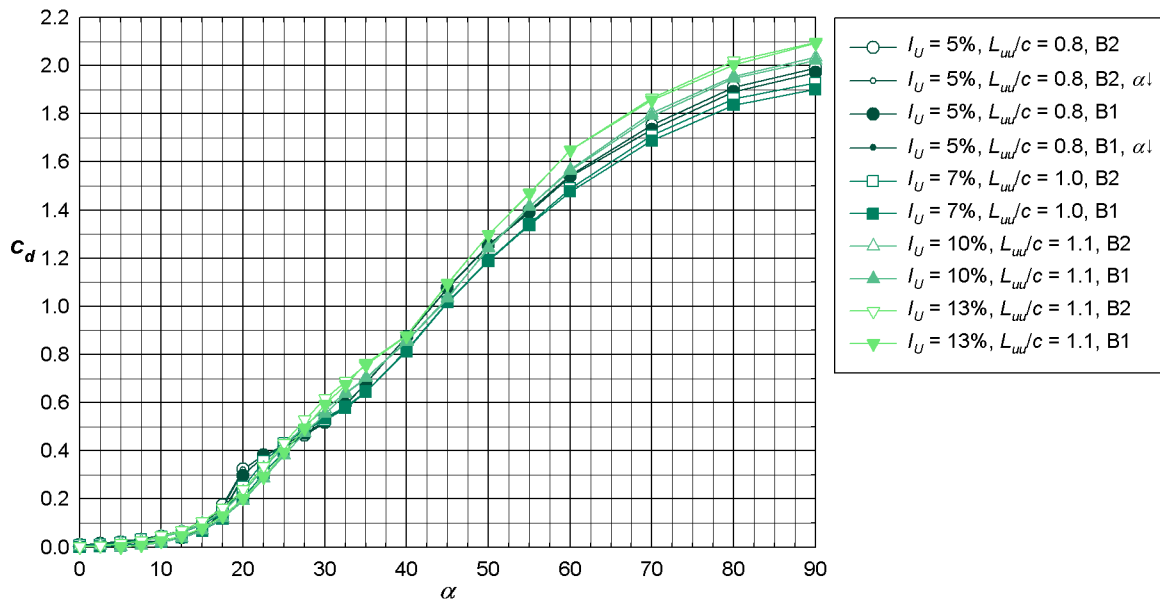
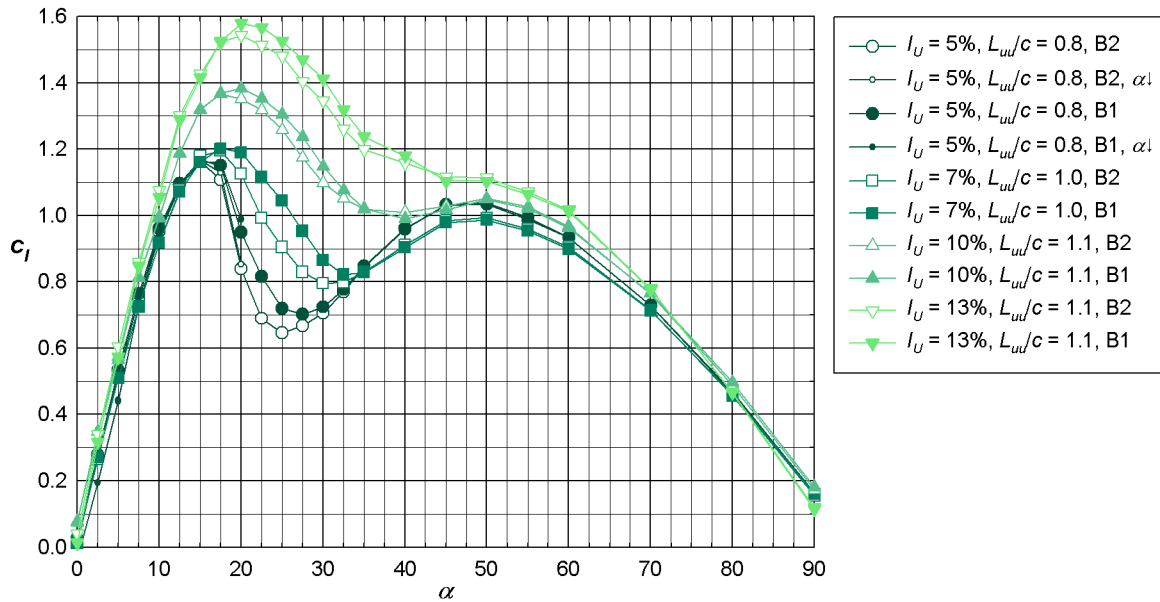


Figure 4-16 - NACA 0021 mean coefficients of lift, drag and moment about the quarter chord with the large grid.

Figure 4-16 also shows coefficients of drag and moment about the quarter chord for the flow conditions with the large grid in the tunnel. There was a slight “hump” associated with stall for the case with the large grid in position E that was smoothed out in the other flows. Compared to the flow with the grid in position E, the maximum drag was reduced with the grid in position D and increased with the grid in positions C and B. A similar smoothing of the jump associated with stall was seen for $c_{m, 1/4c}$, with only the grid in position E producing a sharp jump. The minimum $c_{m, 1/4c}$ was of smaller for the grids in positions D and B compared to that for the grid in position E. However, the grid in position C caused a larger minimum than that of E and the curve for the grid in position B is not of the same shape as the others. It showed reduced values between 30 and 35° before jumping back to similar values seen on the cases at $\alpha = 40^\circ$ to 70° before the curve again assumed a different shape and trended to a different local minimum at $\alpha = 90^\circ$. This “bump” in $c_{m, 1/4c}$ occurs at α where c_l and c_d are similarly changed and appears due to a large leading edge suction peak which remains to very high α in this case, see the C_p and σ plots shown in Figure 4-18(a) and (b).

Figure 4-18(a) shows a good match in C_p at $\alpha = 0^\circ$. Note the very large scale needed for the σ plots. At 5° there is a difference in C_p between the case with the grid in position E and the grid in position B. This is the first case to show such differences before stall, this is possibly due to an earlier transition to a turbulent boundary layer and higher suction pressures due to the turbulent boundary layer. This does happen on a cylinder, see Figure 4-17, although for a cylinder the effect is complicated by the two changing separation points. Otherwise the plots show similar shapes to those seen in the medium grid case until $\alpha = 15^\circ$ (although the scales are different). The plots at 15° for the large grid look similar to those at 12.5° for the medium grid, presumably a thicker turbulent boundary layer is produced by the larger grid causing the separation to be delayed in this case. Note the change in scale for the σ plots at 15° . At 17.5° there is a very large suction peak and similar σ between the plots for the grid in position E and B. For the grid in position E, the σ is different for rows B1 and B2 and slightly different for the increasing and decreasing α cases. There was also the beginning of larger values on the lower surface for the grid in position B compared to those in position E, these larger values on the lower surface continued for the remaining α , this is presumably due to buffeting from the freestream.

By $\alpha = 20^\circ$, the C_p peak has decreased for the grid in position E but the σ is now similar for the two grid positions. However by 22.5° , both the C_p and σ values for the grid in position E had reduced, while those for position B increased or remained similar. These trends continued for 25° and 27.5° . For 30° to 40° the trend while the grid was in position B was for smaller C_p and σ peaks. The plots remained similar for the grid in position E. The C_p at $\alpha = 50^\circ$ the C_p for both grid positions was very similar but the σ very different (note the change in scale). The shape of the σ for the grid in position E is similar to what has been seen earlier, but for the grid in position B the leading edge

has a peak and a similar shape to the plot for the grid in position E near the trailing edge. As the α increases to 70° and 90° , the differences in σ between the grid in position E and in position B decrease at the leading edge and increase further along the chord on the lower surface. In C_p differences increase on the lower surface near the leading edge by 70° and on the leading and trailing edge by 90° .

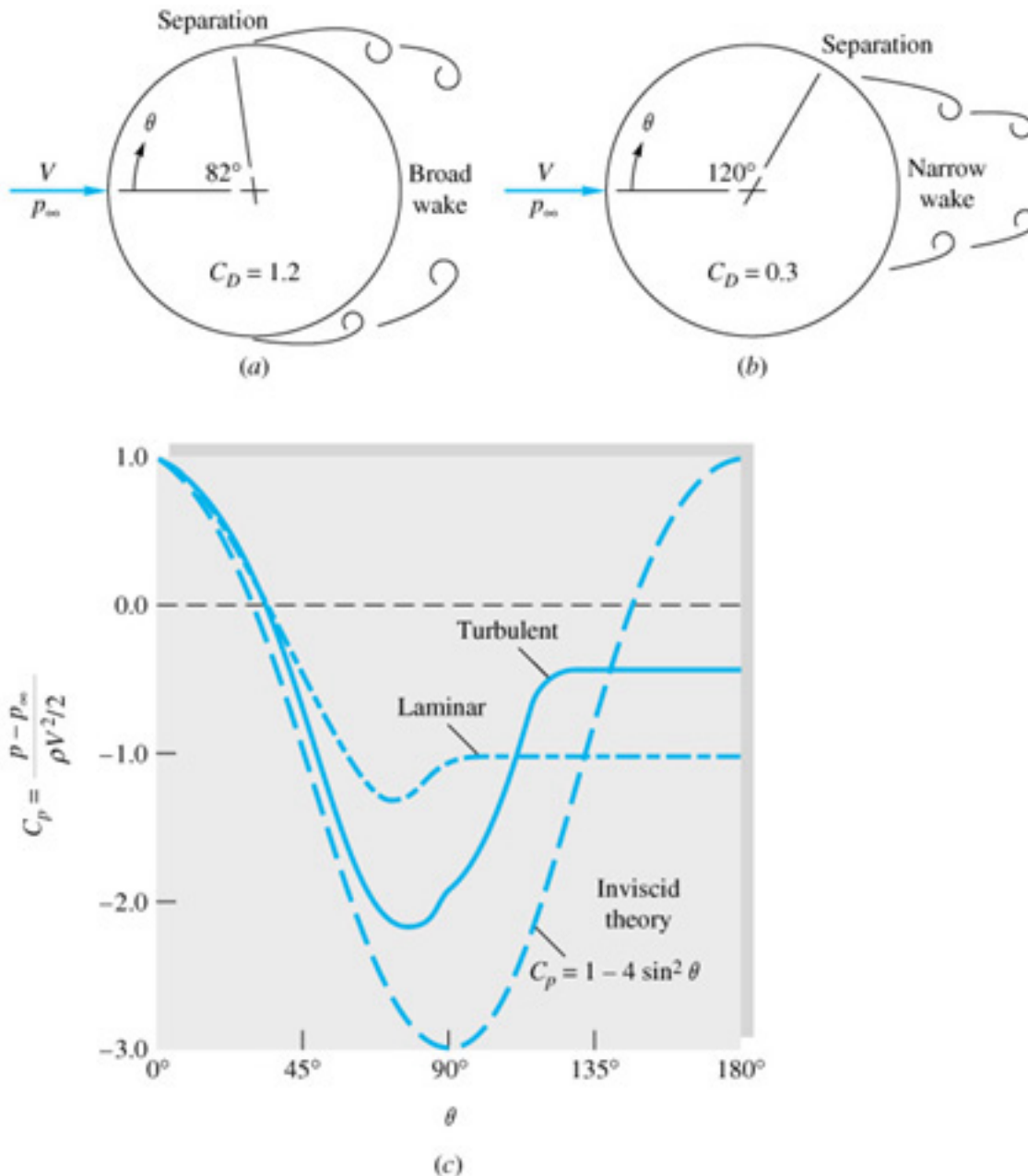


Figure 4-17 – The separation for a laminar boundary layer (a) or a turbulent boundary layer (b) and the associated pressure around a cylinder (c) (from White, 1999, p. 455).

No surface flow visualisation was conducted for the large grid. This was due to the likelihood that the pattern would have begun to dry before the wind tunnel blades reached the appropriate angles to produce the speeds required with the large grid in the tunnel.

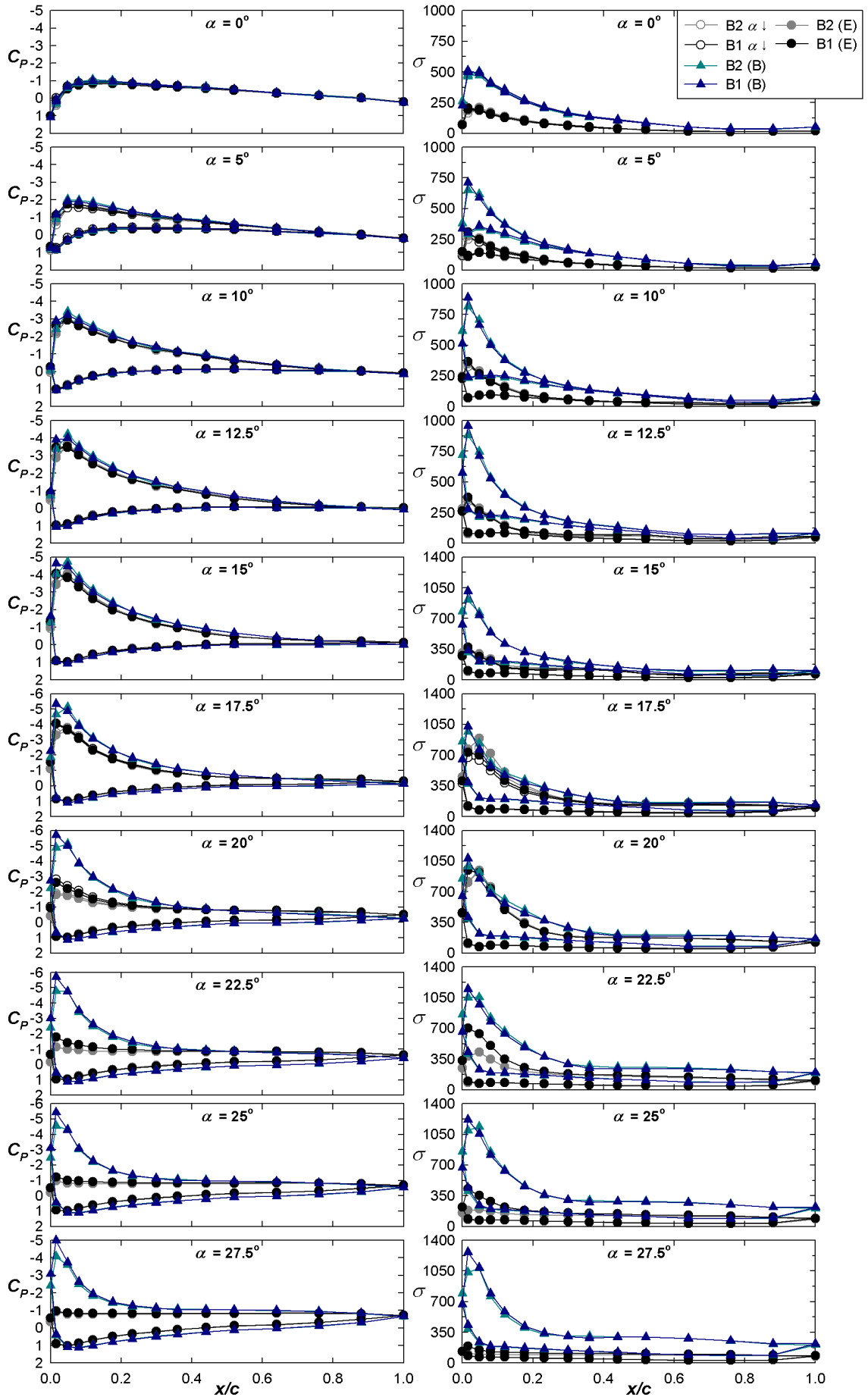


Figure 4-18(a) – NACA 0021 coefficients and standard deviations of the pressures around the aerofoil around stall with the large grid in the tunnel at the closest (B) and furthest positions (E) from the model. Note the changes in scale of the C_p and σ plots.

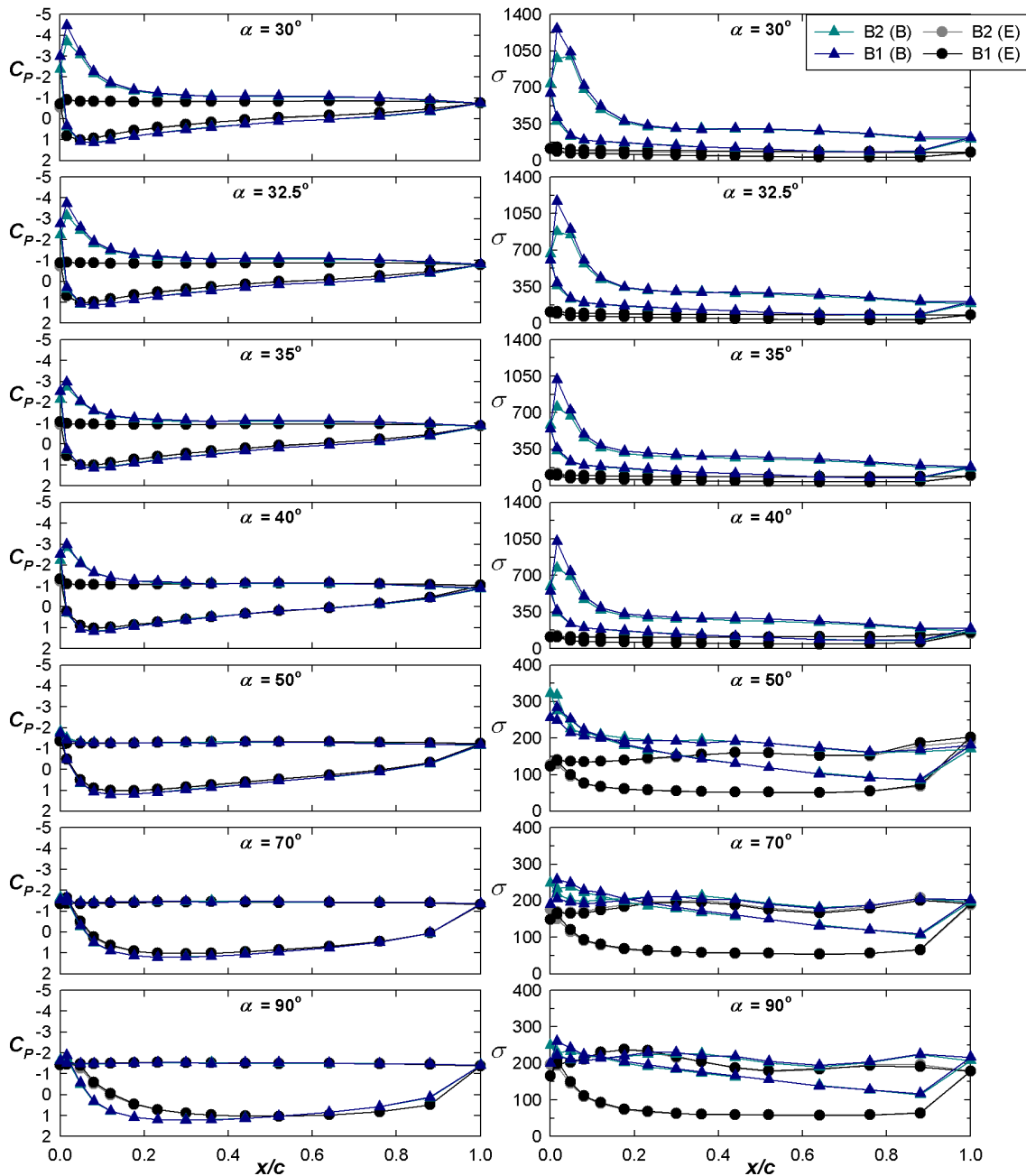


Figure 4-18(b) – NACA 0021 coefficients and standard deviations of the pressures around the aerofoil around stall with the largest grid in the tunnel at the closest (B) and furthest positions (E) from the model. Note the scale of the σ plots changes from a maximum of 1400 $\alpha \leq 40^\circ$ to 400 for the other plots.

Figure 4-19 shows c_l , c_d and c_m at $1/4c$ for the flow conditions where both the increasing and decreasing α cases were tested. This was done for no grid in the tunnel and for each grid in the furthest position from the model (position E). The c_l plot is shown at the top of Figure 4-19. Increasing turbulence intensity decreased c_l for $\alpha = 10^\circ$ and increased c_l for $\alpha = 15^\circ$. All cases were similar for the intermediate value of $\alpha = 12.5^\circ$. Increasing turbulence intensity to 1% reduced the range of α where hysteresis was observed. For $I_u = 2\%$ and 5% the hysteresis loop was eliminated. There was a difference between the increasing and decreasing α cases for $I_u = 2\%$ for $\alpha = 20^\circ$ but this was within the variability of the measurements and does not seem to be an indication of hysteresis. Along with the elimination of the hysteresis loop the two higher turbulence intensities also had a more gradual change in values around stall.

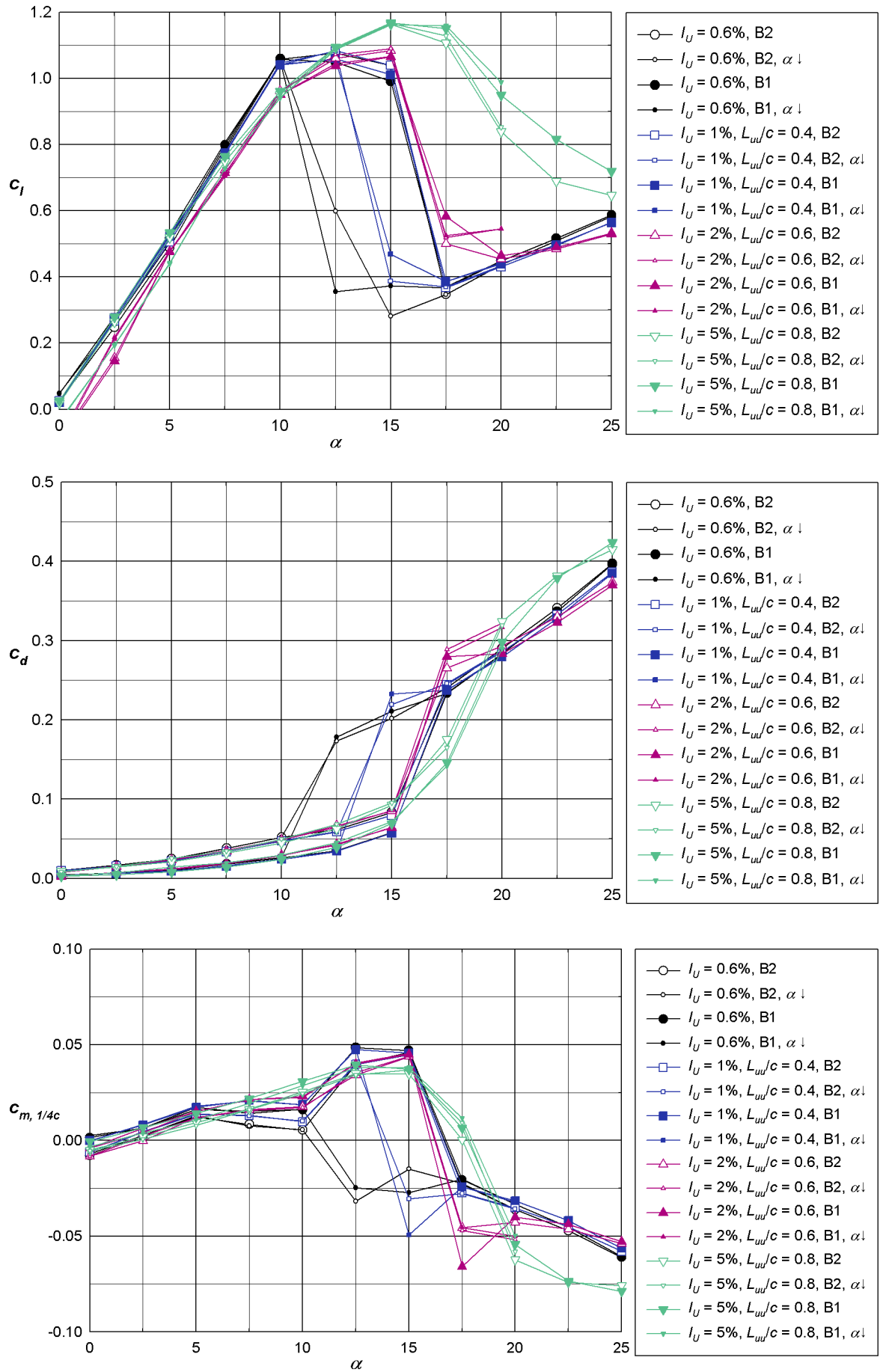


Figure 4-19 – NACA 0021 comparison of hysteresis in different turbulence conditions.

The smaller or eliminated hysteresis loops and softer stall were also seen in the c_d and $c_{m, 1/4c}$ plots. The other interesting feature of the c_d plot is the consistent difference between the values for row B1 and B2 at low α . This difference decreases as α increases and could be an indication of slight differences in placement of the pressure taps at the leading edge which would be the main source of drag at low α . The plot of $c_{m, 1/4c}$ clearly shows that for values where the c_l begins to decrease $c_{m, 1/4c}$ tends to be negative.

The three grids gave three scales of turbulence, the smallest grid provided a turbulence scale of about $c/3$, the medium grid near $c/2$ and the largest grid the scale was comparable to c . The largest and smallest grids did not produce similar turbulence intensities at any position of the grids within the tunnel. However comparisons between the smallest and medium grid and the medium and large grid at similar turbulence intensities are possible. The medium grid at the two furthest positions, E and D, from the model produced similar turbulence intensities to the small grid at the two closest positions to the model, B and A respectively. Similarly the medium grid in positions B and A produced similar turbulence intensities to the large grid in positions E and D respectively. The effect of turbulence intensity has been limited but not removed from the comparison as the turbulence intensities produced by the grids are not exactly the same, see Table 4-1.

Grid Panel Width (m)	Position (m)	Intensity			Scale		
		I_u (%)	I_v (%)	I_w (%)	L_{uu}/c	L_{uv}/c	L_{uz}/c
0.10	E (9.60)	2	4	3	0.6	0.6	1.0
0.04	B (4.60)	2	3	2	0.3	0.4	0.2
0.10	D (7.20)	3	4	3	0.5	1.1	0.5
0.04	A (3.55)	3	3	3	0.3	0.3	0.3
0.30	E (9.60)	5	6	5	0.8	1.3	0.8
0.10	B (4.60)	5	7	5	0.6	0.9	0.4
0.30	D (7.20)	7	8	7	1.0	1.1	0.8
0.10	A (3.55)	6	7	7	0.5	0.6	0.4

Table 4-1 - Characteristics of the grid developed turbulence for the comparison between cases with similar turbulence intensities.

The comparisons for c_l , c_d and $c_{m, 1/4c}$ are shown in Figure 4-20, Figure 4-21 and Figure 4-22 respectively. For the $I_u = 2\%$ case there are some slight differences between the c_l curves for $\alpha < 5^\circ$ and also for the c_l , c_d and $c_{m, 1/4c}$ curves for $30^\circ \leq \alpha \leq 50^\circ$. Similar small differences can be seen in c_l for $20^\circ \leq \alpha \leq 60^\circ$ and for $\alpha \geq 30^\circ$ for c_d and $c_{m, 1/4c}$ for the $I_u = 3\%$ case. There are more differences between the curves for the $I_u = 5\%$ case. Around stall for all the coefficients shown row B2 for an integral length scale of $0.6c$ lies on or between the results for row B1 and B2 for an integral length scale $0.8c$. Row B1 for an integral length scale of $0.6c$ shows increased c_l and $c_{m, 1/4c}$ and decreased c_d in this region. There are also differences between the curves for $\alpha > 30^\circ$ for all coefficients shown, however, unlike the other two coefficients these differences decrease for c_l at high α . The $I_u = 6-7\%$ case shows very similar results in all curves, the biggest differences between the lift results from row B2 for the different grids around stall.

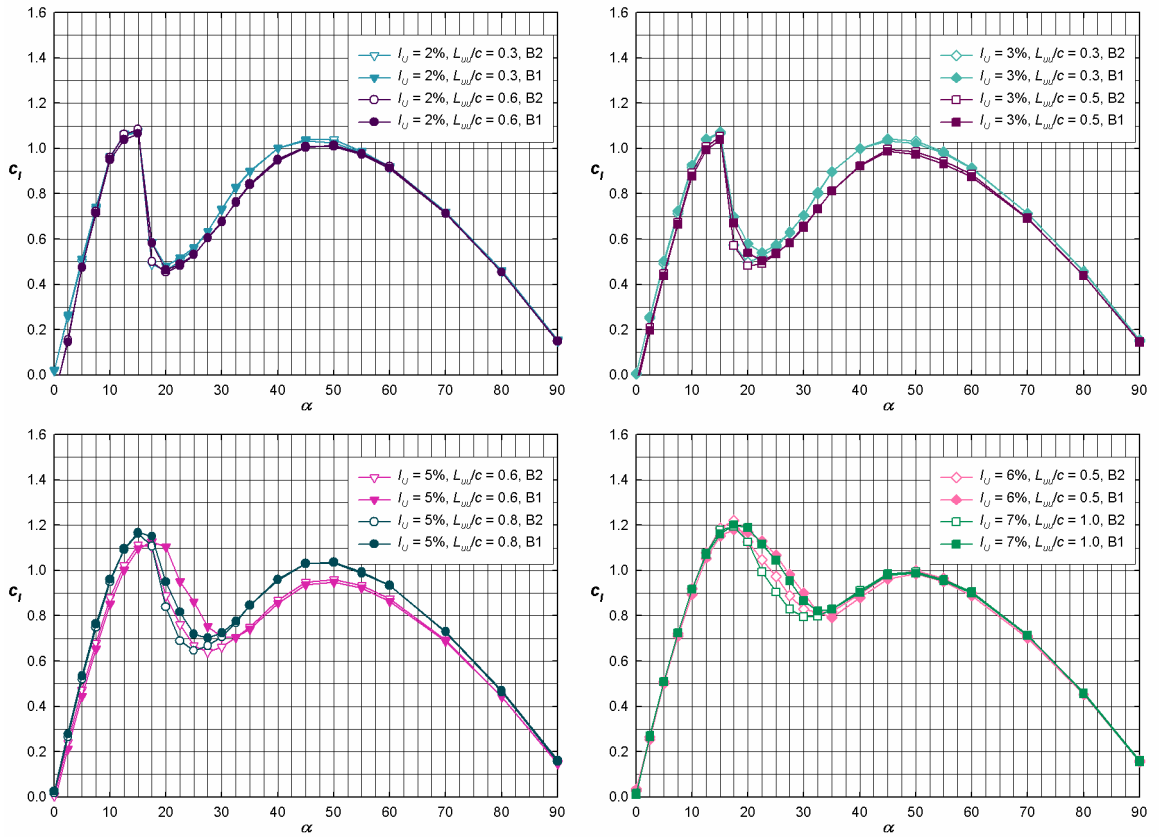


Figure 4-20 – NACA 0021 Comparison of the coefficient of lift at similar turbulence intensities but different integral length scales.

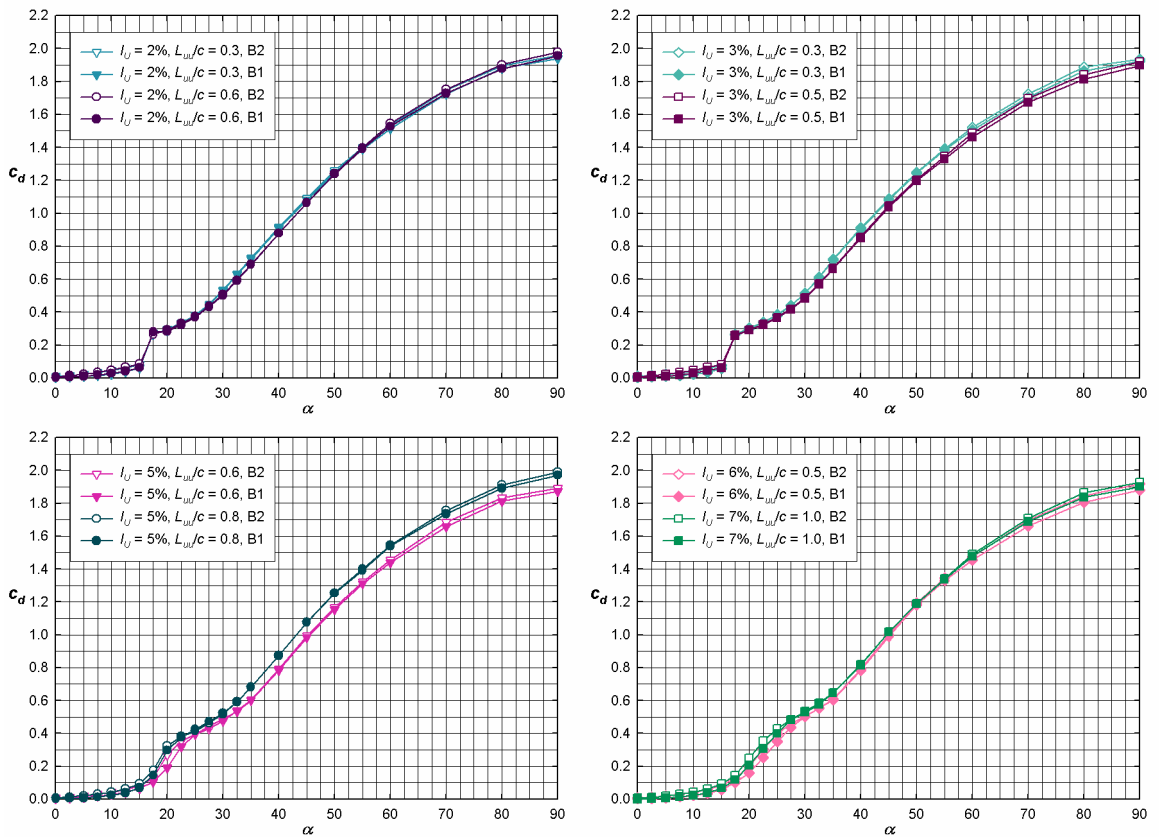


Figure 4-21 – NACA 0021 Comparison of the coefficient of drag at similar turbulence intensities but different integral length scales.

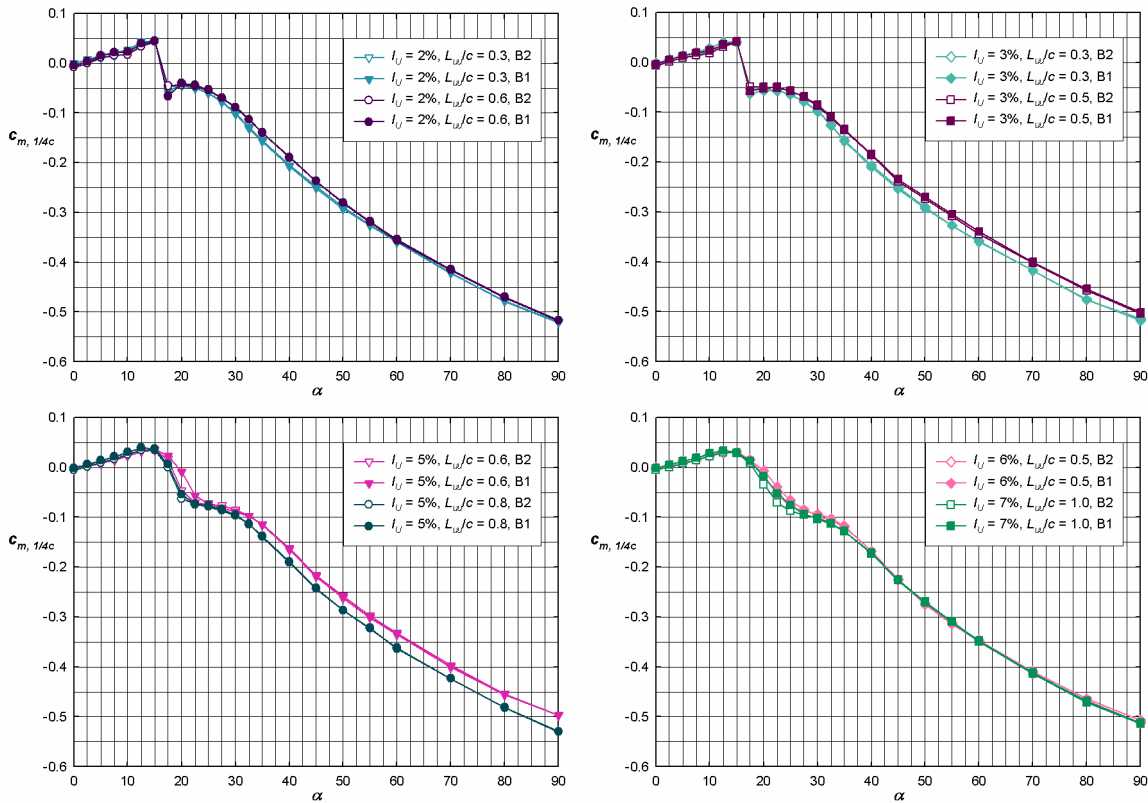


Figure 4-22 – NACA 0021 Comparison of the coefficient of moment at similar turbulence intensities but different integral scales.

At least for the range of integral length scales investigated turbulence intensity seems to have more effect on c_l , c_d and $c_{m, 1/4c}$ than integral length scale. However, as can be seen from the scatter in Figure 4-23, which plots the size of the first local maximum of c_l and the maximum of c_d against I_u , the integral length scale of turbulence also has an effect on results as does the position along the span.

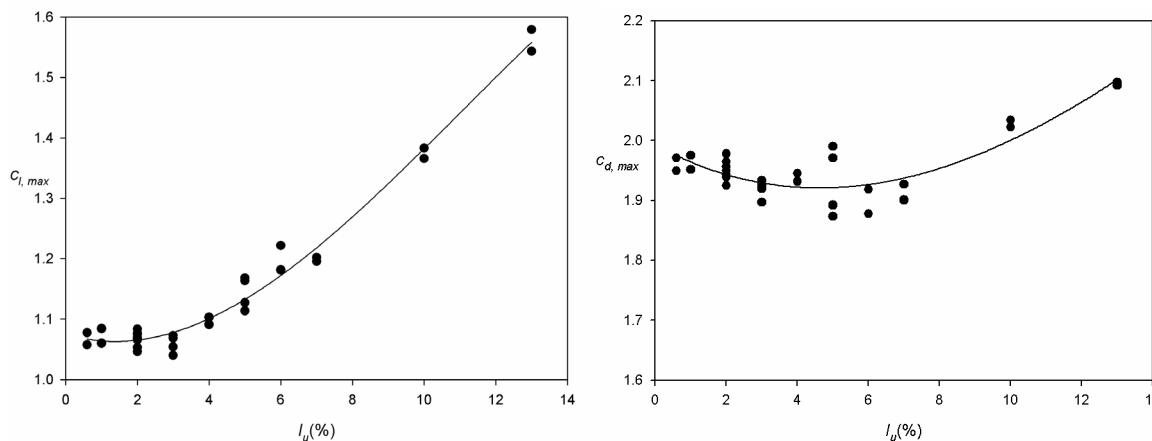


Figure 4-23 - NACA0021 the size of the first local maximum of c_l and the maximum of c_d versus the turbulence intensity for all grids (both row B1 and B2), the lines are third order polynomials fitted to the data. The plots are to the same scale but not over the same range of the coefficients.

This section has shown that turbulence does delay stall on the NACA 0021 aerofoil section. It has reinforced the earlier finding that the structures formed during and after stall are highly three-dimensional. It has also shown that turbulence intensity, at least for the range of turbulence length

scales investigated, produces most of the differences seen with increasing turbulence. This section touched on the fluctuating results in looking at the σ of the pressure signals from the pressure taps. The next section will look at these fluctuations in detail.

4.3 Fluctuating

The literature review presented in Chapter 2 identified surprisingly little prior work on shedding from aerofoils although shedding has been studied extensively for other bluff bodies with a variety of cross sections. Knowledge of the shedding frequencies can enable designers to avoid vortex induced vibrations. This section will examine the low turbulence results in detail before comparing them to computational results and then looking at the effects of added turbulence. The low turbulence data was presented at the 21st AIAA Applied Aerodynamics Conference (Swalwell, Sheridan & Melbourne, 2003b). This data has been used to verify the output of a computational model of a NACA 0012 aerofoil at high α , which is being investigated as part of the European Union's DESider project (Thiele, Mockett & Bunge, 2004). Independently Dr. Keith Weinman, as part the European Union's Flomania project, is planning to model the NACA 0021 and use this data as part of the validation of the Detached Eddy and Large Eddy algorithms in the TAU CFD package (Weinman, 2004).

4.3.1 Lowest Turbulence Case

As described in Chapter 3, the 35 000 data points collected for each tap at each α were corrected for the response of the tubing. This process used a fast Fourier transform and so only used the first 2^{15} (32 768) samples. It was then low pass filtered to 250Hz. This data could then be used to calculate the instantaneous coefficients of lift and drag. It was important to omit the first and last points of the series that were affected by the filter. A small error was introduced as the pressure samples were not taken simultaneously, however the maximum lag between sampling any two taps was less than 0.8 ms, and was unlikely to affect the results.

The time series obtained at two α below stall (0° and 10°) and two α above stall (50° and 90°) for c_l , c_d , c_n and c_t from tapping row B1 are shown in Figure 4-24. As well as the complete time trace, a small section from each signal was enlarged to allow the signals to be seen more clearly. As anticipated, the increase in the variability of the signals above stall is immediately obvious. The intermittency of the shedding, a feature of the wake at these Re as discussed in the literature review, can also be clearly seen, Section 2.10. Comparing the c_l and c_d signals above stall, the c_d signal appears to be more random, especially at $\alpha = 90^\circ$. The c_l and c_d were derived from the c_n and c_t force (according to the equations presented in Section 3.6 the experimental method chapter).

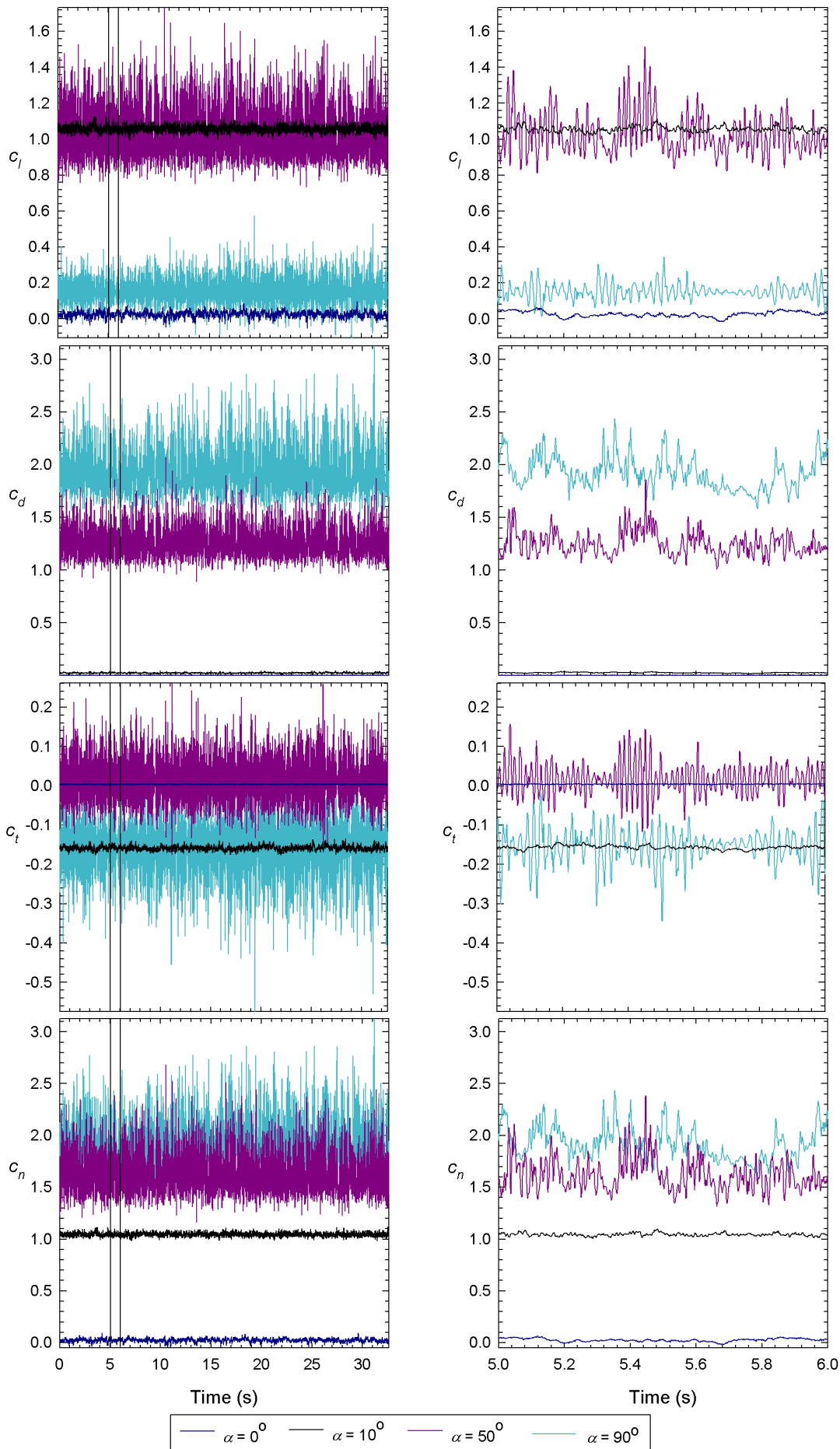


Figure 4-24 - Time series for the coefficient of lift with no grid in the tunnel from tapping row B1 for the NACA 0021 aerofoil section, the plots on the left hand side show the complete filtered data, the two vertical lines in these plots indicate the short section of data which is shown in the plots on the right hand side.

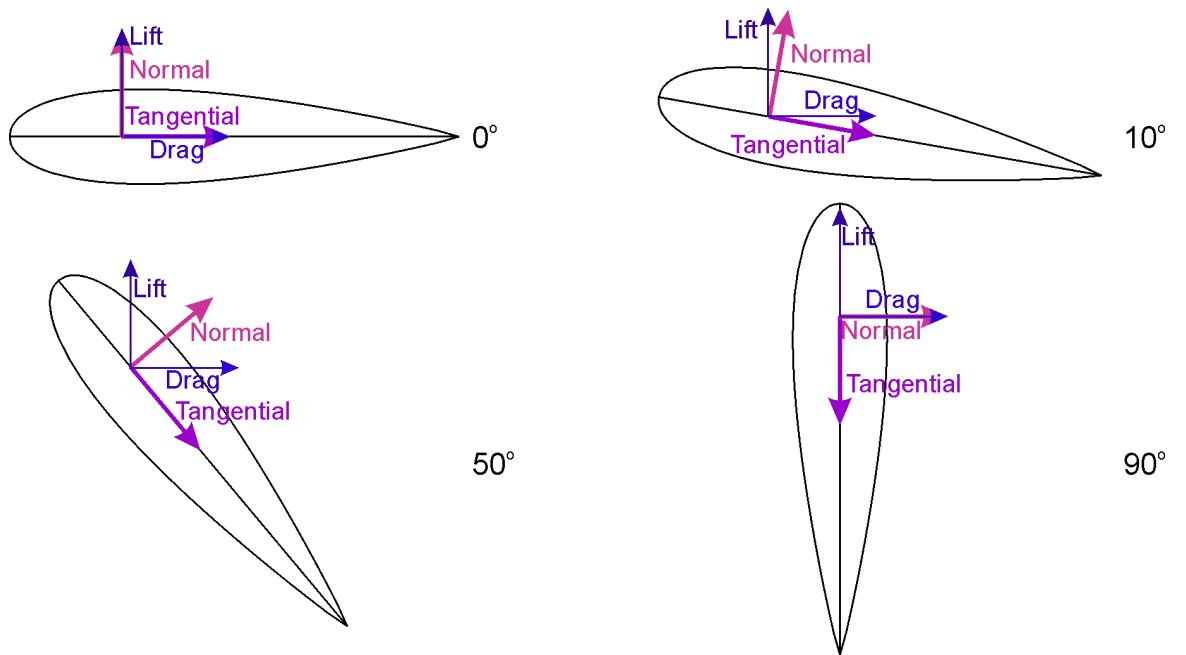


Figure 4-25 - Diagram of the relation of the lift, drag, normal and tangential axes at various α .

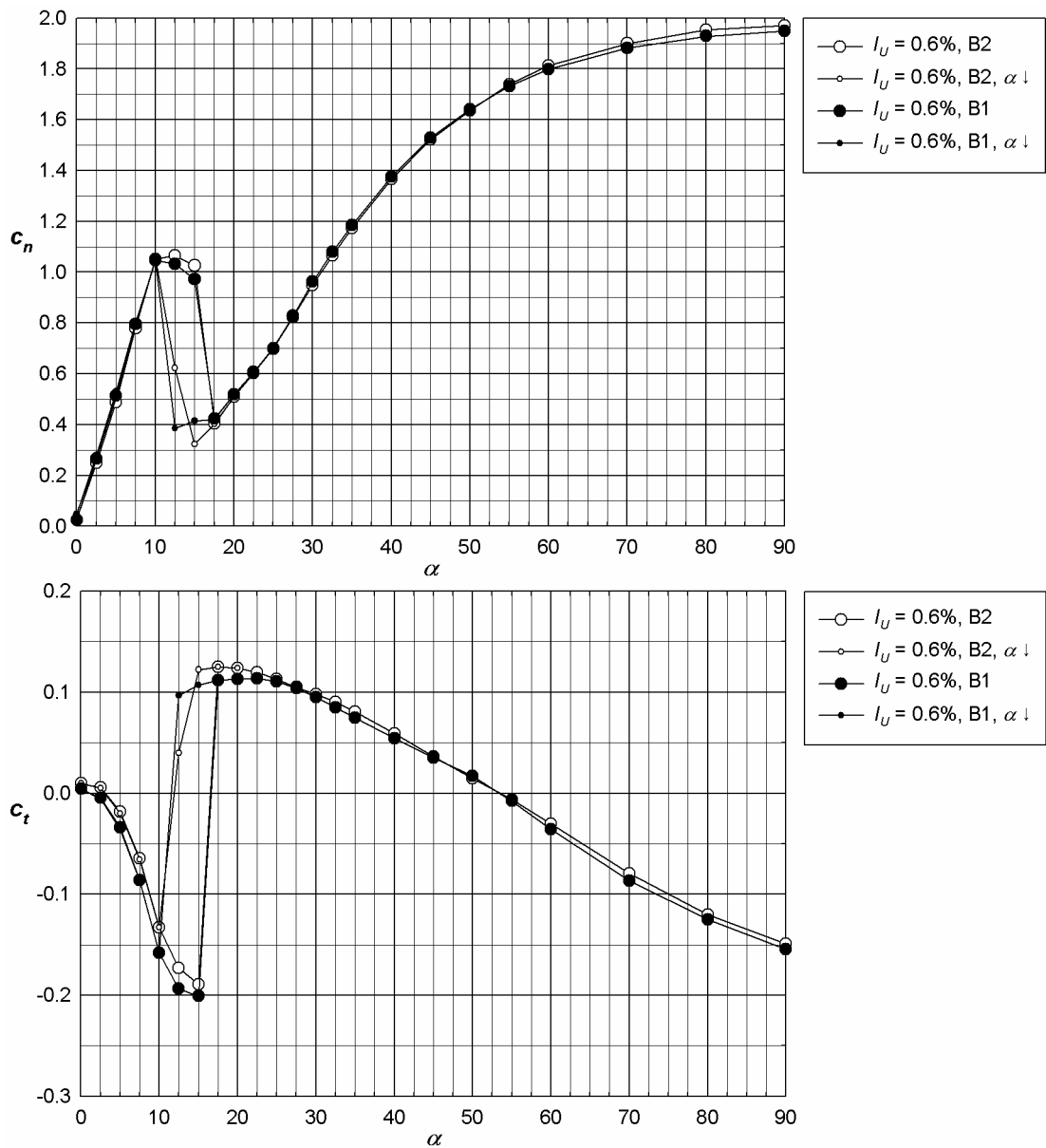


Figure 4-26 - NACA 0021 coefficients of normal and tangential force with no grid in the tunnel.

The relationships between the forces at various α are shown pictorially in Figure 4-25. At $\alpha = 90^\circ$ $c_l = c_t$ and $c_d = c_n$ so the more regular fluctuations of c_t at this angle is unsurprising. What is interesting is that c_t also shows more regular fluctuations than c_n at $\alpha = 50^\circ$. For completeness the plots of mean c_l and c_n are given in Figure 4-26. From the figure, the c_n trace is clearly dominated by the lift at low α and by the drag at high α . The c_t plot is more complex, at low α the larger magnitude of the lift force dominates causing c_t to be negative. At stall there is a change of sign in the c_t signal, as the drop in c_l and increase in c_d means the drag plays more of a role. As α increases toward 45° the c_t component grows in magnitude and dominance of the c_t signal. Past 45° the increase in c_d and decrease in c_l means that although c_t is increasingly in the same plane as c_l , the drag still features until very high α .

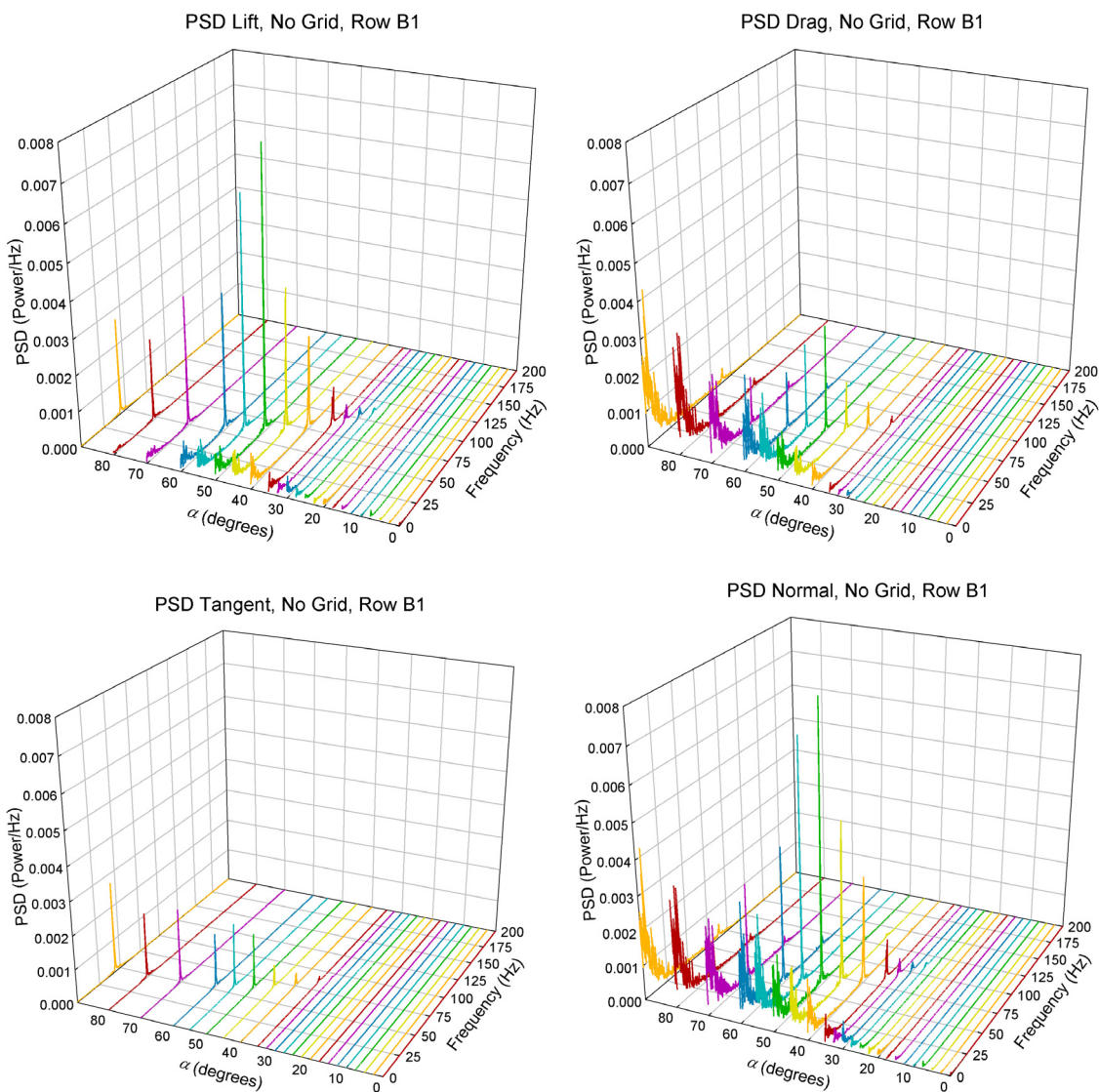


Figure 4-27 – NACA 0021 Power Spectral Density (PSD) plots of the instantaneous coefficient of lift, drag, tangent and normal from row B1 for each α . For the increasing α case with no grid in the tunnel.

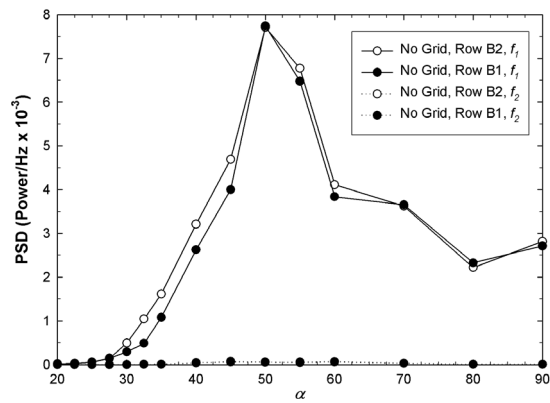
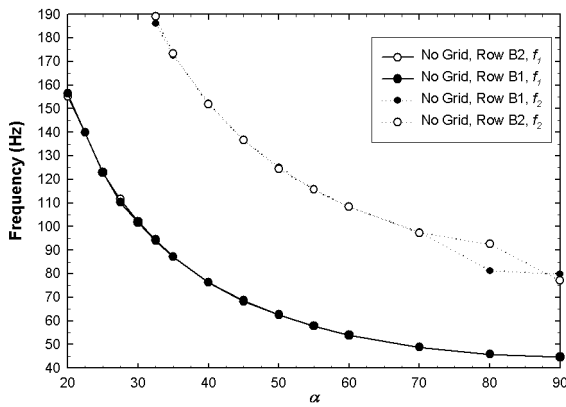
The frequency content of the time series were analysed using Matlab's implementation of the Welch method over small segments. The signals were broken into eight segments with 50% overlap. Each of these segments was windowed with a Hamming window. The Power Spectral

Density of these segments was then determined and the final result averaged to give a clearer indication of the frequency content of the signals. The results for the lift, drag, normal and tangential force coefficients from row B1 are given in Figure 4-27.

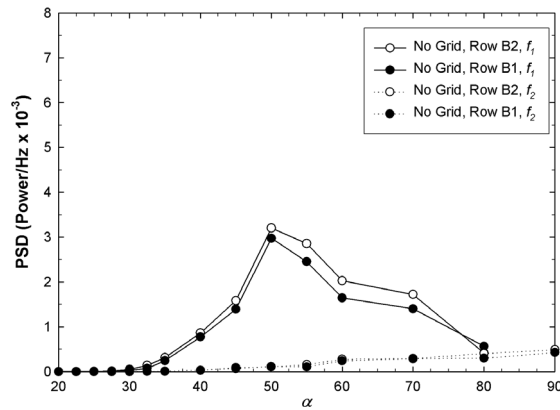
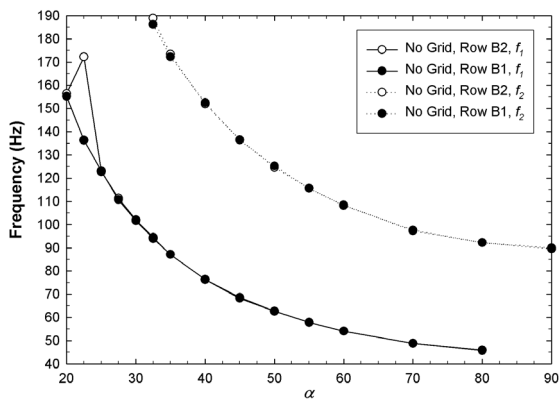
The frequency content of the lift signal shows two main components; a very low frequency noise, which reaches a maximum magnitude at about $\alpha = 50^\circ$ and then decreases until it is indiscernible at $\alpha = 90^\circ$, and a main shedding peak whose frequency decreases as α increases. In addition to these two components in the drag signal frequency content, a small peak at higher α at twice the frequency of the main shedding peak can be seen. For convenience this will be termed the secondary frequency or peak. The first shedding peak decreases in magnitude as α increases to such an extent that at high α it cannot be discriminated from the low frequency content, which increases with α . The most striking feature of Figure 4-27, however, is that the tangential component only shows the main shedding frequency. The normal force coefficient shows all three frequency components in a very similar way to the drag although all the components are larger. The reason for the absence of the low and secondary frequencies from the tangential component will be investigated later in this section. First the attributes of the first and second shedding peaks will be investigated in more detail.

The frequency and magnitude of the peaks found for each of the plots above 20° shown in Figure 4-27 are plotted in Figure 4-28 as a function of α . The smooth trend in the decrease in the frequency components is evident. The second frequency is consistently twice the first frequency. This relationship between the two frequencies is expected. The most likely shedding pattern is alternated shedding of vortices of different signs from the leading and trailing edges of the aerofoil; a sketch of the possible wake is shown in Figure 4-29. For a cylinder at these Re (as discussed in the literature review, see Section 2.10) the alternating vortices over one shedding cycle cause both a positive and negative force maximum in the lift signal (one vortices pulls the cylinder up and the other down) and two positive force maximums in the drag signal (the two vortices pull the aerofoil downstream). Therefore the drag fluctuations are at twice the lift fluctuations. As the aerofoil is inclined with respect to the freestream velocity and there is a positive c_l force, and therefore a wake that inclines downwards, it is not surprising that both frequency components end up in the c_l and c_d signals. It should be noted that the magnitude of the second frequency is small, especially in the lift. The lift and drag tend to be dominated by one of the frequencies only at $\alpha = 90^\circ$ which explains the aberrations from the smooth curves in the c_l case. In the c_d case (and similarly c_n) the first frequency could not be distinguished from the low frequencies at $\alpha = 90^\circ$. At $\alpha = 22.5^\circ$ the frequency from Row B2 in the drag signal has a peak around 170 Hz that is due to the very small magnitude of the frequency shedding peaks at this α .

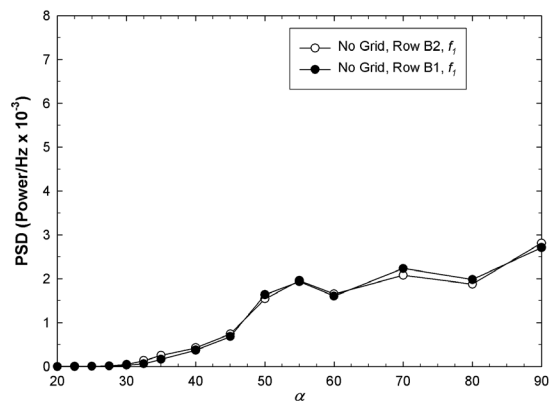
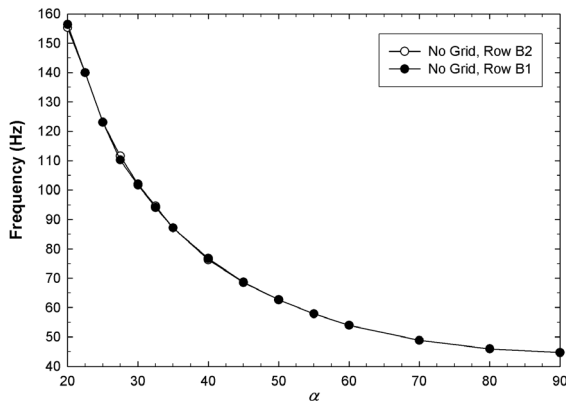
Lift



Drag



Tangential



Normal

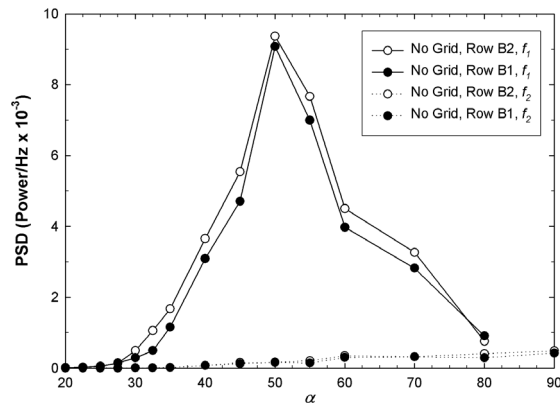
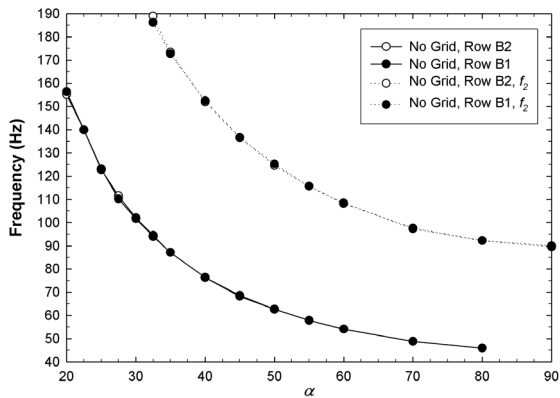


Figure 4-28 – The frequency and magnitude of the first and second shedding peaks in the lift, drag, normal and tangential force components for tapping row B1 for α between 20° and 90° .

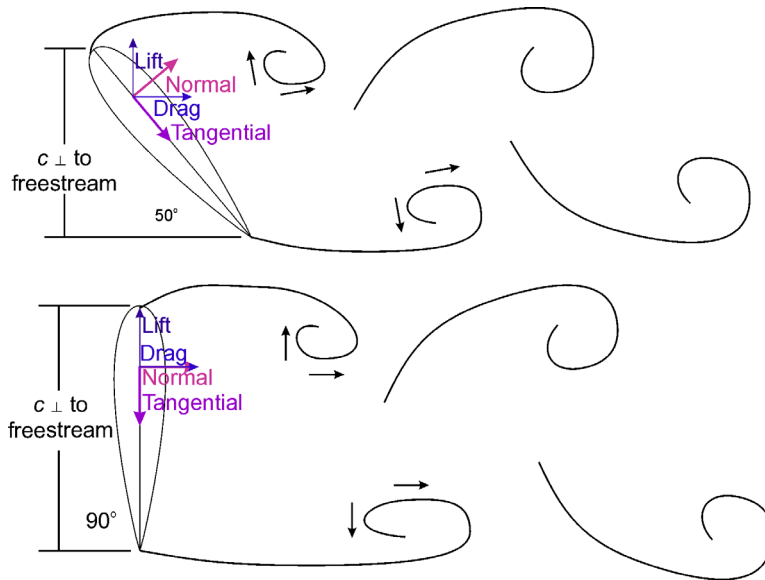


Figure 4-29 - Sketch of possible vortex wake structures, with arrows indicating the directions the vortices might pull on the aerofoil at α of 50° and 90° .

The tangential signal has only one frequency component and unlike the other cases the magnitude generally increases with increasing α . For the other signals a maximum shedding peak was found at $\alpha = 50^\circ$ (note the different scale for the c_n plot in Figure 4-28 to accommodate this peak). This is likely to be due to the vortices from the leading edge being closer to the surface for this α , see Figure 4-29. The magnitude of the secondary peak increases with α for c_d and c_n . This is likely to be for a similar reason, the second vortex would be closer to more of the surface at higher α therefore more of the aerofoil would be exposed to both vortices. The peak of the second frequency is of much smaller magnitude than the peak of the first shedding frequency.

The smooth function of shedding frequency with α seen in Figure 4-28 makes sense considering the relationship between α and wake width. As discussed in the literature review, in Section 2.10, Roshko's universal Strouhal number based on the wake width provides a good collapse of the data. While the wake width in these experiments was not measured directly, the chord length normal to the freestream, as shown in Figure 4-29, gives an indication of the likely wake width. Fage & Johansen (1928) used a similar technique with inclined flat plate results. Defining a Strouhal number based on the length normal to the chord gives

$$St = \frac{f c \sin(\alpha)}{U} \quad \text{Equation 4-1}$$

Plotting this parameter using the frequency results in Figure 4-28 gives Figure 4-30 below. Apart from the results that lay off the smooth frequency curves (which were discussed earlier) these results give an excellent collapse. The Strouhal number declines with increasing α , indicating the wake width is not a purely linear function of the chord normal to the freestream. This is likely to be due to the asymmetric shape of the aerofoil. The aerofoil has a fixed separation point at the

sharp trailing edge and an unfixed separation point at the rounded leading edge. This data will be compared to that from Roshko's (1955) paper to investigate the effect of the shape.

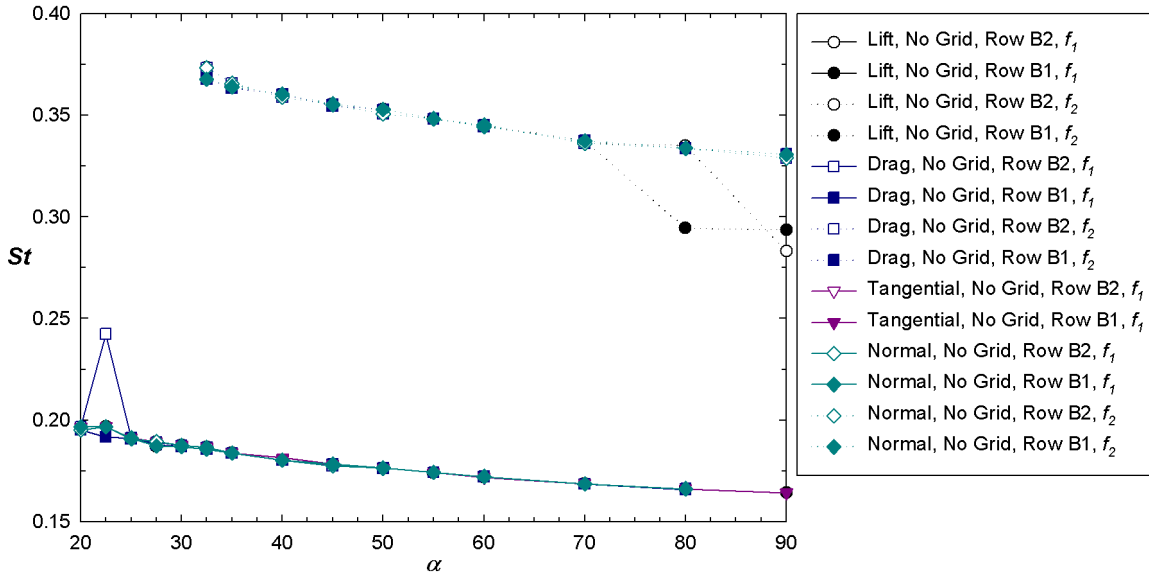


Figure 4-30 - Strouhal number based on the shedding frequencies in Figure 4-28, the chord length normal to the streamline and $U = 34$ m/s versus α .

Using Roshko's universal Strouhal number Equation 2-47 and the results for the NACA 0021 aerofoil section at 20° ($f = 155$ Hz, $U_\infty = 34$ m/s, $D = c \sin(20) = 0.043$ m therefore $St = 0.19$) gives the relationship $D'/D = 0.82 k$. Plotting this on the curves Roshko gives for several generic shapes, see Figure 4-31(a), and using the values given for a circular cylinder gives $k \approx 1.36$ and therefore a predicted coefficient of drag of around 1. The drag coefficient found based on the chord length was $c_d = 0.3$. Normalising this by the chord length normal to the freestream gives $c_d = 0.85$. Similarly for the aerofoil section at 90° , a relationship of $D'/D = 0.97 k$ ($f = 44.7$ Hz, $U_\infty = 34$ m/s, $D = c = 0.125$ m therefore $St = 0.16$) was found. Using the plots, see Figure 4-31(b), the coefficient of drag was estimated based on a 90° wedge to be 1.43 and based on a flat plate to be approximately 2.25. From the pressure measurements the drag was found to be between these values ($c_d = 1.96$) as shown on Figure 4-31(b). These results provide confidence in the values of the shedding frequencies found and show a relationship between α and the generic shape the aerofoil resembles.

The reason for the trend of the shedding frequency with α and the existence of the two frequencies in c_l and c_d has been explained. However, why only one shedding frequency ends up in the c_l signal and the reason for the low frequencies in the other signals still needs to be examined. To investigate the shedding further, the frequencies found from the pressure signals from the taps in rows B1 and B2 at 30° , 50° , 70° and 90° were examined, as is shown in Figure 4-33. The taps in rows B1 and B2 were labelled with numbers starting from 1 at the trailing edge across the upper surface to 15 at the leading edge and back across the lower surface to 28 near the trailing edge.

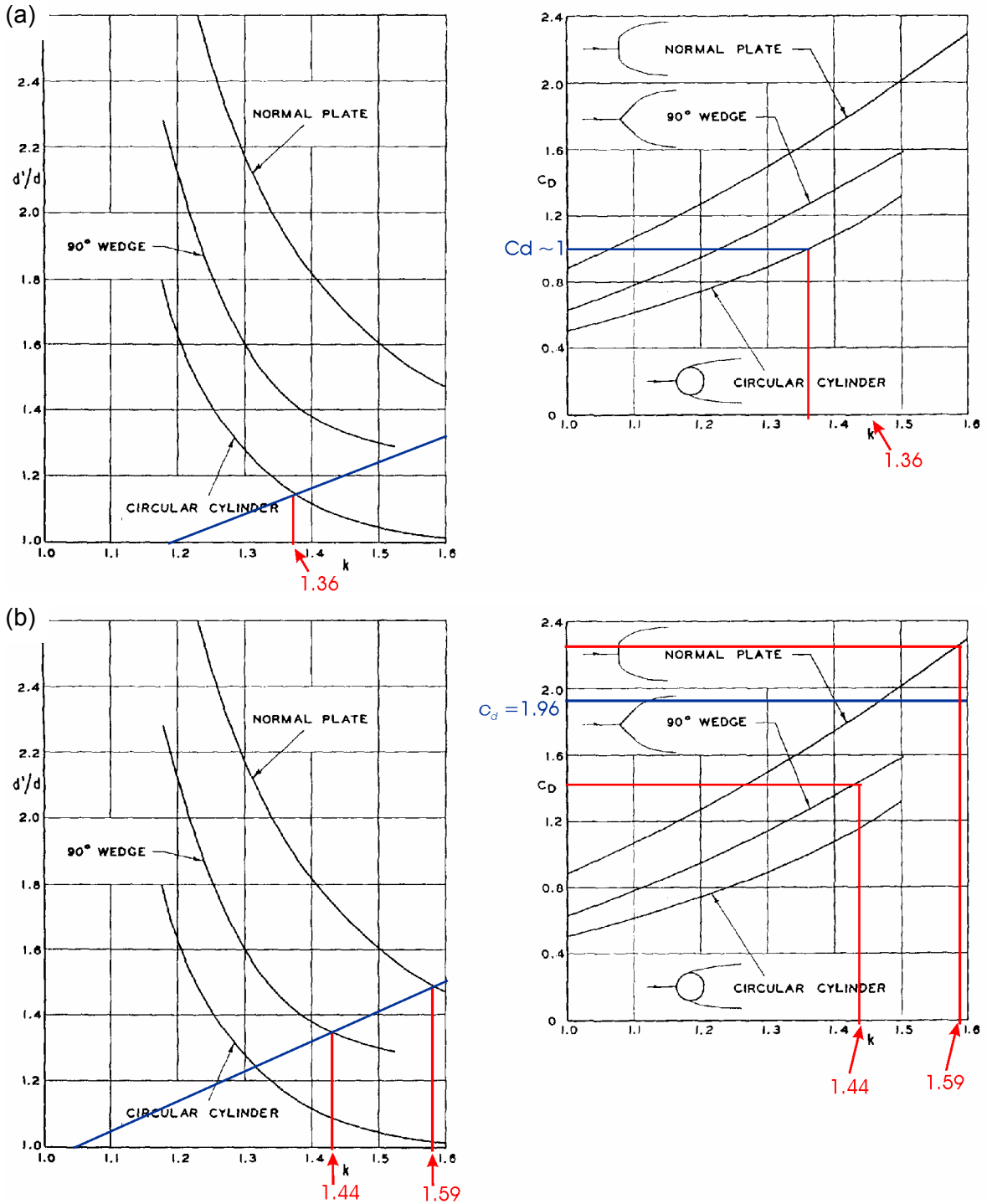


Figure 4-31 - Using Roshko's plots for the relationships between the base pressure parameter k and the ratio of wake width D' to object dimension D and the coefficient of drag for the values found experimentally for an aerofoil at 20° (a) and 90° (b) the value of c_d was estimated and compared to the value found experimentally.

Power spectral densities for both row B1 and B2 are plotted in Figure 4-33 and the similarity between the signals for the taps in the two rows can easily be seen. At 30° there are no major frequency peaks. There is a very small low frequency content on the upper surface (taps 1 to 15) and a very small peak at 100Hz which is the blade passing frequency of the tunnel. The main shedding frequency dominates at 50° except for a small region on the lower surface where there is no discernable frequency content. There are also low frequencies on the upper surface, and the leading and trailing edges, and a very small secondary frequency near the trailing edge at about 125

Hz. At 70° , the first shedding frequency peak has become small and moved to a lower frequency. The second frequency is near the blade passing frequency at about 100Hz and the low frequency components are seen on a similar range of taps but are slightly larger. By 90° the low frequency components are again slightly larger, but seen on a similar range of taps (with the possible exception of tap 15 at the leading edge). The second frequency is seen, with only small contributions from the first frequency, from about mid to three quarter chord on the upper surface. The primary shedding frequency is similar to that seen at 70° except, of course, at a slightly lower frequency.

Using Equation 3-24 and Equation 3-25 c_n and c_t were calculated as the sums of pressures on small segments. An indication of the composition of the small segments is shown in Figure 4-32(a). For clarity, only a limited number of segments were used. The Δx segments are all the same length while the Δy segments are larger towards the leading and trailing edges and the leading and trailing edge segments are larger than all the rest. The percentage of the total length of one surface of each Δy segment is shown in Figure 4-32(b). It is clear that, as the tangential force is calculated from the lengths normal to the chord (Δy), the c_n will be dominated by the signals from the leading and trailing edges.

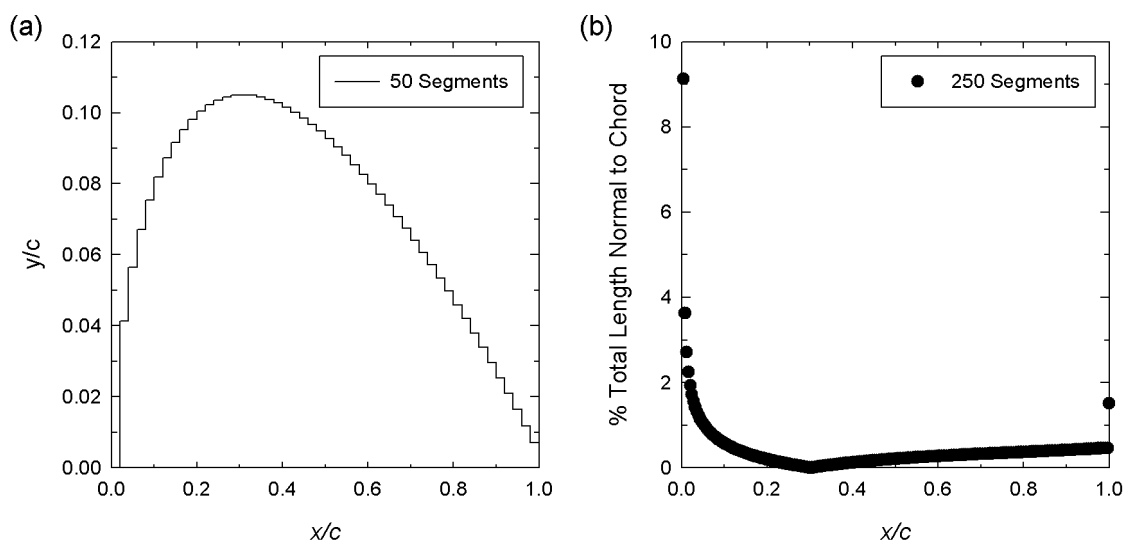


Figure 4-32 – (a) The division of the upper surface of the NACA0021 aerofoil into segments for calculating the normal and tangential forces (number of segments limited for clarity) and (b) the percentage of the total length normal to the chord for each segment (for the number of segments used in the force calculations, there were of course 250 samples from the lower surface as well in these calculations).

Looking at the magnitude of the different frequencies from taps in row B1 and which taps exhibit the different frequencies, as shown in Figure 4-34, it can be seen that the leading and trailing edge are dominated by the primary shedding frequency. This is consistent with only this frequency being seen by c_n . The secondary frequency moves from the trailing edge to mid chord as α increases which correspond to the wakes sketched in Figure 4-29 where, as α increases, the taps that are close to both vortices change from being those near the trailing edge to those near the mid-chord.

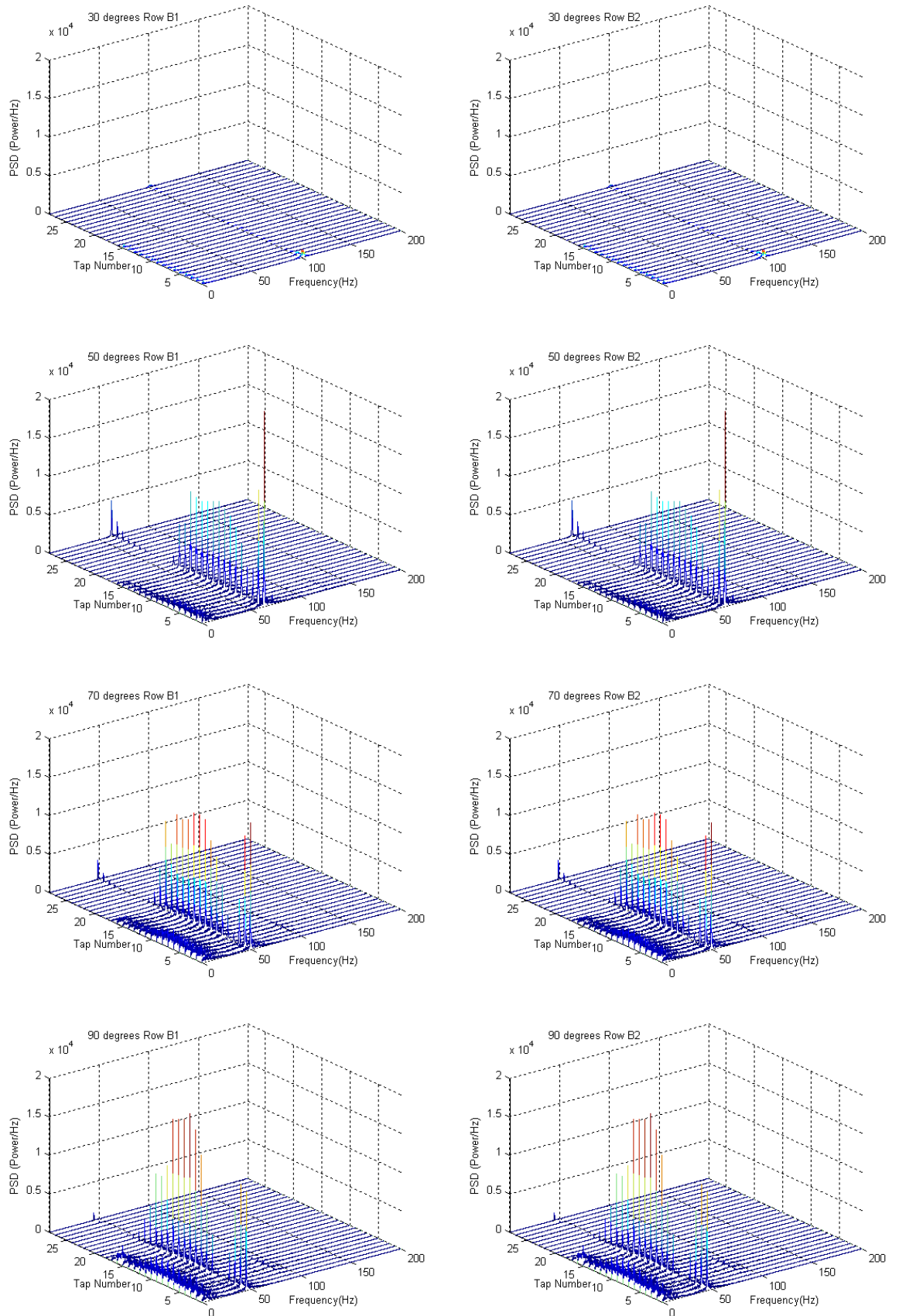


Figure 4-33 – Power Spectral Density (PSD) for each tap in Row B1 and Row B2 for angles of attack of 30°, 50°, 70° and 90°. Tap numbering goes from 1 on the trailing edge across top surface to 15 at the leading edge and along the bottom surface to tap 28.

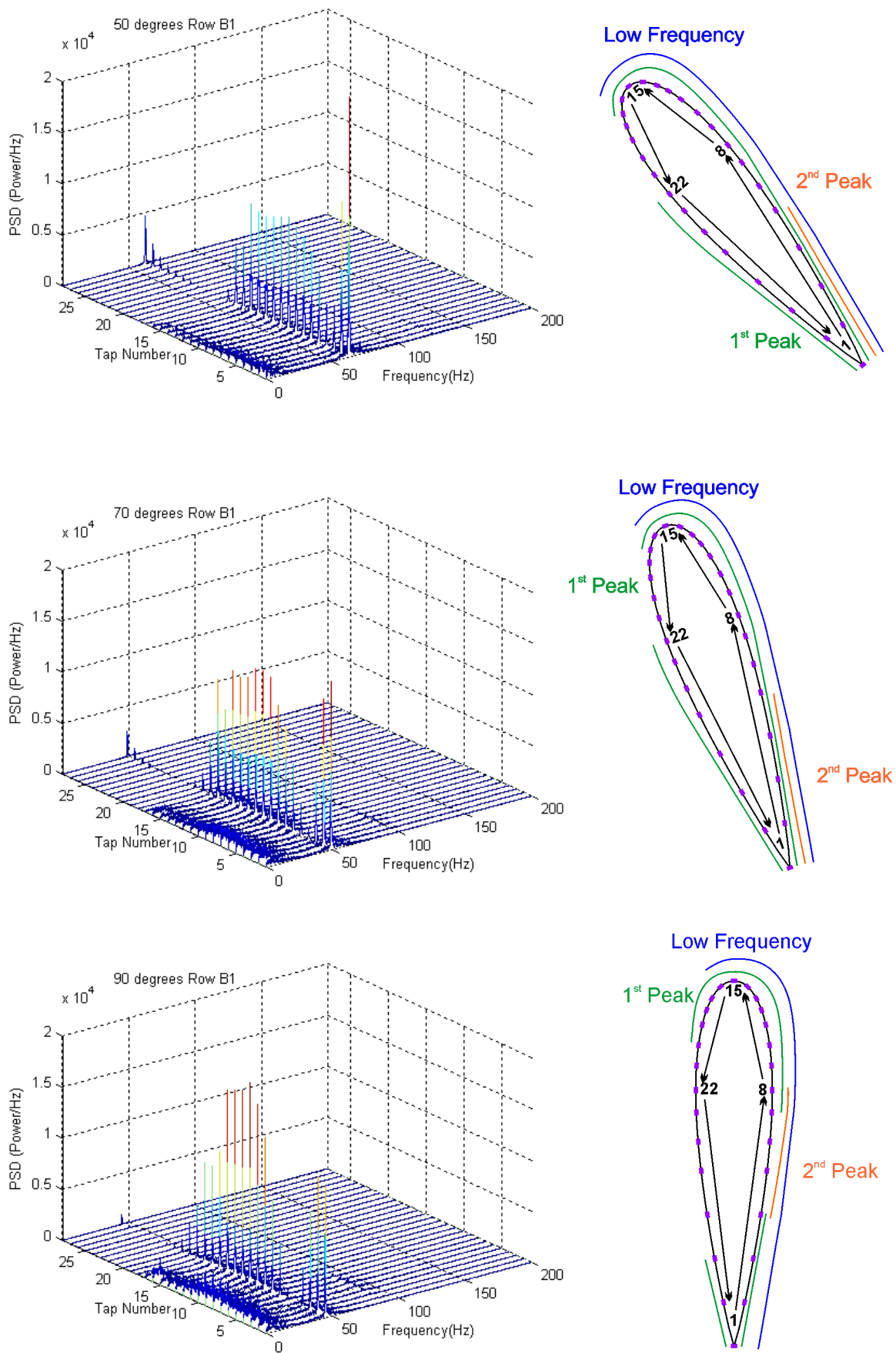


Figure 4-34 – PSD records for each tap for Row B1 and identification of the major shedding locations.

Figure 4-35 shows the low frequency along with the onset of shedding that was also seen by Schewe (2001), although he did not provide an explanation for it. A similar low frequency was seen by Nakamura (1996) in hotwire measurements of the velocity fluctuations downstream of a circular cylinder with the splitter plate extending 0.4D behind the cylinder, similarly no cause was assigned to these low frequency fluctuations. Figure 4-35 also shows the frequency content of $c_{m, 1/4c}$ from row B1 for the present results. This wasn't examined earlier because the scale of the shedding magnitudes is an order of magnitude smaller than for the c_l , c_d , c_n and c_t results. Like for the c_t results the $c_{m, 1/4c}$ results show the magnitude of the primary frequency increasing with α . However unlike for c_t both the low frequencies and secondary frequency can be seen as well as the primary frequency. The existence of the low frequencies in other results is reassuring. The reasons for the low frequencies will be examined further in the subsequent sections on the computational and turbulence results.

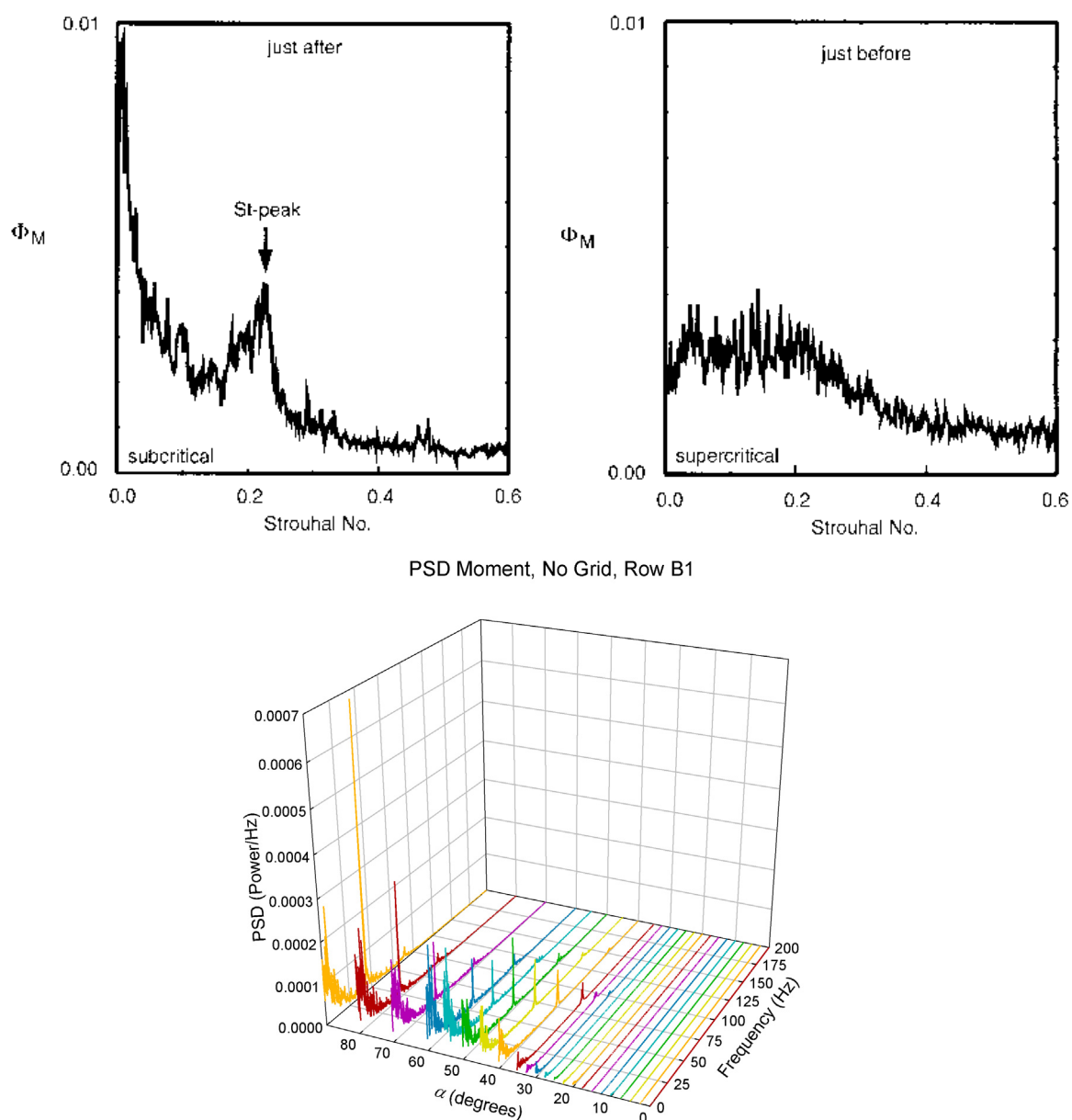


Figure 4-35 - Spectra of the pitching moment, on the upper left hand side just after a separation (laminar) and on the upper right hand side just before separation where the flow is attached and a laminar separation bubble features. From Schewe (2001). Lower plot the spectra of $c_{m, 1/4c}$ from Row B1 for the current results.

4.3.2 Comparison with Computational Results

As mentioned in the introduction to this section, the current experimental results for the NACA 0021 aerofoil section have been used as a benchmark for the results from a Detached Eddy Simulation (DES) of a NACA 0012 aerofoil section conducted by Thiele, Mockett & Bunge (2004). These simulations are being used as a test case of DES as part of the European Union's DESider project, contract number AST3-CT-2003-502842, and their work is partly funded by this project. The simulations have the advantage of allowing the examination of flow structures that can only be inferred from the pressure measurements. Thiele, Mockett & Bunge have kindly allowed the inclusion of some of their, as yet, unpublished results to examine these structures and to compare them with the current experimental findings.

The numerical domains used periodic spanwise boundary conditions and had a spanwise extent of one aerofoil chord. All results are for the NACA 0012 aerofoil section at an $\alpha = 60^\circ$ and $Re = 1 \times 10^5$. The time series results are from calculations on a coarse grid using DES based on the SALSA model (a Linear Strain Adaptive version of the Spalart-Allmaras model (see Rung *et al.*, 2003)). The unsteady pictures are from results from the same method but on a much more refined grid. The averaged plot data was taken from coarse grid calculations using DES based on the Wilcox k- ω model (see Wilcox, 1998).

The computational expense of these calculations limits the amount of time for which the flow field can be simulated. Due to the intermittent nature of the shedding this restriction impacts negatively on the quality of the spectra achieved. When the absence of the low frequency component was found in c_t in the experimental results it was suggested to Charles Mockett that examination of the frequency component of this force component may help alleviate this problem. Time series and spectra for c_l , c_d , c_n and c_t from the simulation are presented in Figure 4-37. As in the experimental results, the intermittency of shedding is seen in all forces, but the c_t force shows less "noise" than the other components. This allowed a clearer spectrum to be produced for the same simulation time. It also provides independent confirmation of the experimental observations of the clarity of the c_t signal. Numerically, the Strouhal number is also close to the value 0.2, the value that was found experimentally. The existence of "bursting" in these time histories which are subject only to periodic boundary conditions support Roshko's proposition, discussed in the literature review in Section 2.10, that this phenomenon is due to the three-dimensional spanwise structures and not just the end conditions.

Two-dimensional slices of the instantaneous Z component of vorticity are shown in Figure 4-38. The expected alternate shedding of vortices can be seen developing into what appears to be a Kármán vortex street. The vorticity field is very irregular near the body, which could account for the low frequencies seen in the c_n time trace. However, averaging the vorticity field as shown in Figure 4-39, demonstrates that the vortices shed from the upper and lower surfaces are the

dominant features of this flow. There are also small areas of vorticity of the opposite sign on the upper surface near the leading and trailing edge vortices. These areas could be due to the shed vortices inducing secondary circulation. This structure is similar to the two dimensional view of shedding from a cylinder, shown in Figure 4-36. Dallmann & Schewe (1987) emphasised that this structure is unstable to three-dimensional disturbances.

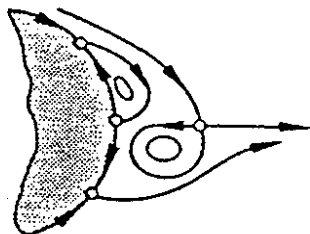


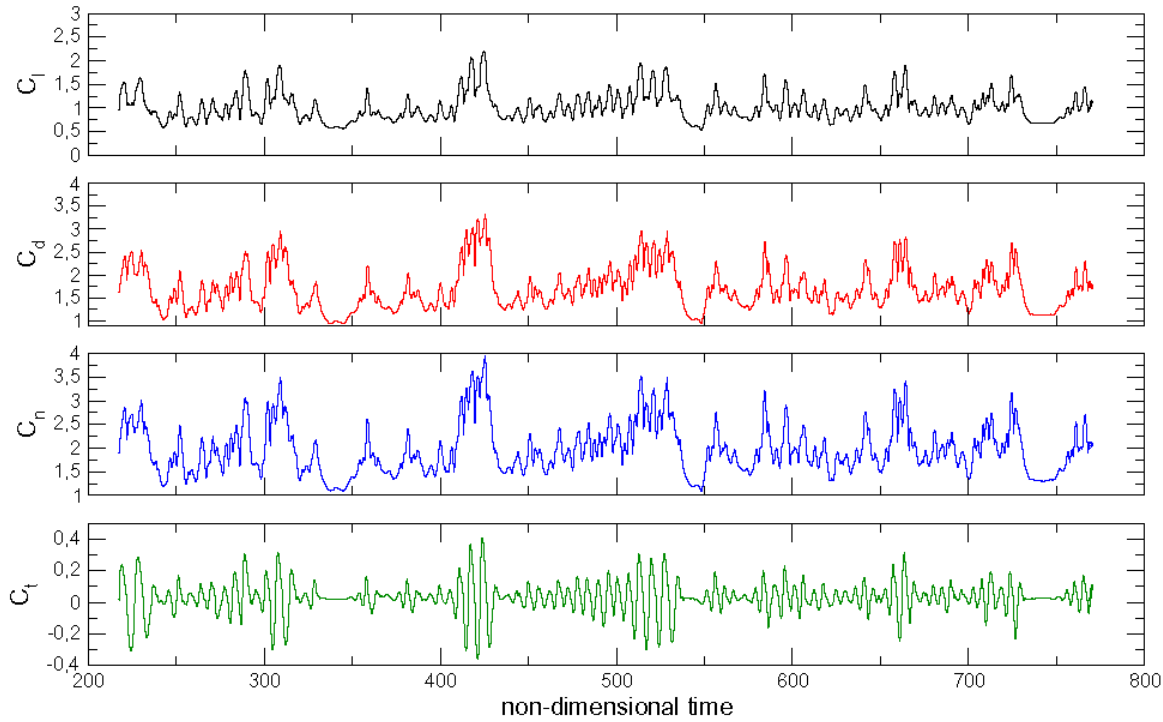
Figure 4-36 - Instantaneous streamlines behind a cylinder for the the onset of vortex shedding. (From Dallmann & Schewe (1987)).

The three-dimensional unsteadiness is evident in other parameters. The instantaneous C_p field, see Figure 4-40, shows the vortex wake and complex structures near the aerofoil surface. The velocity components, also shown in Figure 4-40, show the complexity. The streamwise component of velocity, U , shows the slowing of the fluid in the wake. There is also a clear region of upstream flow near the aerofoil surface caused by the vortex being shed and fine scale structures in the near wake of the aerofoil. The vertical component of velocity, V , also shows these fine scale structures. The expansion of the wake and the movement of the vortices away from the centreline are also apparent. The spanwise component of velocity, W , also shows fine scale structures near the aerofoil surface and larger scale structures in the wake, which probably correspond to the braid vortices seen in Figure 4-38, indicating the three-dimensional structures in the wake.

The three-dimensional structures are especially evident in the λ_2 isosurfaces coloured with normal and tangential velocity shown in Figure 4-41. λ_2 is a widely used criterion for visualising vortex cores based on eigenvalues of the squared strain and squared vorticity tensors, see Jeong & Hussain (1995) for a detailed definition. The highly three-dimensional nature of the wake is immediately evident. Hairpin structures, common in bluff body wakes at higher Re , are also apparent. Given the highly three-dimensional, irregular structures in the near wake, it is unsurprising that there is a low frequency component found in c_n , and therefore in c_l and c_d . The three-dimensionality and hairpin structures are confirmed in Figure 4-42 which shows isosurfaces of vorticity. The positive vorticity shed from the trailing edge and the negative vorticity shed from the leading edge is also apparent. The highly three-dimensional structures with alternate vortex shedding obtained by Thiele, Mockett & Bunge's DES agree with the deductions about the wake made from the surface-pressure measurements made in the wind tunnel earlier in this chapter.

Lift, drag, normal and tangential force components

NACA0012, 60°, DES-SALSA, coarse grid



Spectra of four force components

Hanning window, 7x averaged

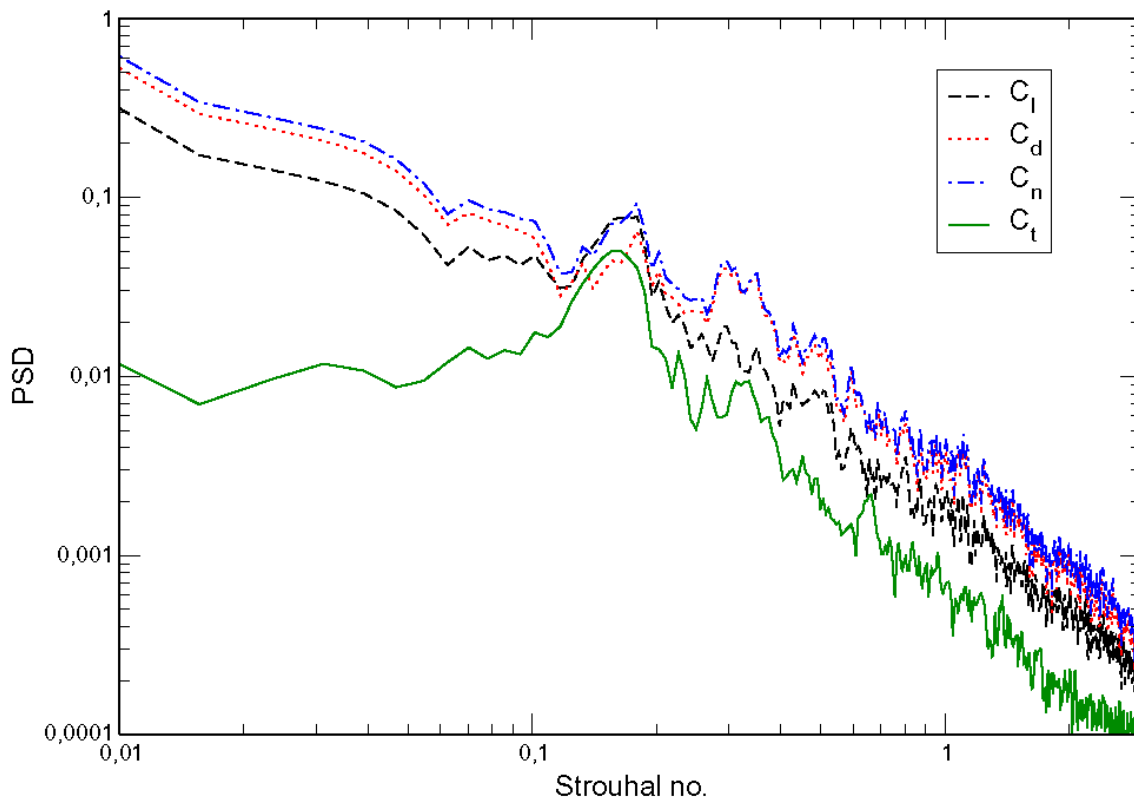


Figure 4-37 - Time series and the frequency content of the lift, drag, normal and tangential force components. Results from a DES based on the SALSA model using a coarse grid by Thiele, Mockett & Bunge (2004), used with permission.

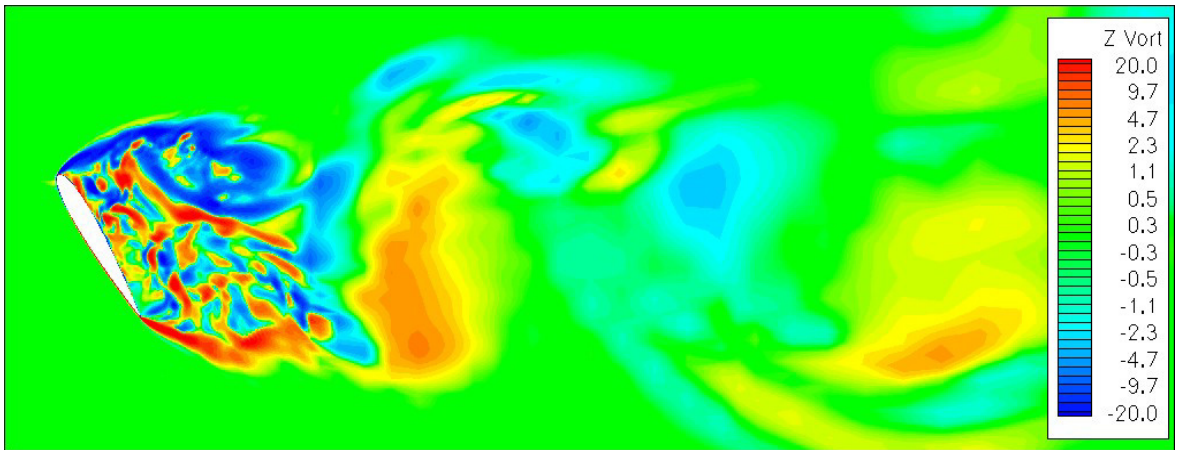
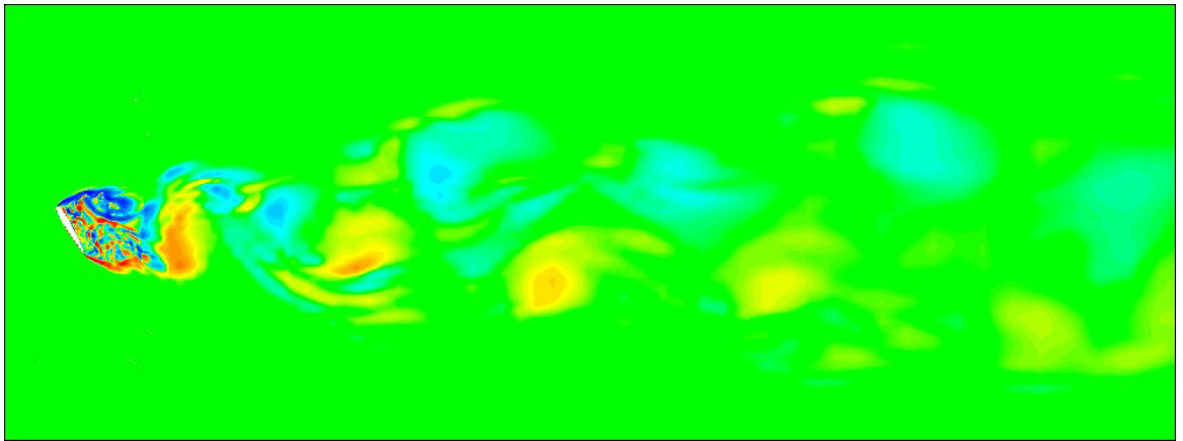


Figure 4-38 – Two dimensional slice about a NACA 0012 section showing contours of Z vorticity for two different magnifications at $\alpha = 60^\circ$. Results from a DES provided by Thiele, Mockett & Bunge (2004), used with permission. The contour levels for the two figures are shown in the lower figure.

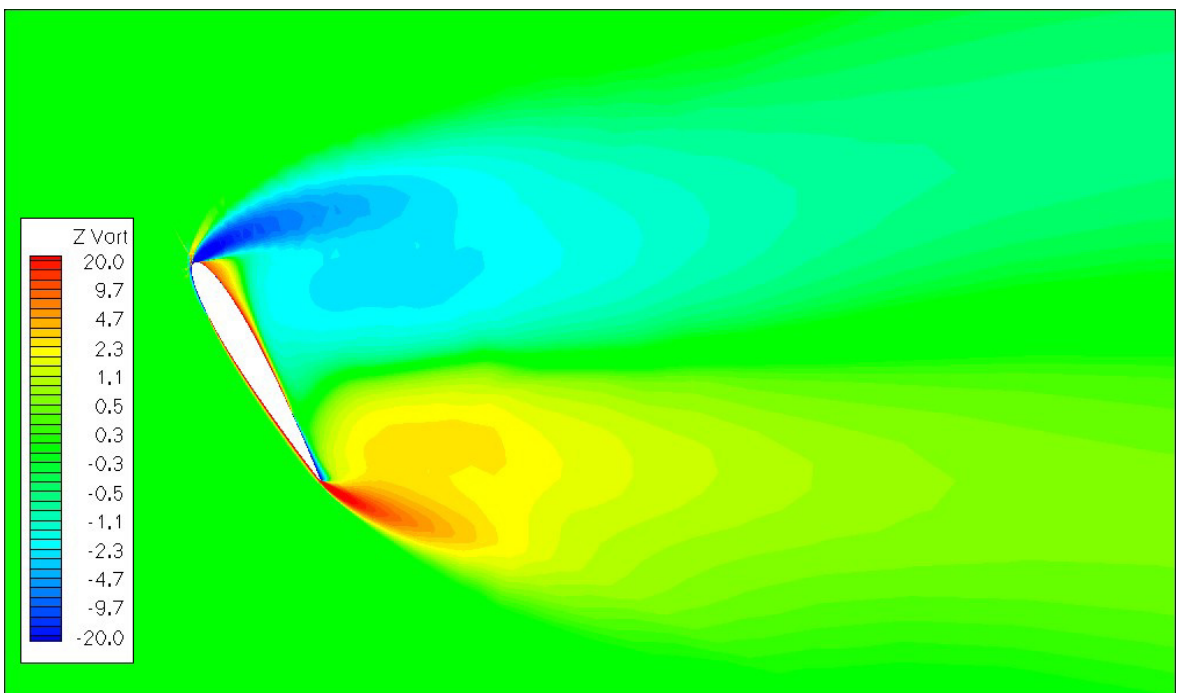


Figure 4-39 – Average of all results for a two dimensional slice about a NACA 0012 section showing contours of Z vorticity at $\alpha = 60^\circ$. Results from coarse grid calculations using DES based on the Wilcox k-omega model provided by Thiele, Mockett & Bunge (2004), used with permission.

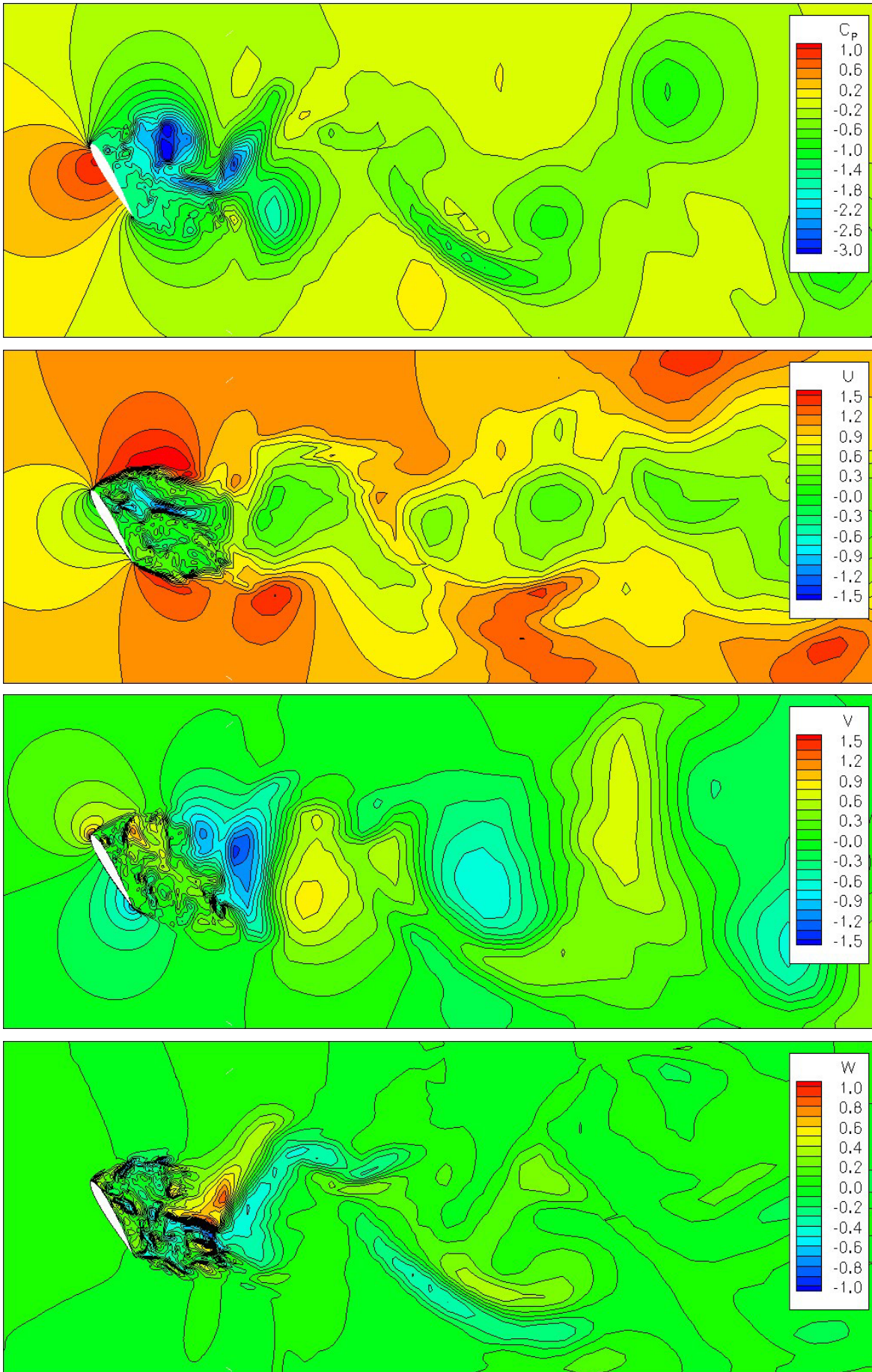


Figure 4-40 – Two dimensional slice about a NACA 0012 section showing contours of the C_p , and the U , V and W components of velocity at $\alpha = 60^\circ$ and $Re = 1 \times 10^5$. Results from a DES by Thiele, Mockett & Bunge (2004), used with permission.

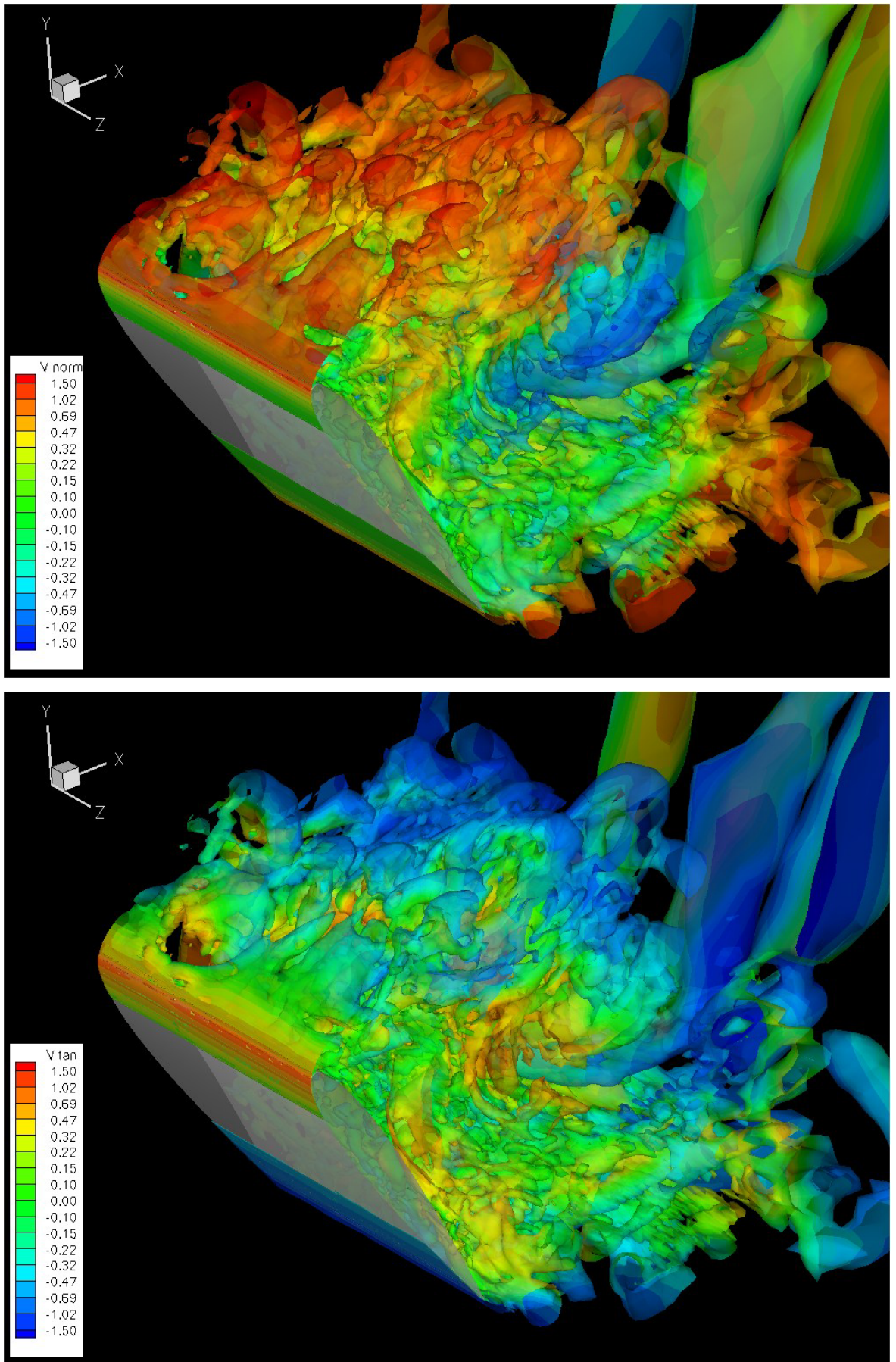


Figure 4-41 – Three Dimensional plot of a NACA 0012 section showing lambda-2 isosurfaces coloured with normal and tangential velocities at $\alpha = 60^\circ$. Results from a DES provided by Thiele, Mockett & Bunge (2004), used with permission.

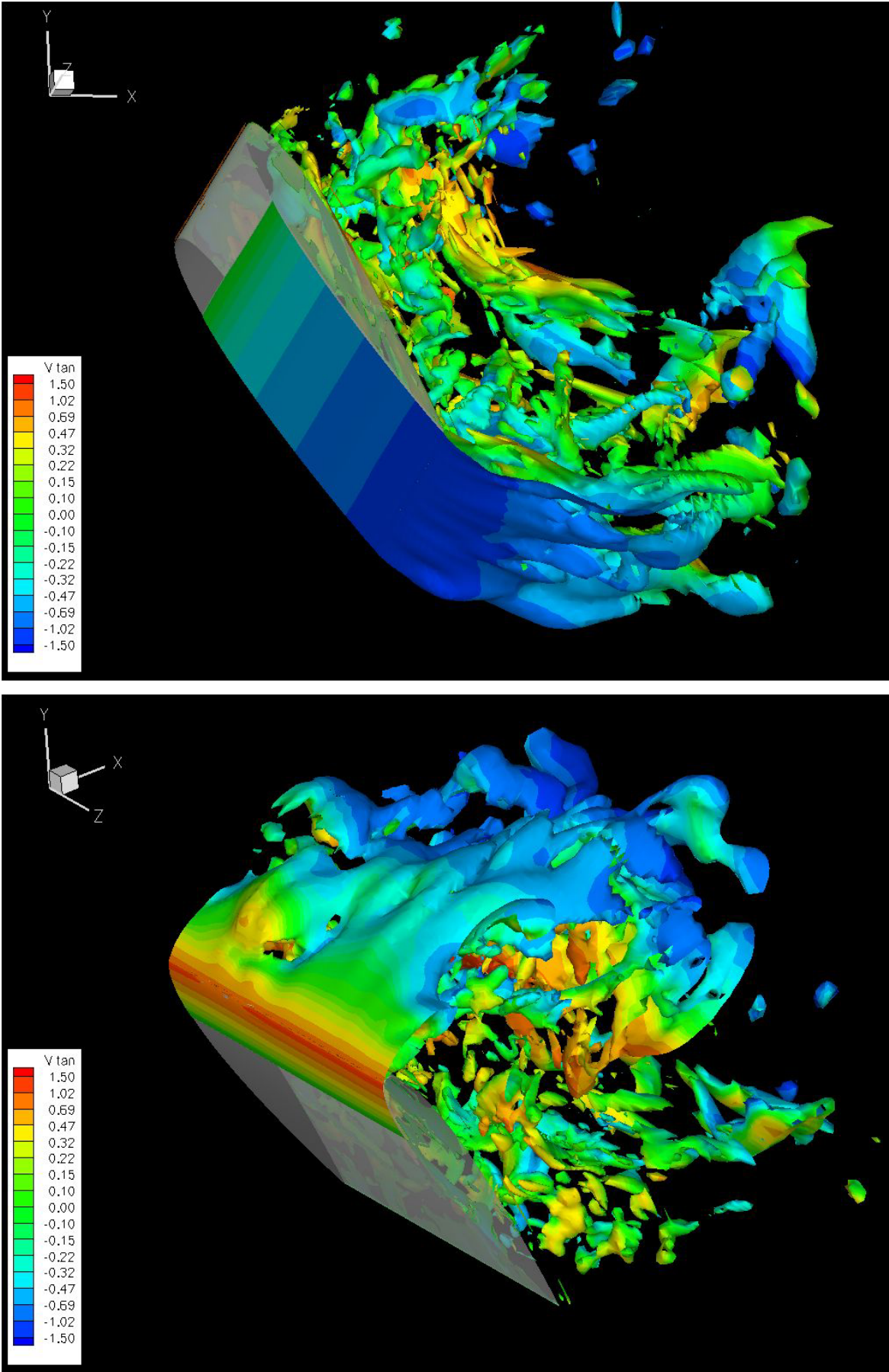


Figure 4-42 – Three Dimensional plot of a NACA 0012 section at $\alpha = 60^\circ$ showing vorticity isosurfaces, the upper plot showing the trailing edge used a velocity contour of +10 and the lower plot -10. The colours indicate normal velocities contours. Results from a DES provided by Thiele, Mockett & Bunge (2004), used with permission.

4.3.3 Effect of Turbulence on Fluctuations

This section examines the effect of turbulence on the fluctuating response. As has been shown, the results can be cleanly separated into those effects normal and tangential to the chord; only the forces in these planes will be presented in this section. The Power Spectral Density (PSD) of the instantaneous tangential and normal forces from Row B1 for all of the increased turbulence flows at all α are presented in this section.

Figure 4-43 shows the results for the flow created by the small grid in all five positions in order of increasing turbulence intensity. The PSD of the tangential force shows only the main shedding frequency for grid positions E, D and C. However, the PSD of the normal force at these positions shows the main shedding frequency, the secondary shedding frequency at twice the value of the main frequency and the low frequency “noise”.

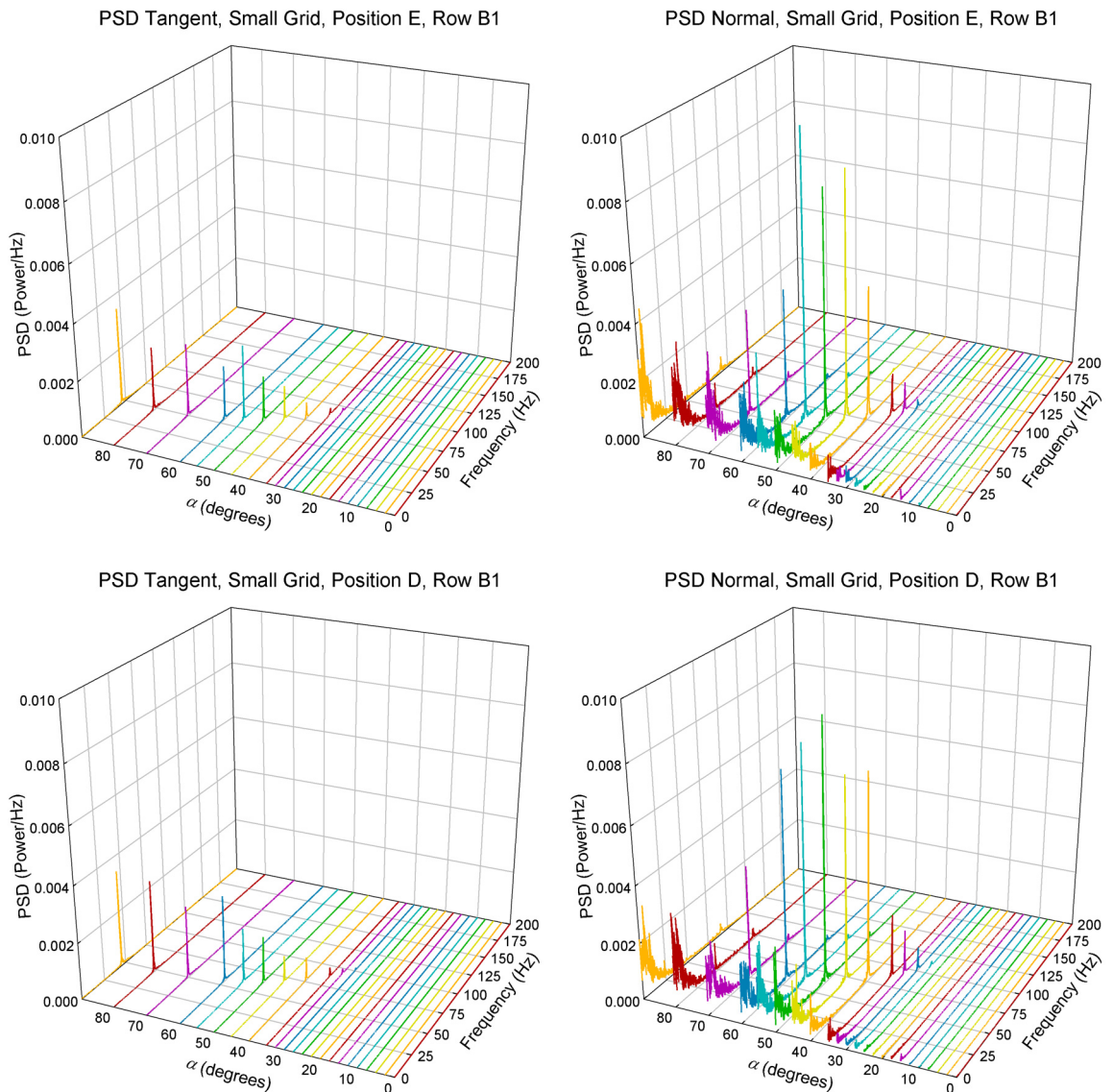
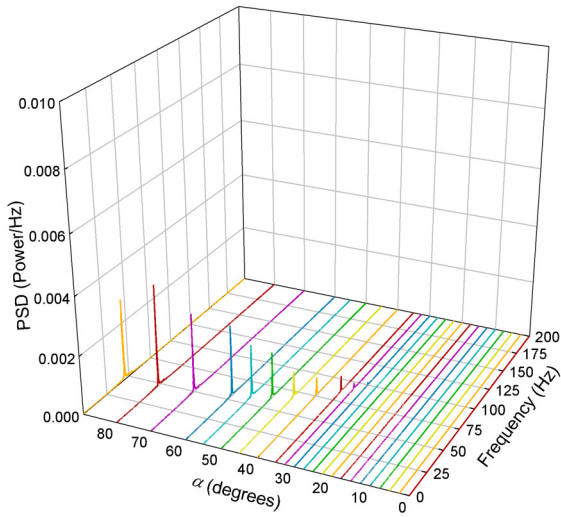
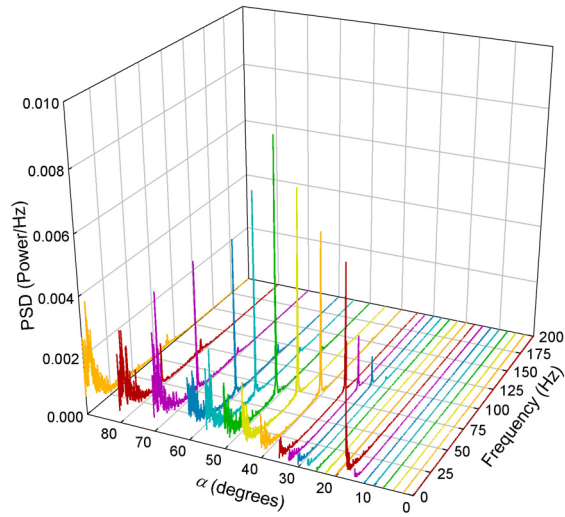


Figure 4-43(a) –NACA 0021 PSD of the c_t and c_n signals for the small grid in all positions. (Where there were increasing or decreasing α cases, the increasing case was used).

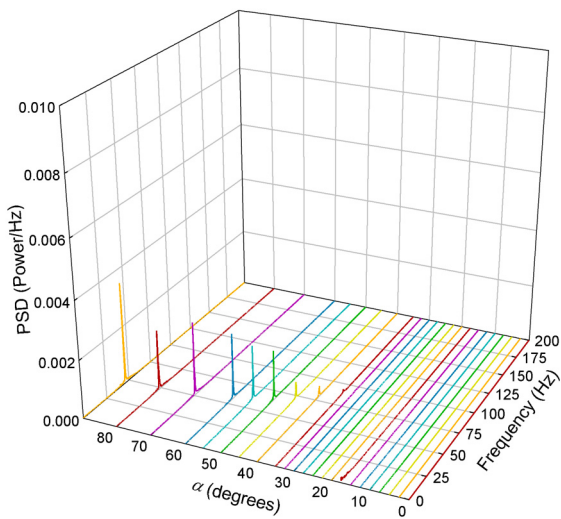
PSD Tangent, Small Grid, Position C, Row B1



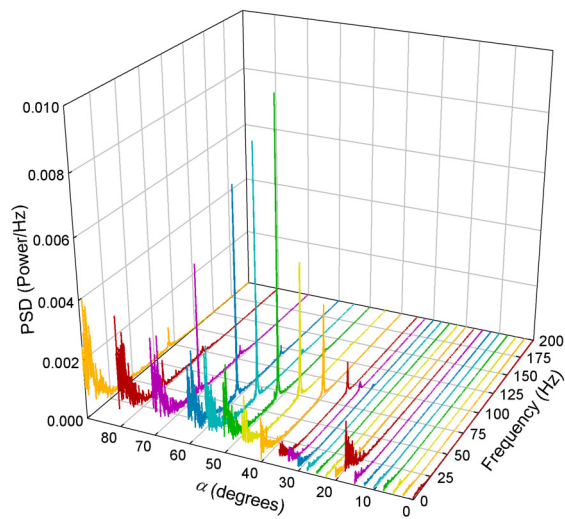
PSD Normal, Small Grid, Position C, Row B1



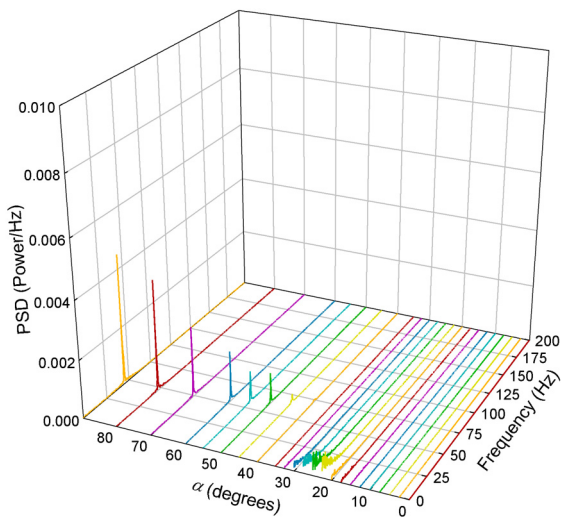
PSD Tangent, Small Grid, Position B, Row B1



PSD Normal, Small Grid, Position B, Row B1



PSD Tangent, Small Grid, Position A, Row B1



PSD Normal, Small Grid, Position A, Row B1

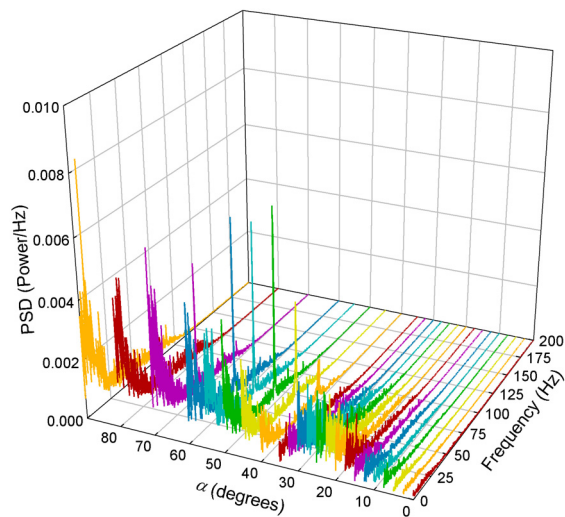
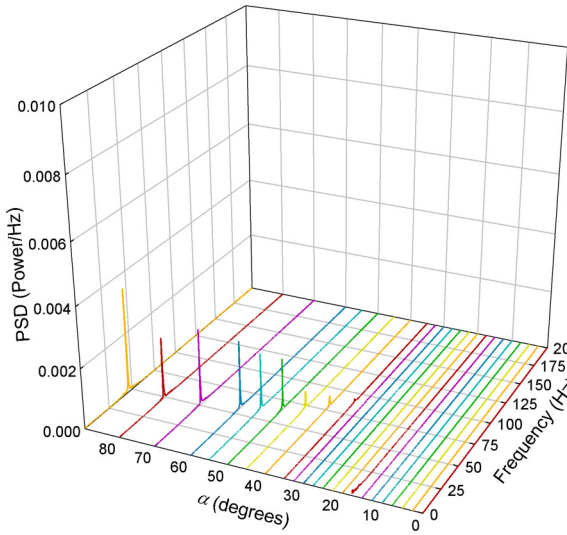
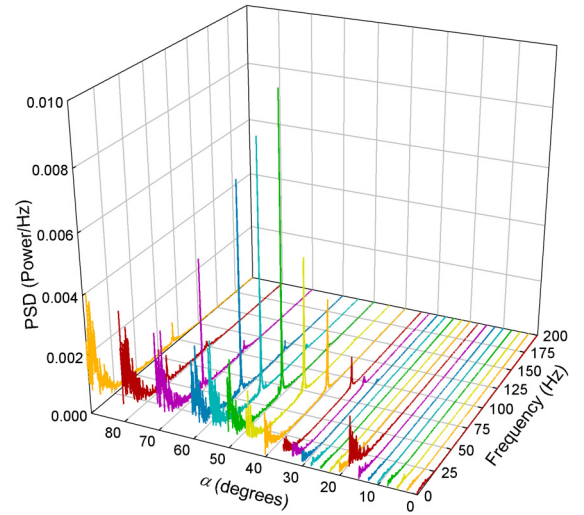


Figure 4-43(b) – NACA 0021 PSD of the c_t and c_n signals for the small grid in all positions. (Where there were increasing or decreasing α cases, the increasing case was used).

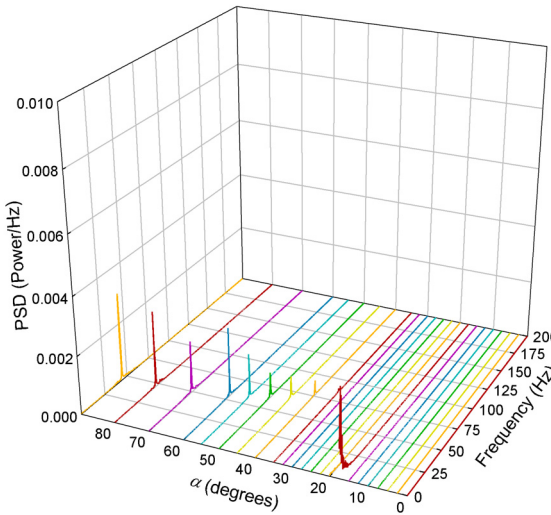
PSD Tangent, Medium Grid, Position E, Row B1



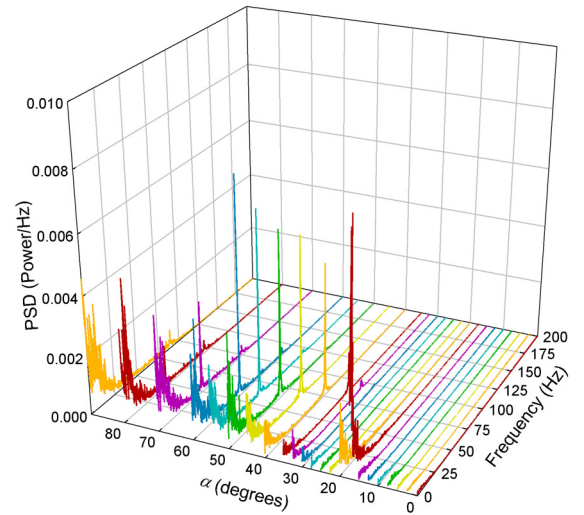
PSD Normal, Medium Grid, Position E, Row B1



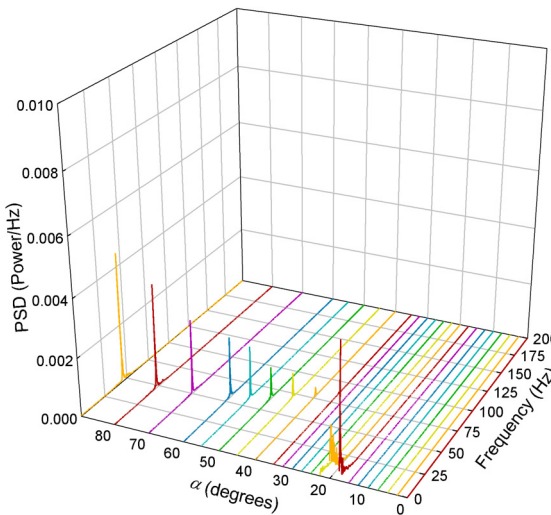
PSD Tangent, Medium Grid, Position D, Row B1



PSD Normal, Medium Grid, Position D, Row B1



PSD Tangent, Medium Grid, Position C, Row B1



PSD Normal, Medium Grid, Position C, Row B1

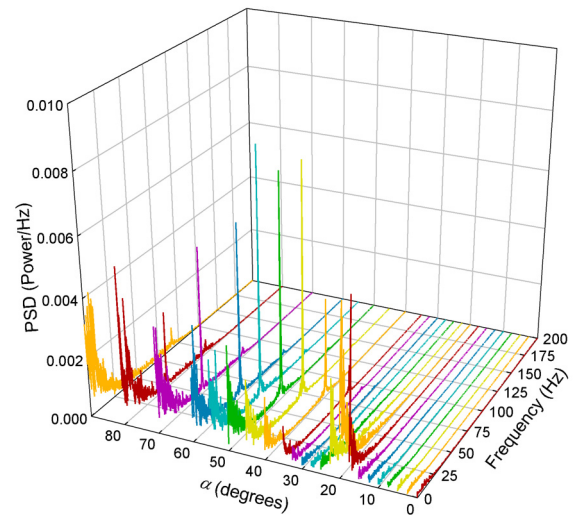


Figure 4-44(a) – NACA 0021 PSD of the c_t and c_n signals for the medium grid in all positions. (Where there were increasing or decreasing α cases, the increasing case was used).

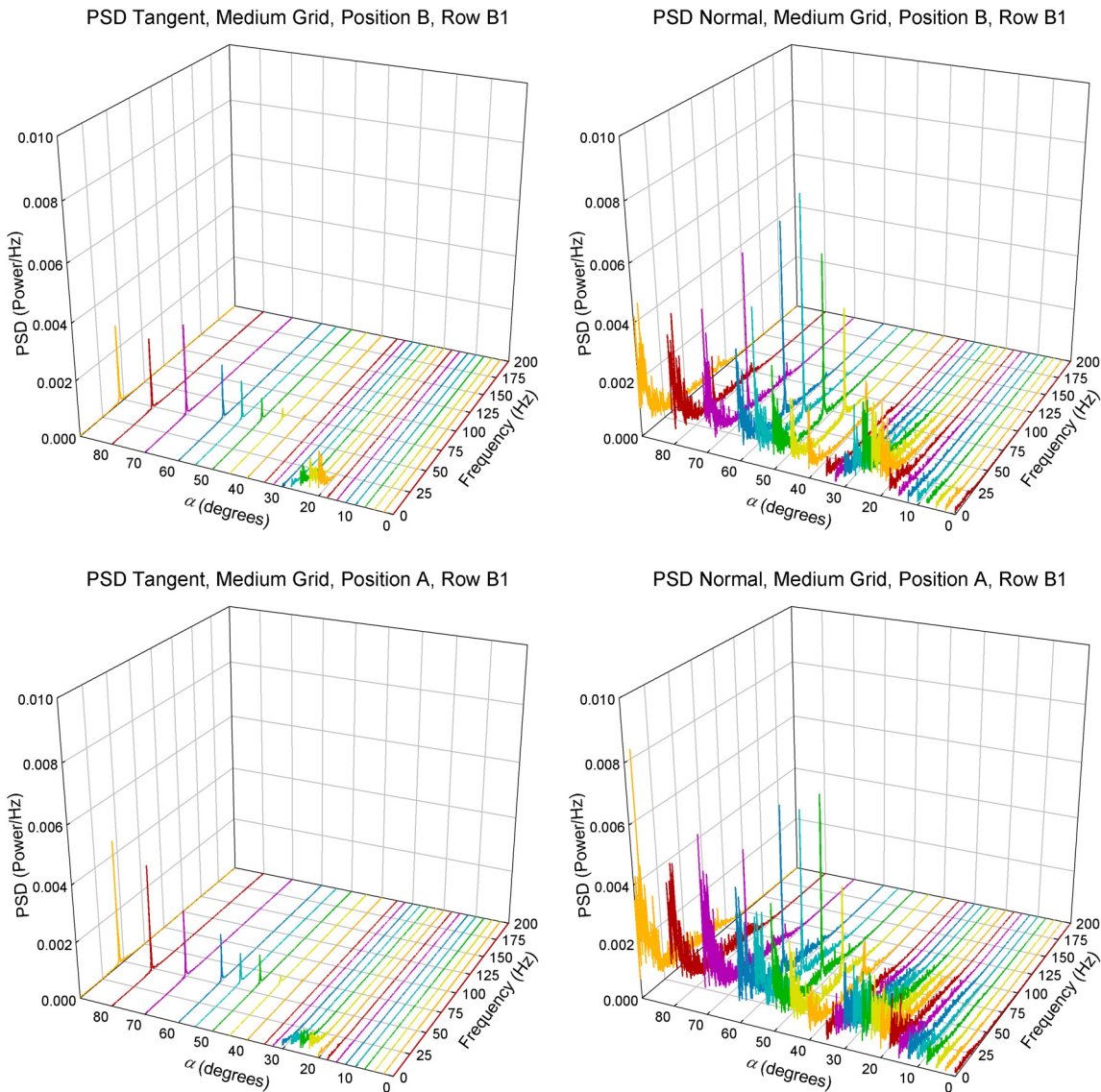


Figure 4-44(b) – NACA 0021 PSD of the c_t and c_n signals for the medium grid in all positions. (Where there were increasing or decreasing α cases, the increasing case was used).

This noise seen in Figure 4-43 becomes visible with the onset of shedding and increases with increasing α and generally increases with increasing turbulence intensity in the flow. There is also a small low frequency component at $\alpha = 15^\circ$. A slight low frequency disturbance for grid position D was observed at $\alpha = 17.5^\circ$, but the peak at $\alpha = 17.5^\circ$ dominates for grid position C. For grid positions E and D, $\alpha = 15^\circ$ is just before the lift curve drops to the local minimum associated with stall. For grid position C, while the large drop in lift occurs between $\alpha = 15^\circ$ and 17.5° , it doesn't drop as much and the local minimum is actually at $\alpha = 20^\circ$. Therefore, in these cases, this peak seems to be associated with the point just before full stall.

For the small grid in position B, see Figure 4-43(b), the largest low α peak in the normal PSD is at the same α (17.5°) as for the grid in position C but is spread out over a wider range of frequencies and the maximum is smaller. There are also corresponding small disturbances in the tangent PSD at this α . In contrast to the earlier cases, the low frequency variations are visible at all α , having

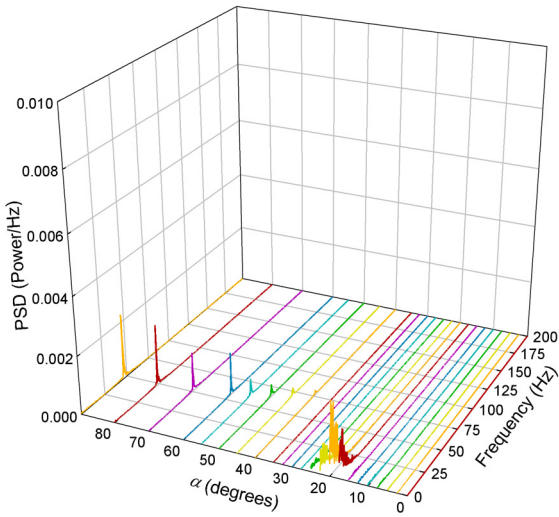
the low α peak discussed earlier at $\alpha=17.5^\circ$ and increasing in intensity with increasing α after the onset of shedding. The magnitude and range of frequencies of these low frequency disturbances increase dramatically with the small grid in position A, making it difficult to locate the second frequency in the normal PSD. There is a local maximum around $\alpha=25^\circ$ (the local minimum in the lift curve was at $\alpha=22.5^\circ$ for this flow). This is echoed by small disturbances in the tangent force PSD around this α .

The medium grid in position E produces a similar turbulence intensity flow to the small grid in position B and the PSD are very similar for these cases, see Figure 4-43(b) and Figure 4-44(a). The small grid in position A also produced a similar turbulence intensity to the medium grid in position D. However the PSD for these cases are quite different, with the medium grid case showing only small amounts of low frequency disturbance at low α in the normal PSD and showing large low frequency peaks at $\alpha=17.5^\circ$ and 20° in the normal and tangential PSD. The lift curve for Row B1 in this flow reaches its local minimum associated with stall at $\alpha=22.5^\circ$ but the local maximum associated with stall was at $\alpha=15^\circ$. Therefore flapping of the separated shear layer may cause these peaks. The larger low frequency response of the small grid flow is probably due to higher turbulence levels at smaller scales and therefore increased impact on the boundary layer.

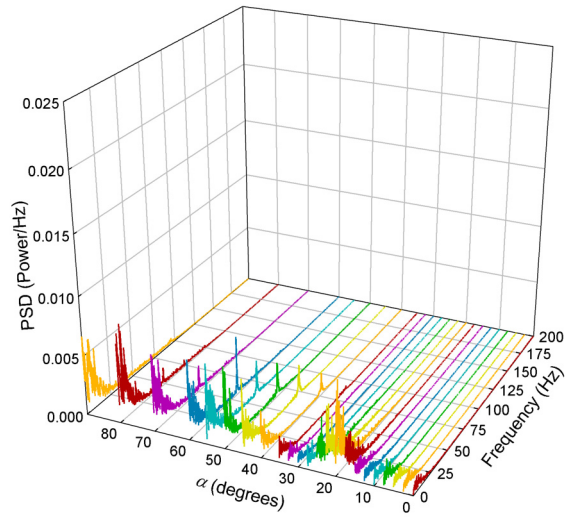
With the medium grid in position C, the low α peaks have spread to $17.5^\circ \leq \alpha \leq 22.5^\circ$ (while there are peaks at all these frequencies in the tangent PSD the peak at 22.5° was very small). For Row B1 the local maximum associated with stall occurs at $\alpha=15^\circ$ for this flow and the local minimum at $\alpha=25^\circ$. Otherwise the plot is fairly similar to that with the grid in position D. For the medium grid in position B and A, the increased low frequency disturbances are centred around 22.5° to 25° (for Row B1 the local maximum and minimum associated with stall occur at 17.5° and 32.5° respectively for grid position B, and 17.5° and 35° respectively for grid position A). Clearly, the range of frequencies at which disturbances are evident in the PSD is increased for the grid in positions B and A, matching the greater separation between the maximum and minimum associated with stall in the c_l curves.

The PSD plots for the large grid positions are presented in Figure 4-45. Note the scale of the normal PSD plots is two and a half times larger than those presented earlier. The medium grid at position B and the large grid in position E produced flows of similar turbulence intensity (although differing in scale). The PSD results for these two cases are similar except the peak at low α is centred around $\alpha=20^\circ$ for the large grid and the PSD levels tend to be larger for the larger grid. For the larger grid the drop in c_l occurred at a lower α (for this flow the local maximum and minimum associated with stall occur at $\alpha=15^\circ$ and $\alpha=22.5^\circ$ respectively) than for the medium grid flow, which explains why the low α peak is at lower α .

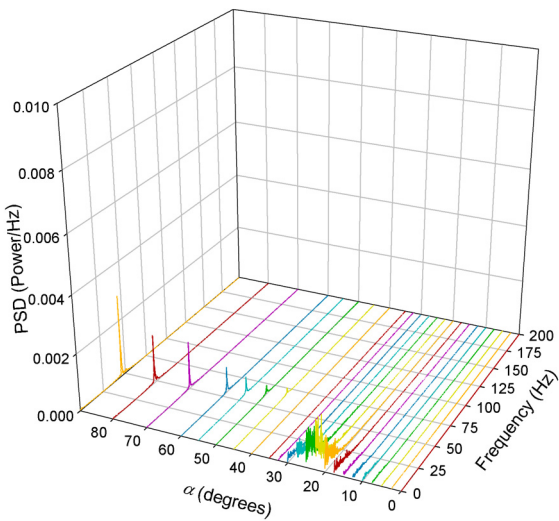
PSD Tangent, Large Grid, Position E, Row B1



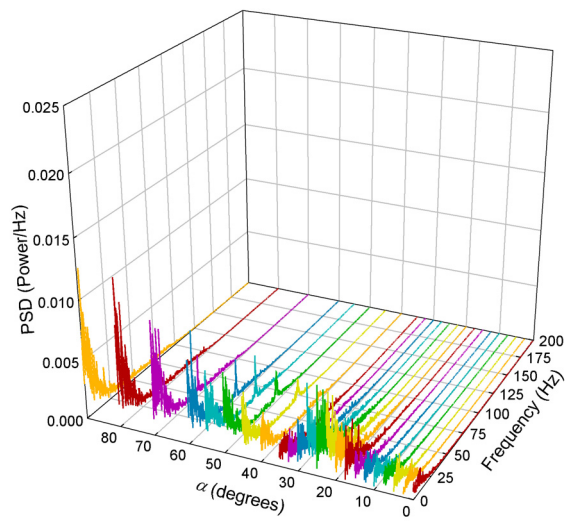
PSD Normal, Large Grid, Position E, Row B1



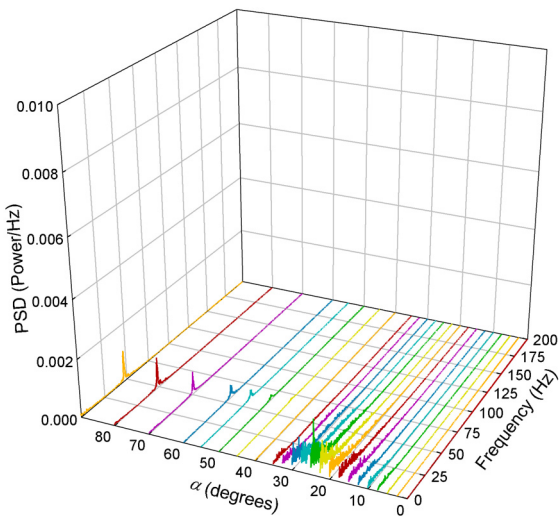
PSD Tangent, Large Grid, Position D, Row B1



PSD Normal, Large Grid, Position D, Row B1



PSD Tangent, Large Grid, Position C, Row B1



PSD Normal, Large Grid, Position C, Row B1

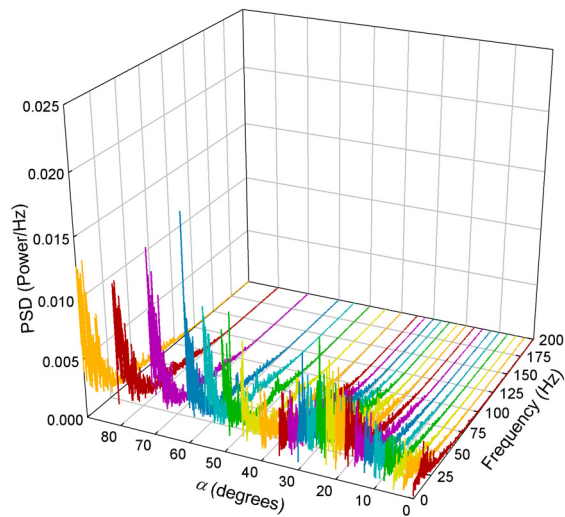


Figure 4-45(a) – NACA 0021 PSD of the c_t and c_n signals for the large grid in all positions. (Where there were increasing or decreasing α cases, the increasing case was used).

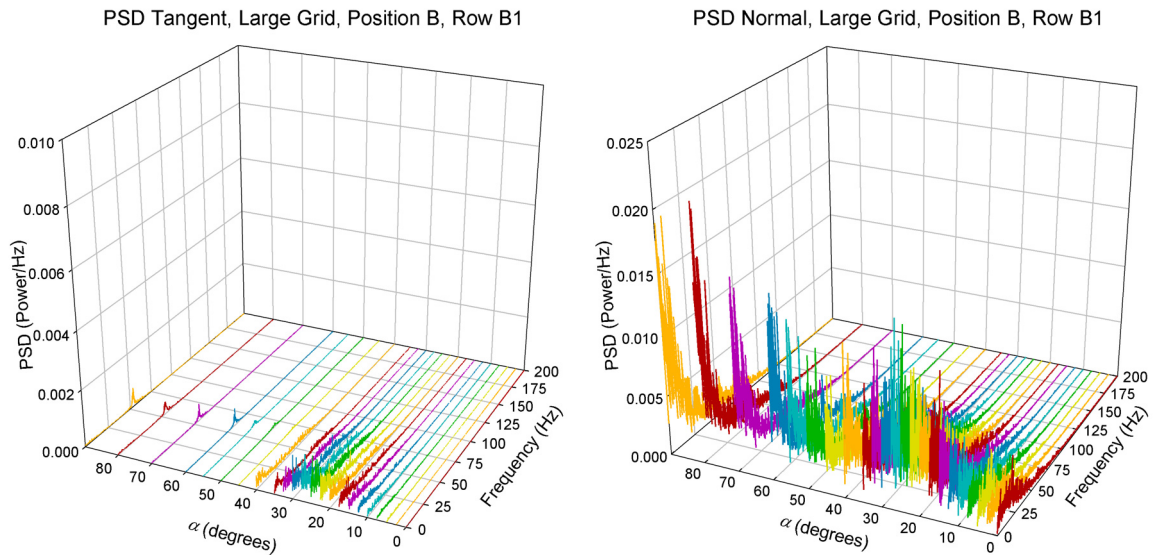


Figure 4-45(b) – NACA 0021 PSD of the c_t and c_n signals for the large grid in all positions. (Where there were increasing or decreasing α cases, the increasing case was used).

The large grid in position D produced similar turbulence intensities to the medium grid in position A and the PSD plots are very similar for these flows as well. The local maximum associated with stall for the large grid in position D occurs at the same α as for the medium grid in position A but the local minimum occurs earlier at $\alpha = 32.5^\circ$, and again the low frequency peak at a low α occurs earlier for the large grid case at about $\alpha = 22.5^\circ$. The large grid in position C and B, Figure 4-45(a) and Figure 4-45(b), shows the low frequencies dominating the normal PSD and those associated with the low α peak are more prominent in the tangent PSD. This makes the shedding peaks difficult to see in the normal PSD, but it is apparent in the tangent PSD that they have decreased in magnitude.

As it is difficult to see the relative magnitude and frequencies of the shedding peaks in the waterfall plots, a Matlab program was written to find the maximums. When searching for the maximum shedding frequency all data below 40Hz was ignored, this was based on the occurrence of low-frequency “noise” in the PSD of the instantaneous normal force being generally below this frequency and the shedding frequencies above this frequency. The maximum PSD and the frequency at which this occurred were found for both the tangential and normal data. If the magnitude of this first maximum was less than 10^{-6} for the tangential data or 10^{-4} for the normal data, it was ignored. To find the second maximum in the normal data the data for 50Hz either side of the first maximum was set to zero as there were no frequencies of interest in this range. In addition, for $-45^\circ \leq \alpha \leq 45^\circ$, all data at lower frequencies from than frequency of the first maximum was set to zero. If the magnitude of this second maximum was less than 10^{-5} it was ignored. Any small α points that did not fit the curve were also deleted manually after this process.

The shedding frequencies and magnitudes for the tangential force PSD are shown in Figure 4-46. The frequency plot shows that the shedding frequencies in all but one flow match very well those

seen earlier for the lowest turbulence flow (no grid, $I_u = 0.6\%$). There are some small differences at low α , but that was probably due to noise as the peaks were small at these angles. The $I_u = 13\%$ flow trended to a higher frequency at high α than for the other cases. This was the largest turbulence intensity at the largest turbulence integral length scale tested, so it is conceivable that the turbulence in this case caused increased curvature of the shear layers and therefore a narrower wake. For the universal Strouhal number to remain constant, a narrower wake would require an increased shedding frequency, see Equation 2-45.

The shedding magnitude plot has large variation between points however it does show a general trend of increasing magnitude with increasing α . Also the smaller scales of turbulence (about $1/3c$ and $1/2c$) tended to produce increased shedding peak magnitudes compared with the lowest turbulence flow ($I_u = 0.6$) and the large turbulence scales (about $1c$) produced flow with a lower shedding peak magnitude than the flow with the lowest turbulence level.

The other frequencies in the normal PSD meant that the shedding frequencies were more difficult to pick out and therefore the frequency curves show more variation than in the tangential case see Figure 4-46. This variation is sufficiently large to make it very difficult to find the higher frequency trend in the highest turbulence intensity data from this plot. The second frequency curve was defined as the second largest peak greater than 50 Hz above the first peak. At $\alpha = 90^\circ$ in some cases the higher frequency peak is larger in magnitude than the lower frequency peak and so some cases jump from one curve to another at this α .

The smaller magnitudes of the peaks at $\alpha = 90^\circ$ for the smaller turbulence flows can be seen in the shedding magnitude plot in Figure 4-46. The normal force shows a peak in shedding magnitude at about $50^\circ \leq \alpha \leq 60^\circ$. In general the smaller intensities show increased shedding magnitude at low α compared to that found for the larger intensities. The larger turbulence integral length scales ($>1c$) don't decline in magnitude at high α as much as for the other flows, though in general, they show lower shedding magnitudes.

The form of this shedding could potentially be a problem for stall controlled wind turbine designs if it was well enough correlated to produce cyclic loading on the blades. This would be especially true normal to the chord around $50^\circ \leq \alpha \leq 60^\circ$ where the shedding was strongest. The next section will look at correlations across the span to examine this possibility.

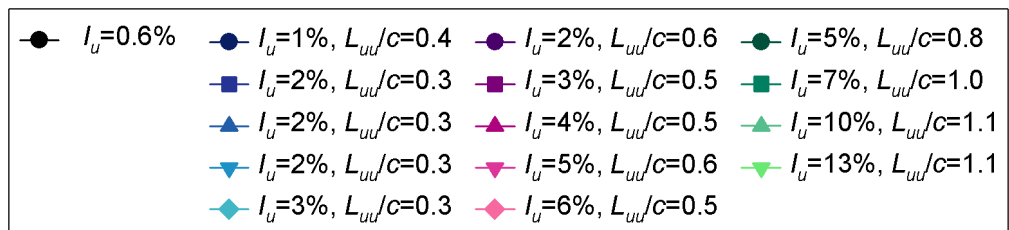
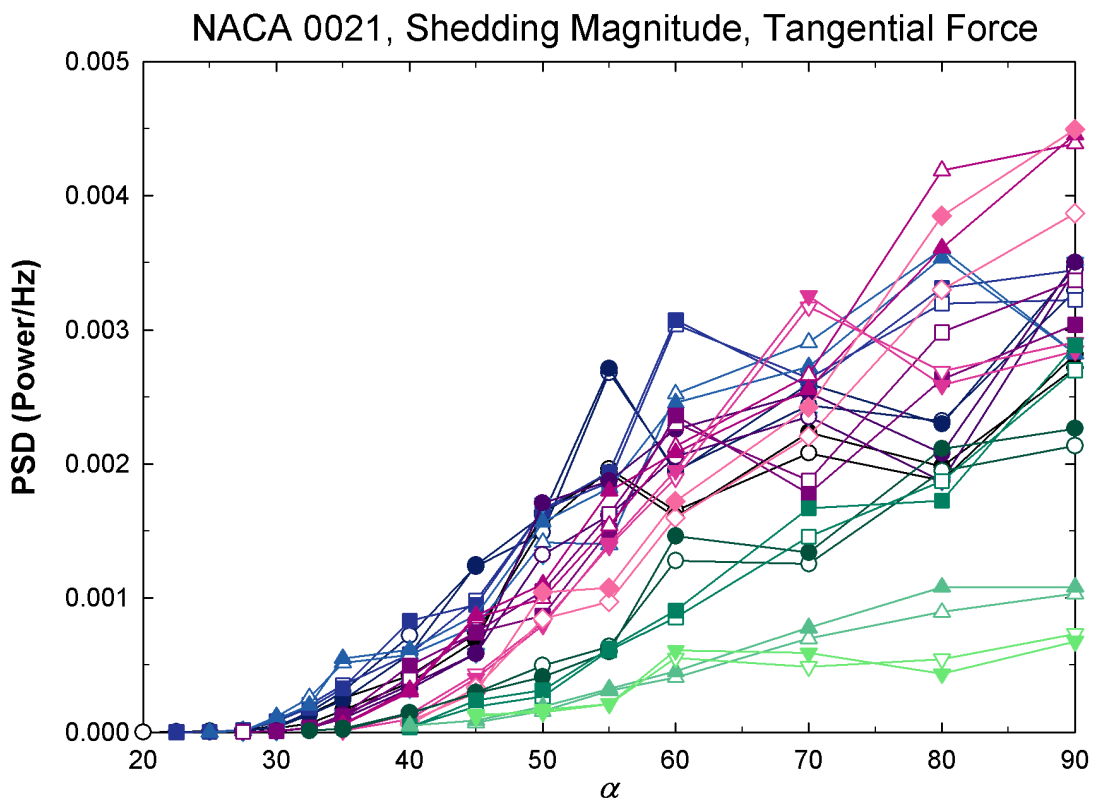
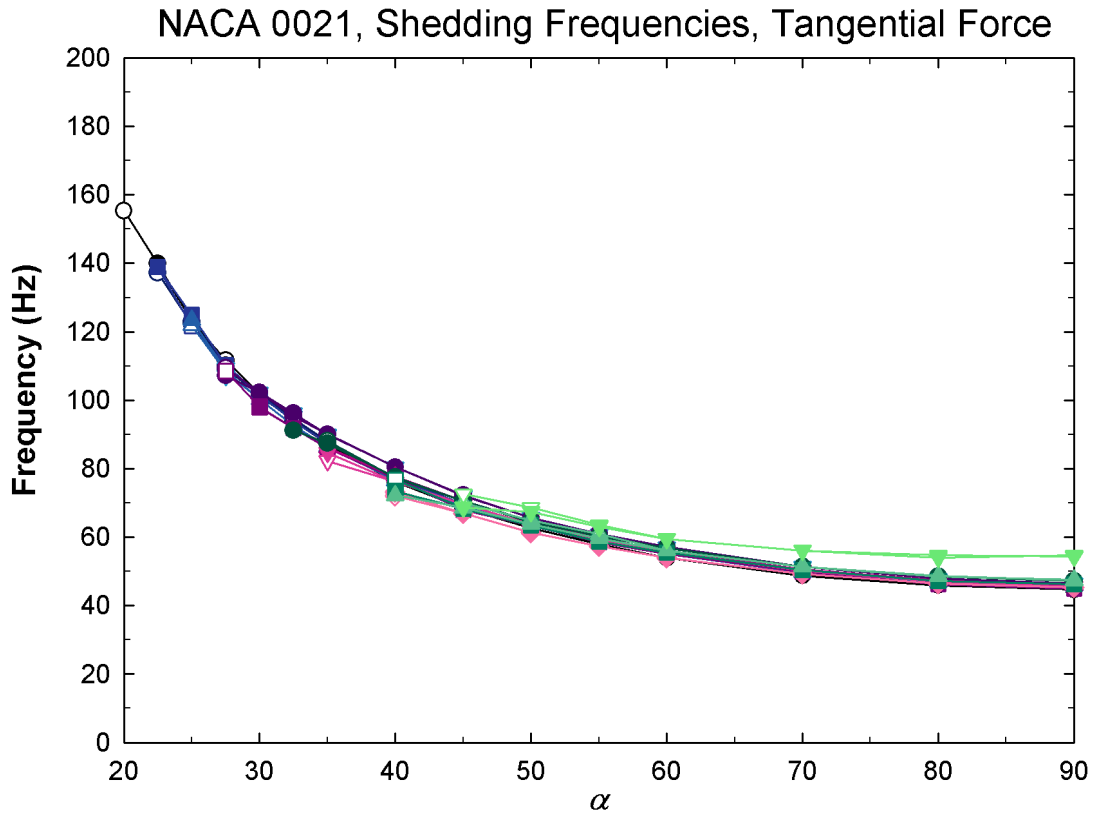
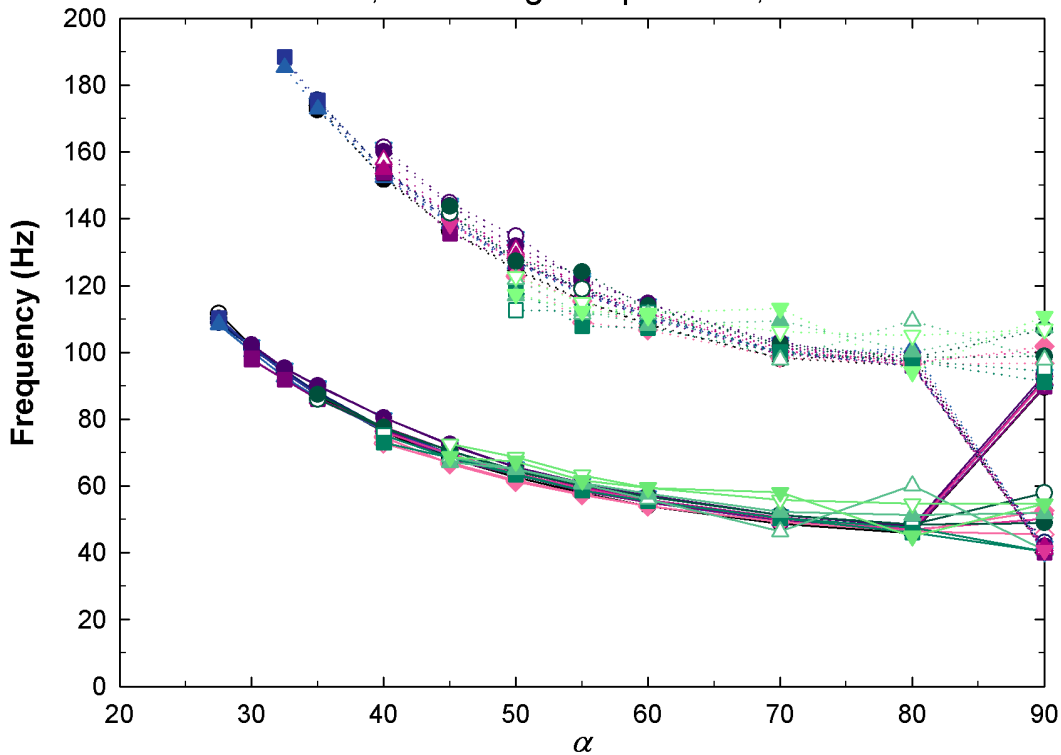


Figure 4-46 - Shedding frequencies and magnitude in the tangential force PSD for all flow conditions. Closed symbols indicate Row B1 and open symbols indicate Row B2.

NACA 0021, Shedding Frequencies, Normal Force



NACA 0021, Shedding Magnitude, Normal Force

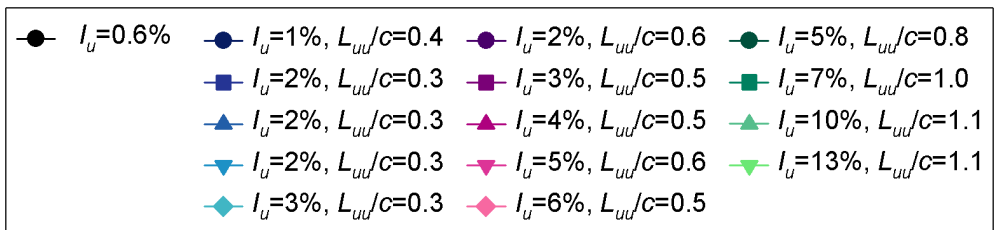
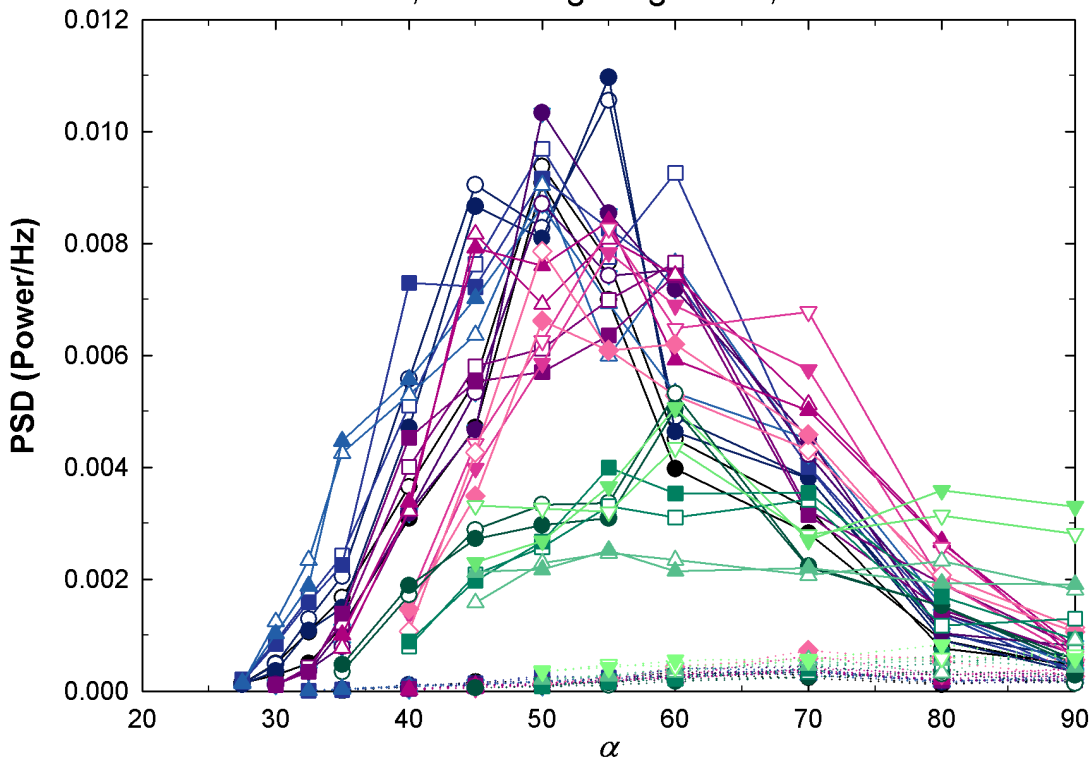


Figure 4-47 - Shedding frequencies and magnitude in the normal force PSD for all flow conditions. Closed symbols indicate Row B1, open symbols indicate Row B2, straight lines the first and dotted lines the second frequency.

4.3.4 Correlations

The correlation coefficient, Equation 3-32, was used to investigate correlation between the pressure signals at various pressure taps as well as the correlations between the instantaneous force coefficients. The force coefficients were only derived for Row B1 and B2. Only the correlations for the increasing α case for the coefficients of tangential force, normal force and moment about the quarter chord between Rows B1 and B2 were investigated as the coefficients of lift and drag can be found from c_t , c_n and α . Correlations of the corrected instantaneous pressure measurements for the four taps in all tapping rows, the taps at the leading edge, trailing edge and the upper and lower surfaces near the point of maximum thickness, will also be shown later in this section.

The correlation coefficients for the c_t , c_n and $c_{m, 1/4c}$ from Rows B1 and B2 are shown in Figure 4-48. As was shown earlier in this chapter, see Section 4.3.1, the tangential force is dominated by measurements taken near the leading and trailing edges. At low α there was very little correlation between the c_t measurements for all flow conditions. However, by $\alpha = 90^\circ$ there was a correlation coefficient of about 0.5 for the highest turbulence flow and between 0.6 and 0.7 for the other flows. The data for $\alpha \geq 45^\circ$ is spread with the higher turbulence intensities having lower correlation coefficients. For $\alpha < 45^\circ$ the large grid tends to have a higher correlation coefficient, with the small and medium grids having lower correlation coefficients than the no grid case. As α increases, the correlations appear to increase and then drop around stall leading to the spread commented on for higher α . The correlation coefficients of the normal force tend to have a similar spread and drop at low α to that of the tangential force. However, at high α the spread is opposite with the highest turbulence intensities showing the highest correlations with the exception of the lowest turbulence case which is intermediate at $\alpha = \pm 90^\circ$. This could be explained by the flow before stall being affected by the attached boundary layers on the pressure surface that are buffeted to a small extent by large turbulence scales in the freestream. The separation associated with stall sees a drop in correlation. The tangential case (c_t) at high α is dominated by vortex shedding from the leading and trailing edge which is less coherent in higher turbulent flows for $\alpha < 90^\circ$ (and at all $\alpha \geq 45^\circ$ for the highest turbulence intensity tested). However, the normal force (c_n) correlation coefficients are also affected by the buffeting from the freestream at high α and therefore are higher for higher turbulence intensities.

The correlation coefficients for the $c_{m, 1/4c}$ data from Row B1 and B2, also shown in Figure 4-48, are similar to the c_t coefficients at low α , show increased correlations for $20^\circ \geq \alpha \geq 30^\circ$ for the lowest turbulence intensities and trend to a similar spread of higher correlations for high turbulence intensities for $\alpha = 90^\circ$. It appears at low α the moment is uncorrelated, that stall increases correlation for $20^\circ \geq \alpha \geq 30^\circ$ for the lower turbulence intensities but it is still small for higher levels of turbulence. However, at high α the shedding produces a more correlated $c_{m, 1/4c}$ and the higher turbulence intensities seem to increase this correlation.

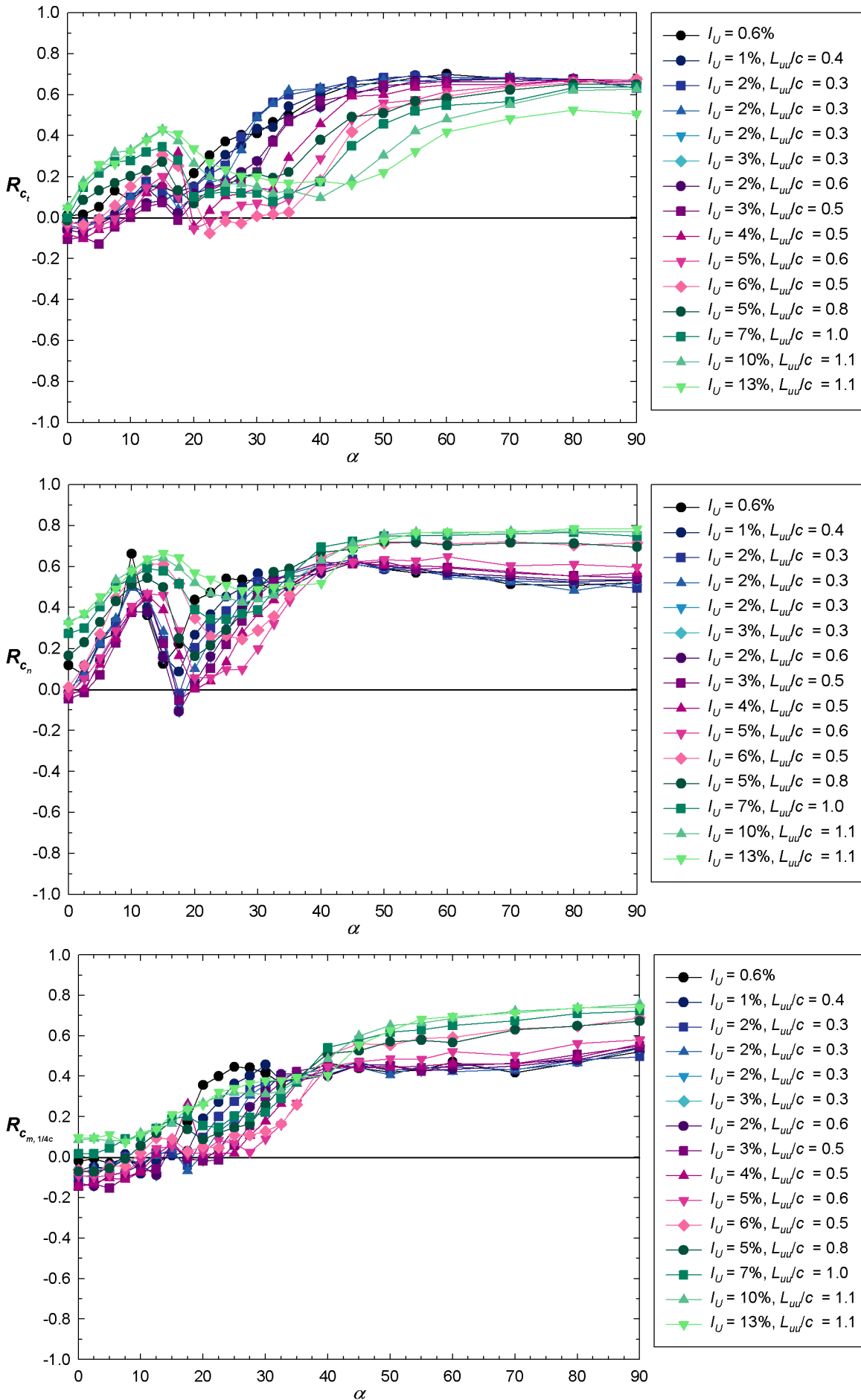


Figure 4-48 – NACA 0021 Correlation coefficients between c_t , c_n and $c_{m, 1/4c}$ calculated from Row B1 and Row B2 data (increasing α data only shown).

The correlation coefficients (R) between the pressure signals for the four taps in all the tapping rows (see Figure 4-49 for the locations of the rows and taps) for the lowest turbulence flow (no grid in the tunnel) is shown in Figure 4-50. At low α ($<20^\circ$) there is a great deal of variation in R associated with stall. This is shown in more detail in Figure 4-51 and this figure should be referred to if the trends noted below for small α are difficult to see in Figure 4-50. It is interesting that, across most α , the correlations trend into bands with those with the closest spacing along the span (one chord length apart for A1B1, B1A2, A2B2 and B2A3) in the top band with the highest correlation and the case the largest spanwise distance apart (four chord lengths apart for A1A3) having the lowest correlation. The spatial limitations of the structures in the shedding and turbulence flow seem to increase the correlation for taps nearer each other and decrease the correlation with increasing distance between taps.

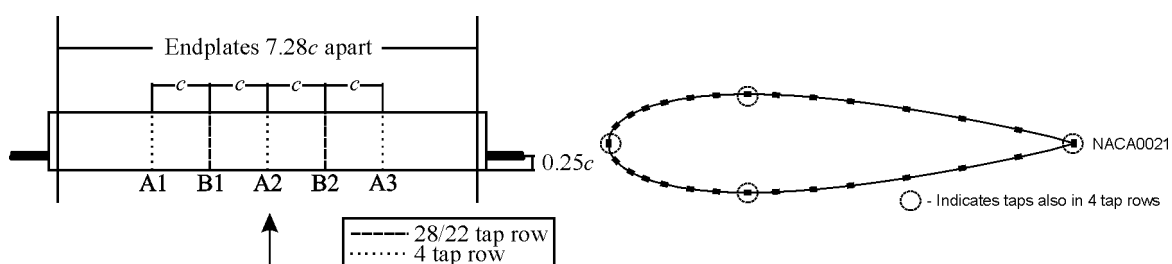


Figure 4-49 – The tapping rows and the taps from which the pressure signals will be compared (the taps in both the 4 tap rows and the 28 tap rows).

There is some correlation at $\alpha = 0^\circ$ ($0.4 \leq R \leq 0.7$) for the taps on the trailing edge which decreases with increasing distance between the taps. The correlation decreases as α increases from 0° . This could be due to different exposures of the taps at the trailing edge to upper and lower surface flow or variation from turbulence in the boundary layer due to reattachment. At 10° the linear attached region of the lift curve ends and there is an increase in correlation at the trailing edge. This could be due to the beginning of separation, where the trailing edge would not be impacted by the turbulent boundary layer. For $\alpha > 10^\circ$, separation moves toward the leading edge, causing larger mushroom patterns and more spanwise variation and therefore lower correlation. The onset of vortex shedding at about $\alpha = 20^\circ$ sees an increase in correlation with increasing α to about $\alpha = 30^\circ$ for the $1c$ spanwise spacing and 40° for the other spanwise spacings. The correlation coefficients then remain fairly constant to $\alpha = 90^\circ$.

The reattachment bubble for the taps in all rows on the upper surface seems to cause a large variation in correlations with the variation increasing with α as the separation bubble becomes more pronounced. At the beginning of separation ($\alpha = 10^\circ$) the Kutta condition no longer needs to be satisfied which perhaps leads to reduced adverse pressure gradients and a smaller separation bubble, a smaller bubble would effect a smaller number of upper surface taps which would increase the correlation observed on the upper surface. For $\alpha > 10^\circ$ the mushroom patterns associated with stall decrease the correlations. In the range $20^\circ < \alpha < 40^\circ$ increasing correlations or fairly constant

levels of the correlation coefficients are seen, this is the region where the vortex shedding begins and the shedding becomes more dominant with increasing α . However, for $\alpha > 40^\circ$, the shed vortices would be further away from the upper tap which explains the slight decrease in the correlation with increasing α .

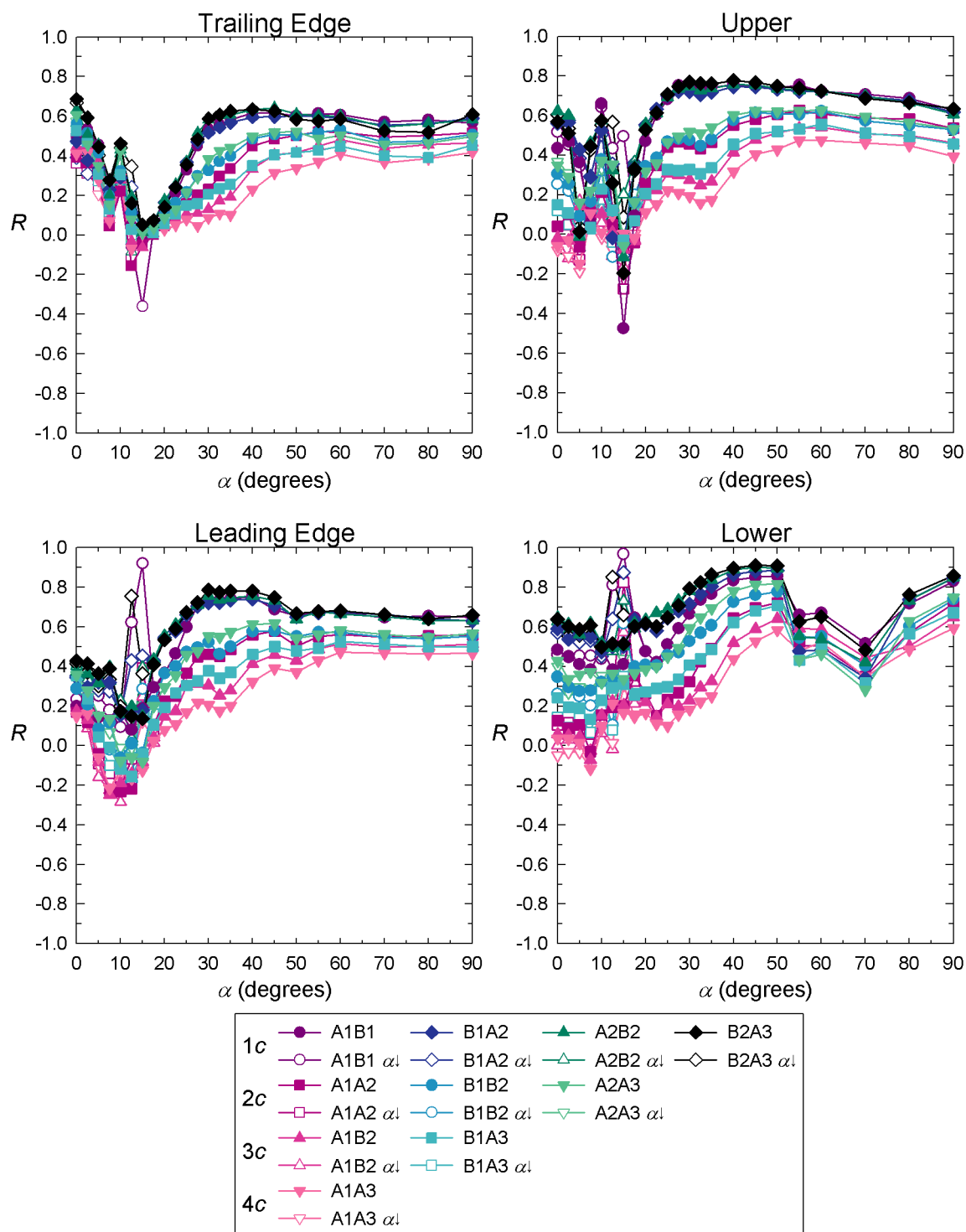


Figure 4-50 – NACA 0021 Correlation coefficients between taps in the 4 tap rows (A1, A2 and A3) and the equivalent taps in the 28 tap rows (B1 and B2) for the lowest turbulence flow ($I_u = 0.6\%$, no grid in the tunnel).

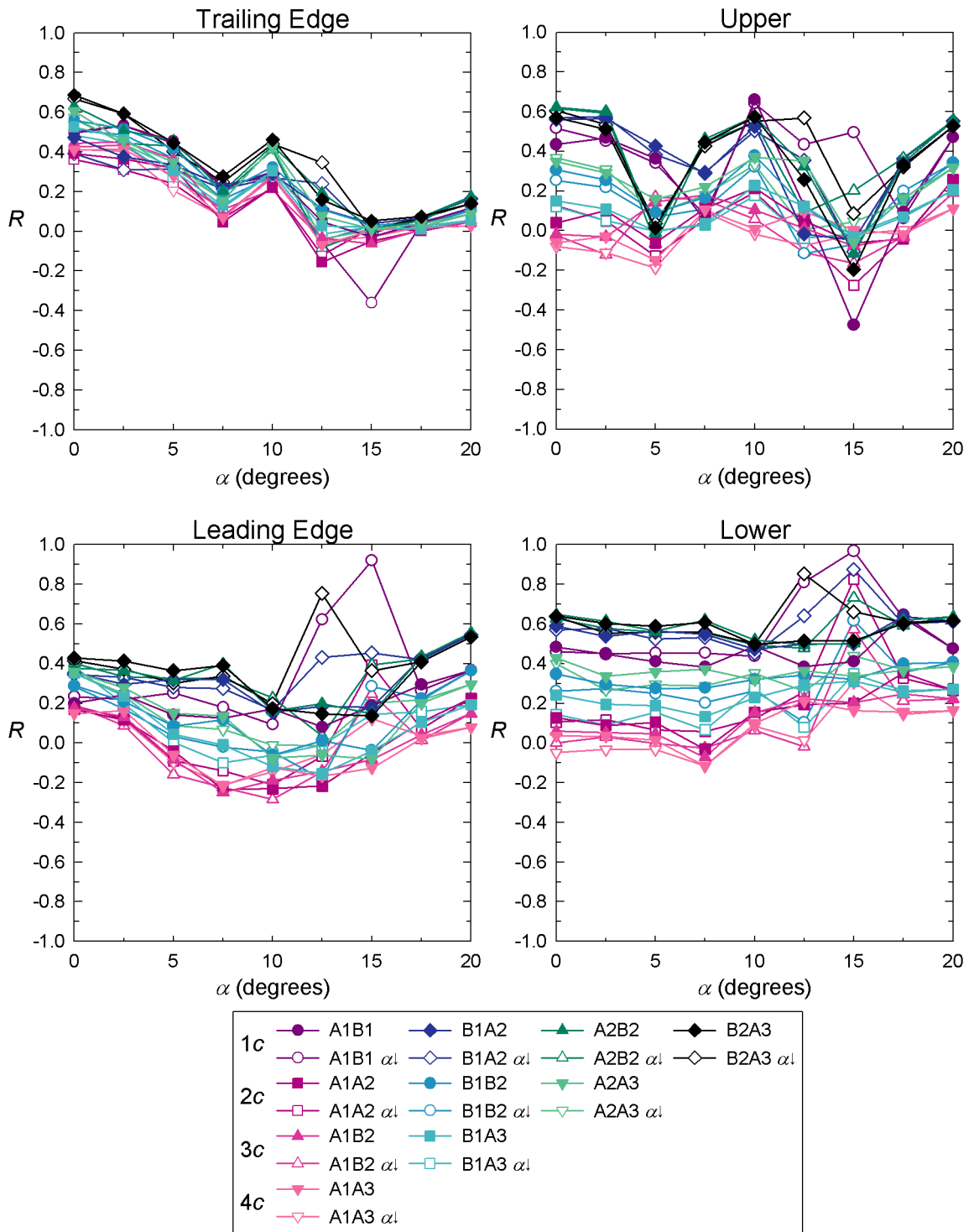


Figure 4-51 – NACA 0021 Correlation coefficients between taps in the 4 tap rows (A1, A2 and A3) and the equivalent taps in the 28 tap rows (B1 and B2) for the lowest turbulence flow ($I_u = 0.6\%$, no grid in the tunnel) for a smaller range of α ($0^\circ \leq \alpha \leq 20^\circ$) than in Figure 4-50.

The leading edge shows low levels of correlation at low α , probably due to variations in the freestream. These correlation coefficients reduce with the correlation coefficients becoming negative in several cases as α increases to about 10° ; however the levels of correlation are still very small. At 12.5° and 15° some of the decreasing α cases show high correlations, this may be due to the shear layer attempting to form a separation bubble, which it does not have sufficient energy to do. The result is a flapping of the shear layer. Alternatively, it is possible that this could have

something to do with end conditions as the two correlations closest to the ends (A1B1 and B2A3) show the large jumps in correlations. This is associated with a jump in σ measured at the taps for the decreasing α case as shown in Figure 4-52. As α is increased further, the correlations at the leading edge increase with the development of vortex shedding. The correlations reduce for $40^\circ < \alpha < 50^\circ$ in agreement with the findings for the upper taps. This may be due to the vortex being further from the tap. For $\alpha > 50^\circ$, the correlation remains fairly constant. It is hypothesised for these taps at high α the position the vortex sheds near the leading edge remains constant.

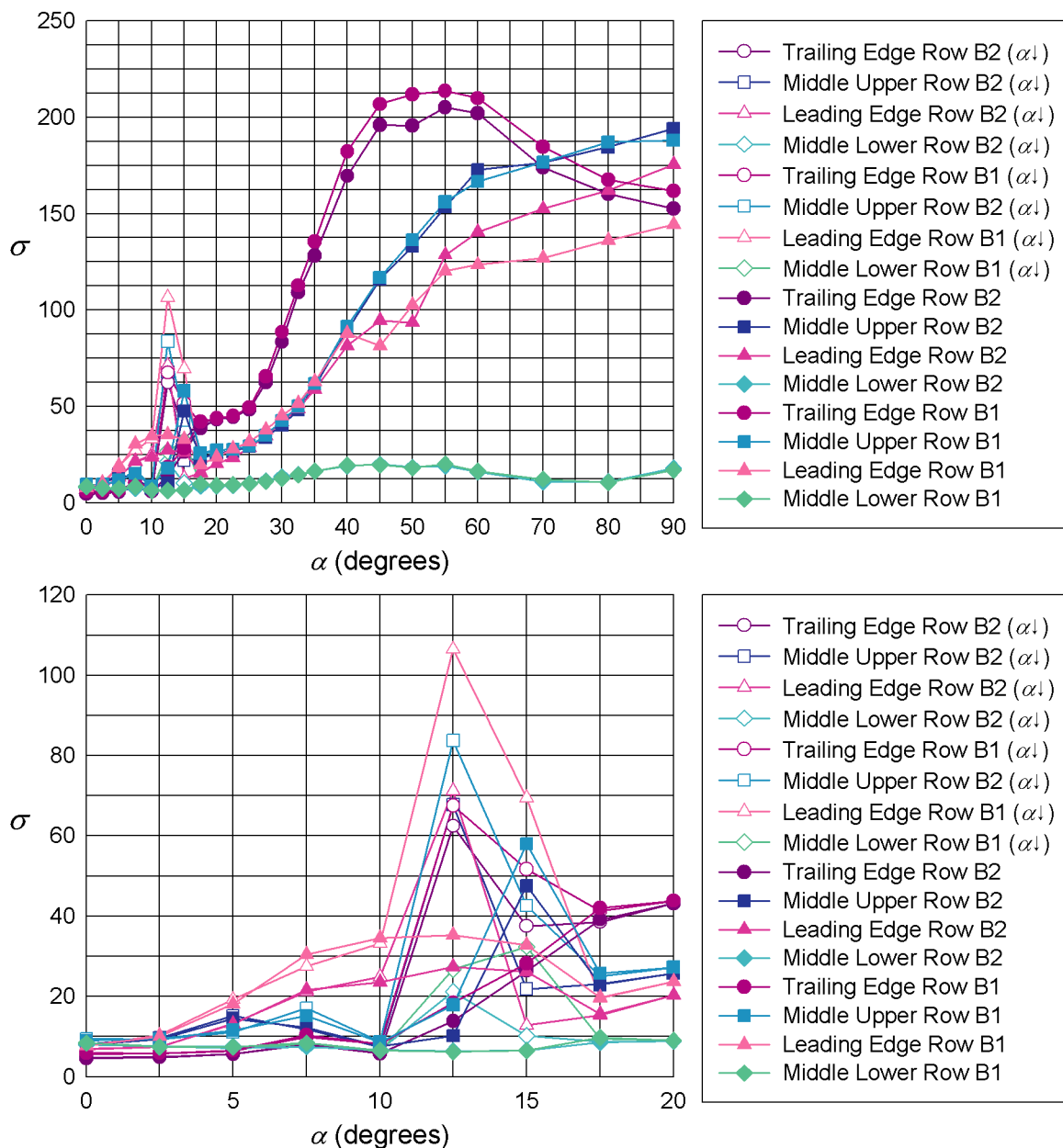


Figure 4-52 – NACA 0021 σ for the 4 taps in Rows B1 and B2 for which correlation coefficients were determined for the lowest turbulence flow (no grid in the tunnel). The lower plot shows the same information but for a smaller range of α ($0^\circ \leq \alpha \leq 20^\circ$) and σ than the upper plot.

The correlations for the lower taps remain fairly constant in bands related to the spanwise distance between the taps. Similar to the leading edge case, there is a jump in correlation for the decreasing α cases at about 12.5° and 15° . This is also associated with an increase, although smaller than seen for the leading edge case, in the σ for the middle lower taps for decreasing α seen in Figure 4-52.

It appears that the effect of the flapping shear layer also affects this tap, perhaps by altering the position of the stagnation point. For $20^\circ \leq \alpha \leq 50^\circ$ the correlations increase with increasing α . However, as α passes from 50° to 55° there is a sudden decrease in correlation. The time traces in Figure 4-53 show very well correlated oscillations at 50° . However, at $\alpha=55^\circ$ these oscillations are disrupted by “bursts” at irregular intervals which would naturally reduce the correlations. Looking back to the frequency analysis of the taps presented earlier, see Section 4.3.3, it can be seen that as α increases the frequency “noise” was observed increasingly further down the lower surface towards the trailing edge. For $\alpha > 70^\circ$ the correlations increase as the tap is becoming more tangential to the freestream and therefore only being exposed to the well correlated normal force.

Figure 4-52 also shows that the upper and leading taps increase in σ with increasing α as might be expected from increasingly stronger shedding. However, the trailing edge shows a decrease in σ for $\alpha > 60^\circ$. It is postulated that as α increases above this angle, it loses “sight” of the vortex from the leading edge since the shear layer from the leading edge moves further away from the trailing edge with increasing α . The lower tap shows smaller σ than the other taps as it was not as exposed to shedding or separation effects.

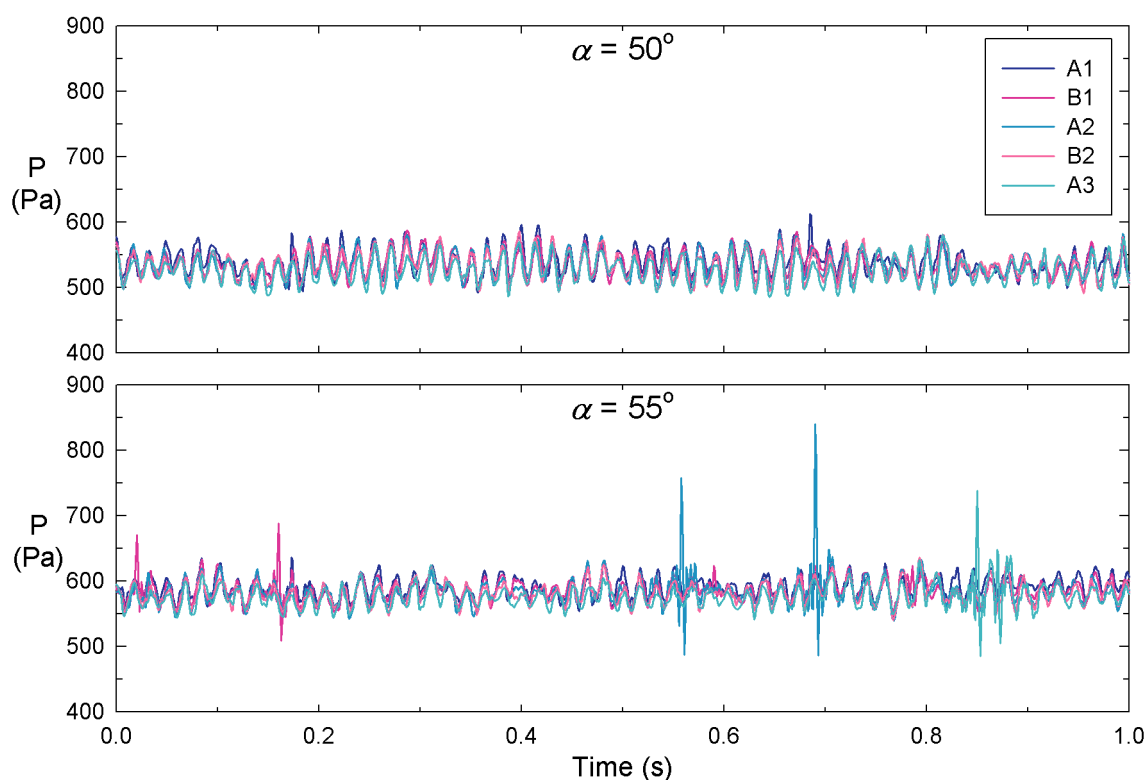


Figure 4-53 - Time traces seen by the lower surface tap in all rows for α of 50° and 55° .

The results obtained with the addition of a small amount of turbulence are shown in Figure 4-54. Comparing the results with the case of the lowest turbulence flow condition, it is seen that increased turbulence slightly reduces the amount of spread in the trailing edge correlation plot and reduces the size of the negative correlation at 15° . This is presumably due to the smaller hysteresis loop; however the general shape of the plots remains similar. The spread in the correlations for the

upper taps is also reduced at low α and the bands related to spanwise spacing become more prominent. Similarly, for the leading edge, the jumps for the decreasing α case at 15° are smaller or result in negative correlations, again presumably due to the smaller hysteresis loop. The lower taps show similar collapse of the bands of results and a smoother decrease for $\alpha > 40^\circ$. The loss of the “jump” is presumably due to lower levels of the bursting in this flow than that seen for the lowest turbulence flow in Figure 4-53 at $\alpha = 55^\circ$.

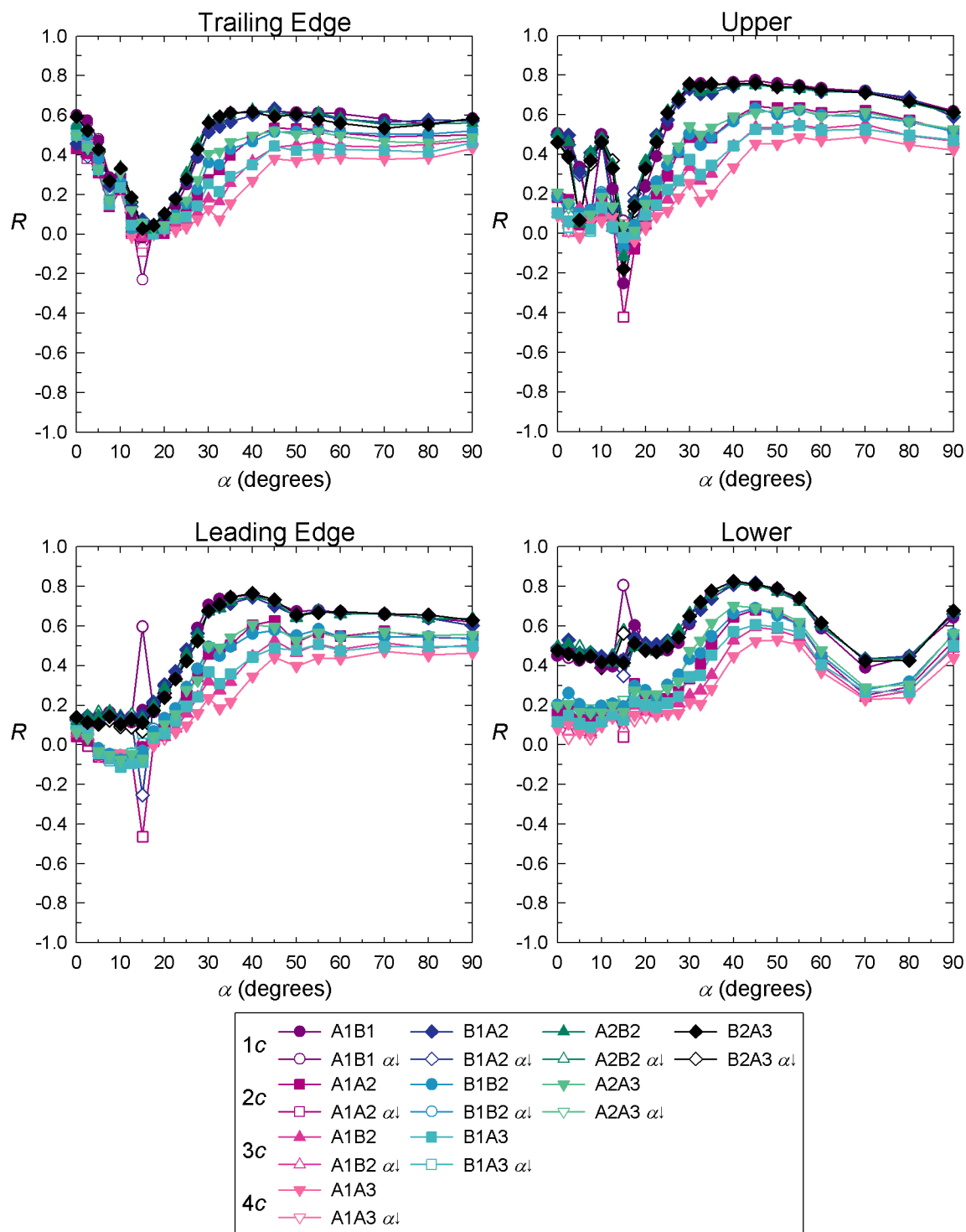


Figure 4-54 – NACA 0021 Correlation coefficients between taps in the 4 tap rows (A1, A2 and A3) and the equivalent taps in the 28 tap rows (B1 and B2) for the lowest turbulence flow ($I_u = 1\%$) with a integral length scale of about $1/3c$ (the small grid in position E).

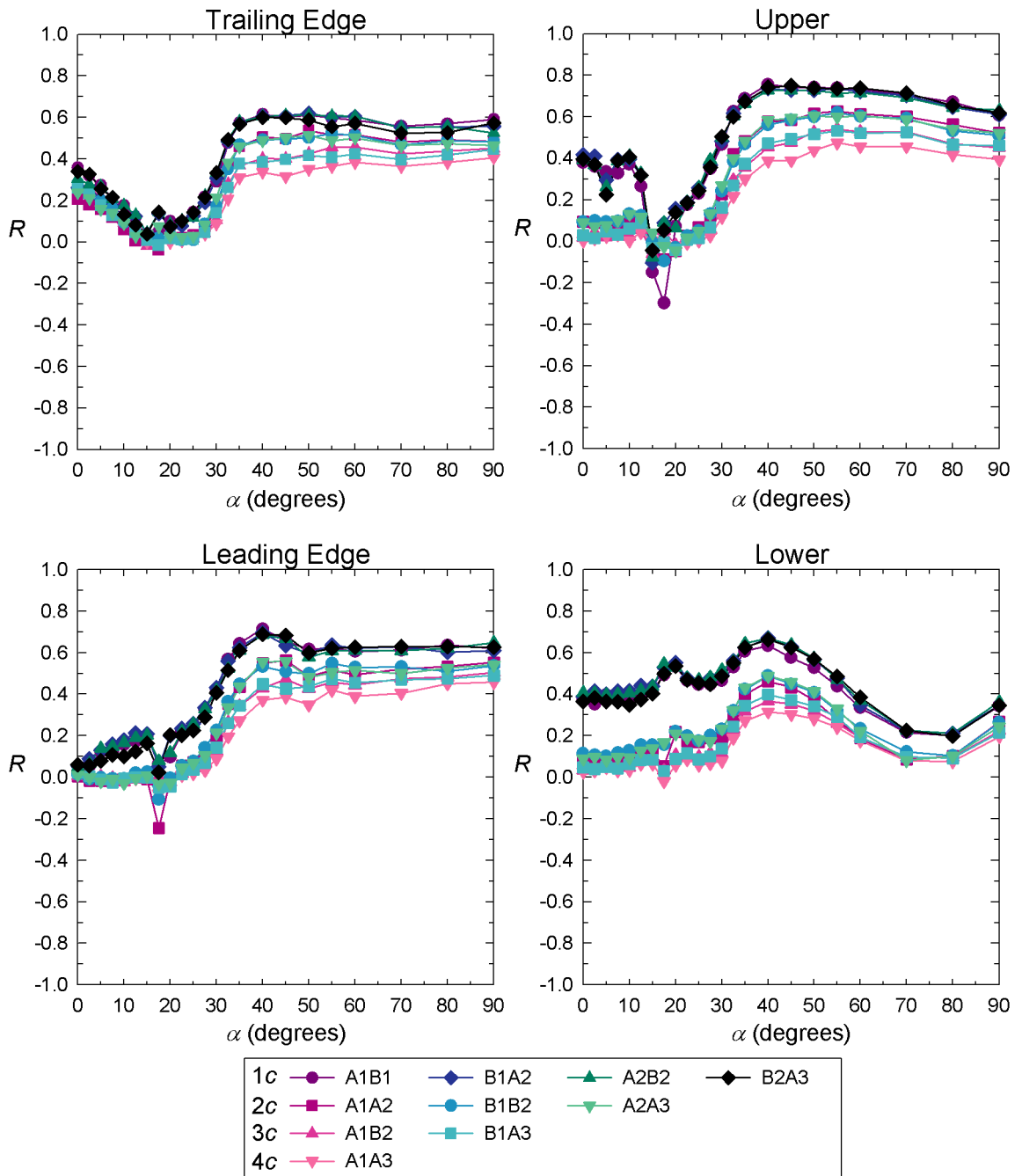


Figure 4-55 – NACA 0021 Correlation coefficients between taps in the 4 tap rows (A1, A2 and A3) and the equivalent taps in the 28 tap rows (B1 and B2) for the highest turbulence flow ($I_u = 3\%$) with a integral length scale of about $1/3c$ (the small grid in position A).

The addition of higher turbulence intensity levels reduces the correlation at small α for the trailing edge taps, as shown in Figure 4-55. This may be due to increased variations in the boundary layer due to the increased turbulence in the freestream. However, the increased turbulence refines the spatial bands in correlation further at high α although shedding clearly dominates correlation levels in this range. Similarly the upper taps show decreased correlation at low α but have much more defined “bands” throughout. The leading edge taps show no negative correlations at low α ; presumably because the signals are dominated by turbulence and so give a zero correlation. Similar “banding” can again be seen. There are small negative jumps in correlation associated with

stall. The lower taps show decreased correlation at all α and increase banding but with the same general shape as the lower turbulence graph. Presumably the increased turbulence in the freestream, and therefore the boundary layer, is reducing the correlation especially at high α for these taps, which are most exposed to boundary layer and turbulence fluctuations and less to wake fluctuations as they are upstream at high α .

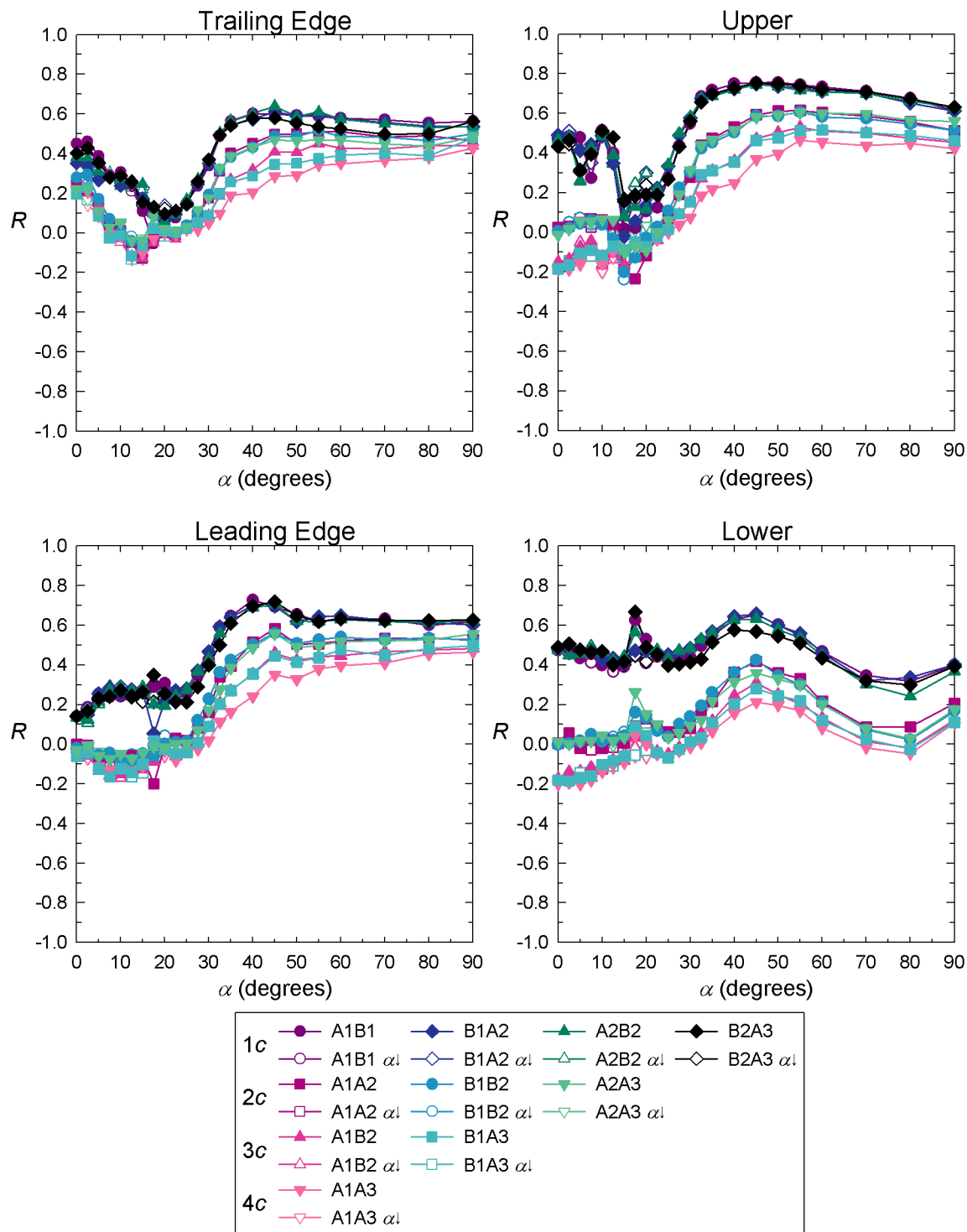


Figure 4-56 – NACA 0021 Correlation coefficients between taps in the 4 tap rows (A1, A2 and A3) and the equivalent taps in the 28 tap rows (B1 and B2) for the lowest turbulence flow ($I_u = 2\%$) with a integral length scale of about $1/2c$ (the medium grid in position E).

Increasing the integral turbulence scale but decreasing the turbulence intensity slightly from the flow condition used for Figure 4-55 (by using the medium grid in position E) gave the correlations

shown in Figure 4-56. The trailing edge and upper taps show pronounced bands at low α . Presumably the scale of the turbulence ($\sim 1/2c$) results in an increase in turbulence in the boundary layer and therefore lowers the correlation at low α , but similar levels were observed at high α where vortex shedding dominates. The leading edge taps at a separation of $1c$ show increased correlations at low α perhaps due to the freestream turbulence, but the correlations are still at very low levels. Again, at high α where vortex shedding dominates, the results are very similar to those seen for the no grid and small grid cases. The jump in correlation associated with stall at the lower tap is more pronounced than in the small grid position A case. The separations of $2c$ and $3c$ & $4c$ show two distinct bands (these separations formed one band in Figure 4-55). The $2c$ is similar to that in Figure 4-56 but $3c$ & $4c$ show slightly more negative correlations for all α .

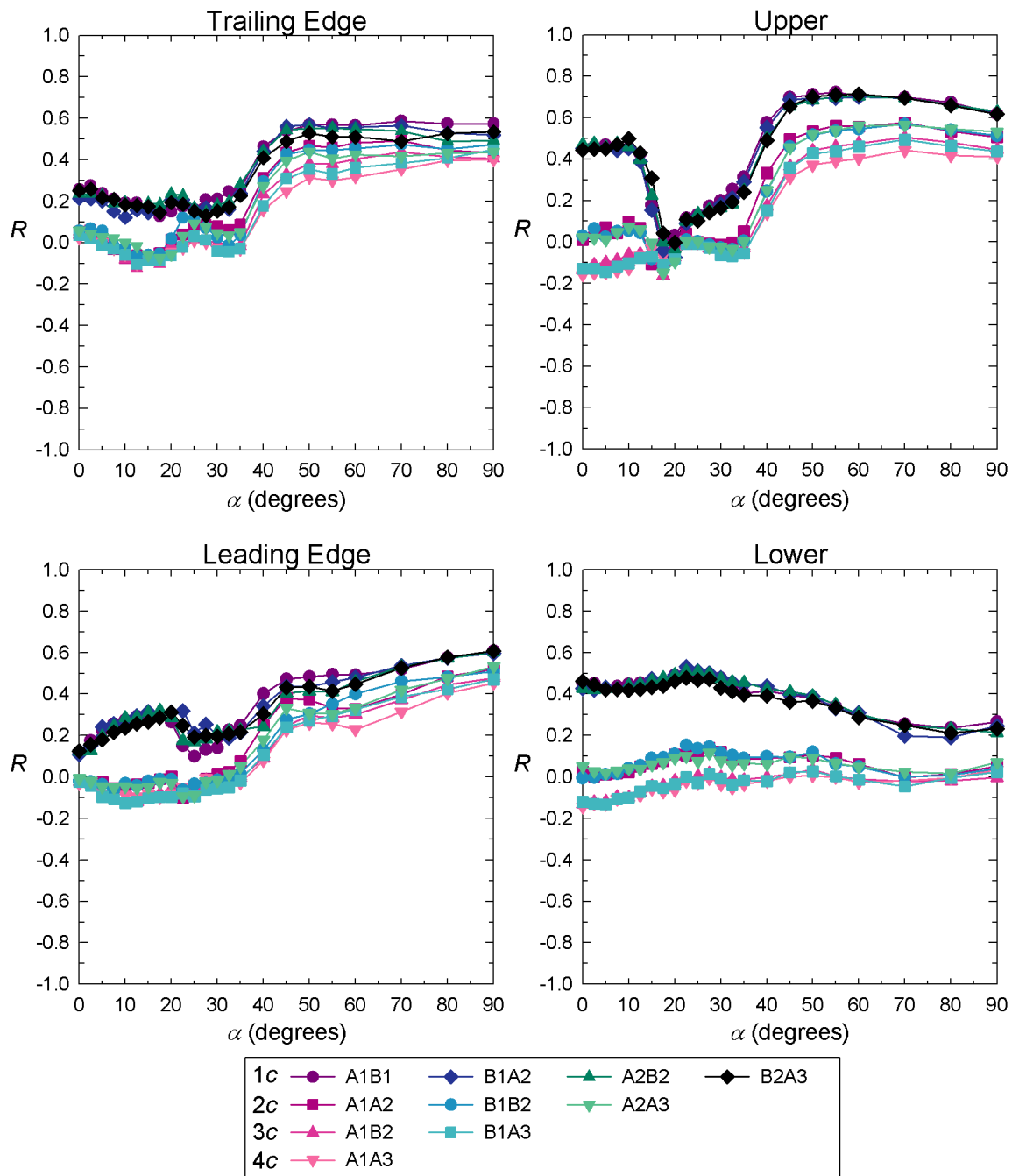


Figure 4-57 – NACA 0021 Correlation coefficients between taps in the 4 tap rows (A1, A2 and A3) and the equivalent taps in the 28 tap rows (B1 and B2) for the highest turbulence flow ($I_u = 6\%$) with a integral length scale of about $1/2c$ (the medium grid in position A).

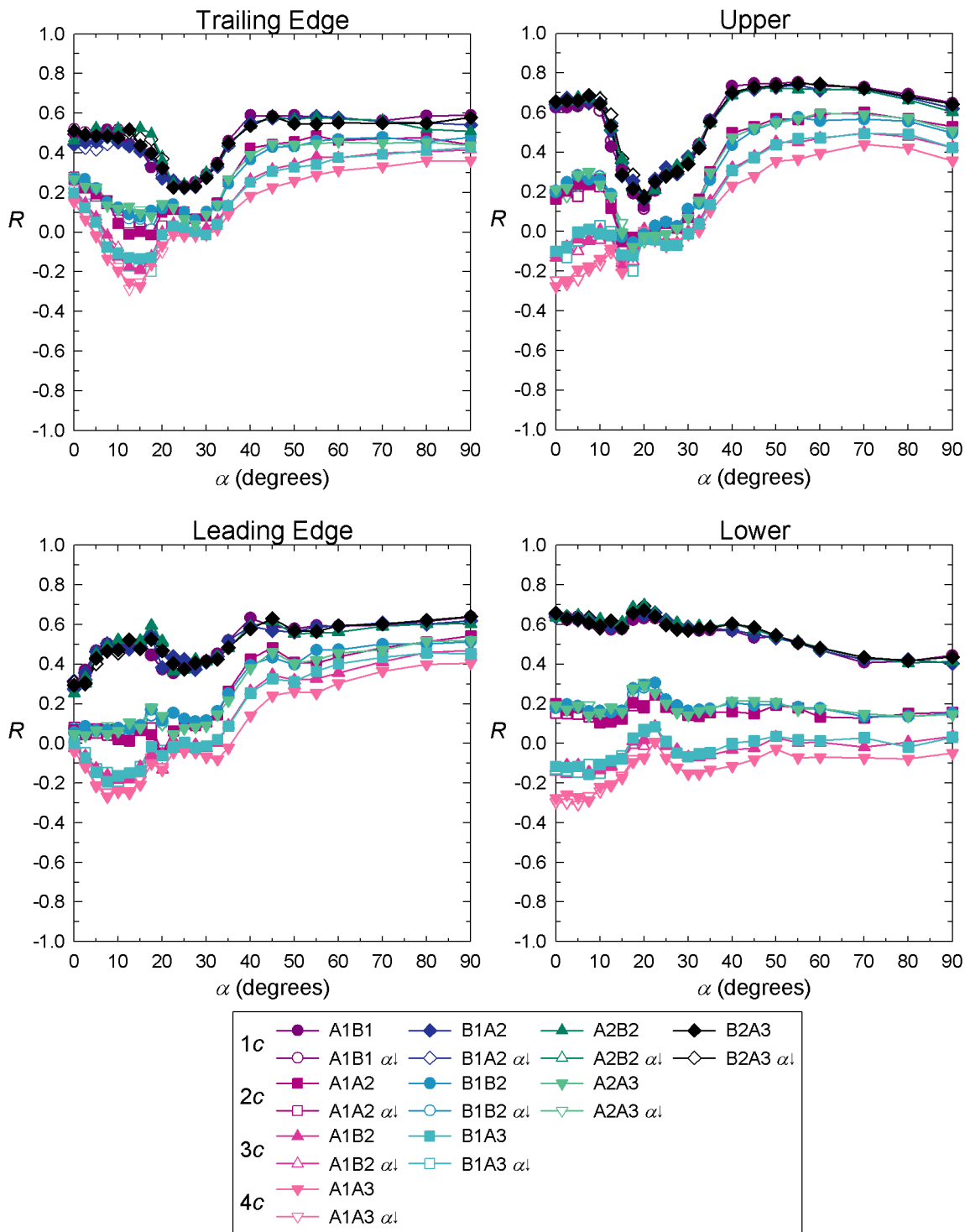


Figure 4-58 – NACA 0021 Correlation coefficients between taps in the 4 tap rows (A1, A2 and A3) and the equivalent taps in the 28 tap rows (B1 and B2) for the lowest turbulence flow ($I_u = 5\%$) with a integral length scale of about $1c$ (the large grid in position E).

A higher turbulence intensity flow at a similar integral length scale to that used for Figure 4-56 (produced by the medium grid in position A) is shown in Figure 4-57. The correlations at low α for the trailing edge taps are reduced and more constant than for the same grid in position E (shown in Figure 4-56). However, at high α where vortex shedding dominates the result are similar to all the cases presented previously in this section. The upper taps show fairly constant correlation until the drop associated with stall. The leading edge taps show small magnitude in correlations and a generally increased trend to the levels of correlation seen earlier due to shedding. The lower

surface taps on the other hand show decreased correlation, presumably due to the effect of increased turbulence in the boundary layer.

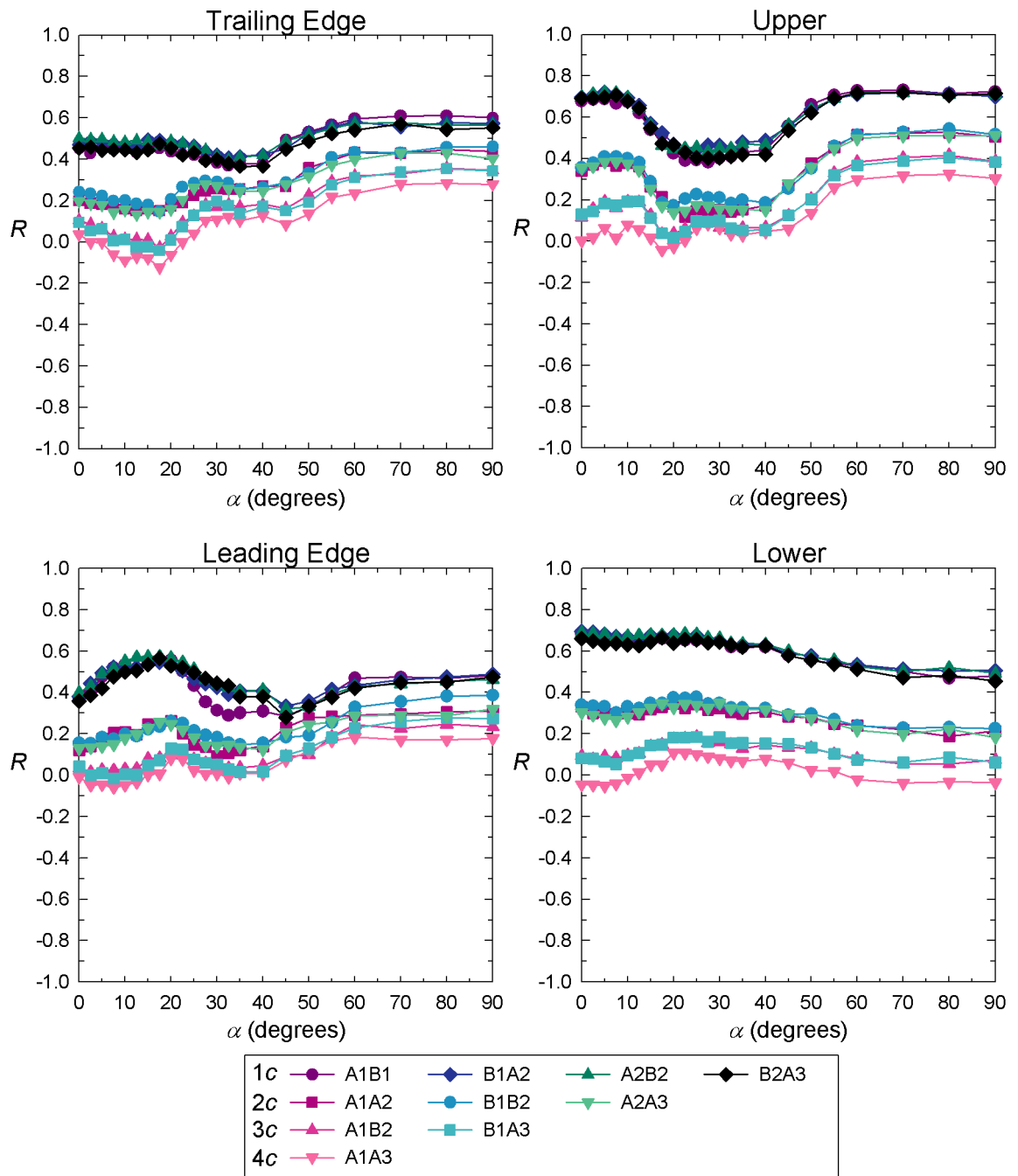


Figure 4-59 – NACA 0021 Correlation coefficients between taps in the 4 tap rows (A1, A2 and A3) and the equivalent taps in the 28 tap rows (B1 and B2) for the highest turbulence flow ($I_u = 13\%$) with a integral length scale of about $1c$ (the large grid in position B).

The large grid in position E produces integral turbulence length scales about $1c$ and a turbulence intensity of 5%; the resulting correlations coefficients are shown in Figure 4-58. The correlations at the trailing edge increase and remain fairly constant for the spanwise spacing of $1c$ until stall. The other separations show a generally decreasing trend. All cases show very distinct bands. At high α , the vortex shedding again dominates and the correlations are at similar levels to seen for the other flow cases presented earlier in this section. The upper taps also show fairly constant

levels before stall and then the correlation coefficients increase to levels seen earlier that were associated with shedding. For small values of α the leading edge shows reduction in variations due to increased turbulence levels in the freestream. As α increases similar correlation levels to those seen earlier due to vortex shedding were observed. The lower tap was dominated by the freestream turbulence and showed fairly of constant correlation coefficients, with only a slight decrease with increasing α and a small rise in correlation associated with stall.

Increasing turbulence intensity further reduces much of the variation in the correlation coefficients, as shown in Figure 4-59. Freestream turbulence levels affected most of the results and reduced some correlations at high α . This corresponds to the different shedding frequencies seen earlier.

The correlation coefficients show that, while the structures associated with stall and vortex shedding were three-dimensional, they were reasonably well correlated over short spanwise distances. The large correlations associated with the decreasing α part of the hysteresis loop near stall and at high α are associated with vortex shedding. Highly correlated shedding across the span of a blade will clearly have a negative impact on the blade's structural loading and may need to be considered in the design of stall controlled wind turbines. However, this effect may be reduced on rotating, tapered and twisted wind turbine blades.

Chapter 5

NACA 4421 Aerofoil

5.1 Introduction

The NACA 4421 aerofoil section has been used on wind turbines and, by making direct comparisons with the results from the NACA 0021 aerofoil section, allows investigation into the effects of camber. Overall comparisons between the three aerofoil sections tested will be left until Chapter 7. This chapter will briefly cover the main results for the NACA 4421 aerofoil section as many features of the results have been covered in detail for the NACA 0021. Some of these results have been presented at conferences (Swalwell, Sheridan & Melbourne, 2003a, , 2004).

5.2 Mean Results

5.2.1 Comparison

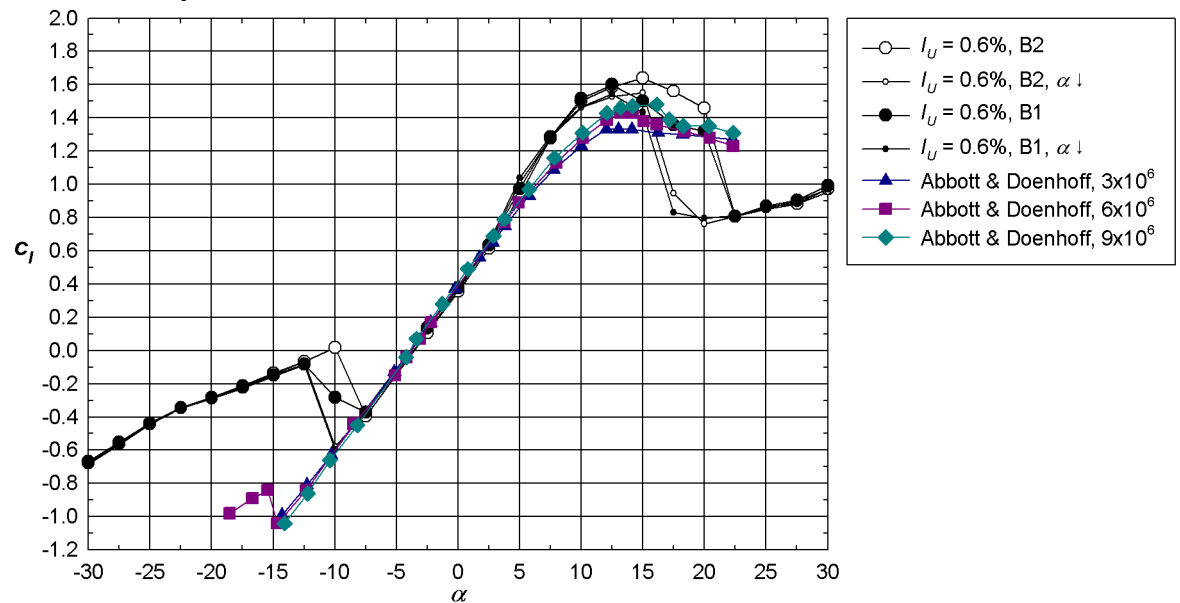


Figure 5-1 - Comparison of the data from the current experiments (black points) at $Re = 2.72 \times 10^5$ with that from Abbot & Doenhoff (1959).

No suitable comparison data for the NACA 4421 aerofoil section was found. The best comparison was from Abbot & Doenhoff (1959) but was at an order of magnitude higher Re than the current experiments, the comparison of the lift coefficients is shown for completeness in Figure 5-1. There is a reasonable match for the lower part of the linear attached region but at higher α the characteristic responses are quite different, as would be expected with the likely absence of separation bubbles for the higher Re flows. However, this aerofoil section used the same method (down to the same chordwise tap placement) as for the NACA 0021 aerofoil. The NACA 0021 aerofoil section results showed good agreement with previous experiments and so the experimental method has been validated.

5.2.2 Effect of Added Turbulence

Because of the asymmetrical shape of the NACA 4421 aerofoil section measurements were taken for $-90^\circ \leq \alpha \leq 90^\circ$. For $0^\circ \leq |\alpha| \leq 30^\circ$ measurements were taken every 2.5° , for $30^\circ < |\alpha| \leq 60^\circ$ every 5° , and for $60^\circ < |\alpha| \leq 90^\circ$ every 10° . Hysteresis was checked for in the lowest turbulence measurements (no grid) and for each grid. Due to an error in construction the model had to be mounted upside-down in the tunnel. This should not affect results and the α have been corrected to reflect the normal frame of reference.

Figure 5-2 shows the mean c_l , c_d and $c_{m, 1/4c}$ calculated from the Row B1 and Row B2 results for increasing α between -90° and 90° , the decreasing α measurements are also shown between 30° and -30° . The negative α results show much the same shape for all three coefficients as the positive α case except that, for c_l and $c_{m, 1/4c}$, the sign of the coefficients has been reversed. For c_l there is a local minimum at $\alpha = -50^\circ$ which corresponds to the local maximum at $\alpha = 45^\circ$. These extremes are caused by the deflection of the stalled flow by the body downwards as discussed for the NACA0021, however the camber of the body shifts the extreme to -50° . The stall region around $\alpha = -10^\circ$ is very sharp. This was expected as the concave surface would make it likely to separate at the leading edge or trailing edge but not in between. Row B2 stalls more sharply than Row B1 in the increasing α case. Presumably this difference is due to three-dimensional spanwise structures. The decreasing α case shows very similar results for both rows. The causes will be examined in more detail shortly when the C_p measurements are examined.

The linear attached region shows results that are generally very well matched from both rows although there is some spread in the results most notably at $\alpha = 5^\circ$. The -5° measurement was omitted from Figure 5-2 because of the possibility of a mistaken repeat of the -2.5° measurement. This measurement for increasing α gave an odd result which was very close to that recorded at $\alpha = -2.5^\circ$. As there should be no difference between increasing and decreasing α in this fully attached flow region, the decreasing α results should indicate the correct measurement.

The maximum c_l for Row B1 was recorded at $\alpha = 12.5^\circ$. It then gradually decreased before a sharp drop at $\alpha = 22.5^\circ$. For Row B2, the increasing α results show a maximum c_l at $\alpha = 15^\circ$ and are higher than the Row B1 results until the sharp drop to the same value at $\alpha = 22.5^\circ$. The decreasing α results show hysteresis between $12.5^\circ < \alpha < 22.5^\circ$. There are differences in this range between the c_l from the two rows with the Row B2 measurements giving larger c_l than the Row B1 measurements except at $\alpha = 20^\circ$. The variation in the measured coefficients between Rows B1 and B2 will be discussed further when the mean C_p results are examined later in this section. There are also slight differences between the c_l calculated from the measurements at the two rows around the next local maximum at $\alpha = 45^\circ$. However the results are almost identical for $\alpha \geq 55^\circ$.

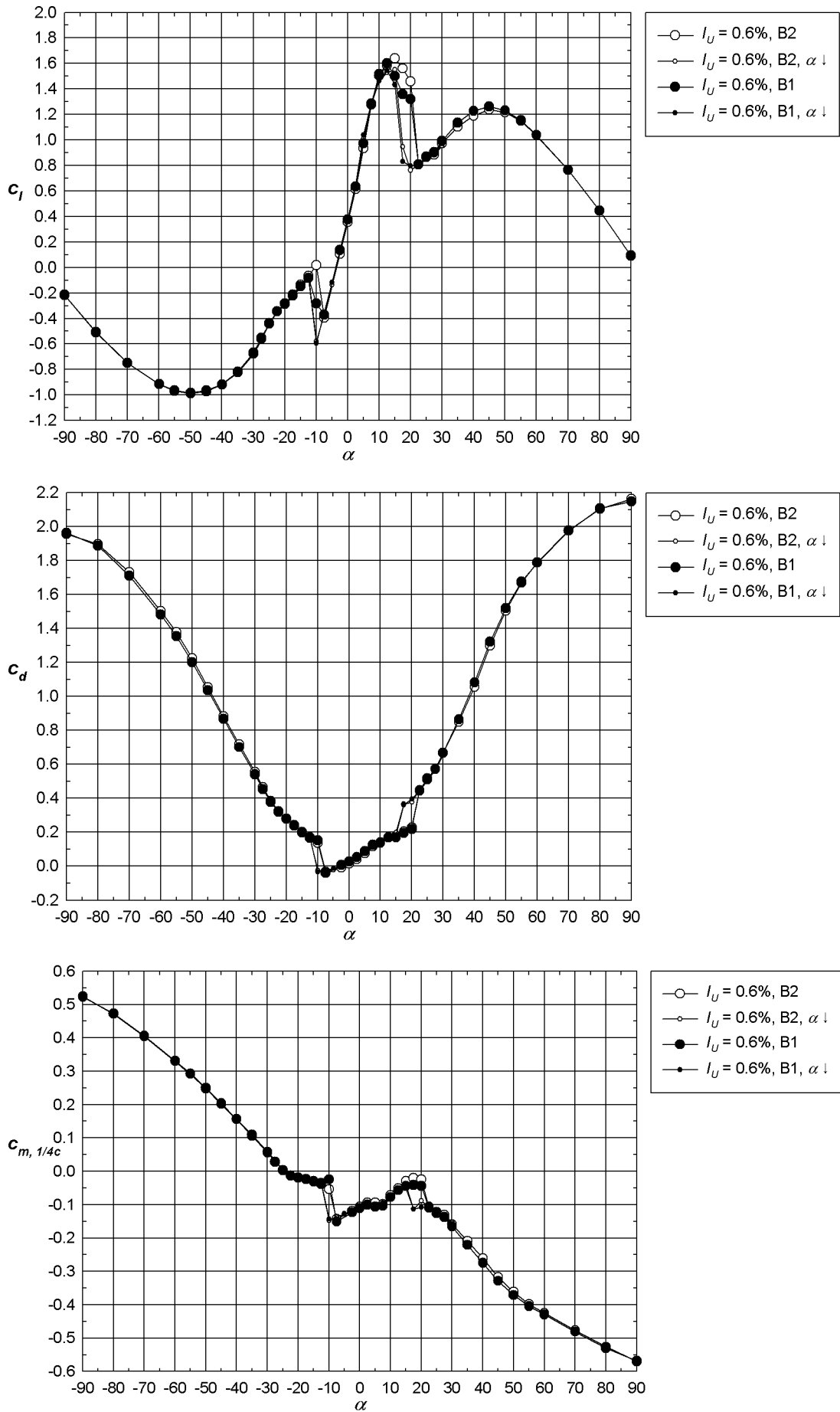


Figure 5-2 – NACA 4421 mean coefficients of lift, drag and of moment about the quarter chord for the lowest turbulence case (no grid).

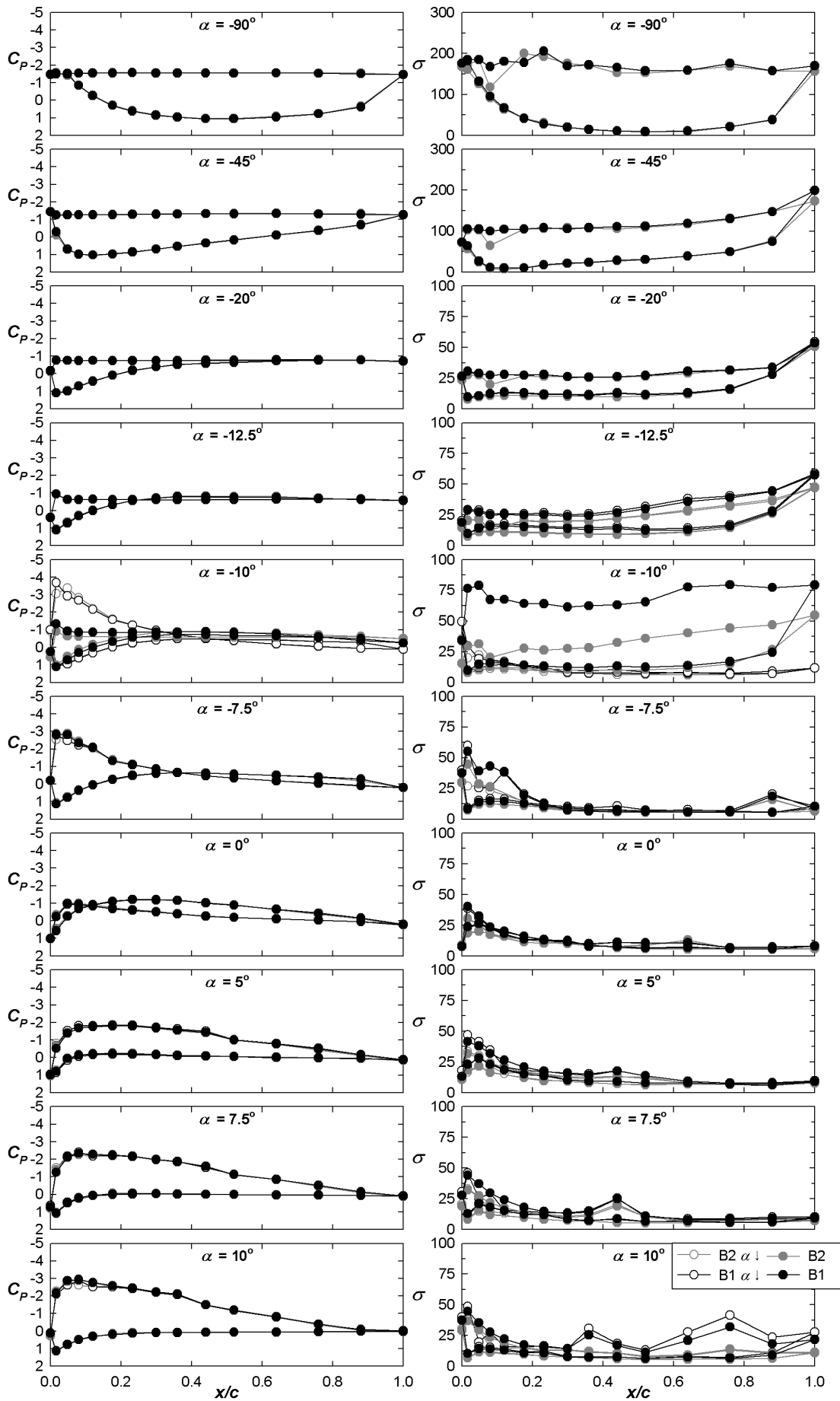


Figure 5-3(a) –NACA 4421 coefficients and standard deviations of the pressures around the aerofoil at selected α for the lowest turbulence flow (no grid). Note the scale of the σ plots changes from a maximum of 300 to a maximum of 100 for $\alpha \geq -20^\circ$.

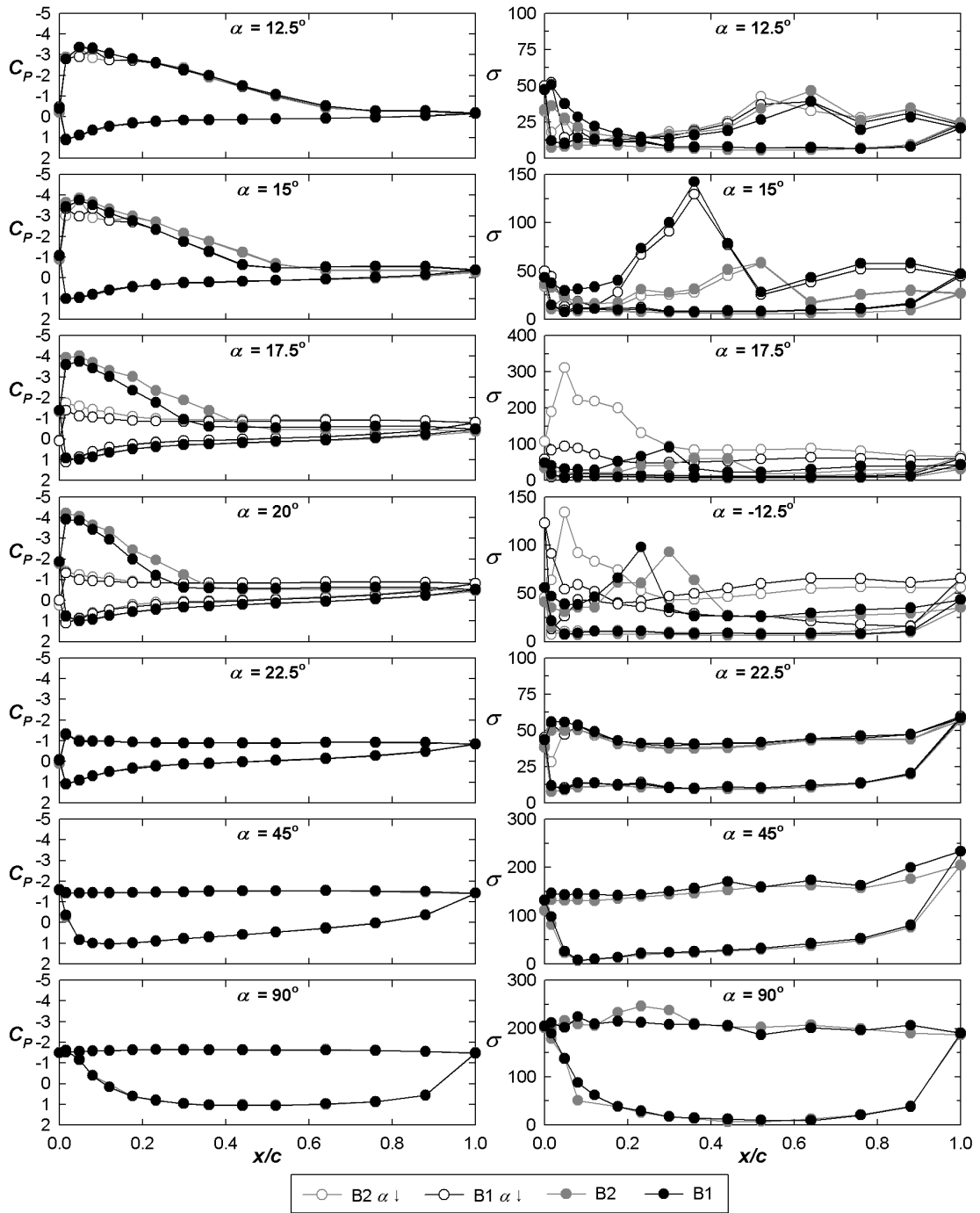


Figure 5-3(b) –NACA 4421 coefficients and standard deviations of the pressures around the aerofoil at selected α for the lowest turbulence flow (no grid). Note the changes of scale of the σ plots.

At $\alpha=90^\circ$ the lift is positive, showing some deflection of the wake downwards. At $\alpha=-90^\circ$ there is some negative lift of a larger magnitude than the positive 90° case. This corresponds to the body which is rounded in the direction of the flow causing more deflection of the flow than the body which is slightly concave. As would be expected the results for c_d are reversed with the smaller magnitude of drag occurring at $\alpha=-90^\circ$ where the slightly rounded profile causes less drag than the slightly concave profile presented at $\alpha=90^\circ$.

There are some slight differences between c_d from the Row B1 and B2 measurements but in general they are very similar. Hysteresis loops are apparent at the same angles as noted for the lift.

The most notable feature of the c_d plot is the negative drag recorded for $-10^\circ \leq \alpha < 0^\circ$. This is due to only measuring the drag on the surface of the aerofoil section and therefore only recording the pressure drag. As the aerofoil has a concave surface, there are some components of drag in the opposite direction to the flow. However the skin friction drag (which was not measured) would exceed the pressure drag at these α .

$c_{m, 1/4c}$ shows a general decrease with increasing α except in the attached flow region where it increases slightly with increasing α . Hysteresis can be seen as for c_l and c_d . Differences between $c_{m, 1/4c}$ calculated from Row B1 and Row B2 measurements are seen within the same range of α where differences were observed in c_l . The magnitude of $c_{m, 1/4c}$ was slightly greater at $\alpha = 90^\circ$ than at $\alpha = -90^\circ$.

Figure 5-3 shows the mean C_p and the σ of the pressure signals at each tap at various α for the lowest turbulence flow. The 5th tap from the leading edge in Row B2 on the concave surface (the lower surface at $\alpha = 0^\circ$) was excluded from the calculation of the force and moment coefficients as it appeared to be blocked as both the C_p and σ were lower than the other measurements. The tap before this one in Row B2 may have been partially blocked as the σ measured at this tap was generally lower although the C_p values seem reasonable. At $\alpha = -90^\circ$ the pressures at the leading edge were very similar on both the concave and convex surfaces and were fairly constant across the downwind concave surface. The convex upwind surface had C_p increasing and σ decreasing from the leading and trailing edges but was fairly constant across the mid-chord after these gradients.

As α increased to -45° the C_p on the lower concave surface stayed much the same while, on the upper convex surface, the local maximum in C_p moved toward the leading edge. The σ generally decreased except at the trailing edge. These trends continued as α increased further as can be seen in the $\alpha = -20^\circ$ and -12.5° cases. By $\alpha = -12.5^\circ$ the σ for Row B1 are slightly higher than for Row B2. At -10° the flow is attached at the leading edge in the decreasing α case which results in the larger magnitude of c_l . For the increasing α cases there is a slightly smaller magnitude for Row B2 than Row B1 near the leading edge which resulted in the large difference in c_l noted earlier. There is also a clear difference in σ with Row B1 having a much higher σ than Row B2. For the decreasing α case the σ is much lower except at the leading edge.

By $\alpha = -7.5^\circ$ all cases have much the same C_p indicating at least some attached flow. There are peaks in σ near the leading edge and a small jump near the trailing edge. Continuing through the attached flow region to 0° , 5° and 7.5° the same general features of smooth C_p plots and generally low σ except at the leading edge are seen. There is a small jump in σ at 7.5° around $0.5c$. This suggests a separation region, but the c_l curve is still linear in this region.

At 10° the C_p is still smooth but the σ near the trailing edge for Row B1 has started to increase. This is true for both tapping rows by 12.5° and there is a flat region in C_p for about the last $\frac{1}{4}c$. By 15° this flat region in C_p has extended towards about $0.5c$. The higher c_l for Row B2 seems to be caused by a slightly increased magnitude of C_p before the flat region. The slightly lower results for α decreasing seem to be due to a smaller peak at the leading edge. The σ has a peak at about $0.4c$ for Row B1. There is a smaller peak for Row B2 at about $0.6c$. These flat regions in C_p and the peaks in σ are associated with separation of the boundary layer as the aerofoil section stalls. The decreasing α cases seem fully stalled by 17.5° with large peaks in σ near the leading edge especially for Row B2 (note change in scale of the σ plots). This is associated with a slightly increased c_l . Similar peaks in σ to that seen at 15° were seen in the decreasing α case.

By 20° the σ for the decreasing α has decreased but there are still large peaks near the leading edge. The peaks in σ for the increasing α case have moved further towards the leading edge as have the separated flat region in C_p . All cases appear fully stalled at 22.5° . Similar C_p and σ as seen for the high negative α were seen as α increased to 90° .

Figure 5-4 shows the mean coefficients of lift, drag and moment about the quarter chord for turbulent flows of integral length scale of about $\frac{1}{3}c$ and various turbulence intensities. In concurrence with Stack's (1931) results, the maximum c_l during stall at positive α was reduced with the addition of turbulence. The size of the hysteresis loops at both positive and negative α was reduced compared to the data taken with no grid in the tunnel even when the lowest turbulence intensity of 1% was applied. The small increase in turbulence intensity to 2% eliminated the hysteresis loop entirely. Decreasing measurements were also taken for the higher turbulence intensity cases but are not shown as hysteresis had been eliminated and the extra lines would have cluttered the figures. However, a clearer plot can be seen of the hysteresis loops can be seen later in this section when the increasing and decreasing α cases for various flow are compared, see Figure 5-10.

Increased turbulence intensity reduced the sharpness of stall at both positive and negative α . This is most easily seen in the c_l plot where the delay in complete stall is remarkable especially at negative α where stall was previously very sharp. Interestingly the magnitude of the local minimum during stall at negative α was increased by the addition of turbulence. However, the magnitude of c_d and the magnitude of $c_{m, 1/4c}$ at $\pm 90^\circ$ were decreased by the addition of turbulence compared to the lowest turbulence case presented in Figure 5-2. The addition of turbulence did not affect the occurrence of negative c_d due to only using surface pressure measurements to determine drag.

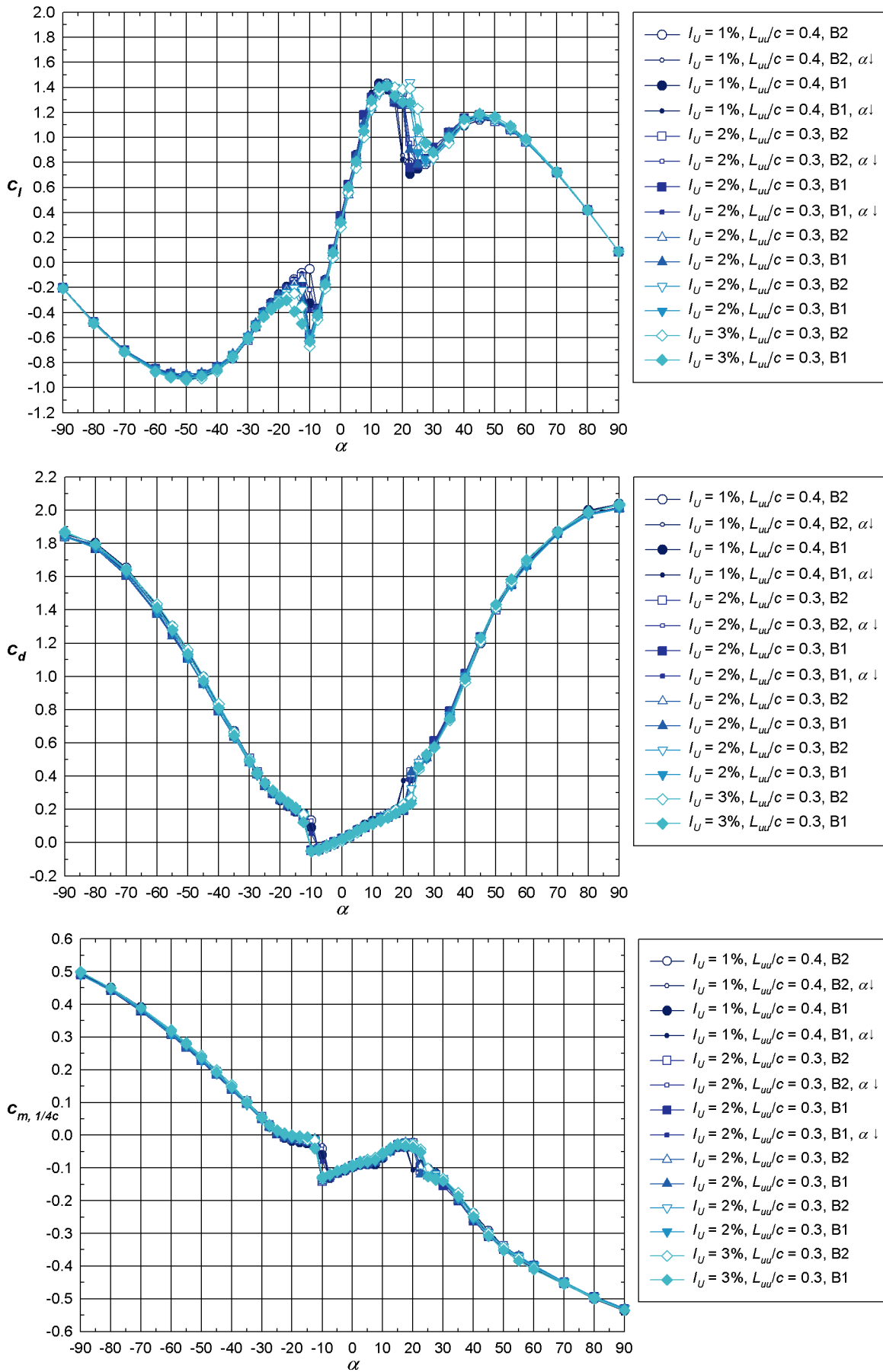


Figure 5-4 – NACA 4421 mean coefficients of lift, drag and of moment about the quarter chord with the integral turbulence length scale $\sim 1/3c$ (small grid).

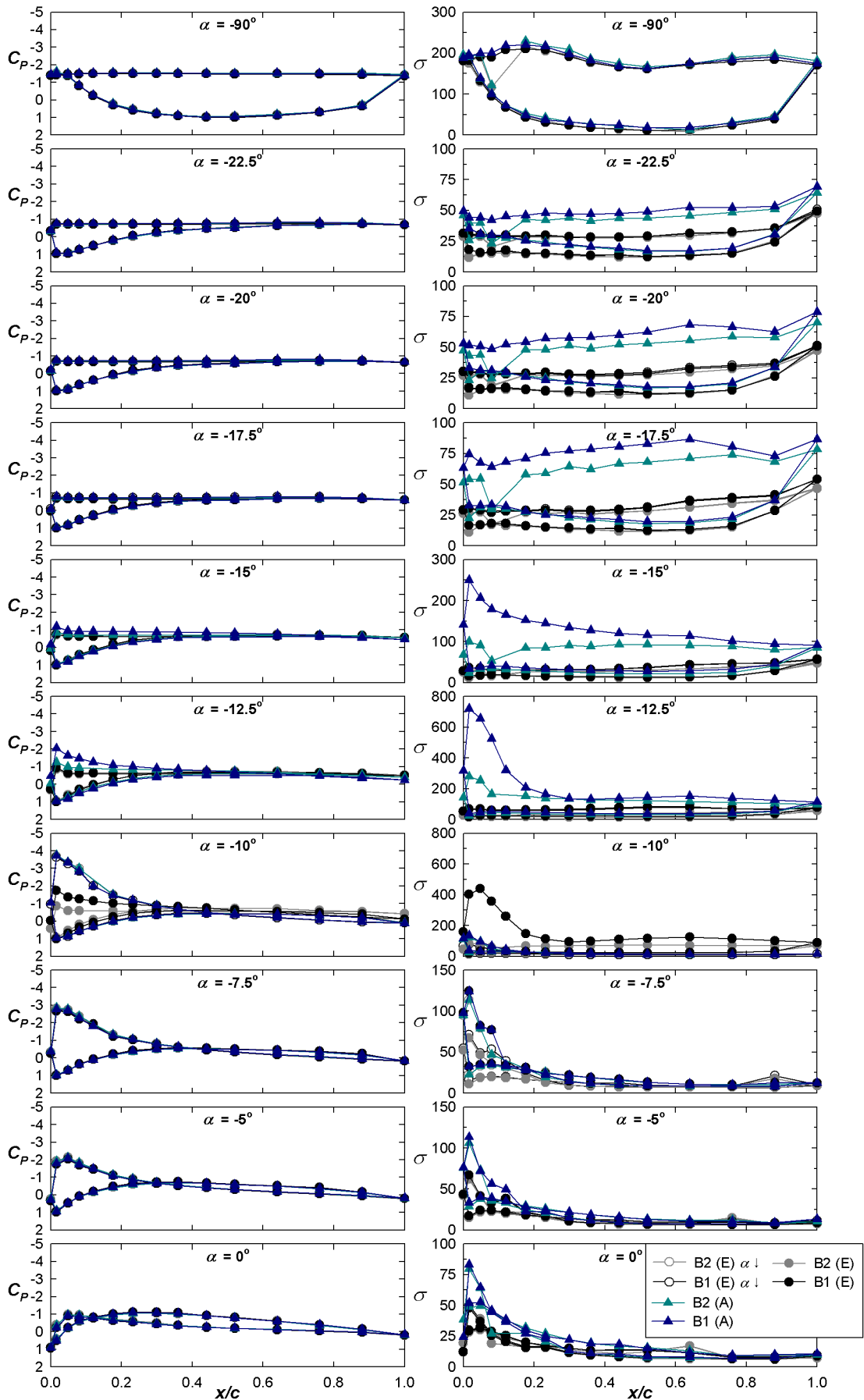


Figure 5-5(a) –NACA 4421 coefficients and standard deviations of the pressures around the aerofoil with turbulence integral length scale $\sim 1/3c$ for the lowest and highest turbulence intensities (small grid at the closest (A) and furthest positions (E) from the model). Note the changes in scale of the σ plots.

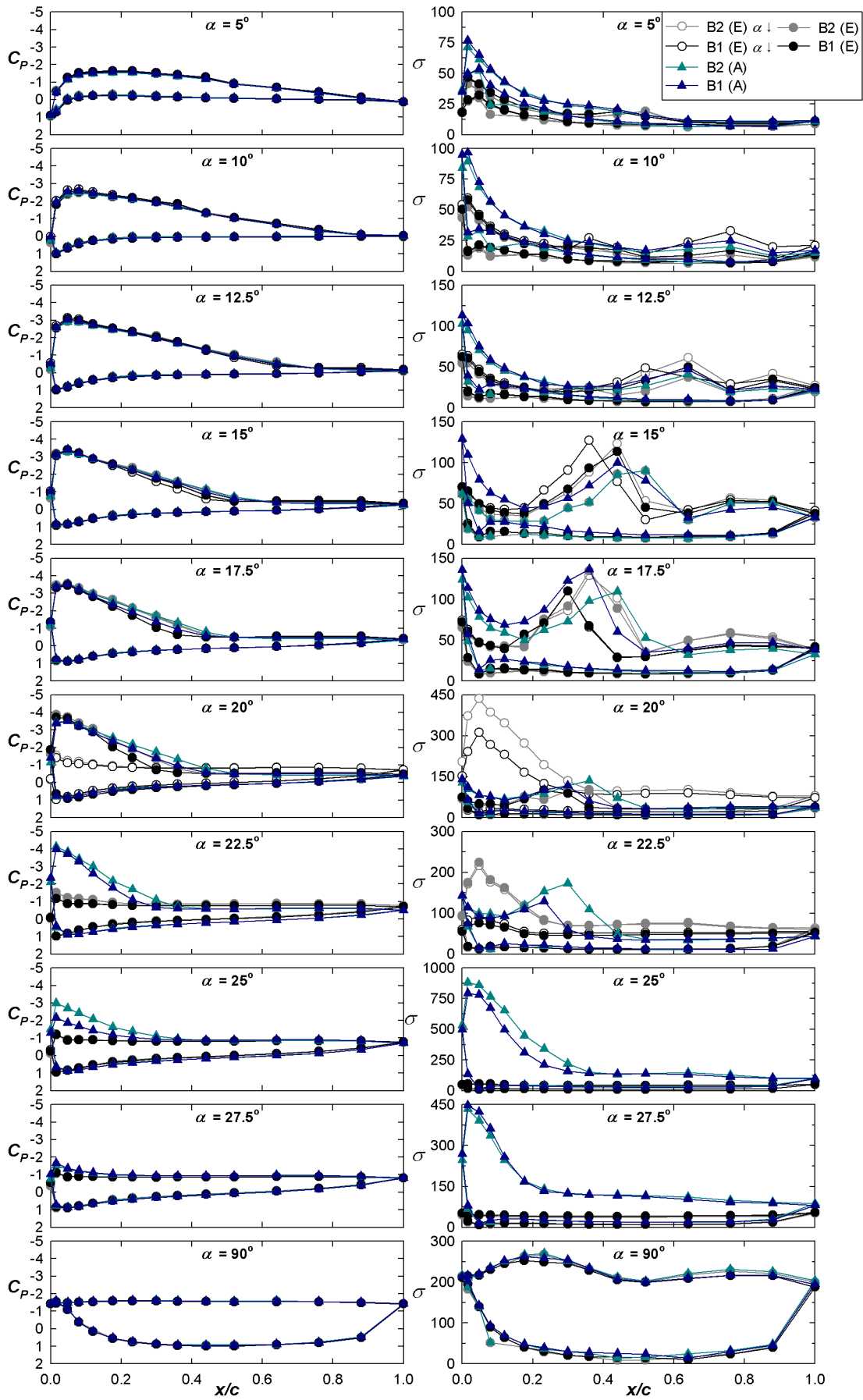


Figure 5-5(b) –NACA 4421 coefficients and standard deviations of the pressures around the aerofoil with turbulence integral length scale $\sim 1/3c$ for the lowest and highest turbulence intensities (small grid at the closest (A) and furthest positions (E) from the model). Note the changes in scale of the σ plots.

Figure 5-5 shows the mean C_p and the σ of the pressure signals from the taps in rows B1 and B2 for the about $1/3c$ integral turbulence length scale (small grid) for the highest and lowest turbulence intensities (grid in positions A and E). The results at $\alpha = -90^\circ$ in Figure 5-5 look very similar to those at the same angle but in a lower turbulence intensity flow presented in Figure 5-3. For $\alpha = -22.5^\circ$, -20° and -17.5° there is little difference in C_p but significantly higher σ for the higher turbulence flow case. By $\alpha = -15^\circ$ there is a slight increase in the magnitude of C_p at the leading edge for the highest turbulence flow case. At this integral length scale, this peak is more pronounced for Row B1 than B2. This corresponds to a jump in σ for this case with the peak in σ near the leading edge also higher for Row B1 than B2. The peaks in C_p and σ increase in magnitude at $\alpha = -12.5^\circ$ for the highest turbulence intensity at this turbulence integral length scale. By $\alpha = -10^\circ$ there are also small suction peaks at the leading edge for the lowest turbulence intensity of this turbulence integral length scale, with Row B1 having a more pronounced peak than B2 as occurred for the higher turbulence intensity case at $\alpha = -15^\circ$. This corresponds to an increase in σ for this tapping row although the σ for the higher turbulence flow have reduced. This increase in σ appears to be associated with partially attached states. By -7.5° where in all the cases the aerofoil is in the linear attached portion of the c_l curve the σ is reduced and slowly reduces further as α goes to 0° .

At $\alpha = 10^\circ$ there is a small peak in σ and a short flat region in C_p on the suction surface near the trailing edge. As α increases to 17.5° the peak in σ moves towards the leading edge as does the start of the flat region in the C_p plots, these features indicate separation of the boundary layer. At $\alpha = 20^\circ$ in the decreasing α case for the lowest turbulence intensity, the flow is mainly separated except for a small peak in C_p near the leading edge associated with a large peak in σ as seen at negative α earlier. The peaks in the other cases are near the onset of the flat region of the C_p curves. By 22.5° , both increasing and decreasing α cases for the lowest turbulence intensity flow of this integral length scale are mostly stalled and the leading edge peaks are especially evident on Row B2. σ peaks associated with the flat region of the higher turbulence intensity C_p plots are also evident. By 25° and 27.5° , leading edge suction peaks associated with high σ peaks are seen for the higher turbulence intensity flow. By $\alpha = 90^\circ$, the plots are very similar to those observed with no grid in the tunnel (see Figure 5-3).

Figure 5-6 shows c_l , c_d and $c_{m, 1/4c}$ for integral turbulence length scales about $1/2c$ for various intensities. At negative α the minimum c_l in the stalling region reduced markedly for the higher turbulence intensities. The local maximum in the stalling region at positive α remained about the same or was reduced, but at both positive and negative α , full stall was delayed by the addition of turbulence. In some cases, the magnitude of c_l around the local minimum at -50° and the local maximum at 45° , was reduced. However, the extremes at $\pm 90^\circ$ in c_l are the same as for the no grid case. In c_d and $c_{m, 1/4c}$ there is a spread of results at $\pm 90^\circ$ around what was seen in the no grid case.

The addition of high turbulence intensities at a turbulence integral length scale of about $1/2c$ smoothed away the jumps associated with stall for positive α .

Figure 5-7(a) and (b) show the C_p and σ for selected α for the lowest and highest turbulence intensities shown in Figure 4-13. At -90° the two flows produce very similar C_p but there are differences in σ . This is presumably due to the increased turbulence in the flow affecting the taps on the upwind and leading edge of the model. An increase in σ is obvious at all taps at -25° in the higher turbulence flow. By -22.5° there is a small attached region at the leading edge which is associated with a peak in σ for this case (note the change in scale of the σ plots). The σ and C_p peaks for this high turbulence intensity flow increase at $\alpha = -17.5^\circ$. By -15° there is a further increase in the C_p magnitude peak for the high turbulence intensity flow (note change in scale of the C_p plot) but a reduction in the σ peak.

By $\alpha = -12.5^\circ$ there is some leading edge attachment for the lower turbulence intensity case as well which produces an associated peak in σ . By $\alpha = -10^\circ$ the flow is mostly attached in both cases. At $\alpha = -5^\circ$ and 0° the flow is attached. However, the σ plot of the higher turbulence intensity case is larger than but of the same general shape as the lower turbulence intensity case. At $\alpha = 10^\circ$ and 15° , the magnitude of C_p on the suction surface near the leading edge is higher for the lower turbulence intensity flow. However, the σ continues to be higher for the larger turbulence intensity case. At $\alpha = 15^\circ$, σ shows a peak associated with a flat section of the C_p plot for all flows. This region moves toward the leading edge as α increases to 20° . By $\alpha = 25^\circ$ the lower turbulence intensity flow has only a small region of attached flow associated with a high σ at the leading edge. The higher turbulence intensity flow still shows separation and the associated local maxima in σ around $0.2c$. This local maxima moves towards the leading edge at 30° and is at the leading edge by 35° . By 30° the lower turbulence intensity case is fully stalled. However, full stall (complete separation of the boundary layer from the top surface) does not occur until around 55° for the higher turbulence intensity case with the increased magnitude of the leading edge C_p and σ evident until that point. At $\alpha = 60^\circ$ and 90° , the increased σ on the upwind surface for the higher turbulence intensity case is evident similar to what was seen at $\alpha = -90^\circ$.

The largest integral length scale of turbulence applied smoothed almost all jumps in coefficients associated with stall as shown in Figure 5-8. The extremes at $\pm 90^\circ$ were close to what was observed with no grid in the tunnel. c_l showed increased magnitude during stall at negative α and a range from slightly less to a much larger magnitude at positive α compared with the no grid case. The largest intensity case is most striking with a drastically increased magnitude of c_l during stall at both positive and negative α .

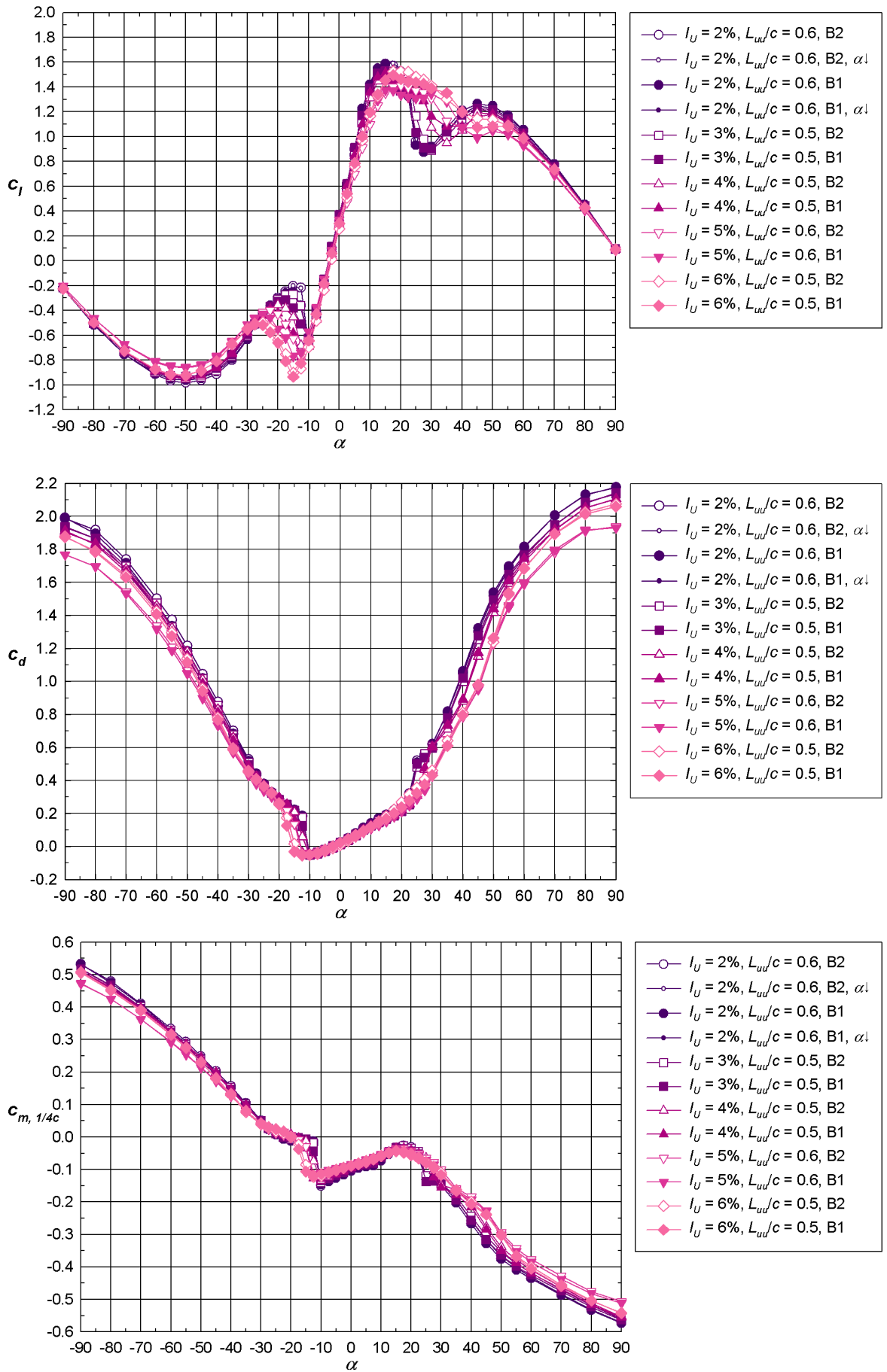


Figure 5-6 – NACA 4421 mean coefficients of lift, drag and of moment about the quarter chord with integral turbulence length scale about $1/2c$ (medium grid).

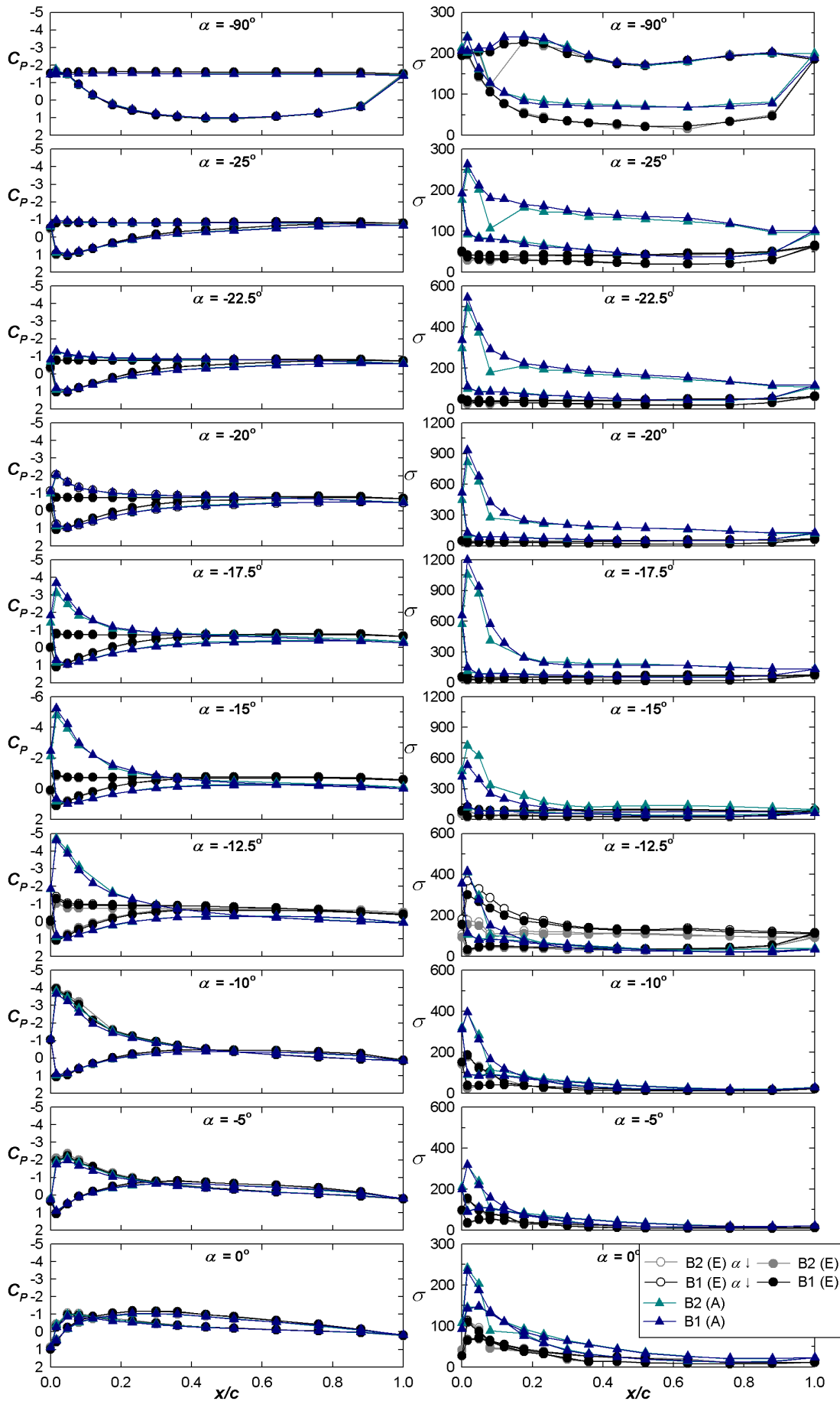


Figure 5-7(a) – NACA 4421 coefficients and standard deviations of the pressures around the aerofoil with turbulence integral length scale $\sim 1/2c$ for the lowest and highest turbulence intensities (medium grid at the closest (A) and furthest positions (E) from the model). Note the changes in scale of the σ and C_p plots.

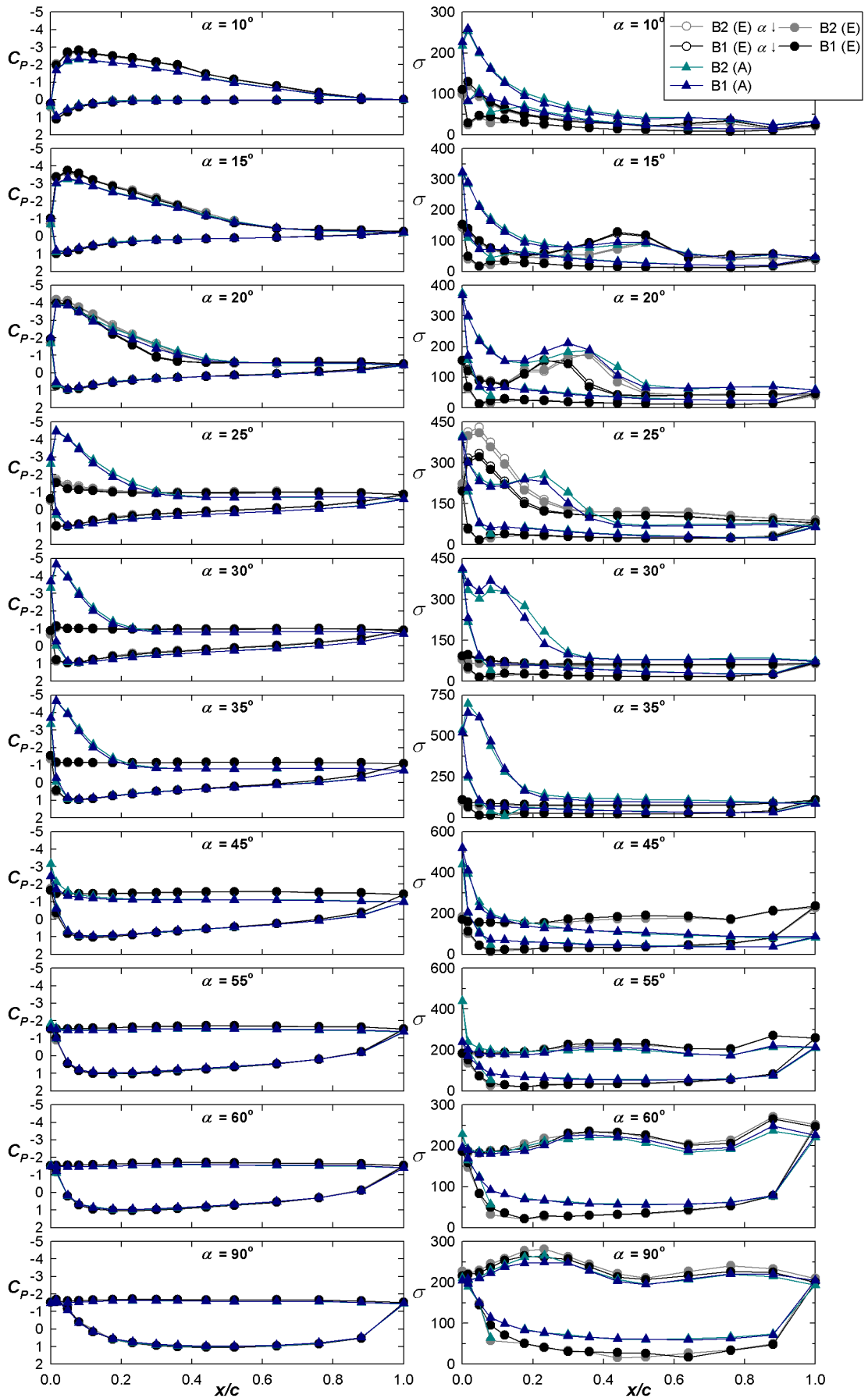


Figure 5-7(b) – NACA 4421 coefficients and standard deviations of the pressures around the aerofoil with turbulence integral length scale $\sim 1/2c$ for the lowest and highest turbulence intensities (medium grid at the closest (A) and furthest positions (E) from the model). Note the changes in scale of the σ plots.

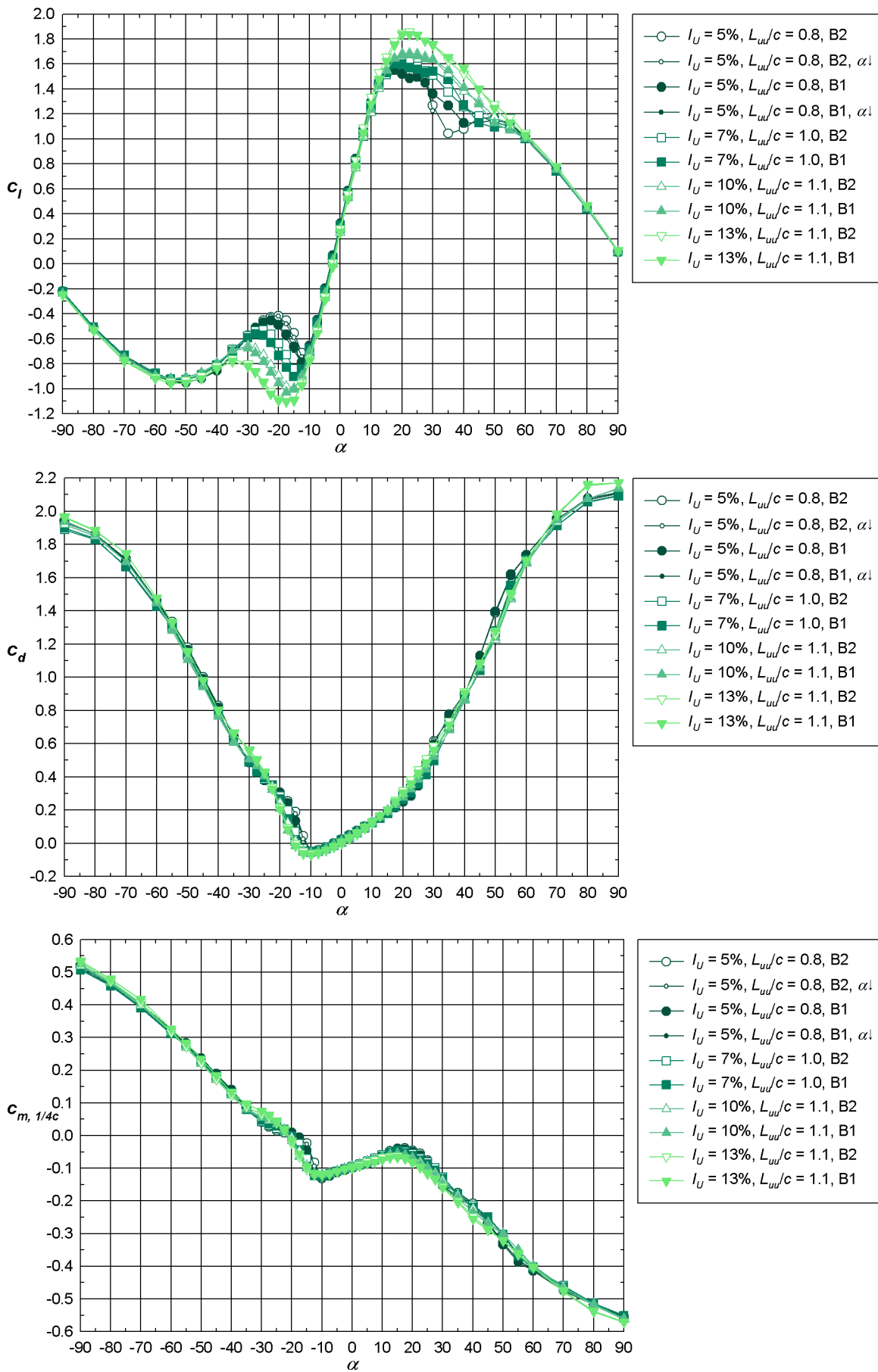


Figure 5-8 - NACA 4421 mean coefficients of lift, drag and of moment about the quarter chord with integral turbulence length scale about $1c$ (large grid).

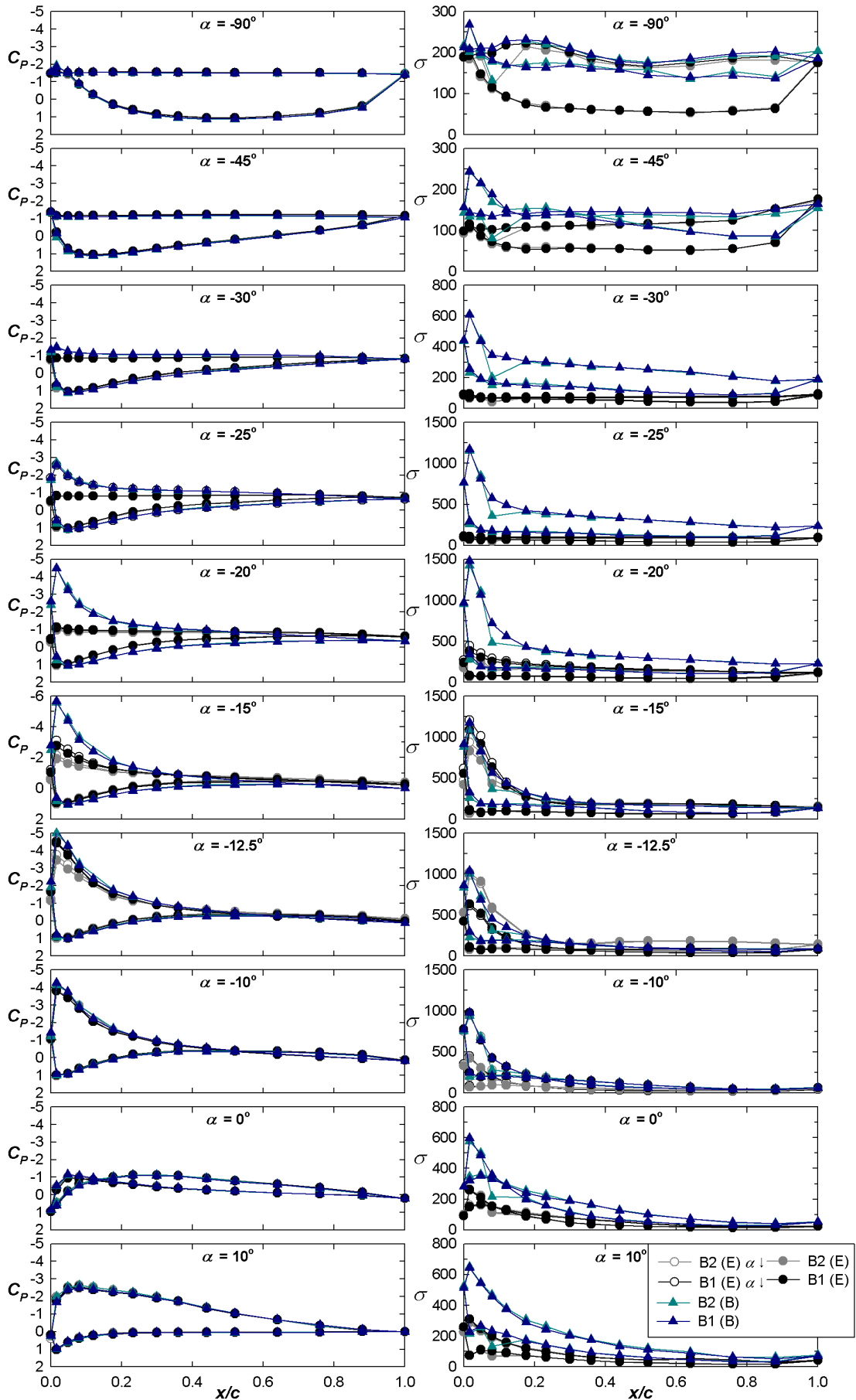


Figure 5-9(a) –NACA 4421 coefficients and standard deviations of the pressures around the aerofoil with turbulence integral length scale $\sim 1c$ for the lowest and highest turbulence intensities (large grid at the closest (B) and furthest positions (E) from the model). Note the changes in scale of the σ and C_p plots.

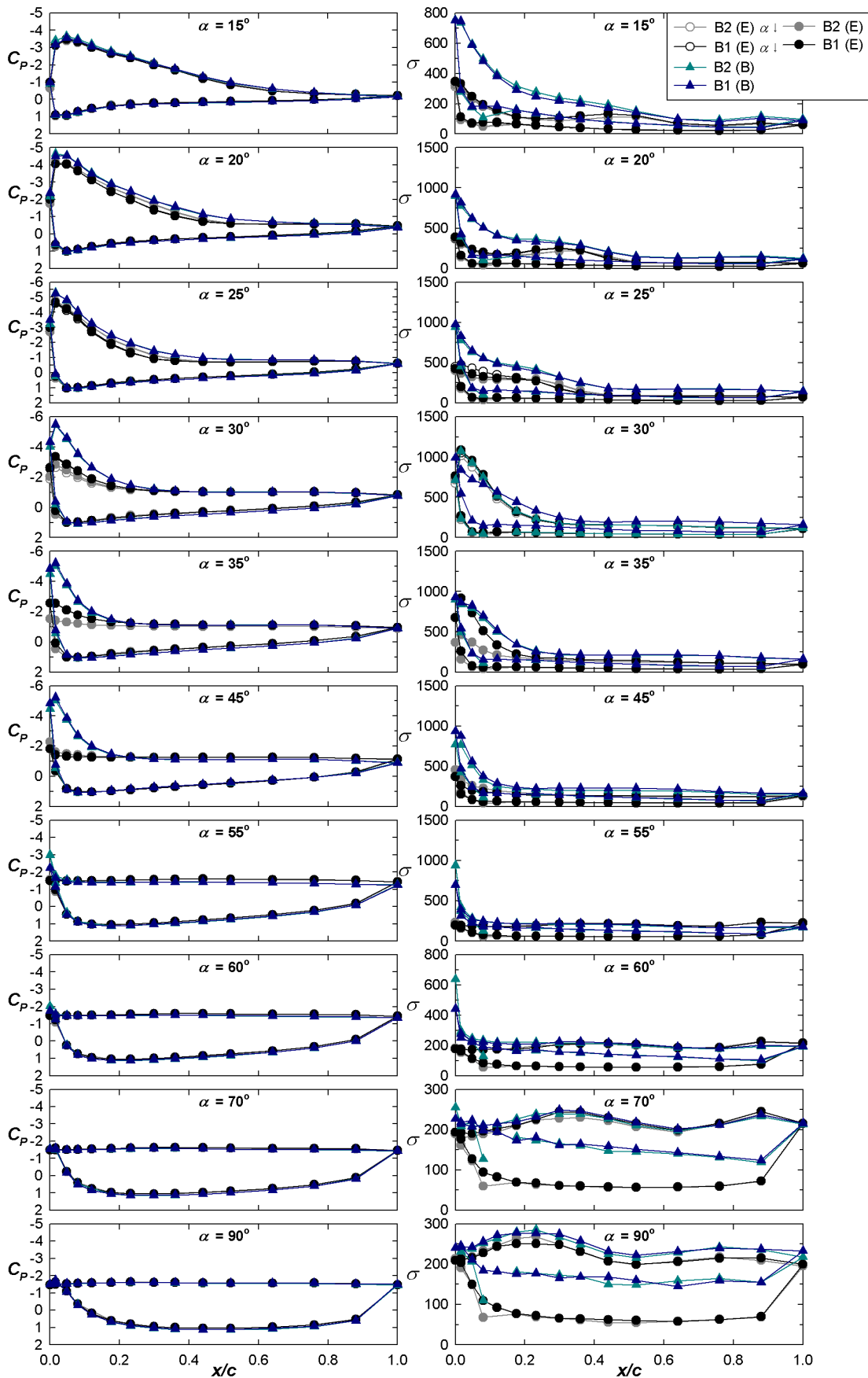


Figure 5-9(b) –NACA 4421 coefficients and standard deviations of the pressures around the aerofoil with turbulence integral length scale $\sim 1c$ for the lowest and highest turbulence intensities (large grid at the closest (B) and furthest positions (E) from the model). Note the changes in scale of the σ and C_p plots.

The highest turbulence intensity case shown in Figure 5-9 disturbs the σ plot so the upwind surface sees σ around the same level as the downwind surface at $\alpha = -90^\circ$. However the C_p is much the same as for the lower turbulence intensity case. This is also evident at -45° . By $\alpha = -30^\circ$, there is a small region of attached flow at the leading edge seen in C_p and a peak in σ for the highest turbulence intensity flow. These peaks increase as α increases to -20° . At $\alpha = -15^\circ$, there starts to be attached flow at the leading edge for the lower turbulence intensity case shown in this figure and a similar level σ peak is seen for all cases. Note the suction peak for the highest turbulence intensity case required the scale of the C_p plot to be changed for this α . As α increased to -12.5° and -10° the two cases began to show similar C_p and σ . However, at 0° , 10° and 15° , although similar in C_p increased σ is again evident for the higher turbulence intensity case. By $\alpha = 15^\circ$ and 20° , there is a small hump in σ about mid-chord associated with a flat region in C_p but the leading edge σ peak in the higher turbulence case still dominates. At $\alpha = 20^\circ$, the C_p on the suction surface from the leading edge to the mid-chord is of slightly higher magnitude for the higher turbulence intensity case.

Note the change in scale in the C_p plots for $\alpha = 25^\circ$ to 45° necessitated by the large leading edge suction peak in the higher turbulence intensity flow. The suction peak for the lower turbulence intensity case drops away along with σ until it appears completely stalled at $\alpha = 55^\circ$. The highest turbulence intensity case does not appear to stall completely until around $\alpha = 60^\circ$. At $\alpha = 70^\circ$ and 90° the increase σ due to the flow on the upstream surface is again evident.

A comparison of the increasing and decreasing α cases for c_l , c_d and $c_{m, 1/4c}$ is shown in Figure 5-10. The most immediately obvious feature is the differences observed for the results from Rows B1 and B2 during stall. The three plots show hysteresis at both positive and negative α for the flow cases with $I_u = 0.6\%$ and $I_u = 1\%$. However, for $I_u = 2\%$ hysteresis is only seen at negative α and it is not seen at all for the other flow conditions. These plots clearly show the way turbulence smoothes the changes in coefficients around stall, the most obvious example of which is the more gradual changes in c_l around stall at negative α with increasing turbulence intensities.

Figure 5-11, Figure 5-12 and Figure 5-13 show comparisons of the c_l , c_d and $c_{m, 1/4c}$ respectively for flows which have similar turbulence intensities but different turbulence integral length scales. The details of the turbulence characteristics of the flows are given in Table 5-1. Figure 5-11 shows that, for c_l around stall at negative α , the turbulence intensity appears to control the lift with similar intensities giving very similar results. However, for stall at positive α , the integral turbulence length scale is important with the larger scales giving increased c_l in all cases. For 2% and 5% intensities there are differences around the local minimum at -50° and local maximum around $+50^\circ$ with the larger turbulence integral length scales giving increased magnitudes. All cases approach the same values at $\pm 90^\circ$.

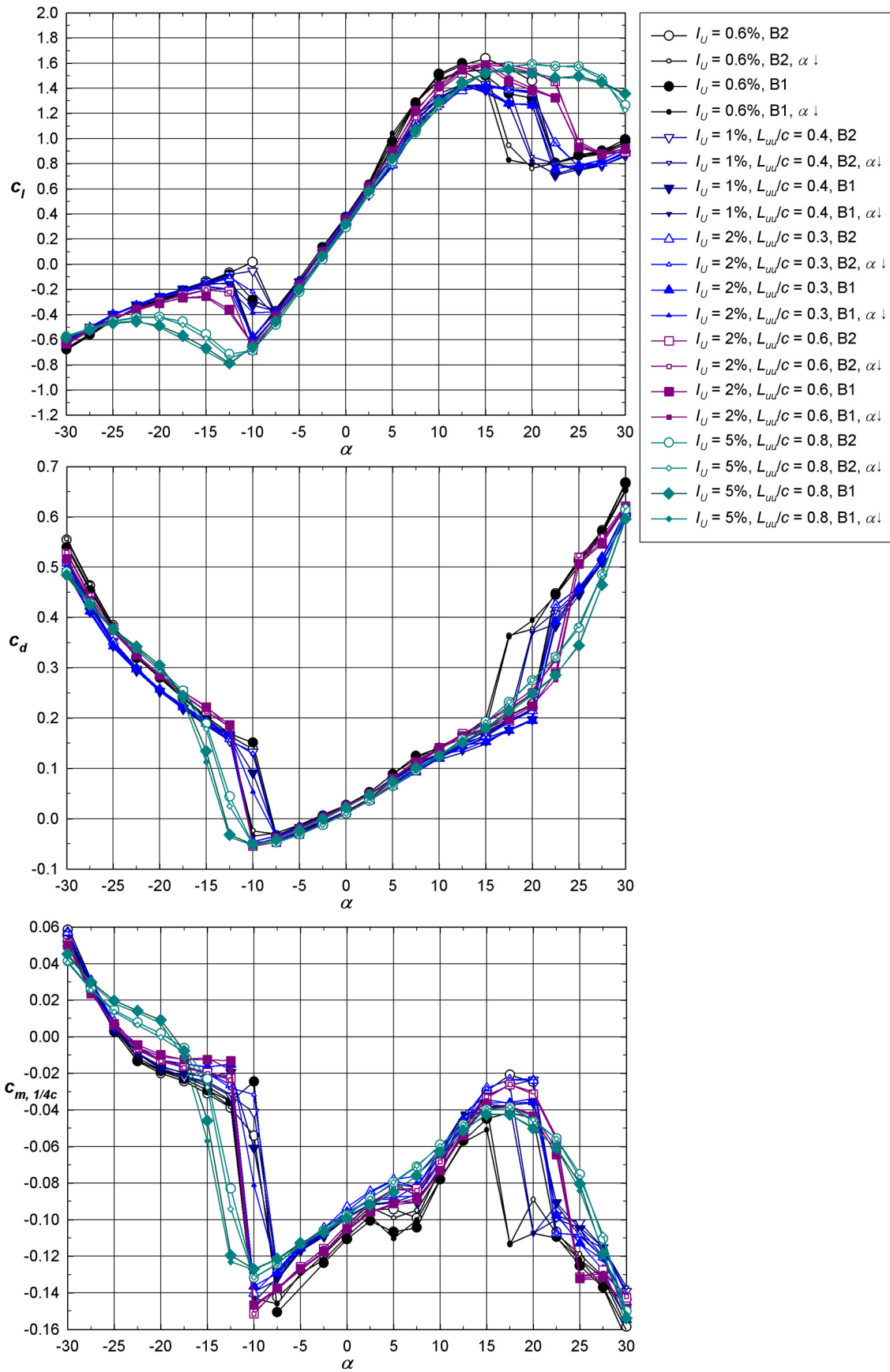


Figure 5-10 - NACA 4421 mean coefficients of lift, drag and moment about the quarter chord for some flow cases with both increasing and decreasing α .

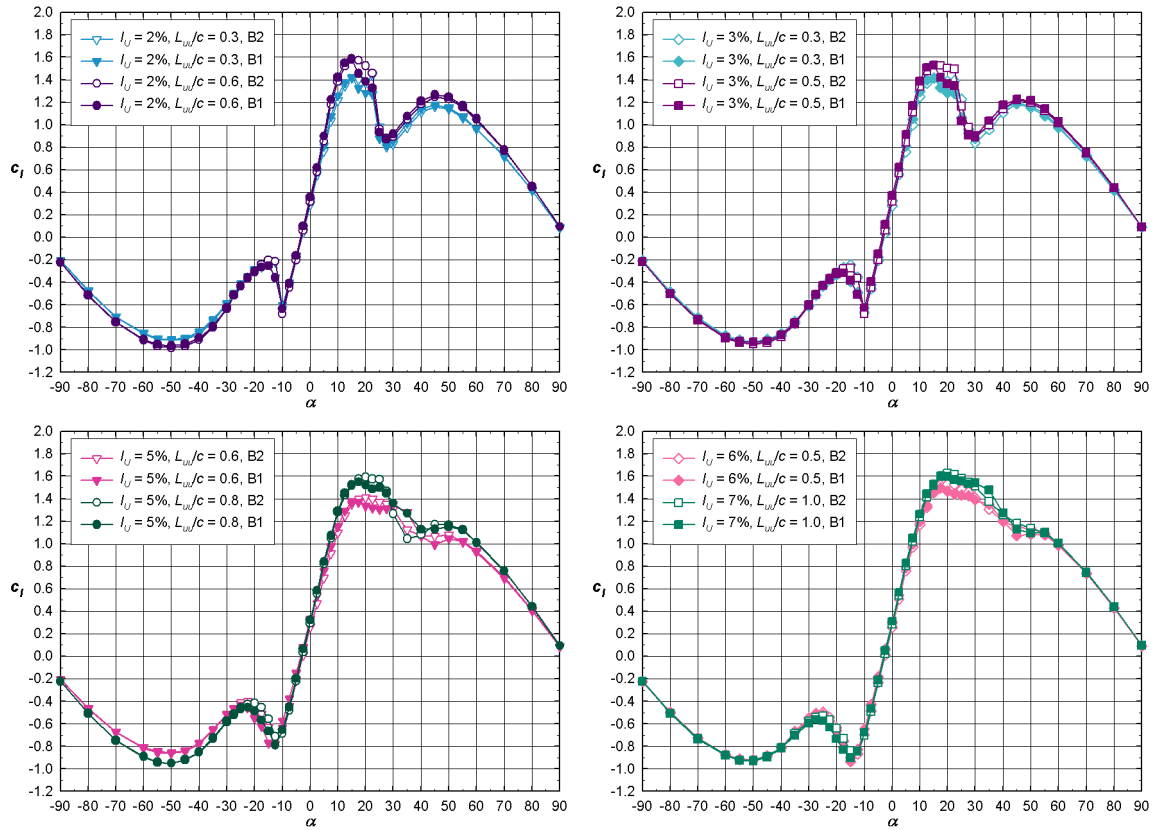


Figure 5-11 – NACA 4421 Comparison of the coefficient of lift at similar turbulence intensities but different integral length scales.

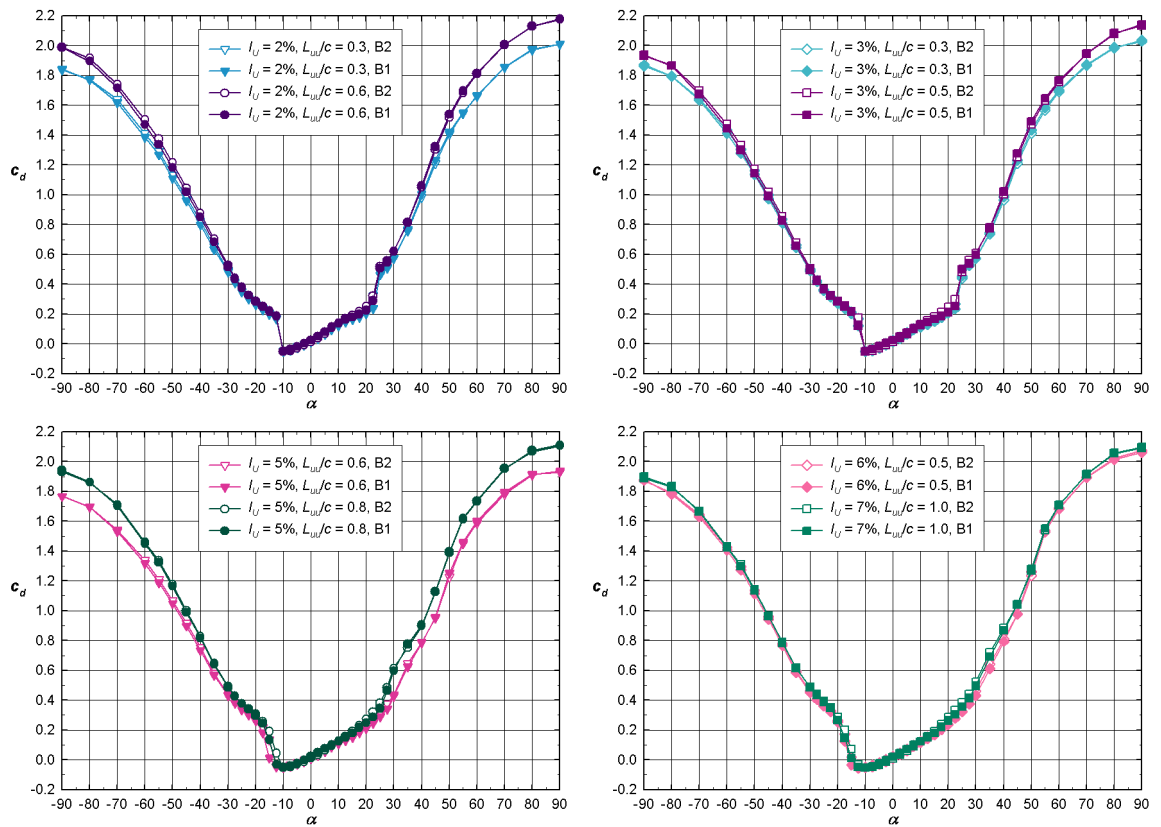


Figure 5-12 – NACA 4421 Comparison of the coefficient of drag at similar turbulence intensities but different integral length scales.

The c_d comparisons shown in Figure 5-12 display different results at the extremes of α ($\pm 90^\circ$) except for the case of turbulence intensity of 6 to 7%. Where there are differences, the larger scale produces higher drag. Similarly for the $c_{m, 1/4c}$ comparisons shown in Figure 5-13, the results are very similar at all α for the 6 to 7% turbulence intensity case but show differences at the extremes of α ($\pm 90^\circ$) in the other cases. Where there are differences, the larger scale of turbulence causes increased magnitude of the local maximum at -90° and the local minimum at $+90^\circ$.

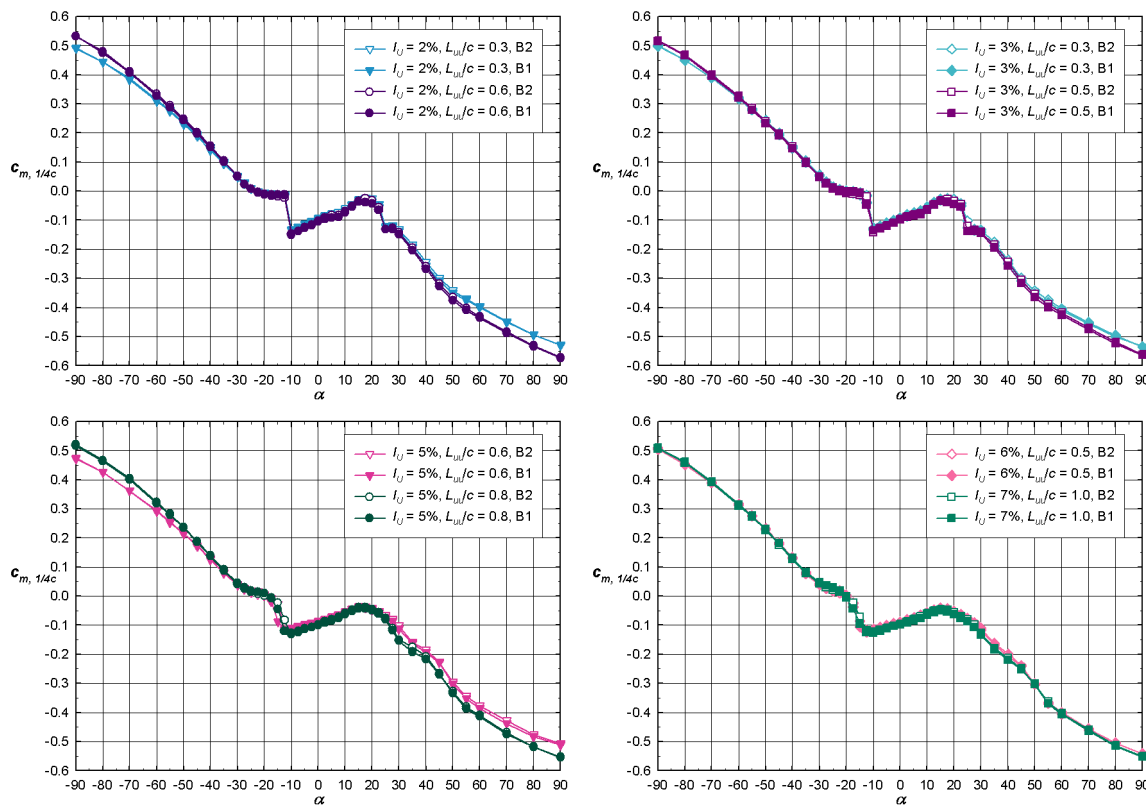


Figure 5-13 – NACA4421 Comparison of the coefficient of moment at similar turbulence intensities but different integral scales.

Grid Panel Width (m)	Position (m)	Intensity			Scale		
		I_u (%)	I_v (%)	I_w (%)	L_{uu}/c	L_{uv}/c	L_{uz}/c
0.10	E (9.60)	2	4	3	0.6	0.6	1.0
0.04	B (4.60)	2	3	2	0.3	0.4	0.2
0.10	D (7.20)	3	4	3	0.5	1.1	0.5
0.04	A (3.55)	3	3	3	0.3	0.3	0.3
0.30	E (9.60)	5	6	5	0.8	1.3	0.8
0.10	B (4.60)	5	7	5	0.6	0.9	0.4
0.30	D (7.20)	7	8	7	1.0	1.1	0.8
0.10	A (3.55)	6	7	7	0.5	0.6	0.4

Table 5-1 - Characteristics of the grid developed turbulence for the comparison between cases with similar turbulence intensities (repeated from Chapter 4).

Figure 5-14 shows the minimum and maximum of c_l associated with stall, the largest magnitude from the increasing or decreasing α case was chosen when there was data for both cases. Third order polynomials have been fitted to these and some of the subsequent plots, they are indented only to aid the eye in following the trends and differences in the data and should not be taken to imply any third order relationship exists in the results. The minima, from results near stall at

negative α , decrease with increasing turbulence intensity with little scatter in the data. However, the maxima from results near stall at positive α are spread. This corresponds to the earlier observation from the similar intensity results shown in Figure 5-11, that turbulence intensity seems to have a strong effect on the minimum lift associated with stall but that turbulence scale seems to affect the maximum lift associated with stall. Figure 5-15 shows the α at which the minima and maxima associated with stall occurred in c_l . There is a general increase in magnitude of α with increasing turbulence intensity although there is a large spread in the data. Finer intervals of α would probably be necessary to determine whether or not intensity has a direct effect on the value of α at which the minimum and maximum c_l associated with stall occurs.

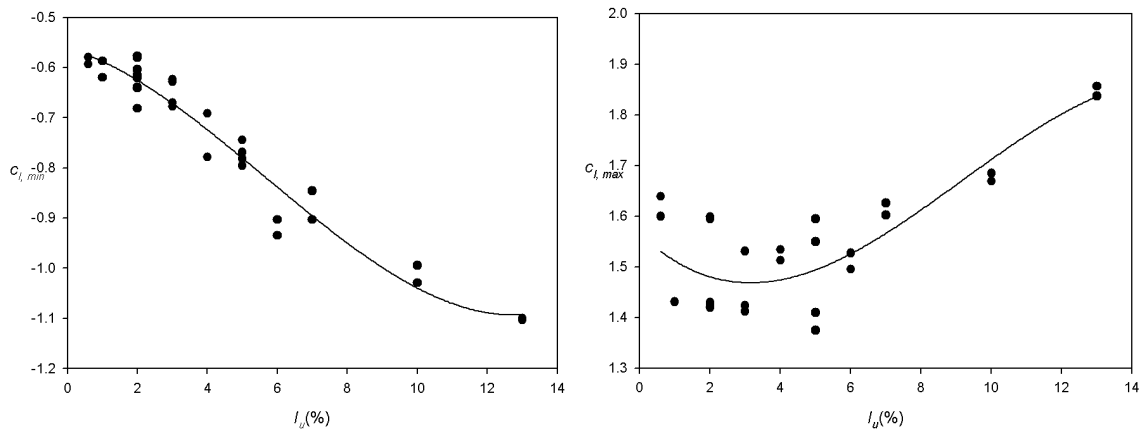


Figure 5-14 – NACA 4421 The local minimum and maximum of c_l associated with stall versus the turbulence intensity for all grids (both row B1 and B2), the lines are third order polynomials fitted to the data. The plots are to the same scale but not over the same range of the coefficients.

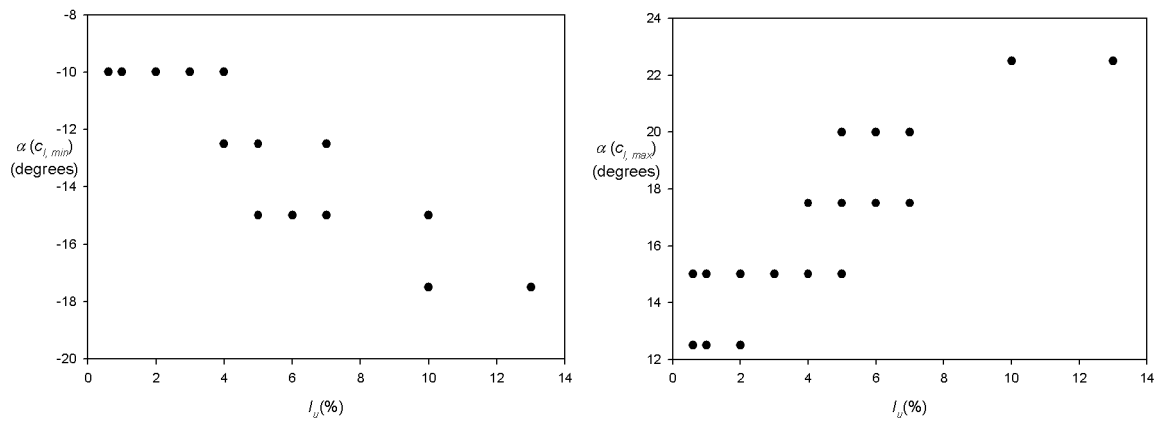


Figure 5-15 – NACA 4421 The α at which the maximum and minimum of c_l associated with stall shown in Figure 4-23 occurs. The plots are to the same scale in degrees but not over the same range of angles.

The maximum c_d at $\pm 90^\circ$ versus the turbulence intensity is shown in Figure 5-16. The scale in both plots is the same as in Figure 4-23 although the range of coefficients is different. The spread of the data indicates turbulence intensity does not have a major effect on the maximum c_d . Figure 5-17 shows the minimum and maximum $c_{m, 1/4c}$ at $\pm 90^\circ$. The range of values of $c_{m, 1/4c}$ is smaller than for the lift and the drag but it appears that, as for the drag and stall at positive α , the lift intensity is not the only cause of the extreme values.

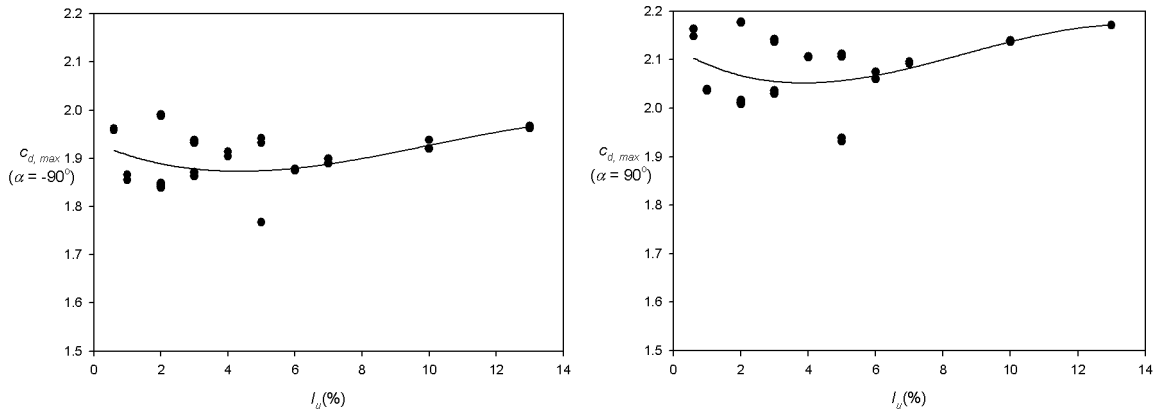


Figure 5-16 – NACA4421 The local maximum of c_d at $\pm 90^\circ$ versus the turbulence intensity for all grids (both row B1 and B2), the lines are third order polynomials fitted to the data.

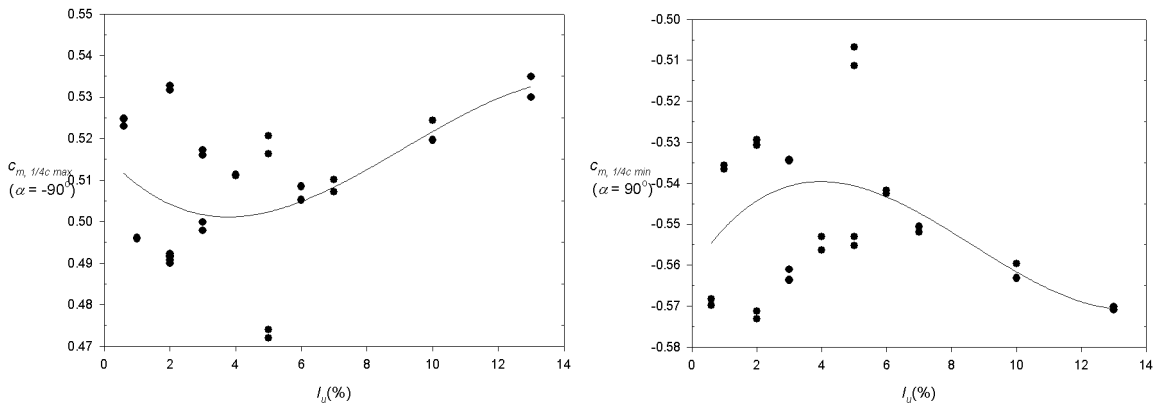


Figure 5-17 – NACA4421 The local maximum at -90° and minimum at $+90^\circ$ of $c_{m, 1/4c}$ versus the turbulence intensity for all grids (both row B1 and B2), the lines are third order polynomials fitted to the data. The plots are to the same scale but not over the same range of the coefficients.

5.3 Fluctuating

As for the NACA 0021 aerofoil section the fluctuations normal to the aerofoil section for the lowest turbulence flow ($I_u = 0.6\%$) were very clean containing only one main frequency component for the force tangential to the chord, see Figure 5-18. The force normal to the chord, see Figure 5-19, contained low frequency components, the main shedding frequency and a secondary shedding frequency at twice the frequency of the main shedding frequency. The causes of these have been discussed in detail for the NACA 0021 in Chapter 4 so this section will just look briefly over the main results for the NACA 4421 aerofoil section.

The best summary plot for the shedding is the frequency and magnitude of the main shedding peak in the PSD of the instantaneous tangential force and the main and secondary shedding peak in the PSD of the instantaneous normal force. The same Matlab program as discussed in Section 4.3.3 was used to find the shedding frequency and magnitude was used; see Section 4.3.3 for a complete description. In addition the data at 120Hz and 173Hz was set to zero as there were small components in the normal PSD at these frequencies, see Figure 5-2. These frequencies may have been due to some disturbance in the tunnel or external electrical source.

PSD Tangent NACA 4421, No Grid, Row B1

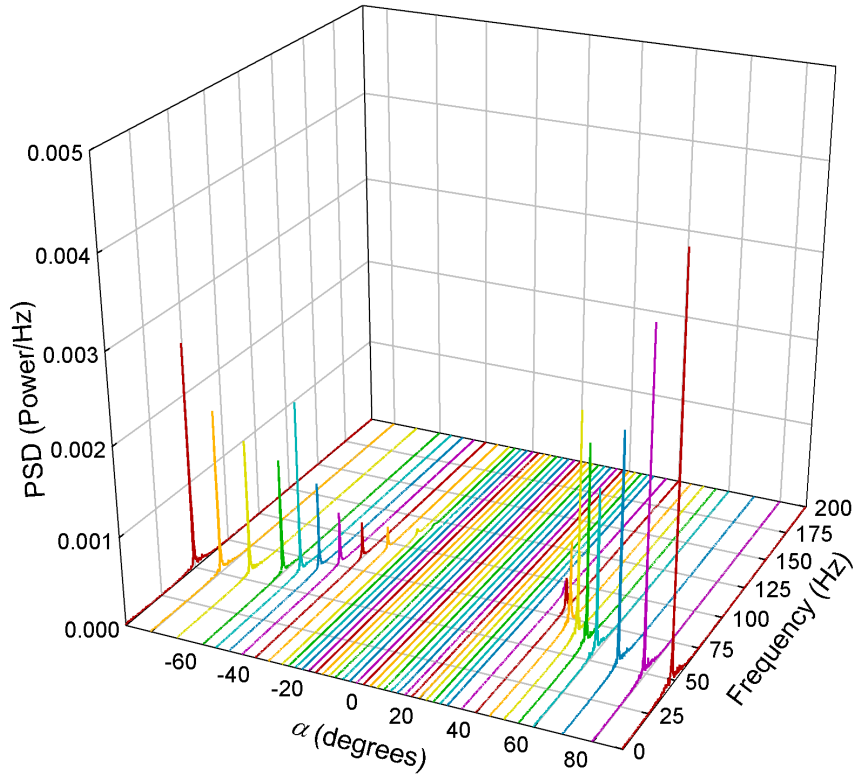


Figure 5-18 – Frequency content of the fluctuations in the tangent force for the increasing α case for the NACA 4421 aerofoil section for the lowest turbulence flow.

PSD Normal NACA 4421, No Grid, Row B1

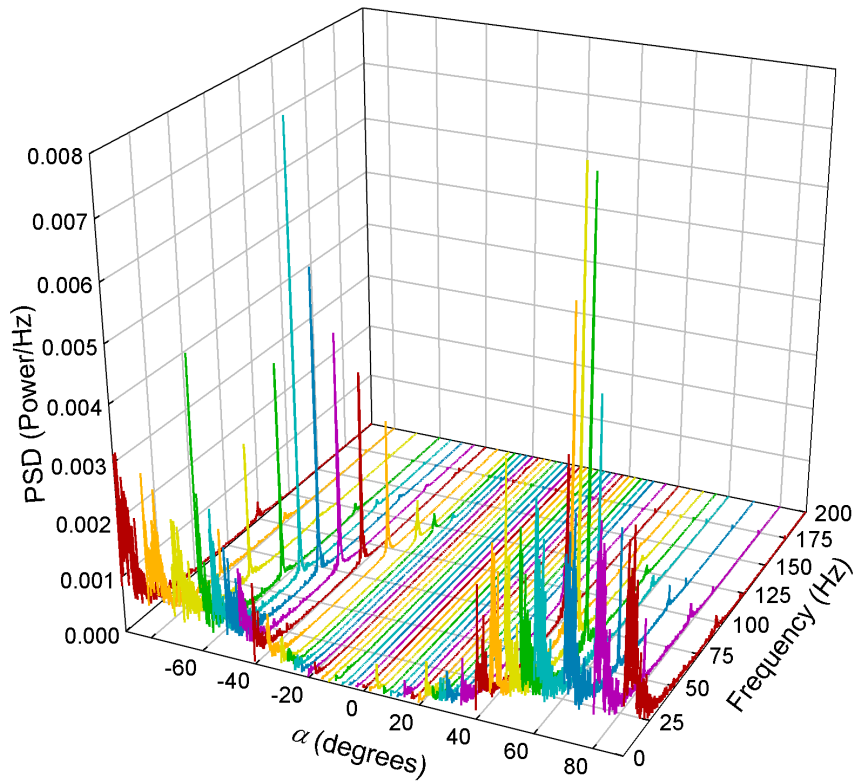


Figure 5-19 – Frequency content of the fluctuations in the normal force for the increasing α case for the NACA 4421 aerofoil section for the lowest turbulence flow.

As the cambered NACA 4421 aerofoil presents a slightly concave surface to the flow at positive α and a convex surface to the flow at negative α the wake would be expected to be narrower for negative α as the flow can more smoothly travel around the surface, this is shown diagrammatically in Figure 5-20. For the universal Strouhal number to remain constant the frequency must increase for a narrower wake width and therefore a higher shedding frequency would be expected for negative α than for positive α . This is indeed what is seen in Figure 5-21 which shows the frequency and magnitude of the shedding peak in the tangential force PSD versus α . The delay in vortex shedding onset with increasing turbulence intensity can also be seen at both positive and negative α . The shedding starts at lower magnitude α for the negative α case as the aerofoil stalls earlier in this orientation. Unlike for the NACA 0021 aerofoil section the highest turbulence intensity flow ($I_u = 13\%$) showed the same trend as in the other cases, the scales and intensities of turbulence used did not alter the wake width for the NACA 4421 aerofoil section.

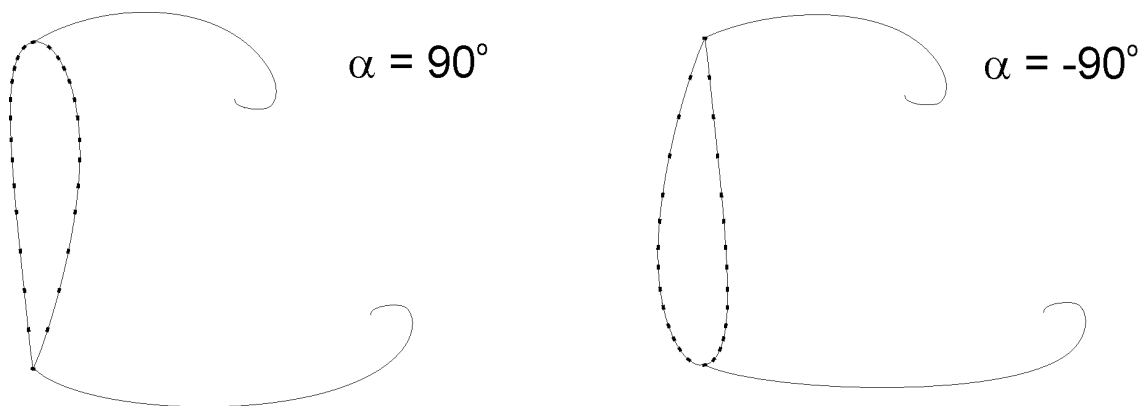


Figure 5-20 - Diagram showing the concave surface presented to the flow at positive α and the convex surface and therefore narrower wake at negative α .

The shedding magnitude in the tangential PSD showed much less smoothness in the trends but showed a general increase with increasing magnitude of α , see Figure 5-21. In general, the lower integral length scales of turbulence (about $1/3c$, blue points, and $1/2c$, purple and pink points) showed higher shedding magnitude, with the largest integral length scales (about $1c$, green points) showing smaller magnitudes with increasing turbulence intensity. The lowest turbulence flow ($I_u = 0.6\%$, black points, note the integral turbulence length scale could not be determined for this flow) showed shedding magnitudes in between these levels.

For the normal component of force, the same general trends in shedding magnitudes can be seen in Figure 5-22 except in this case the flows show a peak in shedding magnitude for the first shedding peak about $|\alpha| = 55^\circ$. The secondary shedding frequency magnitude shows the generally increasing trend seen for the tangential shedding magnitude but is at far smaller magnitudes than both the tangential and normal main shedding frequency magnitudes.

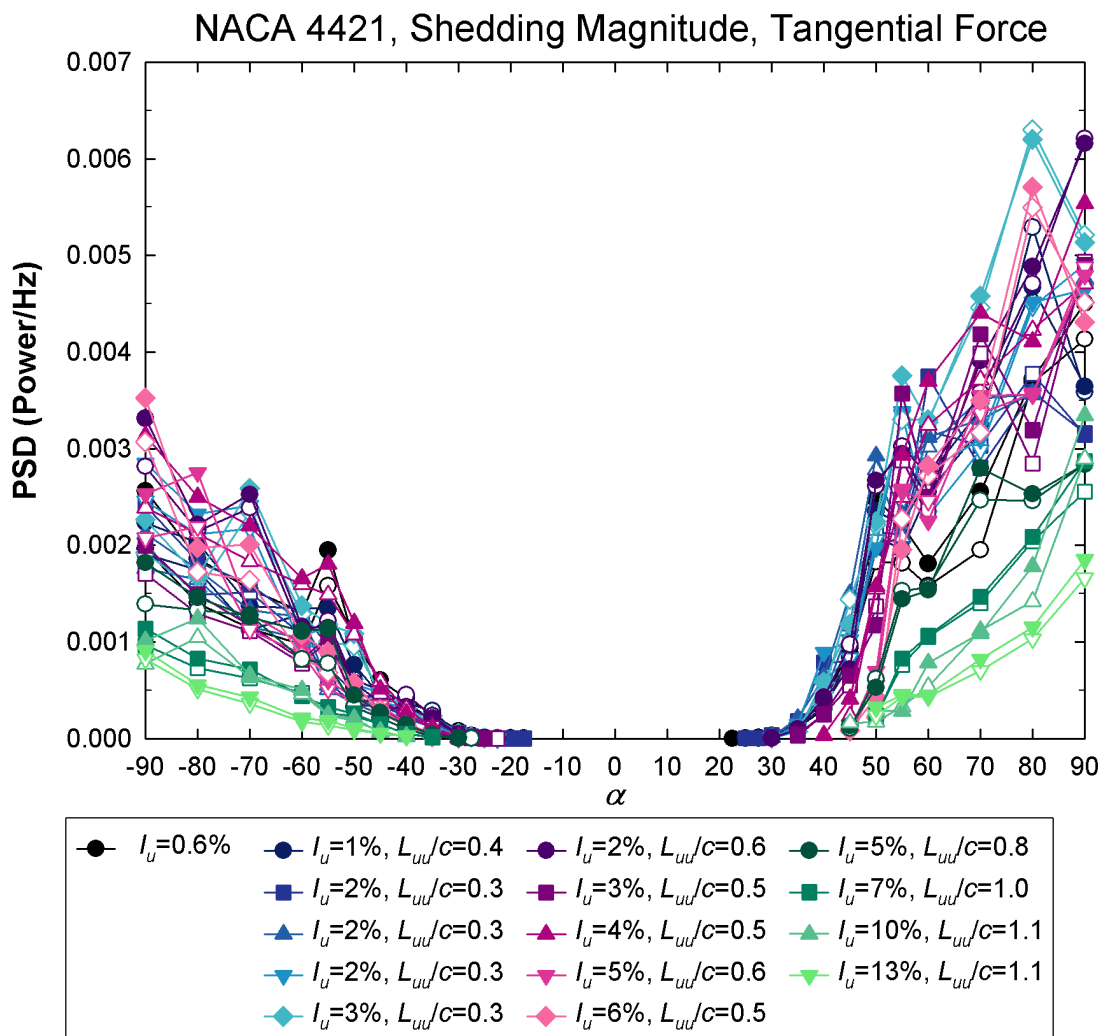
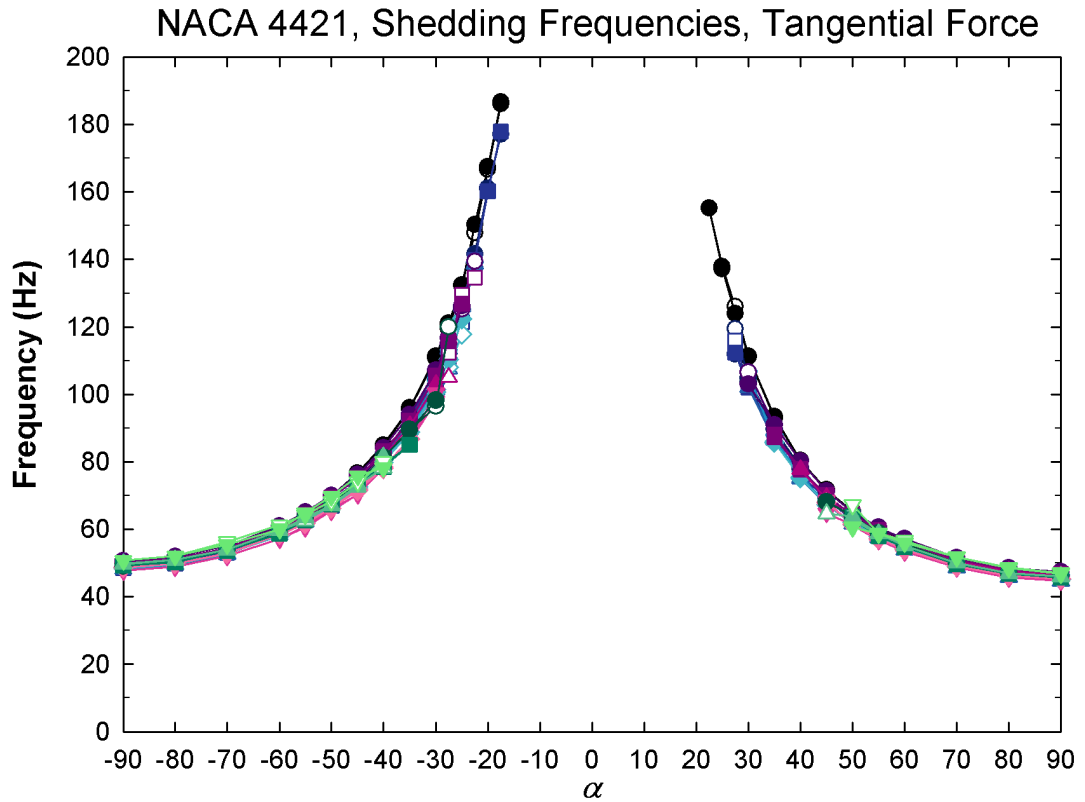
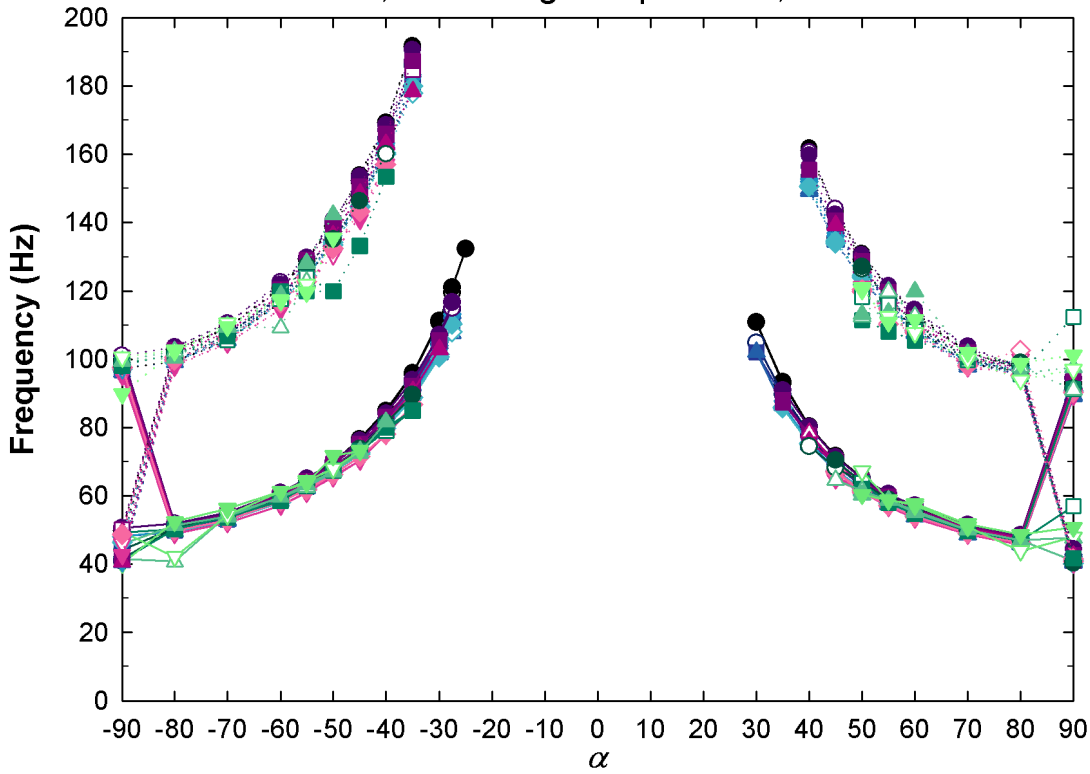


Figure 5-21 - Shedding frequencies and magnitude in the tangential force PSD for all flow conditions. Closed symbols indicate Row B1 and open symbols indicate Row B2.

NACA 4421, Shedding Frequencies, Normal Force



NACA 4421, Shedding Magnitude, Normal Force

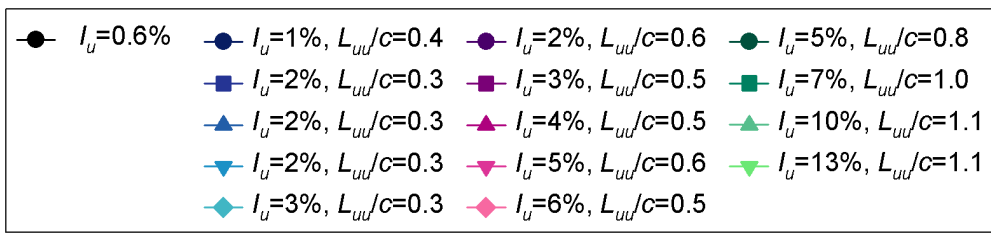
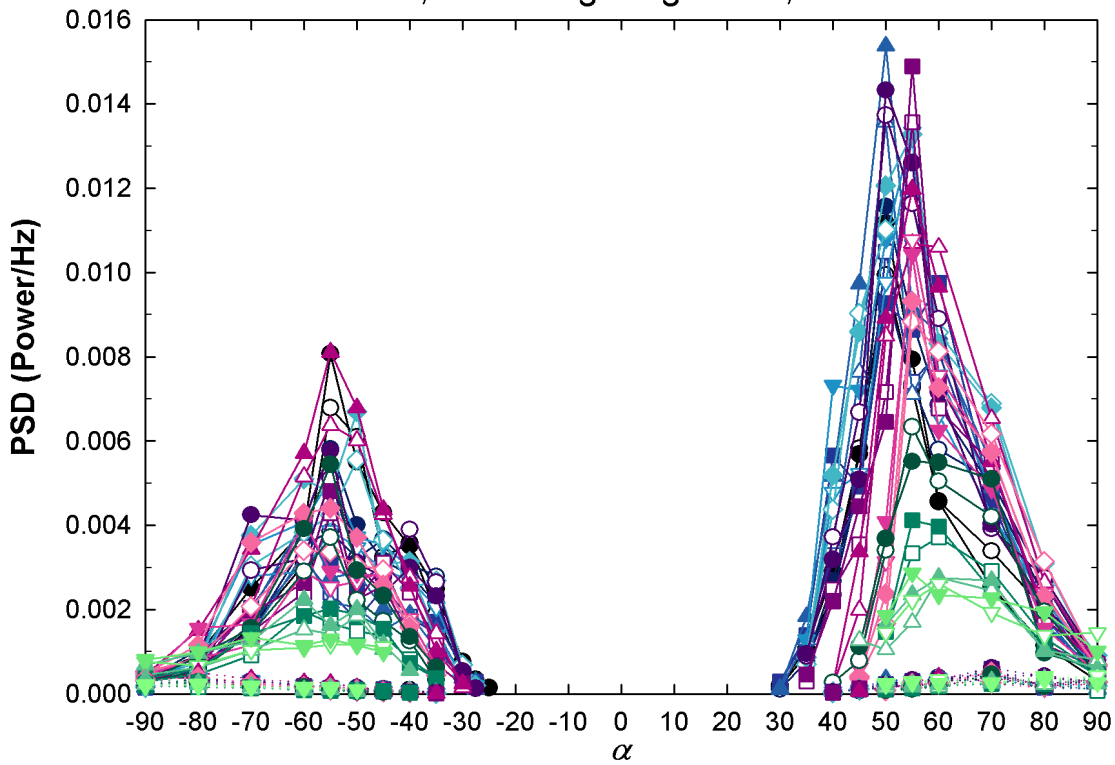


Figure 5-22 - Shedding frequencies and magnitude in the normal force PSD for all flow conditions. Closed symbols indicate Row B1, open symbols indicate Row B2, straight lines the first and dotted lines the second frequency.

As expected the increased noise in the normal force PSD made the shedding frequencies more difficult to detect and there was much more variation in the normal force shedding frequencies, see Figure 5-22. For some curves there is a cross-over between $|\alpha| = 80^\circ$ and $|\alpha| = 90^\circ$ as the secondary frequency is defined as the one with the smaller magnitude and the magnitudes of the main and secondary shedding frequencies PSD at $|\alpha| = 90^\circ$ are similar.

This section has shown no effect of added turbulence on the frequencies at which vortices are shed, although the shedding peaks do alter in magnitude and the α at they begin. The next section will examine whether the vortex shedding is well correlated enough across the span to potentially produce problems with cyclic loading on the stalled aerofoil section.

5.3.1 Correlations

Many of the features of the correlation plots presented in this section have been discussed previously in Chapter 4 in relation to the results for the NACA 0021 aerofoil section. A comparison of the results will be given in the discussion in Chapter so the analysis in this section will be relatively brief. The first plots presented in this section show the correlation coefficients between the instantaneous c_n , c_t and $c_{m, 1/4c}$ from Rows B1 and B2 for various flow conditions. The location of Rows B1 and B2 are shown in Figure 5-23. Later in this section the correlations between the rows of the corrected pressure signals for each tapping present in all rows will be presented. The location of the taps in all rows is indicated by circles in Figure 5-23. The “upper” and “lower” taps refer to the orientation shown in Figure 5-23. To be more correct, the upper and lower taps should really be referred to as the downwind and upwind taps respectively for $\alpha > 0^\circ$ and, for $\alpha < 0^\circ$, the upwind and downwind taps respectively. However the constant designation of upper and lower with respect to the chord will be kept for the sake of simplicity.

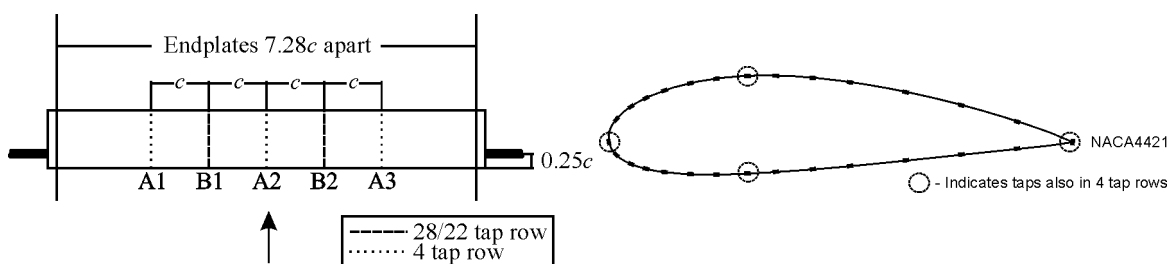


Figure 5-23 - Location of the tapping rows and the four taps located in every tapping row.

At the extremes of $\alpha (\pm 90^\circ)$, the R_{C_t} plot in Figure 5-24 shows higher correlations for smaller levels of turbulence with the correlations decreasing with increasing turbulence intensities. In contrast, the extremes of the R_{C_n} and $R_{C_{m, 1/4c}}$ plots show a mid-band of the lowest turbulence intensities (no grid and small grid, the black and blue plots on the graph). The medium scales (purple points) are below this band and the large scales (green points) are above it.

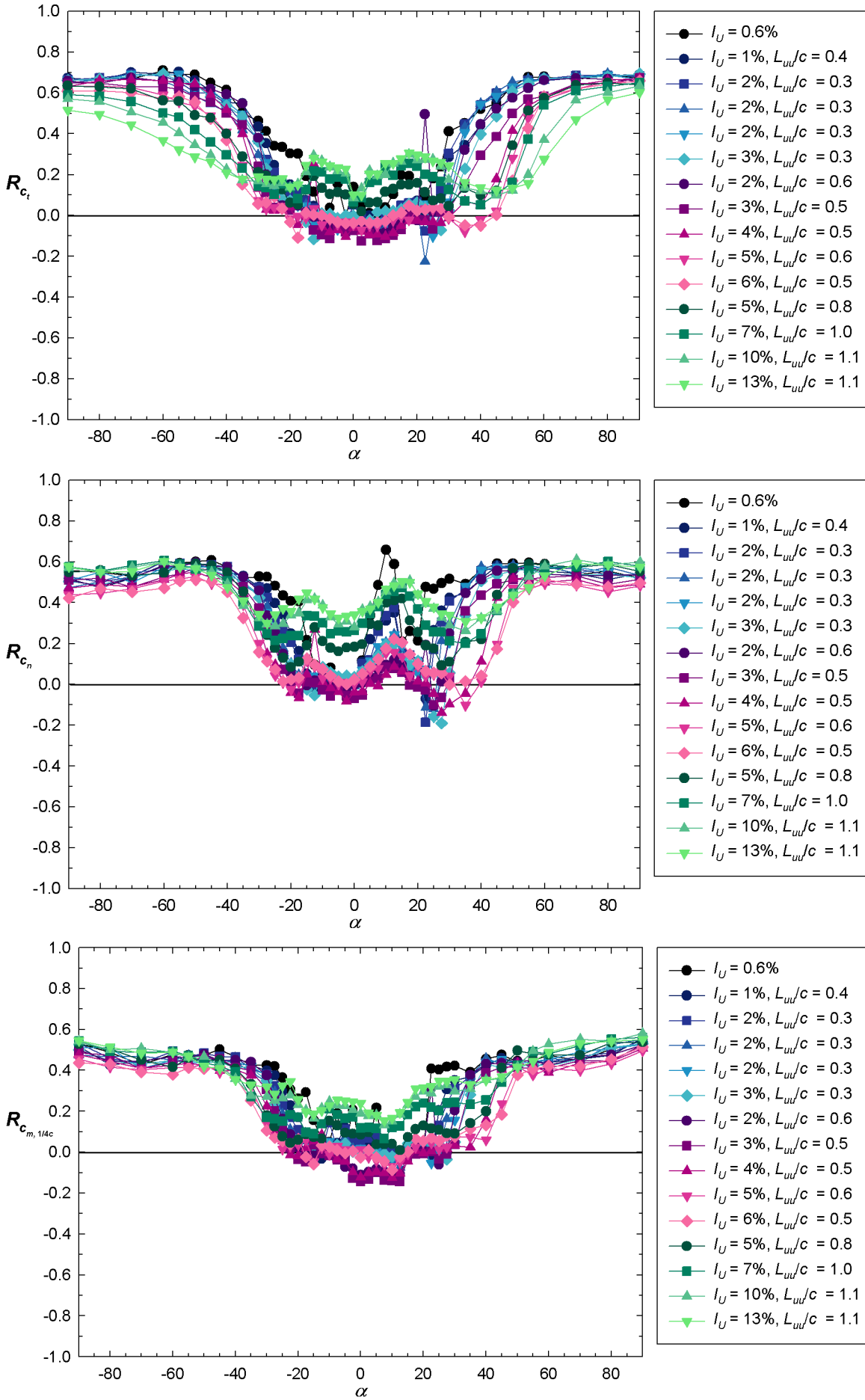


Figure 5-24 – NACA4421 Correlation coefficients between c_t , c_n and $c_{m, 1/4c}$ calculated from Row B1 and Row B2 data (increasing α data only shown).

The tangential force would be expected to be dominated by the shedding force that becomes less coherent with increasing turbulence intensity. In contrast, the normal force and moment about the quarter chord seem to be affected by scale. This may be due to buffeting or curvature of the shear-layers. This will be discussed in Chapter 7 with respect to all aerofoils where more definite conclusions are drawn. The similarities between the R_{C_n} and $R_{C_{m,1/4c}}$ plots were expected as $|\alpha|$ goes to 90° because the normal force would dominate the moment at high α .

Some of the R_{C_i} plots (most notably the high turbulence intensity cases) drop in correlation for decreasing magnitude of α from $\pm 90^\circ$. However, the R_{C_n} and $R_{C_{m,1/4c}}$ plots remain fairly constant for $-90^\circ \leq \alpha \leq -40^\circ$ and $50^\circ \leq \alpha \leq 90^\circ$. The correlations in the attached and stall regions are generally smaller but have more variation with α . Increasing the turbulence level tends to reduce these variations. There are a few extreme points of interest, for instance at $\alpha = 22.5^\circ$ in R_{C_i} . Also for $I_u = 2\%$, $L_{uu}/c = 0.6$ R_{C_n} increases suddenly at $\alpha = 22.5^\circ$ and that for $I_u = 2\%$, $L_{uu}/c = 0.3$ decreases suddenly, see Figure 5-25. This is the angle at which or shortly after the aerofoil stalls. The $I_u = 0.6\%$ case has a peak about $\alpha = 10^\circ$ in R_{C_n} and there are smaller increases for the other low turbulence intensity cases near this α . This angle is at the start of the stalling region so the peaks seem to be related to the start of separation and possibly the effects of the separated boundary layer or a reduced separation bubble.

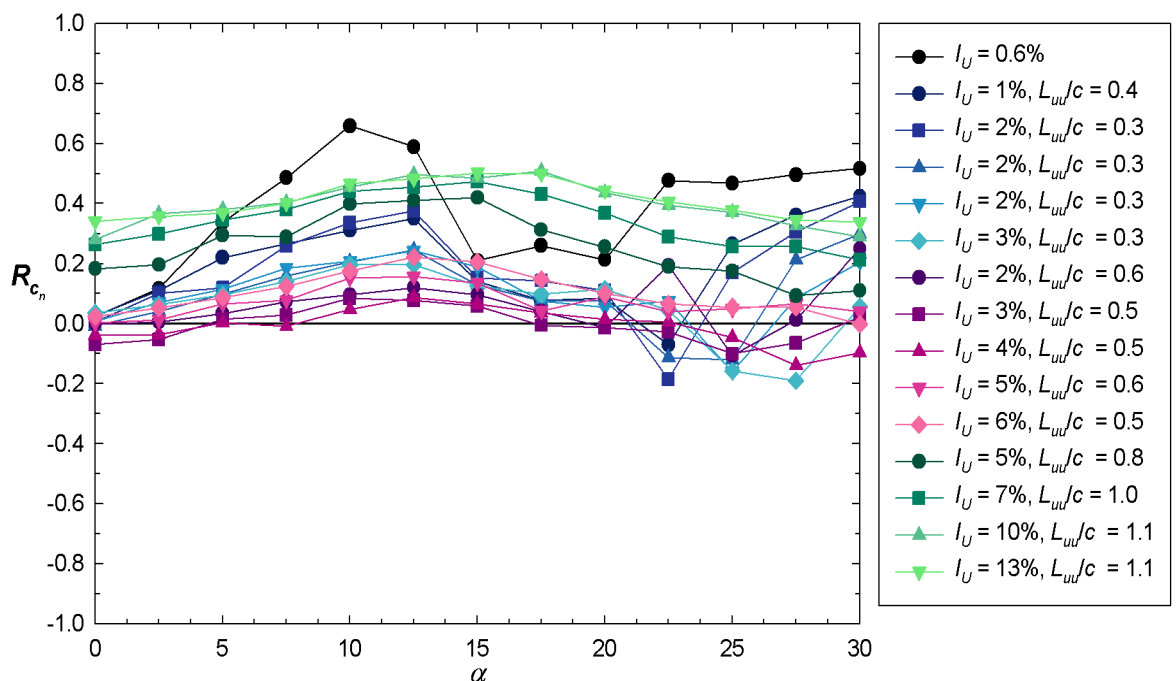


Figure 5-25 – NACA4421 Close up of correlation coefficients between c_n calculated from Row B1 and Row B2 data (increasing α data only shown).

The correlation coefficients between the four pressure tap locations present in all rows are shown Figure 5-26 for the lowest turbulence flow case. The banding based on spanwise spacing and the

dominance at high α of shedding leading to fairly constant correlation coefficients is clear. The “upper” and “lower” tap plots show a dip in correlation for $|\alpha| > 60^\circ$ when the taps are facing upstream. The dip was hypothesised for the NACA0021 aerofoil section to be due to the low frequency “noise” and the increase due to the increasing alignment of the tap with increasing α to the normal flow. The decrease in correlation with increasing α when the taps were downwind was postulated earlier for the NACA 0021 to be due to the increasing distance from the vortex cores as α increased. This is shown diagrammatically for the NACA 4421 aerofoil in Figure 5-27. The smaller decreases in the trailing edge and leading edge correlations may be due to similar effects.

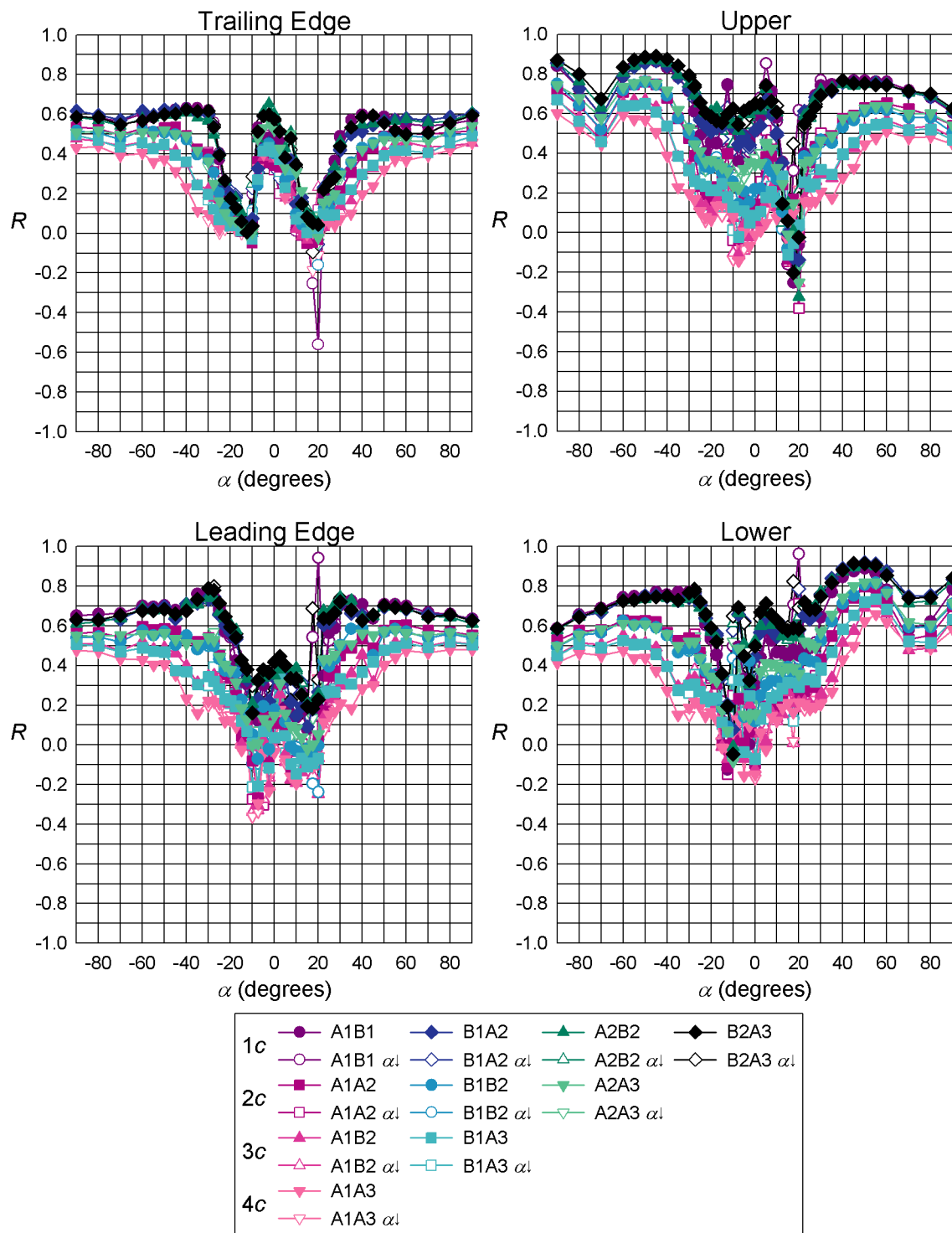


Figure 5-26 - NACA 4421 Correlation coefficients between taps in the 4 tap rows (A1, A2 and A3) and the equivalent taps in the 28 tap rows (B1 and B2) for the lowest turbulence flow ($I_u = 0.6\%$, no grid).

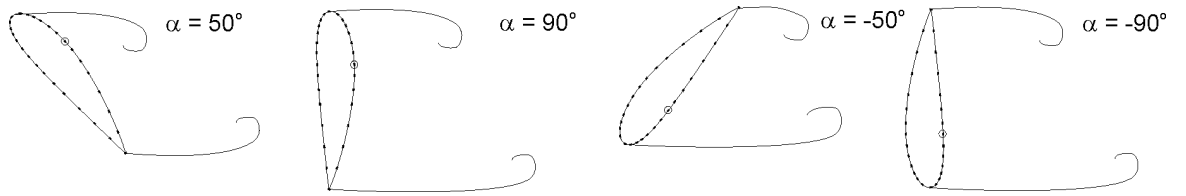


Figure 5-27 – Sketch of vortex shedding with respect to the locations of the upper tap at $\alpha = 50^\circ$ and 90° and with respect to the locations of the lower tap at $\alpha = -50^\circ$ and -90° . The upper and lower taps are circled in the sketch at positive and negative angles respectively.

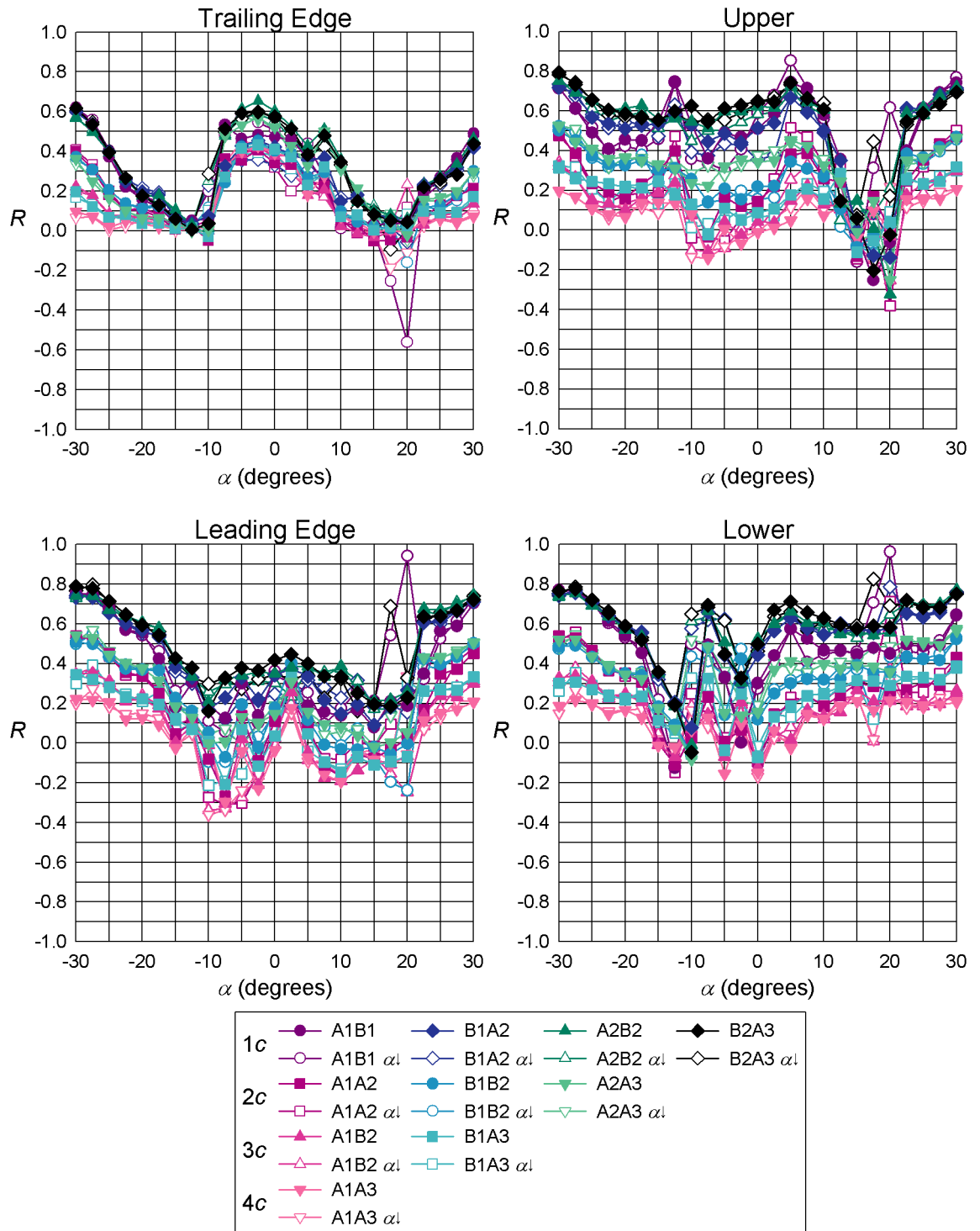


Figure 5-28 - NACA 4421 Correlation coefficients between taps in the 4 tap rows (A1, A2 and A3) and the equivalent taps in the 28 tap rows (B1 and B2) for the lowest turbulence flow ($I_u = 0.6\%$, no grid in the tunnel) for $30 \geq \alpha \geq -30^\circ$.

The behaviour within the range $-30^\circ \leq \alpha \leq 30^\circ$ is shown in Figure 5-28. The trailing edge shows a relatively high correlation for attached flow with drops to minimums about stall (around $\alpha = -10^\circ$ and $\alpha = 15^\circ$) and then increases in correlations as vortex shedding begins. There are extreme peaks for some of the decreasing α cases about $\alpha = 20^\circ$ (also seen in the other taps). This is probably due to attempts to form a separation bubble as discussed for the NACA 0021 aerofoil section. The upper and lower taps show fairly constant, strongly banded correlations for attached flow, dropping with the onset of stall and increasing again as shedding occurs near the tap. The lower taps also show a dip in correlation about -2.5° that may be due to the fairly slow speed of the boundary layer at this α which therefore allows more effect from the freestream. The leading edge shows relatively constant but low correlations before stall (about $\alpha = -10^\circ$ and $\alpha = 20^\circ$ degrees) at low α for the $1c$ separation increasing with the onset and development of shedding. The large spanwise spacings, especially $4c$, show decreasing correlation either side of $\alpha = 2.5^\circ$ before the higher correlations associated with shedding.

The addition of a small amount of turbulence refines the bands based on spanwise spacing but most of the general features identified earlier for the lower turbulence case remain. For example, the extreme points associated with stall and decreasing $|\alpha|$. Note, increasing α is the decreasing $|\alpha|$ case for negative α and so would be expected to show a more abrupt stall given the effect of the aerofoil's camber. Unexpectedly there is an extreme for decreasing α for B1A2 at $\alpha = -12.5^\circ$ in the upper taps and leading edge taps plots. This is after stall for this flow. The increase in turbulence reduces variation in the correlation coefficients for each band with the exception of the dips at large magnitude α ($|\alpha| \rightarrow 90^\circ$) or the upper and lower cases, these are more pronounced for this flow condition.

There are still some extreme points about stall for both increasing and decreasing α for a higher turbulence intensity at about the same scale (small grid in position A), see Figure 5-30. The higher turbulence level has further collapsed the results into bands based on spanwise spacing. The turbulence has also decreased the correlation for attached flow for the leading and trailing edge (perhaps by increasing turbulence in the boundary layer). The correlations at $\alpha = -90^\circ$ for the upper taps and $\alpha = +90^\circ$ for the lower taps are also decreased. This decrease was anticipated from the hypothesis made in the previous section that the correlation in this case was affected by the freestream turbulence; increasing turbulence would therefore be expected to decrease correlation.

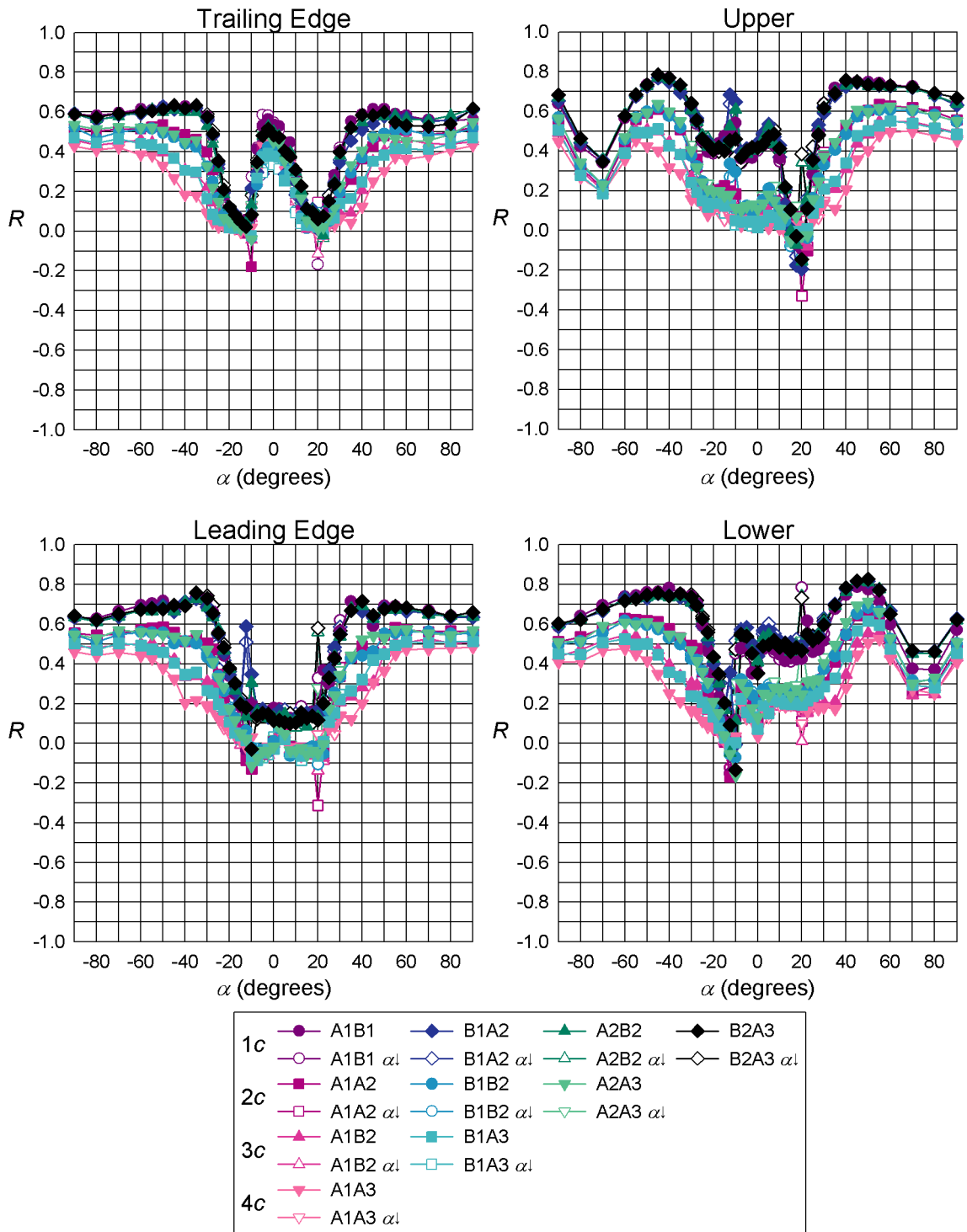


Figure 5-29 - NACA 4421 Correlation coefficients between taps in the 4 tap rows (A1, A2 and A3) and the equivalent taps in the 28 tap rows (B1 and B2) for the lowest turbulence flow ($I_u = 1\%$) with an integral length scale of about $1/3c$ (the small grid in position E).

The medium grid in position E ($I_u = 2\%$, $L_{uu}/c = 0.6$) produces lower turbulence intensity than the small grid in position A ($I_u = 3\%$, $L_{uu}/c = 0.3$) but with a larger integral turbulence length scale. Correspondingly the correlations for the upper taps at $\alpha = -90^\circ$ and the lower taps at $\alpha = 90^\circ$ are slightly higher for the medium grid case shown in Figure 5-31. The other changes noted earlier for the small grid in position A compared with the small grid in position E are also slightly less pronounced. For example, the correlations for the attached flow are slightly higher for the lower turbulence flow (medium grid in position E).

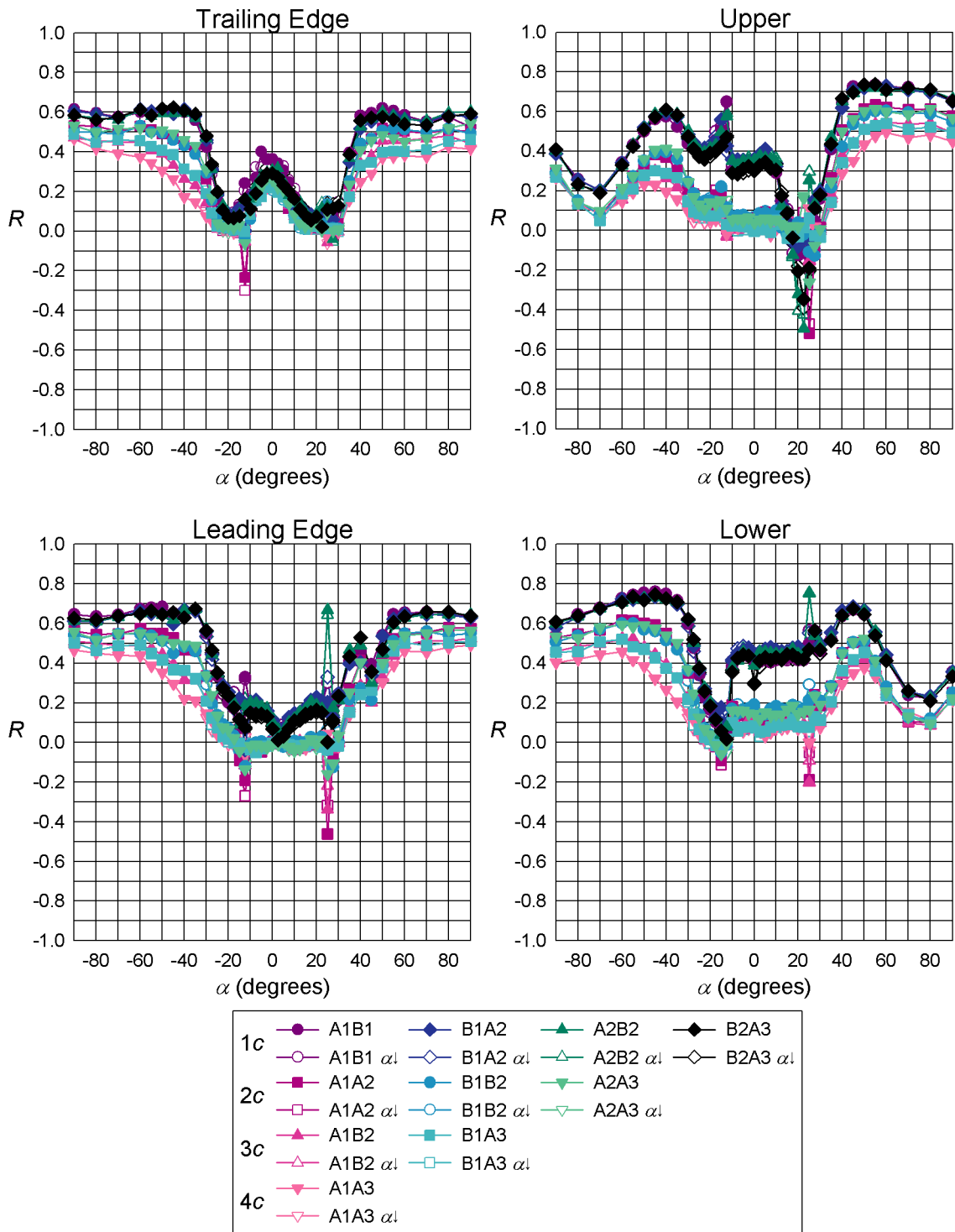


Figure 5-30 - NACA 4421 Correlation coefficients between taps in the 4 tap rows (A1, A2 and A3) and the equivalent taps in the 28 tap rows (B1 and B2) for the highest turbulence flow ($I_u = 3\%$) with an integral length scale of about $1/3c$ (the small grid in position A).

However, the medium grid in position A greatly effects the correlations as shown in Figure 5-32. There are no “jumps” in correlation associated with stall (except for the odd point in the B2A3 comparison at $\alpha = -15^\circ$). The trailing edge shows very little correlation before the onset of shedding. The leading edge shows an increase in correlation for $\alpha > 2.5^\circ$ and $\alpha < 2.5^\circ$ for the 1c spanwise separation cases, beyond this region the correlations decrease again before increasing with the onset of stall. The same phenomena were observed in the correlations for the small grid in

position A for this spacing and, to a lesser extent, for the medium grid in position E. Increasing turbulence intensity appears to increase the size of these “peaks” around $\alpha = 2.5^\circ$ although the correlations are still quite small. This feature in the leading edge taps seems to be an effect of the freestream turbulence intensity, with increasing α causing a decrease in exposure to the freestream turbulence. The reverse trend, a slight decrease in correlation about $\alpha = 2.5^\circ$, can just be observed in Figure 5-31 (medium grid in position E) for spanwise spacings greater than $1c$ and can be more clearly observed in Figure 5-32 (medium grid in position A).

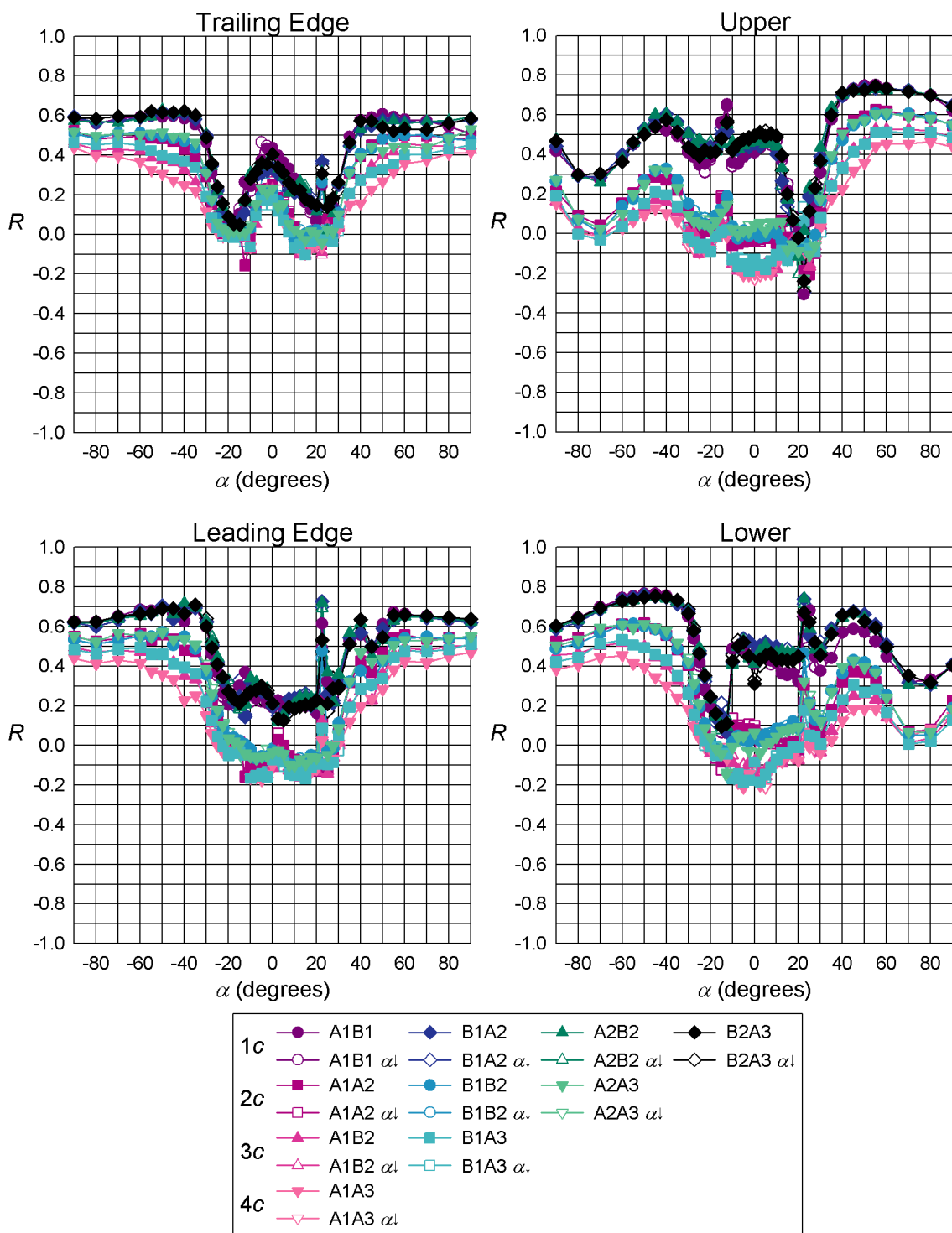


Figure 5-31 - NACA 4421 Correlation coefficients between taps in the 4 tap rows (A1, A2 and A3) and the equivalent taps in the 28 tap rows (B1 and B2) for the lowest turbulence flow ($I_u = 2\%$) with an integral length scale of about $1/2c$ (the medium grid in position E).

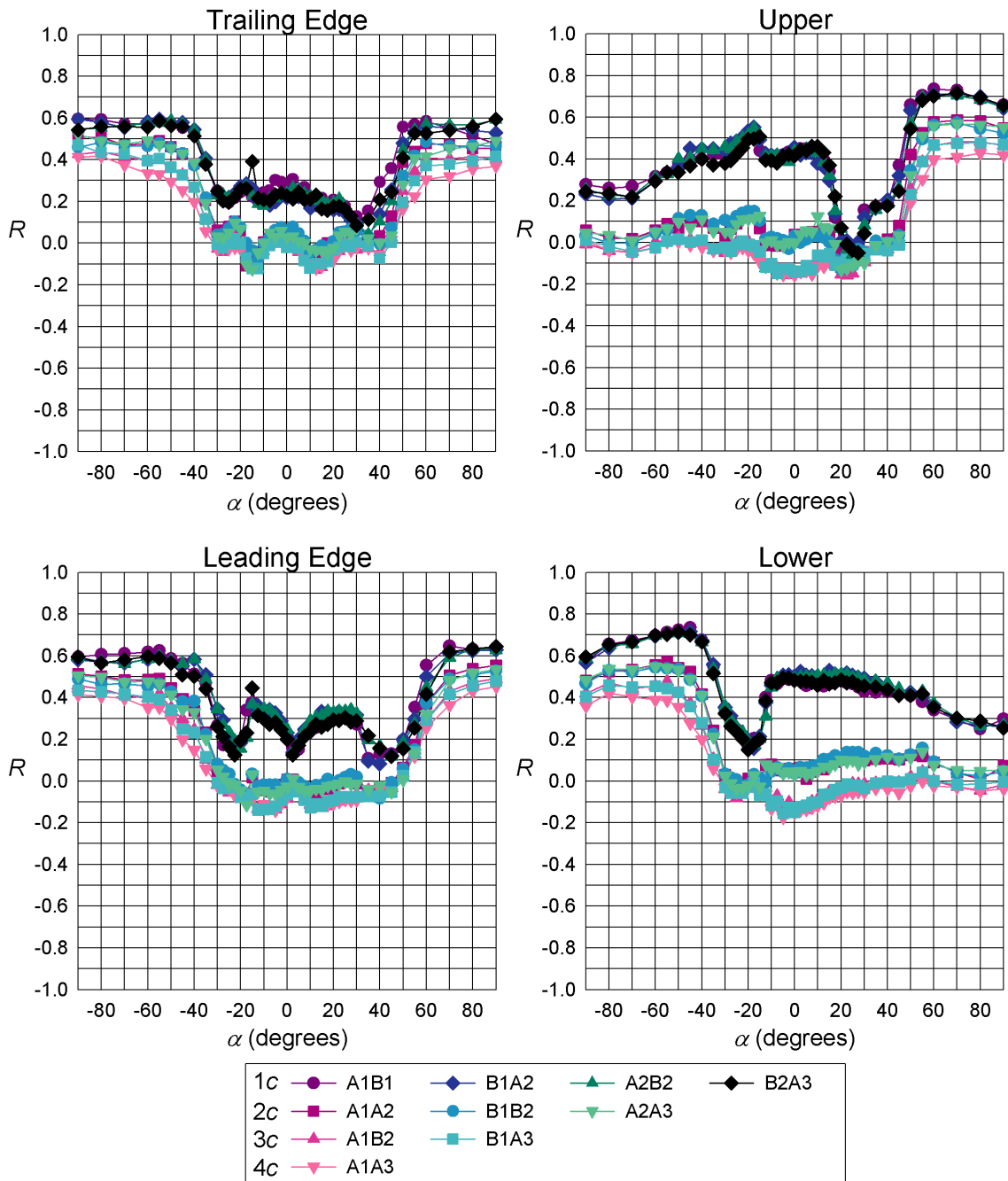


Figure 5-32 - NACA 4421 Correlation coefficients between taps in the 4 tap rows (A1, A2 and A3) and the equivalent taps in the 28 tap rows (B1 and B2) for the highest turbulence flow ($I_u = 6\%$) with an integral length scale of about $1/2c$ (the medium grid in position A).

The correlations for the lower and upper taps in Figure 5-32 show the characteristic increase with α when the tap is downwind. However, there was very little correlation when the tap was upwind and the “dip” seen earlier has almost been wiped out by the high turbulence intensity.

The turbulence intensity for the large grid in position E is lower than for the medium grid in position A, for which the correlation coefficients are shown in Figure 5-33 and Figure 5-32 respectively. As for the earlier lower turbulence intensity case where different scales but similar turbulence intensities were compared (small grid in position A and medium grid in position E), the decrease in turbulence intensity reduces some of the trends noted earlier, e.g. the loss of correlation

for the upstream position of the upper and lower taps is not as severe, but the same general features are seen.

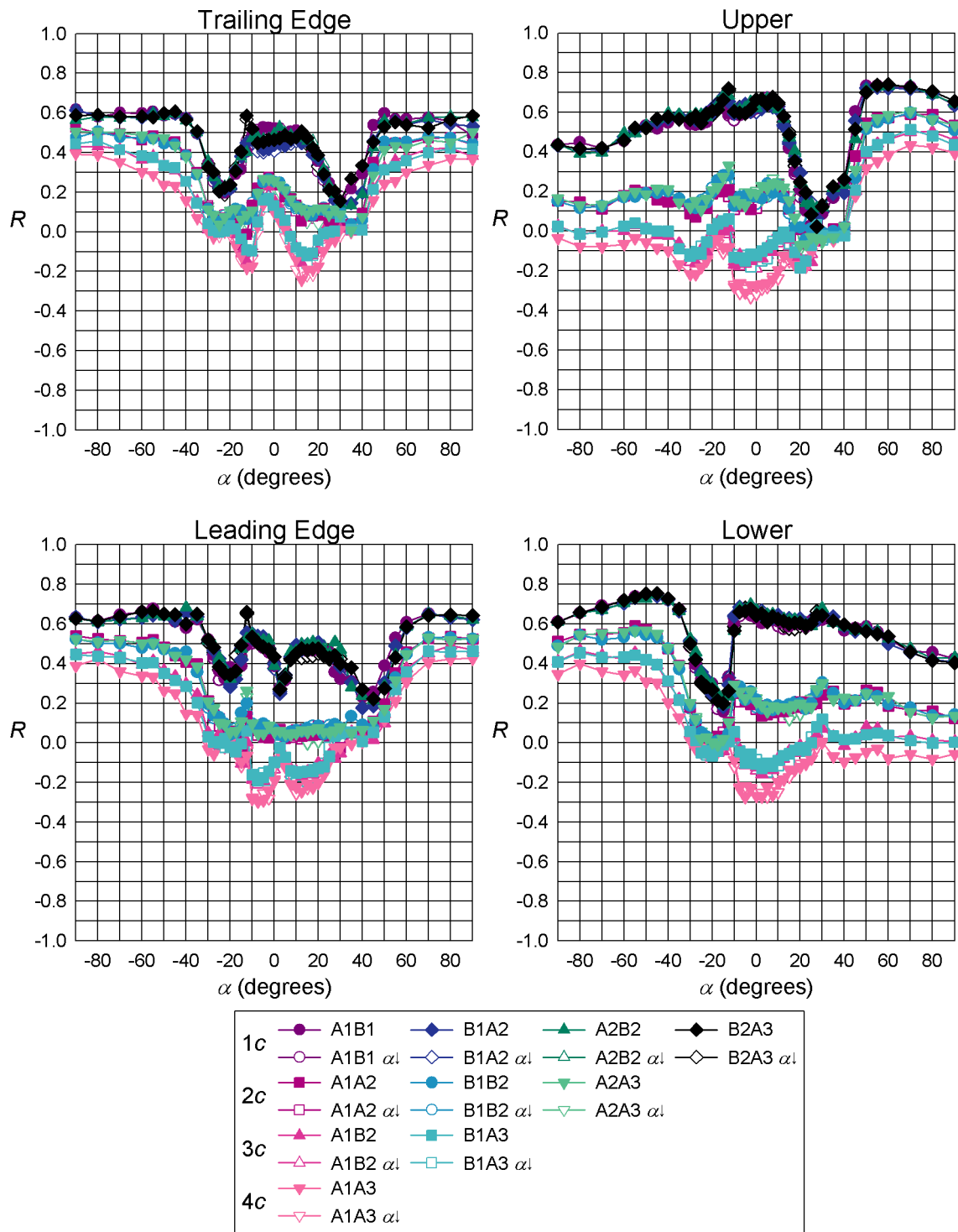


Figure 5-33 - NACA 4421 Correlation coefficients between taps in the 4 tap rows (A1, A2 and A3) and the equivalent taps in the 28 tap rows (B1 and B2) for the lowest turbulence flow ($I_u = 5\%$) with an integral length scale of about $1c$ (the large grid in position E).

The large grid in position B smooths out much of the variation in the correlation coefficients, as seen in Figure 5-34. Note the increase in the local maxima of the leading edge graph for $\alpha < 2.5^\circ$ and $\alpha > 2.5^\circ$ is slightly higher for the increased turbulence intensity supporting the idea that the turbulence is the primary cause of this feature. In general the correlations for spanwise spacings of

$1c$ at $\alpha = \pm 90^\circ$ are very similar to the case of the large grid in position E, Figure 5-33, but the other spacings are less correlated.

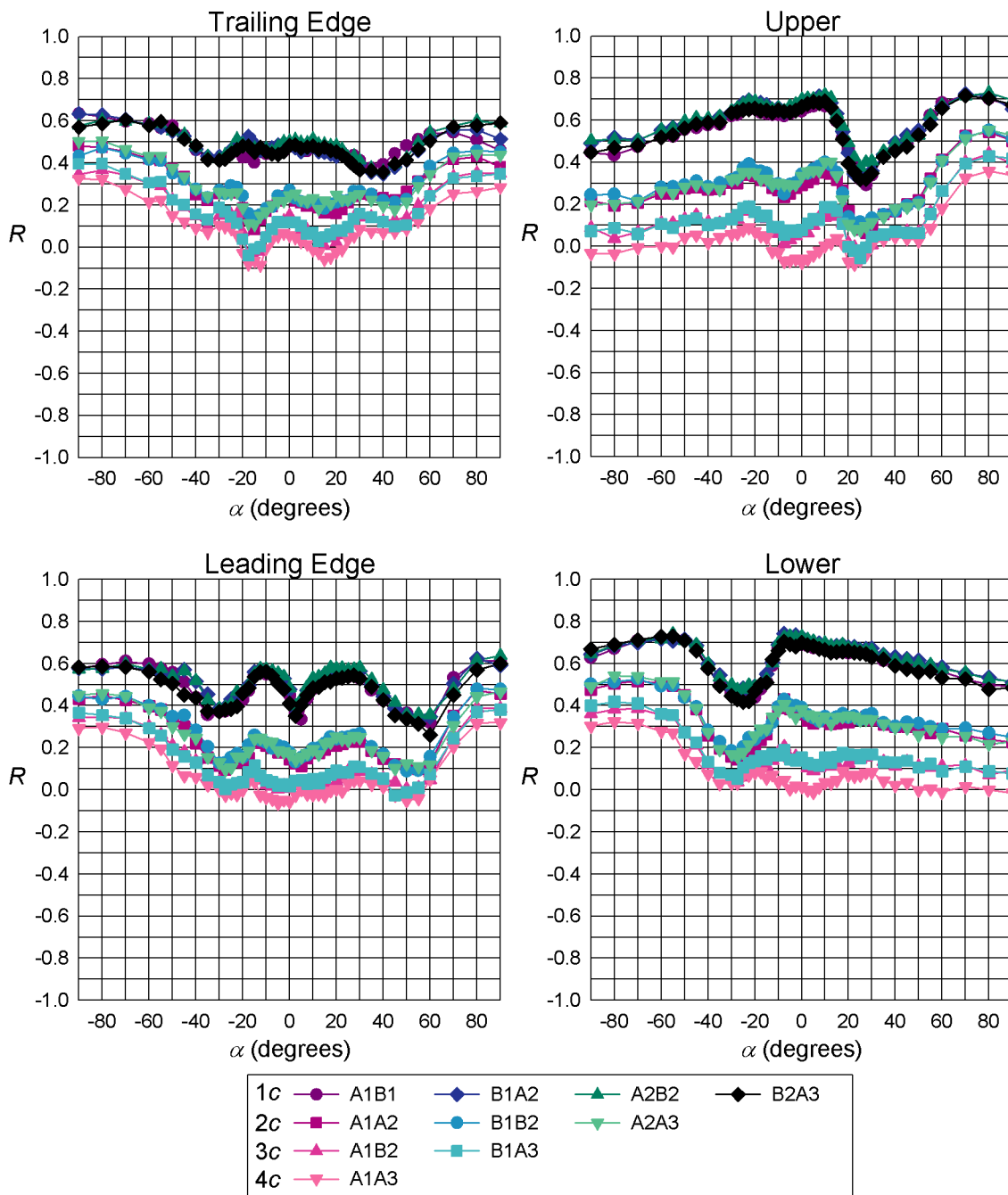


Figure 5-34 - NACA 4421 Correlation coefficients between taps in the 4 tap rows (A1, A2 and A3) and the equivalent taps in the 28 tap rows (B1 and B2) for the highest turbulence flow ($I_u = 13\%$) with an integral length scale of about $1c$ (the large grid in position B).

The general features of these correlations were seen on all the aerofoil sections tested and the possible implications for wind turbine design will be discussed in Chapter 7.

Chapter 6

S809 Aerofoil

6.1 Introduction

The S809 aerofoil section was designed for use on wind turbines and has been extensively tested both in wind tunnels and on operating wind turbine blades, see Section 2.4.2. It was designed to have a restrained maximum lift and gradual stall, see Section 2.2. The current tests provide results from another thick, cambered aerofoil to compare with the results from the previous aerofoil sections. These comparisons will be left until Chapter 7. As many of the general features are similar to the other aerofoils sections, and have been covered in detail in the previous chapters, the discussion of results in this chapter will be relatively brief.

6.2 Mean Results

6.2.1 Comparison

Test	Model	Chord (mm)	Aspect Ratio	Re ($\times 10^6$)	Blockage	
					$\alpha=20^\circ$	$\alpha=90^\circ$
Delft	108 staggered tappings, very smooth model	600	2.08 <i>c</i>	1	12.4%	-
Ohio (OSU)	Same model for OSU and CSU tests. 31 tappings in row in centre of tunnel, positions as on NREL turbine in Phase I tests, model same roughness as NREL blade (made in same mould).	457 (18")	2.17 <i>c</i>	0.75 to 1.5	11.2%	-
Colorado (CSU)				0.3 to 0.65	4%	11.6%
Current	Two rows of 22 tappings (Row B1 and B2), smooth model	125	7.28 <i>c</i>	0.275 to 0.4	2.1%	6.25%

Table 6-1 – Summary of test setups for the comparison data for the S809 aerofoil section.

The S809 aerofoil section was used on the NREL 10m diameter turbine. There have been a number of studies on this aerofoil; these have been discussed in relation to comparisons with the wind turbine performance in Section 2.4.2. A summary of the test setups is given in Table 6-1. The Delft and Ohio State University (OSU) data used for comparison was obtained from Somers (1989) and Reuss Ramsay, Hoffman & Gregorek (1995) and the Colorado State University (CSU) from Butterfield, Musial & Simms (Butterfield, Musial & Simms, 1992). The Delft model used staggered tappings so that the wake from one tapping would not impact on other tappings. However, the three-dimensionality encountered during and post-stall can cause problems with this method, as discussed in Section 2.2. The OSU and CSU data was obtained using the same tapping positions as on the NREL 10m test turbine in the first set of field tests called Phase I had one radial station of 31 pressure taps on straight blades (Phase I, Butterfield, Musial & Simms, 1992). Phase II used 28 of the taps but had four radial pressure locations, and Phase III and IV used 22 taps at

five spanwise locations on twisted blades (Simms *et al.*, 1999a). The tapered and twisted blades used in the Ames tunnel tests also had 22 taps at five spanwise locations (Hand *et al.*, 2001). The positions of the taps for these studies and for the current experiment are shown in Figure 6-1. The large chord lengths for these tests allowed a much higher concentration of taps at the leading edge than was possible in the current experiment.

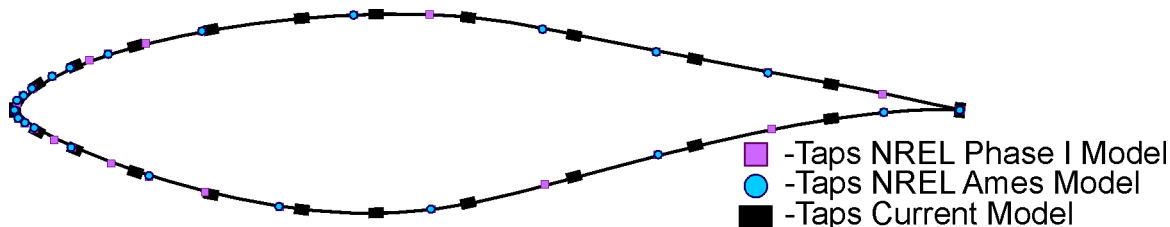


Figure 6-1 - Tap positions for the tapping rows on the NREL 10m diameter turbine tested in the NASA Ames wind tunnel (Schreck, Scott J., 2000), from the Phase I tests (Butterfield, Musial & Simms, 1992) and those in the current study. Note that the Phase I test had all the tapping positions of the NREL test and 9 additional taps.

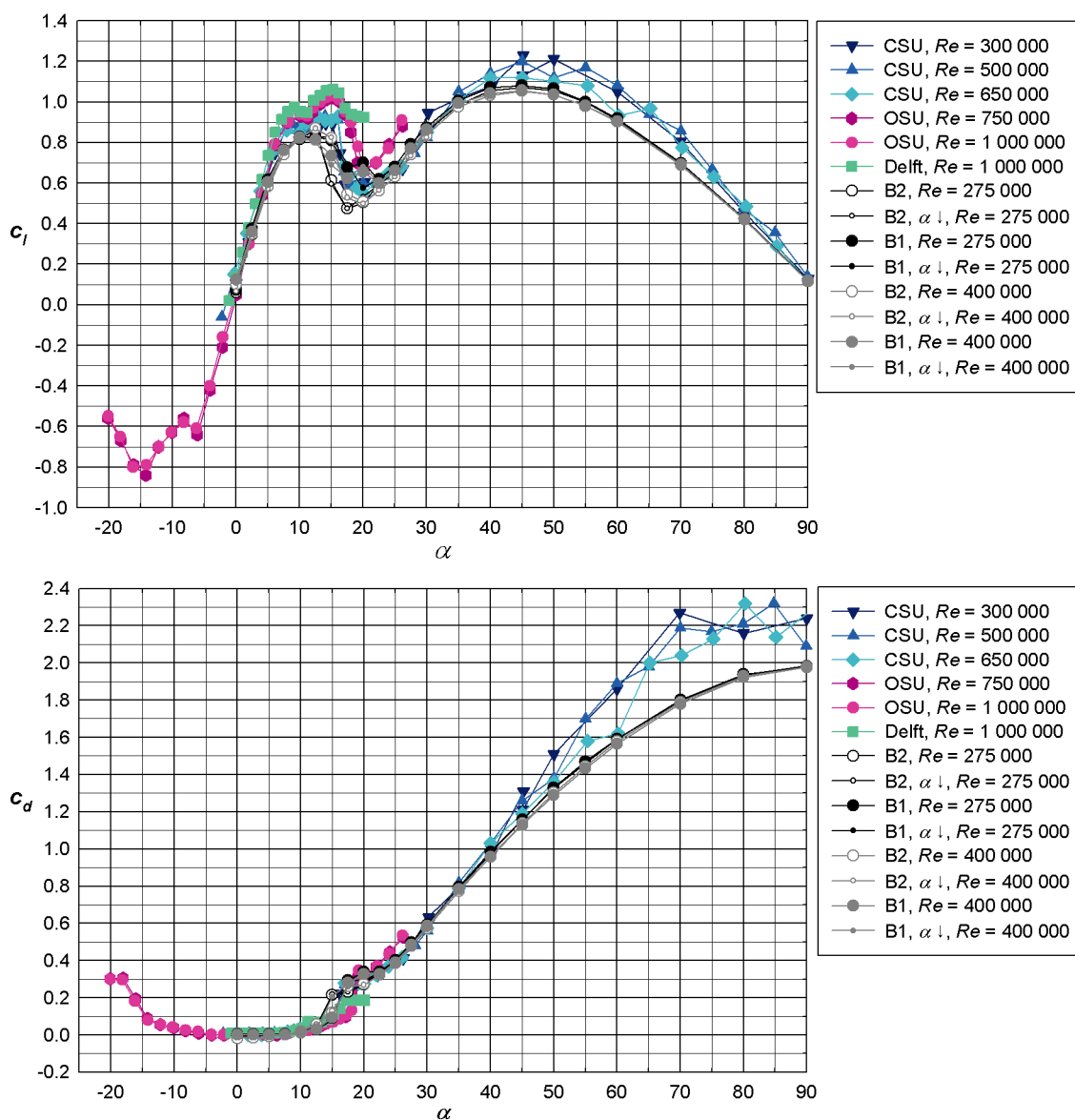


Figure 6-2 - Comparison the coefficients of lift and drag with data from the current experiments with data from other wind tunnel tests of the S809 aerofoil.

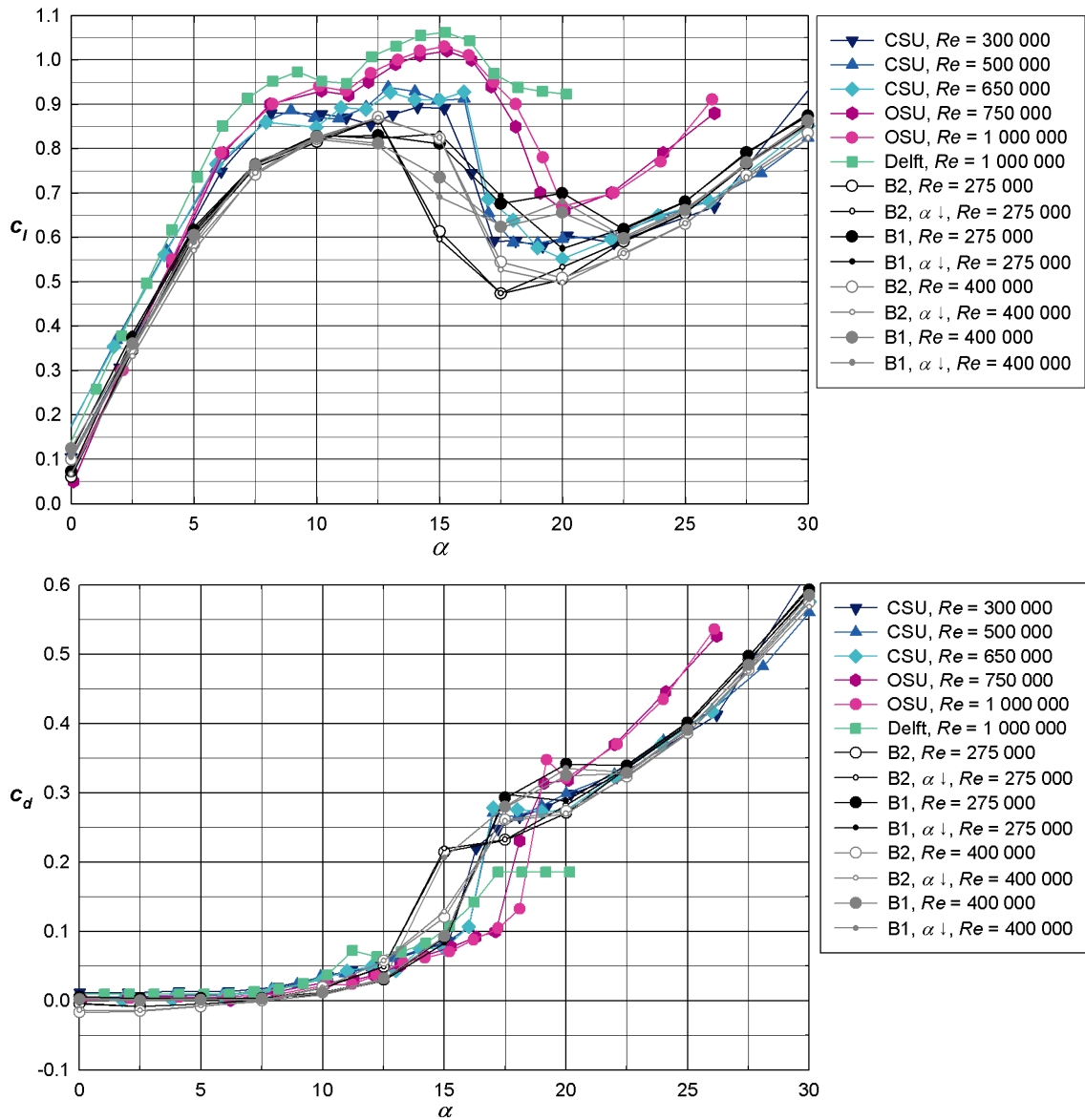


Figure 6-3 - Comparison the coefficients of lift and drag with data from the current experiments with data from other wind tunnel tests of the S809 aerofoil around stall for a smaller range of α than in Figure 6-2.

Figure 6-2 shows the comparison of the experimental results for all α tested. There was a good match for all cases for the c_l curves up until $\alpha = 5^\circ$. The differences in the stall region will be examined in detail later in this section. For $22.5^\circ \leq \alpha \leq 40^\circ$ the current results match the CSU data well. At the largest α tested for the OSU experiments there was a very high blockage (14.5%) so it is not surprising that it does not match the CSU or current results near this angle. The CSU data has higher c_l for $\alpha \geq 40^\circ$ and is more variable than the current experiments, although they both trend to the same c_l at $\alpha = 90^\circ$.

There is a good match for the c_d curves in Figure 6-2 below the jumps associated with stall (the stall region will be examined in more detail later in this section). There is also a good match between the current results and the CSU data past stall for $\alpha < 40^\circ$. However, the CSU data shows

higher c_d for $\alpha \geq 40^\circ$ than the current data set and a great deal of “noise” in the measurements. The CSU data also trends to a larger c_d than the current experimental results.

It is interesting that (except for some variability around stall for the current experiments that will be examined later in this section) comparing the different Re tests in the same facilities were fairly consistent. However, comparing between tests conducted in different facilities, there were far larger differences. Therefore the influence of the testing facility were greater than that of Re , at least for the ranges of Re tested.

Figure 6-3 shows the comparison of c_l and c_d over a limited range of α to allow the differences in the stall region to be observed. The current experiment's c_l curves drop off more quickly at the end of the linear region and are, in general, lower in the stall region than the curves from the other experiments. As would be expected, the current data are closest to the CSU tests, which are the closest in Re . The CSU data, which is also the only data at the same order of magnitude blockage at $\alpha = 20^\circ$, shows a similar drop in c_l between 15° and 17.5° . This is the general trend in the current data (most clearly there is a drop in Row B2 at $Re = 400,000$ between these α). There is quite a deal of difference between all the plots during stall. Some of the differences between the other experiments and the current results could be due to the finer sampling in α of the other tests. The lines connecting points in the current tests may not be an accurate reflection of the behaviour of the aerofoil between these points. Another difference is the much finer sampling at the leading edge of the other tests, see Figure 6-1. This could result in better sampling of the leading edge suction peak and therefore higher calculated c_l . In addition, the current results were from tapping rows one chord length either side of the tunnel centreline. The OSU and CSU results were from a row of tappings on the tunnel centreline and the Delft results were from tappings staggered across the span. Given the three-dimensional structures that are known to exist on stalling aerofoils, the differences in this region are not unexpected.

The drag curves show better matching to the current results during stall, see Figure 6-3. The jump in drag associated with stall occurs at a similar α to the CSU data (except for row B2 $Re = 275\ 000$ where the jump is at slightly lower α than the other cases). The OSU data shows a jump later than the CSU and current data and increased c_d after this jump, but the tunnel blockage was very high at these α for these tests. The Delft data does not show a sudden increase in c_d . This may be due to its staggered tappings. It generally has lower c_d than the other cases at the higher α tested for this model.

While there is a good deal of variation between the current results and previous tests this is also true between all tests. Considering the difficulty in matching results from different facilities, the degree of agreement in results was considered satisfactory.

6.2.2 Effect of Added Turbulence

The lift curve in Figure 6-4 shows a very short linear region (for $\alpha \leq 5^\circ$) before the rate of increase in lift begins to slow. There are some differences between the results from Row B1 and B2 for $\alpha \leq 5^\circ$. The local maximum in lift associated with stall occurs at 12.5° for both rows but the rows show different stalling characteristics from this angle on. The reasons for this will be discussed when the mean C_p and flow visualisation results are discussed later in this section. Row B2 has higher c_l at 12.5° but then stalls sharply to a local minimum at 17.5° . There are slight differences between the increasing and decreasing α cases for Row B2 at 15° and 20° . The lift seen by Row B2 is less than that seen by Row B1 until $\alpha \geq 55^\circ$. Row B1 stalls more gradually. There was a slight difference between the increasing and decreasing α cases at 15° (as was the case for Row B2 but the decreasing α case caused slightly increased c_l) and a large difference at $\alpha = 20^\circ$, where the increasing case showed an increase in c_l and the decreasing case continued the linear decreasing trend to a local minimum. Both the increasing and decreasing cases gave the same lift for $\alpha \geq 22.5^\circ$.

The drag curve in Figure 6-4 has some measurements at low α that are very slightly negative due to only measuring the pressure drag (as discussed in Chapter 5 for the NACA 4421 aerofoil section). The jump in drag for Row B2 associated with stall occurred at 15° and the increasing and decreasing α cases are very similar at all α . The jump for Row B1 occurred at 17.5° and there is a slight difference between the increasing and decreasing α cases at $\alpha = 20^\circ$ with the increasing α case showing higher drag. However, both rows show very similar results for the rest of the range of α and the drag trends to 2.0 (the value that would be expected for a flat plate normal to the flow) at $\alpha = 90^\circ$.

The $c_{m, 1/4c}$ curve showed slight differences between the two rows over the entire range of α , with Row B1 showing increased $c_{m, 1/4c}$ for $0^\circ < \alpha < 10^\circ$ and $\alpha > 15^\circ$. At $\alpha = 15^\circ$ there was a slight drop in $c_{m, 1/4c}$ associated with stall for Row B2; this occurred at 17.5° for Row B1. There were differences in the results from Row B1 at $\alpha = 20^\circ$ for the increasing and decreasing α cases. The decreasing α case showed increased $c_{m, 1/4c}$ compared to the increasing α case. The general decreasing trend in both rows matched well for $\alpha > 20^\circ$.

The C_p and σ results in Figure 6-5 provide more insight into the causes of the features of the c_l , c_d and $c_{m, 1/4c}$ plots. The differences in the coefficients between the two rows for $\alpha \leq 10^\circ$ seem to be related to small differences in C_p near the leading edge. The C_p plots at $\alpha = 0^\circ$ and $\alpha = 5^\circ$ show increased σ at about $0.6c$. By 10° this has spread to a wide range of taps and by 12.5° this σ peak has moved towards the leading edge. At 12.5° this peak and the one at the leading edge are higher for the Row B1 cases. At $\alpha = 10^\circ$ and 12.5° the differences in the C_p and σ are especially evident at the first two taps near the leading edge on the suction side.

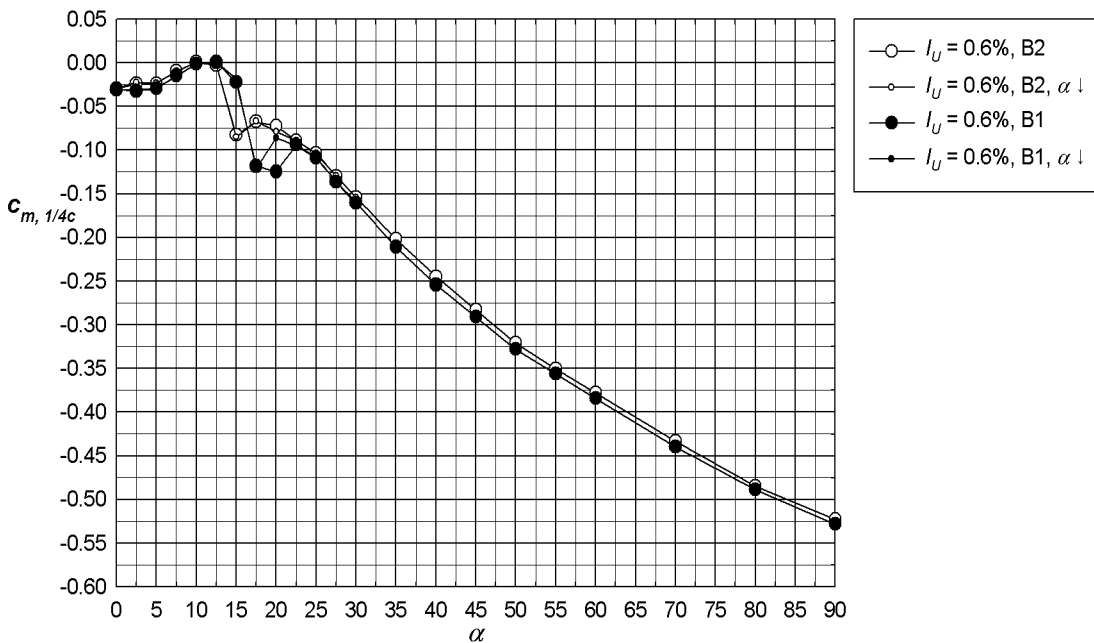
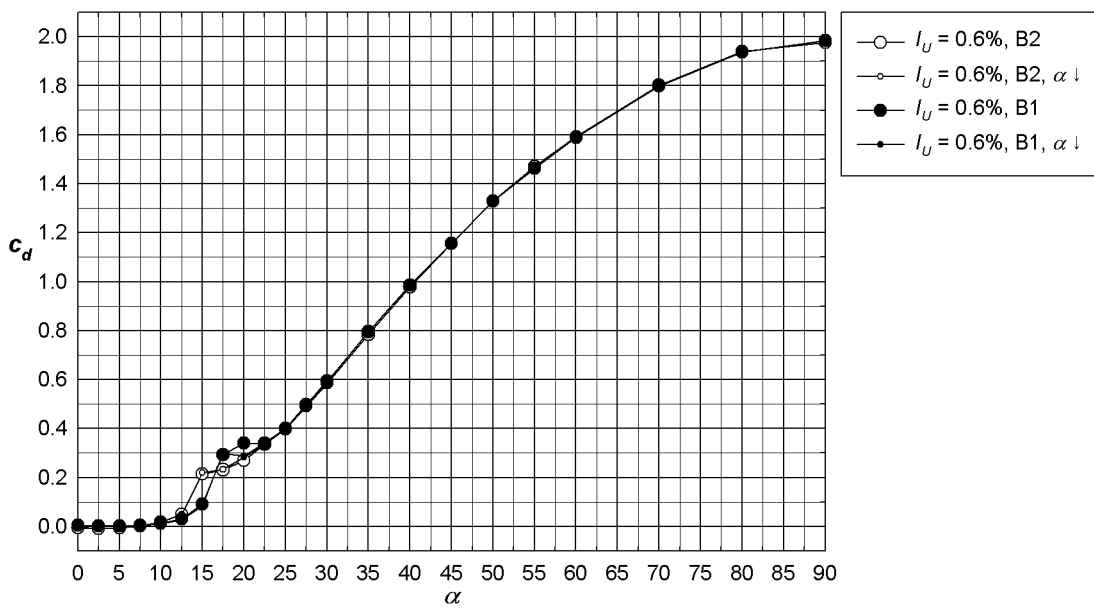
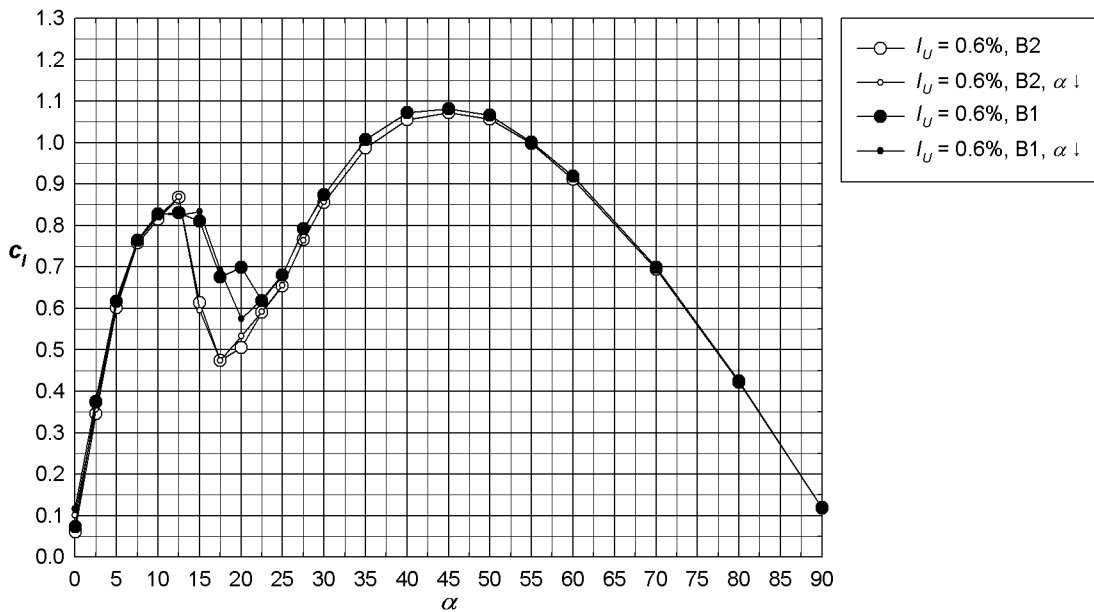


Figure 6-4 - S809 mean coefficients of lift, drag and of moment about the quarter chord for the lowest turbulence case (no grid).

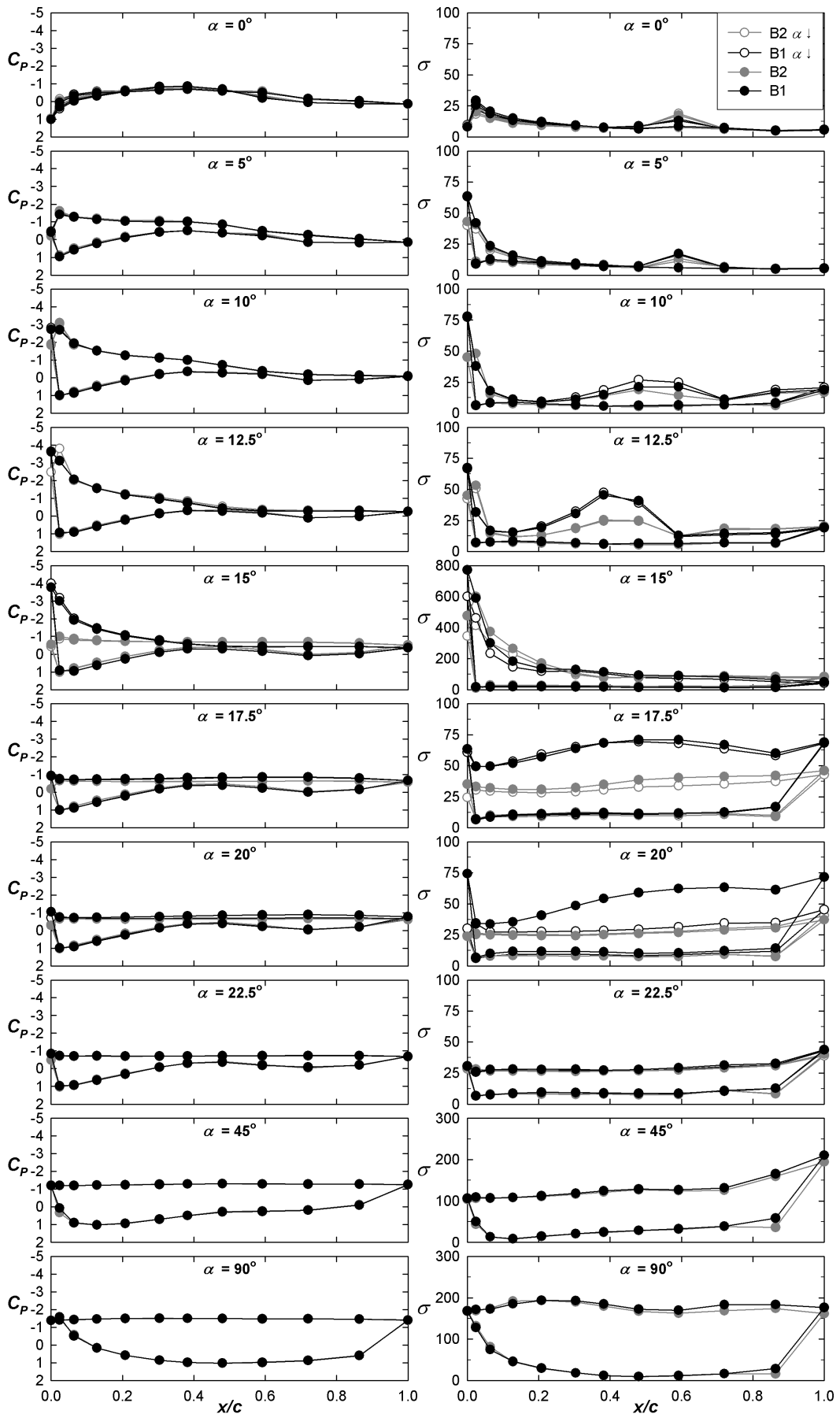


Figure 6-5 - Coefficients and standard deviations of the pressures around the S809 aerofoil at selected α for the lowest turbulence flow (no grid). Note the scale of the σ plots changes from a maximum of 300 to a maximum of 100 for $\alpha \geq -20^\circ$.

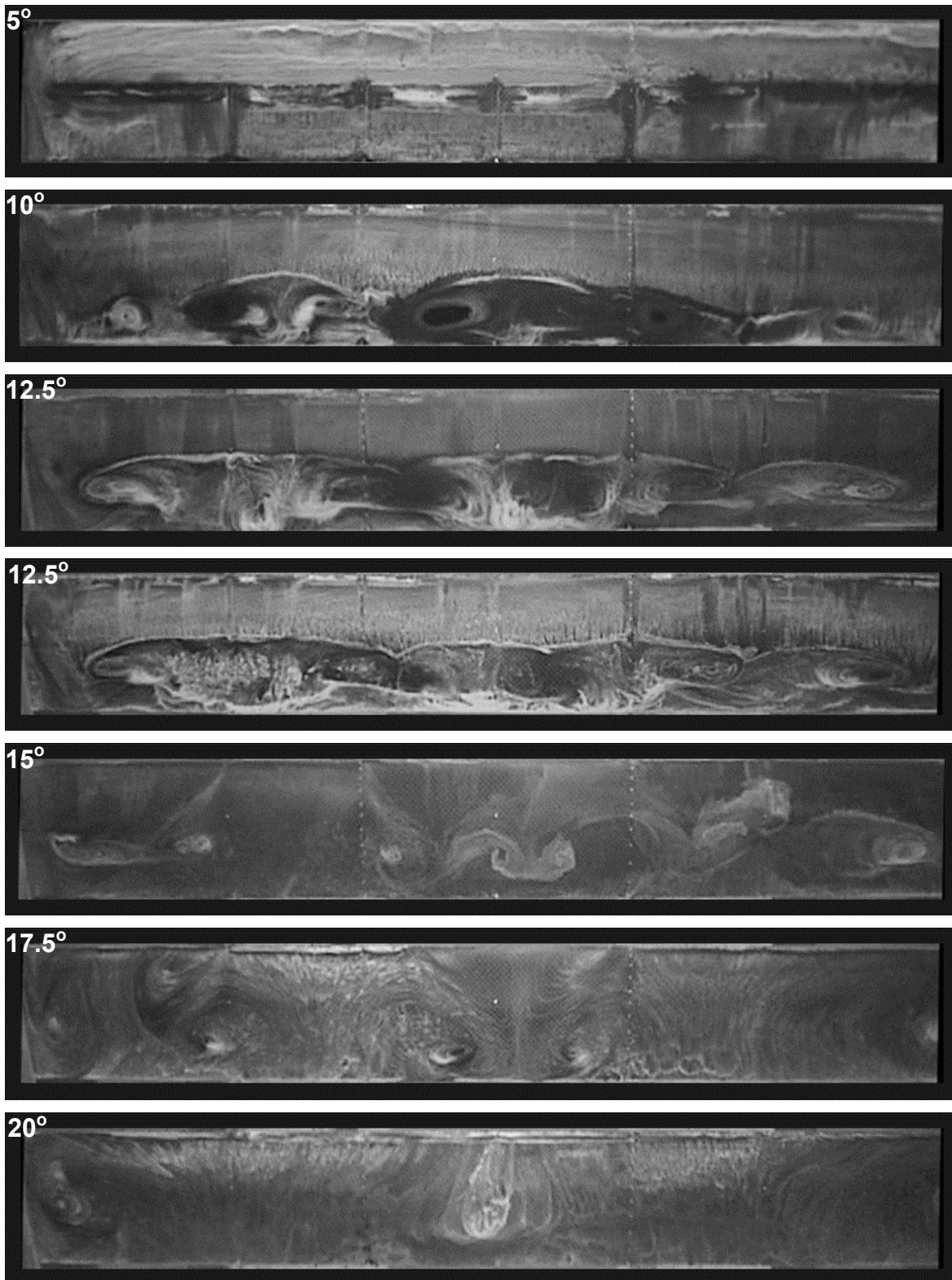


Figure 6-6 - Surface flow visualisation on the S809 around stall for the lowest turbulence case (no grid). The leading edge is at the top of the pictures, taping row B2 on the left hand side and taping row B1 on the right hand side.

By 15°, Row B1 and B2 show very different result in C_p with Row B2 appearing to be stalled. However, the σ results are similar with a large leading edge peak for both rows. By 17.5° both rows have a similar stalled profile but the pressure measurements on the suction surface of Row B1 have slightly greater magnitude resulting in the increased c_l seen in Figure 6-4. The σ for Row B1 is much higher than Row B2. This continues for $\alpha = 20^\circ$ for the case of increasing α for Row B1

only. The decreasing α case looks like the results from Row B2 and therefore has similar c_l . By 22.5° the differences in C_p and σ are mainly near the leading edge resulting in only small differences in c_l . This is also true at $\alpha = 45^\circ$. At 90° the C_p results are very similar for Rows B1 and B2.

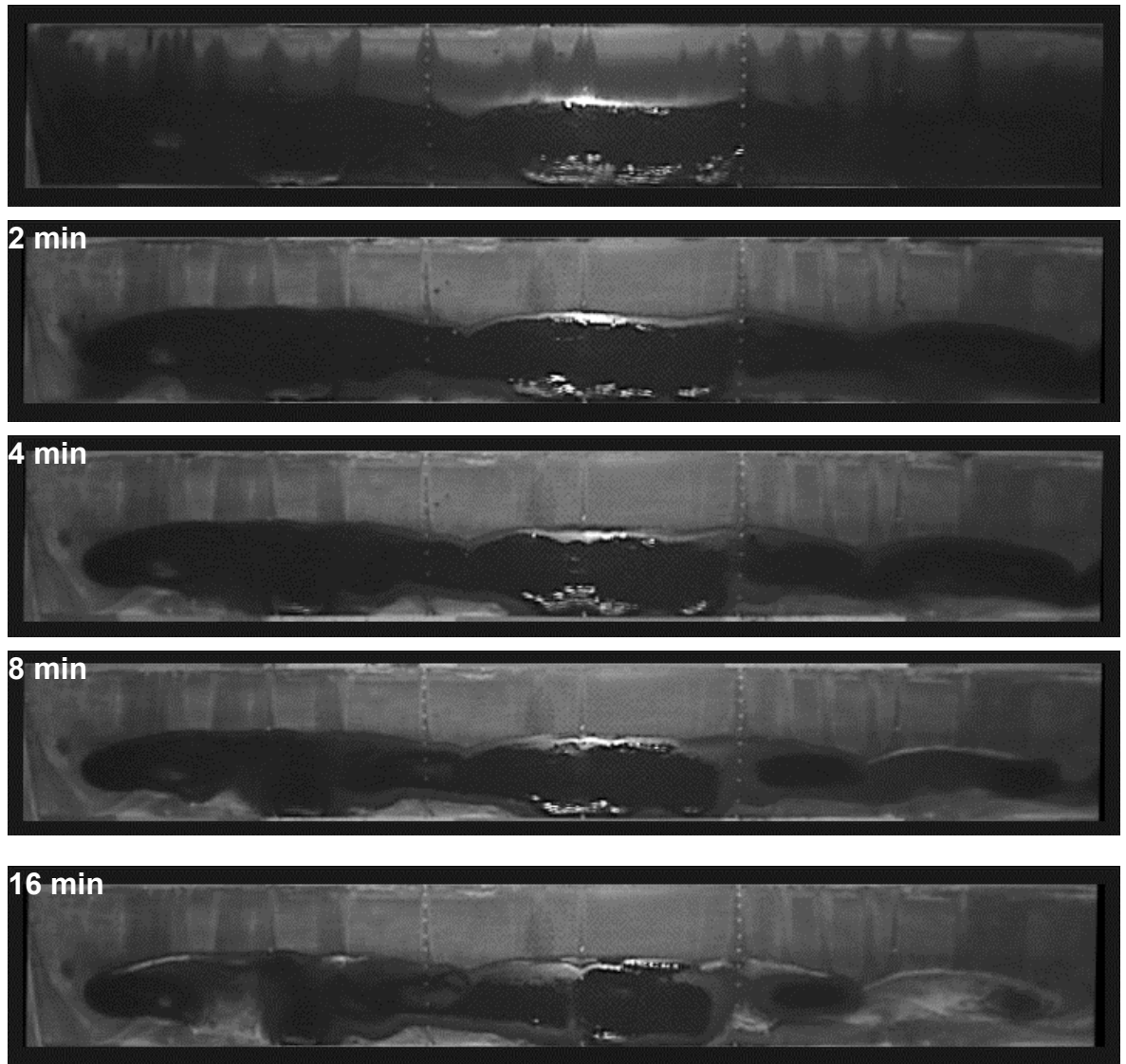


Figure 6-7 - Surface flow visualisation on the S809 at $\alpha = 12.5^\circ$ degrees for the lowest turbulence case (no grid), the first frame was taken just after the tunnel reached full speed and the others were taken at the specified amount of time after the first frame.

Figure 6-6 shows the China Clay surface visualisations for the lowest turbulence (no grid) case. As was emphasised in the description of this method in Chapter 3, the tunnel had to be run up to speed after the paint was applied. Therefore this method is looking at the flow seen in the decreasing α case. At 5° the mixture was a little thick, resulting in brush strokes being visible on the left hand side near the leading edge. However the main feature, a separation bubble about mid-chord, can clearly be seen. By 10° there was an uneven separation with uneven mushroom structures beyond the separation line. This probably caused the differences in mean C_p seen between the rows at the leading edge in Figure 6-5 with the two rows being in different areas of these mushroom structures (Row B1 is on the right hand side of the picture while Row B2 is on the left hand side).

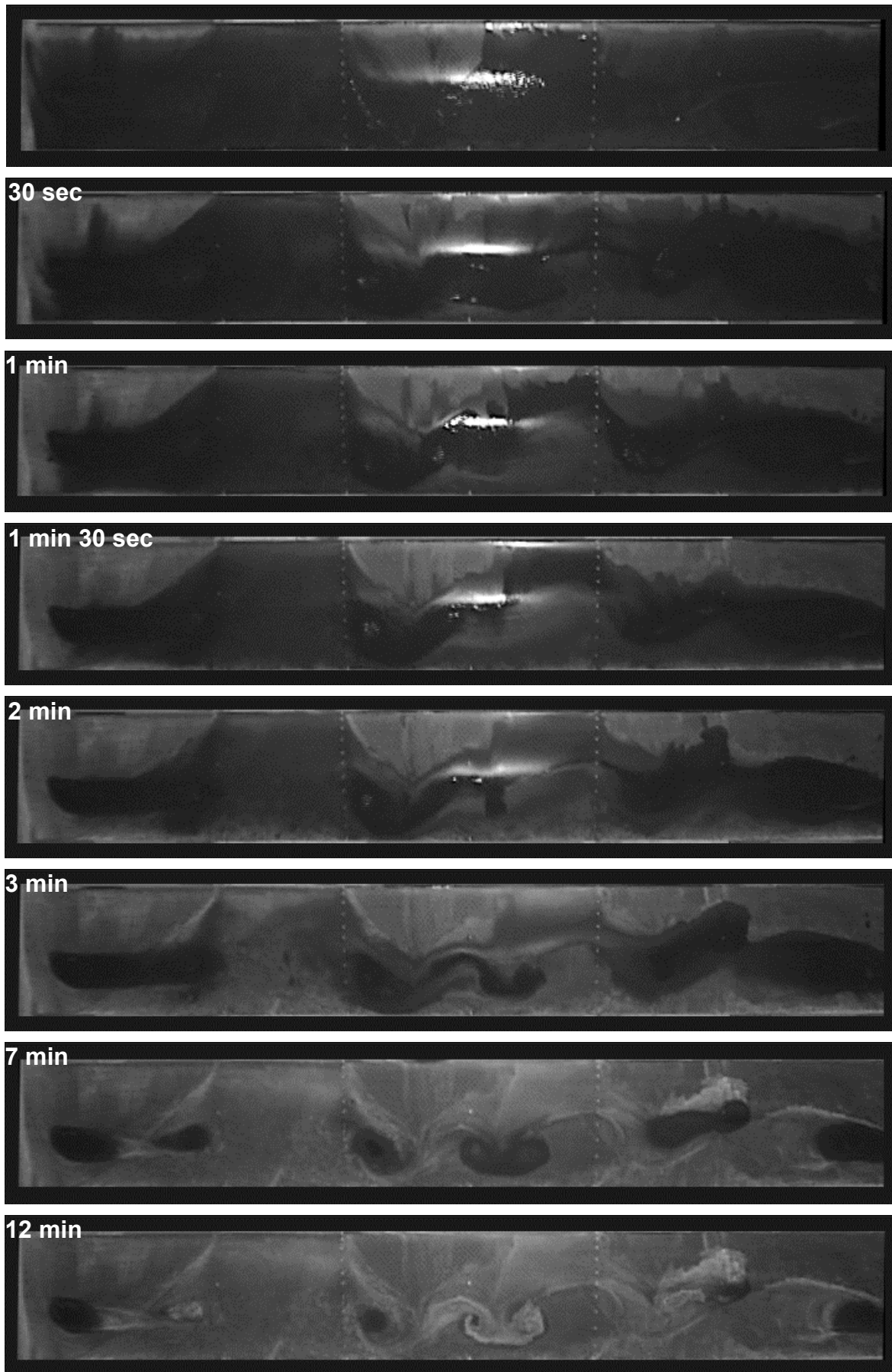


Figure 6-8 - Surface flow visualisation on the S809 at $\alpha = 15^\circ$ degrees for the lowest turbulence case (no grid), the first frame was taken just after the tunnel reached full speed and the others were taken at the specified amount of time after the first frame.

At 12.5° two pictures from different runs are shown in Figure 6-6, the upper picture had less china clay in the mix and so gave a clearer picture but with less detail than seen in the lower picture. The two pictures show very similar patterns with the separation line about mid-chord. By 15° , Row B2 (left hand side) seems to be in a separated mushroom structure, while the right hand side is a region with a number of structures. This clearly accounts for the differences in C_p seen at this angle in Figure 6-5. Figure 6-7 and Figure 6-8 show frames taken from video of the surface flow visualisation for 12.5° and 15° respectively. These figures allow transient features of the surface pattern to be identified, which may otherwise be destroyed as the china clay dries into the final pattern. The first frame in each case was taken just after the tunnel reached the desired speed. The 12.5° results shown in Figure 6-7 took a long time to dry as the paint gathered near the trailing edge but the structures were very stable over this time. For the 15° results shown in Figure 6-8, the large mushroom structure on the left hand side is visible in all frames and remains constant. However, on the right hand side in the first frame a similar mushroom structure is visible but by the second frame there is a pool of liquid in the mid-span of the aerofoil and another to the right hand side. These structures were unstable, with the liquid flowing towards the leading edge and then reforming repeatedly as can be seen in the subsequent frames.

At $\alpha = 17.5^\circ$, Row B1, on the right hand side in Figure 6-6, is closer to the swirling side of the mushroom structure and therefore has more suction across the chord as seen in Figure 6-5. By 20° the aerofoil looks stalled with recirculation zones seen only near the walls. The central feature was due to pools of fluid that formed on the leading edge and the mid-span and lapped across as it dried.

The c_l , c_d and $c_{m, 1/4c}$ results for an integral turbulence length scale of about $1/3c$ (small grid) are presented in Figure 6-9. The flow with 1% turbulence reduced the signs of hysteresis, the only case remaining shows a small difference in c_l (<0.03) between the increasing and decreasing α results for Row B1 at $\alpha = 20^\circ$. The lift curve shows that increased turbulence intensity smoothed out the stalling process but otherwise there was little difference between the results, except that the 3% turbulence case showed slightly higher c_l than for the other flows at α about 45° . Rows B1 and B2 showed very different curves during stall. This is likely to be due to the rows being in different parts of the stall cells as was seen for the lowest turbulence (no grid) case. This, and the differences at $\alpha = 45^\circ$, will be discussed further when the C_p and σ plots are examined later in this section.

The drag and moment about the quarter chord results shown in Figure 6-9 indicate that increasing turbulence intensity reduces the jumps associated with stall. The spread in the results is small apart from this region. The C_p and σ results for the 1% and 3% turbulence intensity cases at selected α are shown in Figure 6-10(a) and (b). For $\alpha = 0^\circ$ and 5° show similar results for the two levels of turbulence intensity. Note the change in scale for the σ plots between 0° and 5° .

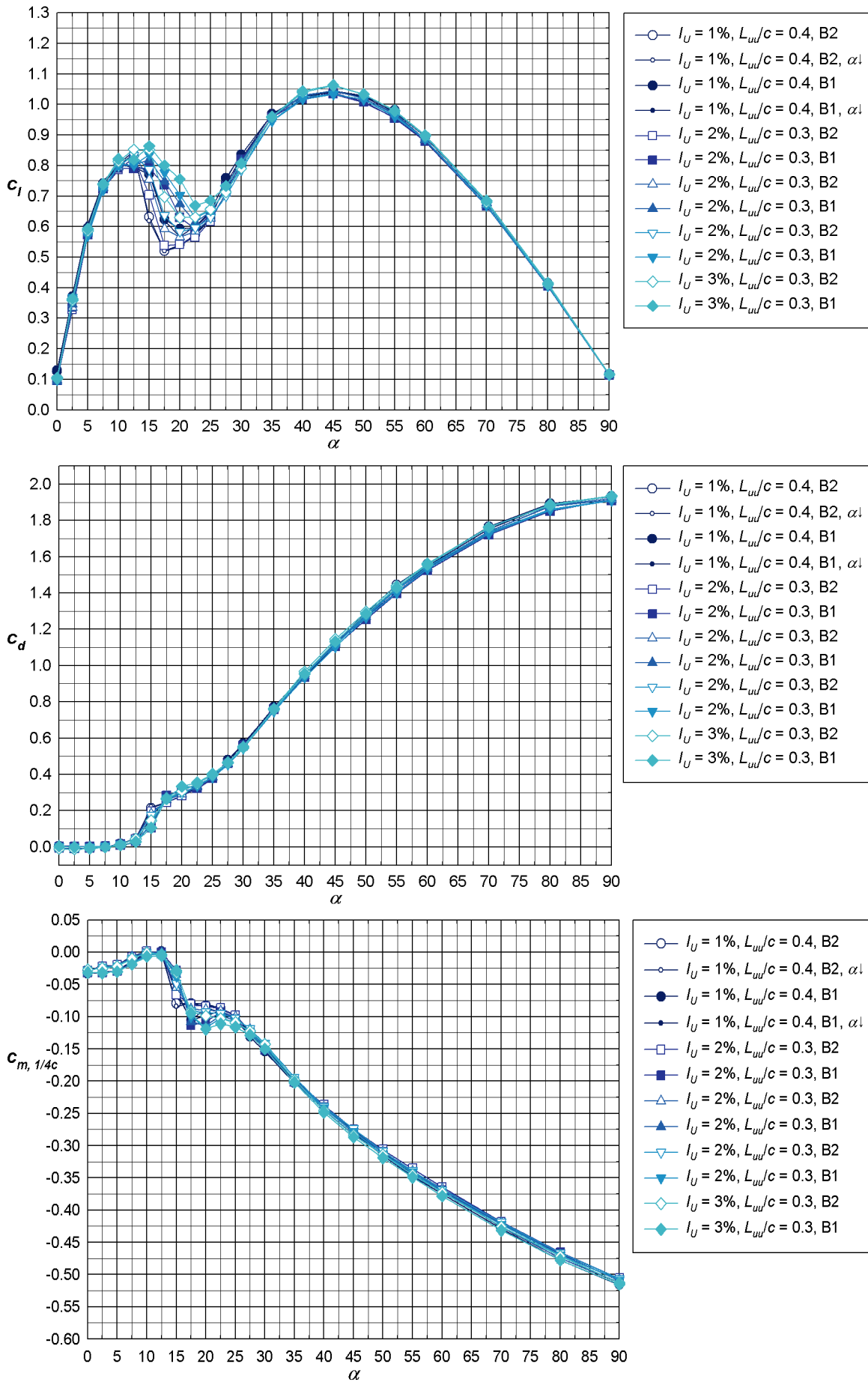


Figure 6-9 - S809 mean coefficients of lift, drag and moment about the quarter chord with the integral turbulence length scale $\sim 1/3c$ (small grid).

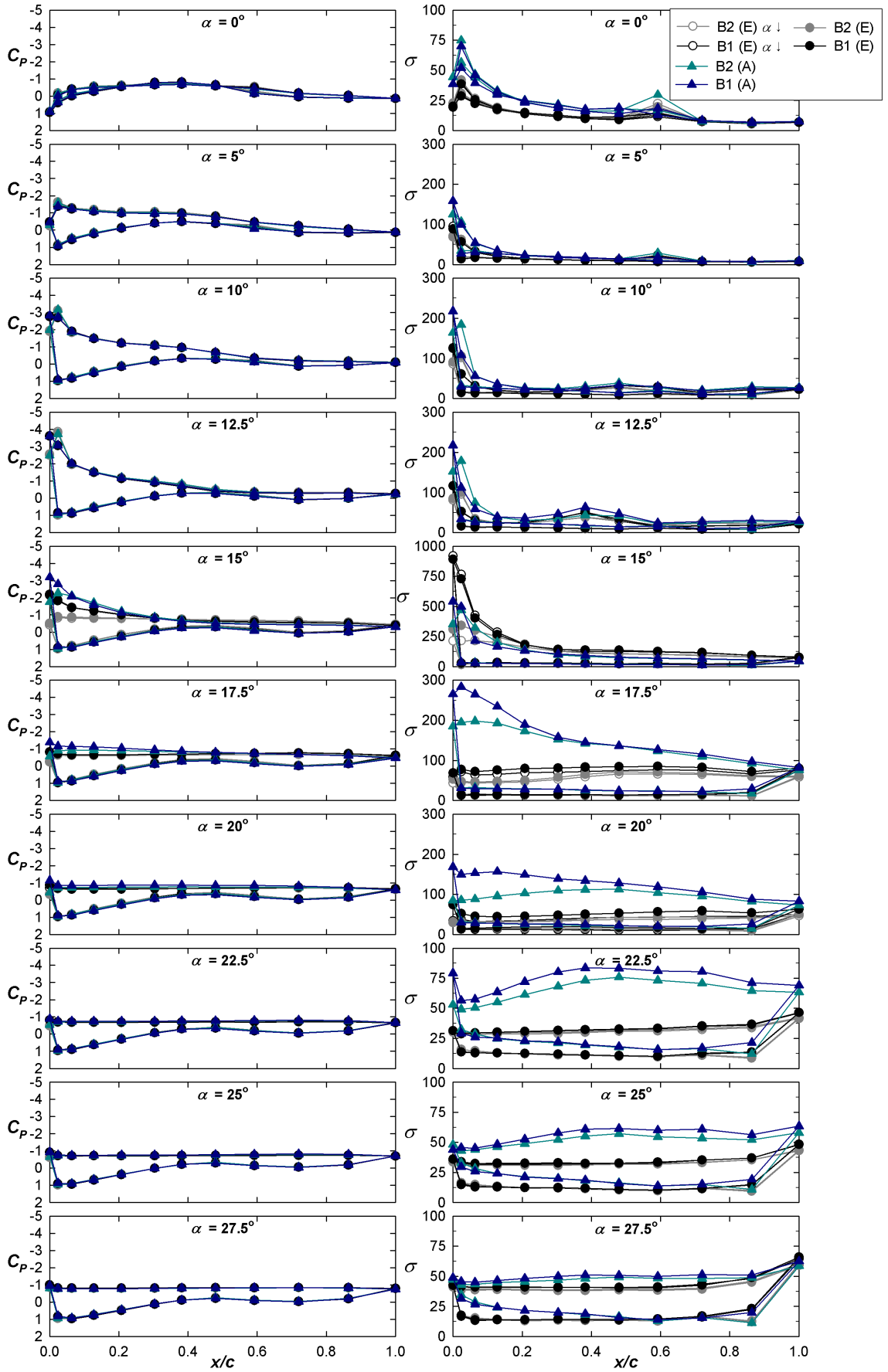


Figure 6-10(a) - Coefficients and standard deviations of the pressures around the S809 aerofoil with turbulence integral length scale $\sim 1/3c$ for the lowest and highest turbulence intensities (small grid at the closest (A) and furthest positions (E) from the model). Note the changes in scale of the σ plots.

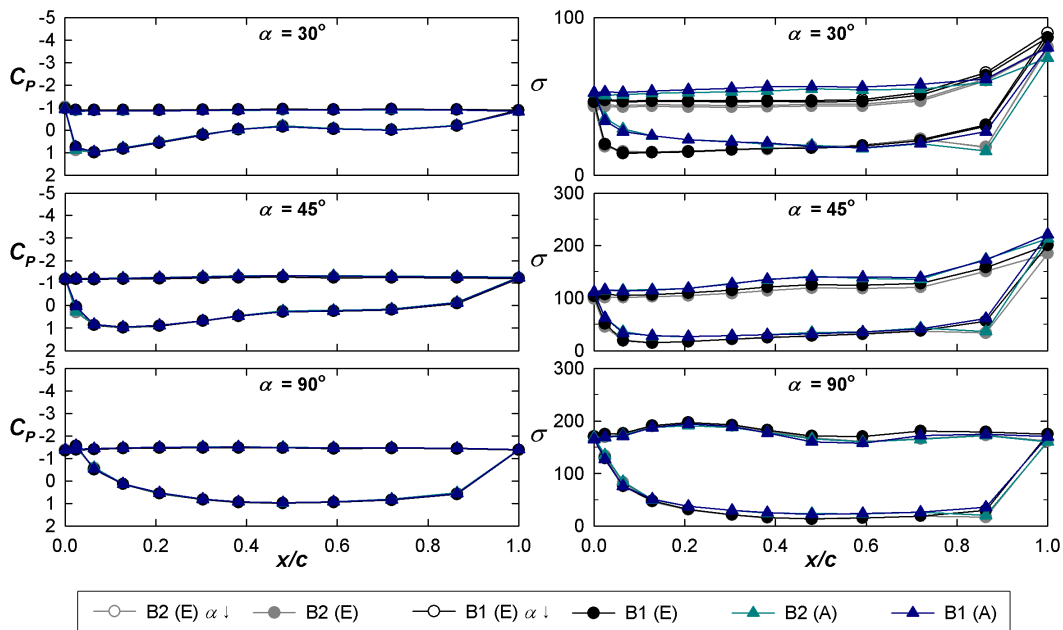


Figure 6-10(b) - Coefficients and standard deviations of the pressures around the S809 aerofoil with turbulence integral length scale $\sim 1/3c$ for the lowest and highest turbulence intensities (small grid at the closest (A) and furthest positions (E) from the model). Note the changes in scale of the σ plots.

However, the σ curves show increased magnitude on the front half of the aerofoil for 3% turbulence intensity, presumably due to the increased turbulence in the flow. There is a small increase in C_p at about $0.6c$ as seen for the no grid case shown earlier in Figure 6-5. This bump moved towards the leading edge for $\alpha = 10^\circ$ and 12.5° and was associated with the beginning of the flat stalled region of the C_p plot. The C_p plots show differences between Row B1 and B2 at the leading edge. This explains the spread in result of the force coefficients at these α . The rows appear to be in different positions within the stall structures leading to different pressures being seen at the leading edge, as was observed for the lowest turbulence case (no grid).

By $\alpha = 15^\circ$ there are also differences between the lower and higher turbulence intensity cases for this grid. For the 1% turbulence intensity case, Row B2 seems completely stalled except that, in the increasing α case, there may be occasional attachment at the leading edge shown by the high σ compared to the decreasing α case (note change of scale in the σ plot). However, this was not visible on the c_l plot in Figure 6-9, so any hysteretic effects are very slight. Row B1 is at least partially attached at the leading edge. Both Row B1 and B2 for the 3% turbulence intensity flow appear to have attached flow regions at the leading edge and the σ plots are similar.

By 17.5° Rows B1 and B2 seem very similar for the 1% turbulence intensity case (small grid in position E), although there are some slight differences in C_p at the leading edge. The σ is higher for Row B1 (and there are very slight differences between the σ for the increasing and decreasing α cases for this row). However, the rows still show some attachment for the 3% turbulence intensity case and there were higher σ across the aerofoils surface. The slight attachment and higher σ for

the 3% case continues, but to a lesser degree, at 20° . The differences in C_p for the 1% turbulence intensity flow that cause the slight hysteresis effect for Row B1 are not visible in this plot.

For $25^\circ \leq \alpha \leq 45^\circ$, the higher turbulence intensity still shows increased σ , but the C_p results for the two flows were very similar. There is a slightly increased σ on the upwind surface (lower σ line) even at $\alpha = 90^\circ$. The differences in the mean c_l at $\alpha = 45^\circ$ seem to have been due to a slight difference at the leading edge in the mean C_p .

The medium grid results shown in Figure 6-11 display an increased turbulence intensity prolonging stall and increasing the maximum c_l associated with stall. There was a spread in results up to $\alpha = 80^\circ$ with the second maximum at $\alpha = 45^\circ$ decreasing with increasing turbulence intensity except for the highest turbulence intensity case of 6%. The stall regions in both the c_d and $c_m, 1/4c$ plots were smoothed by increasing turbulence intensity and the local extrema at $\alpha = 90^\circ$ show two different trends. The 2% and 6% curves trend to similar values, while the $3\% \leq I_u \leq 5\%$ cases trend to a smaller magnitude.

The C_p and σ plots, shown in Figure 6-12, show comparisons between the 2% (medium grid in position E) and 6% (medium grid in position A) turbulence intensity cases. At $\alpha = 0^\circ$, the small peak at about $0.6c$ is difficult to see for position E and seems to be missing for position A due to the large scale of the graph necessitated by the effect of the freestream turbulence on the aerofoil. By $\alpha = 10^\circ$, a small bump in σ is seen about $0.5c$ and the leading edge σ peak has increased markedly. There are some slight differences in C_p near the leading edge for the two flow conditions and for the increasing and decreasing α results. This was also true at $\alpha = 12.5^\circ$. The σ plot shows the “bump” has moved to about $0.4c$.

The leading edge at $\alpha = 15^\circ$ shows different results for the larger and smaller intensities of turbulence. There are also differences for Row B1 and B2 at the smaller intensity. However, the σ plot shows more similarities with a very high leading edge peak in all cases (note the change in scale for this plot). At 17.5° , differences between the cases at the leading edge can be seen and also between the Row B1 and B2 results. The σ peaks at the leading edge have reduced. By 20° , the σ peaks are present only in the higher turbulence case and the size of these has reduced further. The smaller turbulence intensity case has completely stalled but there is still some leading edge attachment for the higher turbulence intensity flow. At $\alpha = 22.5^\circ$, there is still some leading edge attachment seen although the suction peak and the σ peak have reduced further. At 25° and 30° , there are slight differences between the cases and rows at the leading edge but the shape of the σ indicates stall. The difference by 90° can be seen only in the σ where the higher turbulence shows increased buffeting (lower line) and some increasing of the turbulence in the wake (upper line).

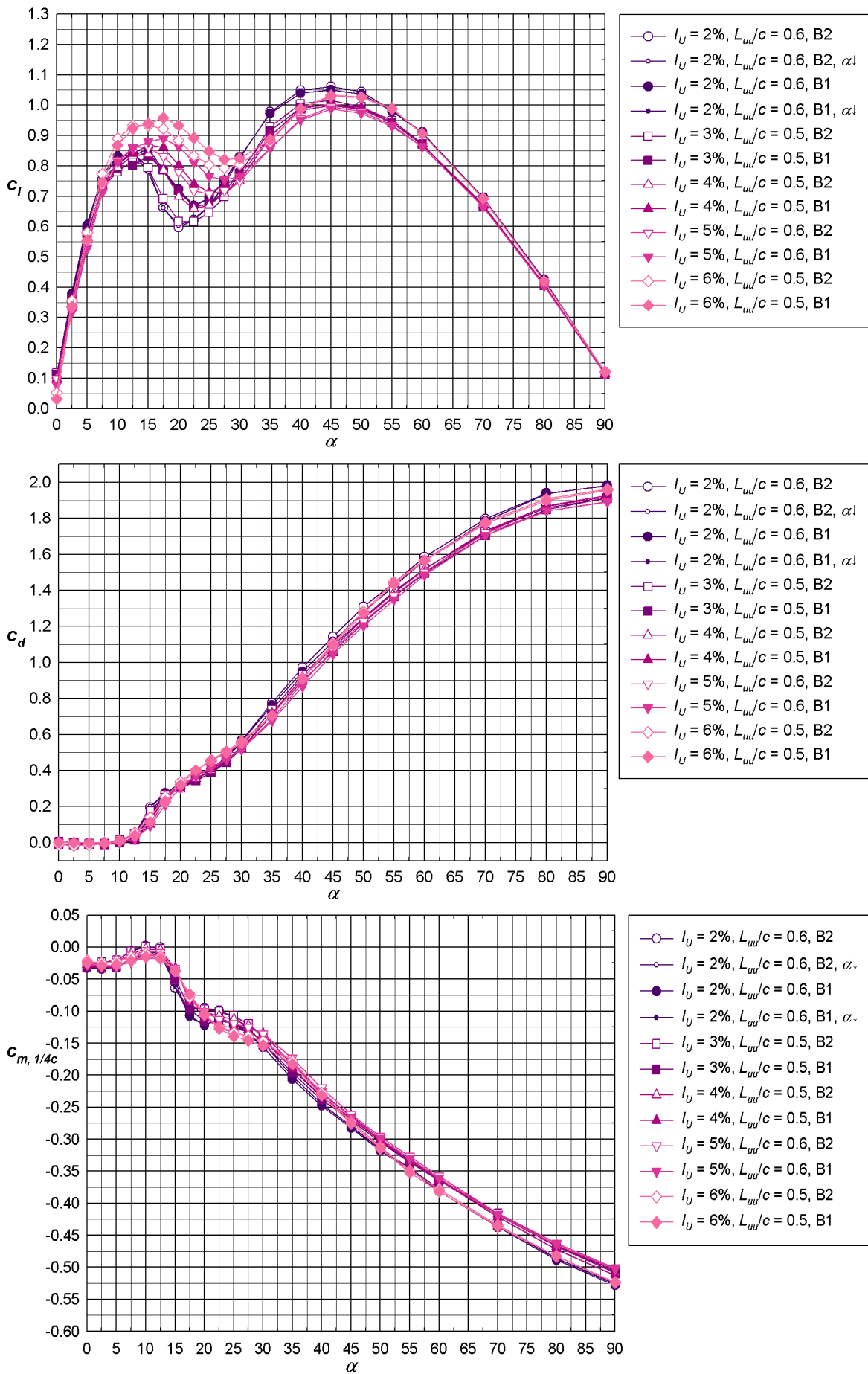


Figure 6-11 - S809 mean coefficients of lift, drag and moment about the quarter chord with integral turbulence length scale about $1/2c$ (medium grid).

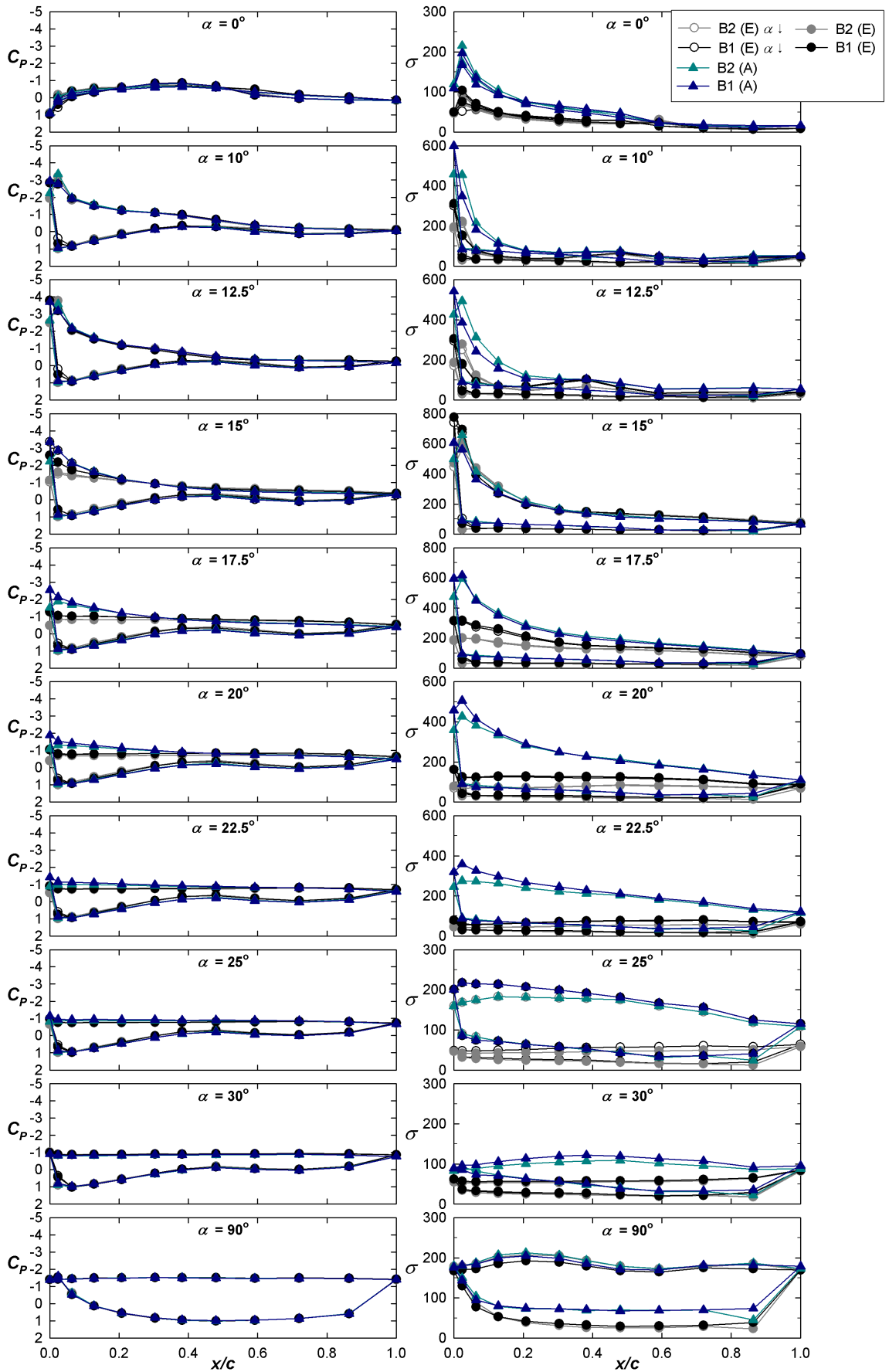


Figure 6-12 - Coefficients and standard deviations of the pressures around the S809 aerofoil with turbulence integral length scale $\sim 1/2c$ for the lowest and highest turbulence intensities (medium grid at the closest (A) and furthest positions (E) from the model). Note the changes in scale of the σ and C_p plots.

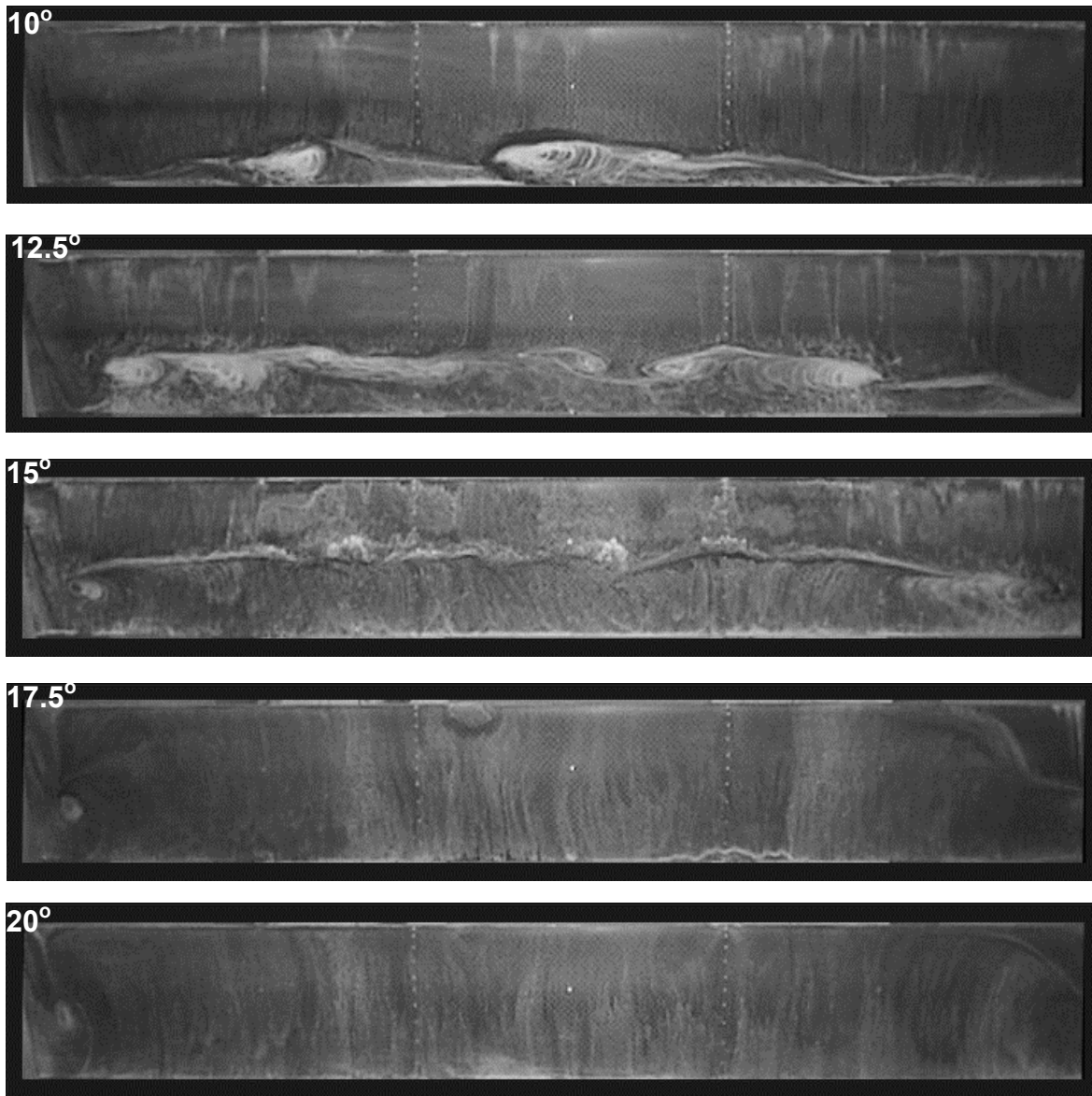


Figure 6-13 - Surface flow visualisation on the S809 around stall with the medium grid in the closest position to the model.

Surface flow visualisations for the highest turbulence intensity flow for which results are shown in Figure 6-11 and Figure 6-12 are given in Figure 6-13. Note that Row B1 is the tapping row with many taps on the left hand side of the photos and Row B2 on the right hand side. There is a separation region at 10° at the trailing edge. The separation line moves towards the leading edge at 12.5° and 15° . In both of these cases, differences in the separation point for the two tapping rows can be seen, which would lead to the differences in the leading edge suction pressures seen in Figure 6-12. The aerofoil by 17.5° looks stalled except perhaps for a small region at the leading edge. The aerofoil looks totally stalled by 20° . This case was repeated but gave much the same result. It is possible that the small region of attachment near the leading edge of Figure 6-12 is intermittent and therefore does not show up in the visualisation or that the added roughness of the china clay paint used for the visualisation has caused earlier stall. However, compared with the earlier visualisations for the lowest turbulence flow, see Figure 6-6, it is clear that turbulence dramatically affects the progress of separation from the trailing edge.

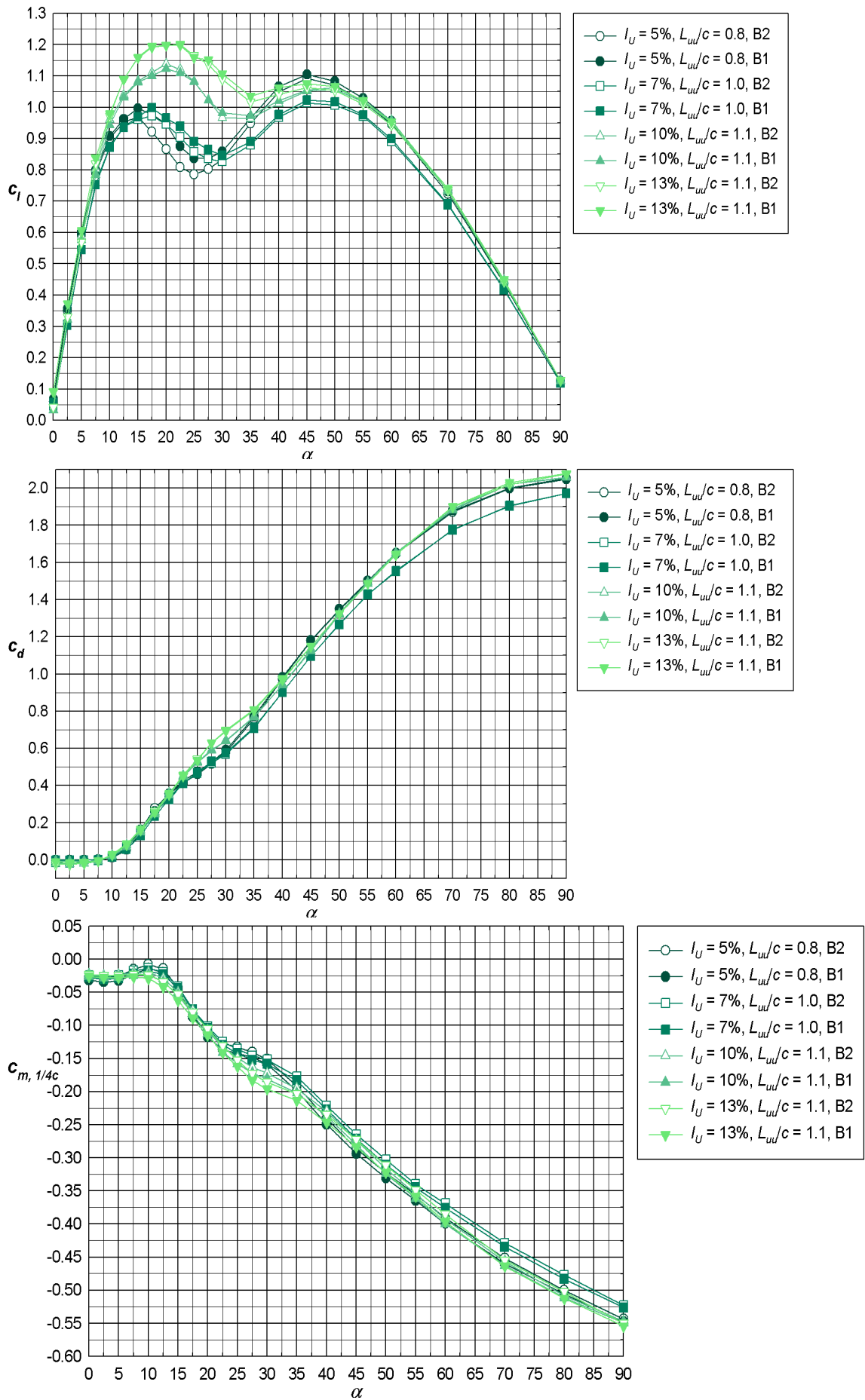


Figure 6-14 - S809 mean coefficients of lift, drag and moment about the quarter chord with integral turbulence length scale about $1c$ (large grid).

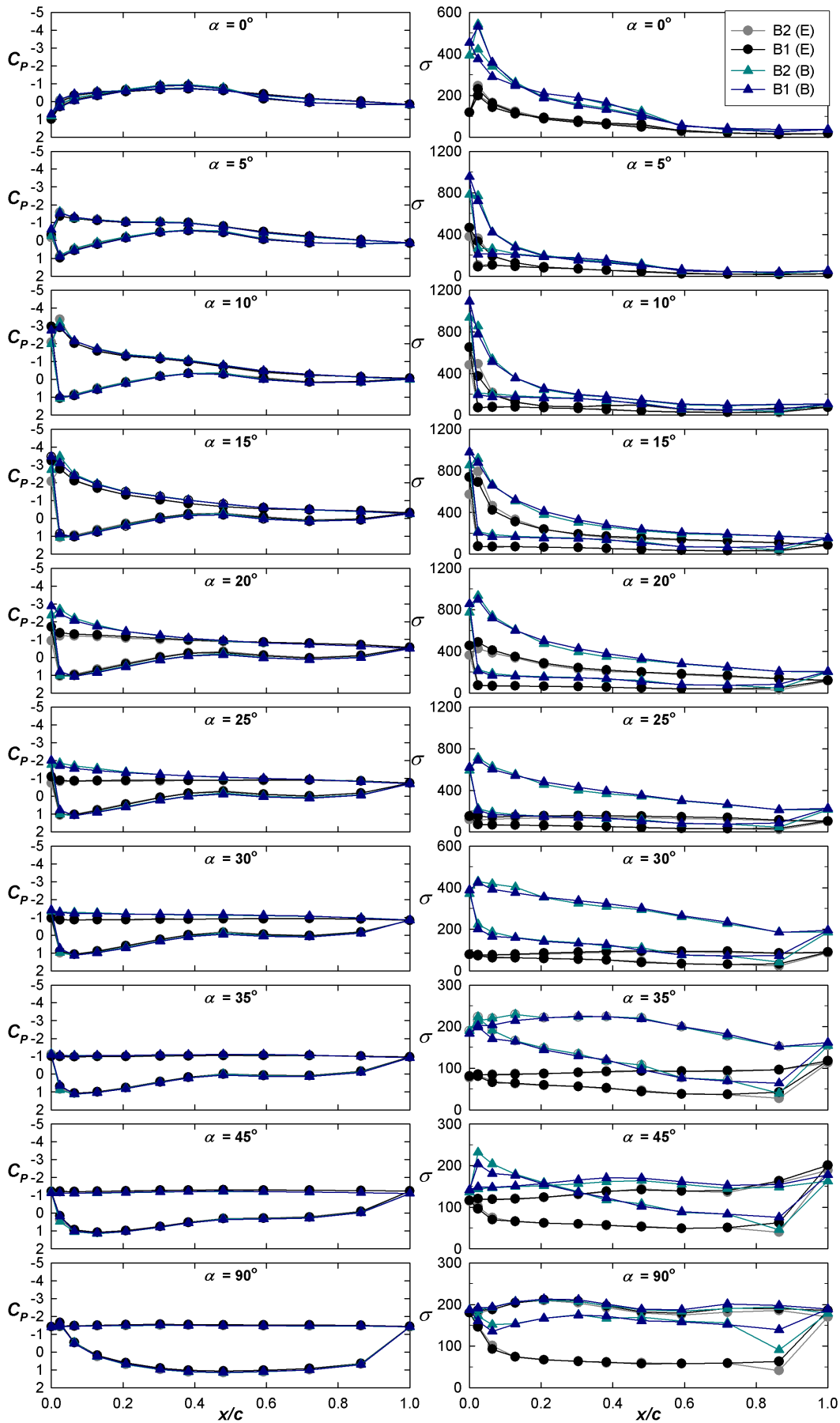


Figure 6-15 - Coefficients and standard deviations of the pressures around the S809 aerofoil with turbulence integral length scale $\sim 1c$ for the lowest and highest turbulence intensities (large grid at the closest (B) and furthest positions (E) from the model). Note the changes in scale of the σ plots.

Figure 6-14 shows the c_l , c_d and $c_{m, 1/4c}$ results for the largest turbulence integral length scale flows (large grid). The two higher turbulence intensities have a dramatic effect on the stalling process, leading to much more gradual changes in c_l and much higher local c_l maxima. There are considerable differences between c_l results for Rows B1 and B2 in the two lower turbulence intensity cases ($I_u \leq 7\%$), as there were for all the previous cases. However, there were only very slight differences between the results for the two rows for the higher turbulence intensities ($I_u \geq 10\%$). The trends at $\alpha = 45^\circ$ are also quite different with the local c_l maximum decreasing from the $I_u = 5\%$ to $I_u = 7\%$ flow but increasing when comparing the $I_u = 7\%$ and $I_u = 10\%$ and the $I_u = 10\%$ and $I_u = 13\%$ flows. The three higher intensity flows ($I_u \geq 7\%$) show the same c_l for $\alpha > 55^\circ$ but the $I_u = 5\%$ flow doesn't give the same c_l until $\alpha = 90^\circ$.

The c_d plot in Figure 6-14 doesn't show differences between the Row B1 and B2 results. However, for $\alpha \geq 25^\circ$, there are differences between the different flows with the higher turbulence intensities showing more gradual changes in the shape of the curve leading to higher c_d for higher turbulence intensities for $25^\circ \leq \alpha \leq 35^\circ$. For $\alpha \geq 35^\circ$, the $I_u = 7\%$ flow shows consistently lower c_d than the other plots. For $40^\circ \leq \alpha \leq 55^\circ$, the c_d for the two higher intensity plots lies between that for the $I_u = 5\%$ and $I_u = 7\%$ flows. However, for higher α , the two higher intensity flows show similar c_d results to the $I_u = 5\%$ flow.

The $c_{m, 1/4c}$ results in Figure 6-14 show some differences between the Row B1 and B2 results and small differences between flows in the "bump" region around $\alpha = 10^\circ$ but otherwise very similar trends to the c_d plots. Like for the drag for $25^\circ \leq \alpha \leq 35^\circ$, the higher turbulence intensities produce greater magnitude $c_{m, 1/4c}$. For $\alpha \geq 35^\circ$ the $I_u = 7\%$ flow shows consistently smaller magnitude $c_{m, 1/4c}$ than the other plots. For $40^\circ \leq \alpha \leq 55^\circ$ the $c_{m, 1/4c}$ for the two higher intensity plots lies between that for the $I_u = 5\%$ and $I_u = 7\%$ flows and for higher α the two higher intensity flows show similar $c_{m, 1/4c}$ results to the $I_u = 5\%$ flow.

The C_p and σ results, corresponding to the force coefficients shown in Figure 6-14 for the lowest and highest turbulence intensities flows, are shown in Figure 6-15. A much larger scale is needed for the σ plots even at $\alpha = 0^\circ$ than for the previous plots of this type due to the higher variations caused by the high turbulence levels in the freestream. The bumps seen in previous cases near the trailing edge in σ due to the onset of separation are not visible in any plot, perhaps merely due to the larger scale of these plots. There are some slight differences at the leading edge in C_p at 10° between the two flow conditions. By 15° , slight differences are apparent along the first half of the suction surface. For $5^\circ \leq \alpha \leq 15^\circ$, the σ shows the familiar peak at the leading edge. However, by 20° the size of this peak has reduced markedly for the lower turbulence intensity flow and the aerofoil seems completely stalled for this case by $\alpha = 25^\circ$. The higher turbulence intensity flow shows higher values of C_p on the suction surface until $\alpha = 35^\circ$ where it appears fully stalled. However, even for α above the stalled flow conditions, the higher turbulence case shows increased

σ . This is most obvious at $\alpha = 90^\circ$ where the buffeting due to the freestream turbulence causes high σ on the downwind taps (lower line).

The S809 aerofoil showed very little signs of hysteresis with the largest difference being for Row B1 at 20° for the $I_u = 0.6\%$ case, see Figure 6-16. This hysteresis has mostly vanished with a turbulence intensity of 1% and is not at all evident for the higher turbulence intensities tested. While the designers did not succeed in entirely eliminating hysteresis from the S809 aerofoil, as discussed in Section 2.2, they did minimise the range of α over which it occurred and the addition of small amounts of turbulence eliminates it entirely. The scale of Figure 6-16 also emphasises the differences in results from Rows B1 and B2 for this aerofoil and the smoothing effect of the addition of turbulence on the c_d curve, as discussed earlier in this section.

Examining cases with similar turbulence intensities but different integral length scales, as in previous chapters, can give an indication of the relative importance of turbulence intensity and integral length scale. The flow conditions are summarised in Table 6-2 and the coefficients of lift, drag and moment about the quarter chord are presented in Figure 6-17, Figure 6-18 and Figure 6-19 respectively. The lift curves for the lower turbulence intensities of 2% and 3% shown in Figure 6-17 for each flow are very similar around stall, but diverge around a local maximum at $\alpha = 45^\circ$. This local maximum for the 2% turbulence intensity flow is higher for the larger integral turbulence length scale but, for the 3% turbulence intensity flow, the opposite is true. At this α the lift is due to deflection of the wake, it seems that for 2% intensity the larger turbulence integral length scale causes more deflection of the wake and therefore higher lift. However, for 3% turbulence integral length scale the deflection is less for the larger integral length scale possibly due to increased curvature of the wake. Measurements in the wake would need to be taken to confirm this. The 5% turbulence intensity case has considerably different lift between the two length scales cases for almost all α , with the larger scale increasing the lift. For the 6 to 7% turbulence intensity flows, the curves are very similar at all α except for some differences around stall.

The c_d and $c_{m, 1/4c}$ results presented in Figure 6-18 and Figure 6-19 respectively for the lower turbulence intensities also show differences between the rows at high α . This is similar to what was seen in c_l around $\alpha = 45^\circ$. As for c_l , the larger turbulence integral length scale shows increased magnitude of c_d and $c_{m, 1/4c}$ for 2% turbulence intensity and the smaller integral length scale shows increase magnitude of c_d and $c_{m, 1/4c}$ for 3% turbulence intensity. For 5% the c_d and $c_{m, 1/4c}$ plots are different at almost all α and for 6% to 7% turbulence intensity the plots are very similar at all α . Again this is similar to c_l .

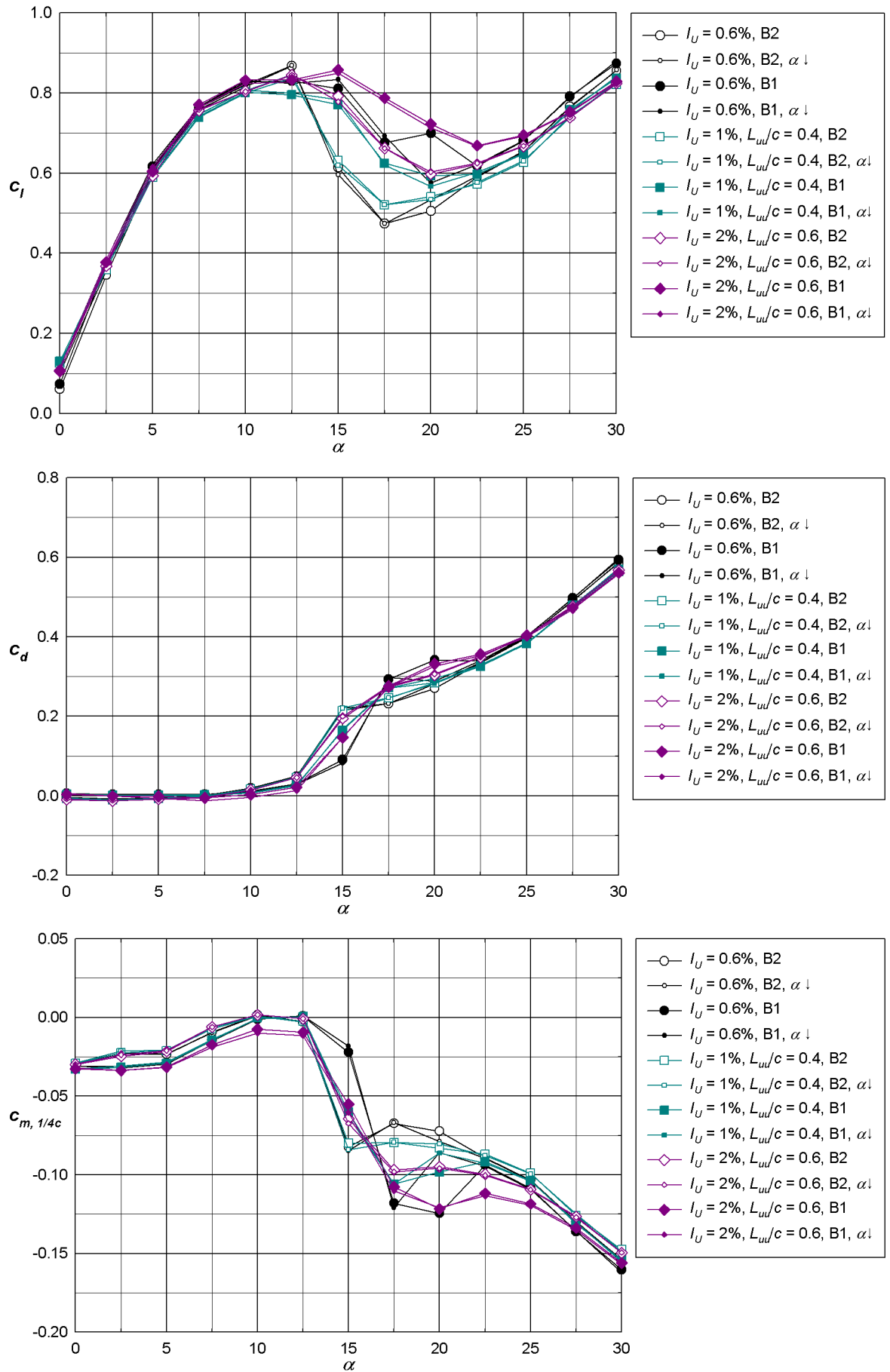


Figure 6-16 - S809 aerofoil mean coefficients of lift, drag and of moment about the quarter chord around stall for the cases where α was both increased and decreased.

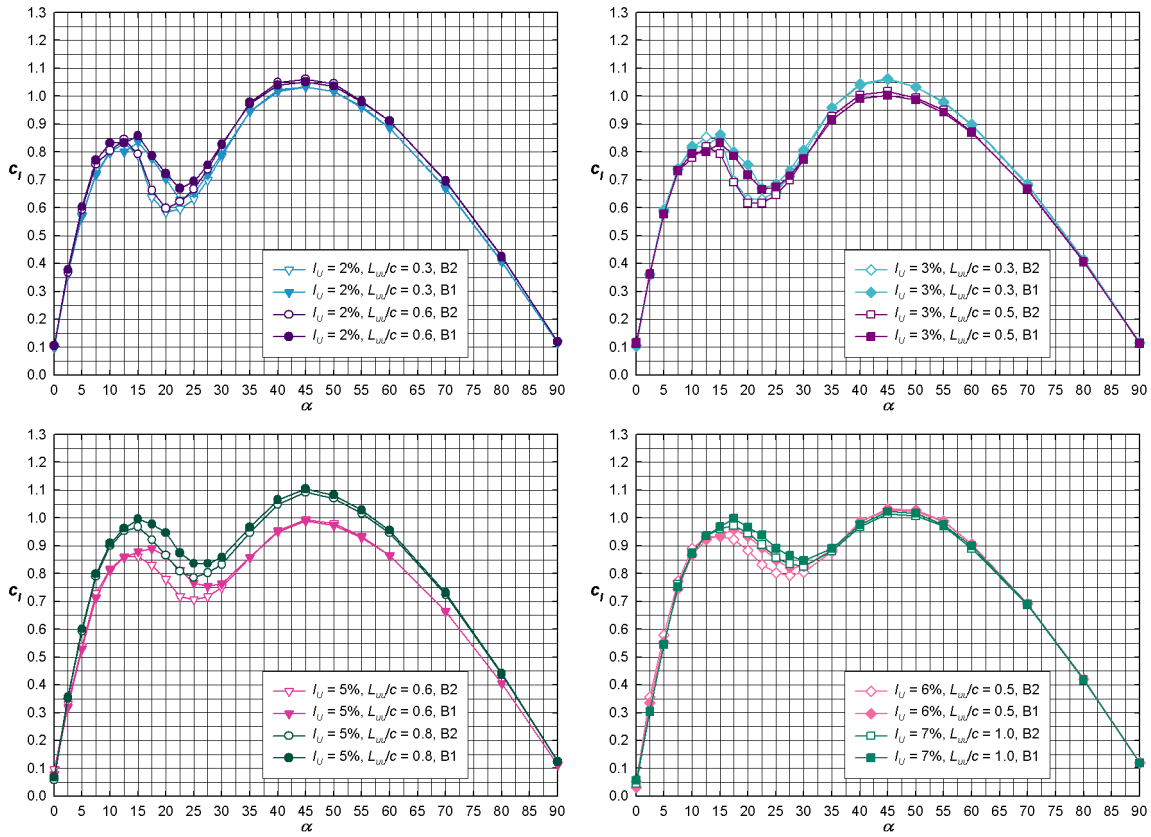


Figure 6-17 – S809 Comparison of the coefficient of lift at similar turbulence intensities but different integral length scales.

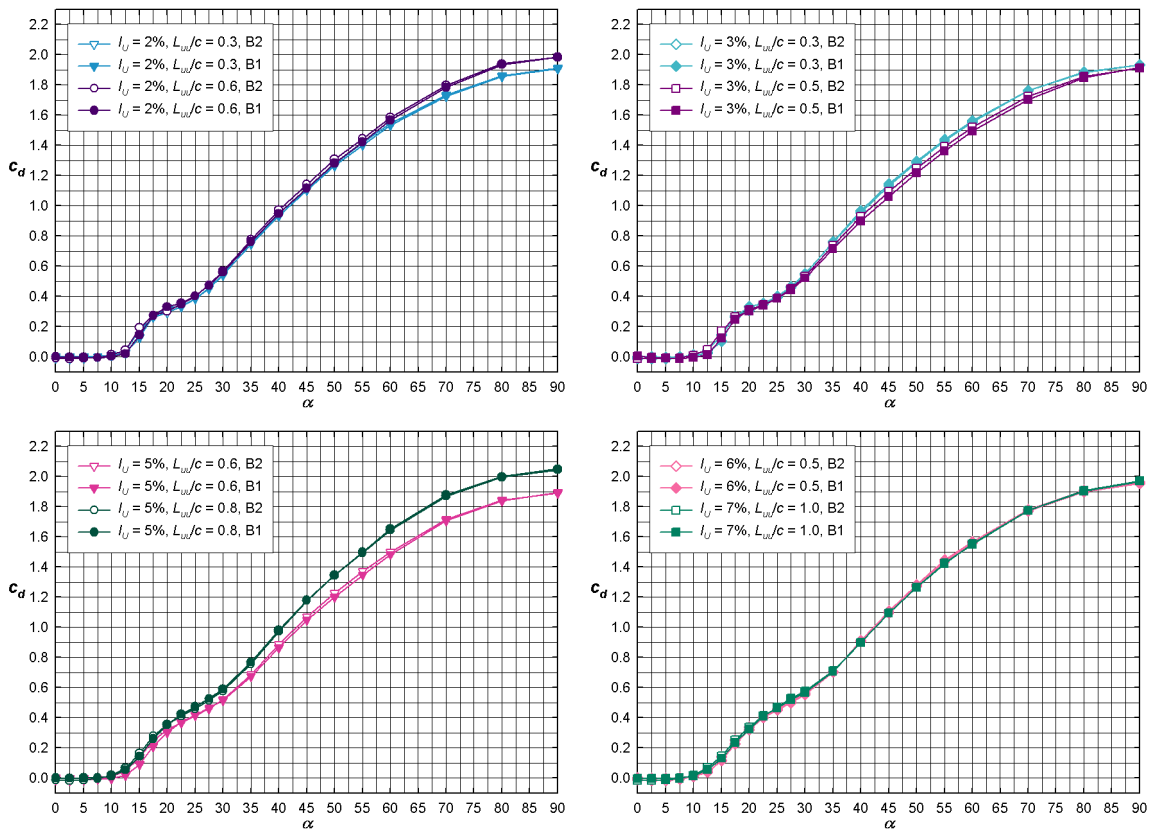


Figure 6-18 – S809 Comparison of the coefficient of drag at similar turbulence intensities but different integral length scales.

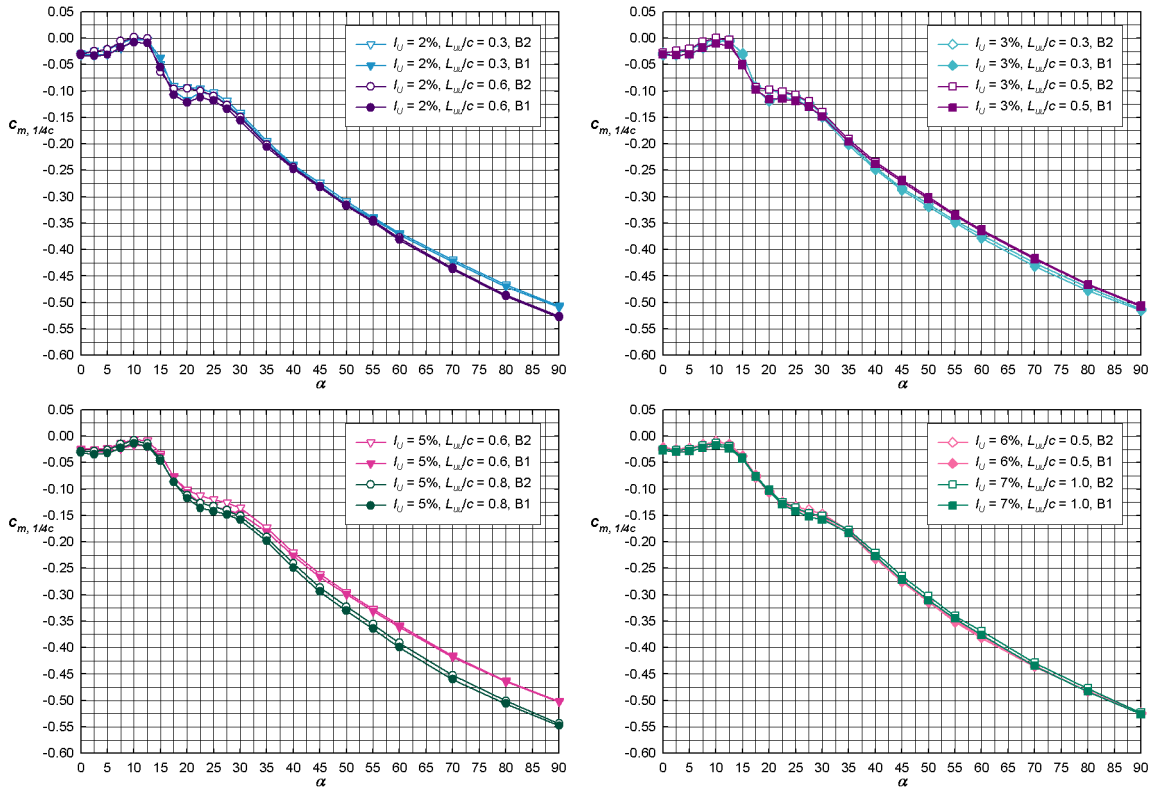


Figure 6-19 – S809 Comparison of the coefficient of moment at similar turbulence intensities but different integral scales.

Grid Panel Width (m)	Position (m)	Intensity			Scale		
		I_u (%)	I_v (%)	I_w (%)	L_{uu}/c	L_{vv}/c	L_{ww}/c
0.10	E (9.60)	2	4	3	0.6	0.6	1.0
0.04	B (4.60)	2	3	2	0.3	0.4	0.2
0.10	D (7.20)	3	4	3	0.5	1.1	0.5
0.04	A (3.55)	3	3	3	0.3	0.3	0.3
0.30	E (9.60)	5	6	5	0.8	1.3	0.8
0.10	B (4.60)	5	7	5	0.6	0.9	0.4
0.30	D (7.20)	7	8	7	1.0	1.1	0.8
0.10	A (3.55)	6	7	7	0.5	0.6	0.4

Table 6-2 - Characteristics of the grid developed turbulence for the comparison between cases with similar turbulence intensities (repeated from Chapter 4).

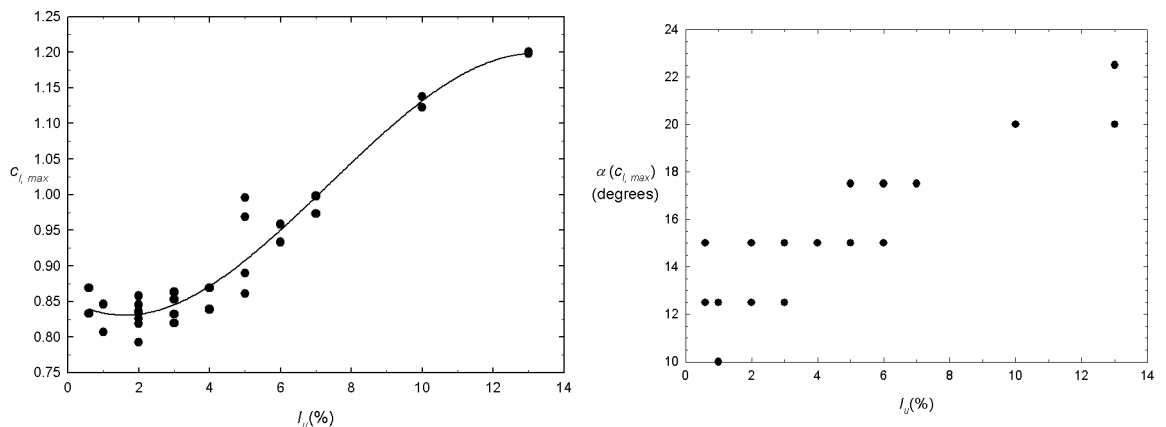


Figure 6-20 – S809 The local maximum of c_l associated with stall and the angle of attack at which this occurs versus the turbulence intensity for all grids (both row B1 and B2). The line is a third order polynomial fitted to the data.

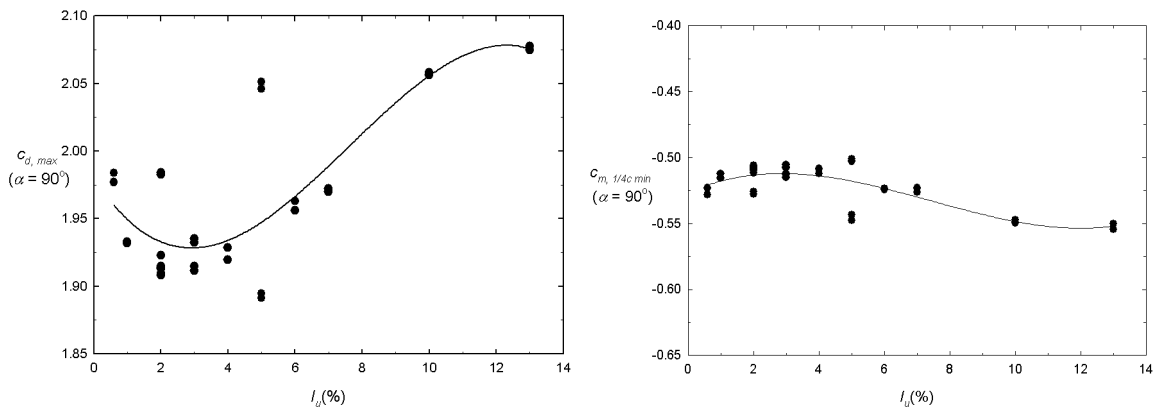


Figure 6-21 – S809 The local maximum of c_d and $c_{m, 1/4c}$ at 90° versus the turbulence intensity for all grids (both row B1 and B2). The lines are third order polynomials fitted to the data.

Figure 6-20 shows the local maximum of c_l associated with stall and the value of α at which it occurs versus the turbulence intensity of the flow. While there is some spread in the data (especially at $I_u = 5\%$), a general increase from 2% in c_l and α can be seen with increasing turbulence intensity. There is more spread in the maximum c_d and less movement in the minimum $c_{m, 1/4c}$ as shown in Figure 6-21. From these results it is apparent that turbulence intensity alone does not predict the performance of the S809 aerofoil section but that both turbulence intensity and scale are involved.

Clearly for the S809 aerofoil section, like the others studied, increasing the turbulence in the flow can have dramatic effects on the aerofoil's performance around stall. A summary of these effects and a comparison of the results for all the aerofoil sections will be given in Chapter 7. The next section in this chapter will look at the fluctuating results from this aerofoil section.

6.3 Fluctuating

The fluctuations normal to the S809 aerofoil section were very clean (see Figure 6-22) as they were for the NACA 0021 and NACA 4421 aerofoil sections. However, in addition to the shedding frequency at high α there was a large low frequency spike at $\alpha = 15^\circ$. This sort of spike was seen in some of the NACA 0021 PSD plots with turbulence in the flow. As in the NACA 0021 cases, the normal PSD spike is associated with low frequency components at low α in the normal PSD which occur between the local maximum and minimums in the mean c_l plot associated with stall (for the S809 aerofoil in the lowest turbulence flow the local maximum associated with stall for Row B1 occurred at 12.5° and the local minimum at 22.5°). The normal PSD also contains other low frequency components associated with shedding which increase in magnitude with increasing α , the main shedding frequency and a secondary frequency at twice the main frequency. The causes of these have been discussed in detail for the NACA 0021 in Chapter 4 so this section will only briefly cover the shedding characteristics for the S809 aerofoil section.

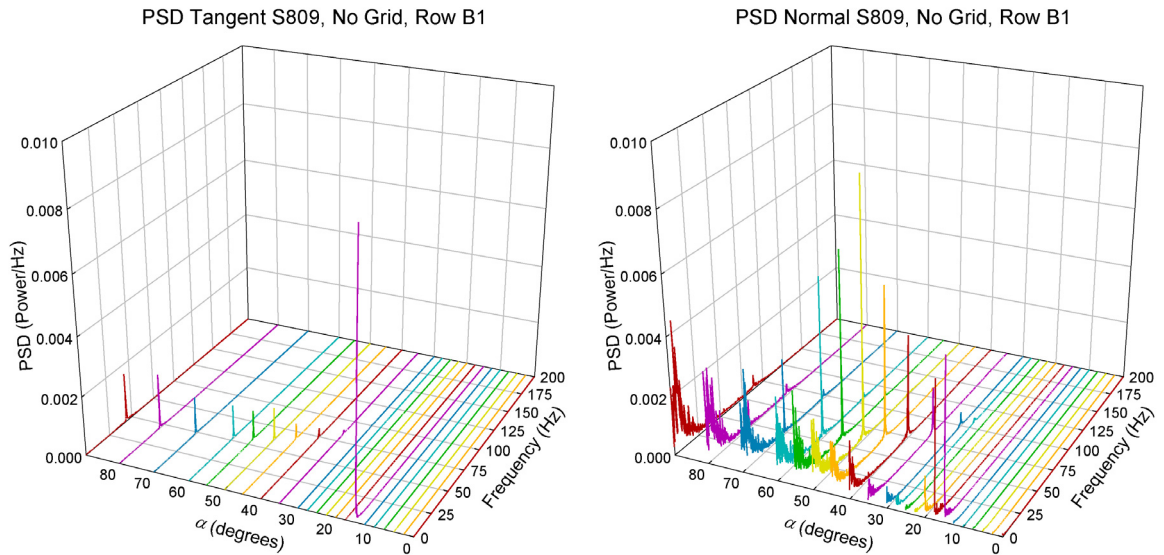


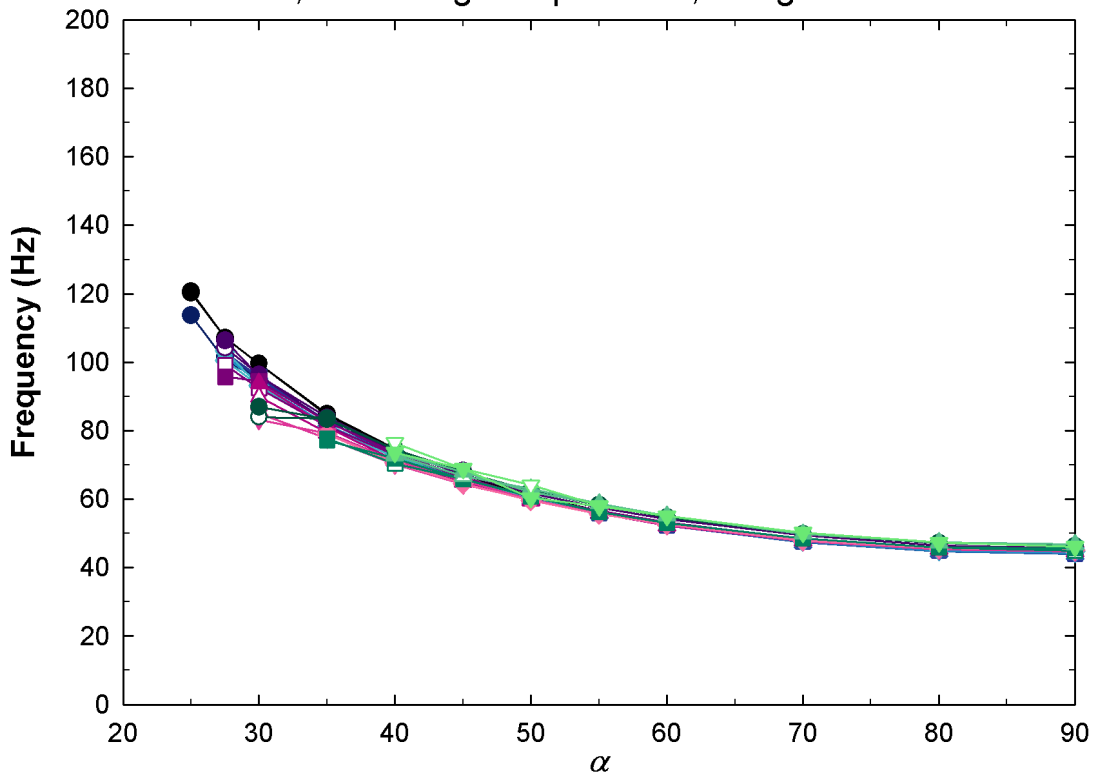
Figure 6-22 – S809 frequency content of the fluctuations in the instantaneous tangent and normal force for the increasing α case for the S809 aerofoil section for the lowest turbulence flow.

The main shedding frequency for the S809 occurs at lower values than for the previous aerofoil sections. Therefore, the Matlab program written to find the maximums associated with shedding for the NACA 0021 PSD plots was modified to only ignore data 38 Hz from the main frequency when finding the secondary frequency. (See Section 4.3.3 for a complete description of the Matlab program.)

The shedding frequencies and magnitude from the tangential force PSD are shown in Figure 6-23. The addition of turbulence delayed the onset of separation as it had for the other aerofoil sections. All turbulence levels and scales tested for this aerofoil section produced very similar frequencies in the wake indicating very similar wake widths. Like the other aerofoils, the smaller integral turbulence length scales (about $1/3c$ and $1/2c$) produced larger shedding magnitudes while the shedding magnitude decreased with increasing turbulence intensity for the largest integral turbulence length scale (about $1c$). However, the lowest turbulence flow results did not lie between these results as for the other aerofoil sections. The lowest turbulence flow for the S809 aerofoil section produced relatively high shedding magnitudes.

The shedding frequencies plot for the normal force, see Figure 6-24, showed more variation between flow cases than the plot for the tangential force. This was expected due to the increased noise in these plots. This was especially evident in the secondary frequency particularly for the highest turbulence intensity where the other signals in the flow would be most dominant. The secondary frequency was defined as the smaller shedding frequency so there are some cases that cross over between $\alpha = 80^\circ$ and 90° as the shedding magnitudes for the two frequencies are comparable at $\alpha = 90^\circ$.

S809, Shedding Frequencies, Tangential Force



S809, Shedding Magnitude, Tangential Force

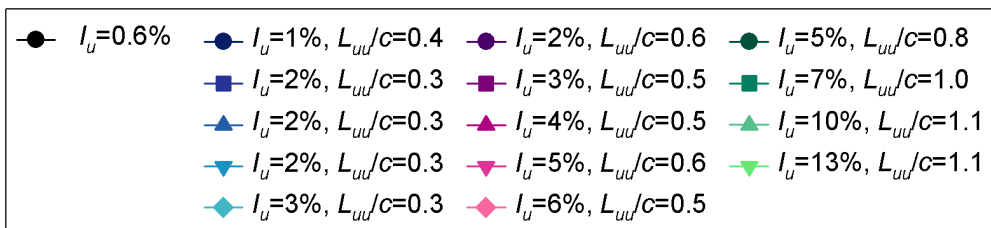
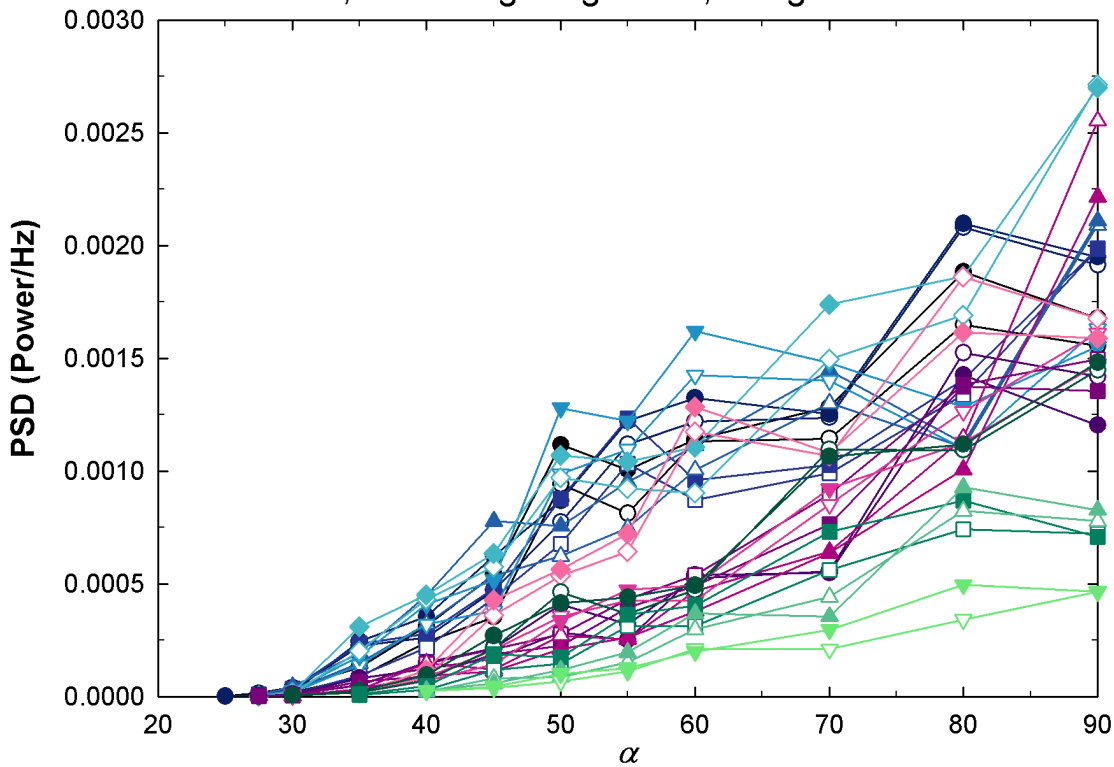
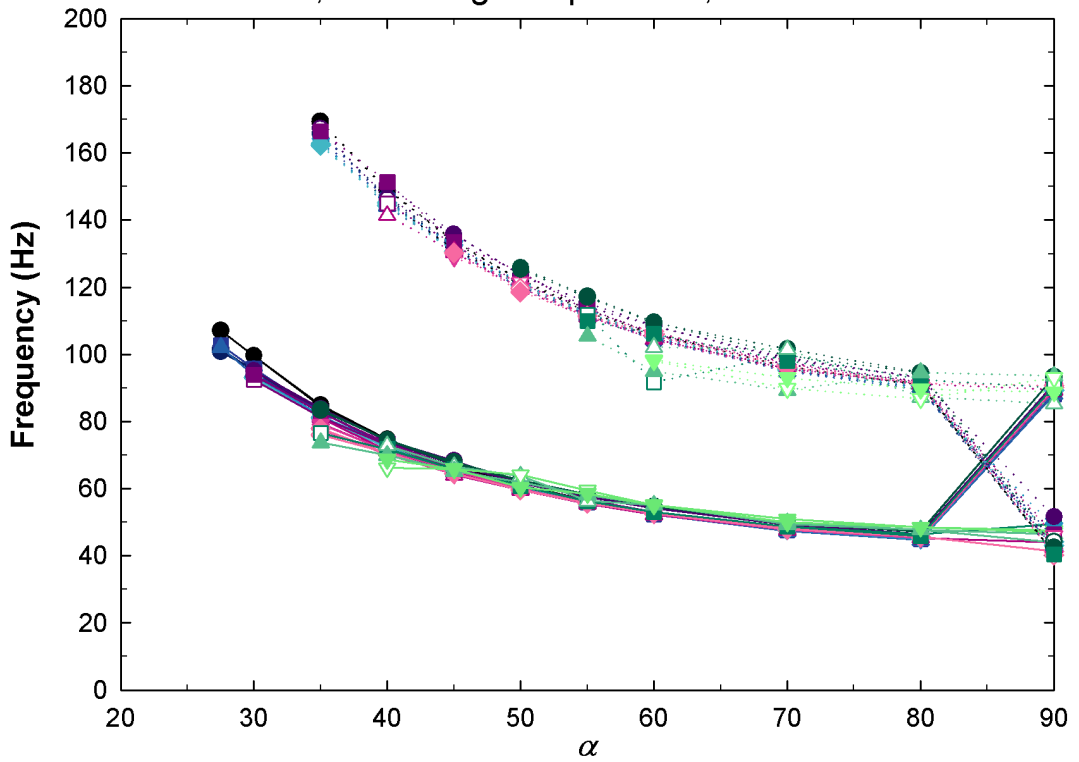


Figure 6-23 - Shedding frequencies and magnitude in the tangential force PSD for all flow conditions. Closed symbols indicate Row B1 and open symbols indicate Row B2.

S809, Shedding Frequencies, Normal Force



S809, Shedding Magnitude, Normal Force

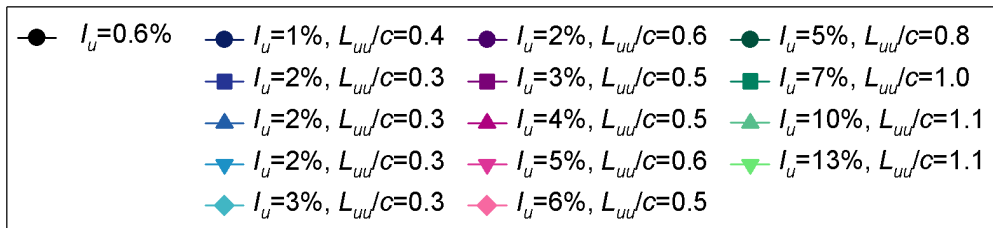
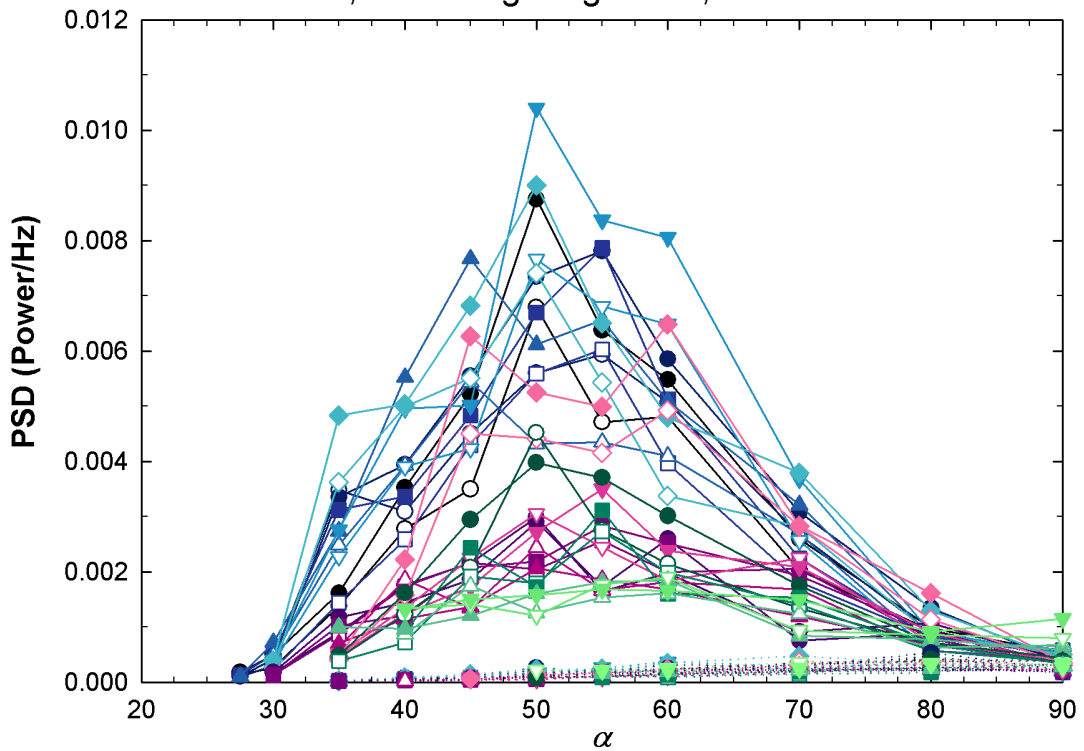


Figure 6-24 - Shedding frequencies and magnitude in the normal force PSD for all flow conditions. Closed symbols indicate Row B1, open symbols indicate Row B2, straight lines indicate the first frequency and dotted lines indicate the second frequency.

The shedding magnitudes for the main shedding frequency in the normal force from the S809 aerofoil section reached maximums around $45^\circ \leq \alpha \leq 55^\circ$. The lowest turbulence scales (about $1/3c$, blue points) and the lowest turbulence flow ($I_u = 0.6\%$) generally had higher shedding magnitudes. Those for the medium turbulence scales (about $1/2c$, pink and purple points) were lower and increased with increasing turbulence intensity and those for the largest turbulence integral length scales (about $1c$, green points) were lower but decreased with increasing turbulence intensity. Only the highest turbulence flow ($I_u = 13\%$) did not decrease in shedding magnitude between $\alpha = 80^\circ$ and 90° . The shedding magnitudes for the secondary shedding frequency increased with increasing α but were much smaller.

As for the other aerofoil sections, the vortex shedding identified above has the potential to impose cyclic loading on a wind turbine blade. The cyclic loading would of course be worse if the vortex shedding was well correlated along the span. The next section will look at the correlations for all the flow cases for the S809 aerofoil section.

6.3.1 Correlations

The discussion of the correlation coefficients plots for the S809 aerofoil section will be kept brief (as it was for the NACA 4421 aerofoil section) as many features are similar to the correlations from the NACA 0021 aerofoil section that were discussed in detail. A comparison between the aerofoil sections will be left until Chapter 7. The location of the tapping rows and the taps to be compared (the circled taps) is presented in Figure 6-25.

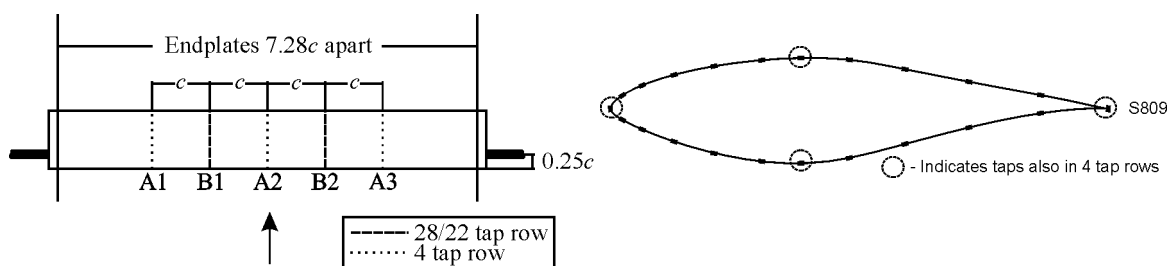


Figure 6-25 - Location of the tapping rows and the four taps present in all tapping rows.

The correlation coefficients between the instantaneous c_t , c_n and $c_{m, 1/4c}$ from Rows B1 and B2 are shown in Figure 6-26. The R_{C_t} plot at high α shows higher correlations for lower turbulence intensities tending to a correlation coefficient of about 0.65 at $\alpha = 90^\circ$ in all cases except for the highest turbulence intensity case. The highest turbulence intensity case shows a lower correlation of about 0.5 at $\alpha = 90^\circ$. The R_{C_n} plot (and the $R_{C_{m, 1/4c}}$ plot which is very similar at high α as would be expected) shows bands roughly based on the size of the grid at $\alpha = 70^\circ$ and $\alpha = 80^\circ$ with the lowest turbulence case (no grid, black points) and those with a turbulence integral length scale of about $1/3c$ (small grid, blue points) in the middle band, plots with a turbulence integral length scale about $1/2c$ (medium grid, pink and purple points) below this band and plots with the

turbulence integral length scale about $1c$ (large grid, green points) above this band. However, at $\alpha = 90^\circ$ there is a jump in correlation for the higher turbulence intensity cases and the correlation coefficients at this angle increase with increasing turbulence intensity. This trend was seen for the NACA 0021 aerofoil section and the “banding” on turbulence integral length scale was seen for the NACA 4421 aerofoil section. Further discussion of this will be left until Chapter 7.

A high negative correlation occurs in the tangential force at $\alpha = 15^\circ$ which is particularly large for the lowest turbulence intensity case, decreases in magnitude quickly as turbulence intensity increases and is eliminated by the largest integral turbulence length scale. This is the α at which there is the greatest difference between the mean c_l between the two rows and the first drop in the mean $c_{m, 1/4c}$ value for the lowest turbulence intensity flow. There are also local minimums at this α for R_{C_n} and $R_{C_{m, 1/4c}}$. This may be due to flapping of the separated shear layer near Row B2. There is a great deal of variation in the correlations for the lowest turbulence case at low α . The variation is greatly reduced for higher turbulence intensities. The local maximum at $\alpha = 7.5^\circ$ in R_{C_n} is associated with the start of trailing edge separation in the lowest turbulence case.

The correlation coefficients for the lowest turbulence intensity flow between the pressure signals measured at taps in the same chordwise position but in different rows (the taps circled in Figure 6-25) is shown in Figure 6-27. A magnified section of this plot over the range $0^\circ \leq \alpha \leq 30^\circ$ is shown in Figure 6-28 and this plot should be referred to if the features at low α discussed below are difficult to see in Figure 6-27. As for the other two aerofoil sections, the correlation coefficients are in “bands” based on the spanwise spacing with the smallest spacing ($1c$) having the highest correlation coefficients. The correlation coefficients for the trailing edge taps are fairly constant (and quite high) until the onset of separation at $\alpha = 7.5^\circ$ where the correlation coefficients begin to decrease. There are jumps in correlation at $\alpha = 15^\circ$ that correspond to those seen earlier in Figure 6-26 (R_{C_n} etc. plots). After this angle the correlations decrease again before increasing with the onset of vortex shedding.

The upper tap shows higher correlations at $\alpha = 0^\circ$ than the leading edge taps for the $1c$ separation but the correlations are smaller for the larger spanwise spacings. There is an increase in correlation for the larger spanwise spacings at $\alpha = 7.5^\circ$ (perhaps due to partial separation causing a smaller separation bubble) but then all curves decrease to small negative values before increasing again to high correlations with the development of vortex shedding. The correlations reduce at high α , presumably due to the increasing distance of the vortices from the upper tap (the shed vortices don't travel as near to the aerofoils surface as for lower α).

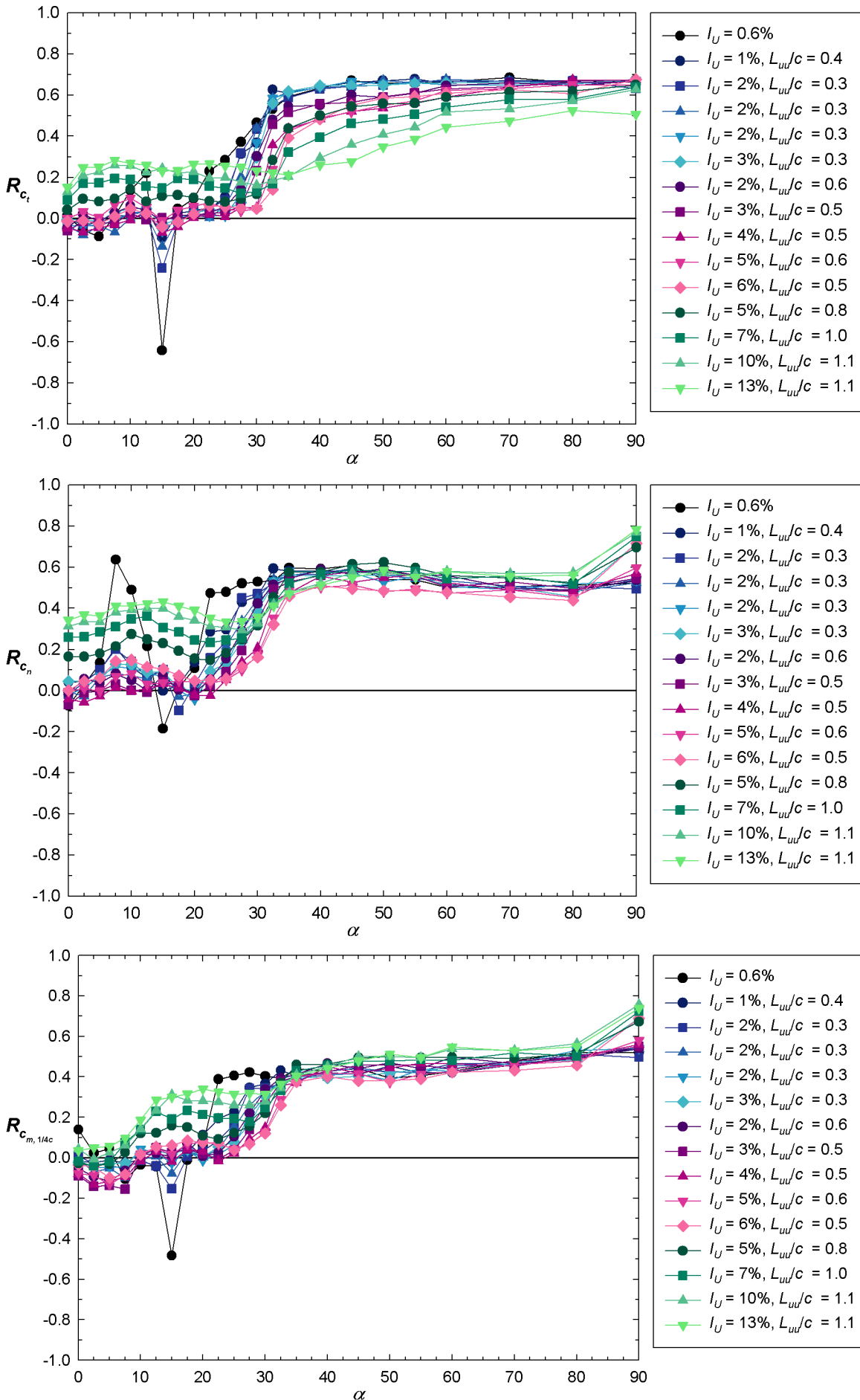


Figure 6-26 – S809 Correlation coefficients between c_t , c_n and $c_{m, 1/4c}$ calculated from Row B1 and Row B2 data (increasing α data only shown).

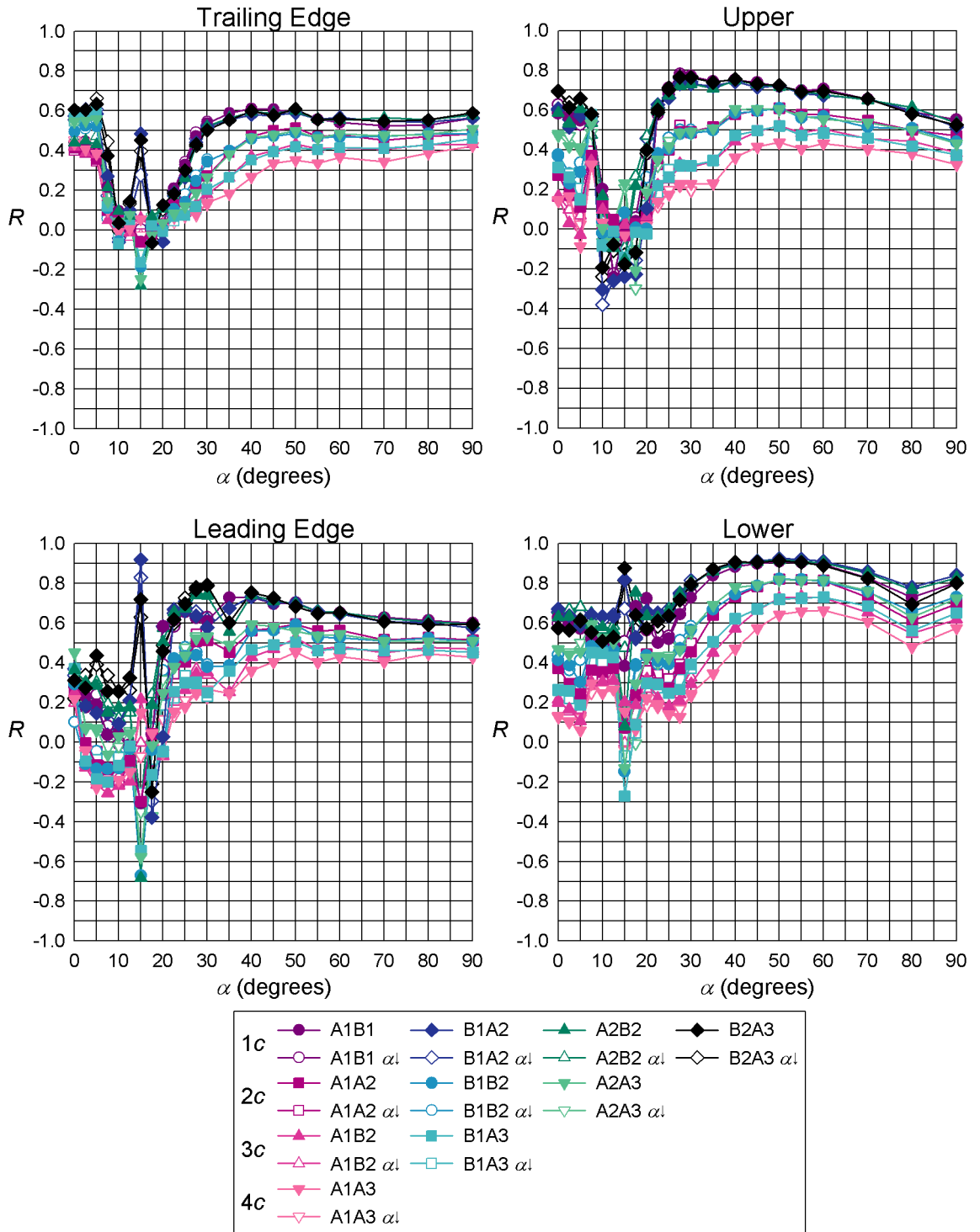


Figure 6-27 - S809 Correlation coefficients between taps in the 4 tap rows (A1, A2 and A3) and the equivalent taps in the 28 tap rows (B1 and B2) for the lowest turbulence flow ($I_u = 0.6\%$, no grid in the tunnel).

The leading edge shows a wide range of fairly low correlation coefficients for low α . However, at $\alpha = 15^\circ$ there was a spike in correlation, as there was for the trailing edge taps. The magnitude of R decreases again before increasing with the onset of stall. The correlations decrease at high α , presumably for a similar reason to the decrease for the upper taps (the decrease is less for the leading edge taps than the upper taps as would be expected).

The lower taps show a similar spread in correlations at $\alpha = 0^\circ$ to the correlations for the upper taps. However, they remain fairly constant at low α except for an increase in R for spanwise spacings greater than $1c$ at $\alpha = 7.5^\circ$. There are jumps in correlation coefficients at $\alpha = 15^\circ$. The $|R|$ then decreases again before the onset of shedding and the associated increase in correlation. The correlation coefficients for the lower taps show a dip in correlation at high α . This was also seen for the other aerofoil sections and was hypothesised to be to do with freestream turbulence effects.

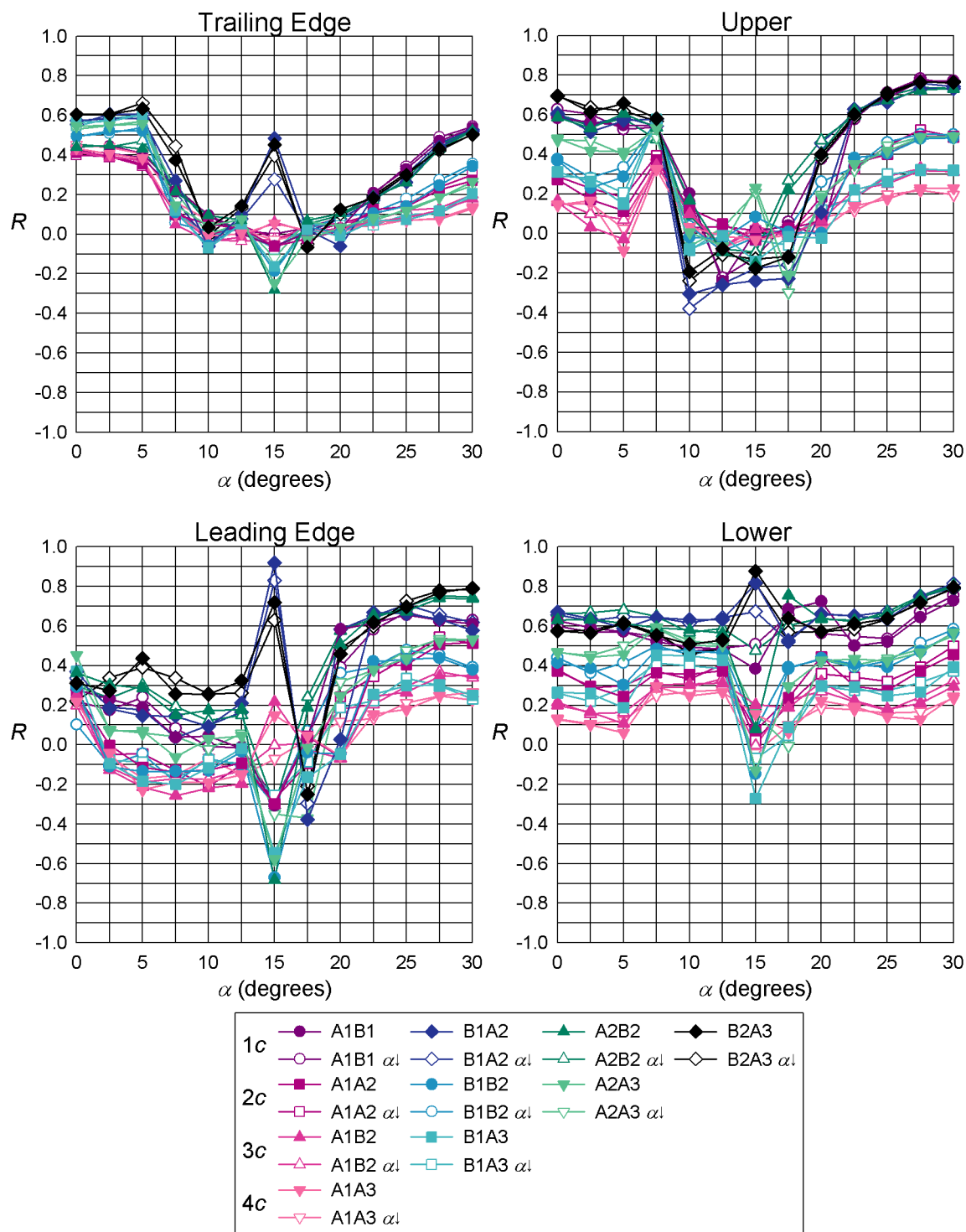


Figure 6-28 - S809 Correlation coefficients between taps in the 4 tap rows (A1, A2 and A3) and the equivalent taps in the 28 tap rows (B1 and B2) for the lowest turbulence flow ($I_u = 0.6\%$, no grid in the tunnel) for $30^\circ \geq \alpha \geq 0^\circ$.

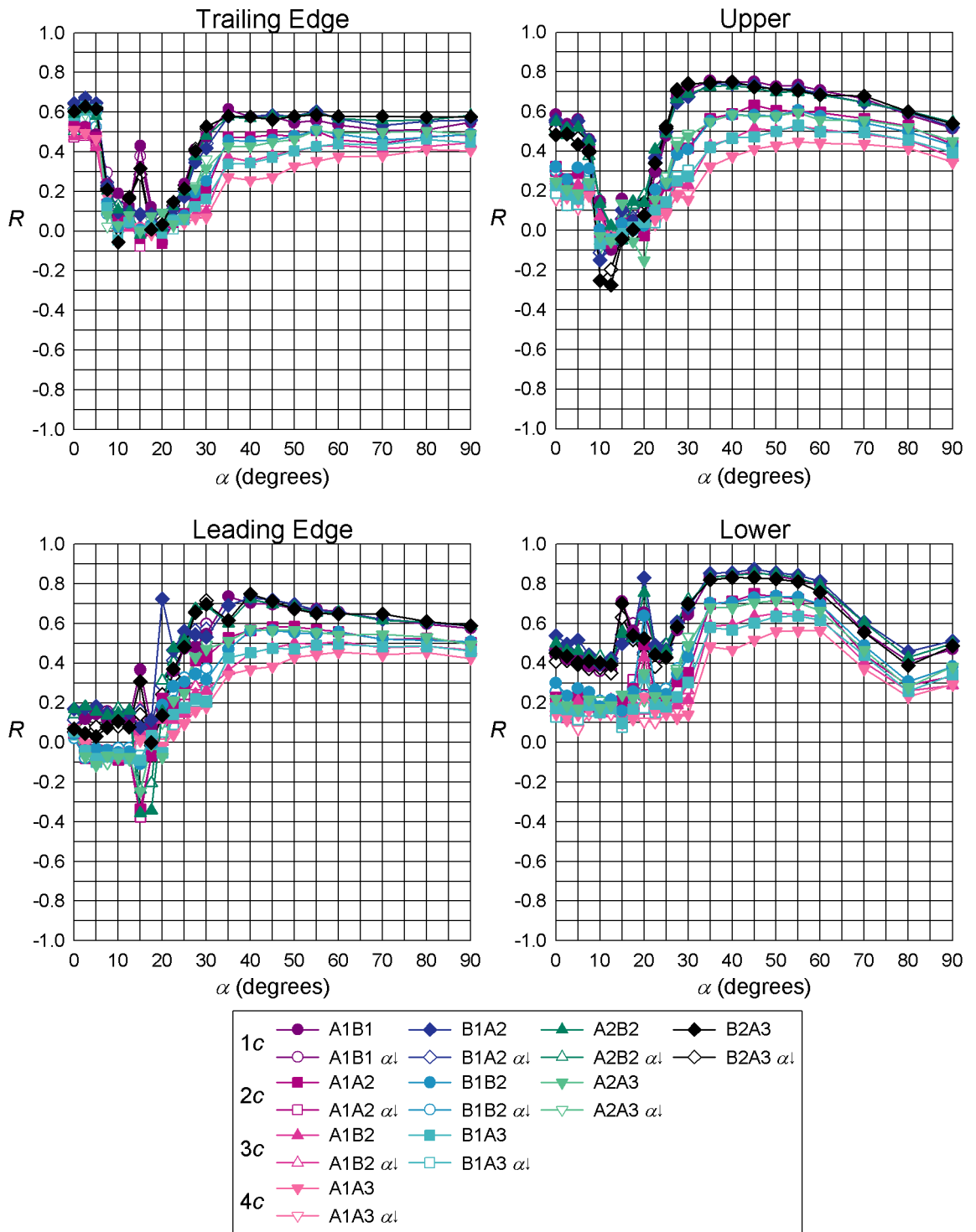


Figure 6-29 - S809 Correlation coefficients between taps in the 4 tap rows (A1, A2 and A3) and the equivalent taps in the 28 tap rows (B1 and B2) for the lowest turbulence flow ($I_u = 1\%$) with an integral length scale of about $1/3c$ (the small grid in position E).

The addition of a small amount of turbulence (small grid furthest from the model, position E) refines the bands based on spanwise position as can be seen in Figure 6-29. It also decreases the jumps in correlation at $\alpha = 15^\circ$. The leading edge shows reduced correlations for low α ($<15^\circ$) and a second jump in correlation at $\alpha = 20^\circ$ for the correlation between Rows B1 and A2. The lower taps show decreased correlations at all α except for a similar jump at $\alpha = 20^\circ$ to the correlation on the leading edge. Most noticeable for this plot was that the “dip” at high α was increased and did

not regain the values of the correlation coefficients seen earlier (at $\alpha = 90^\circ$ for the $1c$ separations it was only about 0.5 compared to about 0.8 for the lower turbulence intensity case).

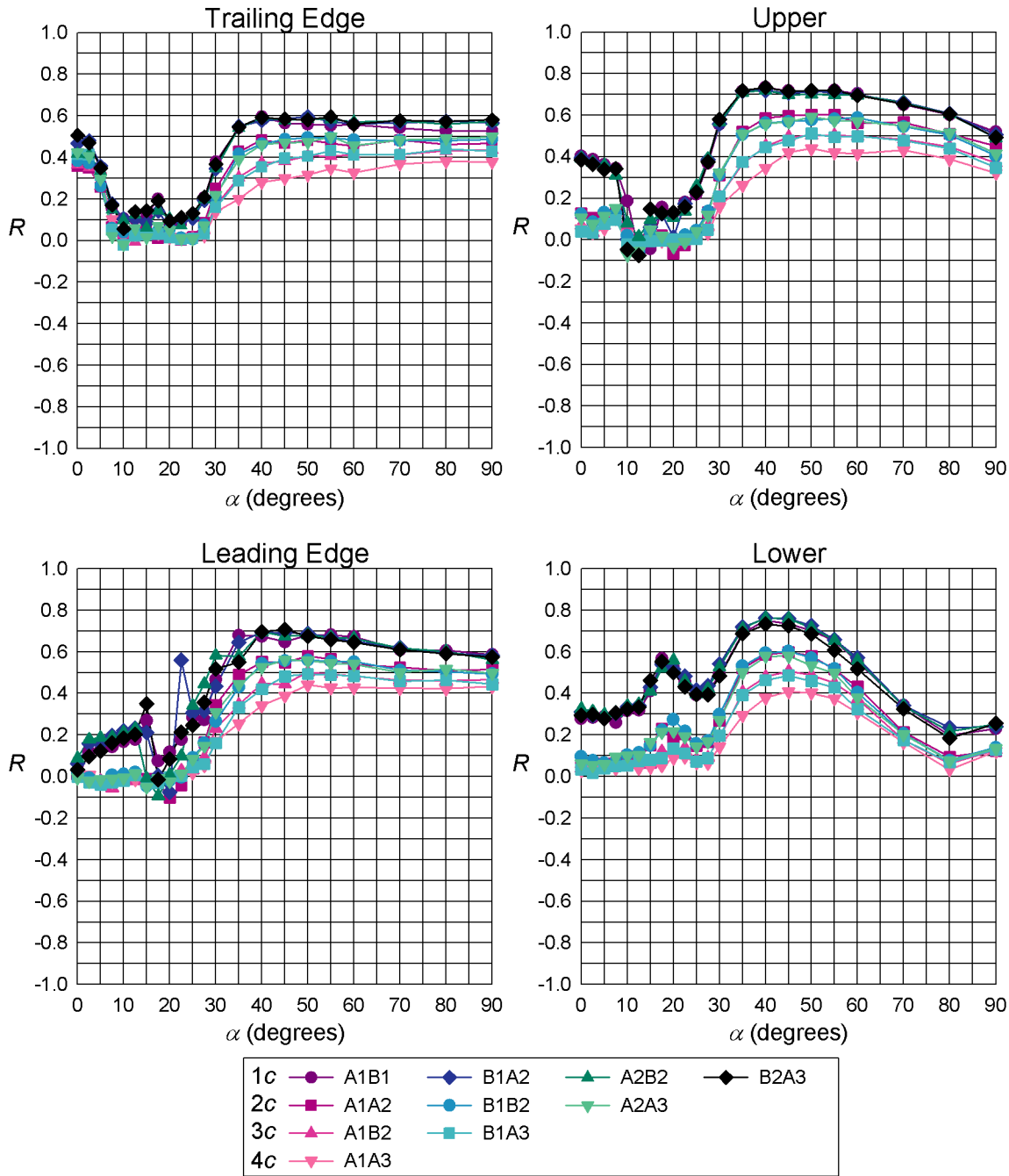


Figure 6-30 - S809 Correlation coefficients between taps in the 4 tap rows (A1, A2 and A3) and the equivalent taps in the 28 tap rows (B1 and B2) for the highest turbulence flow ($I_u = 3\%$) with an integral length scale of about $1/3c$ (the small grid in position A).

Increasing the turbulence intensity further decreases the correlation coefficients for the lower taps further across the range of α as seen in Figure 6-30. The correlation coefficient at $\alpha = 90^\circ$ for the $1c$ separations is only about 0.2. The trailing edge shows a collapse of all bands for low α and no “jumps” at $\alpha = 15^\circ$. The upper taps shows a reduction in R for $1c$ at $\alpha = 0^\circ$ and a collapse of all the other spacings (there were two bands for $\alpha < 7.5^\circ$). There was a small jump at $\alpha = 15^\circ$ for spacings of $1c$, but only to very low levels of R , and then a smooth increase in correlation with the onset of

shedding in all cases followed by the decrease in correlation coefficients with increasing α typical for this tap. There was no correlation for $\alpha = 0^\circ$ for the leading edge tap. There was a slight increase for the $1c$ separation cases for $\alpha < 15^\circ$. At $\alpha = 15^\circ$ there were very small jumps in correlations for some of the $1c$ cases before all correlations went to about zero again. The correlations then increased with the onset of shedding as seen previously. There was a jump at $\alpha = 22.5^\circ$ for the correlations between Rows B1 and A2. This angle is between the maximum and minimum c_l associated with stall.

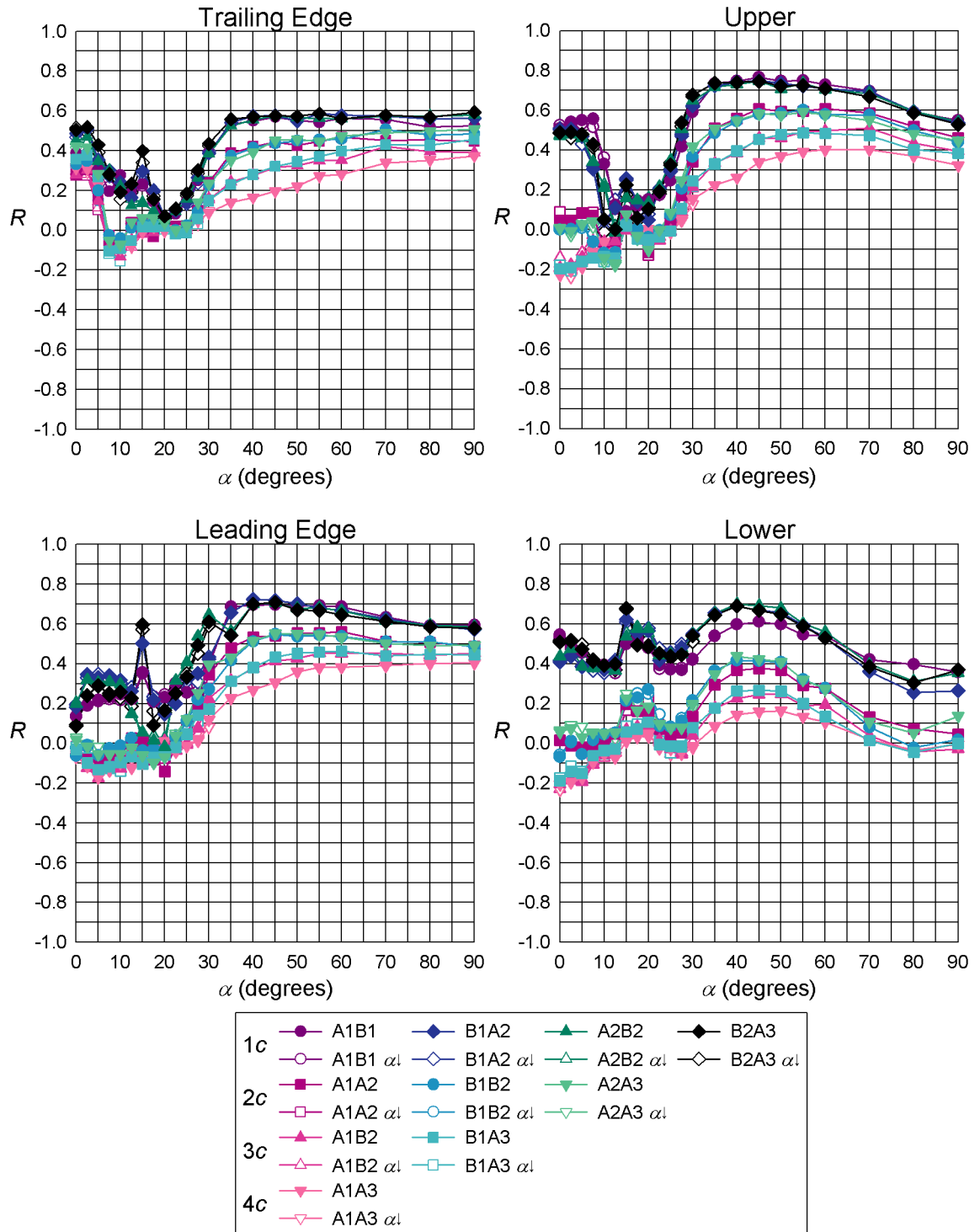


Figure 6-31 - S809 Correlation coefficients between taps in the 4 tap rows (A1, A2 and A3) and the equivalent taps in the 28 tap rows (B1 and B2) for the lowest turbulence flow ($I_u = 2\%$) with an integral length scale of about $1/2c$ (the medium grid in position E).

The medium grid in position E produces a smaller turbulence intensity but larger length scale than the small grid in position A and so the correlations shown in Figure 6-31, are somewhere between those for the small grid in positions A (Figure 6-30) and E (Figure 6-29). For example, the jumps at $\alpha=15^\circ$ are more apparent than for the small grid in position A. Oddly the correlations for A1B1 and A1A2 were different from the other separation results for at high α for the lower taps only. The lower tap in row A1 may have been partially blocked during this run, this could give lower variations in the pressure record and therefore lower correlations.

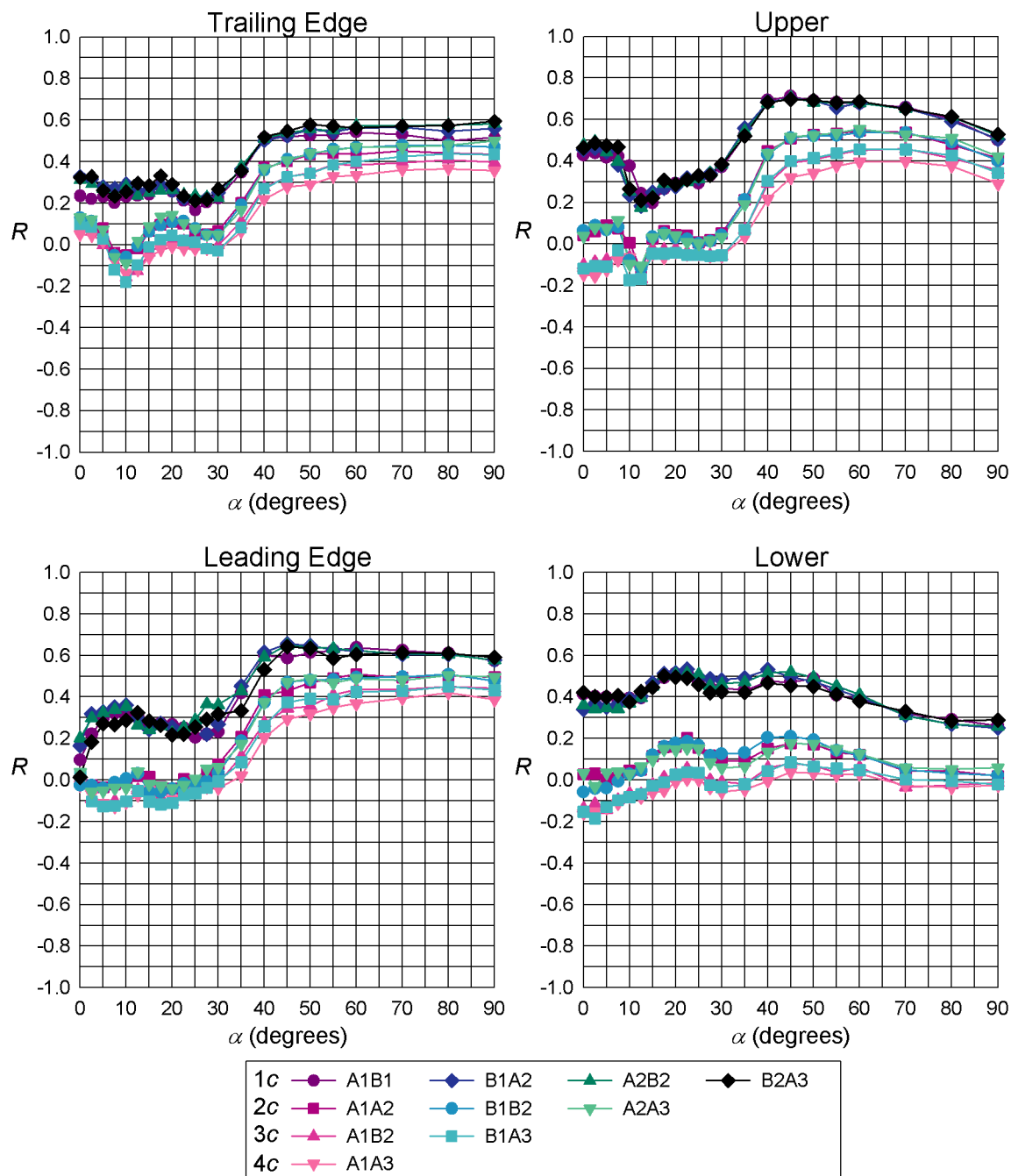


Figure 6-32 - S809 Correlation coefficients between taps in the 4 tap rows (A1, A2 and A3) and the equivalent taps in the 28 tap rows (B1 and B2) for the highest turbulence flow ($I_u = 6\%$) with an integral length scale of about $1/2c$ (the medium grid in position A).

However, increasing the turbulence intensity (medium grid in position A) further reduced the variation at small α and more constant values in the shedding region for the leading and trailing edge taps, see Figure 6-32. Most notable was the very flat plot for the lower tap, clearly the effects of the turbulence dominates the correlations in this case.

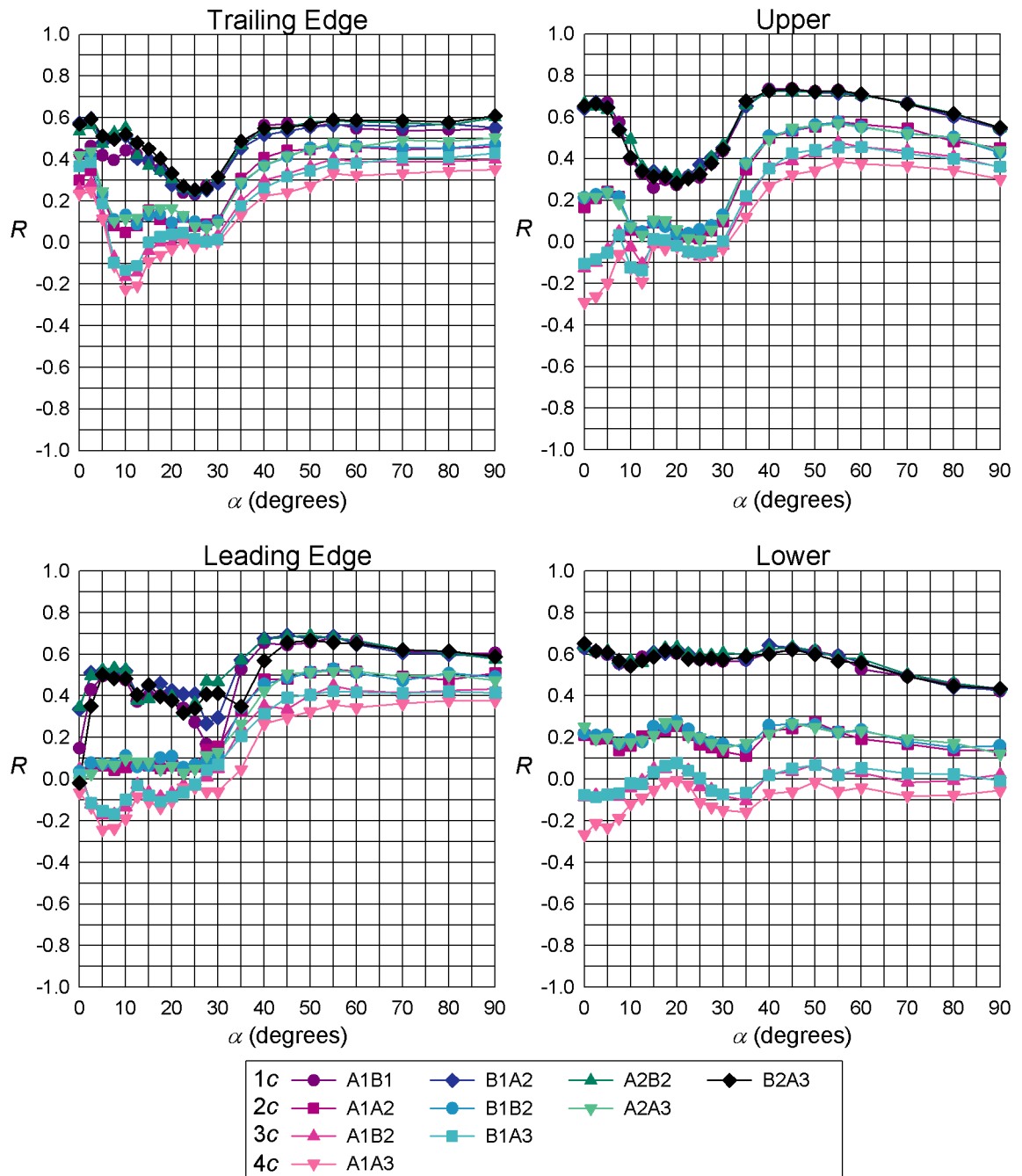


Figure 6-33 - S809 Correlation coefficients between taps in the 4 tap rows (A1, A2 and A3) and the equivalent taps in the 28 tap rows (B1 and B2) for the lowest turbulence flow ($I_u = 5\%$) with an integral length scale of about $1c$ (the large grid in position E).

Increasing the turbulence integral length scale but slightly decreasing the turbulence intensity shows that the intensity is responsible for damping out variations in R (see Figure 6-33). For example the lower turbulence intensity shows more variation in R at low α . However, the scale also had an effect with the correlations for the $1c$ separation cases increasing at α prior to stall.

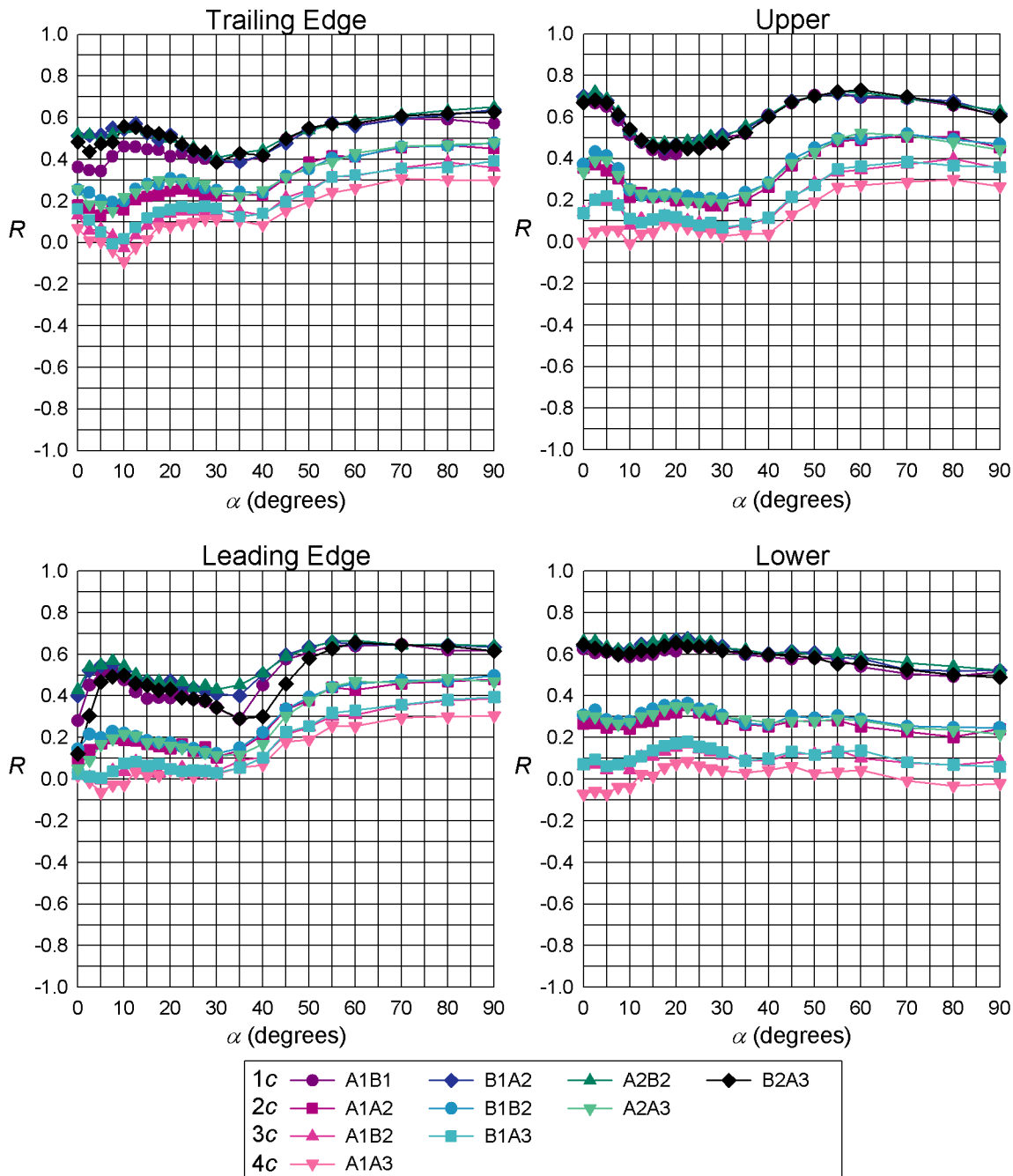


Figure 6-34 - S809 Correlation coefficients between taps in the 4 tap rows (A1, A2 and A3) and the equivalent taps in the 28 tap rows (B1 and B2) for the highest turbulence flow ($I_u = 13\%$) with an integral length scale of about $1c$ (the large grid in position B).

A higher turbulence intensity of similar scale heavily damped out variations in the correlation coefficients, see Figure 6-34. For example the lower taps for a spanwise separation of $1c$ had a variation in R of 0.4 to 0.7 in Figure 6-33 but only 0.5 to 0.7 in Figure 6-34. There was also some variation for the leading edge taps between the $1c$ results for $30^\circ < \alpha < 50^\circ$.

Conclusions from the correlation coefficients with relevance to all the aerofoil sections and likely effects on wind turbines will be drawn in Chapter 7.

Chapter 7

Conclusions

This research has provided detailed measurement of the pressures on three aerofoil sections over a wide range of α in turbulent flows. It has added to the sparse information on the performance of aerofoil sections in turbulence and on the behaviour of aerofoils at high α . The lack of data on aerofoils at high α was demonstrated by the use of some of the NACA 0021 data presented as verification of computational models on the NACA 0012 aerofoil section (Thiele, Mockett & Bunge, 2004) and the decision by another researcher (Weinman, 2004) to computationally model the flow past a NACA 0021 aerofoil section so these experimental results can be used as a direct comparison with the computational results. The experiments have demonstrated that even low intensity turbulence can affect stall on thick aerofoil sections. The major implication of this result is that turbulence should be considered in the design and testing of aerofoil sections for wind turbines and also in the design of new codes for the prediction of the aerodynamic performance of wind turbines.

The high aspect ratio of the wing used was one of the major features of the model design. This was due to Szepessy & Bearman's (1992) findings of the effects of reduced aspect ratio on the vortex shedding on cylinders. Some preliminary testing was done to assess the effects of aspect ratio on the aerofoil and the results showed strong effects. However, as altering the aspect ratio also changed the position of the tapping rows in the stall cells, the exact cause of the changes could not be assigned. Therefore, these results were not included in the thesis. It would be very valuable for future testing of this kind for an investigation to be made of the effect of aspect ratio on aerofoil performance at high α . Such an investigation would require the use of a force balance so that integrated measurements of lift and drag could be made across the span. Given the differences in the current results between Row B1 and B2 due to different positions in the stall cells, especially on the NACA 4421 and S809 aerofoil sections, the use of a force balance to obtain span integrated force measurements would be recommended for future testing. This would allow comparison between the span averaged forces and detailed pressure measurements inside different parts of the stall cells.

The high aspect ratio limited the chord size and therefore the Re of the tests as well as the number of taps that could be included in the model. The Re tested was less than that expected on large wind turbines operating in the field. It is likely the separation bubble would not be present at the higher Re , or at least the size of the hysteresis loop would be reduced. It has been argued that this makes the current results less relevant to wind turbine operation. However, at higher turbulence levels where there is no hysteresis loop, increasing the turbulence intensity still delays stall on the aerofoil section so it is clear that the separation bubble is not the only thing affected by turbulence.

The number of taps is limited by the size of the model as it is with all pressure measurements that use tubing. While more detailed information is often desired, more taps will also add more roughness to the surface of the model. A good compromise seems to have been reached in this case, given the consistency in results.

This next section will look at the independent and dependent variables in order to summarise the results. Five independent variables were investigated; α (including the direction of change), Re , turbulence intensity and integral turbulence length scale and aerofoil shape (which includes camber, thickness etc.). During a run the aerofoil section being tested was in one flow condition (Re , turbulence intensity and integral turbulence length scale). To reduce the parameter space, Re was kept as constant as possible between runs (there was only one case of two runs at different Re for the same flow condition, the S809 in the lowest turbulence flow). The three aerofoil sections were chosen to have the same thickness (21%) and were built with the same chord length (125 mm). They represented a conventional symmetric aerofoil (the NACA 0021), a cambered version of this aerofoil (the NACA 4421) and a cambered aerofoil section specifically designed for wind turbine applications (the S809). Each aerofoil section was tested in 15 different turbulent flow conditions. To check for hysteresis in some flow conditions both increasing and decreasing α runs were conducted at low α . The same grid in different positions in the tunnel provided similar turbulent integral length scales but different turbulence intensities. There were also four flow conditions of similar turbulence intensities but different integral length scales. Although this control of the independent variables allowed comparisons of the effects of changing one variable, the large number of interrelated dependent variables still makes analysis complicated.

Many of the plots were based on the independent variable of α versus the dependent variables of mean lift, drag, moment about the quarter chord, normal force or tangent force. These are calculated from the mean pressure around the aerofoil. The pressure depends on the deflection of the flow around the aerofoil and on the attached or separated boundary layer on the suction surface of the aerofoil. The separation points are fixed on the trailing edge but vary around the rounded leading edge. As all aerofoil sections tested were thick, stall was not very sudden and the free separation point moved towards the leading edge with increasing α . The separation point depends on the boundary layer's ability to withstand the adverse pressure gradient, which depends on the aerofoil shape and α .

Increasing turbulence intensity at scales about the boundary layer size promotes the transition of the boundary layer to turbulence and therefore increases the ability of the boundary layer to withstand adverse pressure gradients. This promotes a slower movement of the separation point towards the leading edge. Large turbulent scales affect the curvature of the separated shear layers. This was most dramatically seen in the higher shedding frequency for the NACA 0021 aerofoil section for the highest turbulence integral length scale and intensity flow. For a constant universal

Strouhal number increasing frequency means decreasing wake width, therefore the higher frequency showed this flow decreased the wake width by increasing curvature of the shear layers.

Figure 7-1 shows the lift curves for all the flow conditions for the three aerofoil sections tested. The most striking features of the plots is how the stalling process is prolonged by the increase in turbulence intensity and for the higher turbulence intensities the increasing c_l region after stall is also increased. There also seems to be some effect of turbulence on the slope of the linear attached region of the lift curve. The effects of turbulence on c_d and $c_{m, 1/4c}$, shown in Figure 7-2 and Figure 7-3 respectively, are not as dramatic, with the main features being the smoothing away of the jump in c_d and $c_{m, 1/4c}$ associated with stall and changes in the extreme values at $|\alpha| = 90^\circ$.

In an attempt to quantify these effects, a series of plots of the extreme points of the c_l , c_d and $c_{m, 1/4c}$ curves will be presented versus the turbulence intensity and integral turbulence length scale. It must be remembered that these values are not entirely independent for this data, i.e. higher turbulence intensities generally had larger integral turbulence length scales. Figure 7-4 shows the slope of the linear attached region of the lift curve with respect to the turbulence intensity and integral length scale. There is a general decrease in slope with increasing turbulence intensity up to $I_u \approx 5\%$ and then an increase in slope. There is no strong trend for the plot versus L_{uu}/c except for the S809 aerofoil section where slope generally increases with increasing integral length scale. However, there is a great deal of scatter in the plots. Perhaps future experiments using balances could examine this relationship further.

Figure 7-5 shows the maximum or minimum c_l associated with stall and the angle at which it occurs versus the turbulence intensity and the integral turbulence length scale. There is a gradual increase in magnitude of c_l and the α at which this occurs with turbulence intensity and turbulence integral length scale (although there is more scatter in the plot versus integral turbulence length scale which indicates a weaker relationship with length scale than turbulence intensity). Compared to the NACA 0021 results, the cambered NACA aerofoil shows increased maximum c_l and the restrained lift S809 aerofoil shows reduced maximum c_l as would be expected.

Figure 7-7 shows the maximum c_d at $\alpha = \pm 90^\circ$ versus I_u and L_{uu}/c . There is a lot of scatter in these plots and, apart from a slight trend to increasing maximum c_d with increasing I_u and L_{uu}/c , there is no discernable trend in the results for each aerofoil section. In comparing aerofoil sections it is interesting that the NACA 0021 and S809 aerofoil sections have comparable maximum c_d and that the NACA 4421 has higher c_d with the concave surface down wind and lower drag with the convex surface upwind. Given the different aerofoil shapes shown in Figure 7-6, the changes in maximum c_d may be due to the thickest part of the S809 aerofoil being closer to mid-chord and therefore encouraging a more even split of the fluid around the aerofoil. For the sake of completeness, Figure 7-8 shows the maximum or minimum $c_{m, 1/4c}$ at $\alpha = \pm 90^\circ$. The changes in this value are small and $c_{m, 1/4c}$ remains fairly constant with increasing I_u and L_{uu}/c .

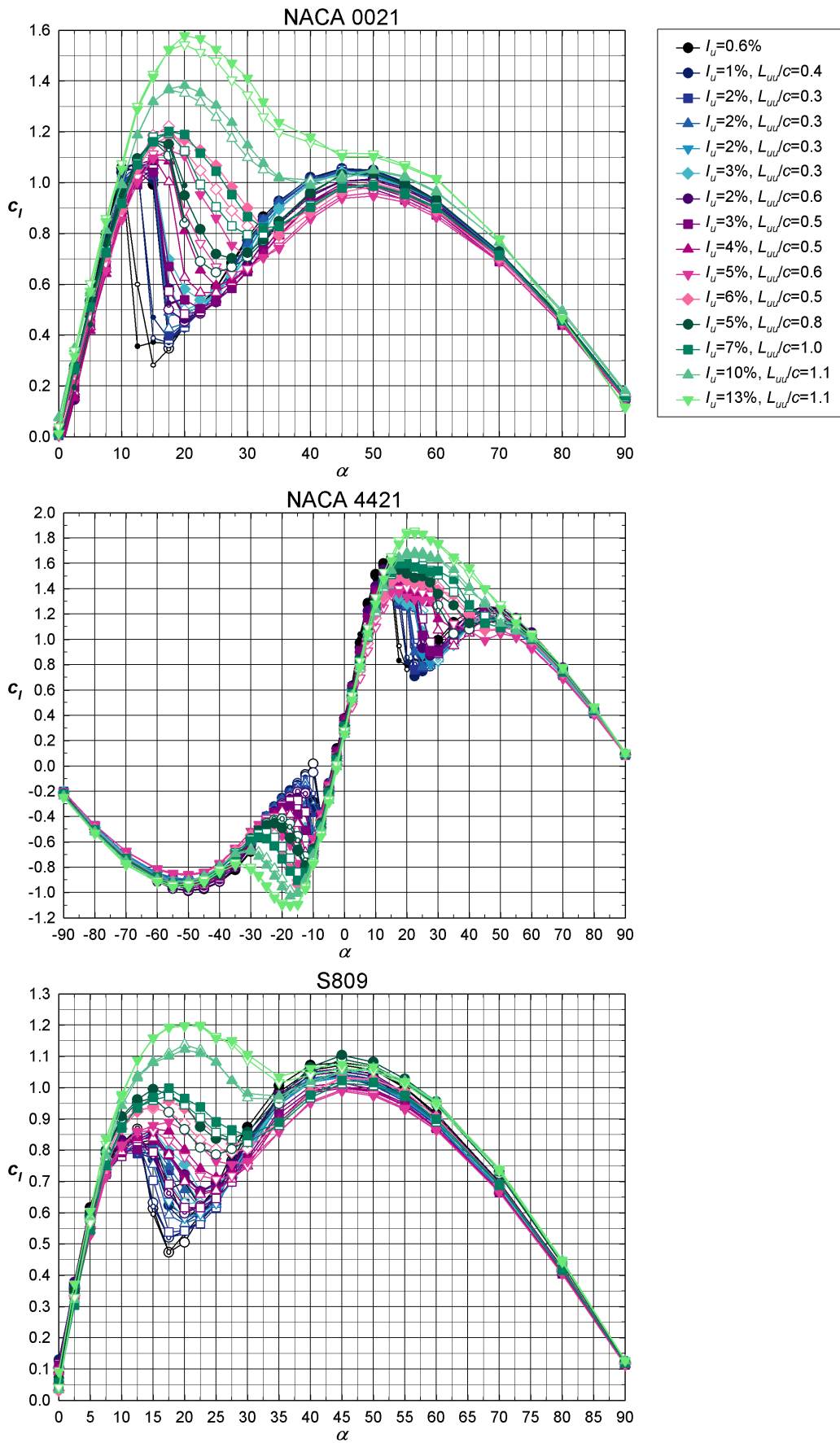


Figure 7-1 - Lift curves for the three aerofoil sections in all flow conditions. Closed symbols indicate Row B1 and open symbols indicate Row B2. Decreasing α is indicated by smaller symbols.

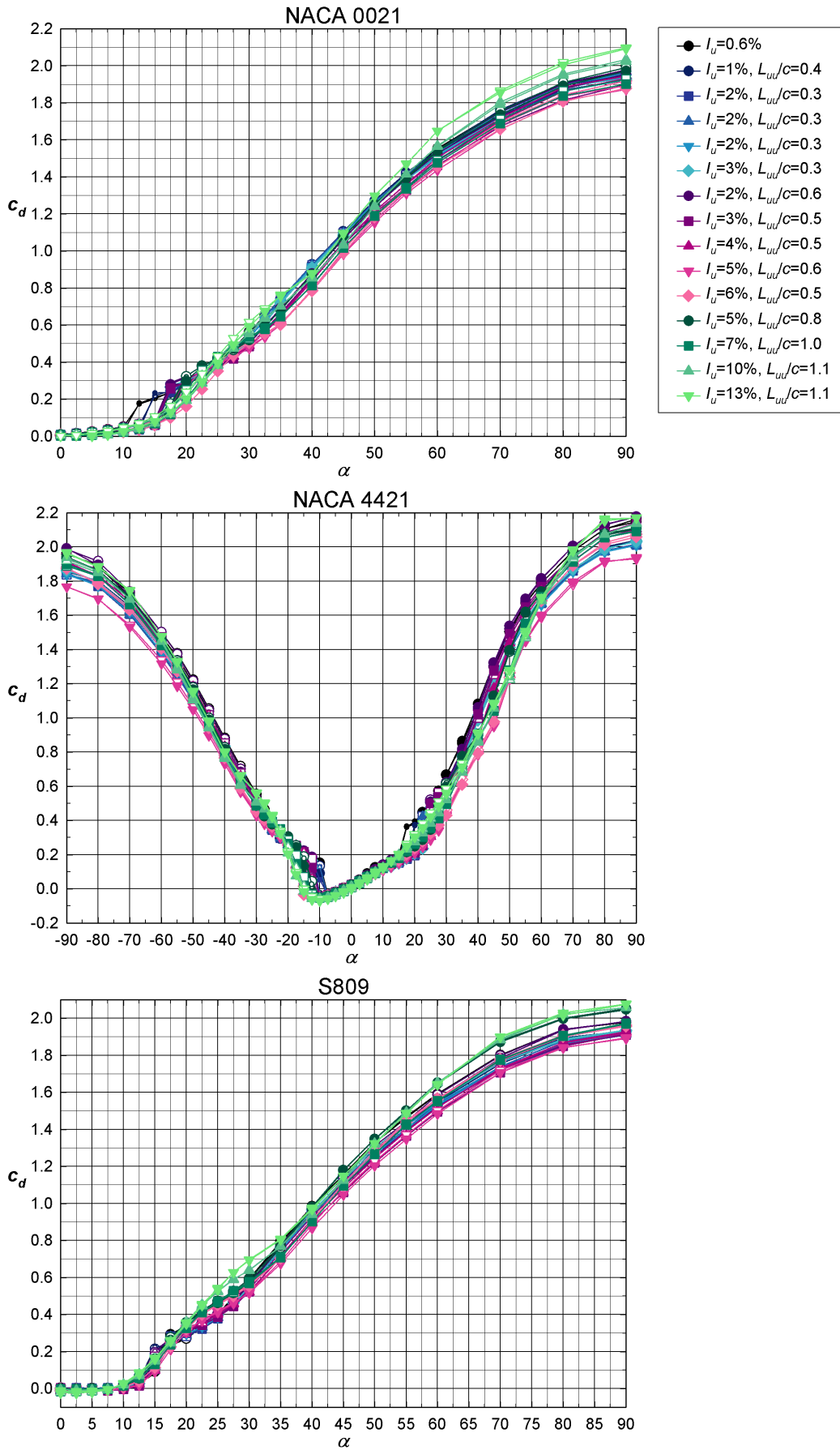


Figure 7-2 - Drag curves for the three aerofoil sections in all flow conditions. Closed symbols indicate Row B1 and open symbols indicate Row B2. Decreasing α is indicated by smaller symbols.

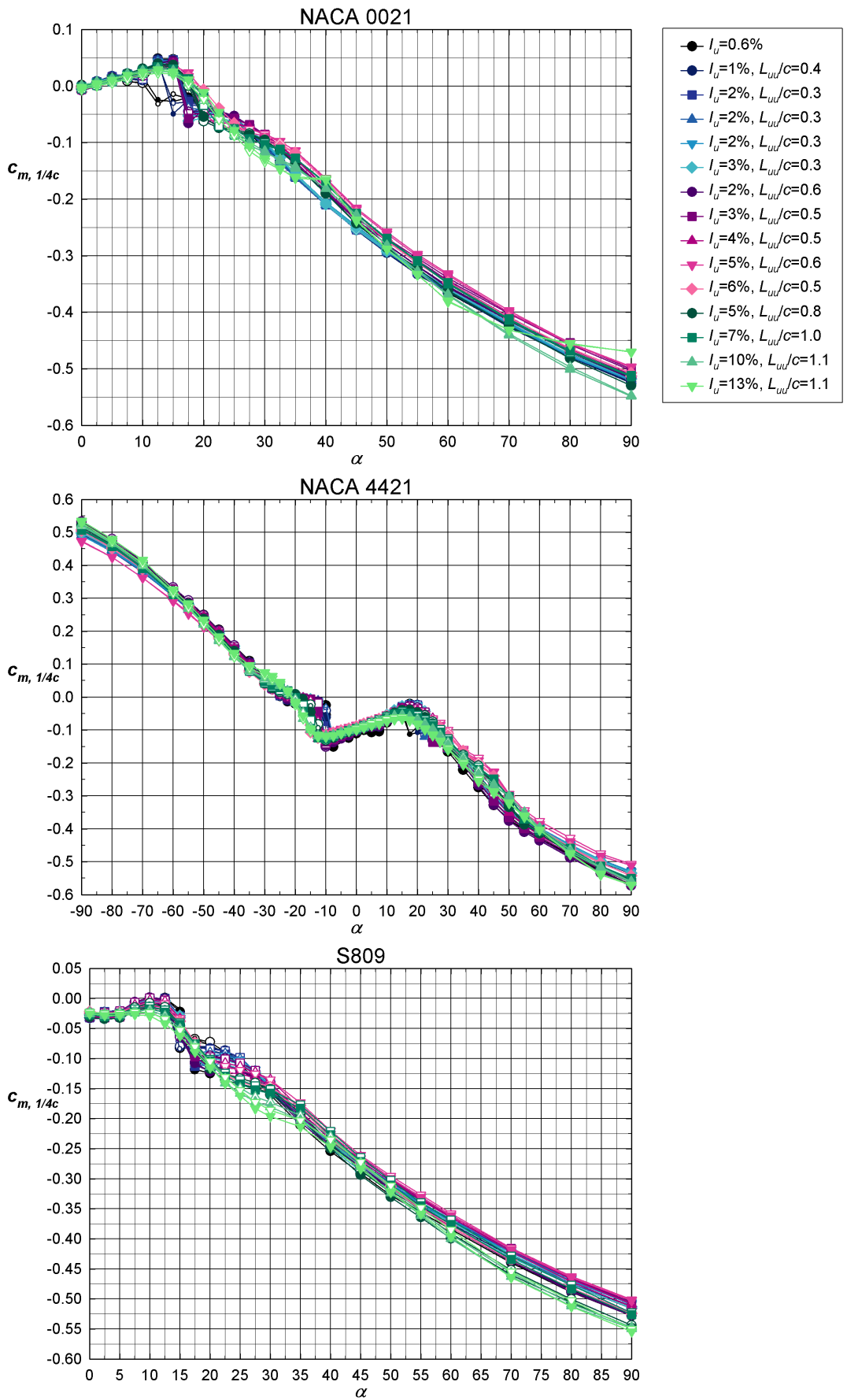


Figure 7-3 – Moment about the quarter chord for the three aerofoil sections in all flow conditions. Closed symbols indicate Row B1 and open symbols indicate Row B2. Decreasing α is indicated by smaller symbols.

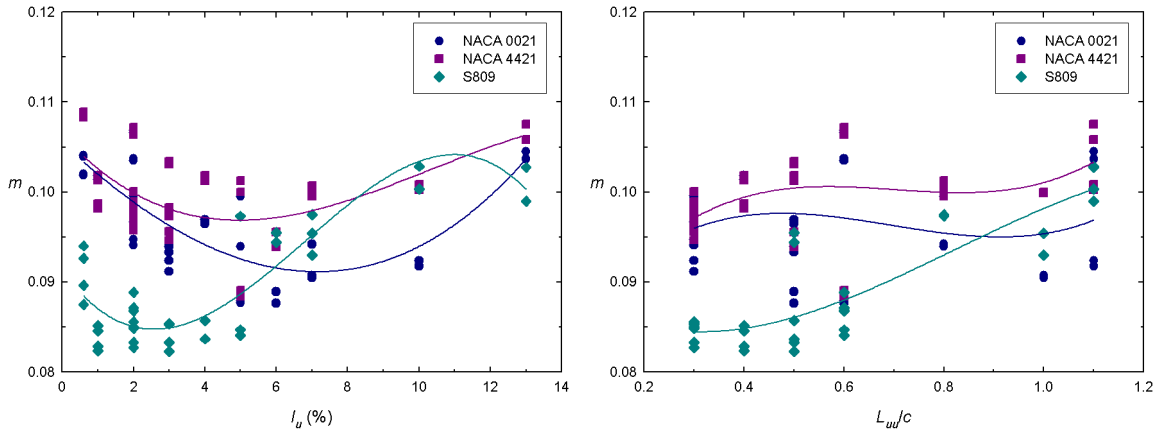


Figure 7-4 - Gradient of the linear region versus turbulence intensity and length scale. The gradient was found with a least squares fit over the α range of 0 to 10 for the NACA 0021, -7.5 to 10 for the NACA 4421 and 0 to 7.5 for the S809. The R^2 values for the linear least squares fit used to find the slopes were greater than 0.995 for all the NACA aerofoil fits and greater than 0.978 for the S809 aerofoil fit. The lines are third order polynomials to aid the eye in following the overall trends in the data.

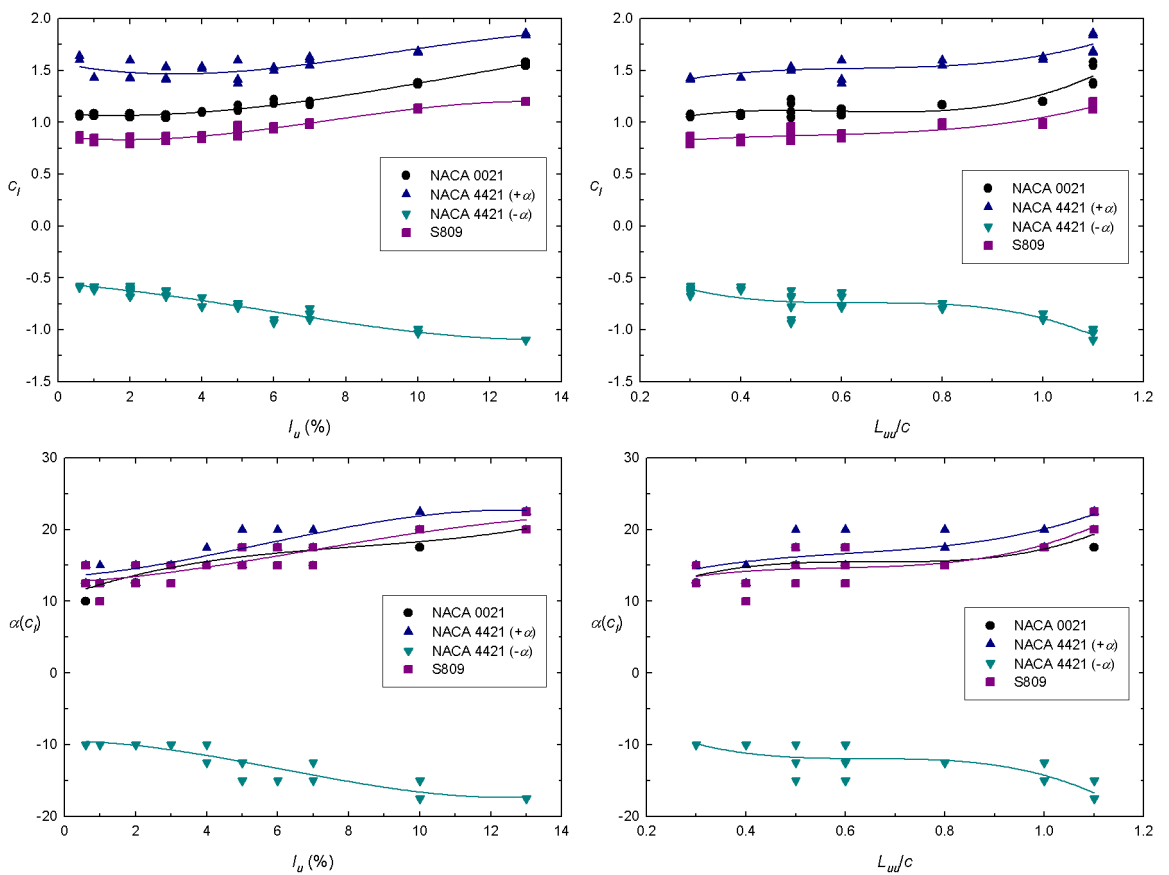


Figure 7-5 - The maximum and minimum c_l associated with stall and the α at which they occurred for all increasing α cases. The lines are third order polynomials to aid the eye in following the overall trends in the data.

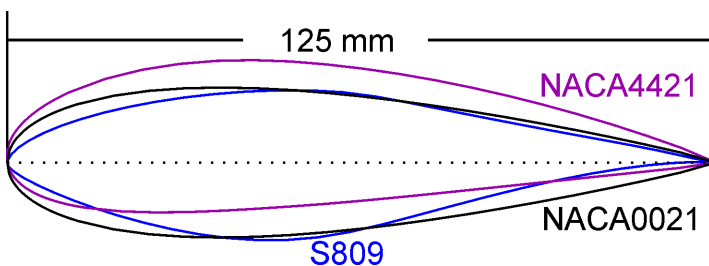


Figure 7-6 - Aerofoil cross-sections of the NACA0021, NACA4421 and NREL's S809 (to scale). Figure repeated from Chapter 3.

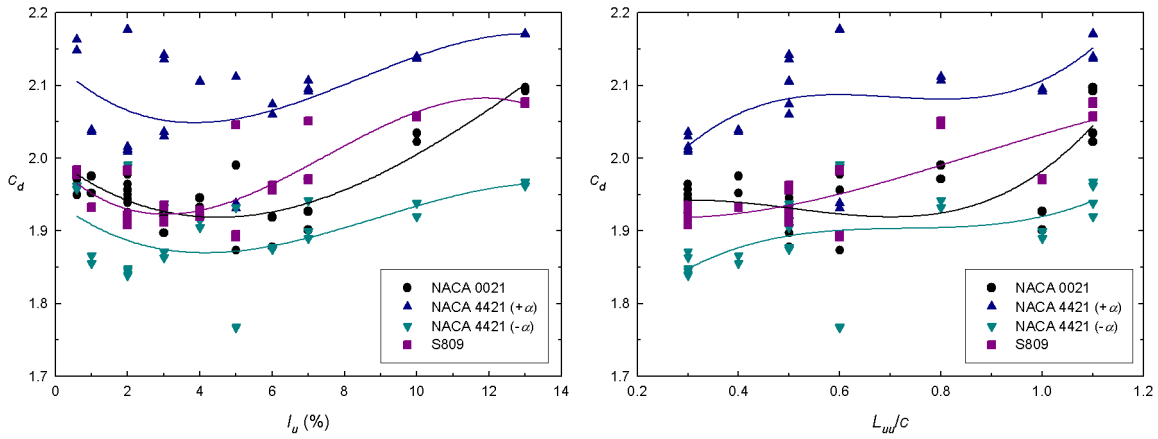


Figure 7-7 - The maximum c_d at $\alpha = \pm 90^\circ$ versus I_u and L_{tu}/c . The lines are third order polynomials to aid the eye in following the overall trends in the data.

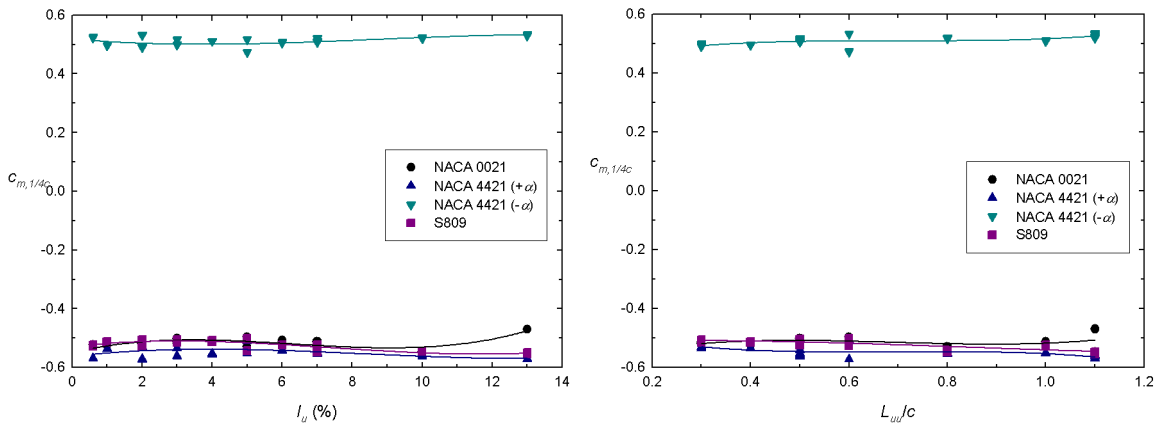


Figure 7-8 - The maximum and minimum $c_{m, 1/4c}$ at $\alpha = \pm 90^\circ$ versus I_u and L_{tu}/c . The lines are third order polynomials to aid the eye in following the overall trends in the data.

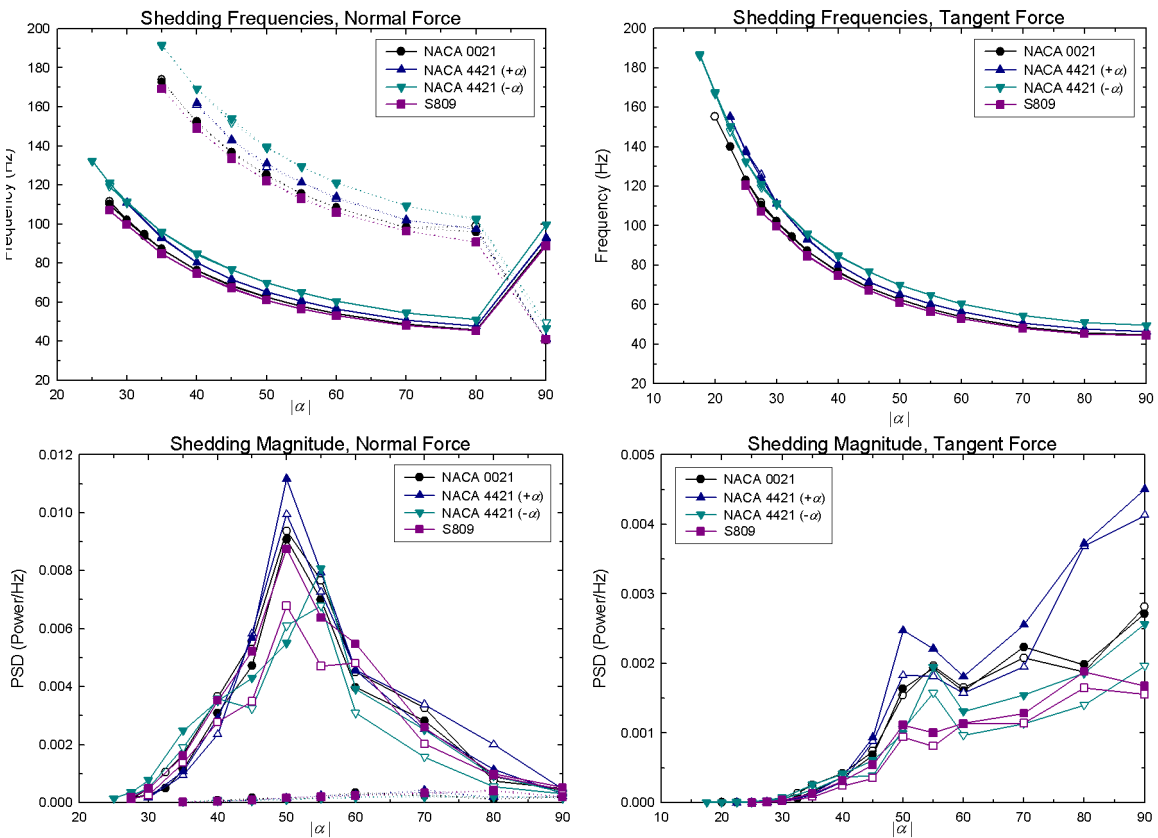


Figure 7-9 - Shedding frequency and magnitude from the tangential and normal force for the lowest turbulence flow. Closed symbols indicate Row B1 and open symbols indicate Row B2. Complete lines indicate the main shedding frequency and dotted lines indicate the second shedding frequency.

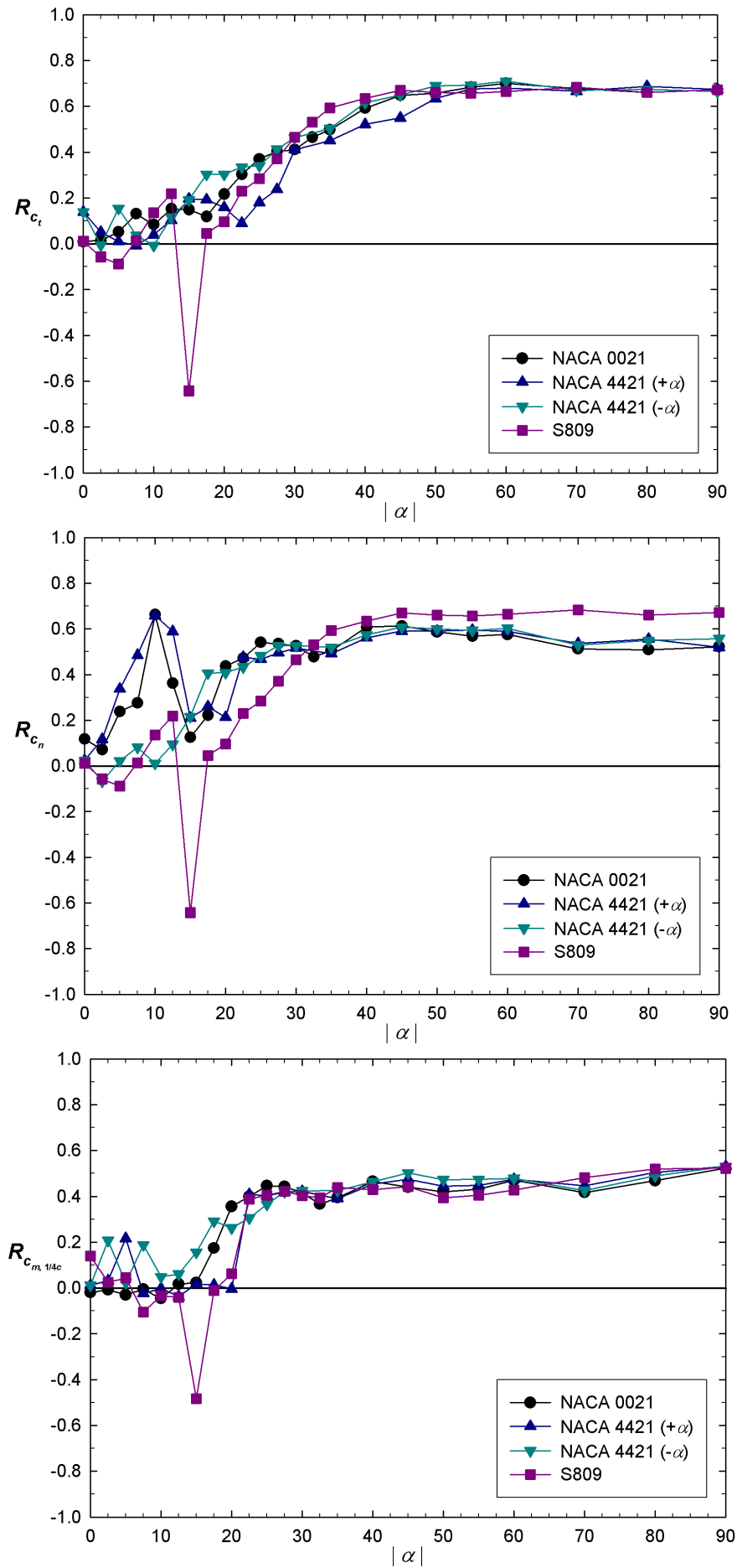


Figure 7-10 - Correlation coefficients between the c_r , c_n and $c_{m, 1/4c}$ from Row B1 and B2 measurements for the lowest turbulence flow.

The fluctuating results for all three aerofoil sections showed a single frequency in the instantaneous c_t measurements. This was because the c_t measurements were dominated by the leading edge and trailing edge taps which were where the vortices were being shed. The instantaneous c_n signals showed a low frequency noise, main shedding frequency and a secondary peak at twice the main shedding frequency. The “noise” has been seen in previous experiments (Schewe, 2001, Nakamura, 1996). This effect and the main and secondary frequencies can also be seen in the time traces presented in Figure 2-62. There were also low frequencies near the onset of stall in some flows in the normal force PSDs. And, in some cases, the tangential force as well. Low frequencies were also seen in c_n for higher turbulence intensity flows. Increasing turbulence intensity delayed the onset of shedding for all aerofoil sections.

For comparison purposes, the shedding frequencies in the normal and tangential force and the magnitude of the shedding peaks from all the aerofoil sections in the lowest turbulence flow are shown in Figure 7-9. At large negative α the NACA 4421 aerofoil section showed the highest frequency of shedding and therefore, to preserve the universal Strouhal number, the lowest wake width. The next smallest wake was for the NACA 4421 at positive α , followed by the NACA 0021 and then the S809 (which was close to the NACA 0021). The NACA 4421 for positive angles showed a different shape to the curve at low α , presumably another side effect of the camber, see Figure 7-6. Figure 7-9 also shows the magnitude of the shedding peaks. For the second frequency (dotted lines) and in the tangential force the magnitude of the shedding frequency peak increases with increasing α . However, the secondary frequency peaks are very small. The main shedding frequency in the normal force has the largest magnitude. The peak occurs at 50° for all aerofoil sections except the NACA 4421 at negative α (where it occurs at $\alpha = -55^\circ$). There is a good deal of difference in the shedding magnitude between tapping rows on the aerofoil sections so it would be unwise to comment on differences between the aerofoil sections based on just this data.

The shedding would need to be well correlated across the span to have a fatiguing effect on a wind turbine blade. The correlation coefficients between Row B1 and B2 results for c_t , c_d and c_m , $1/4c$ for the lowest turbulence flow are shown for the three aerofoil sections in Figure 7-10. They all show reasonably high correlations for high α . They are affected by noise at low α and there is a great deal of variability. The other interesting feature is the peak in negative correlation for the S809 aerofoil section at $\alpha = 15^\circ$ in all plots. This is the same α at which there were large peaks in c_n and c_t associated with stall of the aerofoil section. Peaks of this nature were also seen in the correlations between taps, especially in decreasing α cases where it was hypothesised that the shear layers were flapping as they did not have enough energy to form a separation bubble. The pressure tap correlation results also showed high correlations at high α . The most interesting result for the comparison between taps in the same position in different rows was that the results formed “bands” based on the distance the taps were apart with the closest taps having the highest correlations. Increasing turbulence tended to refine these bands. Increasing turbulence intensity tended to

smooth out the variations in the correlation coefficients between taps and between c_n , c_t and c_m , $1/4c$ signals at low α .

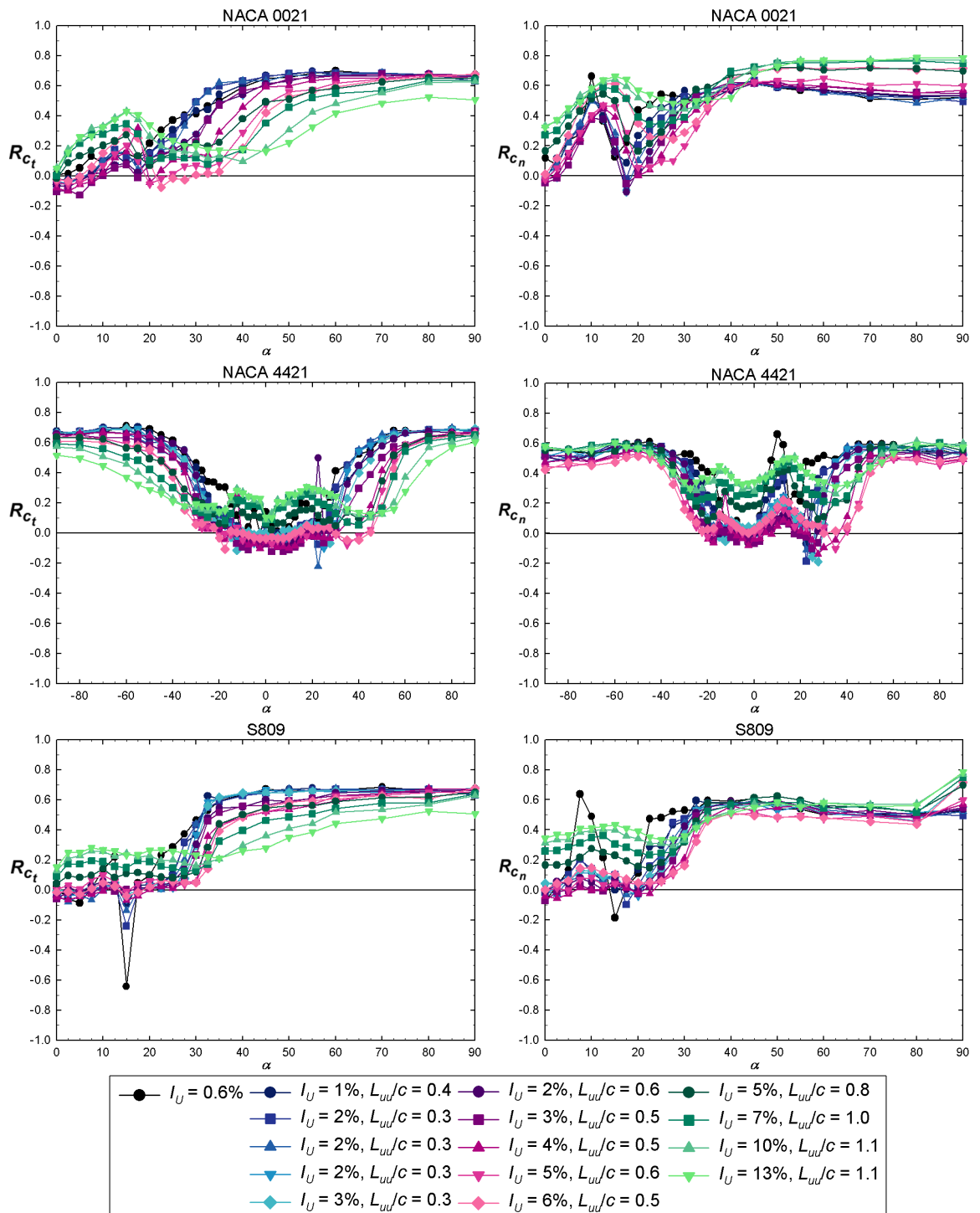


Figure 7-11 - Correlation coefficients between the instantaneous c_t and c_n from Rows B1 and B2 in turbulence.

The correlation coefficients for the c_m , $1/4c$ data are similar to that from the c_t coefficients at low α and the c_n coefficients at high α and so won't be discussed further here. The addition of turbulence does effect R_{C_t} and R_{C_n} as is shown in Figure 7-11. As $|\alpha| \rightarrow 90^\circ$, the R_{C_t} values converge on about 0.6 to 0.7, except for the largest turbulence intensity flow which has a lower correlation for

all three aerofoil sections. Reducing the magnitude of α from $|\alpha| = 90^\circ$ results in the higher turbulence intensity flows dropping in correlation faster and so, for example, at $|\alpha| = 60^\circ$ the correlations increase with decreasing turbulence intensity. It was suggested that this was due to the turbulence in the freestream masking the vortex shedding that dominates the tangential force and therefore reduces the correlations.

The behaviour for R_{C_n} as $|\alpha| \rightarrow 90^\circ$ is more complicated. For the NACA 0021 aerofoil section, the correlations are highest for the highest turbulence intensity flow and generally reduce with decreasing turbulence intensity. However, for the NACA 4421 and S809 aerofoil sections (except for the S809 at $\alpha = 90^\circ$), the extremes of the R_{C_n} plot show a mid-band of the lowest turbulence intensities (no grid and small grid, the black and blue plots on the graph). The medium scales (purple points) are below this band and the large scales (green points) are above it. For the S809 aerofoil at $\alpha = 90^\circ$, there is a jump in correlation for the higher turbulence intensity cases and the correlation coefficients at this angle increase with increasing turbulence intensity. The normal force seems to be affected by scale. Even the NACA 0021 results could be argued to show some banding on turbulence scale. The mechanism that causes this integral turbulence length scale effect deserves further investigation but to do so would probably require taking measurements in the wake.

In conclusion, the possible fatigue effects of well correlated vortex shedding should be considered in the design of wind turbines as should the increase in the mean forces with turbulence. Hopefully the results of this research will be to prompt the use of turbulence in testing of aerofoils for wind turbine applications and the consideration of turbulence in future predictive codes for wind turbine performance. This has the potential to enable the design of more efficient wind turbines which would be more competitive with existing fossil fuel technologies for electricity generation.

Chapter 8

References

- Abbot, I. H. & Doenhoff, A. E. (1959) *Theory of Wing Sections*, Dover Publications, pp. 111-5.
- Akins, R. E. (1978) *Performance Evaluation of Wind Energy Conversion Systems Using the Method of Bins - Current Status*, Sandia Laboratories, SAND77-1375.
- Amiet, R. K. (1975) *Acoustic Radiation from an Airfoil in a Turbulent Stream*, Journal of Sound and Vibration, 41(4), pp. 407-20.
- Anderson, C. G., Niven, A. J., Hamieson, P., Knight, R. R. & Milborrow, D. J. (1987) Flow Visualisation Studies on Rotating Blades, In *Wind Energy Conversion 1987 - Proceedings of the 9th British Wind Engineering Association Conference, Edinburgh 1-3 April 1987*, ed. Galt, J. M., Mechanical Engineering Publications Ltd, pp. 169-76.
- Anderson, M. B., Milborrow, D. J. & Ross, J. N. (1982) *Performance and Wake Measurements on a 3 m Diameter Horizontal Axis Wind Turbine. Comparison of Theory, Wind Tunnel and Field Test Data*, Presented at The Fourth International Symposium on Wind Energy Systems, September 21-24, Stockholm, Sweden, pp. 113-35.
- Barnsley, M. J. & Wellicome, J. F. (1992) *Wind Tunnel Investigation of Stall Aerodynamics for a 1.0 m Horizontal Axis Rotor*, Journal of Wind Engineering and Industrial Aerodynamics, 39, pp. 11-21.
- Bearman, P. W. & Morel, T. (1983) *Effect of Free Stream Turbulence on the Flow Around Bluff Bodies*, Progress in the Aerospace Sciences, 20, pp. 97-123.
- Blackburn, H. M. & Melbourne, W. H. (1996) *The Effect of Free-Stream Turbulence on Sectional Lift Forces on a Circular Cylinder*, Journal of Fluid Mechanics, 306, pp. 267-92.
- Blanch, M. J. (1996) *Reynolds Number Effects on the Stall of a Small Horizontal Axis Wind Turbine*, Presented at Wind Energy Conversion 1996. Proceedings of the 18th British Wind Energy Association Conference, pp. 315-21.
- Brown, C. J. & Graham, J. M. R. (1989) *The Effect of Turbine Rotation on Maximum Lift Coefficient*, Presented at EWEC '89. European and Wind Energy Conference and Exhibition, 10-13 July, Glasgow, pp. 117-21.
- Butterfield, C. P. (1989a) *Aerodynamic Pressure and Flow-Visualization Measurement for a Rotating Wind Turbine Blade*, Presented at the Eighth ASME Wind Energy Symposium, January 22-25, Houston, Texas, pp. 245-55.
- Butterfield, C. P. (1989b) *Three-dimensional airfoil performance measurements on a rotating wing*, Presented at EWEC '89. European Wind Energy Conference and Exhibition, 10-13 July, Glasgow, pp. 90-4.
- Butterfield, C. P., Musial, W. D. & Simms, D. A. (1992) *Combined Experiment Phase I - Final Report*, NREL, TP-257-4655.
- Butterfield, C. P., Scott, G. & Musial, W. (1992) *Comparison of Wind Tunnel Airfoil Performance Data with Wind Turbine Blade Data*, Journal of Solar Energy Engineering - Transactions of the ASME, 114(2), pp. 119-24.
- Carmichael, B. H. (1981) *Low Reynolds Number Airfoil Survey*, NASA.
- Carr, L. W. (1988) *Progress in Analysis and Prediction of Dynamic Stall*, Journal of Aircraft, 25(1), pp. 6-17.
- Chaviaropoulos, P. K. & Hansen, M. O. L. (2000) *Investigating Three-Dimensional and Rotational Effects on Wind Turbine Blades by Means of a Quasi-3D Navier-Stokes Solver*, Transactions of the ASME - Journal of Fluids Engineering, 122, pp. 330- 5.
- Chaviaropoulos, P. K., Sørensen, N. N., Hansen, M. O. L., Nikolaou, I. G., Aggelis, K. A., Johansen, J., Gaunaa, M., Hamraus, T., von Geyr, H. F., Hirsch, C., Shun, K., Voutsinas, S. G., Tzabiras, G., Perivolaris, Y. & Dyrmoose, S. Z. (2003) *Viscous and Aeroelastic Effects on Wind Turbine Blades. The VISCEL Project. Part II: Aeroelastic Stability Investigations*, Wind Energy, 6, pp. 387-403.
- Chen, J. M. & Fang, Y.-C. (1996) *Strouhal numbers of inclined flat plates*, Journal of Wind Engineering and Industrial Aerodynamics, 61, pp. 99-112.

- Clausen, P. D., Piddington, D. M. & Wood, D. H. (1987) *An Experimental Investigation of Blade Element Theory for Wind Turbines. Part 1. Mean Flow Results*, Journal of Wind Engineering and Industrial Aerodynamics, 25, pp. 189-206.
- Clausen, P. D. & Wood, D. H. (1988) *An Experimental Investigation of Blade Element Theory for Wind Turbines. Part 2. Phase-Locked Averaged Results*, Journal of Wind Engineering and Industrial Aerodynamics, 31, pp. 305-22.
- Connell, J. R. & George, R. L. (1987) *Accurate Correlation of Wind Turbine Response with Wind Speed Using a New Characterisation of Turbulent Wind*, Journal of Solar Energy Engineering - Transactions of the ASME, 109, pp. 321-9.
- Corten, G. P. (1999) *The Tip Commands - A Hypothetical Explanation of Double Stall*, Presented at WIND ENERGY. Wind Power Comes of Age. Proceedings of the 1999 Twenty-First BWEA Wind Energy Conference, 1-3 Sept., Cambridge, U.K., pp. 383-9.
- Corten, G. P. (2001) *Flow Separation on Wind Turbine Blades*, PhD thesis, Energieonderzoek Centrum Nederland (ECN).
- Corten, G. P. & Veldkamp, H. F. (2001) *Insects can Halve Wind-Turbine Power*, Nature, 412, pp. 41-2.
- Dallmann, U. & Schewe, G. (1987) *On Topological Changes of Separating Flow Structures at Transition Reynolds Numbers*, Presented at AIAA 19th Fluid Dynamics, Plasma Dynamics and Lasers Conference, June 8-10, Honolulu, Hawaii, p. 18.
- Danish Wind Industry Association (2003) *Generators*, <http://www.windpower.org>, last updated 19 September 2003.
- de Vries, O. (1983) *On the Theory of the Horizontal-Axis Wind Turbine*, Annual Review of Fluid Mechanics, 15, pp. 77-96.
- de Vries, O. (1985) *Comment on the Yaw Stability of a Horizontal - Axis Wind Turbine at Small Angles of Yaw*, Wind Engineering, 9(1), pp. 42-9.
- de Vries, O. & den Blanken, M. H. G. (1981) *Second Series of Wind-Tunnel Tests on a Model of a Two-Bladed Horizontal-Axis Wind Turbine; Influence of Turbulence on the Turbine Performance and Results of a Flow Survey Behind the Rotor*, National Aerospace Laboratory NLR The Netherlands, NLR TR 81069 L.
- Devinant, P., Laverne, T. & Hureau, J. (2002) *Experimental study of wind-turbine airfoil aerodynamics in high turbulence*, Journal of Wind Engineering and Industrial Aerodynamics, 90, pp. 689-707.
- Dodge, D. A. (2002) *Illustrated History of Wind Power*, <http://telosnet.com/wind>.
- Eaddy, M. (2005) *Lift Forces on Smooth and Rough Circular Cylinders in Low And High Turbulence Flows*, Doctoral thesis, Monash, Clayton.
- Ebert, P. R. & Wood, D. H. (1997) *The Near Wake of a Model Horizontal-Axis Wind Turbine - I. Experimental Arrangements and Initial Results*, Renewable Energy, 12(3), pp. 225-43.
- Ebert, P. R. & Wood, D. H. (1999) *The Near Wake of a Model Horizontal-Axis Wind Turbine - II. General Features of the Three-Dimensional Flow Field*, Renewable Energy, 18(4), pp. 513-34.
- Ebert, P. R. & Wood, D. H. (2001) *The near wake of a model horizontal-axis wind turbine Part 3: properties of the tip and hub vortices*, Renewable Energy, 22(4), pp. 461-72.
- ECN (Energieonderzoek Centrum Nederland) (2002) *IEA ANNEX-XIV/XVIII*, <http://www.ecn.nl/wind/other/IEA/index.en.html>, last updated 11th of November 2002.
- Eggers, A. J. & Digumarthi, R. V. (1992) *Approximate scaling of rotational effects of mean aerodynamic moments and power generated by the combined experiment rotor blades operating in deep-stalled flow*, Presented at the Eleventh ASME Wind Energy Symposium, Houston, Texas, pp. 33-43.
- Eggleston, D. M. & Starcher, K. (1990) *A Comparative Study of the Aerodynamics of Several Wind Turbines Using Flow Visualization*, Journal of Solar Energy Engineering - Transactions of the ASME, 112(4), pp. 301-9.
- Eggleston, D. M. & Stoddard, F. S. (1987) *Wind Turbine Engineering Design*, Von Nostrand Reinhold, New York.
- Elliot, D. L. & Cadogan, J. B. (1990) *Effects of Wind Shear and Turbulence on Wind Turbine Power Curves*, Presented at the European Wind Energy Conference and Exhibition, September 10-14, Madrid, Spain, pp. 79-83.
- Fage, A. & Johansen, F. C. (1928) *The Structure of Vortex Sheets*, Phil. Mag. S., 7(28), pp. 417-41.

- Fingersh, L. J., Simms, D. A., Butterfield, C. P. & Jenks, M. D. (1995) *An Overview of the Unsteady Aerodynamics Experiment Phase III Data Acquisition System and Instrumentation*, Presented at Wind Energy 1995, January 29 - February 1, Houston, Texas, pp. 277-9.
- Foussekis, D., Fraunié, P. & Béguier, C. (1992) *Steady and Unsteady Separated Flows around a Profile. Application on the Wind Turbines*, Journal of Wind Engineering and Industrial Aerodynamics, 39, pp. 41-9.
- Fugslang, P. (2002) *Aerodynamic Design Guidelines for Wind Turbine Rotors*, Presented at the 4th GRACM Congress on Computational Mechanics, 27-29 June, Patra, p. 9.
- Fugslang, P. & Bak, C. (2003) *Status of the Risø Wind Turbine Airfoils*, Presented at the European Wind Energy Conference, 16-19 June, Madrid.
- Galbraith, R. A., Coton, F. N., Saliveros, E. & Kokkodis, G. (1987) Aerofoil Scale Effects and the Relevance to Wind Turbines, In *Wind Energy Conversion 1987 - Proceedings of the 9th British Wind Energy Association Conference, Edinburgh 1-3 April 1987*, ed. Galt, J. M., Mechanical Engineering Publications Ltd., pp. 143-53.
- Gipe, P. (1995) *Wind Energy Comes of Age*, Wiley.
- Glauert, H. (1963) Airplane Propellers, In *Aerodynamic Theory - A General Review of Progress*, ed. Durand, W. F., Dover, pp. 324-41.
- Grafton, J. D. (1985) *Boeing Background Information - Wind Energy*, Boeing Aerospace Company Public Relations, A-1478, p. 8.
- Griffin, O. M. (1979) *Universal Similarity in the Wakes of Stationary and Vibrating Bluff Structures*, Presented at the Fifth International Wind Engineering Conference, Colorado State University, USA, pp. 607-17.
- Hand, M. M., Simms, D. A., Fingersh, L. J., Jager, D. W., Cotrell, J., Schreck, S. J. & Larwood, S. (2001) *Unsteady Aerodynamics Experiment Phase VI: Wind Tunnel Test Configurations and Available Data Campaigns*, NREL, TP-500-29955.
- Hansen, A. C. & Butterfield, C. P. (1993) *Aerodynamics of Horizontal-Axis Wind Turbines*, Annual Review of Fluid Mechanics, 25, pp. 115-49.
- Hansen, M. H. (2003) *Improved Modal Dynamics of Wind Turbines to Avoid Stall-induced Vibrations*, Wind Energy, 6, pp. 179-95.
- Hoerner, S. F. (1965) *Fluid-Dynamic Drag*, Published by the Author.
- Holmes, J. D. (2001) *Wind Loading of Structures*, Spon Press, pp. 46-67.
- Horner, M. B., Galbraith, R. A. M., Coton, F. N., Grant, I., Stewart, J. N. & de la Iglesia Moreno, F. (1995) *A Descriptive Model of the Flows Underlying the Impulsive Loading Produced by Blade-Vortex Interaction*, Presented at Wind Energy 1995, January 29 - February 1, Houston, Texas, pp. 175-84.
- Huang, R. F. & Lee, H. W. (1999) *Effects of Freestream Turbulence on Wing-Surface Flow and Aerodynamic Performance*, Journal of Aircraft, 36(6), pp. 965-72.
- Huyer, S. A., Simms, D. & Robinson, M. C. (1996) *Unsteady Aerodynamics Associated with a Horizontal-Axis Wind Turbine*, AIAA Journal, 34(7), pp. 1410-9.
- Ifeachor, E. C. & Jervis, B. W. (1993) *Digital Signal Processing - A practical approach*, Addison-Wesley, pp. 288-90.
- Irwin, H. P. A. H., Cooper, K. R. & Girard, R. (1979) *Correction of distortion effects caused by tubing systems in measurements of fluctuating pressures*, Journal of Wind Engineering and Industrial Aerodynamics, 5, pp. 93-107.
- Iyengar, A. K. S. & Farell, C. (2001) *Experimental Issues in Atmospheric Boundary Layer Simulations: Roughness Length and Integral Length Scale Determination*, Journal of Wind Engineering and Industrial Aerodynamics, 89, pp. 1059-80.
- Jancauskas, E. D. (1983) *The Cross-Wind Excitation of Bluff Structures and the Incident Turbulence Mechanism*, Doctoral thesis, Monash University, Clayton.
- Jeong, J. & Hussain, F. (1995) *On the identification of a vortex*, Journal of Fluid Mechanics, 285, pp. 69-94.
- Kentfield, J. A. C. (1996) *The Influence of Free-Stream Turbulence Intensity on the Performance of Gurney-Flap Equipped Wind-Turbine Blades*, Wind Engineering, 20(2), pp. 93-106.
- Knacke, M. S. T., Thiele, F., Meyer, R., Hage, W. & Bechert, D. W. (2004) *Separation Control by Self-Activated Movable Flaps*, Presented at the 42nd AIAA Aerospace Sciences Meeting and Exhibit, Reno, Nevada, USA.

- Kristensen, L. & Frandsen, S. (1982) *Model for power spectra of the blade of a wind turbine measured from the moving frame of reference*, Journal of Wind Engineering and Industrial Aerodynamics, 10, pp. 249-62.
- Leishman, J. G. (2002) *Challenges in Modelling the Unsteady Aerodynamics of Wind Turbines*, Wind Energy, 5, pp. 85-132.
- Lissaman, P. B. S. (1983) *Low-Reynolds-Number Airfoils*, Annual Review of Fluid Mechanics, 15, pp. 223-39.
- Liu, H. T. (1986) *Atmospheric Turbulence and Gust on the Performance on a Worthmann FX 63-137 Wing*, Presented at Aerodynamics at Low Reynolds Numbers, 15-18 October, London, pp. 9.1-9.25.
- Madsen, H. A. (1991) *Aerodynamics of a Horizontal-Axis Wind Turbine in Natural Conditions*, Risø National Laboratory, Roskilde, Denmark, Risø-M-2903.
- Madsen, H. A. & Christensen, H. F. (1990) *On the Relative Importance of Rotational, Unsteady and Three-Dimensional Effects on the HAWT Rotor Aerodynamics*, Wind Engineering, 14(6), pp. 405-15.
- Maltby, R. L. (1962) *Flow Visualization in Wind Tunnels Using Indicators*, NATO Advisory Group for Aeronautical Research and Development, Report Number 70.
- Marchman III, J. F., Sumantran, V. & Schaefer, C. G. (1987) *Acoustic and Turbulence Influences on Stall Hysteresis*, AIAA Journal, 25(1), pp. 50-1.
- McAlister, K. W. & Carr, L. W. (1979) *Water Tunnel Visualizations of Dynamic Stall*, Journal of Fluids Engineering - Transactions of the ASME, 101(3), pp. 376-80.
- McCroskey, W. J. (1982) *Unsteady Airfoils*, Annual Review of Fluid Mechanics, 14, pp. 285-311.
- McKeough, P. J. & Graham, J. M. R. (1980) *The Effect of Mean Loading on the Fluctuating Loads Induced on Aerofoils by a Turbulent Stream*, Aeronautical Quarterly, 31, pp. 56-69.
- Melbourne, W. H. (1993) *Turbulence and the Leading Edge Phenomenon*, Journal of Wind Engineering and Industrial Aerodynamics, 49, pp. 45-64.
- Michos, A., Bergeles, G. & Athanassiadis, N. (1983) *Aerodynamic Characteristics of NACA 0012 Airfoil in Relation to Wind Generators.*, Wind Engineering, 7(4), pp. 247-62.
- Milborrow, D. J. (1985) *Changes in aerofoil characteristics due to radial flow on rotating blades*, Presented at the 7th British Wind Energy Association Conference, 27-29 March, Oxford, pp. 85-93.
- Milborrow, D. J. (2005) *Goodbye gas and squaring up to coal*, Wind Power Monthly, 21(1), pp. 31-5.
- Miley, S. J. (1982) *A Catalog of Low Reynolds Number Airfoil Data for Wind Turbine Applications*, RFP-3387, UC-60, pp. 13-23.
- Mish, P. F. & Devenport, W. J. (2001) *Mean Loading Effects on the Surface Pressure Fluctuations on an Airfoil in Turbulence*, Presented at the 7th AIAA/CEAS Aeroacoustics Conference, 28-30 May 2001, Maastricht, The Netherlands, p. 17.
- Mouzakis, F., Morfiadakis, E. & Dellaportas, P. (1999) *Fatigue Loading Parameter Identification of a Wind Turbine Operating in Complex Terrain*, Journal of Wind Engineering and Industrial Aerodynamics, 82, pp. 69-88.
- Mueller, T. J. (1985) *The Influence of Laminar Separation and Transition on Low Reynolds Number Airfoil Hysteresis*, Journal of Aircraft, 22(9), pp. 763-70.
- Mueller, T. J. & Batill, S. M. (1980) *Experimental Studies of the Laminar Separation Bubble on a Two-Dimensional Airfoil at Low Reynolds Numbers*, Presented at the AIAA 13th Fluid and Plasma Dynamics Conference, July 14-16, Snowmass, Colorado, pp. 1-12.
- Nakamura, Y. (1996) *Vortex Shedding from Bluff Bodies and a Universal Strouhal Number*, Journal of Fluids and Structures, 10, pp. 159-71.
- Neff, D. E. & Meroney, R. N. (1985) *Measurement in a Wind Tunnel of the Modification of Mean Wind and Turbulence Characteristics Due to Induction Effects Near Wind Turbine Rotors*, Fluid Mechanics and Wind Engineering Program, Department of Civil Engineering, Colorado State University, CER85-86DEN-RNM10.
- Newland, D. E. (1993) *An introduction to random vibrations, spectral and wavelet analysis*, Longman, pp. 21-3.
- Oak Creek Energy (2002) *Oak Creek Energy Systems Main Page*, <http://www.oakcreekenergy.com>, last updated 1st of March, 2002.

- Paulsen, U. S. (1989) *Aerodynamics of a Full-Scale Non Rotating Wind Turbine Blade Under Natural Wind Conditions*, Presented at EWEC '89. European Wind Energy Conference and Exhibition, 10-13 July, Glasgow, pp. 172-7.
- Pederson, T. F. & Antoniou, I. (1989) *Visualisation of Flow Through a Stall-Regulated Wind Turbine Rotor*, Wind Engineering, 13(5), pp. 239-51.
- Pederson, T. F. & Madsen, H. A. (1998) *Location of Flow Separation on an 11m Wind Turbine Blade by Means of Flow Visualization and a Two Dimensional Airfoil Code*, Presented at The 10th British Wind Engineering Conference, Mar 23-35, pp. 155-62.
- Pohlen, L. J. & Mueller, T. J. (1984) *Boundary Layer Characteristics of the Miley Airfoil at Low Reynolds Numbers*, Journal of Aircraft, 21(9), pp. 658-64.
- Raghunathan, S., Harrison, J. R. & Hawkins, B. D. (1988) *Thick Airfoil at Low Reynolds Number and High Incidence*, Journal of Aircraft, 25(7), pp. 669-71.
- Reuss Ramsay, R., Hoffman, M. J. & Gregorek, G. M. (1995) *Effects of Grit Roughness and Pitch Oscillations on the S809 Airfoil*, NREL, TP-442-7817.
- Robinson, M. C., Hand, M. M., Simms, D. A. & Schreck, S. J. (1999) *Horizontal Axis Wind Turbine Aerodynamics: Three-Dimensional, Unsteady, and Separated Flow Influences*, NREL - National Renewable Energy Laboratory, NREL/CP-500-25337.
- Robison, D. J., Coton, F. N., Galbraith, R. A. & Vezza, M. (1995) *Application of a Prescribed Wake Aerodynamic Prediction Scheme to Horizontal Axis Wind Turbines in Axial Flow*, Wind Engineering, 19, pp. 41-51.
- Ronsten, G. (1992) *Static Pressure Measurements on a Rotating and a Non-rotating 2.375 m Wind Turbine Blade. Comparison with 2D Calculations*, Journal of Wind Engineering and Industrial Aerodynamics, 39, pp. 105-18.
- Roshko, A. (1955) *On the wake and drag of bluff bodies*, Journal of the Aeronautical Sciences, 22, pp. 124-32.
- Roshko, A. (1993) *Perspectives on Bluff Body Aerodynamics*, Journal of Wind Engineering and Industrial Aerodynamics, 49, pp. 79-100.
- Rung, T., Bunge, U., Schatz, M. & Thiele, F. (2003) *Restatement of the Spalart-Allmaras Eddy-Viscosity Model in Strain-Adaptive Formulation*, AIAA Journal, 41(7), pp. 1396-9.
- Sacre, C., Flori, J. P. & Duchene-Marullaz, P. (1987) *Preliminary Study of Turbulence in Complex Terrain for Wind Turbine Setting Up*, Presented at the Second Contractors' Meeting, 23-24 November, Brussels, pp. 187-92.
- Saxena, L. S., Fejer, A. A. & Morkovin, M. V. (1978) *Effects of Periodic Changes in Free Stream Velocity on Flows Over Airfoils Near Static Stall*, Presented at Nonsteady Fluid Dynamics, Proceedings of the ASME Winter Meeting, December, San Francisco, CA, pp. 111-6.
- Schepers, J. G., Brand, A. J., Bruining, A., Graham, J. M. R., Hand, M. M., Ingfield, D. G., Madsen, H. A., Maeda, T., Paynter, J. H., van Rooij, R., Shimizu, Y., Simms, D. A. & Stefanatos, N. (2002) *Final Report of IEA Annex XVIII: Enhanced Field Rotor Aerodynamics Database*, ECN, ECN-C--02-016.
- Schepers, J. G., Brand, A. J., Bruining, A., Graham, J. M. R., Hand, M. M., Ingfield, D. G., Madsen, H. A., Paynter, R. J. H. & Simms, D. A. (1997) *Final Report of IEA Annex XIV: Field Rotor Aerodynamics*, International Energy Agency.
- Schewe, G. (2001) *Reynolds-number effects in flow around more-or-less bluff bodies*, Journal of Wind Engineering and Industrial Aerodynamics, 89, pp. 1267-89.
- Schlichting, H. (1979) *Boundary Layer Theory*, McGraw-Hill, pp. 695-6.
- Schreck, S. J. (2000) *Unsteady Aerodynamics Experiment Wind Tunnel Testing and Data Acquisition*, Presented at the Furling Workshop, July 14-15, National Wind Technology Centre, NREL, Golden, Colorado.
- Schreck, S. J. (2002a) *The NREL Full-Scale Wind Tunnel Experiment - Introduction to the Special Issue*, Wind Energy, 5, pp. 77-84.
- Schreck, S. J. (2002b) *Personal Communication*, NREL.
- Schreck, S. J. (2005) *Personal Communication*.
- Schreck, S. J. & Helin, H. E. (1994) *Unsteady Vortex Dynamics and Surface Pressure Topologies on a Finite Pitching Wing*, Journal of Aircraft, 31(4), pp. 899-907.
- Schreck, S. J. & Robinson, M. (2002) *Rotational Augmentation of Horizontal Axis Wind Turbine Blade Aerodynamic Response*, Wind Energy, 5, pp. 133-50.

- Schreck, S. J. & Robinson, M. C. (2005) *Unsteadiness in HAWT Blade Aerodynamic Force and Flow Field Structures During Rotational Augmentation*, Presented at the ASME Wind Energy Symposium at the 42nd AIAA Aerospace Sciences Meeting and Exhibit, 10-13 January, 2005, Reno, Nevada, pp. 278-88.
- Schreck, S. J., Robinson, M. C., Hand, M. M. & Simms, D. A. (2000) *HAWT Dynamic Stall Response Asymmetries Under Yawed Flow Conditions*, National Renewable Energy Laboratory, NREL/CP-500-27898.
- Schreck, S. J., Robinson, M. C., Hand, M. M. & Simms, D. A. (2001) *Contrasting Blade Flow Field Archetypes in the HAWT Operating Regime*, AIAA, AIAA 2001-0036.
- Sheldahl, R. E. & Klimas, P. C. (1981) *Aerodynamic Characteristics of Seven Symmetrical Airfoil Sections Through 180-Degree Angle of Attack for Use in Aerodynamic Analysis of Vertical Axis Wind Turbines*, Sandia National Laboratories, SAND80-2114.
- Shiple, D. E., Miller, M. S. & Robinson, M. C. (1995) *Dynamic Stall Occurrence on a Horizontal Axis Wind Turbine Blade*, Presented at Wind Energy 1995, January 29 - February 1, Houston, Texas, pp. 167-73.
- Simms, D. A., Hand, M. M., Fingersh, L. J. & Jager, D. W. (1999a) *Unsteady Aerodynamics Experiment Phases II-IV Test Configurations and Available Data Campaigns*, National Renewable Energy Laboratory, NREL/TP-500-25950.
- Simms, D. A., Schreck, S., Hand, M., Fingersh, L., Cotrell, J., Pierce, K. & Robinson, M. (1999b) *Plans for Testing the NREL Unsteady Aerodynamics Experiment 10-m Diameter HAWT in the NASA Ames Wind Tunnel*, National Renewable Energy Laboratory, NREL/TP-500-27599.
- Simms, D. A., Schreck, S. J., Hand, M. M. & Fingersh, L. J. (2001) *NREL Unsteady Aerodynamics Experiment in the NASA-Ames Wind Tunnel: A Comparison of Predictions to Measurements*, NREL, NREL/TP-500-29494, p. 51.
- Smith, G. H., Grant, I., Liu, A., Infield, D. & Eich, T. (1991) *The Wind Tunnel Application of Particle Image Velocimetry to the Measurement of Flow Over a Wind Turbine*, Wind Engineering, 15(6), pp. 301-17.
- Snel, H. & Schepers, J. G. (1992) *Engineering Models for Dynamic Inflow Phenomena*, Journal of Wind Engineering and Industrial Aerodynamics, 39(1-3), pp. 267-81.
- Somers, D. M. (1989) *Design and Experimental Results for the S809 Airfoil*, National Renewable Energy Laboratory, NREL/SR-440-6918.
- Somers, D. M. (1992) Subsonic Natural-Laminar-Flow Airfoils, In *Natural Laminar Flow and Laminar Flow Control*, ed. Barnwell, R. W. and Hussaini, M. Y., Springer-Verlag, pp. 143-76.
- Somers, D. M. & Tangler, J. L. (1996) *Wind Tunnel Test of the S814 Thick Root Airfoil*, Journal of Solar Energy Engineering - Transactions of the ASME, 118, pp. 217-21.
- Stack, J. (1931) *Tests in the Variable Density Wind Tunnel to Investigate the Effects of Scale and Turbulence on Airfoil Characteristics*, NACA Langley Memorial Aeronautical Laboratory, NACA-TN-364.
- Stansby, P. K. (1974) *The effects of end plates on the base pressure coefficient of a circular cylinder*, Aeronautical Journal, 78, pp. 36-7.
- Swalwell, K. E., Sheridan, J. & Melbourne, W. H. (2003a) *The Effect of Turbulence Scale and Intensity on Stall of a NACA 4421 Airfoil*, Presented at the 11th International Conference of Wind Engineering, June 2-5, Lubbock, Texas.
- Swalwell, K. E., Sheridan, J. & Melbourne, W. H. (2003b) *Frequency Analysis of Surface Pressures on an Airfoil after Stall*, Presented at the 21st AIAA Applied Aerodynamics Conference, Orlando, Florida, p. 4.
- Swalwell, K. E., Sheridan, J. & Melbourne, W. H. (2004) *The Effect of Turbulence Intensity on Performance of a NACA 4421 Airfoil Section*, Presented at the AIAA/ASME Wind Energy Symposium, January 5-8, Reno, Nevada, p. 10.
- Szepessy, S. & Bearman, P. W. (1992) *Aspect Ratio and End Plate Effects on Vortex Shedding from a Circular Cylinder*, Journal of Fluid Mechanics, 234, pp. 191-217.
- Tangler, J. L. (1999) *Effects of Airfoil Thickness and Maximum Lift on Roughness Sensitivity*, Presented at the Third ASME-JSME Joint Fluid Engineering Conference, July 18-23, San Francisco, CA, p. 4.

- Tangler, J. L. (2000) *The Evolution of Rotor and Blade Design*, Presented at WindPower 2000, American Wind Energy Association, April 30 - May 4, Palm Springs, California, p. 10.
- Tangler, J. L. (2002) *The Nebulous Art of Using Wind Tunnel Aerofoil Data for Predicting Rotor Performance*, *Wind Energy*, 5, pp. 245-57.
- Tangler, J. L. & Somers, D. M. (1995) *NREL Airfoil Families for HAWTs*, National Renewable Energy Laboratory, NREL/TP-442-7109.
- Taylor, G. I. (1963) The 'Rotational Inflow Factor' in Propeller Theory, In *The Scientific Papers of Sir Geoffrey Ingram Taylor*, ed. Batchelor, G. K., Cambridge University Press, pp. 59-65.
- Taylor, G. L. (1987) *Wake Measurements on the Nibe Wind Turbines in Denmark - Part 2: Data Collection and Analysis*, Presented at the Second Contractors' Meeting, 23-24 November, Brussels, pp. 165-76.
- Thiele, F., Mockett, C. & Bunge, U. (2004) *Personal Communication*, Hermann-Föttinger-Institute of Fluid Mechanics, Technical University of Berlin, Sekr. HF1, Strasse des 17. Juni 135, D-10623 Berlin, Germany.
- Vestas (2003) *V80 - 2.0MW*, Vestas Wind Systems A/S.
- Wagner, S. (1987) *Dynamic and Aeroelastic Response of Wind Energy Converter to Dynamic Loads*, Presented at Second Contractors' Meeting, 23-24 November, Brussels, pp. 95-107.
- Watkins, S., Saunders, J. E. & Hoffman, P. H. (1995) *Turbulence experienced by moving vehicles. Part I. Introduction and turbulence intensity*, *Journal of Wind Engineering and Industrial Aerodynamics*, 57, pp. 1-17.
- Weinman, K. (2004) *Personal Communication*, DLR-Braunschweig, Institut für Aerodynamik und Strömungstechnik.
- White, F. M. (1999) *Fluid Mechanics*, McGraw-Hill.
- Wilcox, D. C. (1998) *Turbulence modelling for CFD*, DCW industries.
- Winkelmann, A. E. (1982) *An Experimental Study of Mushroom Shaped Stall Cells*, Presented at the AIAA/ASME 3rd Joint Thermophysics, Fluids, Plasma and Heat Transfer Conference, St. Louis, Missouri.
- Winkelmann, A. E. & Barlow, J. B. (1980) *Flowfield Model for a Rectangular Planform Wing beyond Stall*, *AIAA Journal*, 18(8), pp. 1006-8.
- Wood, D. H. (1987) *Some Effects of Finite Solidity on the Aerodynamics of Horizontal-Axis Wind Turbines*, *Journal of Wind Engineering and Industrial Aerodynamics*, 26, pp. 255-73.
- Wood, D. H. (1991) *A Three-Dimensional Analysis of Stall-Delay on a Horizontal-Axis Wind Turbine*, *Journal of Wind Engineering and Industrial Aerodynamics*, 37, pp. 1-14.
- Yoshida, A., Kurita, T. & Tamura, Y. (2000) *Effects of Tubing System with a Bent Pipe for Wind Pressure Measurement*, Presented at the Fourth International Colloquium on Bluff Body Aerodynamics and Applications, Ruhr-Universität, Bochum, Germany, pp. 91-4.
- Young, W. C. (1989) *Roark's Formulas for Stress and Strain*, McGraw-Hill Book Company.
- Zdravkovich, M. M. (1997) *Flow Around Circular Cylinders*, Oxford University Press, pp. 431-57.
- Zell, P. T. (1993) *Performance and Test Section Flow Characteristics of the National Full-Scale Aerodynamic Complex 80- by 120-Foot Wind Tunnel*, NASA Technical Memorandum 103920.

Appendix A

Blade Element Momentum Method

A.1 Betz Limit

Before going on to the Blade Element Momentum (BEM) method, it is worthwhile to consider the simple one-dimensional actuator disk model that Betz used in order to derive the maximum performance of a wind turbine.

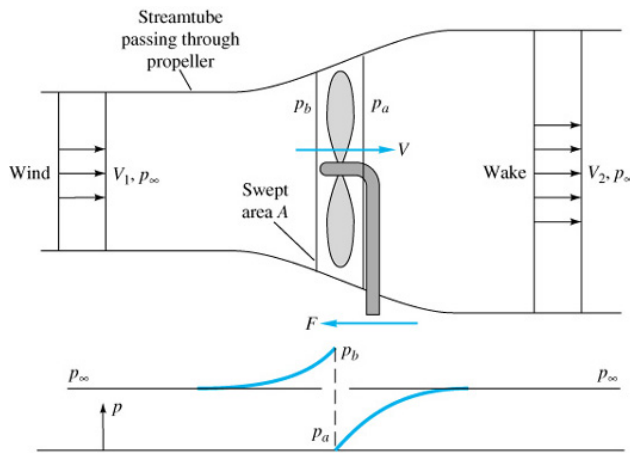


Figure 1– Diagram of the one-dimensional actuator disk model of a wind turbine, from White (1999).

The force on the rotor can be expressed in terms of the velocity drop over the blades,

$$-F = \dot{m}(V_2 - V_1) = \rho AV(V_2 - V_1), \quad \text{Equation 1}$$

or the pressure drop over the blades,

$$-F = (p_a - p_b)A. \quad \text{Equation 2}$$

Combining these two expressions of the force gives the pressure drop across the blades in terms of the velocities,

$$p_b - p_a = \rho V(V_1 - V_2). \quad \text{Equation 3}$$

Applying Bernoulli's equation from far upstream to just before the rotor gives

$$p_\infty + \frac{1}{2}\rho V_1^2 = p_b + \frac{1}{2}\rho V^2, \quad \text{Equation 4}$$

and from just behind the rotor gives

$$p_a + \frac{1}{2}\rho V^2 = p_\infty + \frac{1}{2}\rho V_2^2. \quad \text{Equation 5}$$

Combining these two equations gives

$$p_b - p_a = \frac{1}{2}\rho(V_1^2 - V_2^2). \quad \text{Equation 6}$$

Combining the pressure drop from conservation of mass (Equation 3) and the pressure drop from Bernoulli's equation (Equation 6) gives

$$V = \frac{1}{2}(V_1 - V_2) . \tag{Equation 7}$$

A common representation is that wind at the rotor is slowed by an axial induction factor, a , so the wind at the rotor plane is represented as

$$V = (1 - a)V_1 . \tag{Equation 8}$$

Combining this with Equation 7 gives

$$V_2 = (1 - 2a)V_1 . \tag{Equation 9}$$

Combining the above expression with the earlier expression for the force on the rotor (Equation 1) gives the following for the power (P)

$$P = FV = \rho AV^2 (V_1 - V_2) = 2\rho Aa(1 - a)^2 V_1^3 . \tag{Equation 10}$$

As the power available is

$$P_{available} = \frac{1}{2} \dot{m} V_1^2 = \frac{1}{2} \rho A V_1^3 , \tag{Equation 11}$$

$$C_P = \frac{P}{P_{available}} = 4a(1 - a)^2 , \tag{Equation 12}$$

$$\frac{dC_P}{da} = 4(1 - a)(1 - 3a) . \tag{Equation 13}$$

The only physically possible maximum occurs when $a = 1/3$, which gives the maximum power coefficient possible from a wind turbine as $C_P=16/27$, which is known as the Betz number or Betz limit.

A.2 Blade Element Momentum (BEM) Method

The BEM method divides the flow around the rotor into concentric streamtubes as shown in Figure 1(a). It assumes that each streamtube is independent and that the forces from the blades within each streamtube are constant (which corresponds to a rotor with an infinite number of blades).

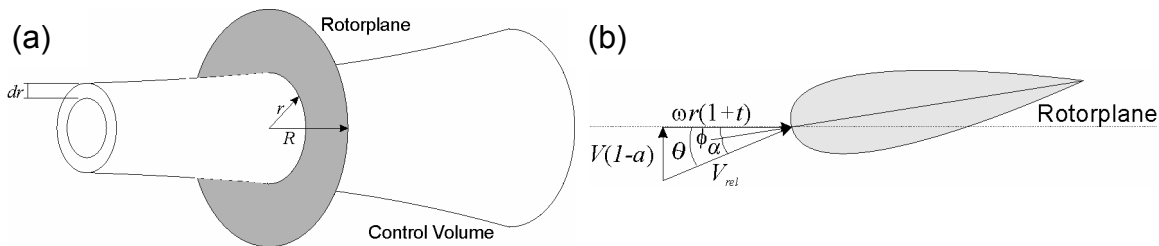


Figure 2 - Streamtubes (a) and a blade element (b).

The actuator disk model used to derive the Betz number assumes there is no rotation in the wake. Of course in a real turbine there is rotation in the wake. A blade element will see a component due to the wind which is slowed by the axial induction factor, a , and a component due rotation which is increased by wake rotation represented by an axial induction factor, t , as shown in Figure 2(b). The

simple trends of increasing α with increasing windspeed and that the α will increase quickest near the hub of the rotor can be seen from this figure. The rotational speed in the wake, V_θ , is defined as

$$V_\theta = 2t\omega r, \quad \text{Equation 14}$$

and from Figure 2(b) the flow angle is

$$\theta = \alpha + \phi = \text{atan}\left(\frac{V(1-a)}{\omega r(1+t)}\right), \quad \text{Equation 15}$$

and relative velocity

$$V_{rel} = \frac{V(1-a)}{\sin\phi} = \frac{\omega r(1+t)}{\cos\phi}. \quad \text{Equation 16}$$

Similarly to the 1D model, see Equation 1, the force on the element, dF , will be

$$-dF = \dot{m}(V_2 - V_1) = \rho 2\pi r V (V_2 - V_1) dr, \quad \text{Equation 17}$$

where $2\pi r dr$ is the cross sectional area of the control volume at the rotor plane. The torque on the annular element, dM , is found using the integral moment of momentum equation on the control volume giving

$$dM = \dot{m} r V_\theta = \rho 2\pi r^2 V V_\theta dr. \quad \text{Equation 18}$$

Using the definition of the axial and tangential induction factors, Equation 8 and Equation 14 respectively, and assuming that Equation 8 is still valid for the case with rotation in the wake, the force and torque can be rewritten in terms of the axial induction factor.

$$dF = 4\rho\pi r V_1^2 (1-a) dr, \quad \text{Equation 19}$$

$$dM = 4\rho\pi r^3 t V \omega (1-a) t dr. \quad \text{Equation 20}$$

If the lift and drag coefficients are known at a particular α , the lift and drag can be derived

$$L = \frac{1}{2} \rho V_{rel}^2 c C_l, \quad \text{Equation 21}$$

$$D = \frac{1}{2} \rho V_{rel}^2 c C_d. \quad \text{Equation 22}$$

The force normal and tangential to the rotor plane is therefore

$$F_N = L \cos\phi + D \sin\phi, \quad \text{Equation 23}$$

$$F_T = L \sin\phi - D \cos\phi. \quad \text{Equation 24}$$

Creating normal and tangential coefficients

$$C_n = \frac{F_N}{\frac{1}{2} \rho V_{rel}^2 c} = C_l \cos\phi + C_d \sin\phi, \quad \text{Equation 25}$$

$$C_t = \frac{F_T}{\frac{1}{2} \rho V_{rel}^2 c} = C_l \sin\phi - C_d \cos\phi. \quad \text{Equation 26}$$

As these are forces per unit length

$$dF = B F_N dr, \quad \text{Equation 27}$$

$$dM = r B F_T dr. \quad \text{Equation 28}$$

Combining these equations with the definitions of the normal and tangential force and Equation 16 for the relative velocity (choosing the definitions that best match those in the earlier definition of normal and tangential force) gives

$$dF = \frac{1}{2} \rho B \frac{V_1^2 (1-a)^2}{\sin^2 \phi} c C_n dr, \quad \text{Equation 29}$$

$$dM = \frac{1}{2} \rho \frac{V_1 (1-a) r \omega (1+t)}{\sin \phi \cos \phi} c C_t r dr. \quad \text{Equation 30}$$

Equating Equation 19 and Equation 29 gives the following expression for the axial induction factor

$$a = \frac{1}{\frac{4 \sin^2 \phi}{\sigma C_n} + 1}, \quad \text{Equation 31}$$

where σ is the local solidity ($\sigma = cB/2\pi r$), the fraction of the annular area covered by the blades. Similarly equating Equation 20 and Equation 30 gives the following expression for the tangential induction factor

$$t = \frac{1}{\frac{4 \sin \phi \cos \phi}{\sigma C_t} - 1}. \quad \text{Equation 32}$$

As the lift and drag coefficients are included in these definitions of a and t and these coefficients are determined by α which is also determined by a and t it is necessary to use an iterative process. Before the steps in the calculation are outlined, the two most important empirical modifications, which need to be incorporated into the method, will be discussed.

A.2.1 Prandtl's Tip Loss Factor

Assuming a lightly loaded rotor, the expansion of the wake behind a wind turbine can be neglected and the trailing vortex sheets from the blades modelled as a regular screw surface, as shown in Figure 3(a). For a finite number of blades there would be gaps between these sheets. Near the slipstream boundary, air would tend to flow around the edges of the vortex sheets. Prandtl modelled these sheets as a system of parallel lines, as shown in Figure 3(b), and calculated the loss caused by the flow around the sheets as described by Glauert (1963).

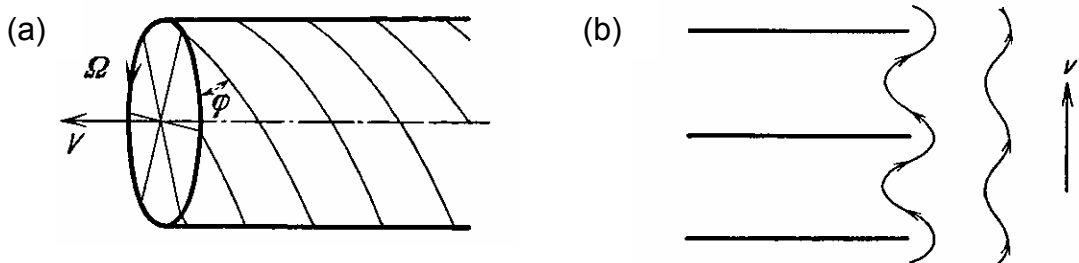


Figure 3 - Vortex sheets forming a screw surface (a) and Prandtl's parallel lines model of this (b). From Glauert (1963).

This lead to the derivation of Prandtl's tip loss factor, which is defined as

$$F = \frac{2}{\pi} \arccos(e^{-f}), \quad \text{Equation 33}$$

$$f = \frac{B}{2} \frac{R-r}{r \sin(\phi)}. \quad \text{Equation 34}$$

The definition of normal and tangential force from the integral momentum and moment of momentum equations respectively, Equation 19 and Equation 20, should be multiplied by this factor to estimate the effect of a finite number of blades. As this factor is carried through the calculations the equations for the axial and tangential induction factors become

$$a = \frac{1}{\frac{4F \sin^2 \phi}{\sigma C_n} + 1}, \quad \text{Equation 35}$$

$$t = \frac{1}{\frac{4F \sin \phi \cos \phi}{\sigma C_t} - 1}. \quad \text{Equation 36}$$

A.2.2 Glauert Correction

The momentum theory breaks down for $a \geq 0.5$ as this implies, from Equation 9, that the wake is either stopped or flowing back toward the rotor. The wake states that occur for a rotor are shown in Figure 4, wind turbines operate in regions II and III.

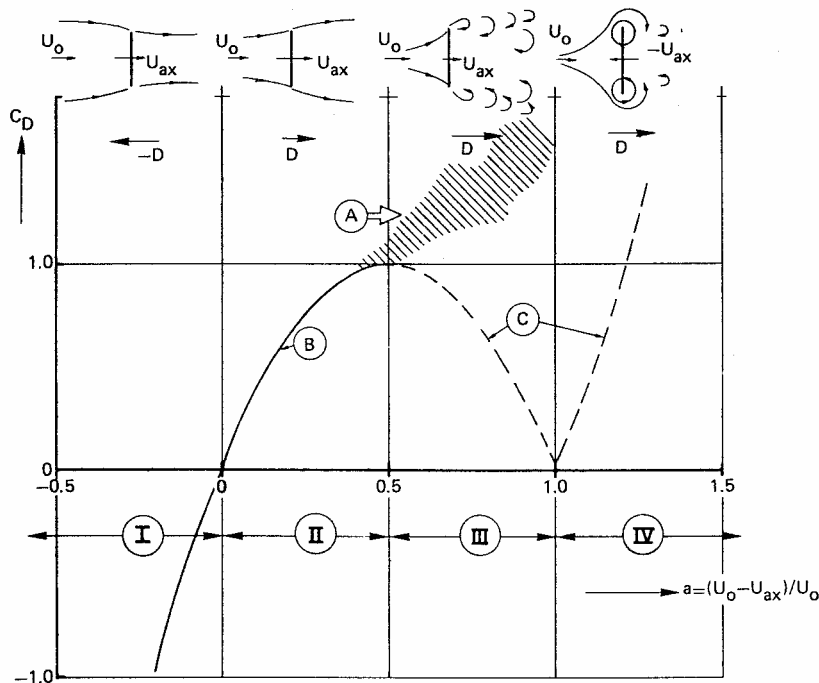


Figure 4 - Wake states characterised by a and the coefficient of rotor drag C_D . I propeller state, II windmill state, III turbulent wake state, IV vortex ring state. A indicates data from helicopters, the solid line indicated by B shows regions where the momentum theory is valid and the dashed line indicated by C shows where it is invalid. Figure from De Vries (1983).

The thrust coefficient (in De Vries figure noted C_D) was matched by Glauert to the following equations

$$C_F = \begin{cases} 4a(1-a)F & a \leq \frac{1}{3} \\ 4a(1 - \frac{1}{4}(5-3a)a)F & a \geq \frac{1}{3} \end{cases}. \quad \text{Equation 37}$$

Another fit provided for Danish certification of wind turbines and quoted by Hansen (1998) is

$$C_F = \begin{cases} 4a(1-a)F & a \leq a_c \\ 4(a_c^2 + (1-2a_c)a)F & a \geq a_c \end{cases}, \quad \text{Equation 38}$$

where a_c is approximately 0.2. Using this fit, the definition of C_F for an angular control volume

$$C_F = \frac{dF}{\frac{1}{2} \rho V_1^2 2\pi r dr}, \quad \text{Equation 39}$$

and the earlier derivation of normal force (Equation 29) the earlier result is obtained for $a \leq a_c$ but for $a \geq a_c$ the equation becomes

$$a = \frac{1}{2} \left[2 + K(1-2a_c) - \sqrt{(K(1-2a_c)+2)^2 + 4(Ka_c^2 - 1)} \right] \text{ where } K = \frac{4F \sin^2 \phi}{\sigma C_n}. \quad \text{Equation 40}$$

A.2.3 Calculation sequence

The calculation for a given turbine design, for a given rotational speed at each windspeed and at each location along the blade follows the following steps.

1. Initialise the axial and tangential induction factors ($a_{initial}=t_{initial}=0$).
2. Calculate the flow angle using these factors in Equation 15 $\left(\theta = \text{atan} \left(\frac{V(1-a)}{\omega r(1+t)} \right) \right)$.
3. Use the known pitch of the blade at this radius (ϕ) and the flow angle from the previous step to compute the angle of attack on the blade segment ($\alpha = \theta - \phi$).
4. Look up the coefficient of lift and drag at this α from the known performance of this aerofoil section.
5. Calculate the normal and tangential force from these coefficients as in Equation 25 and Equation 26 ($C_n = C_l \cos \phi + C_d \sin \phi$ and $C_t = C_l \sin \phi - C_d \cos \phi$).
6. Calculate the tip loss factor from Equation 33 and Equation 34 $\left(F = \frac{2}{\pi} \arccos(e^f) \right)$ where $f = \frac{B}{2} \frac{R-r}{r \sin(\phi)}$.
7. Calculate $K = \frac{4F \sin^2 \phi}{\sigma C_n}$. If $a_{initial} < a_c$, where a_c is usually taken as 0.2, use Equation 35 to calculate $a_{new} \left(a_{new} = \frac{1}{K+1} \right)$ otherwise use Equation 40 $\left(a_{new} = \frac{1}{2} \left[2 + K(1-2a_c) - \sqrt{(K(1-2a_c)+2)^2 + 4(Ka_c^2 - 1)} \right] \right)$.
8. Calculate a new value for the tangential induction factor from Equation 36 $\left(t_{new} = \frac{1}{\frac{4F \sin \phi \cos \phi}{\sigma C_t} - 1} \right)$.

9. If the absolute value of $a_{initial}-a_{new}$ or $t_{initial}-t_{new}$ is greater than the nominated tolerance, repeat from step 2 using the new values of a and t as the initial values.
10. Calculate the tangential force at this radius, using Equation 26 and Equation 16 for the velocity at the rotor, from the tangential force coefficient calculated in step 5

$$\left(F_T = \frac{1}{2} \rho \left(\frac{V(1-a)}{\sin\phi} \right)^2 c C_t \right).$$

11. Repeat from step 1 for the next radius until the tangential force at each radius has been calculated.
12. Assuming that there is a linear relationship between the tangential forces at each radius the tangential force on each section, dr can be calculated.

$$\left(F_T = m_i r + c_i \text{ where } m_i = \frac{F_{T,i+1} - F_{T,i}}{r_{i+1} - r_i} \text{ and } c_i = \frac{F_{T,i} r_{i+1} - F_{T,i+1} r_i}{r_{i+1} - r_i} \right)$$

13. Using Equation 28, an expression for the moment from each section can be developed

$$\left(dM = r B F_T dr = B (m_i r^2 + c_i r) dr, \text{ ignoring the number of blades as this is the same for all sections } M_{i,i+1} = \left[\frac{1}{3} m_i r^3 + \frac{1}{2} c_i r^2 \right] = \frac{1}{3} m_i (r_{i+1}^3 - r_i^3) + \frac{1}{2} m_i (r_{i+1}^2 - r_i^2), \text{ and therefore the total shaft torque from the blades is } M_{total} = B \sum_1^{N-1} M_{i,i+1} \right).$$

14. Repeating from step 1 for the next windspeed until the shaft torque from the blades is known across the range of windspeeds of operation.

The above steps can be expanded to give more aerodynamic forces to help in the structural design but the features for predicting the power curve have been outlined. Other corrections can also be added to attempt to improve predictions.

A.3 References

- de Vries, O. (1983) *On the Theory of the Horizontal-Axis Wind Turbine*, Annual Review of Fluid Mechanics, 15, pp. 77-96.
- Glauert, H. (1963) Airplane Propellers, In *Aerodynamic Theory - A General Review of Progress*, ed. Durand, W. F., Dover, pp. 324-41.
- Hansen, M. O. (1998) *Wind Turbine Technology and Aerodynamics Course Notes*, Fluid Mechanics Section, Department of Energy Engineering, Technical University of Denmark (DTU), p. 128.
- White, F. M. (1999) *Fluid Mechanics*, McGraw-Hill, p. 826.

Appendix B

Notes on Modelling Dynamic Stall

CFD models of this unsteady, separated flow are not yet practical. Many experimental studies have been done on pitching aerofoils, with less on other types of motion. This data has been used to develop semi-empirical models for helicopters, some of which have been adapted for wind turbine use (Leishman (2002) provides a review of some of these models). There are many semi-empirical dynamic stall models. The Beddoes-Leishman model for predicting the effect of dynamic stall on helicopters has been adapted to wind turbines (Simms *et al.*, 1999). Yeznasni, Derdelinckx and Hirsch (1992) compared five semi-empirical dynamic stall models to measurements from two HAWTs in the field (an 8.5 kW and 500 kW).

- The Boeing–Vertol method that is based on aerofoils oscillating in pitch.
- The Strickland method that is once again based on aerofoils oscillating in pitch but also assumes that there is no change in performance below the static stall angle.
- The Machielse model is a similar empirical formula to the first two.
- The Favier method that is based on cyclic changes in the angle of attack and also requires the reduced frequency and magnitude.
- The ONERA method that uses differential equations to simulate the time history of flows and is based on measurements on the OA family of airfoils used in helicopters at high speed.

Yeznasni *et al.* (1992) found that the Machielse, Strickland and ONERA methods provided the worst overestimates of torque for the 8.5 kW turbine and that the Boeing-Vertol and Favier methods slightly underestimated torque, although not as badly as the BEM method without correction. The ONERA method provided the best match for the 500 kW turbine, although it showed some features that were not observed on the turbine, while all other methods underestimated both power and flap moment. They attributed the better performance of the ONERA method in the second case to the aerofoils being more like the OA family. These results show that the corrections, while they can improve prediction, must be treated with caution and that their performance on one type of turbine should not be taken as an indication of how well they will perform on another type.

Similar results were found by Chen & Dexin (1999) who used a dynamic stall model based on a two-dimensional form of the Navier-Stokes equations. They found that the corrections improved predictions slightly in all cases but did not match experimental measurements at low tip speed ratios or at high yaw errors.

'Engineering models' (either BEM models with corrections for dynamic inflow or vortex wake methods) currently give the highest predictive confidence levels for design purposes (Leishman, 2002). Empirical subcomponent models for various effects such as dynamic stall are included but these subcomponents must be validated. The coupling of the subcomponents can also be important as, in some cases, different coupling schemes can give different results.

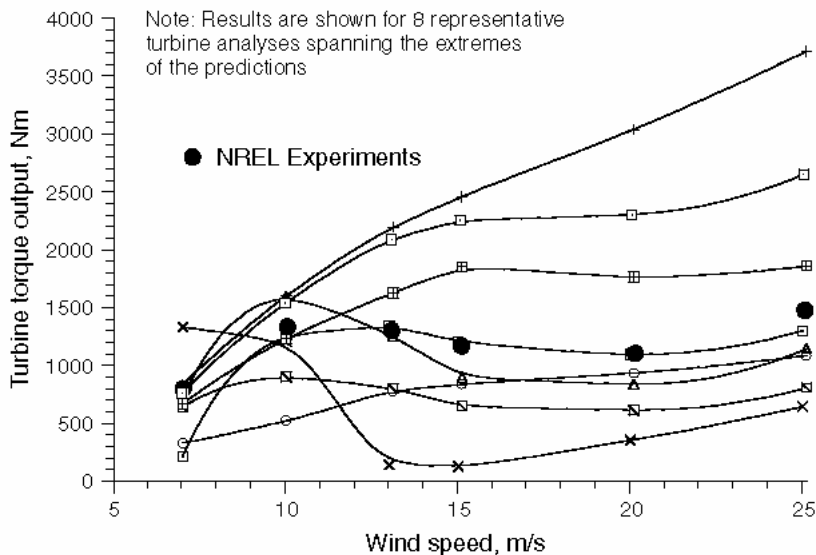


Figure B-1 - Representative 'blind' predictions compared to measurements on the NREL 10m diameter turbine in the NASA Ames wind tunnel. From Leishman (2002).

Results of the NREL blind comparison were extremely mixed, even for unyawed, unstalled operating conditions. The predictions of torque shown in Figure B-1 ranged from a 60% under-prediction to a 150% over-prediction. Most models did not predict net power output well (ranging from a 50% under-prediction to a 200% over-prediction) for the turbine operating under dynamic stall conditions and were particularly bad at predicting the amplitude and phasing of blade loads. Some models predicted dynamic stall onset where there was none or did not predict dynamic stall where the experimental measurements suggested there were extensive regions of stall over the rotor.

Wind turbines can be more subject to flow perturbations than other rotating machinery because of their relatively low rotational velocity (about 1s per rotor revolution) thereby allowing changes in windspeed to cause larger changes in α at the blade elements. Yaw adds to these fluctuations by adding a motion into and out of the wind. The fluctuations can exceed the limits of unsteady aerodynamic models based on the assumption of small perturbations.

The type of motion to be modelled should also be considered carefully. For instance tower shadow is often modelled as resulting in a change of α whereas it should be modelled as a change in velocity field. This can result in an underprediction of the drop in lift (Leishman, 2002). For cases

where there are combinations of different types of motion, the aerodynamic component from each type of motion must be considered separately and combined through superposition.

Three-dimensional effects that are not usually accounted for in these dynamic stall models as they are usually derived from two-dimensional data. However, for dynamic stall on a wind turbine it is unlikely the entire blade is at the same angle of attack. Also, since the finite span of the blade produces a tip vortex, steady state tests suggest that this dominates the flow at the tip and so dynamic stall is unlikely to occur. The effect of rotation of the boundary layer is not considered. Finally, coning of the blades is equivalent to the sweep of a non-rotating wing. Sweep is known to affect the lift near stall, and while the effects for the likely coning angles of wind turbines are small, they do tend to increase lift and delay separation and could affect the dynamic stalling of the wing.

Possible improvements to dynamic stall models include modelling the three-dimensional effect mentioned in the last paragraph and obtaining and using aerofoil data from more typical aerofoils for wind turbine applications (many models have been derived on the basis of thin helicopter rotor aerofoils) and more typical motions.

References

- Chen, W. & Dexin, H. (1999) A dynamic stall model for HAWT performance prediction in yawed flow, In *Wind Engineering into the 21st Century*, ed. Larsen, A., Larose, G. L. & Livesey, F. M., Balkema, pp. 1973-7.
- Leishman, J. G. (2002) *Challenges in Modelling the Unsteady Aerodynamics of Wind Turbines*, *Wind Energy*, 5, pp. 85-132.
- Simms, D. A., Hand, M. M., Fingersh, L. J. & Jager, D. W. (1999) *Unsteady Aerodynamics Experiment Phases II-IV Test Configurations and Available Data Campaigns*, National Renewable Energy Laboratory, NREL/TP-500-25950, p. 117.
- Yeznasni, A., Derdelinckx, R. & Hirsch, C. (1992) *Influence of Dynamic Stall in the Aerodynamic Study of HAWTs*, *Journal of Wind Engineering and Industrial Aerodynamics*, 39, pp. 187-98.